

**Dinitrogen Adsorption and Activation
on Pure and Alloy Metal Cluster Cations
Studied by Cryo Adsorption Kinetics and Infrared Spectroscopy**

vom Fachbereich Chemie der Technischen Universität Kaiserslautern zur Erlangung des
akademischen Grades „Doktor der Naturwissenschaften“ genehmigte

Dissertation

D 386

vorgelegt von

Dipl.-Chem. Matthias Peter Klein

Betreuer: Prof. Dr. G. Niedner-Schatteburg

Tag der wissenschaftlichen Aussprache: 13.09.2021

Technische Universität Kaiserslautern 2021

Die vorliegende Arbeit wurde im Zeitraum von Dezember 2016 bis Juni 2021 im Fachbereich Chemie der Technischen Universität Kaiserslautern unter Betreuung von Prof. Dr. G. Niedner-Schatteburg angefertigt.

Datum des Antrags auf Eröffnung des Promotionsverfahrens: 18.06.2020

Tag der wissenschaftlichen Aussprache: 13.09.2021

Dekanin: Prof. Dr. E. Richling

Promotionskommission:

Vorsitzender: Prof. Dr. W. R. Thiel

1. Berichterstatter: Prof. Dr. G. Niedner-Schatteburg

2. Berichterstatter: PD Dr. Ch. Riehn

Contents

1. Introduction.....	1
2. Experimental and theoretical methods.....	11
2.1 The FRITZ setup	11
2.2 Laser Vaporization (LVAP) cluster ion source	13
2.3 Fourier Transform-Ion Cyclotron Resonance Mass Spectrometry (FT-ICR MS).....	15
2.4 Isothermal Cryo Kinetics.....	17
2.4.1 Relative rate constants.....	18
2.4.2 Absolute rate constants	18
2.5 Cryo Infrared Spectroscopy	20
2.5.1 InfraRed (Multiple) Photon Spectroscopy (IR-(M)PD)	20
2.5.2 Optical Parametric Oscillator / Amplifier (OPO / OPA) IR Laser System.....	22
2.6 Density Functional Theory (DFT)	24
2.7 References.....	26
3. Infrared Spectroscopic Investigation of Structures and N₂ Adsorption Induced Relaxations of Isolated Rhodium Clusters	31
3.1 Preamble	31
3.2 Reprint.....	32
3.3 Supplementary Information.....	46
4. Cryokinetics and Spin Quenching in the N₂ Adsorption onto Rhodium-Cluster Cations	63
4.1 Preamble	63
4.2 Abstract	65
4.3 Introduction.....	65
4.4 Experimental and theoretical methods	67
4.5 Results and Discussion	70
4.5.1 The Limits of N ₂ -Adsorption and its Cluster Size Dependencies.....	70
4.5.2 Adsorption kinetics and rate constants	73
4.5.3 The Gibbs energies	84
4.5.4 DFT modelling.....	86
4.6 Conclusion	90
4.7 Acknowledgements/Funding	91

4.8	Conflicts of interest	91
4.9	References.....	91
4.10	Supplementary Information.....	96
5.	Cryospectroscopy and Spin Quenching in the N₂ Adsorption onto a Rh₆⁺ Cluster Cation	133
5.1	Preamble	133
5.2	Abstract	133
5.3	Introduction.....	134
5.4	Experimental and theoretical methods	135
5.5	Results and discussion.....	137
5.5.1	IR-PD spectroscopy.....	137
5.5.2	DFT calculations.....	140
5.6	Conclusions.....	153
5.7	Acknowledgement	154
5.8	References.....	154
5.9	Supplementary Information.....	157
6.	Cryo Kinetics of N₂ Adsorption onto Bimetallic Rhodium-Iron Clusters in Isolation ...	199
6.1	Preamble	199
6.2	Abstract	199
6.3	Introduction.....	200
6.4	Experimental Methods, Data Evaluation, and Computational Approach.....	203
6.4.1	Experimental Methods.....	203
6.4.2	Data evaluation	204
6.4.3	Computational Approach	205
6.4.4	Nomenclature.....	206
6.5	Results and Discussion	206
6.5.1	The Limits of N ₂ Adsorption and the Cluster Size Dependences	206
6.5.2	Reaction kinetics and rate constants	211
6.5.3	Determination of sticking probabilities $\gamma_{(i,j,m)}$ and Gibbs free energies ΔG_{ad}	227
6.6	Conclusions.....	232
6.7	Acknowledgements.....	232
6.8	References.....	232
6.9	Supplementary Information.....	238

7. Cryo Infrared Spectroscopy of N₂ Adsorption onto Bimetallic Rhodium-Iron Clusters in Isolation.....	247
7.1 Preamble	247
7.2 Abstract	247
7.3 Introduction.....	248
7.4 Experimental Methods and Computational Approach	250
7.5 Results and Discussion	253
7.5.1 The computed structures and spin states of bare [Rh ₃ Fe ₃] ⁺ and [Rh ₄ Fe ₄] ⁺ clusters	253
7.5.2 IR spectroscopy of N ₂ adsorption onto [Rh _{<i>i</i>} Fe _{<i>j</i>}] ⁺ <i>i</i> = <i>j</i> = 3,...,8 clusters	256
7.5.3 Modelling of the [Rh ₃ Fe ₃ (N ₂) ₇] ⁺ vibrational spectra	265
7.6 Conclusion	269
7.7 Acknowledgement	269
7.8 References.....	270
7.9 Supplementary Information.....	274
8. Observation and mechanism of cryo N₂ cleavage by a tantalum cluster.....	293
8.1 Preamble	293
8.2 Reprint.....	294
8.3 Supplementary Information.....	305
9. N₂ Adsorption onto Ta_{<i>n</i>}⁺ <i>n</i> = 4,5 Clusters: IR-PD Spectroscopy, Cryo-Kinetics, and DFT Modelling	337
9.1 Preamble	337
9.2 Abstract	337
9.3 Introduction.....	338
9.4 Experimental and theoretical methods	338
9.5 Results and Discussion	341
9.5.1 [Ta ₄ (N ₂) _{<i>m</i>}] ⁺	341
9.5.2 [Ta ₅ (N ₂) _{<i>m</i>}] ⁺	343
9.6 Conclusion	352
9.7 Acknowledgement	353
9.8 References.....	353
9.9 Supplementary Information.....	356
10. Summary and Outlook	365

11. Zusammenfassung und Ausblick	371
12. Appendix 1: Manuals for kinetic fit procedures.....	379
12.1 Evofit.....	379
12.1.1 Introduction.....	379
12.1.2 Preparatory work	379
12.1.3 The actual <i>evofit</i> procedure	380
12.1.4 Illustrations for the evofit procedure.....	384
12.2 Manufit.....	387
12.2.1 Introduction.....	387
12.2.2 The actual <i>manufit</i> procedure.....	387
12.2.3 The code	389
12.3 Normalize kinetic data	393
12.4 Literature.....	395
13. Appendix 2: Further Joint Publications.....	397
13.1 Cryo IR Spectroscopy of N ₂ and H ₂ on Ru ₈ ⁺ : The Effect of N ₂ on the H-Migration	397
13.1.1 Preamble	397
13.1.2 Reprint.....	398
13.2 A Phosphino-Carboxylic Acid-Based Ru Dimeric Complex.....	405
13.2.1 Preamble	405
13.2.2 Reprint.....	406
13.3 Generation of a zinc and rhodium containing metallomacrocycle by rearrangement of a six-coordinate precursor complex.....	413
13.3.1 Preamble	413
13.3.2 Reprint.....	414
13.4 Complexes of Platinum Group Elements Containing the Intrinsically Chiral Cyclopentadienide Ligand (Cp ^C) ⁻¹	419
13.4.1 Preamble	419
13.4.2 Reprint.....	420
Curriculum Vitae	433
List of Publications.....	435
Conference Contributions	437
Danksagung	441
Eidesstattliche Erklärung.....	443

1. Introduction

Transition metals are widely used as catalysts in chemical processes [1-5], e.g. in the production of fertilizers [6, 7] or the cleaning of exhaust gases [8]. In automobile catalytic converters, rhodium sites catalyze the simultaneous reduction of nitrous oxides and oxidation of CO to form selectively N₂ and CO₂. [8-11] Rhodium catalysts find application in various additional reactions. [12-16] Doping rhodium catalysts with iron also may have a promoting effect towards chemical processes such as steam reforming or the generation of hydrocarbons from syngas. [17-19] Iron catalyzes the ammonia production from H₂ and N₂ in the Haber-Bosch-process. [20]

The investigation of the processes enabling the catalysis are of great importance for a better basic understanding and for possible improvements of the catalytic systems. Nitrogen served for a long time to characterize the surfaces of catalytically active materials and is able to reveal a variety of surface sites and binding stated therein. [21-30] However, the complexity and extent of catalyst surfaces impedes such understanding and studies of model systems are an important tool. [31] Elementary steps in catalysis often proceed on steps or in regions with high surface curvature. Clusters may provide for a high number of low coordinated surface atoms and an analogy between clusters and surfaces has been postulated. [9, 32-39] In this regard, size selected small transition metal clusters that consist mainly of surface atoms or even single atoms constitute suitable model systems for catalytically active surfaces. [40-46] The properties of such small transition metal clusters with a size of less than 50 atoms reveal a pronounced and often unpredictable dependency of size, shape and charge state. [47-51]

A variety of guided ion beam studies with a focus on iron clusters investigated the thermochemistry of their reactions with small molecules as H₂, O₂, H₂O, CO, CO₂, CH₄, and NH₃. [47, 52-66] N₂ complexes of Fe atoms and small Fe_n clusters revealed an end-on coordination of N₂. [67-70] Isolated rhodium containing species in the gas phase react with small molecules such as H₂, CO, NO and N₂O. [71, 72] Particularly CO adsorbates have provided insights into the clusters' reactivities, structures and the effect of the cluster-molecule-bond on the vibrational spectra of these cluster adsorbate complexes. [73-80] As for catalyst surfaces, a multitude of studies and reviews has recognized the value of N₂ adsorption for the characterization of such size selected clusters [47, 67-70, 73, 81-92] and the activation of N₂ by isolated metal ions and clusters in the gas phase has been examined extensively [90, 93-

96]. The investigation of isolated clusters in the gas phase requires a mass spectrometer equipped with a mass filter and an area where the clusters can react with the molecules of interest. The development of cryogenically cooled ion traps facilitated the attachment of weakly bound messenger atoms or molecules onto clusters and molecules.[97-99] The low bonding energies of those complexes allow to record one-photon dissociation spectra of bare transition metal clusters and of cluster adsorbate complexes.[100-102]

We utilize such instrumentation to depose N_2 under well-defined cryo conditions onto size selected clusters and to record their adsorption kinetics and the IR-PD spectra of the adsorbates.[103] This combined approach facilitates the investigation of the morphology of transition metal clusters and the properties of the N_2 adsorbate molecules as well.[36-38, 45, 103-109] The work presented in chapters 3,4,6, and 7 was started in the course of the diploma theses of Amelie Ehrhard and myself.[110, 111] The present thesis continues and extends this work.

This thesis comprises three sections, which represent three classes of metal cluster cores. They are divided in seven research chapters, each of which contains individual introduction, experimental, and discussion parts. A general overview of the applied experimental setup as well as of the experimental and computational methods is provided in chapter 2.

Chapters 3 – 5 focus on the N_2 adsorption onto cationic rhodium clusters. In a first step, we investigate the infrared spectra of cluster adsorbate complexes with a single N_2 molecule and high amounts of N_2 . We identify trends of shifts of the N_2 stretching vibration and determine cluster structures by help of DFT calculations. Our analysis allows us to identify an adsorbate induced spin quench and it indicates the presence of several isomers.

Chapter 4 studies the adsorption/desorption kinetics of N_2 onto the rhodium clusters and analyzes them in terms of *rough* and *smooth* cluster surfaces. A special focus is on the Rh_5^+ cluster, which turns out to be particularly reluctant towards N_2 adsorption. The introduction of spin valley plots helps to visualize and investigate spin relaxations in the course of the stepwise N_2 adsorption. Desorption rate constants are utilized to determine equilibrium constants and upper limits of Gibbs energies for adsorption/desorption equilibria.

We accomplish our studies of rhodium clusters by recording the IR-PD spectra of each cluster adsorbate complex $[Rh_6(N_2)_m]^+$, $m = 1, \dots, 12$, N_2 and correlate them with the results of extensive DFT modelling (chapter 5). Primarily, open questions from the previous chapters are

addressed, like adsorbate induced spin quench and isomerization. Additionally, a trend of shifting IR bands could be correlated with changes in charge and spin distribution, which allows to enhance the known charge dilution model by the concept of adsorbate-induced charge dilution.

The second section of the present thesis (chapters 6 and 7) investigates the cluster adsorbate complexes of mixed rhodium-iron alloy clusters near equiatomic stoichiometry. N₂ adsorption/desorption kinetics (chapter 6) serve to identify rough and smooth cluster surfaces and second shell weakly bound N₂ molecules. We complement our kinetic study by recording IR-PD spectra of the equiatomic rhodium-iron clusters (chapter 7). DFT modelling helps us to obtain structural information about the corresponding cluster adsorbate complexes. This approach facilitates the assignment of alloy-like cluster cores. The observed ranges of the N₂ stretching bands are specific for the chemical nature of the adsorption site and we conclude on a preferential N₂ adsorption onto rhodium atoms.

The last section of this thesis investigates the N₂ adsorption and activation by Ta₄⁺ and Ta₅⁺ clusters. The previous observation of N₂ dissociation on small Ta_n⁺ clusters by help of mass spectrometry and DFT modelling inspired us to complement these studies with our combined approach of adsorption kinetics and IR-PD spectroscopy. The investigation of the Ta₄⁺ cluster in chapter 8 reveals strongly varying adsorption rate constants and no IR-PD bands for the two initial adsorption steps. DFT calculations reveal activation pathways with barriers that either enable or impede a complete N₂ cleavage. An activated intermediate can be identified by its characteristic vibrational band. In chapter 9, we extend our investigations of [Ta₄(N₂)_m]⁺ cluster adsorbate complexes up to $m = 12$. In addition, we present the N₂ adsorption kinetics onto the Ta₅⁺ cluster and record IR-PD spectra of its [Ta₅(N₂)_m]⁺ cluster adsorbate complexes both of which provide no indication of possible N₂ cleavage. Our combined approach indeed turns out to be a suitable tool for the investigation of reactants, products and even intermediates in isolated cluster adsorbate complexes.

References

1. Somorjai, G.A., *Introduction to Surface Chemistry and Catalysis*. **1994**, New York: John Wiley & Sons.

2. Deutschmann, O., Knözinger, H., Kochloefl, K., and Turek, T., *Heterogeneous Catalysis and Solid Catalysts*, in *Ullmann's Encyclopedia of Industrial Chemistry*. **2000**, Wiley-VCH Verlag GmbH & Co. KGaA.
3. Bligaard, T. and Nørskov, J.K., *Chapter 4 - Heterogeneous Catalysis*, in *Chemical Bonding at Surfaces and Interfaces*. **2008**, Elsevier: Amsterdam. 255-321.
4. Schlögl, R., *Heterogeneous Catalysis*. *Angew. Chem., Int. Ed.* **2015**, *54*, 3465-3520.
5. Friend, C.M. and Xu, B., *Heterogeneous Catalysis: A Central Science for a Sustainable Future*. *Acc. Chem. Res.* **2017**, *50*, 517-521.
6. Schlögl, R., *Ammonia Synthesis*, in *Handbook of Heterogeneous Catalysis*. 2501-2575.
7. Schlögl, R., *Catalytic Synthesis of Ammonia—A “Never-Ending Story”?* *Angew. Chem., Int. Ed.* **2003**, *42*, 2004-2008.
8. Votsmeier, M., Kreuzer, T., Gieshoff, J., and Lepperhoff, G., *Automobile Exhaust Control*, in *Ullmann's Encyclopedia of Industrial Chemistry*. **2009**.
9. Ertl, G., *Reactions at Surfaces: From Atoms to Complexity (Nobel Lecture)*. *Angew. Chem., Int. Ed.* **2008**, *47*, 3524-3535.
10. Harrison, B., Cooper, B.J., and Wilkins, A.J.J., *Control of Nitrogen Oxide Emissions from Automobile Engines*. *Platin. Met. Rev.* **1981**, *25*, 14-22.
11. Dey, S. and Dhal, G.C., *Applications of Rhodium and Ruthenium Catalysts for CO Oxidation: an Overview*. *Polytechnica* **2020**, *3*, 26-42.
12. *Rhodium Catalysis in Organic Synthesis: Methods and Reactions*, ed. Tanaka, K. **2019**, Weinheim: Wiley-VCH.
13. Doyle, M.P., *Electrophilic metal carbenes as reaction intermediates in catalytic reactions*. *Acc. Chem. Res.* **1986**, *19*, 348-356.
14. Werlé, C., Goddard, R., Philipps, P., Farès, C., and Fürstner, A., *Structures of Reactive Donor/Acceptor and Donor/Donor Rhodium Carbenes in the Solid State and Their Implications for Catalysis*. *J. Am. Chem. Soc.* **2016**, *138*, 3797-3805.
15. *Rhodium Catalyzed Hydroformylation*. *Catalysis by Metal Complexes*, ed. van Leeuwen, P.W.N.M. and Claver, C. Vol. 22. **2002**, Dordrecht: Springer.
16. Cheung, H., Tanke, R.S., and Torrence, G.P., *Acetic Acid*, in *Ullmann's Encyclopedia of Industrial Chemistry*. **2000**, Wiley-VCH Verlag GmbH & Co. KGaA.
17. Burch, R. and Hayes, M.J., *The Preparation and Characterisation of Fe-Promoted Al₂O₃-Supported Rh Catalysts for the Selective Production of Ethanol from Syngas*. *Journal of Catalysis* **1997**, *165*, 249-261.
18. Chen, L., Choong, C.K.S., Zhong, Z., Huang, L., Ang, T.P., Hong, L., and Lin, J., *Carbon monoxide-free hydrogen production via low-temperature steam reforming of ethanol over iron-promoted Rh catalyst*. *Journal of Catalysis* **2010**, *276*, 197-200.
19. Li, F. and Qian, W., *DRIFTS study of Fe promoter effect on Rh/Al₂O₃ catalyst for C₂ oxygenates synthesis from syngas*. *Applied Petrochemical Research* **2019**, *9*, 211-219.
20. Ertl, G., *Surface Science and Catalysis—Studies on the Mechanism of Ammonia Synthesis: The P. H. Emmett Award Address*. *Catal. Rev.: Sci. Eng.* **1980**, *21*, 201-223.
21. Brunauer, S., Emmett, P.H., and Teller, E., *Adsorption of Gases in Multimolecular Layers*. *J. Am. Chem. Soc.* **1938**, *60*, 309-319.
22. Rakić, V. and Damjanović, L., *Temperature-Programmed Desorption (TPD) Methods*, in *Calorimetry and Thermal Methods in Catalysis*, Auroux, A., editor. **2013**, Springer Berlin Heidelberg: Berlin, Heidelberg. 131-174.
23. Rosowski, F., Hinrichsen, O., Muhler, M., and Ertl, G., *The temperature-programmed desorption of N₂ from a Ru/MgO catalyst used for ammonia synthesis*. *Catalysis Letters* **1996**, *36*, 229-235.

-
24. Langmuir, I., *The Adsorption of Gases on Plane Surfaces of Glass, Mica and Platinum*. J. Am. Chem. Soc. **1918**, *40*, 1361-1403.
 25. Freund, H.J., Bartos, B., Messmer, R.P., Grunze, H., Kühlenbeck, H., and Neumann, M., *The adsorption of N₂ on Fe(111): Angle resolved photoemission and theoretical model studies*. Surf. Sci. **1987**, *185*, 187-202.
 26. King, D.A. and Wells, M.G., *Molecular beam investigation of adsorption kinetics on bulk metal targets: Nitrogen on tungsten*. Surf. Sci. **1972**, *29*, 454-482.
 27. King, D.A. and Wells, M.G., *Reaction Mechanism in Chemisorption Kinetics: Nitrogen on the Plane of Tungsten*. Proceedings of the Royal Society A: Mathematical, Physical and Engineering Sciences **1974**, *339*, 245-269.
 28. Ertl, G., Lee, S.B., and Weiss, M., *Kinetics of nitrogen adsorption on Fe(111)*. Surf. Sci. **1982**, *114*, 515-526.
 29. Grunze, M., Golze, M., Hirschwald, W., Freund, H.J., Pulm, H., Seip, U., Tsai, M.C., Ertl, G., and Küppers, J., *π -Bonded N₂ on Fe(111): The Precursor for Dissociation*. Phys. Rev. Lett. **1984**, *53*, 850-853.
 30. Böhme, D.K. and Schwarz, H., *Gas-Phase Catalysis by Atomic and Cluster Metal Ions: The Ultimate Single-Site Catalysts*. Angew. Chem., Int. Ed. **2005**, *44*, 2336-2354.
 31. Somorjai, G.A., Contreras, A.M., Montano, M., and Rioux, R.M., *Clusters, surfaces, and catalysis*. Proceedings of the National Academy of Sciences **2006**, *103*, 10577.
 32. Muetterties, E.L., Rhodin, T.N., Band, E., Brucker, C.F., and Pretzer, W.R., *Clusters and surfaces*. Chem. Rev. **1979**, *79*, 91-137.
 33. Muetterties, E.L., *Molecular metal clusters*. Science **1977**, *196*, 839-48.
 34. Muetterties, E.L., *Metal Clusters in Catalysis III. — Clusters as Models for Chemisorption Processes and Heterogeneous Catalysis*. Bulletin des Sociétés Chimiques Belges **1975**, *84*, 959-986.
 35. Shustorovich, E., *Cluster-Surface Analogy: New Developments*, in *Quantum Chemistry: The Challenge of Transition Metals and Coordination Chemistry*, Veillard, A., editor. **1986**, Springer Netherlands: Dordrecht. 445-464.
 36. Mohrbach, J., Dillinger, S., and Niedner-Schatteburg, G., *Probing cluster surface morphology by cryo kinetics of N₂ on cationic nickel clusters*. J. Chem. Phys. **2017**, *147*, 184304.
 37. Dillinger, S., Mohrbach, J., and Niedner-Schatteburg, G., *Probing cluster surface morphology by cryo spectroscopy of N₂ on cationic nickel clusters*. J. Chem. Phys. **2017**, *147*, 184305.
 38. Mohrbach, J., Dillinger, S., and Niedner-Schatteburg, G., *Cryo Kinetics and Spectroscopy of Cationic Nickel Clusters: Rough and Smooth Surfaces*. J. Phys. Chem. C **2017**, *121*, 10907-10918.
 39. Tombers, M., Barzen, L., and Niedner-Schatteburg, G., *Inverse H/D Isotope Effects in Benzene Activation by Cationic and Anionic Cobalt Clusters*. J. Phys. Chem. A **2013**, *117*, 1197-1203.
 40. Bohme, D.K. and Schwarz, H., *Gas-phase catalysis by atomic and cluster metal ions: the ultimate single-site catalysts*. Angew Chem Int Ed Engl **2005**, *44*, 2336-54.
 41. Johnson, G.E., Mitrić, R., Bonačić-Koutecký, V., and Castleman, A.W., *Clusters as model systems for investigating nanoscale oxidation catalysis*. Chemical Physics Letters **2009**, *475*, 1-9.
 42. Lang, S.M. and Bernhardt, T.M., *Gas phase metal cluster model systems for heterogeneous catalysis*. Phys. Chem. Chem. Phys. **2012**, *14*, 9255-9269.
-

43. Asmis, K.R. and Fielicke, A., *Size-Selected Clusters as Model Systems for Catalysis*. Top. Catal. **2018**, *61*, 1-2.
44. Schröder, D. and Schwarz, H., *C-H and C-C Bond Activation by Bare Transition-Metal Oxide Cations in the Gas Phase*. Angew Chem Int Ed Engl **1995**, *34*, 1973-1995.
45. Niedner-Schatteburg, G., *Cooperative Effects in Clusters and Oligonuclear Complexes of Transition Metals in Isolation*, in *Clusters – Contemporary Insight in Structure and Bonding*, Dehnen, S., editor. **2017**, Springer International Publishing: Cham. 1-40.
46. Liu, L. and Corma, A., *Metal Catalysts for Heterogeneous Catalysis: From Single Atoms to Nanoclusters and Nanoparticles*. Chem. Rev. **2018**, *118*, 4981-5079.
47. Knickelbein, M.B., *Reactions of transition metal clusters with small molecules*. Ann. Rev. Phys. Chem. **1999**, *50*, 79-115.
48. Luo, Z., Castleman, A.W., Jr., and Khanna, S.N., *Reactivity of Metal Clusters*. Chem Rev **2016**, *116*, 14456-14492.
49. Haberland, H., Kleinermanns, K., and Träger, F., *Cluster*, in *Lehrbuch der Experimentalphysik Band 5 - Gase, Nanosysteme, Flüssigkeiten*, Kleinermanns, K., editor. **2005**, De Gruyter. 819.
50. Heiz, U. and Landman, U., *Nanocatalysis*. NanoScience and Technology. **2007**, Berlin Heidelberg: Springer-Verlag.
51. Landman, U., Yoon, B., Zhang, C., Heiz, U., and Arenz, M., *Factors in gold nanocatalysis: oxidation of CO in the non-scalable size regime*. Top. Catal. **2007**, *44*, 145-158.
52. Parks, E.K., Liu, K., Richtsmeier, S.C., Pobo, L.G., and Riley, S.J., *Reactions of iron clusters with hydrogen. II. Composition of the fully hydrogenated products*. J. Chem. Phys. **1985**, *82*, 5470-5474.
53. Richtsmeier, S.C., Parks, E.K., Liu, K., Pobo, L.G., and Riley, S.J., *Gas phase reactions of iron clusters with hydrogen. I. Kinetics*. J. Chem. Phys. **1985**, *82*, 3659-3665.
54. Jones, N.O., Beltran, M.R., Khanna, S.N., Baruah, T., and Pederson, M.R., *Hydrogen adsorption and magnetic behavior of Fe_n and Co_n clusters: Controlling the magnetic moment and anisotropy one atom at a time*. Phys. Rev. B **2004**, *70*, 165406.
55. Parks, E.K., Weiller, B.H., Bechthold, P.S., Hoffman, W.F., Nieman, G.C., Pobo, L.G., and Riley, S.J., *Chemical probes of metal cluster structure: Reactions of iron clusters with hydrogen, ammonia, and water*. J. Chem. Phys. **1988**, *88*, 1622-1632.
56. Conceição, J., Loh, S.K., Lian, L., and Armentrout, P.B., *Guided ion beam studies of the reactions of Fe_n^+ ($n=2-15$) with D_2 : Cluster–deuteride bond energies as a chemical probe of cluster structures*. J. Chem. Phys. **1996**, *104*, 3976-3988.
57. Griffin, J.B. and Armentrout, P.B., *Guided ion beam studies of the reactions of Fe_n^+ ($n=2-18$) with O_2 : Iron cluster oxide and dioxide bond energies*. J. Chem. Phys. **1997**, *106*, 4448-4462.
58. Gutsev, G.L., Mochena, M.D., and Bauschlicher, C.W., *Interaction of water with small Fe_n clusters*. Chem. Phys. **2005**, *314*, 291-298.
59. Weiller, B.H., Bechthold, P.S., Parks, E.K., Pobo, L.G., and Riley, S.J., *The reactions of iron clusters with water*. J. Chem. Phys. **1989**, *91*, 4714-4727.
60. McNary, C.P. and Armentrout, P.B., *Iron cluster–CO bond energies from the kinetic energy dependence of the Fe_n^+ ($n = 4-17$) + CO association reactions*. Phys. Chem. Chem. Phys. **2014**, *16*, 26467-26477.
61. Griffin, J.B. and Armentrout, P.B., *Guided ion-beam studies of the reactions of Fe_n^+ ($n=1-18$) with CO_2 : Iron cluster oxide bond energies*. J. Chem. Phys. **1997**, *107*, 5345-5355.

-
62. Liyanage, R., Zhang, X.-G., and Armentrout, P.B., *Activation of methane by size-selected iron cluster cations, Fe_n^+ ($n=2-15$): Cluster- CH_x ($x=0-3$) bond energies and reaction mechanisms.* J. Chem. Phys. **2001**, *115*, 9747-9763.
63. Liyanage, R., Griffin, J.B., and Armentrout, P.B., *Thermodynamics of ammonia activation by iron cluster cations: Guided ion beam studies of the reactions of Fe_n^+ ($n=2-10,14$) with ND_3 .* J. Chem. Phys. **2003**, *119*, 8979.
64. Parks, E.K., Nieman, G.C., Pobo, L.G., and Riley, S.J., *The reaction of iron clusters with ammonia. I. Compositions of the ammoniated products and their implications for cluster structure.* J. Chem. Phys. **1988**, *88*, 6260-6272.
65. Fossan, K.O. and Uggerud, E., *Reactions of cationic iron clusters with ammonia, models of nitrogen hydrogenation and dehydrogenation.* Dalton transactions **2004**, 892-897.
66. Irion, M.P. and Schnabel, P., *FT-ICR studies of sputtered metal cluster ions. 5. The chemistry of iron cluster cations with ammonia and hydrazine.* The Journal of Physical Chemistry **1991**, *95*, 10596-10599.
67. Tan, L., Liu, F., and Armentrout, P.B., *Thermochemistry of the activation of N_2 on iron cluster cations: Guided ion beam studies of the reactions of Fe_n^+ ($n = 1-19$) with N_2 .* J. Chem. Phys. **2006**, *124*, 084302.
68. Liu, F., Li, M., Tan, L., and Armentrout, P.B., *Guided ion beam studies of the reactions of Co_n^+ ($n=1-18$) with N_2 : Cobalt cluster mononitride and dinitride bond energies.* J. Chem. Phys. **2008**, *128*, 194313.
69. Duarte, H.A., Salahub, D.R., Haslett, T., and Moskovits, M., *$Fe(N_2)_n$ ($n = 1-5$): Structure, Bonding, and Vibrations from Density Functional Theory.* Inorganic Chemistry **1999**, *38*, 3895-3903.
70. Haslett, T.L., Fedrigo, S., Bosnick, K., Moskovits, M., Duarte, H.A., and Salahub, D., *Binary Iron-Dinitrogen Compounds Synthesized by Co-deposition of Mass-Selected Fe , Fe_2 , and Fe_3 with N_2 .* J. Am. Chem. Soc. **2000**, *122*, 6039-6044.
71. Andersson, M., Holmgren, L., and Rosén, A., *Rhodium-cluster reactivity: Sticking probabilities of some diatomic molecules.* Surf. Rev. Lett. **1996**, *3*, 683-686.
72. Zhao, Y.-X., Zhao, X.-G., Yang, Y., Ruan, M., and He, S.-G., *Rhodium chemistry: A gas phase cluster study.* J. Chem. Phys. **2021**, *154*, 180901.
73. Mafuné, F., Tawarayama, Y., and Kudoh, S., *Reactivity Control of Rhodium Cluster Ions by Alloying with Tantalum Atoms.* J. Phys. Chem. A **2016**, *120*, 861-867.
74. Fielicke, A., Gruene, P., Meijer, G., and Rayner, D.M., *The adsorption of CO on transition metal clusters: A case study of cluster surface chemistry.* Surf. Sci. **2009**, *603*, 1427-1433.
75. Swart, I., de Groot, F.M., Weckhuysen, B.M., Rayner, D.M., Meijer, G., and Fielicke, A., *The effect of charge on CO binding in rhodium carbonyls: from bridging to terminal CO.* J. Am. Chem. Soc. **2008**, *130*, 2126-2127.
76. Fielicke, A., von Helden, G., Meijer, G., Pedersen, D.B., Simard, B., and Rayner, D.M., *Size and charge effects on the binding of CO to late transition metal clusters.* J. Chem. Phys. **2006**, *124*, 194305.
77. Fielicke, A., von Helden, G., Meijer, G., Pedersen, D.B., Simard, B., and Rayner, D.M., *Size and Charge Effects on the Binding of CO to Small Isolated Rhodium Clusters.* J. Phys. Chem. B **2004**, *108*, 14591-14598.
78. Fielicke, A., von Helden, G., Meijer, G., Simard, B., Dénomée, S., and Rayner, D.M., *Vibrational Spectroscopy of CO in Gas-Phase Rhodium Cluster-CO Complexes.* J. Am. Chem. Soc. **2003**, *125*, 11184-11185.
-

79. Shetty, S., Strych, S., Jansen, A.P.J., and van Santen, R.A., *Theoretical investigation of CO adsorption on Rh_n (n = 3–13) clusters*. Canadian Journal of Chemistry **2009**, *87*, 824–831.
80. Tian, F.-Y. and Shen, J., *Density-functional study of CO adsorbed on Rh_N (N= 2–19) clusters*. Chinese Physics B **2011**, *20*, 123101.
81. Morse, M.D., Geusic, M.E., Heath, J.R., and Smalley, R.E., *Surface reactions of metal clusters. II. Reactivity surveys with D₂, N₂, and CO*. J. Chem. Phys. **1985**, *83*, 2293–2304.
82. Bérces, A., Hackett, P.A., Lian, L., Mitchell, S.A., and Rayner, D.M., *Reactivity of niobium clusters with nitrogen and deuterium*. J. Chem. Phys. **1998**, *108*, 5476–5490.
83. Ho, J., Parks, E.K., Zhu, L., and Riley, S.J., *Reactions of small cobalt clusters with N₂: implications for cluster structure*. Chem. Phys. **1995**, *201*, 245–261.
84. Riley, S.J., *The atomic structure of transition metal clusters*. Journal of Non-Crystalline Solids **1996**, *205–207*, 781–787.
85. Parks, E.K., Zhu, L., Ho, J., and Riley, S.J., *The structure of small nickel clusters. I. Ni₃–Ni₁₅*. J. Chem. Phys. **1994**, *100*, 7206–7222.
86. Parks, E.K., Zhu, L., Ho, J., and Riley, S.J., *The structure of small nickel clusters. II. Ni₁₆–Ni₂₈*. J. Chem. Phys. **1995**, *102*, 7377–7389.
87. Parks, E.K. and Riley, S.J., *Nickel cluster structure determined from the adsorption of molecular nitrogen Ni₄₉–Ni₇₁*. Zeitschrift für Physik D Atoms, Molecules and Clusters **1995**, *33*, 59–70.
88. Parks, E.K., Kerns, K.P., and Riley, S.J., *The structure of nickel-iron clusters probed by adsorption of molecular nitrogen*. Chem. Phys. **2000**, *262*, 151–167.
89. Parks, E.K., Nieman, G.C., Kerns, K.P., and Riley, S.J., *The thermodynamics of nitrogen adsorption on nickel clusters: Ni₁₉–Ni₇₁*. J. Chem. Phys. **1998**, *108*, 3731–3739.
90. Mou, L.-H., Jiang, G.-D., Li, Z.-Y., and He, S.-G., *Activation of dinitrogen by gas-phase species*. Chinese Journal of Chemical Physics **2020**, *33*, 507–520.
91. Mafuné, F., Tawarayama, Y., and Kudoh, S., *Nitrogen Molecule Adsorption on Cationic Tantalum Clusters and Rhodium Clusters and Desorption from Their Nitride Clusters Studied by Thermal Desorption Spectrometry*. J. Phys. Chem. A **2016**, *120*, 4089–4095.
92. Cui, C., Jia, Y., Zhang, H., Geng, L., and Luo, Z., *Plasma-Assisted Chain Reactions of Rh₃⁺ Clusters with Dinitrogen: N≡N Bond Dissociation*. J Phys Chem Lett **2020**, *11*, 8222–8230.
93. Pillai, E.D., Jaeger, T.D., and Duncan, M.A., *IR Spectroscopy and Density Functional Theory of Small V⁺(N₂)_n Complexes*. J. Phys. Chem. A **2005**, *109*, 3521–3526.
94. Pillai, E.D., Jaeger, T.D., and Duncan, M.A., *IR Spectroscopy of Nb⁺(N₂)_n Complexes: Coordination, Structures, and Spin States*. J. Am. Chem. Soc. **2007**, *129*, 2297–2307.
95. Kerpál, C., Harding, D.J., Lyon, J.T., Meijer, G., and Fielicke, A., *N₂ Activation by Neutral Ruthenium Clusters*. J. Phys. Chem. C **2013**, *117*, 12153–12158.
96. Brathwaite, A.D., Abbott-Lyon, H.L., and Duncan, M.A., *Distinctive Coordination of CO vs N₂ to Rhodium Cations: An Infrared and Computational Study*. J. Phys. Chem. A **2016**, *120*, 7659–7670.
97. Wolk, A.B., Leavitt, C.M., Garand, E., and Johnson, M.A., *Cryogenic ion chemistry and spectroscopy*. Acc Chem Res **2014**, *47*, 202–210.
98. Gerlich, D., Jašík, J., Andris, E., Navrátil, R., and Roithová, J., *Collisions of FeO⁺ with H₂ and He in a Cryogenic Ion Trap*. Chemphyschem : a European journal of chemical physics and physical chemistry **2016**, *17*, 3723–3739.

-
99. Wu, Z., Płucienik, A., Liu, Y., Naschitzki, M., Wachsmann, W., Gewinner, S., Schöllkopf, W., Kühlenbeck, H., and Freund, H.-J., *Surface action spectroscopy with rare gas messenger atoms*. Rev. Sci. Instrum. **2018**, *89*, 083107.
 100. Duncan, M.A., *Infrared spectroscopy to probe structure and dynamics in metal ion-molecule complexes*. Int. Rev. Phys. Chem. **2003**, *22*, 407-435.
 101. MacAleese, L. and Maître, P., *Infrared spectroscopy of organometallic ions in the gas phase: From model to real world complexes*. Mass Spectrometry Reviews **2007**, *26*, 583-605.
 102. Gruene, P., Butschke, B., Lyon, J.T., Rayner, D.M., and Fielicke, A., *Far-IR Spectra of Small Neutral Gold Clusters in the Gas Phase*. Zeitschrift für Physikalische Chemie **2014**, *228*, 337-350.
 103. Dillinger, S. and Niedner-Schatteburg, G., *Cryo trapping by FT-MS for kinetics and spectroscopy*, in *Fundamentals and Applications of FTMS*, Schmitt-Kopplin, P. and Kanawati, B., editors. **2018**, Elsevier: Cambridge. 593-621.
 104. Dillinger, S., Mohrbach, J., Hewer, J., Gaffga, M., and Niedner-Schatteburg, G., *Infrared spectroscopy of N₂ adsorption on size selected cobalt cluster cations in isolation*. Phys. Chem. Chem. Phys. **2015**, *17*, 10358-10362.
 105. Mohrbach, J., *Cryo Tagging Infrared Spectroscopy and Temperature Controlled Kinetic Studies in a Tandem Trap Mass Spectrometer*. 2017, TU Kaiserslautern: Kaiserslautern.
 106. Dillinger, S., *Cryo Spectroscopy and Kinetics of Isolated Transition Metal Clusters and Complexes* 2017, TU Kaiserslautern: Kaiserslautern.
 107. Dillinger, S., Klein, M.P., Steiner, A., McDonald, D.C., Duncan, M.A., Kappes, M.M., and Niedner-Schatteburg, G., *Cryo IR Spectroscopy of N₂ and H₂ on Ru₈⁺: The Effect of N₂ on the H-Migration*. J. Phys. Chem. Lett. **2018**, *9*, 914-918.
 108. Straßner, A., Wiehn, C., Klein, M.P., Fries, D.V., Dillinger, S., Mohrbach, J., Armentrout, P.B., and Niedner-Schatteburg, G., *Kinetics of stepwise nitrogen adsorption by size-selected iron cluster cations: Evidence for some size-dependent nitrophobia*. under review at J. Chem. Phys.
 109. Straßner, A., Wiehn, C., Klein, M.P., Fries, D.V., Dillinger, S., Mohrbach, J., Armentrout, P.B., and Niedner-Schatteburg, G., *Cryo spectroscopy of N₂ on cationic iron clusters*. under review at J. Chem. Phys.
 110. Klein, M.P., *Cryo-Infrarotspektroskopie von Stickstoff-Adsorbaten auf kationischen Rhodium- und Rhodium-Eisen-Clustern*. 2016, TU Kaiserslautern: Kaiserslautern.
 111. Ehrhard, A.-A., *Kryokinetische Untersuchungen zur Adsorption von Stickstoff an kationischen Rhodium-Clustern und Rhodium-Eisen-Mischclustern*. 2016, TU Kaiserslautern: Kaiserslautern.

2. Experimental and theoretical methods

2.1 The FRITZ setup

All experiments were performed at the FRITZ (Fouriertransform Reactive Investigation Test Zoo) setup (Fig. 1). This instrument is a heavily modified Fourier Transform-Ion Cyclotron Resonance (FT-ICR) mass spectrometer (cf. chapter 2.3). A Laser VAPorization (LVAP) source and an Electrospray Ionization (ESI) source (*Apollo II*, Bruker [1-4]) serve for ion generation, both mounted perpendicularly to the instrument axis. Gate valves connect both sources with the remaining vacuum system and allow for individual operation.

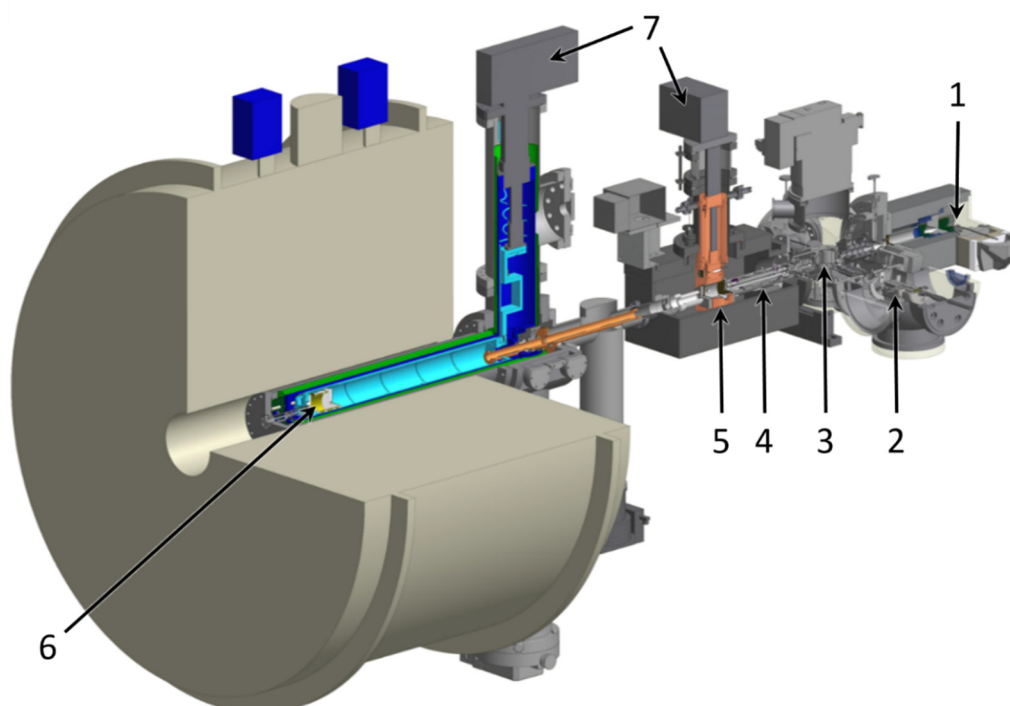


Fig. 1 Schematic drawing of the FRITZ setup, a modified *Bruker Apex Ultra* FT-ICR mass spectrometer. The ESI source (1) is displayed on the magnetic field axis. In the actual setup, the ESI source is mounted in opposite to the LVAP source (2), perpendicular to the magnetic field axis. Coming from the sources, the ions are deflected by the quadrupole ion beam bender (3) onto the magnetic field axis. The ions are mass selected by the quadrupole mass filter (4), stored in the hexapole ion trap (5) and transferred into the ICR cell (6). Both ion traps are cooled by a two-stage closed cycle He cryostat (7).

The cluster ions investigated in the present thesis were produced via laser vaporization (cf. chapter 2.2) that generates cluster clouds consisting of M_n^z metal clusters in a certain size distribution (n) with a selectable charge z ($z = -,0,+$). This thesis focuses on cationic clusters.

Behind the source, a home-built stack of ion optics guides the skimmed cluster beam to a home-built electrostatic quadrupole ion beam bender that deflects it by 90° onto the magnetic field axis and serves to remove neutral clusters.[5, 6]

Through another home-built stack of ion optics, the ions are guided to a quadrupole mass filter that serves to select a cluster with a certain number of metal atoms n from the cluster size distribution (Fig. 2).

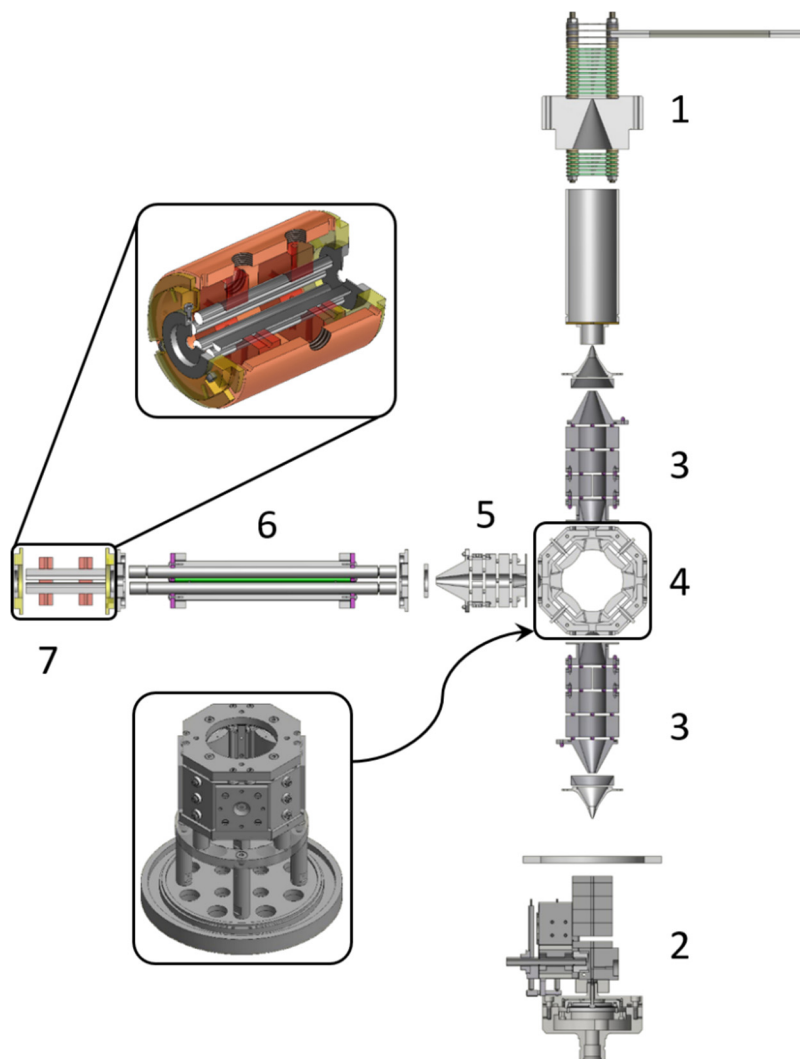


Fig. 2 Scheme of the ion sources and optics leading to the hexapole collision cell: ESI source (1) LVAP source (2), ion optics (3) and (5), quadrupole ion beam bender (4), quadrupole mass filter (6), and hexapole collision cell (7).

After the mass filter, the ions enter a first ion trap, the hexapole collision cell. This trap is mounted on the second stage of a 4 K two-stage closed cycle He cryostat (*Sumitomo* SRDK-101E with a HC-4E compressing unit) and the temperatures of both stages are monitored by temperature sensors (*LakeShore*, Cernox™ CX-1060-CO-HT-P-1.4M, calibrated

from 1.4 to 420 K). In order to adjust the temperature heating resistors (*Janis research*, Cartridge Heater, $R = 50 \Omega$) are attached to both cooling stages. Sensors and heating resistors are connected to a temperature controller (LakeShore, Model 336), which serves to monitor and adjust the temperature. The hexapole collision cell is filled by a continuous flow of He ($3.0 - 5.0 \times 10^{-6}$ mbar) that serves to trap and thermalize the cluster ions within the ion trap. Buffer and reaction gases can be introduced via two gas lines into the hexapole collision cell. Therefore, the hexapole collision cell is connected to various continuous and pulsed gas inlets. In our experiments, we added continuously N_2 ($2.0 - 5.0 \times 10^{-7}$ mbar) into the hexapole collision cell to react with the cluster ions.

After a variable storage time (0 – 20 s), the ions are transferred to the ICR cell, which is located in the high field region of a superconducting solenoid ($B = 7$ T). The ICR cell is connected to the second stage of a 10 K two-stage closed cycle He cryostat (*Sumitomo* SRDK-408S2 with a W-71D compressing unit). Two actively cooled and three passively cooled shielding tubes serve to diminish the cluster heating effects of black body radiation [7]. Three temperature sensors (*LakeShore*, Cernox™ CX-1050-CO-HT-P, calibrated from 4 to 325 K) monitor the temperature and are mounted on the second stage of the cold head, on a shield mounted on the first cooling stage and on the backside of the ICR cell. The temperature can be monitored and adjusted by a temperature controller (LakeShore, Model 340). As for the hexapole collision cell, gases can be introduced in a pulsed or continuous manner. The ICR cell is located in the ultra-high vacuum region of the instrument. At the back end of the instrument, a diamond window (*DiamondMaterials*) enables coupling of an IR laser beam into the ICR cell. Thus, the ICR cell may serve as a reaction chamber, mass selector and mass analyzer.

The FRITZ setup enables measuring of isothermal cryogenic adsorption kinetics (cf. chapter 2.4) and cryogenic InfraRed (Multiple) Photon Dissociation spectra (IR-(M)PD, cf. chapter 2.5) of isolated and cooled metal clusters and their cluster adsorbate complexes.[8]

2.2 Laser Vaporization (LVAP) cluster ion source

As the experimental setup is a mass spectrometer, and this thesis focuses on cluster ions, a suitable ion source is needed [9, 10]. The metal cluster cations investigated in the present work were produced with a home-built Laser VAPorization (LVAP) cluster ion source. This type of cluster source was first described by Bondybey and English [11, 12], as well as Smalley [13, 14].

The source mainly consists of three essential parts: A home-built piezoelectric valve [15], an expansion / interaction block, and an expansion channel (Fig. 3).

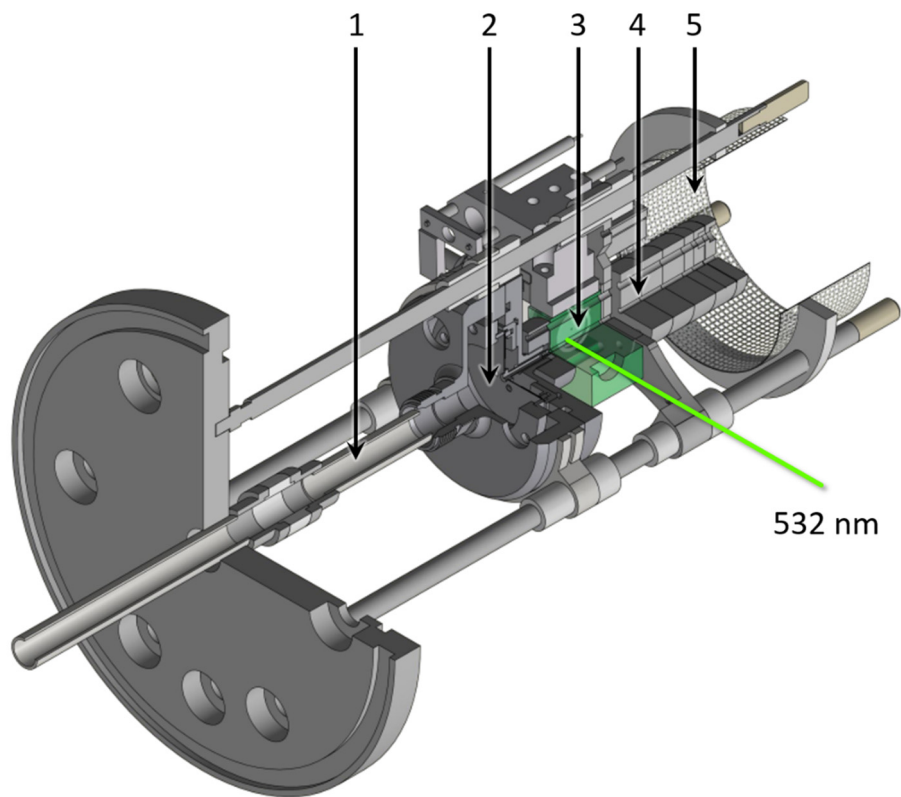


Fig. 3 Schematic drawing of an LVAP source: gas line (1), piezoelectric valve (2), expansion / interaction block (3), expansion channel (4), mesh (5).

The second harmonic of a Nd:YAG laser (Innolas, Spitlight 300, 20 Hz) is focused on a rotating metal target foil (thickness 0.1 – 0.5 mm) that consists of the metal or alloy of interest. The resulting plasma consists of neutral, cationic and anionic species. A transversal gas pulse created by the home-built piezoelectric valve entrains the plasma through the expansion channel (69 mm long). The valve operates in synchronization with the laser at 20 Hz, with an opening time of approximately 40 μ s, and with a backing pressure of 15 – 20 bar. The gas pulse expands into the source vacuum chamber and raises the chamber pressure from 2×10^{-7} mbar to 4×10^{-4} mbar. The supersonic expansion of helium effects the cooling of the entrained metal plasma and metal cluster ions form within the expansion channel. After leaving the expansion channel, the cluster ions cloud is confined by a mesh and skimmed. The intensity maximum of the resulting cluster ion size range (2 to 40 atoms) can be influenced by variation of backing pressure, laser-valve-delay, valve opening time and the applied source voltages.

The polarity of the source voltages and of the subsequent ion optics controls the charge state of the produced cluster ions.

The rhodium foil (purity 99.8%) and the tantalum foil (purity 99.95%) were purchased from *Alfa Aesar*. The rhodium-iron foil (^{103}Rh : ^{56}Fe molar ratio 1:1) was purchased from *MaTeck* and produced using monoisotopic iron.

2.3 Fourier Transform-Ion Cyclotron Resonance Mass Spectrometry (FT-ICR MS)

In the year 1930, Lawrence and Edlefsen first described the principles of a cyclotron that is able to accelerate ions in a limited space without utilization of high voltages.[16-18] This technology was implemented 20 years later in a first ion cyclotron resonance (ICR) mass spectrometer [19] and Comisarow and Marshall adapted these results to introduce a Fourier Transform-Ion Cyclotron Resonance (FT-ICR) mass spectrometer [20, 21]. In the following decades, the performance of these instruments has benefitted from other technological developments, in particular from the combination with superconducting magnets.[22, 23]

$$F_L = qv_{yx}B \quad 2-1$$

$$F_{cf} = \frac{mv_{xy}^2}{r} \quad 2-2$$

$$\omega_c = v_{xy}/r \quad 2-3$$

$$\omega_c = 2\pi f_c = \frac{qB}{m} \quad 2-4$$

$$f_c = \frac{qB}{2\pi m} \quad 2-5$$

F_L Lorentz force

F_{cf} centrifugal force

q charge on the ion ($q = z \cdot e$)

z number of charges

e elementary charge

v_{xy} velocity of the ion in the xy plane

B magnetic field

m ion mass

r radius of the ion's orbit

The key component of an FT-ICR mass spectrometer is the ICR cell (Fig. 4) that is located within a strong homogeneous magnetic field. Ions of interest are stored within this ion trap and forced on a circular trajectory by the magnetic field. The radius of this trajectory is determined by two opposing forces: The Lorentz and the centrifugal force. If both forces are in balance, the ions move on stable circular trajectories with a certain angular velocity ω_c , which is inversely proportional to the mass-to-charge ratio (m/z) and proportional to the cyclotron frequency f_c . The cyclotron frequency is independent of the initial velocity in the xy plane and the radius of the orbit.

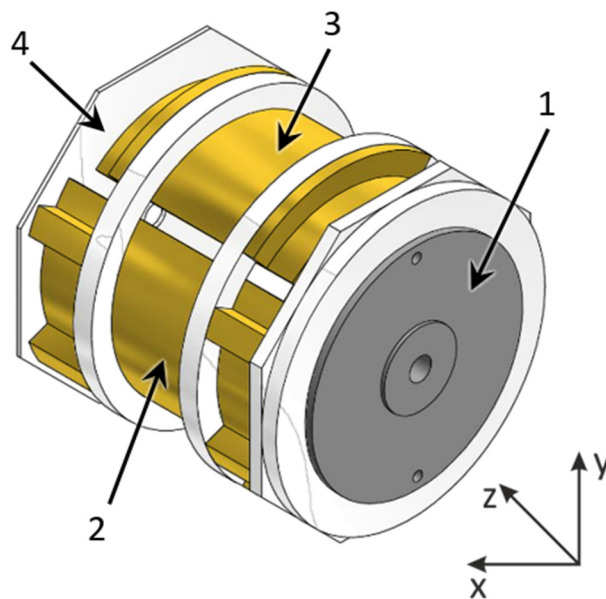


Fig. 4 Schematic drawing of an ICR cell (*Bruker, infinity cell* [24]); front trapping plate (1), excitation plate (2), detection plate (3), back trapping plate (4).

An ICR cell consists of at least six plates (Fig. 4): The front and the back plate serve to produce an electrostatic field, which traps the ions in the cell along the magnetic field axis (z axis). The trapping motion describes the oscillation of the trapped ions between the two trapping plates. This motion adds to the circular motion effected by the magnetic field. Two excitation plates, which are opposed to each other, serve to accelerate and excite the ions onto larger orbits by an alternating electric field. A frequency sweep of this alternating field serves to excite a variety of ions with different m/z ratios. The oscillating ions pass the two opposed detection plates and induce an image current. The oscillation frequency is specific for each m/z ratio. An analysis of the recorded oscillating image currents including Fourier transform yields a mass spectrum.

The total motion of the ions within the ICR cell consists of three components (Fig. 5): The above mentioned trapping motion and cyclotron motion superpose with an electric field induced magnetron motion that is mass independent.

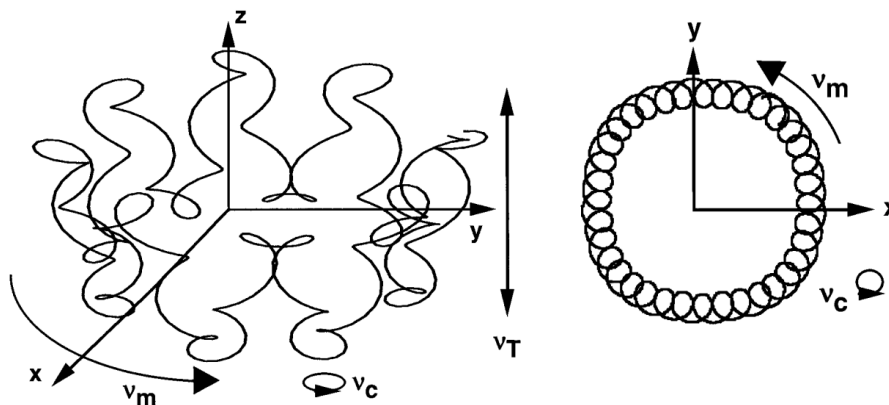


Fig. 5 Representation of the overall ion motion within an ICR cell consisting of the magnetron motion v_m , trapping motion v_T and the cyclotron motion v_c , and its projection on the xy -plane.[22, 25] Republished with permission of John Wiley & Sons - Books, from [22]; permission conveyed through Copyright Clearance Center, Inc.

The ions with a specific m/z ratio can be mass selected within the ICR cell by applying either a frequency sweep or a frequency shot. In the first case, a frequency sweep excluding the resonance frequency of ions with the wanted m/z ratio excites all other ions to much higher orbits than required for detection. These orbits are unstable and the ions are removed from the cell. In the second case, ions of a specific m/z ratio are excited to unstable orbits by applying their specific resonance frequency. Ions can be stored in the cell for a long time, even up to several days, depending on the quality of the ultra-high vacuum.[22, 26] Irradiating the stored and isolated ions with an infrared laser and recording photon energy dependent fragmentation allows for recording of vibrational spectra (cf. chapter 2.5).

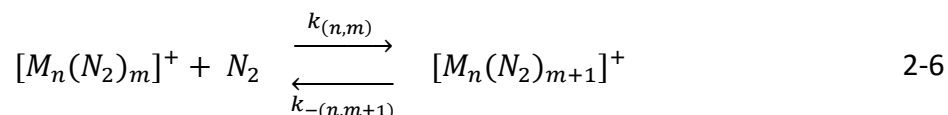
2.4 Isothermal Cryo Kinetics

The mass selected cluster ions can be stored for a variable time in the cryogenic hexapole collision cell and thermalized by collisions with the buffer gas. The thermalized ions can react with a continuously added reaction gas. The temperature of the cell is well defined as well as the pressure of the reaction gas in the hexapole collision cell. By varying the storage time, isothermal cryo kinetics can be recorded. The reaction products appear as additional masses

in the respective mass spectrum. With increasing reaction time, the product intensities increase while the parent intensity decreases. In the present thesis, the reactive gas is nitrogen (N_2) that can adsorb onto mass selected metal clusters.

2.4.1 Relative rate constants

Relative rate constants $k_{(n,m)}$ are obtained by analysis of the mass spectra at various reaction times. The normalized time dependent parent and product ion intensities are fitted as pseudo-first-order kinetics with the genetic algorithm program *evofit*. [27] The program allows for fits that yields relative rate constants for adsorption and possible desorption steps according to the equation 2-6. Note that we observe a consecutive chain of these adsorption/desorption steps. We have chosen a fully self consistent nomenclature, that is described in more detail in chapter 4 ([28] Supplement Text S1 therein).



The obtained relative adsorption and desorption rates can be used for further evaluations. The ratios of relative rate constants of adsorption and desorption yield the equilibrium constant of the $(m+1)^{th}$ N_2 adsorbate, $k_{(n,m)}/k_{-(n,m+1)} = K_m$, and its Gibbs free energy $\Delta_{ads}G$.

$$K_{(n,m)} = k_{(n,m)}/k_{-(n,m+1)} \quad 2-7$$

$$\Delta G_{(n,m)} = -RT \ln(K_{(n,m)}) \quad 2-8$$

Note, that thermodynamic properties are pressure dependent. To determine an according pressure, the measured pressure has to be corrected by the geometry factor c_{app} (cf. chapter 2.4.2).

2.4.2 Absolute rate constants

An adsorption of N_2 onto a cluster adsorbate complex requires a collision of a $[M_n(N_2)_m]^+$ cluster adsorbate complexes with an N_2 molecule. The collision rate of polar and or polarizable molecules with a charged molecule can be calculated via ‘average dipole orientation’ (ADO) theory. [29-32] The charged molecule is considered a point charge. The ADO collision rate provides for a theoretical limit of the reaction rate. It is an extension of the classical Langevin

collision rates and the ADO collision rate simplifies to the Langevin rate in the case of a negligible dipole moment.

$$k_{coll} = \frac{q}{2\varepsilon_0\sqrt{\mu}} \left(\sqrt{\alpha} + c\mu_D \sqrt{\frac{2}{\pi k_B T}} \right) \quad 2-9$$

q	charge on the ion
μ	reduced mass
α	polarizability
c	parameter between 0 and 1, expressed by polarizability volume α' and μ_D [32]
μ_D	dipole moment of the molecule
T	temperature
k_B	Boltzmann constant
ε_0	vacuum permittivity

Thus, this theory is useful for the collisions of transition metal cluster ions with small molecules, but it often underestimates the reaction rates.[33, 34] In order to take account of these effect, Kummerlöwe and Beyer introduced two additional models that include a spherical geometry of the charged particle and different positions of the charge within this sphere.[35] These models are the 'Hard Sphere Average dipole orientation' model (HSA) and the 'Surface Charge Capture' model (SCC).

From our experimental relative rate constants, absolute rate constants $k_{(n,m)}^{abs}$ can be derived by division with the absolute number density of the reaction gas $\rho_{N_2}(T)$:

$$k_{(n,m)}^{abs} = k_{(n,m)} / \rho_{N_2}(T) \quad 2-10$$

$$\rho_{N_2}(26\text{ K}) = \frac{c_{app} p_c^{300\text{ K}}}{k_B T_{300\text{ K}}} \quad 2-11$$

c_{app}	geometry factor
$p_c^{300\text{ K}}$	pressure in the chamber
$T_{300\text{ K}}$	temperature at the point of pressure measurement
k_B	Boltzmann constant

After numerous kinetic studies, we evaluated the geometry factor c_{app} to be 1.8 at 26 K with a net uncertainty of $\pm 50\%$. The ratios of the absolute rate constants to the collision rates yield the sticking probabilities γ , which represent an absolute reaction efficiency.

$$\gamma = \frac{k_{abs}}{k_{coll}} \quad 2-12$$

2.5 Cryo Infrared Spectroscopy

2.5.1 InfraRed (Multiple) Photon Spectroscopy (IR-(M)PD)

InfraRed (IR) spectroscopy is a well-established tool for characterization and structural elucidation of molecules. In condensed phase, IR radiation can be resonantly absorbed by the sample and the extinction is evaluated as a function of the IR wavenumber. Studying isolated molecules in the gas phase would exclude solvent effects as well as packing effects and would enable the examination of ions without the influence of counterions. However, isolated molecules in the gas phase lack a sufficient particle number density to gain a measurable extinction. To address this impediment methods of *action spectroscopy* have established and proved valuable tools for the investigation of neutral and ionic isolated molecules and clusters.[36]

These methods base on mass spectrometry. Their approach is to observe the photon energy dependent effects of laser irradiation on the molecule instead of photon energy dependent extinction. Ionic precursors and products of irradiation can be observed via mass spectrometry. Vibrational spectra of trapped and isolated gaseous ions can be recorded via InfraRed (Multiple) Photon Dissociation (IR-(M)PD).[37, 38] A tunable laser irradiates the gaseous ion, which absorbs a photon if the laser frequency is in resonance with a vibrational transition. The absorbed energy redistributes by internal vibrational redistribution (IVR) into other internal degrees of freedom of the ion.[39] The original absorbing vibrational mode can now absorb another IR photon. If the ion is irradiated by intense and/or multiple laser pulses, this process can repeat until the energy within the ion is sufficient to break a weak bond (Fig. 6).[37, 40-42]

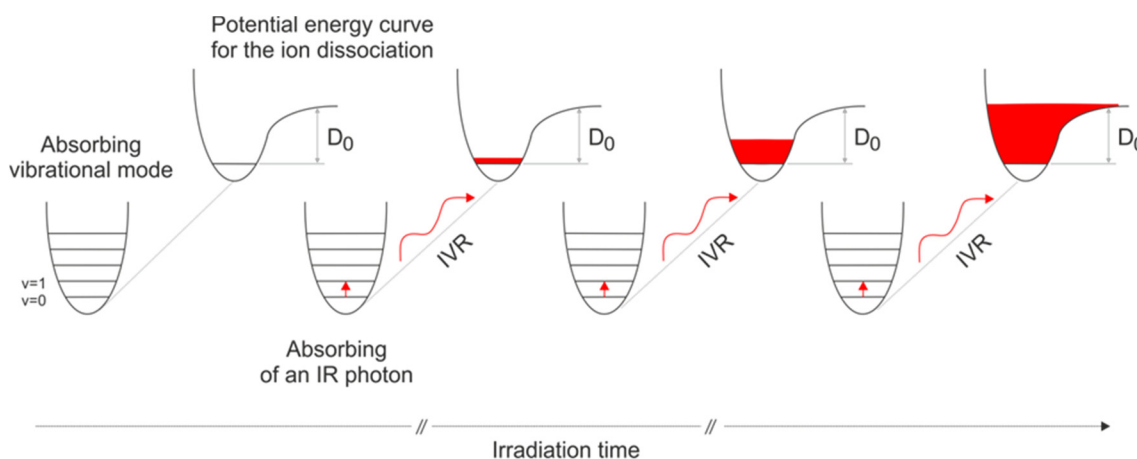


Fig. 6 Schematic representation of the IR-MPD process, adapted from [40]. The ion absorbs a resonant IR photon and the energy is redistributed via IVR. This process repeats until the dissociation threshold is reached and the ion dissociates. Republished with permission of The Royal Society of Chemistry, from [40]; permission conveyed through Copyright Clearance Center, Inc.

The resulting fragments can be detected by mass spectrometry and the IR-(M)PD spectrum is obtained by plotting the fragmentation efficiency (*frag. eff.*) as a function of the laser frequency.

$$frag. eff. = \left(\frac{\sum_i I_i^{fr}}{\sum_j I_j^p + \sum_i I_i^{fr}} \right) \quad 2-13$$

I_i^{fr} intensity of the fragment ions

I_j^p intensity of the parent ions

If the dissociation of the ion is a multiphoton process, the fragmentation efficiency does not necessarily correlate linearly with the laser intensity and the absorption cross section of the irradiated ion. Thus, the absorption intensities of IR-MPD spectra may vary from those of calculated linear absorption spectra and those of condensed phase spectra.[40, 43, 44] Heating of the ions by the irradiation can lead to a slight red shift.[37]

To achieve such dissociation, the bond dissociation energy of a weak bond within the ion has to be absorbed. The energy of an IR photon generated by the laser system described below is usually in the range of $800 - 4000 \text{ cm}^{-1}$ ($10 - 50 \text{ kJ/mol}$) and thus far below typical covalent bond energies in a molecule [40-42]. The application of messenger or tagging techniques may enable single photon dissociation of the ions of interest [45]: An unreactive atom or small

molecule (He, Ar, H₂, N₂,...) is attached to the molecule of interest and is only weakly bound. The attachment requires low temperatures as achieved by use of supersonic expansion jets or cryogenically cooled ion traps.[45] The effect of these messenger molecules on the vibrational spectrum of the molecule is supposed to be small and the low bonding energies lead to a reduced dissociation threshold.

An experimental upper limit of the N₂ physisorption energy on iron surfaces is 21 kJ/mol.[46, 47] The calculated N₂ adsorption enthalpies on stepped rhodium and iron surfaces are 54 kJ/mol and 34 kJ/mol, respectively.[48] Our own calculations of [M_n(N₂)_m]⁺ M = Rh, Ta cluster adsorbate complexes yielded a similar upper limit for the adsorption energies. For more details, refer to chapters 4, 5, 8, and 9. The IR induced dissociation processes of [M_n(N₂)_m]⁺ cluster adsorbate complexes investigated here seem to be on the edge between single and multiphoton processes.

2.5.2 Optical Parametric Oscillator / Amplifier (OPO / OPA) IR Laser System

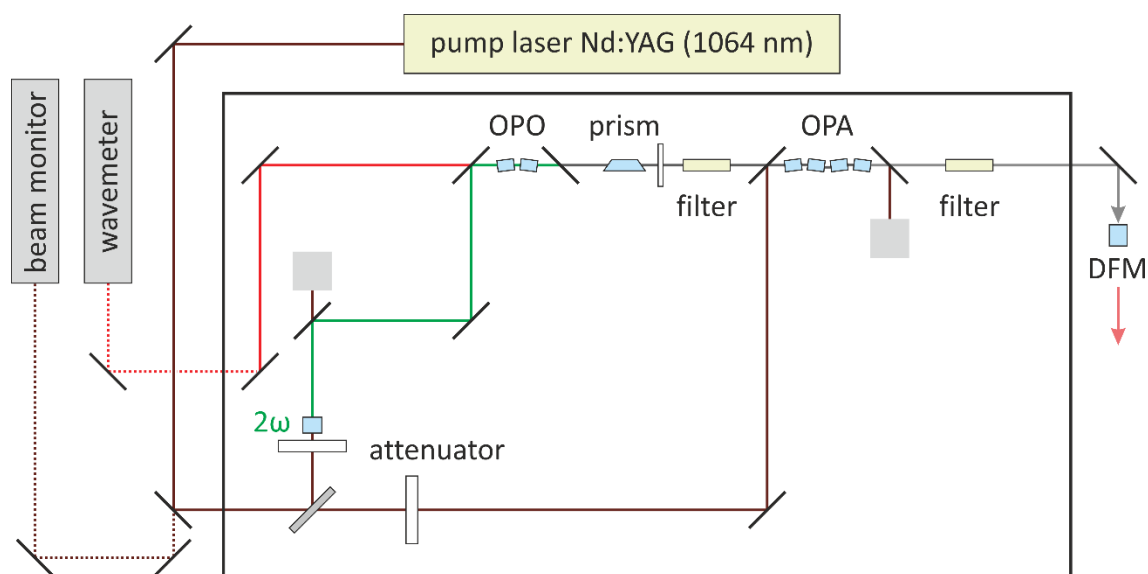


Fig. 7 Optical setup of the *LaserVision* broadband OPO/OPA laser system. Lines indicate the beam paths.

The recording of IR-(M)PD spectra over a wide frequency range requires an intense and tunable light source. Suitable IR radiation for our experiments is provided by an Optical Parametric Oscillator [49] (OPO) / Optical Parametric Amplifier [50] (OPA) laser system (*LaserVision*, Fig. 7). This laser system is pumped by a pulsed injection seeded Nd:YAG laser (*Continuum Powerlite DLS 8000*, 10 Hz, 7 ns, 530 – 600 mJ/pulse) that provides for an intense laser

radiation of 1064 nm ($\omega = 9394 \text{ cm}^{-1}$). The processes occurring within the OPO/OPA laser system and the corresponding frequency ranges are depicted in Fig. 8.

A beam splitter serves to divide the fundamental into two beam lines (Fig. 8): one third of the original intensity is frequency doubled (second harmonic generation, SHG) to 532 nm ($2\omega = 18789 \text{ cm}^{-1}$) by a potassium titanyl phosphate crystal (KTP) [51]. The second harmonic is guided into the OPO resonator and the residual fundamental beam is dumped. The OPO consists of two KTP crystals that splits the 532 nm laser beam into the signal 1 and idler 1 waves of which the signal wave is defined to have a higher frequency than the idler wave. The photon energy 2ω is conserved such that the sum of signal and idler photon energies is equal to that of the 532 nm beam. The photon energy of signal and idler is tuneable by variation of the angles between the KTP crystals and the incident 532 nm beam.

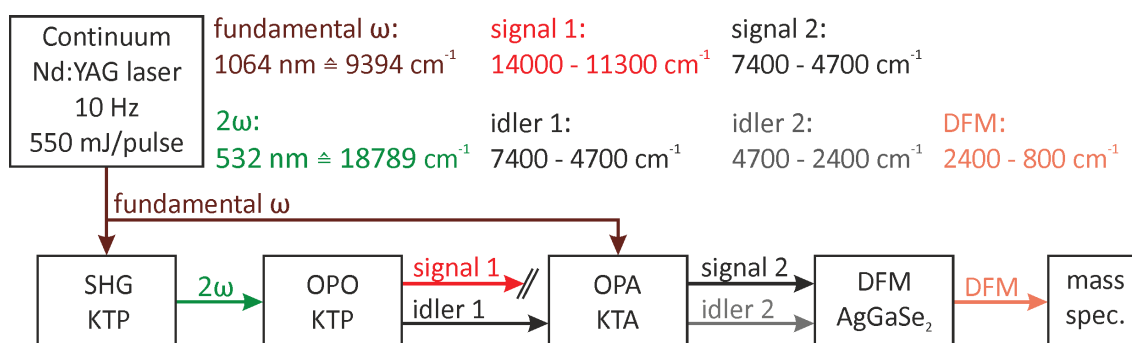


Fig. 8 Schematic representation of the non-linear optical processes and frequency conversions within the OPO / OPA laser system. Potassium titanyl phosphate (KTP) crystals serve for second harmonic generation (2ω) and constitute the optical parametric oscillator (OPO). Potassium titanyl arsenate (KTA) crystals enable the optical parametric amplification (OPA) process. Difference frequency mixing is achieved by a AgGaSe₂ crystal.

The idler 1 beam is guided to the OPA stage and the signal 1 beam is dumped by a silicon filter. A prism rotates the beam profile by 90°. The OPA stage consists of four potassium titanyl arsenate (KTA) crystals and therein, the idler 1 beam is combined with the remaining two thirds of the fundamental beam. This process generates signal 2 and idler 2 waves, where signal 2 has the same photon energy as idler 1 which thus is amplified. The remaining fundamental is dumped. The linear polarizations of signal 2 and idler 2 differ by 90° and a silicon filter tuned to the respective brewster angle may serve to dump either of them. The other beam is guided towards the mass spectrometer in order to be utilized for spectroscopy. Alternatively, both signal 2 and idler 2 are guided to a difference frequency mixing (DFM)

stage, where the difference frequency of both beams is generated. This stage consists of a silver gallium diselenide (AgGaSe₂) crystal that generates the DFM wave [52] followed by a zinc selenide (ZnSe) crystal that serves to dump the residual signal 2 and idler 2 waves.

Signal 2 and idler 2 waves provide for IR radiation in the ranges of 7400 – 4700 cm⁻¹ and 4700 – 2400 cm⁻¹, respectively. The DFM stage generates IR radiation in the range of 800 – 2400 cm⁻¹ and makes CO stretching modes, C-H bending modes and the stretching mode of adsorbed N₂ accessible for IR-(M)PD spectroscopy.

Overall, this OPO / OPA laser system provides for intense IR radiation, which can be tuned in the range of 7400 – 800 cm⁻¹, a pulse energy between 0.1 – 20 mJ/pulse and a spectral resolution of 0.9 cm⁻¹. Typical laser pulse energy curves for the measured wavenumber ranges are presented in the supplements of the following chapters. The laser system is calibrated with a wavemeter (*Bristol Instruments*, 821B-NIR) that continuously monitors the signal 1 wavelength. The beam profile of the fundamental pump beam is continuously monitored by a beam profiler camera (*DataRay Inc.*, WinCamD).

2.6 Density Functional Theory (DFT)

Comparison of the experimental results with quantum chemical calculations is crucial for a conclusive interpretation. Density Functional Theory (DFT) has established as a routinely used method for performing geometry optimizations and frequency calculations.[53-59]

The basic idea of DFT is that all properties of a quantum chemical system can be described as a functional of the electron density. This idea was first formulated by Thomas and Fermi.[60, 61] Hohenberg and Kohn proved its correctness formulating their first theorem [62] and applied the variational principle with their second theorem. Kohn and Sham concluded on a simplified expression for the energy as a functional of the electron density as follows [63]:

$$E(\rho) = T_0(\rho) + \int dr \rho(\vec{r}) \left(V_{ext}(\vec{r}) + \frac{1}{2} \varphi(\vec{r}) \right) + E_{XC}(\rho) \quad 2-14$$

$T_0(\rho)$ kinetic energy

$V_{ext}(\vec{r})$ external potential: electron in nuclear field

$\varphi(\vec{r})$ Coulomb potential

$E_{XC}(\rho)$ Exchange correlation functional

The Kohn-Sham wavefunction is a single Slater determinant that is constructed from a set of Kohn-Sham orbitals Φ_i , which are lowest energy solutions to the Schrödinger equation (2-15).

$$\left(-\frac{\hbar^2}{2m} \nabla^2 + V_{eff}(\vec{r}) \right) \Phi_i(r) = \varepsilon_i \Phi_i(r) \quad 2-15$$

$V_{eff}(\vec{r})$ effective potential

$\Phi_i(r)$ Kohn-Sham orbital i

ε_i orbital energy

Thus, the calculation simplifies from the solution of a single N-electron Schrödinger equation to the solution of N one-electron Schrödinger equations. The electron density of the entire system can now be described as:

$$\rho(\vec{r}) = \sum_i^N |\Phi_i(r)|^2 \quad 2-16$$

The solution proceeds in analogy to the Hartree-Fock formalism. In addition, the computation of the exchange-correlation energy $E_{XC}(\rho)$ is the most involving part as it comprises all unknown parts and its contribution to the energy is significant. The approximation of $E_{XC}(\rho)$ depends strongly on the used functional. Thus, the choice of the functional is crucial for the accuracy of the calculation. Local density approximation (LDA) assumes a uniform density at a local point [58] and general gradient approximation (GGA) considers a local change of density. Hybrid functionals incorporate exchange terms from Hartree-Fock theory and provide for accurate results for many systems.[64, 65] The amount of required exact exchange depends strongly on the investigated system. Commonly used functionals like B3LYP [64, 66, 67] and PBE0 [68] incorporate 20% and 25% exact Hartree-Fock exchange respectively.

Structural properties of the investigated systems base on a geometry optimization where the potential energy surface is scanned for stationary points. There the first derivative of energy as a function of the spatial coordinates equals zero. This happens at local energy minima (minimum structures) and saddle points. An evaluation of the second derivative allows for discrimination between the two cases. All positive second derivatives indicate a local minimum structure; a single negative value indicates a transition state. Starting from a multitude of initial geometries allows finding different local minima. The global minimum can

be found by comparing the relative energies of the obtained structures. Comparison of calculated linear infrared absorption spectra with experimental IR-(M)PD spectra allows for an isomer assignment and transition state calculations allow conclusions on possible reaction pathways.

In the present work, most geometry optimizations and frequency calculations were performed using the Gaussian 09 package [69]. The choice of the specific functionals and basis sets is addressed in the respective chapters. The calculations were gratefully performed on the computing clusters of the Theoretical Chemistry department under supervision of Prof. Dr. Christoph van Wüllen. The calculations of the N₂ activation and dissociation pathways in chapter 8 [70] were performed using the Gaussian 16 package [71] on the Elwetritsch HPC cluster operated by RHRK.

2.7 References

1. Dole, M., Mack, L.L., Hines, R.L., Mobley, R.C., Ferguson, L.D., and Alice, M.B., *Molecular Beams of Macroions*. J. Chem. Phys. **1968**, *49*, 2240-2249.
2. Yamashita, M. and Fenn, J.B., *Negative ion production with the electrospray ion source*. J. Phys. Chem. **1984**, *88*, 4671-4675.
3. Yamashita, M. and Fenn, J.B., *Electrospray ion source. Another variation on the free-jet theme*. J. Phys. Chem. **1984**, *88*, 4451-4459.
4. Fenn, J.B., Mann, M., Meng, C.K., Wong, S.F., and Whitehouse, C.M., *Electrospray ionization for mass spectrometry of large biomolecules*. Science **1989**, *246*, 64-71.
5. Peredkov, S., Savci, A., Peters, S., Neeb, M., Eberhardt, W., Kampschulte, H., Meyer, J., Tombers, M., Hofferberth, B., Menges, F., and Niedner-Schatteburg, G., *X-ray absorption spectroscopy of mass-selected transition metal clusters using a cyclotron ion trap: An experimental setup for measuring XMCD spectra of free clusters*. J. Electron Spectrosc. Relat. Phenom. **2011**, *184*, 113-118.
6. Dillinger, S., *Spektroskopische Untersuchungen von Stickstoff Adsorbaten auf kationischen Cobalt Clustern bei tiefen Temperaturen*. 2014, TU Kaiserslautern.
7. Kampschulte, H., *Entwicklung einer Tieftemperatur-FT-ICR Zelle und ihre Charakterisierung mittels Reaktionskinetiken und Synchrotron-Spektroskopie*. 2011.
8. Dillinger, S. and Niedner-Schatteburg, G., *Cryo trapping by FT-MS for kinetics and spectroscopy*, in *Fundamentals and Applications of FTMS*, Schmitt-Kopplin, P. and Kanawati, B., editors. **2018**, Elsevier: Cambridge. 593-621.
9. Gross, J.H., *Mass Spectrometry*. **2017**: Springer International Publishing.
10. Duncan, M.A., *Invited Review Article: Laser vaporization cluster sources*. Rev. Sci. Instrum. **2012**, *83*, 041101.
11. Berg, C., Schindler, T., Niedner-Schatteburg, G., and Bondybey, V.E., *Reactions of Simple Hydrocarbons with Nb_n⁺: Chemisorption and Physisorption on Ionized Niobium Clusters*. J. Chem. Phys. **1995**, *102*, 4870-4884.

12. Bondybey, V.E. and English, J.H., *Laser induced fluorescence of metal clusters produced by laser vaporization: Gas phase spectrum of Pb₂*. J. Chem. Phys. **1981**, *74*, 6978-6979.
13. Maruyama, S., Anderson, L.R., and Smalley, R.E., *Direct injection supersonic cluster beam source for FT-ICR studies of clusters*. Rev. Sci. Instrum. **1990**, *61*, 3686-3693.
14. Dietz, T.G., Duncan, M.A., Powers, D.E., and Smalley, R.E., *Laser Production of Supersonic Metal Cluster Beams*. J. Chem. Phys. **1981**, *74*, 6511-6512.
15. Proch, D. and Trickl, T., *A high-intensity multi-purpose piezoelectric pulsed molecular beam source*. Rev. Sci. Instrum. **1989**, *60*, 713-716.
16. Lawrence, E.O. and Edlefsen, N.E., *On the production of high speed protons*. Science **1930**, *72*, 372-8.
17. Lawrence, E.O. and Livingston, M.S., *The production of high speed light ions without the use of high voltages*. Phys. Rev. **1932**, *40*, 19-35.
18. Lawrence, E.O. and Cooksey, D., *On the apparatus for the multiple acceleration of light ions to high speeds*. Phys. Rev. **1936**, *50*, 1131-1140.
19. Sommer, H., Thomas, H.A., and Hipple, J.A., *The Measurement of e/M by Cyclotron Resonance*. Phys. Rev. **1951**, *82*, 697-702.
20. Comisarow, M.B. and Marshall, A.G., *Frequency-sweep fourier transform ion cyclotron resonance spectroscopy*. Chemical Physics Letters **1974**, *26*, 489-490.
21. Comisarow, M.B. and Marshall, A.G., *Fourier transform ion cyclotron resonance spectroscopy*. Chemical Physics Letters **1974**, *25*, 282-283.
22. Marshall, A.G., Hendrickson, C.L., and Jackson, G.S., *Fourier transform ion cyclotron resonance mass spectrometry: A primer*. Mass Spectrom Rev **1998**, *17*, 1-35.
23. Marshall, A.G., *Milestones in Fourier transform ion cyclotron resonance mass spectrometry technique development*. Int. J. Mass Spectrom. **2000**, *200*, 331-356.
24. Caravatti, P. and Allemann, M., *The 'infinity cell': A new trapped-ion cell with radiofrequency covered trapping electrodes for fourier transform ion cyclotron resonance mass spectrometry*. Org. Mass Spectrom. **1991**, *26*, 514-518.
25. Schweikhard, L., Ziegler, J., Bopp, H., and Lutzenkirchen, K., *The Trapping Condition and a New Instability of the Ion Motion in the Ion-Cyclotron Resonance Trap*. Int. J. Mass Spectrom. **1995**, *141*, 77-90.
26. Church, D.A., *Collision measurements and excited-level lifetime measurements on ions stored in Paul, Penning and Kingdon ion traps*. Physics Reports **1993**, *228*, 253-358.
27. Graf, M., *Entwicklung eines auf Evolutionsstrategien basierenden Computerprogrammes zum optimierten Anpassen kinetischer Daten aus FT-ICR-Massenspektrometrie-Messungen*. September 2006, TU Kaiserslautern.
28. Ehrhard, A.A., Klein, M.P., Mohrbach, J., Dillinger, S., and Niedner-Schatteburg, G., *Cryokinetics and spin quenching in the N₂ adsorption onto rhodium cluster cations*. Mol. Phys. **2021**, e1953172.
29. Su, T. and Bowers, M.T., *Ion-polar molecule collisions. Effect of molecular size on ion-polar molecule rate constants*. J. Am. Chem. Soc. **1973**, *95*, 7609-7610.
30. Su, T. and Bowers, M.T., *Ion-polar molecule collisions. Proton transfer reactions of H₃⁺ and CH₅⁺ to the geometric isomers of difluoroethylene, dichloroethylene, and difluorobenzene*. J. Am. Chem. Soc. **1973**, *95*, 1370-1373.
31. Su, T. and Bowers, M.T., *Theory of ion-polar molecule collisions. Comparison with experimental charge transfer reactions of rare gas ions to geometric isomers of difluorobenzene and dichloroethylene*. J. Chem. Phys. **1973**, *58*, 3027-3037.

32. Su, T. and Bowers, M.T., *Ion-Polar molecule collisions: the effect of ion size on ion-polar molecule rate constants; the parameterization of the average-dipole-orientation theory*. Int. J. Mass Spectrom. **1973**, *12*, 347-356.
33. Balteanu, I., Balaj, O.P., Fox-Beyer, B.S., Rodrigues, P., Barros, M.T., Moutinho, A.M.C., Costa, M.L., Beyer, M.K., and Bondybey, V.E., *Size- and Charge-State-Dependent Reactivity of Azidoacetonitrile with Anionic and Cationic Rhodium Clusters Rh_n^\pm* . Organometallics **2004**, *23*, 1978-1985.
34. Anderson, M.L., Ford, M.S., Derrick, P.J., Drewello, T., Woodruff, D.P., and Mackenzie, S.R., *Nitric Oxide Decomposition on Small Rhodium Clusters, Rh_n^+* . J. Phys. Chem. A **2006**, *110*, 10992-11000.
35. Kummerlöwe, G. and Beyer, M.K., *Rate estimates for collisions of ionic clusters with neutral reactant molecules*. Int. J. Mass Spectrom. **2005**, *244*, 84-90.
36. Polfer, N.C. and Oomens, J., *Vibrational Spectroscopy of Bare and Solvated Ionic Complexes of Biological Relevance*. Mass Spectrometry Reviews **2009**, *28*, 468-494.
37. Polfer, N.C., *Infrared multiple photon dissociation spectroscopy of trapped ions*. Chem Soc Rev **2011**, *40*, 2211-2221.
38. Oomens, J., Sartakov, B.G., Meijer, G., and von Helden, G., *Gas-phase infrared multiple photon dissociation spectroscopy of mass-selected molecular ions*. Int. J. Mass Spectrom. **2006**, *254*, 1-19.
39. Fung, Y.M.E., Kjeldsen, F., Silivra, O.A., Chan, T.W.D., and Zubarev, R.A., *Facile Disulfide Bond Cleavage in Gaseous Peptide and Protein Cations by Ultraviolet Photodissociation at 157 nm*. Angew. Chem., Int. Ed. **2005**, *44*, 6399-6403.
40. Roithova, J., *Characterization of reaction intermediates by ion spectroscopy*. Chem Soc Rev **2012**, *41*, 547-59.
41. Lupo, D.W. and Quack, M., *IR-laser photochemistry*. Chem. Rev. **1987**, *87*, 181-216.
42. Grant, E.R., Schulz, P.A., Sudbo, A.S., Shen, Y.R., and Lee, Y.T., *Is Multiphoton Dissociation of Molecules a Statistical Thermal Process?* Phys. Rev. Lett. **1978**, *40*, 115-118.
43. Schröder, D., Schwarz, H., Milko, P., and Roithová, J., *Dissociation Routes of Protonated Toluene Probed by Infrared Spectroscopy in the Gas Phase*. J. Phys. Chem. A **2006**, *110*, 8346-8353.
44. Simon, A., Joblin, C., Polfer, N., and Oomens, J., *Infrared spectroscopy of $[XFeC_{24}H_{12}]^+$ ($X = C_5H_5, C_5(CH_3)_5$) complexes in the gas phase: Experimental and computational studies of astrophysical interest*. J. Phys. Chem. A **2008**, *112*, 8551-8560.
45. Wolk, A.B., Leavitt, C.M., Garand, E., and Johnson, M.A., *Cryogenic ion chemistry and spectroscopy*. Acc Chem Res **2014**, *47*, 202-210.
46. Atkins, P.W. and De Paula, J., *Atkins' Physical chemistry*, in. **2006**, Oxford University Press: Oxford ; New York. 630.
47. Trapnell, B.M.W. and Hayward, D.O., *Chemisorption*. 2d ed. **1964**, London: Butterworths.
48. Bligaard, T. and Nørskov, J.K., *Chapter 4 - Heterogeneous Catalysis*, in *Chemical Bonding at Surfaces and Interfaces*. **2008**, Elsevier: Amsterdam. 255-321.
49. Eckardt, R.C., Nabors, C.D., Kozlovsky, W.J., and Byer, R.L., *Optical Parametric Oscillator Frequency Tuning and Control*. J Opt Soc Am B **1991**, *8*, 646-667.
50. Brida, D., Manzoni, C., Cirimi, G., Marangoni, M., De Silvestri, S., and Cerullo, G., *Generation of broadband mid-infrared pulses from an optical parametric amplifier*. Opt Express **2007**, *15*, 15035-15040.

-
51. Franken, P.A., Weinreich, G., Peters, C.W., and Hill, A.E., *Generation of Optical Harmonics*. Phys. Rev. Lett. **1961**, 7, 118-119.
 52. Gerhards, M., *High energy and narrow bandwidth mid IR nanosecond laser system*. Opt. Commun. **2004**, 241, 493-497.
 53. Szabo, A. and Ostlund, N.S., *Modern quantum chemistry : introduction to advanced electronic structure theory*. **1996**, Mineola, N.Y.: Dover Publications.
 54. Capelle, K., *A bird's-eye view of density-functional theory*. Brazilian Journal of Physics **2006**, 36, 1318-1343.
 55. Koch, W. and Holthausen, M.C., *A chemist's guide to density functional theory*. 2nd ed. **2001**, Weinheim ; New York: Wiley-VCH.
 56. Peter W. Atkins, R.S.F., *Molecular Quantum Mechanics*. **2011**, Oxford, New York: Oxford University Press.
 57. Levine, I.N., *Quantum Chemistry*. **2014**, Boston: Pearson.
 58. Kohn, W., Becke, A.D., and Parr, R.G., *Density Functional Theory of Electronic Structure*. The Journal of Physical Chemistry **1996**, 100, 12974-12980.
 59. Parr, R.G. and Yang, W., *Density-functional theory of the electronic structure of molecules*. Annu Rev Phys Chem **1995**, 46, 701-28.
 60. Thomas, L.H., *The calculation of atomic fields*. Mathematical Proceedings of the Cambridge Philosophical Society **1927**, 23, 542-548.
 61. Fermi, E., *Eine statistische Methode zur Bestimmung einiger Eigenschaften des Atoms und ihre Anwendung auf die Theorie des periodischen Systems der Elemente*. Zeitschrift für Physik **1928**, 48, 73-79.
 62. Hohenberg, P. and Kohn, W., *Inhomogeneous Electron Gas*. Phys. Rev. B **1964**, 136, B864-B871.
 63. Kohn, W. and Sham, L.J., *Self-Consistent Equations Including Exchange and Correlation Effects*. Phys. Rev. **1965**, 140, A1133-A1138.
 64. Becke, A.D., *Density-functional thermochemistry. III. The role of exact exchange*. J. Chem. Phys. **1993**, 98, 5648-5652.
 65. Becke, A.D., *A new mixing of Hartree-Fock and local density-functional theories*. J. Chem. Phys. **1993**, 98, 1372-1377.
 66. Lee, C., Yang, W., and Parr, R.G., *Development of the Colle-Salvetti correlation-energy formula into a functional of the electron density*. Physical review. B, Condensed matter **1988**, 37, 785-789.
 67. Stephens, P.J., Devlin, F.J., Chabalowski, C.F., and Frisch, M.J., *Ab Initio Calculation of Vibrational Absorption and Circular Dichroism Spectra Using Density Functional Force Fields*. The Journal of Physical Chemistry **2002**, 98, 11623-11627.
 68. Adamo, C. and Barone, V., *Toward reliable density functional methods without adjustable parameters: The PBE0 model*. J. Chem. Phys. **1999**, 110, 6158-6170.
 69. Frisch, M.J., Trucks, G.W., Schlegel, H.B., Scuseria, G.E., Robb, M.A., Cheeseman, J.R., Scalmani, G., Barone, V., Mennucci, B., Petersson, G.A., Nakatsuji, H., Caricato, M., Li, X., Hratchian, H.P., Izmaylov, A.F., Bloino, J., Zheng, G., Sonnenberg, J.L., Hada, M., Ehara, M., Toyota, K., Fukuda, R., Hasegawa, J., Ishida, M., Nakajima, T., Honda, Y., Kitao, O., Nakai, H., Vreven, T., Montgomery Jr., J.A., Peralta, J.E., Ogliaro, F., Bearpark, M.J., Heyd, J., Brothers, E.N., Kudin, K.N., Staroverov, V.N., Kobayashi, R., Normand, J., Raghavachari, K., Rendell, A.P., Burant, J.C., Iyengar, S.S., Tomasi, J., Cossi, M., Rega, N., Millam, N.J., Klene, M., Knox, J.E., Cross, J.B., Bakken, V., Adamo, C., Jaramillo, J., Gomperts, R., Stratmann, R.E., Yazyev, O., Austin, A.J., Cammi, R., Pomelli, C., Ochterski, J.W., Martin, R.L., Morokuma, K., Zakrzewski, V.G., Voth, G.A., Salvador, P.,
-

- Dannenberg, J.J., Dapprich, S., Daniels, A.D., Farkas, Ö., Foresman, J.B., Ortiz, J.V., Cioslowski, J., and Fox, D.J., *Gaussian 09, Revision D.01*. 2009, Gaussian, Inc.: Wallingford, CT, USA.
70. Fries, D.V., Klein, M.P., Steiner, A., Prosenc, M.H., and Niedner-Schatteburg, G., *Observation and Mechanism of Cryo N₂ Cleavage by a Tantalum Cluster*. *Phys. Chem. Chem. Phys.* **2021**, *23*, 11345-11354.
71. Frisch, M.J., Trucks, G.W., Schlegel, H.B., Scuseria, G.E., Robb, M.A., Cheeseman, J.R., Scalmani, G., Barone, V., Petersson, G.A., Nakatsuji, H., Li, X., Caricato, M., Marenich, A.V., Bloino, J., Janesko, B.G., Gomperts, R., Mennucci, B., Hratchian, H.P., Ortiz, J.V., Izmaylov, A.F., Sonnenberg, J.L., Williams, Ding, F., Lipparini, F., Egidi, F., Goings, J., Peng, B., Petrone, A., Henderson, T., Ranasinghe, D., Zakrzewski, V.G., Gao, J., Rega, N., Zheng, G., Liang, W., Hada, M., Ehara, M., Toyota, K., Fukuda, R., Hasegawa, J., Ishida, M., Nakajima, T., Honda, Y., Kitao, O., Nakai, H., Vreven, T., Throssell, K., Montgomery Jr., J.A., Peralta, J.E., Ogliaro, F., Bearpark, M.J., Heyd, J.J., Brothers, E.N., Kudin, K.N., Staroverov, V.N., Keith, T.A., Kobayashi, R., Normand, J., Raghavachari, K., Rendell, A.P., Burant, J.C., Iyengar, S.S., Tomasi, J., Cossi, M., Millam, J.M., Klene, M., Adamo, C., Cammi, R., Ochterski, J.W., Martin, R.L., Morokuma, K., Farkas, O., Foresman, J.B., and Fox, D.J., *Gaussian 16, Revision C.01*. 2016: Wallingford, CT.

3. Infrared Spectroscopic Investigation of Structures and N₂ Adsorption Induced Relaxations of Isolated Rhodium Clusters

Matthias P. Klein, Amelie A. Ehrhard, Jennifer Mohrbach, Sebastian Dillinger,
and Gereon Niedner-Schatteburg

*Fachbereich Chemie and Forschungszentrum OPTIMAS,
Technische Universität Kaiserslautern, 67663 Kaiserslautern, Germany*

3.1 Preamble

The following chapter is a reprint of a publication in the journal „Topics in Catalysis“.

An experimental team consisting of A. Ehrhard, S. Dillinger, J. Mohrbach and me conducted the experiments. I conducted the data evaluation and the quantum chemical calculations. I wrote the initial manuscript and revised it with the help of G. Niedner-Schatteburg and S. Dillinger.

Full Reference:

Infrared Spectroscopic Investigation of Structures and N₂ Adsorption Induced Relaxations of Isolated Rhodium Clusters

M. P. Klein, A. A. Ehrhard, J. Mohrbach, S. Dillinger, and Gereon Niedner-Schatteburg, *Topics in Catalysis* **2018**, *61*, 106-118.

<https://doi.org/10.1007/s11244-017-0865-2>

3. Infrared Spectroscopic Investigation of Structures and N₂ Adsorption Induced Relaxations of Isolated Rhodium Clusters

3.2 Reprint

Reprinted by permission from Springer Nature Customer Service Centre GmbH: Springer Nature Topics in Catalysis, **M. P. Klein**, et al. *Topics in Catalysis* 2018, **61**, 106-118., Copyright 2018.

<https://doi.org/10.1007/s11244-017-0865-2>

This Agreement between Mr. Matthias Klein ("You") and Springer Nature ("Springer Nature") consists of your license details and the terms and conditions provided by Springer Nature and Copyright Clearance Center.

License Number	5100390621819
License date	Jul 01, 2021
Licensed Content Publisher	Springer Nature
Licensed Content Publication	Topics in Catalysis
Licensed Content Title	Infrared Spectroscopic Investigation of Structures and N ₂ Adsorption Induced Relaxations of Isolated Rhodium Clusters
Licensed Content Author	Matthias P. Klein et al
Licensed Content Date	Nov 8, 2017
Type of Use	Thesis/Dissertation
Requestor type	academic/university or research institute
Format	print and electronic
Portion	full article/chapter
Will you be translating?	no
Circulation/distribution	50000 or greater
Author of this Springer Nature content	yes
Title	Dinitrogen Adsorption and Activation on Pure and Alloy Metal Cluster Cations Studied by Cryo Adsorption Kinetics and Infrared Spectroscopy
Institution name	TU Kaiserslautern
Expected presentation date	Jul 2021
Requestor Location	Mr. Matthias Klein Erwin-Schroedinger-Str. 52 Kaiserslautern, 67663 Germany Attn: TU Kaiserslautern
Total	0.00 EUR



Infrared Spectroscopic Investigation of Structures and N₂ Adsorption Induced Relaxations of Isolated Rhodium Clusters

Matthias P. Klein¹ · Amelie A. Ehrhard¹ · Jennifer Mohrbach¹ · Sebastian Dillinger¹ · Gereon Niedner-Schatteburg¹

Published online: 8 November 2017
© Springer Science+Business Media, LLC 2017

Abstract This paper presents a combined IR photo dissociation (IR-PD) spectroscopic and DFT computational study of cold Rhodium cluster N₂ adsorbate complexes, [Rh_i(N₂)_m]⁺ = (i,m), in the ranges of i = 6, ..., 15 and m = 1, ..., 16. DFT modelling of naked Rhodium clusters Rh_i⁺, i = 6, 7, 9 reveals high spin states (10tet, 13tet, and 17tet) of octahedral structures (i = 6, 7), and a tricapped trigonal prism (i = 9). The IR spectra of single N₂ adsorptions red shift in line with the established charge dilution model, and they reveal evidence for structural and/or spin isomers in cases of larger clusters (i, 1), i ≥ 12. The IR spectra of cluster adsorbate complexes at or close to N₂ saturation indicate strong vibrational couplings and likely isomorphism. Together, the IR-PD and DFT spectra of the [Rh₇(N₂)₁₂]⁺ = (7,12) complex reveal spin quenching into a triplet state—as compared to the 13tet state of naked Rh₇⁺. This study is the starting point for systematic investigations of Rhodium cluster N₂ adsorbates and of Rhodium Iron hetero cluster N₂ adsorbates, which are work in progress.

Keywords Rhodium clusters · N₂ adsorption · Infrared spectroscopy · Adsorbate induced surface relaxation

Electronic supplementary material The online version of this article (doi:10.1007/s11244-017-0865-2) contains supplementary material, which is available to authorized users.

✉ Gereon Niedner-Schatteburg
gns@chemie.uni-kl.de

¹ Fachbereich Chemie and Forschungszentrum OPTIMAS,
TU Kaiserslautern, 67663 Kaiserslautern, Germany

1 Introduction

The study of the physical properties of isolated clusters and of their molecular adsorption kinetics, structures, and vibrational dynamics may enhance our understanding of elementary steps in the early parts of heterogeneous catalytic cycles which are most often based on transition metal compounds. Despite its high price, Rhodium catalysts find widespread applications in many industrial catalytic processes such as cyclopropanation [1, 2], hydroformylation [3], and the manufacturing of acetic acid [4]. Nitrogen containing compounds form by Rhodium catalysis in processes such as hydrocyanation, hydroamination, and ammonia oxidation. Rhodium catalysts achieve deoxygenation [5, 6] and hydrogenation [7] of nitrogen compounds. Rhodium finds wide spread practical use in car exhaust catalytic converters, where nitrogen oxides are reduced to N₂ [8], and it finds some use in stationary power plant exhaust cleaning [9].

In many cases the active catalyst is nanostructured, and the initial adsorption steps from gas phase are rate limiting—whether recognized or overlooked. It is obviously beneficial to study fundamental processes such as molecular adsorption and desorption, and to characterize suitable model systems such as size selected Rhodium clusters, and their adsorbates and products.

There are numerous studies on Rh gas phase clusters and complexes. Isolated Rh(I) atoms hexacoordinate a first layer of Ar atoms [10]. Numerous diatomic molecules (D₂, O₂, CO, and NO) were found to stick readily to Rhodium clusters by room temperature single collisions—except for N₂, which requires precooling of the clusters (by lq. N₂) [11, 12]. An early study found an anticorrelation between D₂ and N₂ reactivity and the Fermi energy of the neutral Rh_n clusters [13].

CO Mineva et al. found a strong effect of the spin state (and local electronics/NBOs) on vibrational frequencies of Rh_x(CO)_y, and a weaker effect of cluster size x [14]. CO proved instrumental to unravel size and charge dependencies in adsorption to Rh cluster cations and anions alike, convincingly concluding in a charge dilution model [15–19]. Subsequent studies identified CO on top and on bridge throughout all Rh clusters studied except for Rh₄ and Rh₁₁ where CO on hollow site was observed instead [20]. For larger clusters, Tian et al. found a transition to layered structures in Rh clusters at $n = 11$ – 12 and three types of CO adsorption, not scalable with size: atop, bridge, and face [21]. Non hybrid DFT functional modelling of Rh_i(CO)₁^{+0/-} complexes found trigonal prismatic and cubic structural motifs of the cluster core [22] and end on bridging μ_2/μ_3 adsorption motifs of CO on the charged clusters up to $i = 6$ and a end on μ_1 motif for the larger clusters [23].

NO_x Biexponential kinetics of the initial adsorption step in the Rh₆⁺ + NO system suggested the co-existence of stable isomers [24] that quench upon collisional cooling, while the co-existing isomers of Rh₁₁⁺ and Rh₁₂⁺ persist [25, 26]. DFT modelling elucidated the likely structures of the reactive [Rh₆NO]⁺ system [27] and of the [Rh_{3,4,6,13}NO]^{+/-} systems [28] in detail. NO adsorption was found with Rhodium clusters of any size, while NO reduction takes clusters Rh_n⁺, $n > 5$ and elevated temperatures ($T > 850$ K) [29]. A series of studies identified nitrogen-bound NO and N₂O on various Rh_n⁺ clusters and IR driven or collisional decomposition [30–34]. The Tantalum alloying of Rhodium clusters was found to control NO reduction [35]. Relativistic ZORA level calculations found the N₂O reduction on Rh₆⁻ and Rh₆⁺ sensitive to the cluster charge, rather than to its geometry [36]. The adsorption of a second NO was identified as rate limiting step in CO oxidation on Rh₇⁺ by DFT modelling [37], other calculations modelling NO reduction by CO on Rh₄⁺ [38].

Hydrocarbon Reactions Rhodium cluster Argon complexes modulate CH₄ activation by the level of Ar coating [10, 39]. Benzene adsorption and activation compete on Rh_n⁺ clusters for $n < 19$, the larger ones becoming inert [40] and cluster charge having unexpectedly little effect on the dehydrogenation reactivity [41]. Partial dehydrogenation of small alkanes by Rh_n⁺, $n < 30$ indicated a bi-icosahedral shape of Rh₁₉⁺ [42], supported by lack of reactivity with ethane at $n = 17$ – 19 , 21 [43]. Azidoacetonitrile (N₃CH₂CN) was found to readily releases N₂ + H₂ upon contact to Rh_n⁺ generating either interstitial carbides and nitrides, or yielding surface nitriles [44].

Electronics and Magnetism Rhodium cluster geometries by model potentials and magnetism by tight binding have reached limits in simulating magnetic moments of Rhodium clusters [45]. A more recent relativistic modelling study spent high effort on an appropriate description of the

electronics of such Rh_n clusters in order to determine the magnetic moments by their spin and orbital contributions. It suffered, however, from little effort on the nuclear coordinates merely assuming fcc lattices of spherical shape without geometric relaxation [46]. DFT modelling of single and multiple charges was found to exert strong influence on the structure and magnetism of Rhodium clusters [47]. Choice of a large basis sets in DFT modelling was found crucial before in order to obtain converged predictions on structures of Rh_n, $n \leq 6$ [48]. Simultaneously performed magnetic and electric deflection measurements of Rhodium clusters (Rh_n, $6 \leq n \leq 40$) reveal ferromagnetism and ferroelectricity at low temperatures neither of which property exists in the bulk metal [49]. Nevertheless, our knowledge of the electronic and magnetic properties of small Rhodium clusters is still limited, and the different structural and spin isomers are very close in energy [50].

A significant advance on the structural elucidation of Rh_n⁺ clusters arose through free electron laser and Argon tagging enabled vibrational spectroscopy in conjunction with corresponding DFT modelling (PBE(1)/LanL2DZ) of the obtained spectra [26, 51]. The following was found: octahedral structure motifs for the Rh₆⁺ and Rh₈⁺ cluster, a pentagonal bipyramidal structure for the Rh₇⁺ cluster, a trigonal prismatic structure for the Rh₉⁺ cluster, and icosahedral structural motif for larger clusters up to Rh₁₂⁺. This as well as another DFT study [52] left some room for improvement in terms of the usage of more advanced basis sets. These investigations are the first to demonstrate the importance of hybrid functionals for the investigation of Rhodium clusters.

Basin hopping DFT calculations predicted various properties of Rh_xS_y^{+0/-} ($x = 1$ – 9 ; $y = 0, 1$) clusters and emphasized the importance of hybrid_GGA functionals (e.g. PBE0) while questioning the appropriate percentage of exact Hartree–Fock exchange, and concluding on ambiguities in current spin state determination [53].

Prior N₂ Vibrations FT-IR studies of laser ablated Rh atoms in N₂ doped Ar matrix revealed numerous bands in the 600–2200 cm⁻¹ range which were attributed to Rh(N₂)_{1–4} and other small Rh_xN_y products [54]. Investigation of an isolated Rh(N₂)₄⁺ complex by IRMPD spectroscopy obtained an N₂ stretch at 2297 cm⁻¹ band [55] which is much less red shifted than in the neutral complexes and close to the free N₂ stretch at 2330 cm⁻¹ [56]. This is likely due to less back bonding by cationic Rh.

Our Study We present an IR spectroscopic study of Dinitrogen on cold Rhodium cluster adsorbate complexes with support by some DFT calculations in three cases, Rh_i⁺ ($i = 6, 7, \text{ and } 9$), and we chose the experimental and calculated IR spectra of the [Rh₇(N₂)₁₂]⁺ cluster adsorbate complex for an analysis in more detail. Considering conceivable Rh cluster isomerization barriers on the order of N₂ heats of adsorption we expect considerable structural relaxation in the cluster

adsorbate complexes as of relevance in the context of catalytically active clusters and nanoparticles in operando.

2 Experimental

The experiments were performed by a customized 7 T Fourier Transform-Ion Cyclotron Resonance (FT-ICR)-mass spectrometer (Apex Ultra, Bruker Daltonics). We produced the cluster ions in a home-built laser vaporization source as described before [57–59]. The second harmonic of a Nd:YAG laser is focused on a rotating Rhodium-target (99.8%, Alfa Aesar, 0.1 mm thick). The resulting plasma is entrained in a helium gas pulse (40 μ s, 10–15 bar), which was generated by a homemade piezoelectric valve [60], synchronized to the evaporating laser at 20 Hz. The pressure of the laser vaporization chamber rises from roughly 3.5×10^{-7} to 1.6×10^{-4} mbar during He pulsing. The plasma contains atoms and ions and while they cool down, they aggregate to clusters in the subsequent jet expansion through a 50 mm long channel (2 mm diameter) into vacuum (3×10^{-7} mbar). The cluster beam is skimmed and the cluster ions are accelerated and guided through a 90° static quadrupole ion bender. The required cluster ions are selected by an RF quadrupole mass filter and stored into a cryogenic hexapole ion trap at 26 K which is held at 3.0×10^{-6} mbar He buffer gas pressure. We achieve Nitrogen attachment by constantly adding 3.0 – 3.8×10^{-7} mbar N_2 . Then we use He to increase the pressure in the ion trap to roughly 4.0×10^{-6} mbar. Within ion storage times of up to 2 s all Rhodium clusters reach adsorbate saturation, and we randomly checked for much longer times no further attachment being observed. Subsequently, all stored ions are gently extracted with as little potential gradient as possible, accelerated, steered and decelerated into the ICR-cell by a high definition electrostatic ion lense setup [61, 62]. Transfer and trapping efficiency is about 10%. The ICR-cell of the infinity-type [63] is cooled to 10 K by a closed cycle He cryostat [64, 65] in order to prevent activation of the clusters by black body radiation [66, 67]. In order to record IR-PD spectra of $[Rh_i(N_2)_m]^+$ cluster adsorbate complexes by their sizes (i,m) we isolate the parent cluster ion of interest by RF exciting and removing all other ions from the cell.

For the acquisition of the IR-PD spectra the FT-ICR cell is coupled to a tunable IR laser ($\delta n = 0.9 \text{ cm}^{-1}$, $\delta t = 7 \text{ ns}$, $E_{\text{puls}} = 0.4$ – 1.3 mJ). This laser is a KTP/KTA optical parametric oscillator/amplifier (OPO/A, LaserVision) system which is pumped by a pulsed 10 Hz injection seeded Nd:YAG laser (PL8000, Continuum). The difference frequency (DF) between the OPA signal and idler waves is generated in an AgGaSe₂ crystal. This generates IR radiation in the range of 1000–2400 cm^{-1} . Each trapped and isolated package of ions is irradiated by multiple laser pulses (up to

7) in order to accumulate fragment ions. The IR-PD spectra were recorded as ion chromatograms while continuously scanning the IR wavelength. The IR-PD signal was evaluated as $\sum_i F_i / (\sum_i F_i + \sum_i P_i)$, where F_i and P_i indicate fragment and the parent ion signals, respectively. An experimental IR-PD spectrum arises from a plot of the fragmentation efficiency as a function of laser frequency. We employed the IR-PD spectroscopy in the 2140–2310 cm^{-1} range on the $[Rh_i(N_2)_m]^+$ species (i=6–15). In this range we expected the N_2 stretching frequencies of the species. For all complexes the loss of the N_2 was the only observed fragmentation channel. Note, that IR-PD spectra of (i,m) species with high m likely originate from single photon absorption, whereas those of low m likely originate from two or even multiple photon absorption—rendering the latter IRMPD spectra.

Density functional modelling was performed by the Gaussian 09 package [68] and with the ECCE interface [69]. We chose the PBE0/ECP(Rh); cc-PVTZ(N) level of theory [70] as proven suitable before [57, 71, 72]. We utilize Stuttgart RSC 1997 ECP(Rh) basis sets of double zeta quality throughout [73] which are of significantly higher quality than the often applied basis set LanL2DZ. We did not correct for dispersion effects which we expect small. We do not cover spin orbit coupling which might alter some of our findings. We achieved convergence of our calculation only at the expense of a relaxed convergence criterion of only 10^{-6} , which is well understood in terms of the exceedingly high electronic state density of transition metal clusters [39]. We chose an anharmonic linear scaling factor of 0.9385 to match the calculated free N_2 stretching frequency (2483 cm^{-1}) to the Raman band of free N_2 at 2330 cm^{-1} [56]. We checked the results for spin contamination, and we observed a small rise of the S^2 value merely in cases of the lowest multiplicities and negligible spin state mixing otherwise. We regard our theoretical approach as well gauged by considering our single N_2 adsorption enthalpies of about 50 kJ/mol (lower limit) in comparison to 56 kJ/mol on stepped Rh surfaces as obtained before [74, 75].

3 Results and Discussion

3.1 DFT Modelling of Naked Rh_i^+ Clusters (i = 6, 7, and 9)

In order to lay ground for the characterization of N_2 adsorption to the Rh clusters we set off with DFT modelling of the naked Rh clusters in the first place. We focused on Rh_i^+ (i = 6, 7, and 9) in order to identify most stable structures and competing isomers. In particular, we strived to elucidate the prevailing spin states and their interplay with nuclear geometries, and we have investigated Rh_7^+ in depth. We checked the obtained minimum structures for imaginary vibrational

frequencies and found all reported isomers to be true minimum structures.

3.1.1 Rh₆⁺

In the case of the Rh₆⁺ cluster we started from the three suggested geometries of Harding et al.: a boat like structure (boat), a capped square prism (csp), and an octahedron (oct). We found it appropriate to consider a trigonal prism (tp) as well. Upon investigating these structures, we utilized an extended range of spin multiplicity $2S + 1 = 2–18$. We found the Rh₆⁺ clusters to isomerize significantly upon optimization, in remarkable contrast to the cases of Rh₇⁺ and Rh₉⁺ clusters, and we provide for a comprehensive overview over the found evolution of starting structures towards optimized structures in the supplementary material (Table S2).

The 10tet spin state in octahedral geometry (oct) is the optimum of Rh₆⁺ at the level of our DFT calculation (Fig. 1). At all lower spin states down to the doublet the octet minimum structure persists with slight distortions. Increasing total spin beyond 10tet is possible at the expense of reorganization towards a boat like structure. The stability gain by turning two fourfold coordinated Rh atoms into fivefold coordinated ones overcompensates the loss by turning two other fourfold coordinated Rh atoms into threefold coordination. Note, that spin quenching from 10tet to 8tet affords 27 kJ/mol while an isomerization of octet into capped square pyramid (csp) amounts 78 kJ/mol.

The dominance of octahedral cluster structures is in accordance with a previous study that assigned a distorted octahedron with a 10tet electronic state to their experimental

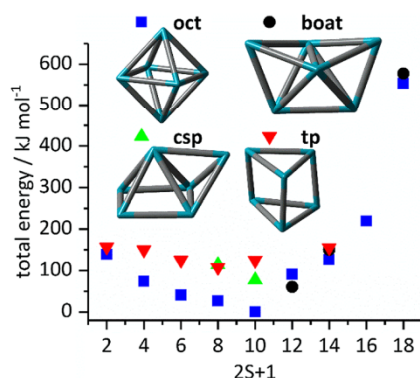


Fig. 1 Total energies of four possible Rh₆⁺ cluster structures as a function of the spin multiplicity $2S + 1$ in relation to the obtained minimum (oct 10tet). In addition a capped square prism (csp), a trigonal prism (tp), and an octahedron (oct) were considered as starting geometries. The calculated minimum structures for each structural motif are shown as insets. Remarkably, the starting structures are subject to major isomerization. The calculated minimum structure is a distorted octahedron with a 10tet spin state

spectra of a naked Rh₆⁺ cluster [51]. Our present investigation extends that work by covering spins and geometries beyond the predicted optimum. Note, that spin–orbit coupling effects in Rh are on the order of 18 kJ/mol and thus may mediate dynamic spin quenching.

3.1.2 Rh₇⁺

We find a clearly limited variation of spin couplings, while there is a considerable flexibility in nuclear rearrangement: The meridional square in octahedral geometry (coh) may open into a fivefold ring and convert into pentagonal bipyramid (pbp). In most stable 13tet spin state this isomerization would take at least ~47 kJ/mol, with a possible barrier adding on top. Spin quenching of coh 13tet into 11tet would take only 12 kJ/mol and subsequent isomerizations to a pbp structure are facile.

We optimized possible geometries and spin states of the Rh₇⁺ cluster, and we found most stable capped octahedron (coh) in 13tet and 11tet spin states which differ by ~12 kJ/mol (Fig. 2). Interestingly, the next stable pentagonal bipyramid structure is almost degenerate in 11tet, 13tet and 15tet states, yet less stable than coh by at least 29 kJ/mol. The pbp structure thus allows for considerable spin variation, while the coh is in favour of a sole spin state. The capped trigonal prism (ctp) is slightly less stable than pbp and considerably less stable than coh. Not that all of this may change through spin orbit coupling effects and/or through antiferromagnetic couplings—both of which are much beyond our current DFT approach.

Harding et al. assigned Rh₇⁺ a distorted pbp structure [51], and Hang et al. calculated most stable Rh₇⁰ as a distorted pentagonal pyramid and a capped octahedron mere 3.8 kJ/mol less stable [52]. On the other hand, electric

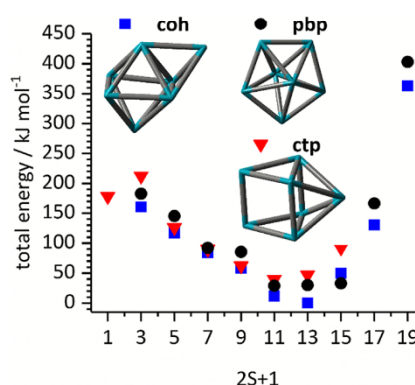


Fig. 2 Total energies of Rh₇⁺ cluster structures as a function of the spin multiplicity $2S + 1$ relative to the most stable capped 13tet of an octahedron (coh). Other structural motifs are capped trigonal prisms (ctp) and pentagonal bipyramids (pbp) as depicted by the insets

deflection studies support the dominance of a capped octahedral structure [76].

We found it appropriate to gauge our computational findings in the case of Rh_7^+ coh 13tet against other studies and species, and we took the Rh–Rh distances as elucidating indicators (see Table 1). Our found coh structure is distorted from C_{3v} symmetry of a perfect capped octahedron, and the interatomic distances deviate. All of the next neighbor distances in Rh_7^+ are considerably longer than in the dimer and somewhat shorter than the solid state values indicating a bond between the next neighbors. The calculated distances in the neutral pbp structure are in the same range.

3.1.3 Rh_9^+

In order to model the Rh_9^+ cluster we have chosen four structural archetypes for optimization: tricapped trigonal prism (tri), capped trigonal antiprismatic structure (trig-ap), double-capped pentagonal bipyramid (dc-pbp), and capped square antiprism (ac-top), and we checked for spin multiplicities $2S + 1 = 9, \dots, 21$ (Fig. 3). We find most stable a slightly distorted tricapped trigonal prism (tri, 17tet, D_{3h}), and this motif stays most stable upon total spin variation from 13tet up to 19tet. A previous study concluded in a 15tet tricapped trigonal prism with likely contributions of a dc-pbp like structure to a recorded far IR spectrum [51]. Note, that the neutral Rh_9 cluster seems to persist in a distorted tri structure type geometry in nearly degenerate 12tet and 16tet spin states [52].

3.2 IR-PD Spectra of Single N_2 Adsorbates on Rhodium Cluster Cations

We have recorded IR-PD spectra of $[\text{Rh}_i(\text{N}_2)_m]^+$ cluster adsorbate complexes. Even upon single N_2 adsorption we found a multitude of bands (Fig. 4) which are red shifted

Table 1 Calculated atomic distances (in Å) for nearest neighbors for the coh Rh_7^+ clusters in comparison with crystal structures, experimental data and calculations on a neutral 14tet pbp structure

	Dimer	Rh_7	Rh_7^+	Bulk
Calc.	2.21 ^a 2.27 ^{b1}	2.61 ^a 2.58 ^{b2} 2.37–2.60 ^{b3}	2.446–2.665 ^{tw}	
Exp.	2.3855 ^c			2.69 ^d

^{tw} this work; PBE0, coh 13tet cation

^aRef [77]. VASP PW91 GGA/LDA; Rh_7^+ : neutral pbp 14tet

^b[78] TZVP, ECP28MWB; ^{b1}neutral dimer quintet; ^{b2}neutral pentagonal bipyramid, 14tet; ^{b3}neutral capped trigonal prism, 12tet

^c[79] crystal structure of $[\text{Rh}_2(\text{O}_2\text{CCH}_3)_4(\text{H}_2\text{O})_2]$

^d[80] distance of next neighbors in fcc crystal, lattice parameter $a = 3.8032 \text{ \AA}$

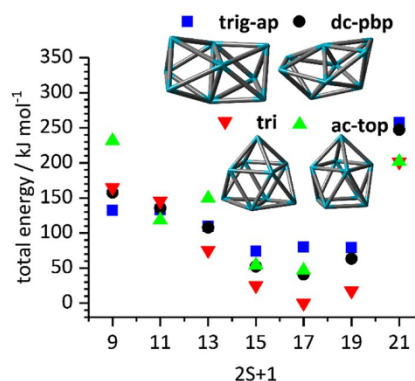


Fig. 3 Total energies of Rh_9^+ cluster structures by their spin multiplicity $2S + 1$ relative to the most stable 17tet of a tricapped trigonal prism (tri). Other structural motifs are trigonal antiprisms (trig-ap), double-capped pentagonal bipyramids (dc-pbp), and capped anti-cubes (ac-top) as depicted by the insets

by 55–120 cm^{-1} with respect to the free N_2 stretching vibration at 2330 cm^{-1} [56]. For ease of reference we will utilize in the following the abbreviating nomenclature $[\text{Rh}_i(\text{N}_2)_m]^+ = (i,m)$. The obtained band positions range from 2210 to 2275 cm^{-1} which is a range similar to the range of observed vibrations of N_2 adsorbates on cobalt clusters [57] as well as to those of nickel and iron clusters [71, 81, 82]. As for these and Ruthenium clusters [57, 71, 83], we expect a μ_1 binding motif of N_2 . There are some fluctuations of the exact band positions around the overall trend of red shift with cluster size. There are some additional strong bands ($i = 9, 12, 13, 15$) and some additional weak side bands ($i = 8, 10$ and 11) which are 20 cm^{-1} to the red (marked by red circles). This is reminiscent of similar effects in the previously reported cobalt cluster spectra [57], all of which are non-scalable cluster size effects.

The spectra of (6,1), (7,1), (8,1) (10,1) and (11,1) are dominated by a single strong peak which we assign to the stretching vibration of an N_2 adsorbate end on to the cluster surface. In these cases, we conclude in the absence of geometric isomers of the Rh cluster core, in the dominance of single spin isomers, and in the equivalence of all occupied N_2 binding sites. The additional “red circle” bands might relate to hot bands, which would arise through de-excitation of some soft Rh core vibrations—yet somewhat unlikely in view of the isothermal cryo conditions of our experiment. Other interpretations are conceivable, such as highly coordinated, semi-internal adsorption sites or even some low spin isomers. The latter come into mind when relating the most stable Rh_6^+ structures of Fig. 1 to the previously found convincing evidence of isomeric reactivity in NO attachment to Rh_6^+ [24]. It is puzzling, however, that the present (6,1) IR-PD spectra of single N_2 attachment do not reveal any evidence of geometric or electronic

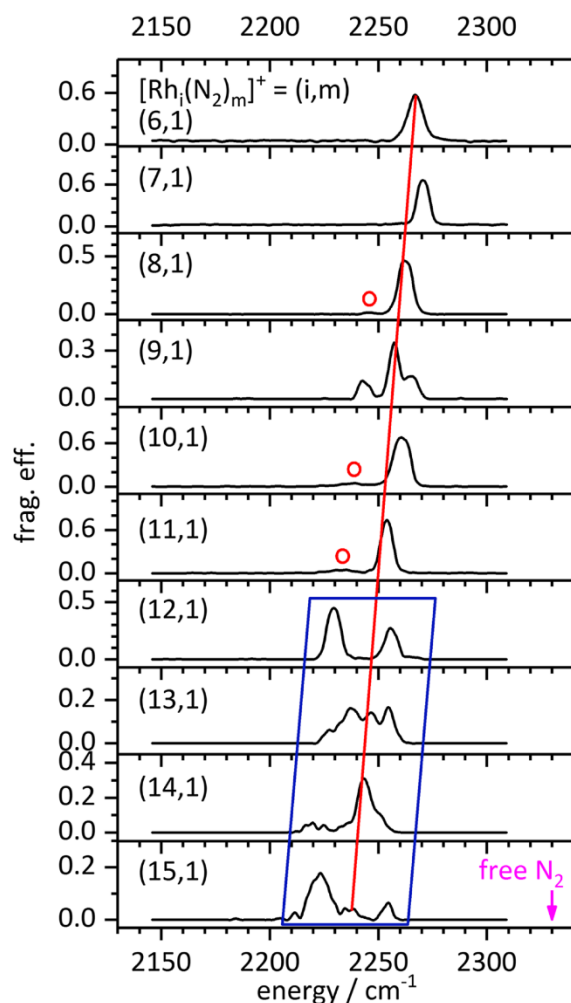


Fig. 4 IR-PD spectra of Rhodium cluster cation single N₂ adsorbate complexes $[\text{Rh}_i(\text{N}_2)_m]^+ = (i,m)$, $i=6-15$ as recorded after 26 K He buffer gas cooling. The red line and the tilted blue box serve to guide the eye indicating the red shift with cluster size i . The red circles mark possible hot bands—or possible isomers (see text for further discussion)

isomers. It takes further experiments and calculations to resolve this puzzle.

In remarkable contrast the spectra of (9,1), (12,1), (13,1) (14,1) and (15,1) reveal two, three or multiple adsorption bands within the same range. This is clear indication for some kind of isomeric co-existence. Three types of isomers come to our minds: within the cluster adsorbate complexes there might be structural isomers of the Rh cluster core. There might be coexisting complexes in different spin states. There might be adsorption site isomers. Yet conceivable, we do not find evidence for changes in coordination geometry (μ_1 , μ_2 or μ_3) which would likely lead to much larger jumps

of band positions much beyond what we observe. Note, that there is in none of the recorded cases any change of spectral features by the applied laser power (cf. Fig. S2 in the supplement).

The general red shift with respect to the free N₂ vibration is conceivable in terms of the Blyholder model [84]. This model has been developed for the explanation of the IR spectra of CO adsorbed to metal surfaces and may be applied to the isoelectronic N₂ molecule. The synergism of σ -donor and π -acceptor properties of N₂, similar to the Dewar–Chatt–Duncanson model [85, 86], leads to a weakening of the N–N bond and a red shift of the N–N stretching frequency.

There are previous studies on spectral shifts of CO adsorbates on Rhodium clusters which have been interpreted in terms of a charge dilution model [17]. We have utilized this model before in order to explain N₂ red shifts when adsorbed to Cobalt and Nickel clusters [57, 71]: An increasing dilution of the positive charge by cluster size leads to a higher electron density at each surface site and thus to an increase of the π backdonation into an antibonding π^* adsorbate orbital which causes red shift of the stretching vibration.

The structure of the Rh cluster core and the occurrence of non-equivalent adsorption sites influence the N₂ vibrations. The Rh surface atoms differ by number and arrangement of next neighbors. *Rough* cluster surfaces originate from a multitude of different adsorption sites, *smooth* cluster surfaces from equivalent ones. The occurrence of internal, inaccessible non surface atoms sets in at cluster sizes of 13 metal atoms in case of icosahedral Rh structures. Note, that in particular the Rhodium clusters are known for stiff bonds (little bond length variation) in favor of close packing and at the expense of structural ambiguity and co-existing isomers [87]. It thus seems likely that N₂ adsorption may induce cluster surface reorganization to some extent. Our own calculations reveal a strong preference of N₂ adsorbates in an end on μ_1 arrangement (on top). Any of our attempts with μ_2 (bridge) starting geometries swiftly relaxed $\mu_2 \rightarrow \mu_1$. Any adsorption site thus coincides with a single Rh surface atom.

In the light of all of the above we analyze each of the recorded (i,1) IR-PD spectra in the following: The recorded single band of the (6,1) spectrum reveals a single type of adsorption sites as e.g. by an Rh₆⁺ octahedron, in line with present and previous structure calculations [51]. The single N₂ band in the (7,1) spectrum is less red shifted indicating less π back donation as e.g. by the low coordinated Rh capping atom in our calculated octahedron Rh₇⁺ structure, which has merely three next neighbors. This is in contrast to the previous pentagonal bipyramid Rh₇⁺ structure [51] which would not provide for such a

low coordinated Rh site. It is conceivable that adsorbates induce structural relaxation. If indeed so, this would imply that π back donation of N_2 makes the difference with respect to Ar which lacks this option/effect—polarizabilities of both being almost identical. Further computations might focus onto this issue. The single strong IR-PD band of (8,1) may originate from either of two conceivable Rh cluster core geometries: a bicapped octahedron or an almost as stable bicapped trigonal prism (+ 17 kJ/mol) [26, 51] with likely swift isomerization into each other, possibly adsorption induced. Marked by a red circle in Fig. 4, this weak band to the red may originate from an N_2 at a higher coordinated Rhodium site. It is the (9,1) cluster N_2 adsorbate complex which reveals a triplet of IR-PD bands which comes as somewhat of a surprise. This work and previous computations [51] agree on Rh_9^+ in a tricapped trigonal prism geometry [88]. As such structure comes with four- and fivefold coordinated Rh atoms, it provides for two adsorption sites and accordingly, it would explain two N_2 vibrational bands. We take the observation of three N_2 vibrational bands as likely evidence for an adsorption induced relaxation and symmetry reduction of the Rh_9^+ cluster core in (9,1). In contrast to previous studies on the Rh_i^+ $i=6-8$ clusters [24, 25] we do not find any evidence for the existence of multiple isomers in the IR-PD spectra of the correspondent $[Rh_i(N_2)_m]^+$, $i=6-8$, $m=1$, Rhodium cluster single N_2 adsorbate complexes.

The single strong IR-PD band of (10,1) and (11,1) indicates a homogeneous cluster adsorbate ensemble void of N_2 binding site isomers and void of Rh cluster core structural isomers. Due to the reduced red shift of the observed N_2 vibrational bands we tentatively assign these bands to μ_1 adsorbates on top of low coordinated adsorption sites some of which occur in all suggested structures of $Rh_{10,11}^{-/0/+}$ clusters [51, 52]. Initial N_2 adsorption at higher coordinated sites stabilize into the above low coordinated sites via high adsorbate mobility on the surface of the Rh cluster cores. Once more marked by red circles in Fig. 4, these weak bands to the red may originate from N_2 at higher coordinated Rhodium sites.

The two widely split, strong IR-PD bands of (12,1) indicate a transition in the structure of the Rh cluster core and a loss of adsorbate mobility. Note, that the coexistence of cluster adsorbate isomers seems rather unlikely with regard to the considerable heat of N_2 adsorption (56 kJ/mol [74]) which is likely sufficient for annealing of the cluster structure. The predicted layered Rh_{12}^+ structure would provide for two highly coordinated central Rh atoms and ten peripheral low coordinated Rh atoms. We tentatively assign the observed two bands to these adsorption sites, the higher coordinated Rh sites causing the larger red shifts in their N_2 adsorbates. Harding et al. assigned a structure consisting of two centered pentagonal layers [51]. Thus, we can assume

the existence of two different adsorption sites reflected in the IR-PD spectra of (12,1).

The multitude of partially resolved IR bands of (13,1), (14,1), and (15,1) ask questions which hardly obtain answers without input from computations. These are not available as of now. We tentatively conclude in the occurrence of several adsorption sites and in reduced N_2 adsorbate mobility. Further insights may arise from future modelling.

3.3 IR-PD Spectra of Multiple N_2 Adsorbates on Rhodium Cluster Cations

The Rhodium clusters Rh_i^+ may adsorb N_2 up to a *maximum adsorption limit*, which is clearly related to the actual cluster structure. It is conceivable, that the $[Rh_i(N_2)_m]^+$ reorganize upon stepwise adsorption of further N_2 , and we find clear evidence in at least one case.

In the course of the present study, we recorded IR spectra of the $[Rh_i(N_2)_m]^+$ $i=6-11$ cluster adsorbate complexes at or close to N_2 saturation (Fig. 5) in order to augment/complement the IR spectra of single N_2 adsorption discussed before.

All spectra of multiple N_2 adsorptions reveal higher red shifts than those of single N_2 adsorptions. Note, that the Blyholder model would predict the opposite, a reduction of red shift upon N_2 saturation: The more N_2 molecules compete for the electrons of the cluster core, the less electron density is transferred into the π^* orbital of each N_2 molecule. Also, the Rh cluster size dependent charge dilution diminishes upon N_2 saturation, while it is clearly in effect upon attachment of the first N_2 adsorbate.

The second finding in all but one of the N_2 saturated IR-PD spectra is a significant *increase* in spectral complexity by multitudes of bands spreading out across up to 110 cm^{-1} , which is not observed upon single adsorptions. The sole exception of (9,9) is to be discussed in the following, where we will discuss the spectral features of each cluster adsorbate complex in detail.

3.3.1 $[Rh_6(N_2)_{11}]^+$, $[Rh_7(N_2)_{13}]^+$

The IR-PD spectra reveal seven partially resolved bands in the range of $2194-2268\text{ cm}^{-1}$. This multitude of the bands likely indicates the presence of diverse adsorption sites, which is in noteworthy difference to the DFT predictions of naked Rh_6^+ clusters, and to the IR-PD spectra of single N_2 adsorption, (6,1) and (7,1), see Fig. 4. We take this as a strong indication for N_2 adsorbate induced relaxation of the Rh cluster core geometries, in conjunction with possible spin state quenching. As evidenced before in the case of $[Ni_9(N_2)_2]^+$ there are symmetric and asymmetric coupling of stretching modes in adjacent N_2 adsorbates with

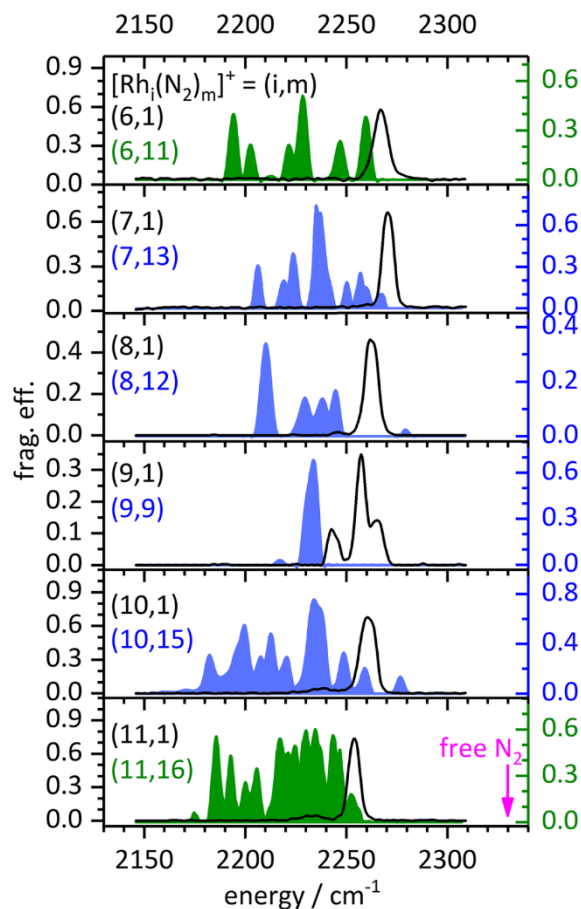


Fig. 5 IR-PD spectra of single (black line) and multiple dinitrogen adsorption on Rhodium clusters at (blue) or close to (green) saturation. The blue areas represent N₂ saturation (at 26 K), the green areas represent spectra of one N₂ adsorbate less in cases of experimental constraints

splittings on the order of 10 cm⁻¹ [71]. We expect such couplings within saturated N₂ layers on Rh cluster surfaces as well. It is hard to conceive, however, that these might make up for all of the observed spread of 70 cm⁻¹.

3.3.2 [Rh₈(N₂)₁₂]⁺

With four bands in the range of 2210–2245 cm⁻¹ the spectrum of the (8,12) cluster adsorbate complex reveals less bands than the spectrum of the smaller clusters, likely indicating a high symmetry of the cluster core with less diverse adsorption sites and less or weaker N₂–N₂ couplings. Other than at *i* = 6, 7 there is an additional weak band at 2279 cm⁻¹ which we tentatively assign to a stretch–wag combination band.

3.3.3 [Rh₉(N₂)₉]⁺

Remarkably, N₂ saturation arises at mere 1:1 stoichiometry in (9,9) while all other studied Rh_{*i*}(N₂)_{*m*}⁺ clusters saturate at significantly higher N₂ loads close to a 1:2 ratio. In the (9,9) cluster adsorbate complex, [Rh₉(N₂)₉]⁺, the small increase in red shift comes with a *reduction* of complexity: Three bands in (9,1) seem to collapse into a single intense band at 2234 cm⁻¹ in (9,9): while single N₂ adsorption reduces symmetry, stoichiometric N₂ saturation seems to recover it. We have assigned a distorted tricapped trigonal prism to the Rh₉ core geometry in (9,1), cf. above, and it may regain full D_{3h} symmetry in (9,9). This implies two types of Rh surface atoms in slightly diverse coordination geometries. If this assumed structure actually prevailed, our spectra would tell that all of the Rh–N₂ pairs are equivalent. Nevertheless, strong electronic Rh–Rh couplings would mediate a coupling between the Rh–N₂ pairs. The weak IR-PD feature at 2217 cm⁻¹ may arise from a hot band.

3.3.4 [Rh₁₀(N₂)₁₅]⁺ and [Rh₁₁(N₂)₁₆]⁺

Similar to the (6,11), (7,13), and the (8,12) cluster adsorbate complexes, the multiple adsorptions of N₂ to the Rh₁₀⁺ and Rh₁₁⁺ clusters reveal a multitude of bands at 2175–2277 cm⁻¹, lacking assignments as of now. In principle, they may arise from diverse adsorption sites, from co-existing cluster core or spin isomers, and from vibrational couplings of adjacent N₂ oscillators, likely in conjunction with Rh_{*i*} cluster core relaxation upon N₂ adsorption and saturation. As in the spectrum of (8,12) the weak band of (10,15) at 2277 cm⁻¹ may be a stretch–wag combination.

Finally, we review together all of the discussed spectral features upon N₂ saturation (Fig. 5) and upon single N₂ attachment (Fig. 4). This allows to sort the [Rh_{*i*}(N₂)_{*m*}]⁺ cluster adsorbate complexes into three classes: we label the *i* = 6–8, 10, 11 species as *small complexes*, and the *i* = 12–15 species as *large complexes*—the latter demarcation based on the spectral complexity of [Rh_{*i*}(N₂)₁]⁺ *i* = 12–15 complexes (Fig. 4). The sole *i* = 9 complex makes up for its own class of *smooth surface complexes*, *high symmetry complexes*, *exceptional complexes*.

3.4 Modelling of the Vibrational Spectrum of the [Rh₇(N₂)₁₂]⁺ Cluster Adsorbate Complex

Up to here, we have presented spectra of single N₂ adsorption and of N₂ saturation. We chose the (7,*m*) complexes for DFT modelling, and we supported this by an additional IR-PD spectrum of (7,12) (Fig. 6). This spectrum reveals a band pattern similar to that of (7,13), with an extra most red shifted strong band at 2192 cm⁻¹. These two findings allow for two interesting conclusions: (1) spectral complexity does not require a

completely saturated N_2 adsorption but sets in earlier. Future studies on IR-PD spectra of intermediate N_2 adsorption levels shall elucidate this aspect further. (2) Even the addition of a single, 13th N_2 does change spectral patterns considerably, indicating strong vibrational and electronic couplings.

With these findings in mind, we spent effort to optimize (7,12) geometries, utilizing as starting geometries the three

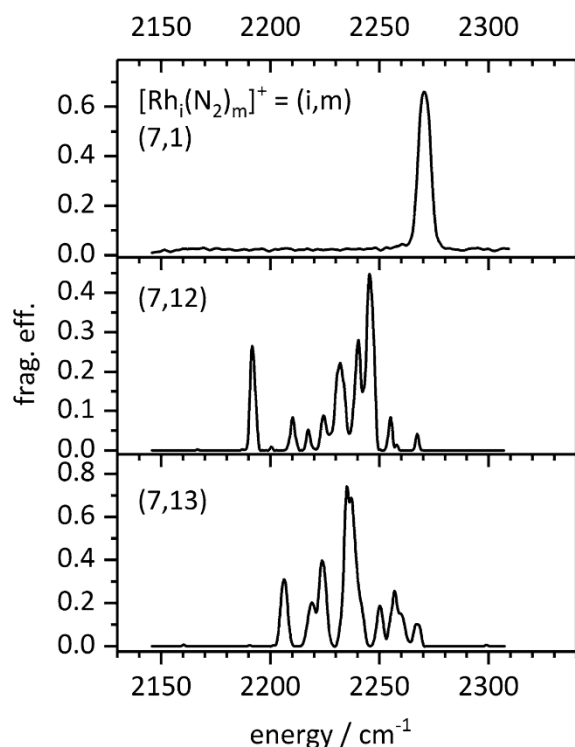


Fig. 6 IR-PD spectra of the $[Rh_i(N_2)_m]^+$ cluster for $m=1, 12,$ and 13 . With an increasing number of N_2 adsorbates there is a spreading out of bands which shift to the red

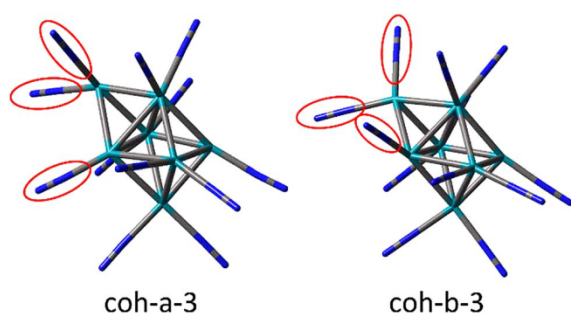


Fig. 7 Two most stable structures of the (7,12) $[Rh_7(N_2)_{12}]^+$ cluster adsorbate complexes. Both cluster Rh_7 cores are capped octahedral structures of similar shape; the $[Rh_7(N_2)_{12}]^+$ complexes distinguish by the orientations of two adjacent N_2 adsorbates highlighted by red circles

mentioned Rh_7^+ cluster core structures with spin multiplicities $2S + 1 = 1, \dots, 17$ and checking for conceivable N_2 adsorbate distributions. Calculating linear IR absorptions of converged (7,12) structures (Fig. 7 and supplement Figs. S6, S8, S10) and folding with apparatus functions of 5 cm^{-1} yielded IR spectra to compare with the recorded IR-PD spectrum (Fig. 8, further spectra in supplement Figs. S7, S9).

The calculated spectra of the four lowest energy calculated structures (coh-a-3 and coh-b-3, see supplement) show qualitative agreement to the measured IR-PD spectrum. All of these structures are capped octahedral with either a Rh_7

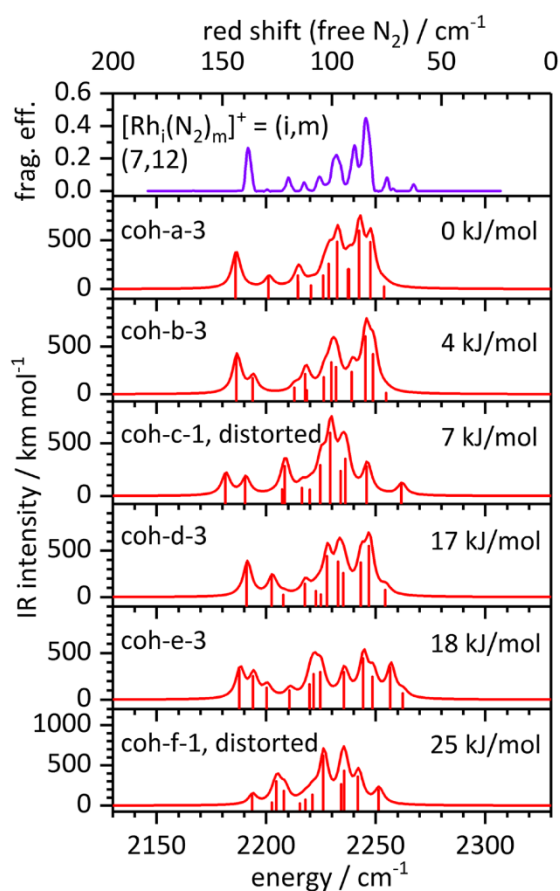


Fig. 8 Experimental IR-PD spectrum of the $[Rh_7(N_2)_{12}]^+$ cluster and calculated linear absorption spectra of some isomers (scaled by 0.9385). The calculated spectra represent the six lowest energy structures and the line spectra were convoluted with a 5 cm^{-1} FWHM Gaussian. The three letters indicate the arrangement of the metal atoms in the calculated structures followed by a code for the arrangement of the N_2 molecules and the spin multiplicity. Remarkably all structures have a singlet or triplet multiplicity. The first two calculated spectra satisfactorily resemble the experimental spectrum. The coh-a-3 structure started as a capped trigonal prism and self-optimized into a capped octahedron. The auxiliary axis (on top) indicates the red shift with respect to the IR inactive free N_2 vibration

core distortion or with some torsional polymorphism in the N₂ adsorbate arrangements. All but two Rh atoms accept two N₂ adsorbates, the remaining two Rh atoms just one N₂ each. The 12 N₂ adsorbates have quenched the 13tet spin state of the naked Rh₇⁺ cluster into a mere triplet state of the (7,12) cluster adsorbate complex.

Inspection of all the calculated vibrational mode characteristics reveals categories as listed in Table 2: N₂ wagging modes (36–91 cm⁻¹, unscaled), Rh cluster core modes (101–238 cm⁻¹), N₂ bending modes (247–439 cm⁻¹), and the N₂ stretching modes (2186–2254 cm⁻¹, scaled). A closer look on the calculated vibrational modes of the ctp-c-3 cluster supports our assumption that the band at 2267 cm⁻¹ is an N₂ stretch wag combination band.

Based on our prior and present investigation of [Ni_n(N₂)_m]⁺ complexes [71, 72] we expect strong couplings amongst geminal N₂ adsorbates on the same Rh site or on neighboring Rh sites, and no couplings amongst the two lone N₂ adsorbates at the Rh2 and Rh6 sites. Indeed, we assign the two most red shifted bands to the uncoupled lone N₂ molecules. These oscillators do not compete for electron density with another geminal N₂ molecule and they thus achieve higher back donation into their antibonding π* orbitals, which leads to the observed larger red shifts.

The strong N₂ couplings render an assignment of the stretching bands difficult; yet, there are some recognizable

characteristics (listed in Table 2). In particular, we identify symmetric and antisymmetric couplings of geminal and vicinal N₂ oscillators. The single stiffest N₂ stretching mode is delocalized over all N₂ oscillators and an all in phase motion (at 2254 cm⁻¹). By an according analysis, we obtain a similar picture of all the vibrational modes in the coh-b-3 cluster adsorbate complex.

4 Summary and Conclusions

We have presented the calculated minimum structures of Rh_i⁺ (i = 6, 7, and 9) clusters and [Rh₇(N₂)₁₂]⁺ cluster adsorbate complexes, in conjunction with the recorded IR-PD spectra of [Rh_i(N₂)_m]⁺ clusters adsorbate complexes (i, m) with a single N₂ (i = 6–15, m = 1) and with multiple N₂ adsorbates at or close to saturation (i = 6–11). In particular, we have compared recorded and calculated spectra of [Rh₇(N₂)₁₂]⁺, and we assign capped octahedral structures of the Rh₇ cores in all (7, m) species. We explain observed red shifts of the various N₂ stretching modes by electronic interactions between adsorbate molecules and cluster cores. For sure, high loads of N₂ adsorbates close to saturation quench high spin states of naked clusters significantly towards much lower multiplicities. Earlier investigations confirmed that assumed isomerization of the cluster

Table 2 Calculated vibrational modes of the coh-a-3 cluster in triplet state

Mode	Type/site	Frequency/cm ⁻¹	Scaled frequency/cm ⁻¹	IR intensity/km mol ⁻¹
1–23	N ₂ wagging modes Wagging	36–91		0.0055–0.15
24–39	Rh skeleton modes Cluster core vibrations	101–238		0.050–2.19
40–75	N ₂ bending modes N ₂ bending	247–439		0.64–18
76	Single N ₂ stretching modes @ Rh2	2329	2186	375
77	@ Rh6	2345	2201	115
78, 79	Coupled N ₂ stretching modes (asym. coupling @ Rh4) with (asym. @ Rh1) and (asym. @ Rh3)	2360	2215	137, 75
80	asym. @ Rh7	2366	2220	36
81	asym. @ Rh5	2372	2226	138
82	(asym. coupling @ Rh4) with (asym. @ Rh1) and (asym. @ Rh3)	2375	2229	259
83	sym. @ Rh4	2379	2233	485
84	asym. coupling of (sym. @ Rh5) and (sym. @ Rh7)	2384	2237	199
85	sym. @ Rh3	2389	2242	597
86	sym. coupling of (sym. @ Rh5) and (sym. @ Rh7)	2395	2248	483
87	All N ₂ in phase	2402	2254	26

The N₂ stretching frequencies are given unscaled and scaled by 0.9385. The Rh atom numbering is provided by Fig. S6 in the supplement. In the case of the stretching vibrations, the position of the oscillators on the cluster is given. The coh-b-3 cluster shows very similar bands

cores as well as the spin quenching may be understood as a result of multiple non-reactive collisions [25]. Our cryogenic hexapole ion trap likely provides for effective thermalization, and we may see an enhancement of such effects. Experiments where reactions takes place in the ICR cell with a much lower pressure reveal a variety of isomers [24, 25].

The present study is meant to provide first insights into N_2 adsorbate localization at Rhodium cluster surfaces and to elucidate adsorbate induced cluster core relaxation, as evidenced in the case of (6,11) and (7,13).

While the current study is a first step in a larger framework, which is work in progress: it is subject of work in progress to systematically vary the number of N_2 adsorbates, and to study the N_2 stretch couplings and the concomitant stepwise spin quenching in the $[Rh_i(N_2)_m]^+$ complexes is subject of work in progress. Also, work in progress are: the N_2 saturation studies of $[Rh_i(N_2)_m]^+$, $i > 11$, the calculation of N_2 adsorbate tilting barriers amongst complex structures of Fig. 7 and their spin state dependencies, the N_2 adsorption kinetics of pure Rh cations and of Fe Rh alloys, and the cryo spectroscopy of the latter.

We emphasize the fundamental value of our above findings for the understanding of the dynamic metal surface adsorbate interplay as of relevance in heterogeneous catalysis with nano-structured surfaces, such as e.g. the annealing of pre-catalyst deposits on substrate surfaces. Able members of the DFT modelling community are invited to join and augment our own efforts.

Acknowledgements This work was supported by the DFG founded transregional collaborative research center SFB/TRR 88 “3MET.de” and by the state research center OPTIMAS. We thank Thomas Kolling for technical assistance and valuable discussions. We acknowledge valuable comments and suggestions by the reviewers.

References

- Doyle MP (1986) Electrophilic metal carbenes as reaction intermediates in catalytic reactions. *Acc Chem Res* 19(11):348–356. doi:10.1021/ar00131a004
- Werlé C, Goddard R, Philipps P, Farès C, Fürstner A (2016) Structures of reactive donor/acceptor and donor/donor rhodium carbenes in the solid state and their implications for catalysis. *J Am Chem Soc* 138(11):3797–3805. doi:10.1021/jacs.5b13321
- van Leeuwen PWNM, Claver C (2002) Rhodium catalyzed hydroformylation, vol 22. *Catalysis by metal complexes*. doi:10.1007/0-306-46947-2
- Cheung H, Tanke RS, Torrence GP (2000) Acetic acid. *Ullmann's encyclopedia of industrial chemistry*. Wiley-VCH Verlag GmbH & Co. KGaA, Weinheim. doi:10.1002/14356007.a01_045
- Kaneda K, Fujita K, Takemoto T, Imanaka T (1991) Selective deoxygenation of various N-O bonds catalyzed by rhodium carbonyl clusters in the presence of H_2O and CO and their heterogenization using amino-substituted polystyrenes. *Bull Chem Soc Jpn* 64(2):602–612. doi:10.1246/bcsj.64.602
- Kaneda K, Takemoto T, Imanaka T (1988) Aminated polystyrene-bound rhodium carbonyl clusters as a catalyst for deoxygenation of various N-O bonds. *Chem Lett* (10):1759–1762. doi:10.1246/cl.1988.1759
- Murahashi S-I, Imada Y, Hirai Y (1987) Rhodium catalyzed hydrogenation of nitrogen heteroaromatics under water gas shift conditions. Selective synthesis of 1,2,3,4-tetrahydroquinolines and -formyl-1,2,3,4-tetrahydroisoquinolines. *Tetrahedron Lett* 28(1):77–80. doi:10.1016/S0040-4039(00)95653-3
- Votsmeier M, Kreuzer T, Gieshoff J, Lepperhoff G (2009) Automobile exhaust control. *Ullmann's encyclopedia of industrial chemistry*. doi:10.1002/14356007.a03_189.pub2
- Jung HJ, Becker ER (1987) Emission control for gas turbines. *Platinum Metals Rev* 31(4):162–170
- Albert G, Berg C, Beyer M, Achatz U, Joos S, Niedner-Schatteburg G, Bondybey VE (1997) Methane activation by rhodium cluster argon complexes. *Chem Phys Lett* 268(3):235–241. doi:10.1016/S0009-2614(97)00202-9
- Andersson M, Holmgren L, Rosén A (1996) Rhodium-cluster reactivity: sticking probabilities of some diatomic molecules. *Surf Rev Lett* 03(01):683–686. doi:10.1142/S0218625X96001236
- Mafuné F, Tawaraya Y, Kudoh S (2016) Nitrogen molecule adsorption on cationic tantalum clusters and rhodium clusters and desorption from their nitride clusters studied by thermal desorption spectrometry. *J Phys Chem A* 120(24):4089–4095. doi:10.1021/acs.jpca.6b03479
- Zakin MR, Cox DM, Kaldor A (1988) Gas-phase rhodium cluster chemistry: Influence of adsorbate electronic structure on reaction rate. *J Chem Phys* 89(2):1201–1202. doi:10.1063/1.455234
- Mineva T, Russo N, Freund H-J (2001) CO interaction with small rhodium clusters from density functional theory: spectroscopic properties and bonding analysis. *J Phys Chem A* 105(47):10723–10730. doi:10.1021/jp0116398
- Fielicke A, von Helden G, Meijer G, Simard B, Dénommée S, Rayner DM (2003) Vibrational spectroscopy of CO in gas-phase rhodium cluster–CO complexes. *J Am Chem Soc* 125(37):11184–11185. doi:10.1021/ja036897s
- Fielicke A, von Helden G, Meijer G, Pedersen DB, Simard B, Rayner DM (2004) Size and charge effects on the binding of CO to small isolated rhodium clusters. *J Phys Chem B* 108(38):14591–14598. doi:10.1021/jp049214j
- Fielicke A, von Helden G, Meijer G, Pedersen DB, Simard B, Rayner DM (2006) Size and charge effects on the binding of CO to late transition metal clusters. *J Chem Phys* 124(19):194305. doi:10.1063/1.2196887
- Swart I, de Groot FM, Weckhuysen BM, Rayner DM, Meijer G, Fielicke A (2008) The effect of charge on CO binding in rhodium carbonyls: from bridging to terminal CO. *J Am Chem Soc* 130(7):2126–2127. doi:10.1021/ja0772795
- Fielicke A, Gruene P, Meijer G, Rayner DM (2009) The adsorption of CO on transition metal clusters: a case study of cluster surface chemistry. *Surf Sci* 603(10–12):1427–1433. doi:10.1016/j.susc.2008.09.064
- Shetty S, Strych S, Jansen APJ, van Santen RA (2009) Theoretical investigation of CO adsorption on Rhn (n = 3–13) clusters. *Can J Chem* 87(7):824–831. doi:10.1139/V09-015
- Tian F-Y, Shen J (2011) Density-functional study of CO adsorbed on RhN(N = 2–19) clusters. *Chin Phys B* 20(12):123101. doi:10.1088/1674-1056/20/12/123101
- Dutta A, Mondal P (2016) Structural evolution, electronic and magnetic manners of small rhodium Rhn+/- (n = 2–8) clusters: a detailed density functional theory study. *RSC Adv* 6(9):6946–6959. doi:10.1039/c5ra21600a

23. Dutta A, Mondal P (2017) Density functional study on structure and bonding nature of CO adsorbed Rh n +/- ($n=2-8$) Clusters. *J Cluster Sci*. doi:[10.1007/s10876-017-1241-x](https://doi.org/10.1007/s10876-017-1241-x)
24. Ford MS, Anderson ML, Barrow MP, Woodruff DP, Drewello T, Derrick PJ, Mackenzie SR (2005) Reactions of nitric oxide on Rh6 + clusters: abundant chemistry and evidence of structural isomers. *Phys Chem Chem Phys* 7(5):975–980. doi:[10.1039/b415414b](https://doi.org/10.1039/b415414b)
25. Harding D, Ford MS, Walsh TR, Mackenzie SR (2007) Dramatic size effects and evidence of structural isomers in the reactions of rhodium clusters, Rh n +/-, with nitrous oxide. *Phys Chem Chem Phys* 9(17):2130–2136. doi:[10.1039/B618299B](https://doi.org/10.1039/B618299B)
26. Harding DJ, Walsh TR, Hamilton SM, Hopkins WS, Mackenzie SR, Gruene P, Haertelt M, Meijer G, Fielicke A (2010) Communications: the structure of Rh(8) (+) in the gas phase. *J Chem Phys* 132(1):011101. doi:[10.1063/1.3285266](https://doi.org/10.1063/1.3285266)
27. Torres MB, Aguilera-Granja F, Balbas LC, Vega A (2011) Ab initio study of the adsorption of NO on the Rh6(+) cluster. *J Phys Chem A* 115(30):8350–8360. doi:[10.1021/jp202511w](https://doi.org/10.1021/jp202511w)
28. Romo-Avila SL, Guirado-Lopez RA (2012) Adsorption of nitric oxide on small Rh(n) +/- clusters: role of the local atomic environment on the dissociation of the N-O bond. *J Phys Chem A* 116(3):1059–1068. doi:[10.1021/jp208847r](https://doi.org/10.1021/jp208847r)
29. Tawaraya Y, Kudoh S, Miyajima K, Mafune F (2015) Thermal desorption and reaction of NO adsorbed on rhodium cluster ions studied by thermal desorption spectroscopy. *J Phys Chem A* 119(31):8461–8468. doi:[10.1021/acs.jpca.5b04224](https://doi.org/10.1021/acs.jpca.5b04224)
30. Anderson ML, Ford MS, Derrick PJ, Drewello T, Woodruff DP, Mackenzie SR (2006) Nitric oxide decomposition on small rhodium clusters, Rh n +. *J Phys Chem A* 110(38):10992–11000. doi:[10.1021/jp062178z](https://doi.org/10.1021/jp062178z)
31. Hamilton SM, Hopkins WS, Harding DJ, Walsh TR, Gruene P, Haertelt M, Fielicke A, Meijer G, Mackenzie SR (2010) Infrared induced reactivity on the surface of isolated size-selected clusters: dissociation of N₂O on rhodium clusters. *J Am Chem Soc* 132(5):1448–1449. doi:[10.1021/ja907496c](https://doi.org/10.1021/ja907496c)
32. Hamilton SM, Hopkins WS, Harding DJ, Walsh TR, Haertelt M, Kerpel C, Gruene P, Meijer G, Fielicke A, Mackenzie SR (2011) Infrared-induced reactivity of N₂O on small gas-phase rhodium clusters. *J Phys Chem A* 115(12):2489–2497. doi:[10.1021/jp201171p](https://doi.org/10.1021/jp201171p)
33. Hermes AC, Hamilton SM, Hopkins WS, Harding DJ, Kerpel C, Meijer G, Fielicke A, Mackenzie SR (2011) Effects of coadsorbed oxygen on the infrared driven decomposition of N₂O on isolated Rh5 + clusters. *J Phys Chem Lett* 2(24):3053–3057. doi:[10.1021/jz2012963](https://doi.org/10.1021/jz2012963)
34. Parry IS, Kartouzian A, Hamilton SM, Balaj OP, Beyer MK, Mackenzie SR (2013) Collisional activation of N₂O decomposition and CO oxidation reactions on isolated rhodium clusters. *J Phys Chem A* 117(36):8855–8863. doi:[10.1021/jp405267p](https://doi.org/10.1021/jp405267p)
35. Mafuné F, Tawaraya Y, Kudoh S (2016) Reactivity control of rhodium cluster ions by alloying with tantalum atoms. *J Phys Chem A* 120(6):861–867. doi:[10.1021/acs.jpca.5b11898](https://doi.org/10.1021/acs.jpca.5b11898)
36. Francisco H, Bertin V, Soto JR, Castro M (2016) Charge and geometrical effects on the catalytic N₂O reduction by Rh6- and Rh6 + clusters. *J Phys Chem C* 120(41):23648–23659. doi:[10.1021/acs.jpcc.6b08172](https://doi.org/10.1021/acs.jpcc.6b08172)
37. Xie H, Ren M, Lei Q, Fang W, Ying F (2012) Explore the catalytic reaction mechanism in the reduction of NO by CO on the Rh7 + cluster: a quantum chemical study. *J Phys Chem C* 116(14):7776–7781. doi:[10.1021/jp2118357](https://doi.org/10.1021/jp2118357)
38. Su B-F, Fu H-Q, Yang H-Q, Hu C-W (2015) Catalytic reduction of NO by CO on Rh4 + clusters: a density functional theory study. *Catal Sci Technol* 5(6):3203–3215. doi:[10.1039/C5CY00119F](https://doi.org/10.1039/C5CY00119F)
39. Niedner-Schatteburg G (2017) Cooperative effects in clusters and oligonuclear complexes of transition metals in isolation. In: Dehnen S (ed) *Clusters—contemporary insight in structure and bonding*. Springer, Cham, pp 1–40
40. Berg C, Beyer M, Schindler T, Niedner-Schatteburg G, Bondybey VE (1996) Reactions of benzene with rhodium cluster cations: competition between chemisorption and physisorption. *J Chem Phys* 104(20):7940–7946. doi:[10.1063/1.471510](https://doi.org/10.1063/1.471510)
41. Berg C, Beyer M, Achatz U, Joos S, Niedner-Schatteburg G, Bondybey VE (1998) Effect of charge upon metal cluster chemistry: reactions of Nb n and Rh n anions and cations with benzene. *J Chem Phys* 108(13):5398–5403. doi:[10.1063/1.475972](https://doi.org/10.1063/1.475972)
42. Adlhart C, Uggerud E (2005) C-H activation of alkanes on Rh + n ($n=1-30$) clusters: size effects on dehydrogenation. *J Chem Phys* 123(21):214709. doi:[10.1063/1.2131066](https://doi.org/10.1063/1.2131066)
43. Balteanu I, Balaj OP, Beyer MK, Bondybey VE (2006) Size-dependent dehydrogenation of ethane by cationic rhodium clusters in the gas phase. *Int J Mass Spectrom* 255–256:71–75. doi:[10.1016/j.ijms.2005.08.019](https://doi.org/10.1016/j.ijms.2005.08.019)
44. Balteanu I, Balaj OP, Fox-Beyer BS, Rodrigues P, Barros MT, Moutinho AMC, Costa ML, Beyer MK, Bondybey VE (2004) Size- and charge-state-dependent reactivity of azidoacetone nitrile with anionic and cationic rhodium clusters Rh n ±. *Organometallics* 23(9):1978–1985. doi:[10.1021/om049946y](https://doi.org/10.1021/om049946y)
45. Aguilera-Granja F, Rodríguez-López JL, Michaelian K, Berlanga-Ramírez EO, Vega A (2002) Structure and magnetism of small rhodium clusters. *Phys Rev B* 66(22):224410
46. Šipr O, Ebert H, Minár J (2015) Trends in magnetism of free Rh clusters via relativistic ab-initio calculations. *J Phys Condens Matter* 27(5):056004. doi:[10.1088/0953-8984/27/5/056004](https://doi.org/10.1088/0953-8984/27/5/056004)
47. Ahmadi S, Zhang X, Gong Y, Zhu W, Sun CQ (2016) Catalytic and magnetic behaviors of excessively charged silver, copper, platinum, and rhodium atomic clusters. *J Phys Chem C* 120(31):17527–17536. doi:[10.1021/acs.jpcc.6b05380](https://doi.org/10.1021/acs.jpcc.6b05380)
48. Chien C-H, Blaisten-Barojas E, Pederson MR (1998) Magnetic and electronic properties of rhodium clusters. *Phys Rev A* 58(3):2196–2202
49. Ma L, Moro R, Bowlan J, Kirilyuk A, de Heer WA (2014) Multiferroic rhodium clusters. *Phys Rev Lett* 113(15):157203. doi:[10.1103/PhysRevLett.113.157203](https://doi.org/10.1103/PhysRevLett.113.157203)
50. Sen P (2016) Magnetism in simple metal and 4d transition metal clusters. *J Cluster Sci* 27(3):795–815. doi:[10.1007/s10876-016-0986-y](https://doi.org/10.1007/s10876-016-0986-y)
51. Harding DJ, Gruene P, Haertelt M, Meijer G, Fielicke A, Hamilton SM, Hopkins WS, Mackenzie SR, Neville SP, Walsh TR (2010) Probing the structures of gas-phase rhodium cluster cations by far-infrared spectroscopy. *J Chem Phys* 133(21):214304. doi:[10.1063/1.3509778](https://doi.org/10.1063/1.3509778)
52. Hang TD, Hung HM, Thiem LN, Nguyen HMT (2015) Electronic structure and thermochemical properties of neutral and anionic rhodium clusters Rh n , $n=2-13$. Evolution of structures and stabilities of binary clusters Rh m M ($M=Fe, Co, Ni$; $m=1-6$). *Comput Theor Chem* 1068:30–41. doi:[10.1016/j.comptc.2015.06.004](https://doi.org/10.1016/j.comptc.2015.06.004)
53. Lecours MJ, Chow WCT, Hopkins WS (2014) Density functional theory study of Rh n S $0,±$ and Rh $n+10,±$ ($n=1-9$). *J Phys Chem A* 118(24):4278–4287. doi:[10.1021/jp412457m](https://doi.org/10.1021/jp412457m)
54. Citra A, Andrews L (1999) Reactions of laser ablated rhodium atoms with nitrogen atoms and molecules. Infrared spectra and density functional calculations on rhodium nitrides and dinitrogen complexes. *J Phys Chem A* 103(18):3410–3417. doi:[10.1021/jp9846274](https://doi.org/10.1021/jp9846274)
55. Brathwaite AD, Abbott-Lyon HL, Duncan MA (2016) Distinctive coordination of CO vs N₂ to rhodium cations: an infrared and computational study. *J Phys Chem A* 120(39):7659–7670. doi:[10.1021/acs.jpca.6b07749](https://doi.org/10.1021/acs.jpca.6b07749)

56. Bendtsen J (1974) The rotational and rotation-vibrational Raman spectra of $^{14}\text{N}_2$, $^{14}\text{N}^{15}\text{N}$ and $^{15}\text{N}_2$. *J Raman Spectrosc* 2(2):133–145. doi:10.1002/jrs.1250020204
57. Dillinger S, Mohrbach J, Hewer J, Gaffga M, Niedner-Schatteburg G (2015) Infrared spectroscopy of N_2 adsorption on size selected cobalt cluster cations in isolation. *Phys Chem Chem Phys* 17(16):10358–10362. doi:10.1039/C5CP00047E
58. Maruyama S, Anderson LR, Smalley RE (1990) Direct injection supersonic cluster beam source for FT-ICR studies of clusters. *Rev Sci Instrum* 61(12):3686–3693. doi:10.1063/1.1141536
59. Berg C, Schindler T, Niedner-Schatteburg G, Bondybey VE (1995) Reactions of simple hydrocarbons with $\text{Nb} + n$: chemisorption and physisorption on ionized niobium clusters. *J Chem Phys* 102(12):4870–4884
60. Proch D, Trickl T (1989) A high-intensity multi-purpose piezoelectric pulsed molecular beam source. *Rev Sci Instrum* 60(4):713–716. doi:10.1063/1.1141006
61. Kofel P, Allemann M, Kellerhals H, Wanczek KP (1985) External generation of ions in ICR spectrometry. *Int J Mass Spectrom Ion Processes* 65(1):97–103. doi:10.1016/0168-1176(85)85056-4
62. Kofel P, Allemann M, Kellerhals H, Wanczek KP (1986) Time-of-flight ICR spectrometry. *Int J Mass Spectrom Ion Processes* 72(1):53–61. doi:10.1016/0168-1176(86)85033-9
63. Caravatti P, Allemann M (1991) The ‘infinity cell’: a new trapped-ion cell with radiofrequency covered trapping electrodes for fourier transform ion cyclotron resonance mass spectrometry. *Org Mass Spectrom* 26(5):514–518. doi:10.1002/oms.1210260527
64. Peredkov S, Savci A, Peters S, Neeb M, Eberhardt W, Kampshulte H, Meyer J, Tombers M, Hofferberth B, Menges F, Niedner-Schatteburg G (2011) X-ray absorption spectroscopy of mass-selected transition metal clusters using a cyclotron ion trap: an experimental setup for measuring XMCD spectra of free clusters. *J Electron Spectrosc* 184(3–6):113–118. doi:10.1016/j.elspec.2010.12.031
65. Meyer J, Tombers M, van Wüllen C, Niedner-Schatteburg G, Peredkov S, Eberhardt W, Neeb M, Palutke S, Martins M, Wurth W (2015) The spin and orbital contributions to the total magnetic moments of free Fe, Co, and Ni clusters. *J Chem Phys* 143(10):104302. doi:10.1063/1.4929482
66. Schindler T, Berg C, Niedner-Schatteburg G, Bondybey VE (1996) Protonated water clusters and their black body radiation induced fragmentation. *Chem Phys Lett* 250(3):301–308. doi:10.1016/0009-2614(96)00002-4
67. Niedner-Schatteburg G, Bondybey VE (2000) FT-ICR studies of solvation effects in ionic water cluster reactions. *Chem Rev* 100(11):4059–4086. doi:10.1021/cr990065o
68. Frisch MJ, Trucks GW, Schlegel HB, Scuseria GE, Robb MA, Cheeseman JR, Scalmani G, Barone V, Mennucci B, Petersson GA, Nakatsuji H, Caricato M, Li X, Hratchian HP, Izmaylov AF, Bloino J, Zheng G, Sonnenberg JL, Hada M, Ehara M, Toyota K, Fukuda R, Hasegawa J, Ishida M, Nakajima T, Honda Y, Kitao O, Nakai H, Vreven T, Montgomery JA Jr, Peralta JE, Ogliaro F, Bearpark MJ, Heyd J, Brothers EN, Kudin KN, Staroverov VN, Kobayashi R, Normand J, Raghavachari K, Rendell AP, Burant JC, Iyengar SS, Tomasi J, Cossi M, Rega N, Millam NJ, Klene M, Knox JE, Cross JB, Bakken V, Adamo C, Jaramillo J, Gomperts R, Stratmann RE, Yazyev O, Austin AJ, Cammi R, Pomelli C, Ochterski JW, Martin RL, Morokuma K, Zakrzewski VG, Voth GA, Salvador P, Dannenberg JJ, Dapprich S, Daniels AD, Farkas Ö, Foresman JB, Ortiz JV, Cioslowski J, Fox DJ (2009) Gaussian 09, Revision D.01. Gaussian, Inc., Wallingford
69. Black G, Schuchardt K, Gracio D, Palmer B (2003) The extensible computational chemistry environment: a problem solving environment for high performance theoretical chemistry. In: Sloot PMA, Abramson D, Bogdanov AV, Gorbachev YE, Dongarra JJ, Zomaya AY (eds) *Computational Science—ICCS 2003: International Conference, Melbourne, Australia and St. Petersburg, Russia, June 2–4, 2003 Proceedings, Part IV*. Springer Berlin Heidelberg, Berlin, Heidelberg, pp 122–131. doi:10.1007/3-540-44864-0_13
70. Adamo C, Barone V (1999) Toward reliable density functional methods without adjustable parameters: the PBE0 model. *J Chem Phys* 110(13):6158–6170. doi:10.1063/1.478522
71. Mohrbach J, Dillinger S, Niedner-Schatteburg G (2017) Cryo kinetics and spectroscopy of cationic nickel clusters: rough and smooth surfaces. *J Phys Chem C* 121(20):10907–10918. doi:10.1021/acs.jpcc.6b12167
72. Dillinger S, Mohrbach J, Niedner-Schatteburg G (2017) Probing cluster surface morphology by cryo spectroscopy of N_2 on cationic nickel clusters. *J Chem Phys* (accepted)
73. Andrae D, Häußermann U, Dolg M, Stoll H, Preuß H (1990) Energy-adjusted ab initio pseudopotentials for the second and third row transition elements. *Theoret Chim Acta* 77(2):123–141. doi:10.1007/bf01114537
74. Bligaard T, Nørskov JK (2008) Chapter 4—heterogeneous catalysis. *Chemical bonding at surfaces and interfaces*. Elsevier, Amsterdam, pp 255–321
75. Comelli G, Dhanak VR, Kiskinova M, Prince KC, Rosei R (1998) Oxygen and nitrogen interaction with rhodium single crystal surfaces. *Surf Sci Rep* 32(5):165–231. doi:10.1016/S0167-5729(98)00003-x
76. Beyer MK, Knickelbein MB (2007) Electric deflection studies of rhodium clusters. *J Chem Phys* 126(10):104301. doi:10.1063/1.2698320
77. Mokkath JH, Pastor GM (2012) Interplay between chemical and magnetic order in FeRh clusters. *J Phys Chem C* 116(32):17228–17238. doi:10.1021/jp3032176
78. Beltran MR, Zamudio FB, Chauhan V, Sen P, Wang H, Ko YJ, Bowen K (2013) Ab initio and anion photoelectron studies of Rh_n ($n = 1–9$) clusters. *Eur Phys J D* 67(3):63. doi:10.1140/epjd/e2013-30547-2
79. Cotton FA, DeBoer BG, LaPrade MD, Pipal JR, Ucko DA (1971) The crystal and molecular structures of dichromium tetraacetate dihydrate and dirhodium tetraacetate dihydrate. *Acta Crystallogr B* 27(8):1664–1671. doi:10.1107/S0567740871004527
80. Lide DR (2010) *CRC handbook of chemistry and physics*, 90th edn. CRC Press, Boca Raton
81. Whetten RL, Cox DM, Trevor DJ, Kaldor A (1985) Free iron clusters react readily with oxygen and hydrogen sulfide, but are inert toward methane. *J Phys Chem* 89(4):566–569. doi:10.1021/j100250a004
82. Dillinger S, Mohrbach J, Ehrhard A, Klein M, Niedner-Schatteburg G, unpublished data
83. Kerpál C, Harding DJ, Lyon JT, Meijer G, Fielicke A (2013) N_2 activation by neutral ruthenium clusters. *J Phys Chem C* 117(23):12153–12158. doi:10.1021/jp401876b
84. Blyholder G (1964) Molecular orbital view of chemisorbed carbon monoxide. *J Phys Chem* 68(10):2772–2777. doi:10.1021/J100792a006
85. Dewar JS (1951) A review of the Pi-complex theory. *Bull Soc Chim Fr* 18(3–4):C71–C79
86. Chatt J, Duncanson LA (1953) 586. Olefin co-ordination compounds. Part III. Infra-red spectra and structure: attempted preparation of acetylene complexes. *J Chem Soc*. doi:10.1039/JR9530002939
87. Rapps T, Ahlrichs R, Waldt E, Kappes MM, Schooss D (2013) On the structures of 55-atom transition-metal clusters and their relationship to the crystalline bulk. *Angew Chem* 52(23):6102–6105. doi:10.1002/anie.201302165
88. Robertson BE (1977) Coordination polyhedra with nine and ten atoms. *Inorg Chem* 16(11):2735–2742. doi:10.1021/ic50177a014

3.3 Supplementary Information

Content

Table S1 Measuring conditions for the IR-PD spectra

Fig. S1 The recorded maximum adsorption limits and intermittent adsorption limits of N₂ adsorbates to Rh_i⁺-clusters

Fig. S2 Laser pulse energy in dependence of photon energy

Table S2 Starting and optimized geometries of the calculated Rh₆⁺ clusters

Table S3 Starting and optimized geometries of the calculated Rh₇⁺ clusters

Table S4 Starting and optimized geometries of the calculated Rh₉⁺ clusters

Fig. S3 IR-PD spectra of single N₂ adsorption on rhodium cluster cations Rh_i⁺ as a function of the cluster core size *i* (*i* = 6 – 15)

Fig. S4 IR-PD spectra of single (black line) and multiple N₂ adsorption on rhodium clusters at (blue) or close to (green) saturation

Fig. S5 IR-PD spectra of the [Rh₆(N₂)_{*m*}]⁺ cluster for *m* = 1, 8, and 11

Table S5 Calculated atomic distances (in Å) for nearest neighbors for the coh Rh₇⁺ clusters in comparison with crystal structures, experimental data and calculations on a neutral 14tet pbp structure.

Fig. S6 Two most stable structures of the (7,12) [Rh₇(N₂)₁₂]⁺ cluster adsorbate complexes

Fig. S7 Calculated structures of the [Rh₇(N₂)₁₂]⁺ cluster adsorbate complex, correspondent to the calculated spectra in Fig. 8

Fig. S8 Calculated structures of the [Rh₇(N₂)₁₂]⁺ cluster adsorbate complex, correspondent to the calculated spectra in Fig. S9

Fig. S9 Experimental IR-PD spectrum of the [Rh₇(N₂)₁₂]⁺ cluster and calculated linear absorption spectra of the isomers shown in Fig. S8

Fig. S10 Calculated structures of the [Rh₇(N₂)₁₂]⁺ cluster adsorbate complex, correspondent to the calculated spectra in Fig. S11

Fig. S11 Experimental IR-PD spectrum of the [Rh₇(N₂)₁₂]⁺ cluster and calculated linear absorption spectra of the isomers shown in Fig. S10

Table S6 Calculated vibrational modes of the coh-b-3 cluster

Table S1 Measuring conditions for the IR-PD spectra of the $[\text{Rh}_i(\text{N}_2)_m]^+$ clusters at 26 K, 15 shots of vaporization laser.

Cluster (l,m)	p(He) / 10^{-6} mbar	p(N ₂) / 10^{-7} mbar	Collision Cell Delay / s	IR-PD time / s	OPA / °	Range / nm	Scanning speed/ nm/s
(6,1)	4.8	--	0.3	0.7	45	767.9- 772.7	0.003
(6,8)	3.2	3.8	0.7	0.7	45	767.9- 772.7	0.003
(6,11)	3.3	3.0	2.0	0.7	45	767.9- 772.7	0.003
(7,1)	4.8	--	0.3	0.7	45	767.9- 772.7	0.003
(7,12)	4.9	3.0	2.0	0.7	24	767.9- 772.7	0.002
(7,13)	4.9	3.0	2.0	0.7	24	767.9- 772.7	0.002
(8,1)	4.8	--	0.3	0.7	45	767.9- 772.7	0.003
(8,12)	4.9	3.0	2.0	0.7	24	767.9- 772.7	0.002
(9,1)	4.8	--	0.3	0.7	45	767.9- 772.7	0.003
(9,9)	4.9	3.0	1.5	0.7	24	767.9- 772.7	0.003
(10,1)	4.8	--	0.2	0.7	45	767.9- 772.7	0.003
(10,15)	4.7	3.0	2.0	0.7	24	767.9- 772.7	0.002
(11,1)	4.8	--	0.2	0.7	45	767.9- 772.7	0.003
(11,16)	4.7	3.0	2.0	0.7	24	767.9- 772.7	0.002
(12,1)	4.8	--	0.2	0.7	45	767.9- 772.7	0.003
(13,1)	4.8	--	0.2	0.7	45	767.9- 772.7	0.003
(14,1)	4.4	--	0.2	0.7	45	767.9- 772.7	0.003
(15,1)	4.4	--	0.2	0.7	45	767.9- 772.7	0.003

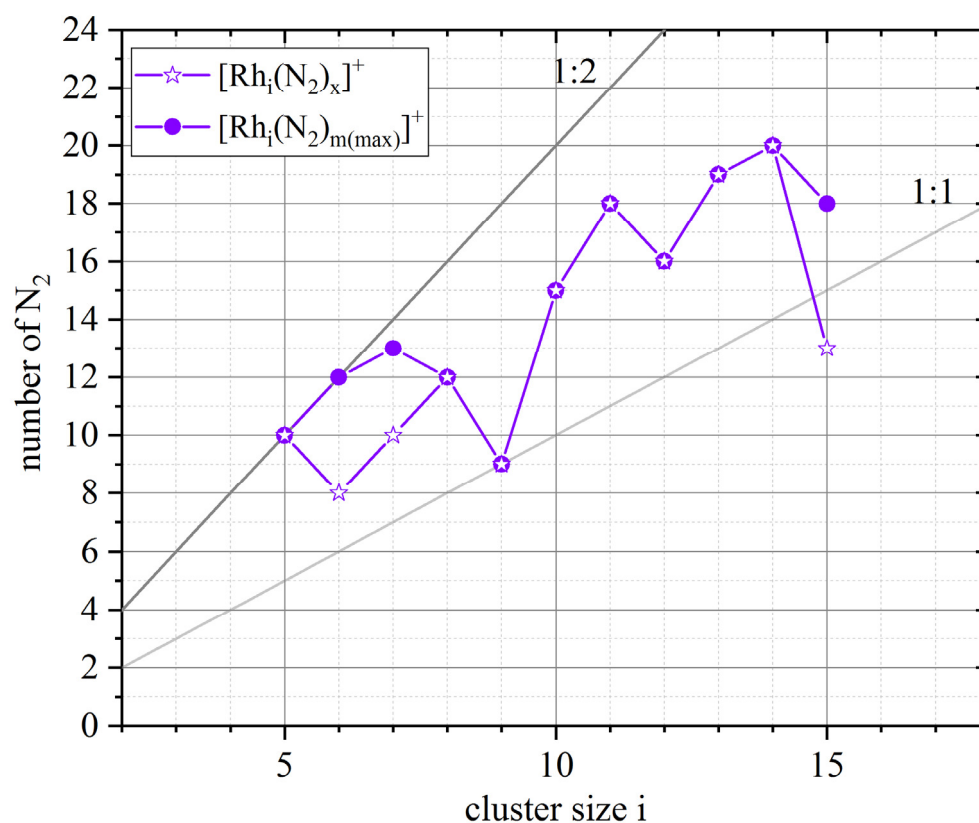


Fig. S1 The recorded maximum adsorption limits and intermittent adsorption limits of N₂ adsorbates to Rh_{*i*}⁺-clusters (*m*_{max}, purple circles; *m*_{*x*}, purple stars). The grey lines indicate stoichiometries of *i* : *m*_{max} = (1 : 1), (1 : 2), namely one and two hypothetical “monolayers” of adsorbates, respectively.

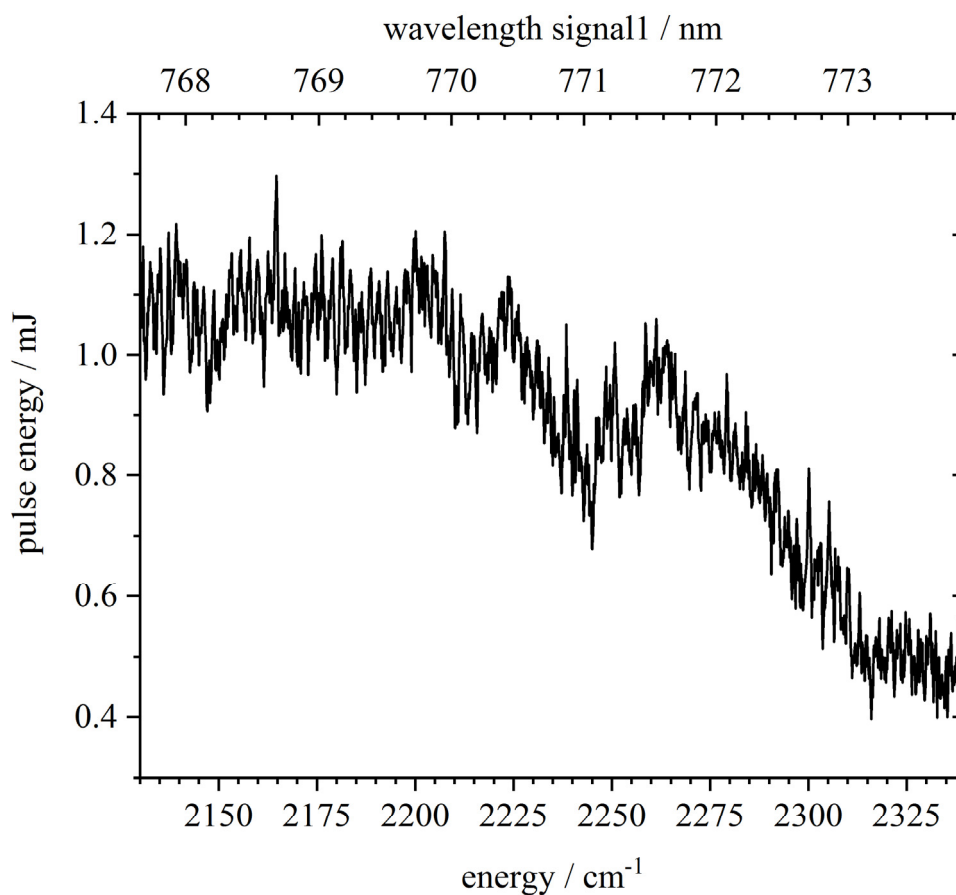


Fig. S2 Laser pulse energy in dependence of photon energy.

Table S2 Starting and optimized geometries of the calculated Rh_6^+ clusters in dependence of spin multiplicity.

Starting geometry	csp	boat	tp	oct
2S+1				
2	oct	oct	tp	oct
4	oct	oct	tp	oct
6	oct	oct	tp	oct
8	csp	oct	tp	oct
10	csp	oct	tp	oct
12	boat	boat	boat	oct
14	boat	boat	tp	oct
16	oct	oct	oct	oct
18	boat	boat	oct	oct

3. Infrared Spectroscopic Investigation of Structures and N₂ Adsorption Induced Relaxations of Isolated Rhodium Clusters

Table S3 Starting and ending geometries of the calculated Rh₇⁺ clusters in dependence of spin multiplicity.

Starting geometry	coh	ctp	pbp
2S+1			
1	ctp	ctp	ctp
3	coh	ctp	pbp
5	coh	ctp	pbp
7	coh	ctp	pbp
9	coh	ctp	pbp
11	coh	ctp	pbp
13	coh	ctp	pbp
15	coh	ctp	pbp
17	coh	coh	pbp
19	coh	coh	pbp

Table S4 Starting and ending geometries of the calculated Rh₉⁺ clusters in dependence of spin multiplicity.

Starting geometry	trig-ap	dc-pbp	tri	ac-top
2S+1				
9	trig-ap	dc-pbp	tri	actop
11	trig-ap	dc-pbp	tri	actop
13	trig-ap	dc-pbp	tri	actop
15	trig-ap	dc-pbp	tri	actop
17	trig-ap	dc-pbp	tri	actop
19	trig-ap	dc-pbp	tri	tri
21	trig-ap	dc-pbp	tri	actop

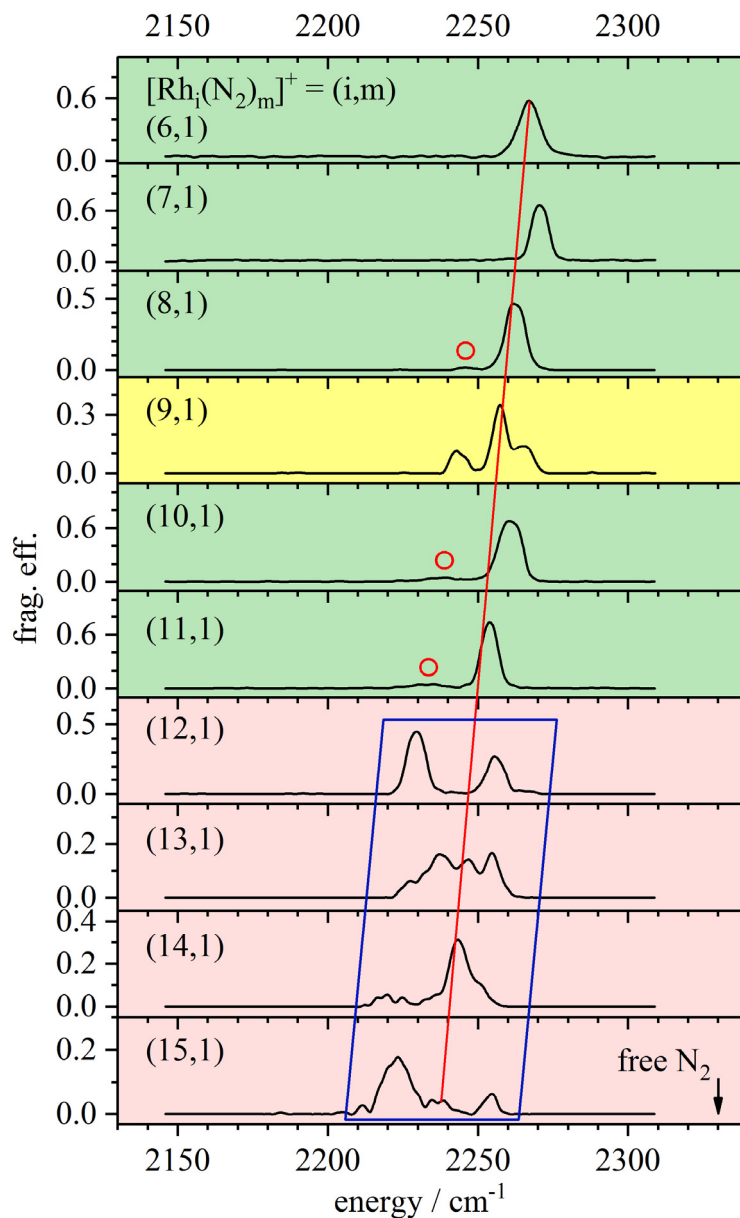


Fig. S3 IR-PD spectra of single N_2 adsorption on rhodium cluster cations Rh_i^+ as a function of the cluster core size i ($i = 6 - 15$). The red line and the blue box serves as a guide to the eye and serve to indicate the red shift with increasing number of Rhodium atoms within the cluster. The red circles mark possible hot bands. There is no correlation between the spectral features and the laser power (Fig. S2). The green and red shaded areas serve to discriminate *small* and *large* cluster adsorbate complexes respectively. The yellow shaded area marks the exceptional $[\text{Rh}_9(\text{N}_2)_1]^+$ complex.

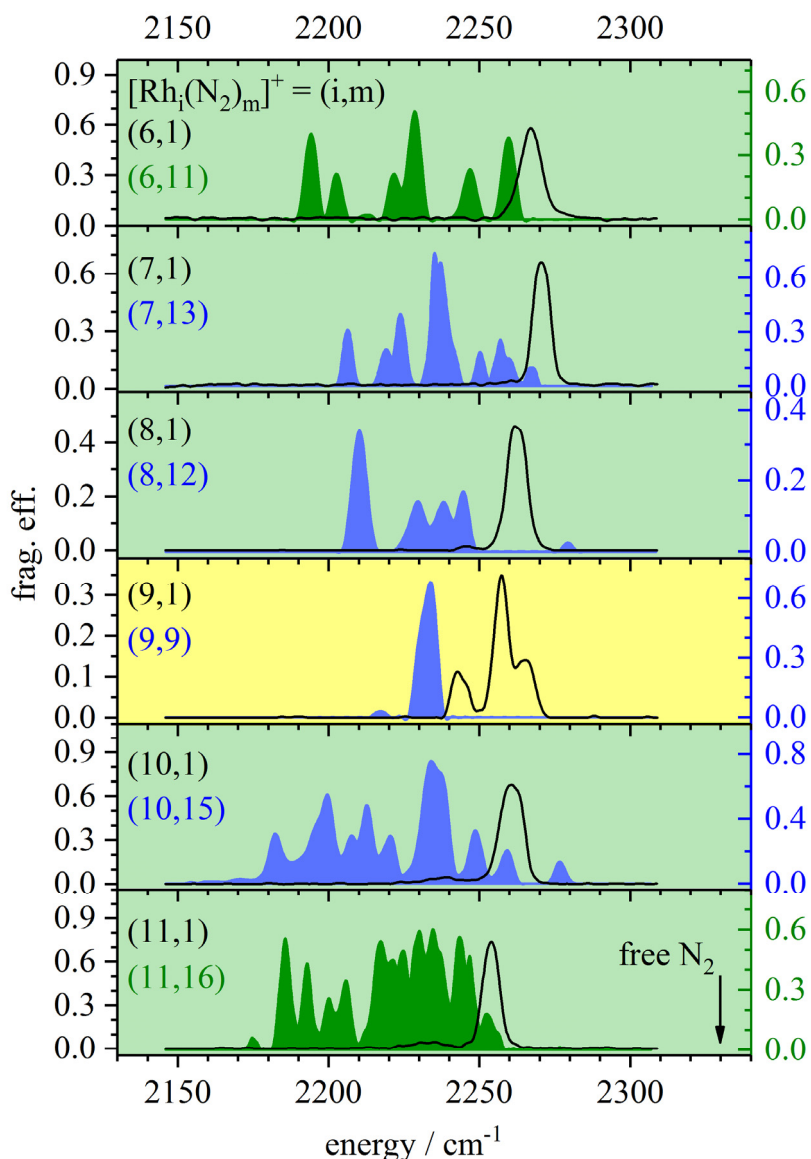


Fig. S4 IR-PD spectra of single (black line) and multiple N₂ adsorption on rhodium clusters at (blue) or close to (green) saturation. The blue areas represent maximum adsorption limits, the green areas represent spectra of one N₂ adsorbate less in cases of experimental constraints. There is no correlation between the spectral features and the laser power (Fig. S2). The green shaded areas mark *small* cluster adsorbate complexes respectively. The yellow shaded area marks the spectra of the exceptional [Rh₉(N₂)_m]⁺ complexes.

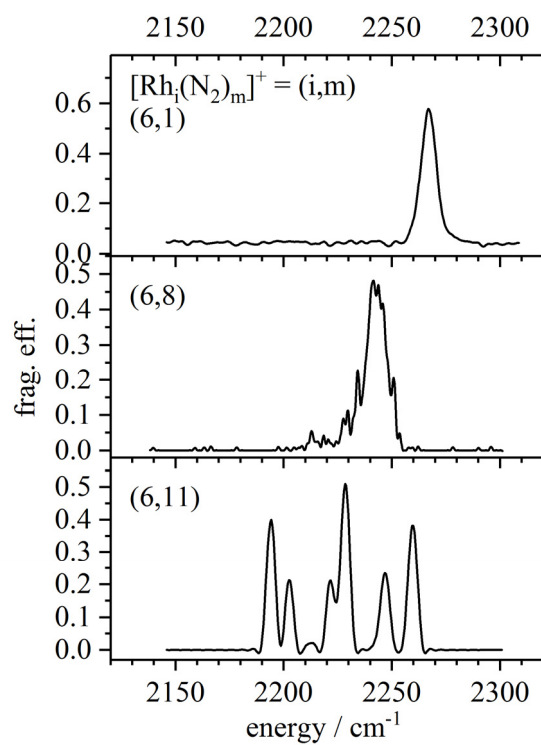


Fig. S5 IR-PD spectra of the $[\text{Rh}_6(\text{N}_2)_m]^+$ cluster for $m = 1, 8,$ and 11 . With increasing number of N_2 adsorbed a broadening and an overall red shift is observed.

3. Infrared Spectroscopic Investigation of Structures and N₂ Adsorption Induced Relaxations of Isolated Rhodium Clusters

Table S5 Calculated atomic distances (in Å) for nearest neighbors for the coh Rh₇⁺ clusters in comparison with crystal structures, experimental data and calculations on a neutral 14tet pbp structure.

	dimer	Rh ₇	[Rh ₇ (N ₂) ₁₂] ⁺			bulk
			ctp 13tet	ctp-c-3	coh-c-3	
Calc.	2.21 ^a	2.61 ^a	2.446 - 2.665	2.548 - 2.822	2.535 - 2.773	
	2.27 ^b					
Exp.	2.3855 ^c					2.69 ^d

a Ref. [1] VASP PW91 GGA / LDA; Rh₇⁺: neutral pbp 14tet

b [2] TZVP, ECP28MWB

c [3] crystal structure of [Rh₂(O₂CCH₃)₄(H₂O)₂]

d [4] distance of next neighbors in fcc crystal, lattice parameter a = 3.8032 Å

tw this work: PBE0, coh 13tet cation

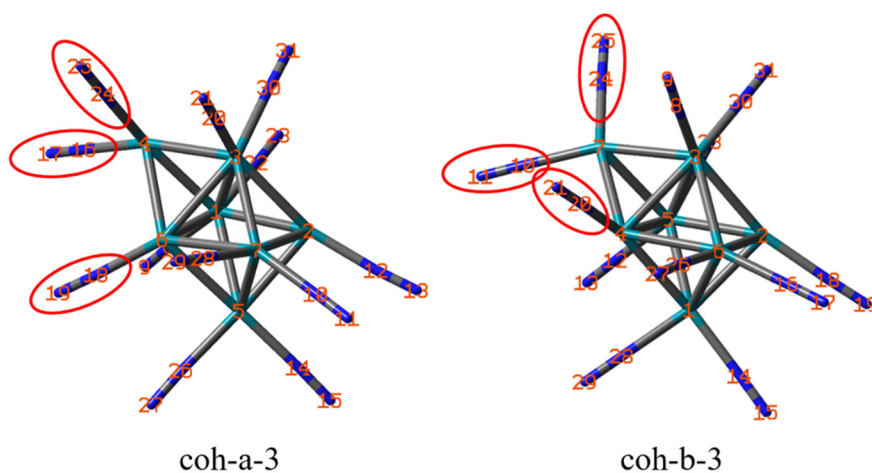


Fig. S6 Two most stable structures of the (7,12) $[\text{Rh}_7(\text{N}_2)_{12}]^+$ cluster adsorbate complexes. Both cluster Rh_7 cores are capped octahedral structures of similar shape; the $[\text{Rh}_7(\text{N}_2)_{12}]^+$ complexes distinguish by the orientations of two adjacent N_2 adsorbates highlighted by red circles.

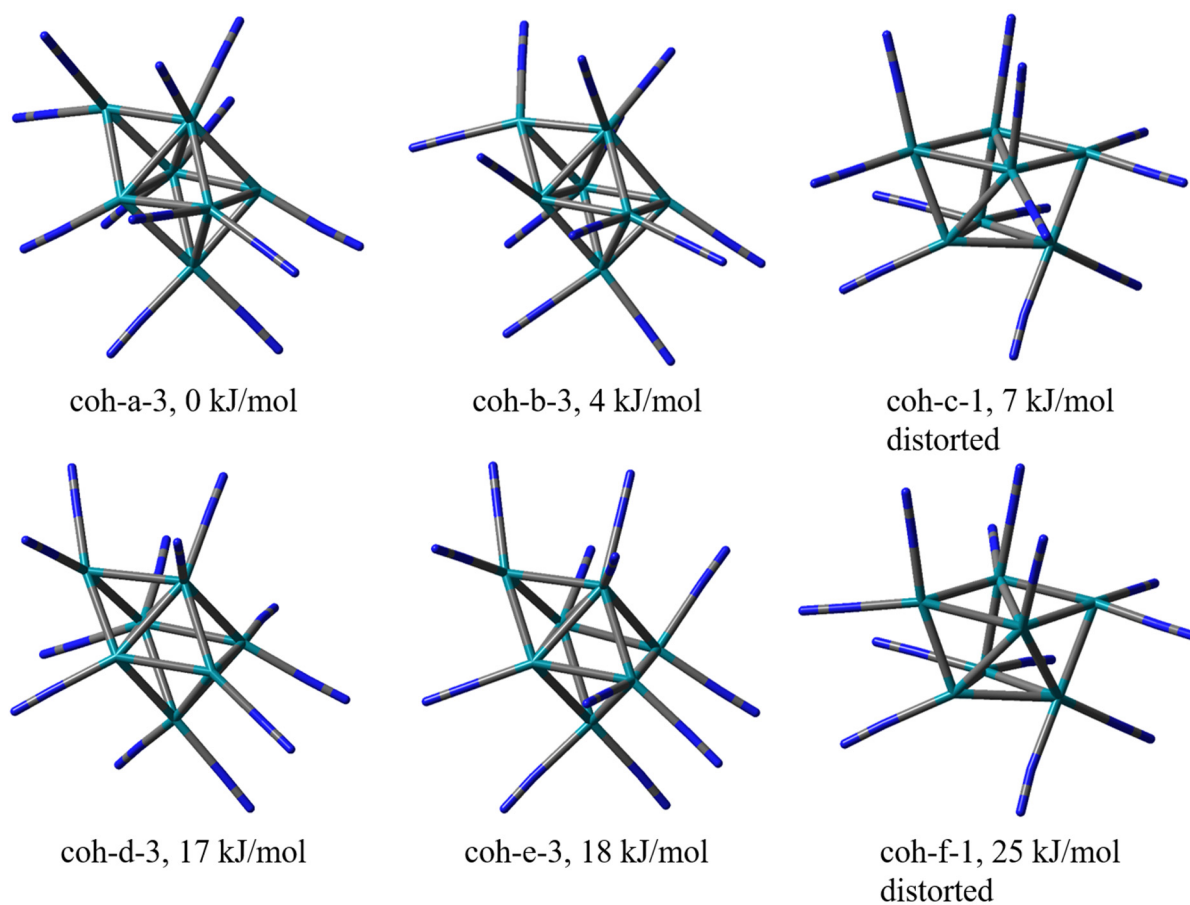


Fig. S7 Calculated structures of the [Rh₇(N₂)₁₂]⁺ cluster adsorbate complex, correspondent to the calculated spectra in Fig. 8.

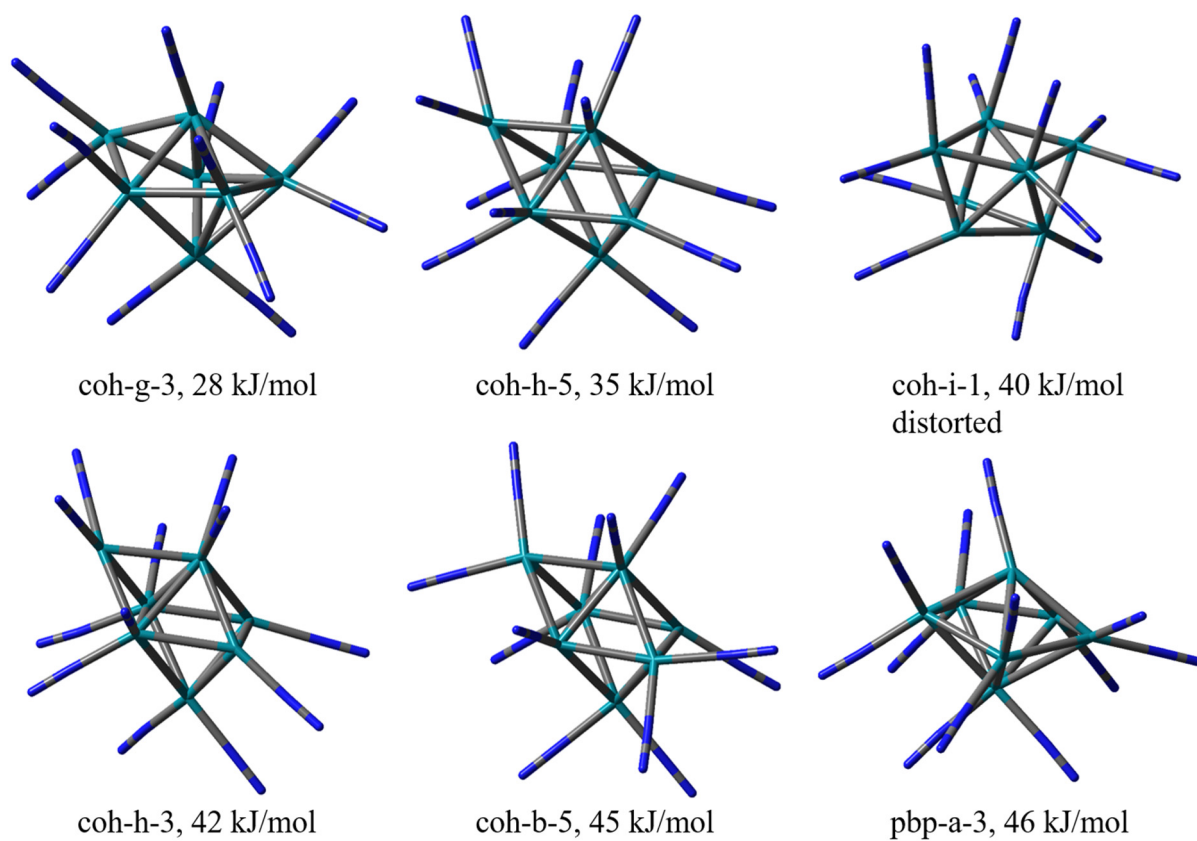


Fig. S8 Calculated structures of the $[\text{Rh}_7(\text{N}_2)_{12}]^+$ cluster adsorbate complex, correspondent to the calculated spectra in Fig. S9.

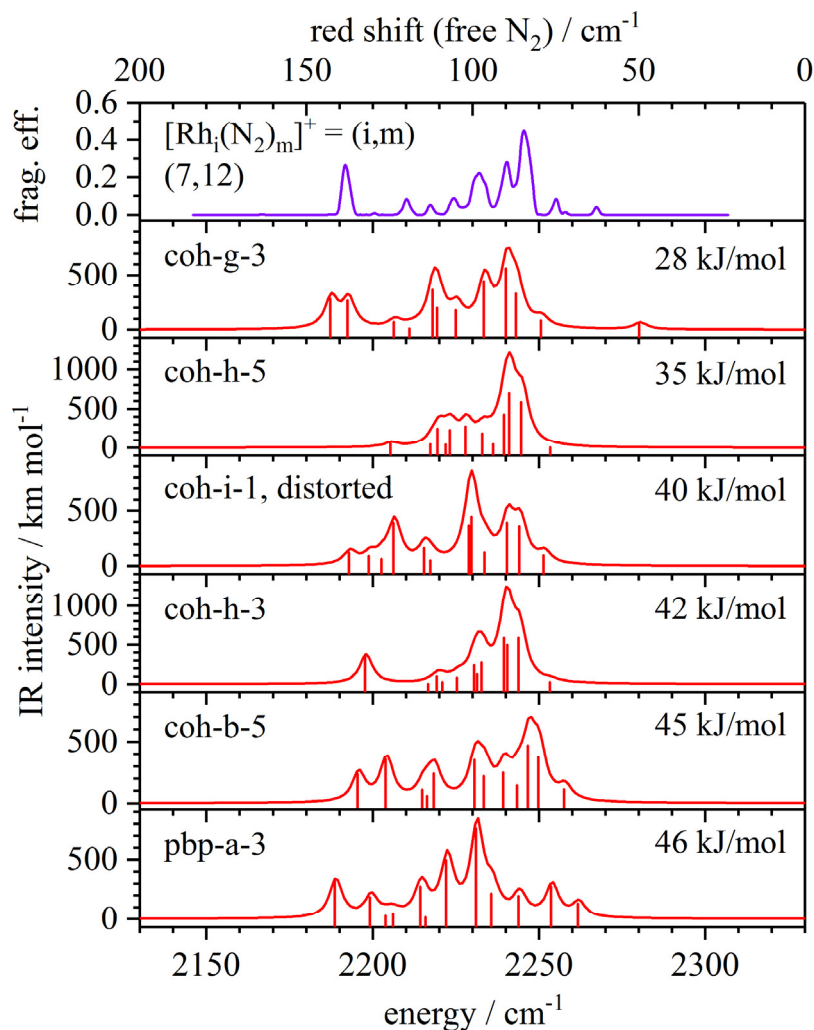


Fig. S9 Experimental IR-PD spectrum of the $[\text{Rh}_7(\text{N}_2)_{12}]^+$ cluster and calculated linear absorption spectra of the isomers shown in Fig. S8 (scaled by 0.9385). The line spectra were convoluted with a 5 cm^{-1} FWHM Gaussian. The three letters indicate the arrangement of the metal atoms in the calculated structures followed by a code for the arrangement of the N_2 molecules and the spin multiplicity. The auxiliary axis (on top) indicates the red shift with respect to the IR inactive free N_2 vibration.

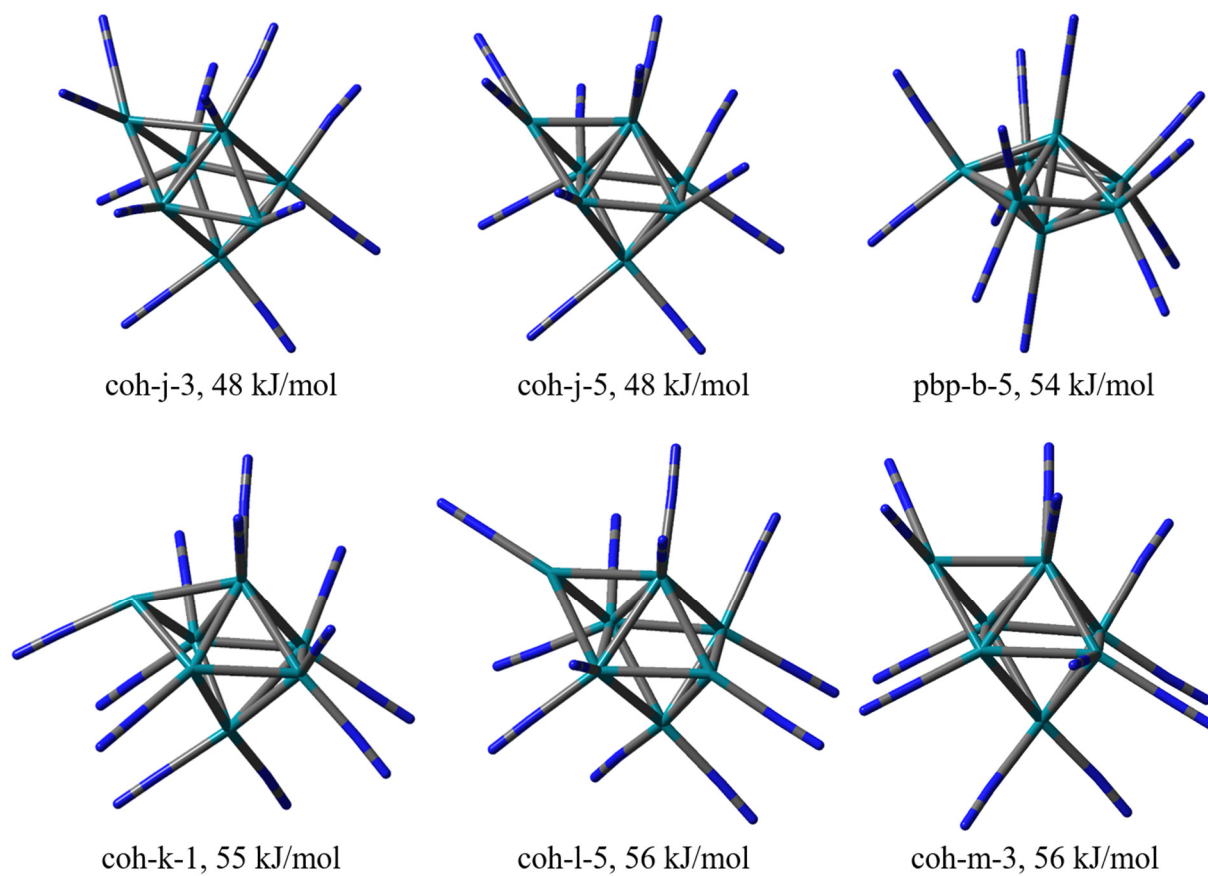


Fig. S10 Calculated structures of the $[\text{Rh}_7(\text{N}_2)_{12}]^+$ cluster adsorbate complex, correspondent to the calculated spectra in Fig. S11.

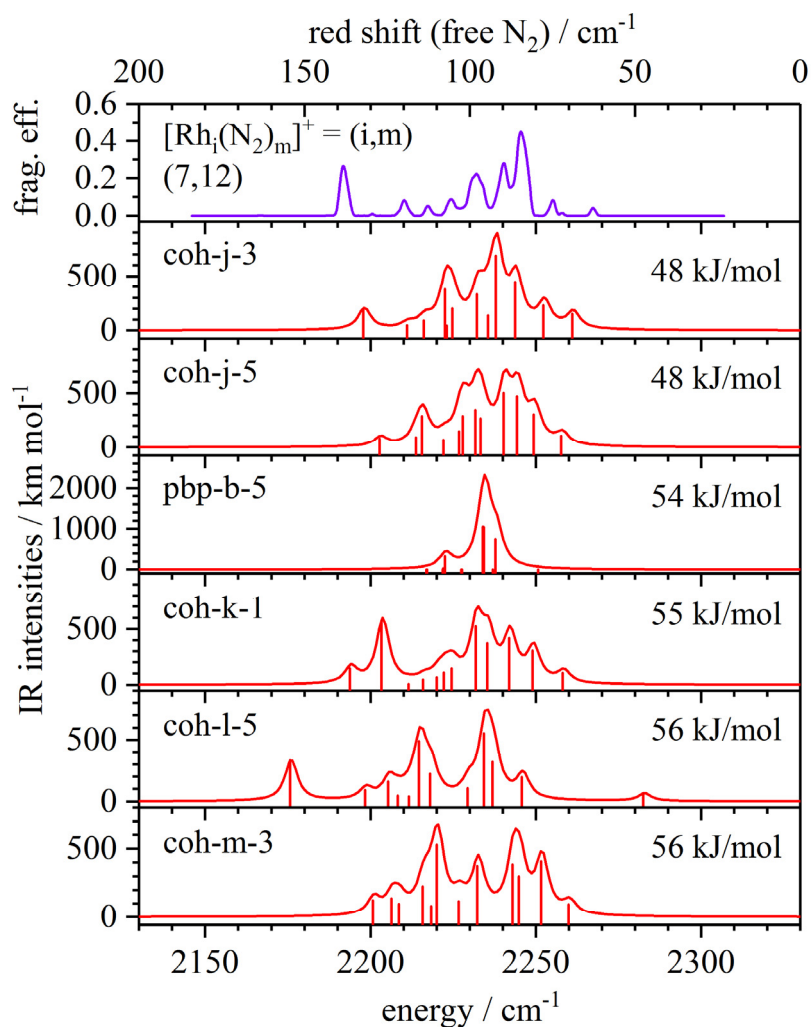


Fig. S11 Experimental IR-PD spectrum of the $[\text{Rh}_7(\text{N}_2)_{12}]^+$ cluster and calculated linear absorption spectra of the isomers shown in Fig. S10 (scaled by 0.9385). The line spectra were convoluted with a 5 cm^{-1} FWHM Gaussian. The three letters indicate the arrangement of the metal atoms in the calculated structures followed by a code for the arrangement of the N_2 molecules and the spin multiplicity. Remarkably all structures have a spin multiplicity of 1 or 3. The auxiliary axis (on top) indicates the red shift with respect to the IR inactive free N_2 vibration.

Table S6 Calculated vibrational modes of the coh-b-3 cluster. The N₂ stretching frequencies are given unscaled and scaled by 0.9385. The Rh atom numbering is corresponding to Fig. S6. In the case of the stretching vibrations, the position of the oscillators on the cluster is given.

mode	type / site	frequency / cm ⁻¹	scaled frequency / cm ⁻¹	IR intensity / km mol ⁻¹
N₂ wagging modes				
1-24	wagging	35-102		0.007-0.24
Rh skeleton modes				
25-39	cluster core vibrations	111-240		0.064-3.7
N₂ bending modes				
40-75	N ₂ Bending	246-437		0.43-25
Single N₂ stretching modes				
76	@ Rh2	2330	2187	408
77	@ Rh4	2338	2194	169
78	asym. coupling of (asym. @ Rh3) and (asym. @ Rh7)	2358	2213	67
79	asym. @Rh7	2363	2218	212
80	asym. @Rh1	2364	2219	42
81	asym. @Rh6	2372	2226	177
82,83	(asym. @ Rh7) with (asym. @ Rh5)	2376, 2378	2230, 2232	334, 285
84	sym. coupling of (sym. @ Rh6) and (sym. @ Rh1)	2386	2239	232
85	sym. @ Rh5	2392	2245	606
86	(sym. @ Rh1) with (sym. @ Rh3)	2396	2249	421
87	all N ₂ in phase	2402	2254	13

References

1. Mokkath JH, Pastor GM (2012) Interplay between Chemical and Magnetic Order in FeRh Clusters. *The Journal of Physical Chemistry C* 116 (32):17228-17238
2. Beltran MR, Zamudio FB, Chauhan V, Sen P, Wang H, Ko YJ, Bowen K (2013) Ab initio and anion photoelectron studies of Rh_n (n = 1-9) clusters. *Eur Phys J D* 67 (3):63.
3. Cotton FA, DeBoer BG, LaPrade MD, Pipal JR, Ucko DA (1971) The crystal and molecular structures of dichromium tetraacetate dihydrate and dirhodium tetraacetate dihydrate. *Acta Crystallographica Section B* 27 (8):1664-1671.
4. CRC Handbook of Chemistry and Physics (2010). 90 edn. CRC Press, Boca Raton.

4. Cryokinetics and Spin Quenching in the N₂ Adsorption onto Rhodium-Cluster Cations

Amelie A. Ehrhard^{1, 2}, Matthias P. Klein², Jennifer Mohrbach, Sebastian Dillinger,
and Gereon Niedner-Schatteburg³

*Fachbereich Chemie and Forschungszentrum OPTIMAS,
Technische Universität Kaiserslautern, 67663 Kaiserslautern, Germany*

4.1 Preamble

The following chapter is an original manuscript of a publication in the journal „Molecular Physics” published by Taylor & Francis.

An experimental team consisting of A. Ehrhard, S. Dillinger, J. Mohrbach and me conducted the experiments. A. Ehrhard and I conducted the data evaluation. An initial manuscript was written by A. Ehrhard and continued by me. The DFT calculations were conducted and evaluated by myself. The manuscript was revised by G. Niedner-Schatteburg and me. A. Ehrhard and I contributed equally.

Full Reference:

Cryokinetics and spin quenching in the N₂ adsorption onto rhodium cluster cations

A. A. Ehrhard, **M. P. Klein**, J. Mohrbach, S. Dillinger, and G. Niedner-Schatteburg, *Mol. Phys.* **2021**, e1953172.

<https://doi.org/10.1080/00268976.2021.1953172>

¹ Present address: Max-Planck-Institut für Polymerforschung, 55128 Mainz, Germany

² These authors contributed equally

³ Corresponding author: Prof. Dr. Gereon Niedner-Schatteburg, Erwin-Schrödinger-Straße 52, 67663 Kaiserslautern, gns@chemie.uni-kl.de

4.2 Abstract

The kinetics of N₂ adsorption onto gas phase Rh_{*i*}⁺-clusters (*i* = 5-15) within 26 K He buffer gas have been investigated by Fourier transform ion cyclotron resonance (FT-ICR) mass spectrometry, with particular focus to clusters *i* = 5,6,7,9. The adsorption limits $m = m_{max}$ of [Rh_{*i*}(N₂)_{*m*}]⁺ clusters are strongly cluster size dependent. Some cluster sizes reveal an intermittent adsorption limit m_x , which implies a rough cluster surface. Most of the clusters reveal smooth surfaces, which constitute of Rh atoms with similar next neighbour coordination. The kinetic fits and relative rate constants reveal the sequential adsorption of N₂ as the only significant reaction channel. In some cases, we find N₂ desorption steps at high N₂ loads indicating adsorption - desorption equilibria. For these steps, we determined Gibbs energies from the relative rate constants. Absolute rate constants compare favourably to those by the 'Hard Sphere Average dipole orientation model'. We observed a significant reluctance towards N₂ adsorption for the Rh₅⁺ cluster, indicated by significant desorption at low N₂ coverage. Our DFT calculations model the energetics of the N₂ adsorption onto Rh₅⁺ in terms of coverage dependent 'spin valley' curves, and we conclude in an adsorption induced spin quenching upon considerable N₂ coverage, $m > 4$.

Keywords: Transition metal clusters, adsorption kinetics, spin quenching

4.3 Introduction

Characterizing surfaces at the molecular level. Throughout the last 90 years, adsorption behavior of small molecules to solid surfaces has been serving to investigate the surface structure and existence of distinct surface sites. Brunauer, Emmett and Teller utilised N₂ adsorption to gain information on active surface sites [1], and Temperature Programmed Desorption (TPD) has become a routine method for surface analytics. In particular, N₂ adsorption/desorption gained a key role in metal surface analysis, and its adsorption kinetics became subject of fundamental research [2-4]. Successively more elaborate techniques of surface analysis gained strong evidence for distinguishable adsorption N₂ adsorption geometries on Fe surfaces [5, 6].

Isolated clusters as model systems. Investigation of size selected clusters construct a bridge between bulk surfaces and isolated atomic systems. In this regard, clusters may serve as model

systems for the adsorbate – surface interaction. Studies of isolated metal cluster ions thus serve to elucidate elementary processes in catalysis [7]. Mere atomic ions (or their oxides) are able to catalyse various elementary reactions of relevance to industrial catalysis [8]. On the other side, the investigation of nanosized particles has led to the coinage of the term ‘nanocatalysis’ [9]. In between of these extreme sizes – very small and very large – size selected clusters of less than 50 atoms have come into the focus of particular interest as model systems for active centers/sites in heterogeneous catalysts or as reactive species themselves [10]. A multitude of studies and reviews has recognised the value of N₂ adsorption for the characterization of such size selected clusters throughout the last 30 years [11-22].

Clusters and aliphatic hydrocarbons. It soon became a vivid field of research to investigate the kinetics of aliphatic hydrocarbon adsorption and activation on clusters [23-27]. Most recently, focused attention was shed on the gas phase chemistry of size selected Rhodium clusters, and we refer the reader to the collection of studies within a most exhaustive review [28]. Few selected examples deserve explicit mentioning in the current context: It repeatedly emerged as a reaction motif that multiple CH activation steps occur through multiple consecutive oxidative additions, which are followed by reductive elimination of H₂ from dihydride intermediate cluster species. These elementary steps were characterised by their kinetics, and they were found cluster size dependent in an often-unpredictable manner, charge state matters [24, 27, 29-33].

Rh clusters and N₂ adsorption. It is confirmed that N₂ undergoes molecular adsorption to Rh_n⁺ clusters under isothermal conditions [34]. The efficiency of adiabatic N₂ adsorption benefits from precooling of neutral Rh_n clusters, and the sticking probability decline with reducing the cluster size, even vanishing at n < 12 [35]. Nitride and Oxide products of Rhodium clusters become readily available under hot conditions [36, 37].

IR spectroscopy of rhodium clusters. IRMPD spectroscopy of [Rh_n(CO)_x]^{-/0/+} clusters revealed novel correlations: Observed CO stretching band shifts correlate with the cluster core size and receive interpretation through a ‘charge dilution model’ [38-41]. Subsequent IRMPD studies confirmed N₂O reduction by Rh₄₋₈⁺ clusters [42]. Far-IR-MPD studies of naked Rh₆₋₁₂⁺ clusters served to verify DFT model calculations that predicted tetrahedral and octahedral structures rather than cubic ones [43]. This prediction found support through analogous findings for neutral and anionic clusters [44].

Cluster surface morphologies. In the last years, we have successfully correlated results from IR spectroscopic and kinetic measurements as well as DFT modelling [45, 46] of nickel cluster cations and were able to identify several types of cluster surface morphologies as *rough* and *smooth* surfaces. Recently, we performed IR-PD measurements together with DFT modelling of $[\text{Rh}_i(\text{N}_2)_m]^+ = (i,m)$ cluster adsorbate complexes. We assigned an octahedral structure for the Rh_6^+ cluster, a capped octahedron for the Rh_7^+ cluster and a tricapped trigonal prism to the Rh_9^+ cluster.[47] Furthermore we found evidence for adsorption induced relaxation of the cluster core for the $(6,m)$ and the $(7,m)$ cluster adsorbate complexes.

The structures of $\text{Rh}_5^{-,0,+}$ clusters have been subject of numerous investigations. DFT modelling of $[\text{Rh}_5(\text{N}_2\text{O})\text{Ar}]^+$ cluster complexes revealed a low energy difference of square-based pyramidal and trigonal bipyramidal Rh_5 motifs beyond a definite assignment [42]. Other studies at various levels of theory report similar results on neutral and anionic Rhodium clusters [27, 44, 48-51]: There are low energy differences of nonet square pyramid and trigonal bipyramid isomers.

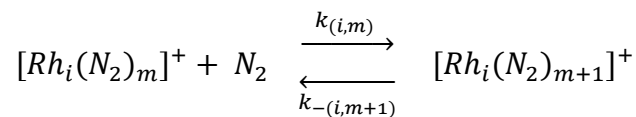
It is a recently emphasized question how coupled electronic surfaces enable metal ligand interactions and reactions through changes of spin multiplicities [52]. Most notably J. Troe and co-workers analysed the reaction kinetics of such nonadiabatic processes involving $\text{Fe}^+ + \text{NO}$, N_2O , NO_2 , and $\text{FeO}^+ + \text{CH}_4$, H_2 , CO , NO [53-58].

In the present study, we report and discuss the stepwise adsorption kinetics of N_2 on Rh_i^+ clusters under isothermal cryo conditions, and we evaluate the recorded rate constants in the light of available kinetic models. We extract thermodynamic parameters, and we elucidate our findings in the light of concomitant DFT modelling. We find evidence for stepwise spin quenching by stepwise N_2 adsorption, and we coin the concept of *spin valley* potential curves.

4.4 Experimental and theoretical methods

A customised 7 T Fourier Transform-Ion Cyclotron Resonance (FT-ICR)-mass spectrometer (Apex Ultra Bruker Daltonics) was used to perform the kinetics experiments. The second harmonic of a Nd:YAG laser (Innolas *Spitlight 300*, 20 Hz) was guided in the home-built laser vaporization cluster ion source chamber as described before [23, 59]. In brief, the laser beam is focused on a rotating Rh-target (99.8%, Alfa Aesar, 0.1 mm thick) and the resulting plasma is entrained in a helium gas pulse (40 μs , 10 – 15 bar). The gas pulse was generated by using a

home-built piezoelectric valve [60], operating in synchronization with the laser at 20 Hz. In the subsequent jet expansion through a 69 mm long channel (2 mm diameter) into vacuum (10⁻⁷ mbar), the atoms and ions in the plasma cool down and aggregate to clusters. The cluster beam is skimmed and the clusters are guided through a 90 degree ion beam bender and a quadrupole mass filter, before they are stored into a cryogenic hexapole ion trap at 26 K. By a continuous gas inlet we introduce 3.0-3.1 · 10⁻⁷ mbar N₂ and 3.0 · 10⁻⁶ mbar He into the cryo ion trap. After storing the cluster ions for a variable storage time (0–10 s), the ions are extracted and steered into the ICR-cell of the so called ‘infinity’ type [61], using various electrostatic lenses. The ICR-cell is cooled down to 10 K by a closed cycle He cryostat to prevent heating of the clusters by black body radiation. For kinetic investigations of the reaction of Rh_i⁺ clusters with N₂, we isolate the parent ion in the quadrupole. The ICR-cell serves for the detection of the formed cluster adsorbate complexes [Rh_i(N₂)_m]⁺. By analysis of the mass spectra at various reaction times and pseudo-first-order kinetic fits with the genetic algorithm program ‘evofit’ [62] we obtain relative rate constants $k_{(i,m)}$ for each N₂ adsorption step $m \rightarrow m+1$, and $k_{-(i,m+1)}$ for each N₂ desorption step $m+1 \rightarrow m$ alike:



The chosen nomenclature is in line with our previous publications. It is fully self-consistent, but might become a possible cause of misinterpretation. For the ease of comprehension the reader finds a short excerpt in the supplement, *cf.* Text S1.

Our thus determined adsorption rate constants are normalised to the experimental conditions of the [Rh₇(N₂)_m]⁺ species (recorded at p(N₂) = 3.0 · 10⁻⁷ mbar). The relative rate constants k_{rel} are transformed to absolute rate constants k_{abs} , using the number density $\rho_{\text{N}_2}(T)$ as conversion factor.

$$k_{(m)}^{abs} = k_{(m)} / \rho_{\text{N}_2}(T) \quad (1)$$

This number density is determined indirectly from the pressure in the surrounding chamber and $p_c^{(300\text{K})}$ and an effective geometry factor c_{app} .

$$\rho_{\text{N}_2}(26\text{ K}) = \frac{c_{app} p_c^{300\text{ K}}}{k_B T_{300\text{ K}}} \quad (2)$$

The geometry factor c_{app} reveals a significant temperature dependence. After numerous kinetic studies, we evaluated this factor to 1.8 at 26 K with an uncertainty of $\pm 50\%$. The ratios of the absolute rate constants to the collision rates yield the sticking probabilities γ :

$$\gamma = \frac{k_{abs}}{k_{coll}} \quad (3)$$

We evaluated collision rates by three models:

(1) The average dipole orientation theory [63-66] (ADO) assumes a classical trajectory of a linear dipole in the field of a point charge:

$$k_{coll} = \frac{q}{2\varepsilon_0\sqrt{\mu}} \left(\sqrt{\alpha} + c\mu_D \sqrt{\frac{2}{\pi k_B T}} \right) \quad (4)$$

μ is the reduced mass (of the cluster adsorbate complex), α is the polarizability and μ_D is the dipole moment in (Debye). The parameter c lies between 0 and 1, and can be expressed by the polarizability volume α' and μ_D [66]. It simplifies to the Langevin rate in the case of a negligible dipole moment.

(2) In some cases, the measured reaction rates for charged metal clusters exceed the ADO collision rate [30]. Kummerloewe and Beyer [67] devised a 'Hard Sphere Average dipole orientation' (HSA) model. They determined collision rates of finite size ionic clusters with neutral molecules treating both as hard spheres, and assuming a point charge in the centre of the cluster. The attraction between point charge and the neutral reactant is represented by an ADO type interaction potential.

(3) The alternative 'Surface Charge Capture' (SCC) model assumes an ideally conducting cluster instead. The point charge is free to move within the geometric boundaries of the cluster, and it interacts attractively with the neutral molecule, such that it migrates to the surface of the cluster. This model predicts significantly larger collision rates than ADO, and it is in good agreement with experimental rate constants. Even the SCC collision rates, however, are exceeded by experimental findings in some cases, for example in the reaction of Rh_n^\pm with CO [67, 68].

The kinetic fits include N_2 desorption whenever appropriate. Such desorption rates at hand, the according adsorption – desorption ratios of relative rate constants yield the equilibrium constant of the $(m+1)^{\text{th}}$ N_2 adsorbate, $k_{(i,m)}/k_{-(i,m+1)} = K_m$ (Table S10), and its Gibbs free energy

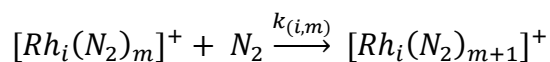
$\Delta_{\text{ads}}G$ (Fig. 6, Table S11). Where our fits include only negligible desorption or none, we set the value of their relative rate constants $k_{-(i,m+1)}$ to an upper limit of 0.001 s⁻¹.

Quantum chemical modelling. Density functional modelling was performed by the Gaussian 09 package [69]. We chose the PBE0/cc-pVTZ(N) level of theory [70] and we utilise Stuttgart RSC 1997 ECP(Rh) basis sets of double zeta quality throughout [71] as proven suitable before [47]. We did not correct for dispersion effects, which we expect small. We do not cover spin orbit coupling which might alter some of our findings. We achieved convergence of our calculation only at the expense of a relaxed convergence criterion of only 10⁻⁶, which is well understood in terms of the exceedingly high electronic state density of transition metal clusters [72]. We checked the obtained structures for imaginary frequencies. For low spin states and low N₂ coverage, we obtained occasionally some spin contamination that is denoted throughout the documentation of results whenever significant.

4.5 Results and Discussion

4.5.1 The Limits of N₂-Adsorption and its Cluster Size Dependencies

We have investigated the cryo adsorption of N₂ to a selected subset of [Rh_{*i*}(N₂)_{*m*}]⁺ clusters – abbreviated as (*i,m*) – in the range of *i* = 5,...,15 by recording their cryogenic mass spectra and their storage time dependent product distributions under isothermal conditions at 26 K. Together with the corresponding kinetic fits these data are presented in the supplementary information to this paper (*cf.* SI Fig.s S1 – S12). Here, we want to present and discuss two archetypical examples in more depth, namely the temporal evolution (t = 0–5 s) of [Rh₆(N₂)_{*m*}]⁺ and [Rh₉(N₂)_{*m*}]⁺ intensities by exposure to ~ 3.0 · 10⁻⁷ mbar N₂ (Fig. 1). The N₂ adsorptions of these clusters demonstrate key features, which are representative for other investigated clusters as well. Starting from the bare rhodium cluster, the temporal evolution of the mass spectra reveal a successive increase of 28 m/z. This indicates the adsorption of molecular N₂. For all cluster sizes studied, there is taking place an apparently dominating, sequential adsorption of N₂ to the clusters:



Plain inspection of the recorded mass spectra does not reveal any evidence for further reactions. Later on – invoking explicit kinetic fits – we will find evidence for N_2 desorption in some cases.

The two clusters $(6,m)$ and $(9,m)$ reveal a stepwise N_2 uptake up to strict adsorption limits m_{max} . These limits mark some points of saturation. Thus, the largest observable clusters are $(6,12)$ and $(9,9)$, respectively. We find an according adsorption limit in all of our recorded spectra of (i,m) clusters ($i = 5, \dots, 15$). Closer inspection of the mass spectra reveals subtle details: In the case of $(6,m)$, we observe an N_2 adsorbate, namely $(6,8)$, which reacts slower to consecutive N_2 -species. This causes some retardation, but does not suppress further N_2 adsorption. We define this as an *intermittent adsorption limit/level* m_x . In the case of $(9,m)$, there is a sole N_2 adsorption limit m_{max} at $m = 9$ and no intermittent adsorption limit.

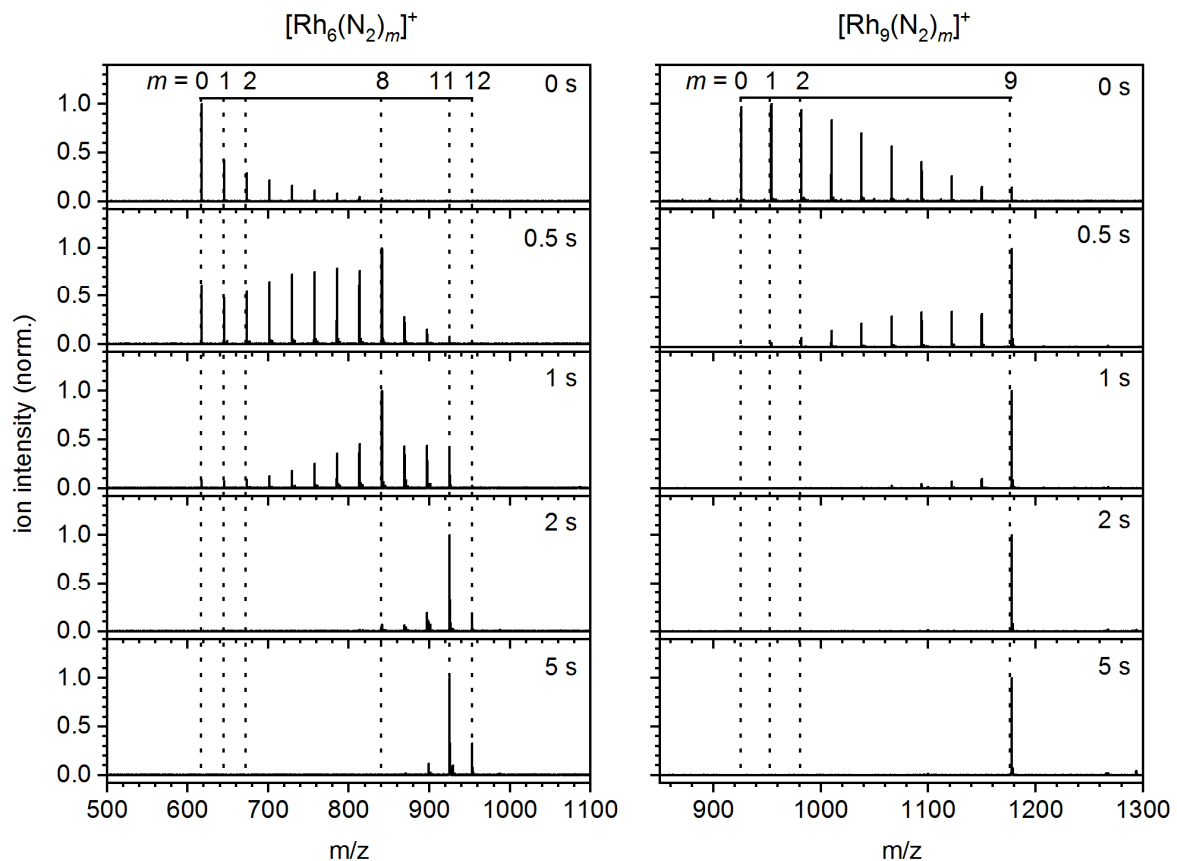


Fig. 1 Temporal evolution of the FT-ICR mass-spectra of Rh_6^+ and Rh_9^+ exposed to $3.0 \cdot 10^{-7}$ mbar and $3.1 \cdot 10^{-7}$ mbar N_2 at a temperature of 26 K at various storage times in the cryogenic hexapole ion trap. Note, that the N_2 adsorption stops after the uptake of 12 N_2 and 9 N_2 , respectively.

A compilation of the m_{max} and the m_x values for each studied cluster core Rh_i^+ (Fig. 2) reveals adsorption limits of $i \leq m_{max} \leq 2i$ with remarkable fluctuations. For the Rh_5^+ and Rh_6^+ clusters the found m_{max}/i ratio is 2; for Rh_7^+ and beyond there is a decrease of observed ratios towards as low as $m_{max}/i = 1.2$ for Rh_{15}^+ .

The Rh_9^+ cluster shows adsorption up to $m_{max} = 9$ – an m_{max}/i ratio of 1 – and reveals no m_x . Such intermittent adsorption limits $m_x < m_{max}$ are observed merely in the cases of Rh_5^+ , Rh_6^+ , Rh_7^+ and Rh_{15}^+ , namely (5,7), (6,8), (7,10), and (15,13).

We expect small clusters ($i \leq 12$) to constitute exclusively of easily accessible surface atoms. One can imagine a limit of a single adsorbate monolayer with twofold occupation of all Rh atoms. Indeed, the Rh atoms of the clusters $i < 7$ tend to prefer such double adsorbate occupation. Intermediate clusters $7 \leq i \leq 12$ may provide for some higher coordinated and therefore less accessible surface atoms that can only adsorb one N₂. Rh_{13}^+ and larger clusters do possess one or more inner Rh atoms, which are completely surrounded by other Rh (surface) atoms, and which become thus inaccessible for exterior adsorbates.

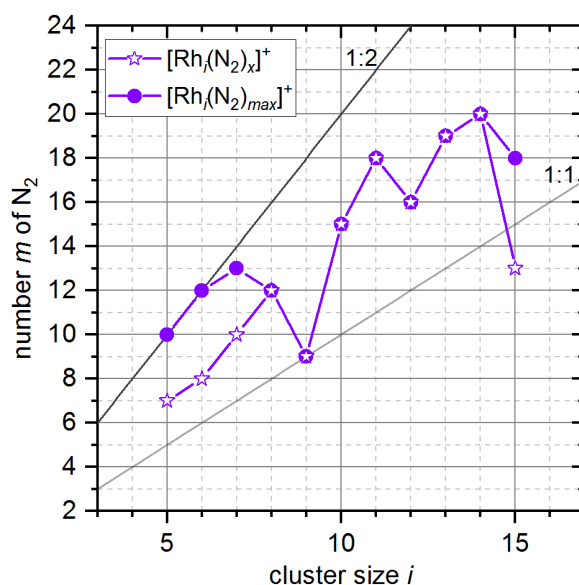


Fig. 2 The recorded *adsorption limits* m_{max} (purple circles) and the intermittent adsorption limits m_x (purple stars) of N₂ adsorbates to Rh_i^+ -clusters. The grey lines indicate adsorbate to cluster size ratios of $m:i = (1:1)$, $(2:1)$, namely a monolayer and a double occupation of all Rhodium atoms, respectively [47]. Note, that in correction to the previous publication ([47], Fig. S1 therein), we assign an intermittent adsorption limit (5,7) at $m = 7$ to the $[Rh_5(N_2)_m]^+$ cluster that is clearly supported by the present kinetic investigations.

In the following discussion, we will find that clusters without an intermittent adsorption limit m_x reveal a *smooth* cluster surface, which holds true in most cases. More precisely these are the cases of $i = 8, \dots, 14$. There are just four clusters, where an intermittent adsorption limit m_x occurs, which are $i = 5, 6, 7$ and 15 . We will regard these as clusters with *rough* surfaces.

4.5.2 Adsorption kinetics and rate constants

We further investigated the stepwise N_2 adsorption onto selected Rh_i^+ clusters at 26 K by recording their adsorption kinetics in more detail. By assuming pseudo-first order kinetics, it is possible to fit the temporal evolution of kinetic data with our genetic algorithm routine. This confirms consecutive N_2 adsorption steps. All of our investigated Rh_i^+ clusters decay mono exponentially without any indication of a second component or isomer. From this and the good overall quality of these fits, it is possible to extract a single relative stepwise rate constant for each consecutive adsorption and for each desorption step of N_2 . We present relative values at this point, with relative uncertainties of as low as $\pm 20\%$. Conversion to absolute rate constants by pressure normalization does imply considerable absolute uncertainties of almost one order of magnitude. For these absolute values, refer to the supplement (Table S7). In the following, we will compare and discuss the recorded kinetic fits and the obtained rate constants for the selected clusters Rh_5^+ , Rh_6^+ , Rh_7^+ and Rh_9^+ in detail. The kinetic data of the other investigated clusters are provided in the supplementary material.

Our kinetic data confirm what we found by MS spectra at long storage times: The kinetic curves of Rh_5^+ (Fig. 3a), Rh_6^+ (Fig. 3b), Rh_7^+ (Fig. 4a) and Rh_9^+ (Fig. 4b) reveal adsorption limits $m_{max} = 10, 12, 13,$ and $9,$ respectively. The kinetic curves of Rh_5^+ , Rh_6^+ and Rh_7^+ reveal intermittent adsorption limits at $m_x = 7, m_x = 8$ and $m_x = 10,$ respectively. In effect, we find strong support for the identification of Rh_9^+ as a cluster with an all *smooth* surface. Rh_5^+ and Rh_6^+ behave like clusters with *rough* surfaces, they possess preferred and less preferred adsorption sites which shows in the kinetic curves. The Rh_7^+ falls somewhat in between; it behaves like a largely smooth surface with some but limited roughness – likely through some low coordinated surface atom.

The Rh_5^+ case seems special as the N_2 uptake is overall slower than in all other cases. A closer look to the values of the fitted rate constants may help to understand.

Relative Rate constants. Next, we take a more detailed look at the rate constants of each adsorption and desorption step for the selected clusters Rh_5^+ (Fig. 3c), Rh_6^+ (Fig. 3d), Rh_7^+

(Fig. 4c), and Rh₉⁺ (Fig. 4d). At first glance we see that the three sets of N₂ adsorption rate constants of Rh₅⁺, Rh₆⁺ and Rh₇⁺ show some step like decline towards $k_{(5,7)}$, $k_{(6,8)}$ and $k_{(7,10)}$, respectively. Rh₉⁺ does not. N₂ desorption is specific by the size of the cluster.

Rh₅⁺ - N₂ adsorption. The relative rate constants of N₂ adsorption to the Rh₅⁺ cluster increase throughout $m = 0, \dots, 2$ by almost a factor of 6. The first adsorption step $k_{(5,0)}$ is rate limiting, and all subsequent steps $k_{(5,m)}$ are faster. For $m = 2, \dots, 6$ they are more or less constant; this is within error margins between 4.8 s^{-1} and 6.2 s^{-1} (Fig. 3c). There is a steep decline at the intermittent adsorption limit $m_x = 7$: The rate constants diminish by a factor of 4.2 from $k_{(5,6)}$ to $k_{(5,7)}$. The rate constants $k_{(5,8)}$ and $k_{(5,9)}$ increase slightly, up to a value of $k_{(5,9)} = 2.9 \text{ s}^{-1}$. Thus, there is a remarkably slow uptake of the first and of the seventh N₂ adsorbate.

Rh₅⁺ - N₂ desorption. We emphasise a particularly noteworthy outcome of the kinetic fits of our recorded data in the case of Rh₅⁺: There is a significant amount of N₂ desorption, $k_{-(5,1)}$ through $k_{-(5,5)}$, which we do not observe in any of the other investigated cases, $[\text{Rh}_i(\text{N}_2)_m]^+$, $i = 6, \dots, 15$. Note, that the N₂ desorption off $[\text{Rh}_5(\text{N}_2)_1]^+$, $k_{-(5,1)} = 6.1 \text{ s}^{-1}$, is much faster than the N₂ adsorption onto Rh₅⁺, $k_{(5,0)} = 0.97 \text{ s}^{-1}$. In order to balance it would take six times higher N₂ partial pressures than applied.

The subsequent desorption steps slow down, and $[\text{Rh}_5(\text{N}_2)_7]^+$ ceases to desorb at all, with a stated upper limit of $k_{-(5,m>5)} < 0.001 \text{ s}^{-1}$. The fits indicate even lower values, e.g. $k_{-(5,6)} < 8 \cdot 10^{-7} \text{ s}^{-1}$. The kinetic fit quality of the Rh₅⁺ cluster is not satisfactory at short and long storage times. An analysis of a reduced data set from storage times of 0.2 to 2.6 s (*cf.* Fig. S2) allows for a kinetic fit with an improved quality, that yields reasonably similar rate constants as before.

In summary, the genetic algorithm modelling of Rh₅⁺ + N₂ kinetics yields a pronounced desorption and thus an equilibrium for the first adsorption step and the subsequent steps up to $m = 5$. With an equilibrium constant of 0.16, the equilibrium $(5,0) \rightleftharpoons (5,1)$ is clearly on the educt side (*cf.* Tables S7 and S10). The bare Rh₅⁺ cluster seems reluctant against adsorption of a first N₂ molecule. The intermittent adsorption limit at $m_x = 7$ may be a first hint towards a trigonal bipyramidal structure with a single N₂ molecule at each of the three equatorial Rh atoms and two N₂ adsorbates at each of the two apical Rh atoms. This core structure comprises for higher coordination of Rh atoms (18 Rh-Rh next neighbor interactions, an average coordination number of 3.6, *cf.* Table S19) than a square pyramid would do (16 Rh-

Rh next neighbor interactions, an average coordination number of 3.2). Moreover, the adsorption limit $m_{max} = 10$ is nicely rationalised by a trigonal bipyramid structure: It makes up for two geminal N_2 per Rh atom.

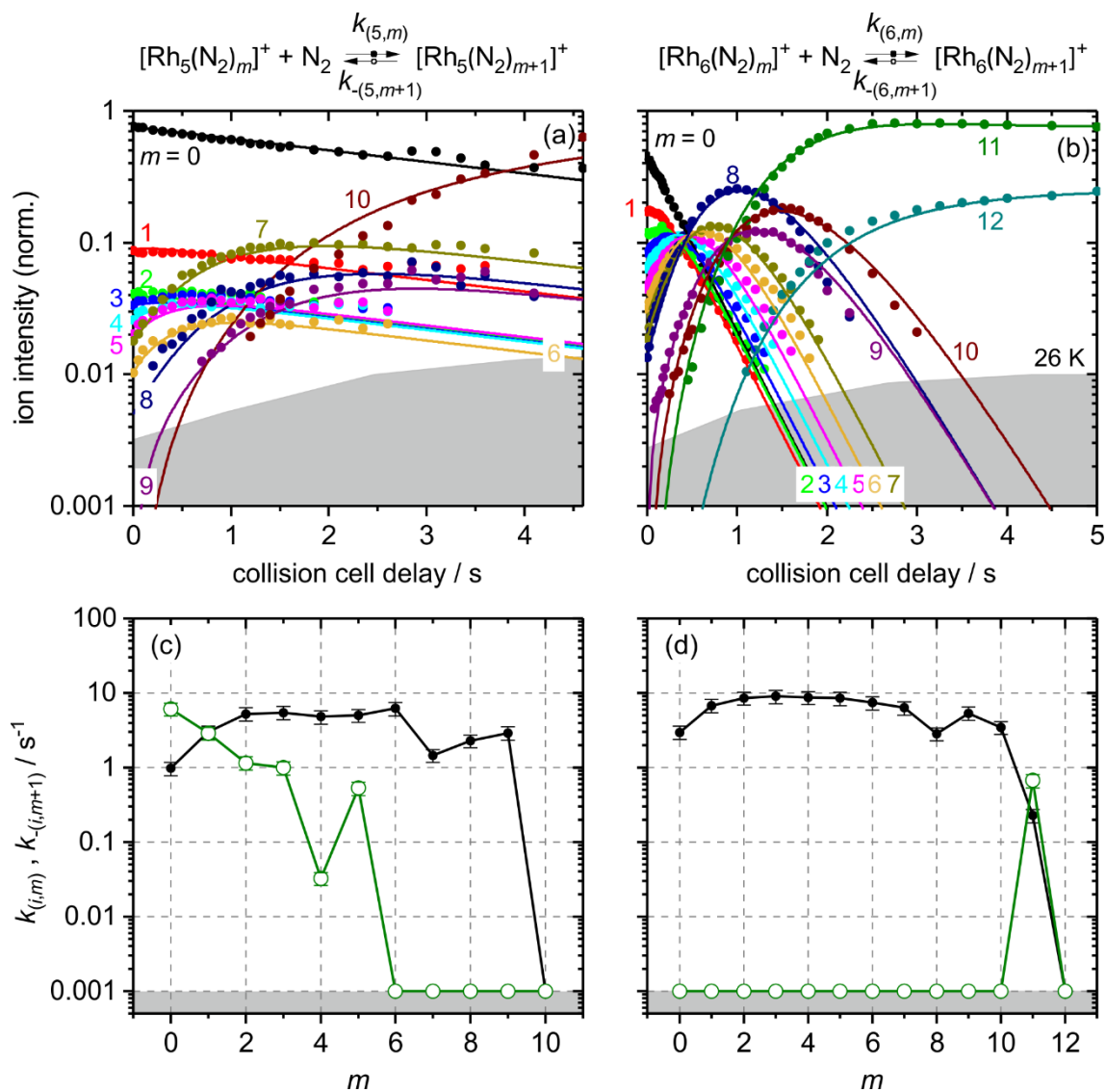


Fig. 3 Isothermal kinetics of the stepwise N_2 adsorption at 26 K (a) by isolated Rh_5^+ clusters and (b) by isolated Rh_6^+ clusters (solid symbols). The fits (solid lines) assume pseudo-first-order kinetics in an adsorption chain of up to 10 consecutive steps for Rh_5^+ and up to 12 for Rh_6^+ clusters. Fitted values of relative rate constants (c) of Rh_5^+ and (d) of Rh_6^+ as a function of the stepwise N_2 adsorption (level m). The grey shaded areas indicate the approximate background noise level. Note, that the fitted rate constants for the adsorption ($k_{(i,m)}$, black filled circles) are nearly 4 orders of magnitude higher than those of the desorption ($k_{-(i,m+1)}$, green open circles, upper limits). Rate constants $k_{(5,10)}$ and $k_{(6,12)}$ are at the noise level and indicate an adsorption limit.

Rh₆⁺ - N₂ adsorption. The relative rate constants of N₂ adsorption to the Rh₆⁺ cluster increase throughout $m = 0, \dots, 2$ by almost a factor of three (Fig. 3d). The increase, however, is less than in the case of the Rh₅⁺ cluster. We find very similar rate constants, $k_{(6,m)} \sim 7.5 \text{ s}^{-1}$, for the subsequent N₂ adsorption steps $m = 2, \dots, 7$. Up to $m = 7$, the first step, $k_{(6,0)}$, is rate limiting for all of the subsequent adsorptions. Beyond the intermittent adsorption limit $m_x = 8$ the rate constants $k_{(6,8)}$, $k_{(6,9)}$, and $k_{(6,10)}$ diminish by a factor of 2.2 (*cf.* Table S2). This drop corresponds to a similar drop in the case of Rh₅⁺, but smaller by almost a factor of two. The subsequent adsorption of a 12th N₂ molecule, $k_{(6,11)} = 0.23 \text{ s}^{-1}$ proceeds more than an order of magnitude slower than any of the previous adsorption steps, and it is in equilibrium with desorption, likely indicating saturation. The overall average of N₂ adsorption rate constants of Rh₆⁺ is higher by almost a factor of two compared to those of the Rh₅⁺ cluster (*cf.* Table S2).

The intermittent adsorption limit at (6,8) is somewhat in contrast to our previous computational results. The then predicted, highly symmetric octahedral cluster structure would rather suggest an intermittent adsorption limit at $m_x = 6$, or even a Langmuir type saturation limit $m_{max} = 6$ [47]. Instead, the presently determined intermittent adsorption limit $m_x = 8$ rather fits to a structure, that comprises two Rh atoms of enhanced propensity of *e.g.* twofold N₂ uptake. It is conceivable to find such behavior upon lower Rh-Rh next neighbor coordination. We can imagine obtaining such coordination motifs by distortion of an octahedral structure towards a boat like structure (*cf.* Fig. S15).

Rh₆⁺ - N₂ desorption. In contrast to the Rh₅⁺ cluster, our fits of the Rh₆⁺ - N₂ kinetics do not reveal any N₂ desorption but for the last step $k_{-(6,12)} = 0.67 \text{ s}^{-1}$. This N₂ desorption off (6,12) is faster by a factor of 2.9 than the N₂ adsorption to (6,11). Thus, the adsorption-desorption equilibrium constant is 0.34 (*cf.* Tables S7 and S10).

At saturation (maximum adsorption limit (6,12)) all Rh centres are doubly occupied by geminal N₂. One of these N₂ is only loosely bound and the equilibrium is on the (6,11) side. We acknowledge the possibility that the observed adsorption – desorption equilibrium may involve an isomerization of the adsorbate shell, and we note in passing that some of our exploratory DFT calculations have revealed indication of such N₂ adsorbate shell reorganization before [46].

Rh₆⁺ cluster surface seems smoother than that of Rh₅⁺. Swift N₂ stabilization is possible without risk of desorption. We have no indication of major electronic effects or relaxation. Saturation

load seems in equilibrium with single desorption. Geminal N₂ occupation of single Rh centres seems ubiquitous.

Rh₇⁺ - N₂ adsorption. The relative adsorption rate constants of the Rh₇⁺ cluster of the consecutive steps $m = 0, \dots, 9$ are roughly constant around $k_{(6,m)} \sim 8.5 \text{ s}^{-1}$ (Fig. 4c). In contrast to Rh₅⁺ and Rh₆⁺, we obtain no initial increase of the rate constants and no clearly rate limiting step up to $k_{(7,10)}$. Similar to Rh₅⁺ and Rh₆⁺, beyond the intermittent adsorption limit $m_x = 10$ the rate constants diminish by a factor of 1.4 from $k_{(7,9)}$ to $k_{(7,10)}$ (cf. Table S2).

Obviously, the step height of the drop at the intermittent adsorption limit decreases with increasing number of metal atoms i through $i = 5, \dots, 7$. The values of the rate constants are in the same range as for Rh₆⁺, thus higher than for Rh₅⁺. The final adsorption of a 13th N₂ molecule is slower by at least a factor of almost two, $k_{(7,12)} = 2.8 \text{ s}^{-1}$, compared to all previous adsorption steps.

Rh₇⁺ - N₂ desorption. As for the Rh₆⁺ cluster, our fit reveals desorption only for the last step $k_{-(7,13)} = 2.6 \text{ s}^{-1}$, and for the second but last desorption step an insignificantly low rate constant $k_{-(7,12)} = 6.0 \cdot 10^{-7} \text{ s}^{-1}$ which is far below our upper accuracy limit of 0.001 s^{-1} (cf. Table S5). Thus, the final adsorption – desorption equilibrium involves a single N₂ molecule. The desorption off (7,13) is essentially as fast as N₂ adsorption onto (7,12) with an equilibrium constant $K_{(7,12)} = 1.1$ (cf. Tables S7 and S10).

At saturation (maximum adsorption limit $m_{max} = 13$) each Rh centre but one is doubly occupied by a geminal N₂ pair. In the course of our previous work, we have managed to assign a capped octahedron structure for the (7,12) clusters by reference to recorded IR spectra. There are geminal N₂ pairs at all but two Rh centres, and single N₂ ligands on two highly coordinated Rh centres: one Rh centre with four and one with five Rh-Rh next neighbour contacts [47]. As for the previous Rh₆⁺ case, the adsorption – desorption equilibrium may come about with adsorbate shell isomerization.

Rh₉⁺ - N₂ adsorption/desorption. The N₂ adsorption desorption cryo kinetics of Rh₉⁺ are particularly noteworthy in two regards: Firstly, all rate constants are roughly equal, $k_{(9,m)} \sim 8.5 \text{ s}^{-1}$ (Fig. 4d), and there is neither an intermittent limit nor a decline towards saturation at $m_{max} = 9$. Secondly, this low value of saturation is in remarkable contrast to the found values $m_{max} = 12$ of Rh₈⁺ and $m_{max} = 15$ of Rh₁₀⁺, (8,12) and (10,15), cf. Fig. 2, and Fig.s S5 and S7. All adsorption sites of Rh₉⁺ seem equivalent, which points towards a *smooth* cluster

surface. Thirdly, Rh₉⁺ runs into $m_{max} = 9$ without indication of any N₂ desorption whatsoever – not even at saturation.

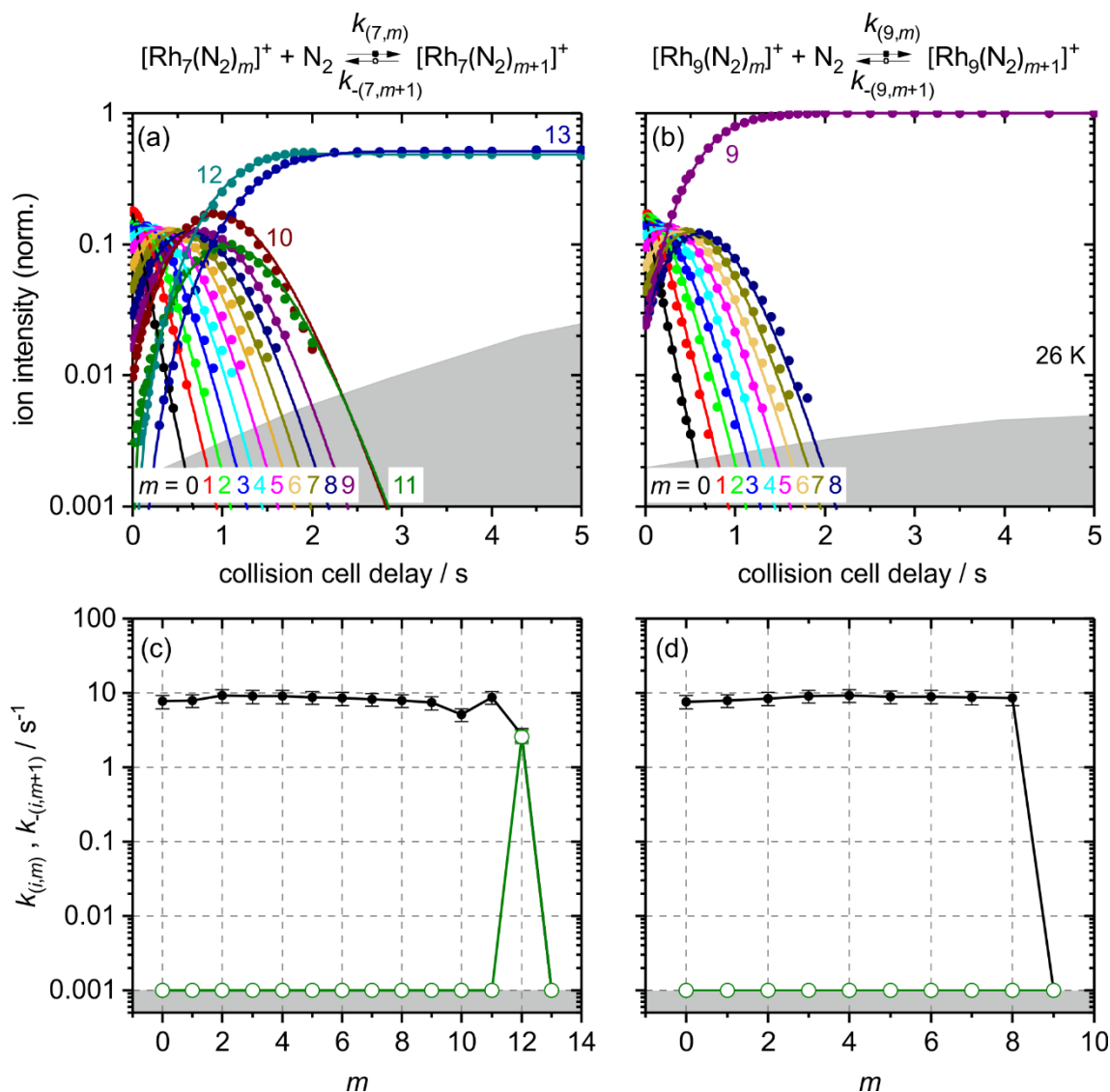


Fig. 4 Isothermal kinetics of the stepwise N₂ adsorption at 26 K (a) by isolated Rh₇⁺ clusters and (b) by isolated Rh₉⁺ clusters (solid symbols). The fits (solid lines) assume pseudo-first-order kinetics in an adsorption chain of up to 13 consecutive steps for Rh₇⁺ and up to 9 for Rh₉⁺ clusters. Fitted values of relative rate constants (c) of Rh₇⁺ and (d) of Rh₉⁺ as a function of the stepwise N₂ adsorption level m . The grey shaded areas indicate the approximate background noise level. Note, that the fitted rate constants for the adsorption ($k_{(i,m)}$, black filled circles) are nearly 4 orders of magnitude higher than those of the desorption ($k_{-(i,m+1)}$, green open circles, upper limits). Rate constants $k_{(7,13)}$ and $k_{(9,9)}$ are at the noise level and indicate an adsorption limit.

The observation of a swift adsorption process and thus a high equivalence of the adsorption sites is in line with our earlier IR results: We have observed merely one strong IR band for all

of the nine N₂ oscillators in the previous reported IR spectrum of (9,9) [47], which emphasises the similarity of the N₂ oscillators and the seeming equivalence of their locations on the cluster surface. This is remarkable in view of the non-equivalence of Rh atoms in any of the identified Rh₉⁺ structures, *cf.* Table S16 and Fig. S15. Differences in next neighbour coordination prevail.

Intermittent limits and cluster surface roughness. All together, when inspecting the relative rate constants of the chosen clusters $i = 5, 6, 7$ and 9 in detail, we evoke the following conclusions: The drop of rate constants at the intermittent adsorption limits (5,7), (6,8), and (7,10) indicates a particularly slow adsorption step for Rh₅⁺, Rh₆⁺, and Rh₇⁺ at $m_x = 7, 8, 10$, respectively. Thus the eighth, ninth, or eleventh N₂ molecule adsorbs slower than any of the previous ones to Rh₅⁺, Rh₆⁺, or Rh₇⁺. We imagine that at this point, each Rh atom has accepted at least one single N₂ molecule, and the most accessible Rh atoms might accept a geminal N₂ pair. The following adsorption steps would yield at less accessible Rh sites, probably those with a higher number of Rh-Rh next neighbours, and thus these steps become slower.

In terms of this interpretation, the observed kinetic drops arise from the presence of at least two essentially different types of adsorption sites on the cluster surfaces. The depths of the kinetic drops seem to indicate the inaccessibility of the corresponding N₂ adsorption site. Previously, we have interpreted the existence of a variety of distinct adsorption sites as an indication for *rough* cluster surfaces [45, 46]. A decrease of such a drop indicates that the different adsorption sites become increasingly similar. For Rh₉⁺ (as well as Rh₈⁺ and Rh₁₀⁺) we do not observe any drop at all. Along with the increase of the cluster size, we expect that the average next neighbour coordination numbers increase such that low coordinated rough atoms diminish. In total, the properties of the surface atoms unify, they are practically similar; the cluster surface becomes more and more *smooth*.

All of these observations and their interpretation indicate: The Rh₅⁺ cluster is *rough* all over its surface and Rh₆⁺ and Rh₇⁺ are less *rough* and more *smooth*. The average coordination numbers of the Rh atoms increase for the conceivable isomers with increasing cluster size (*cf.* Table S16 and Fig. S15). Rh₈⁺ and Rh₁₀⁺ are similar to the case of Rh₉⁺ (*cf.* supplement Figs. S5, S7 and Table S2) in terms of their smooth cluster surface. Both are accepting large amounts of geminal N₂ loads, however, which is in remarkable contrast to the Rh₉⁺ case that strictly supports mere single N₂ load per surface atom.

Equilibria and thermochemistry. As postulated earlier [47], the equilibrium between the last and second last adsorption step on the Rh₆⁺ and the Rh₇⁺ clusters may arise from two different isomers. These isomers may easily interconvert, preliminary calculations revealing a lower limit of the single N₂ adsorption enthalpies of -50 kJ/mol as compared to -56 kJ/mol for stepped Rh surfaces [73, 74].

We expect the cluster N₂ binding energies to decline with N₂ load; in case of observed equilibrium the last adsorption step is necessarily close to thermoneutral. Thus, the final N₂ is very weakly bound, maybe roaming or side-on. Both cases are more likely at higher coordinated Rh centres and / or in cases of geminal N₂ adsorptions. Calculations on (5,*m*) *m* = 0,...,3 indeed indicate decreasing adsorption energies for the first three adsorption steps starting from -65 kJ/mol.

Our calculated (5,0), (5,1) (5,7) structures (*cf.* chapter 3.4 in the following) and the obtained N₂ adsorption energies that depend on the spin state of the clusters. We obtained values that range around -65 kJ/mol stay as high up to *m* = 6.

Absolute rate constants for the first adsorption steps. From the relative rate constants, we obtain, by eq. (1), absolute rate constants in the range of 0.1 – 30 · 10⁻¹⁰ cm³s⁻¹. These values compare favourably with published values of related systems: For example, the reactions Rh_{*i*}[±] + N₂O proceed with absolute rate constants of 0.02 – 10 · 10⁻¹⁰ cm³s⁻¹ [75] and those of Rh_{*i*}[±] + CO with 0.05 – 11 · 10⁻¹⁰ cm³s⁻¹ [68].

In general, we observe a gradual increase of the rate constants with increasing cluster core size *i*. This is commonly observed in reactions of metal clusters with small molecules, as for example the reaction of Rh_{*i*}⁺ clusters with CO [68] as well as the adsorption of N₂ on Ni clusters [45].

We focus on this finding by discussing the first N₂ adsorption step in more detail (Fig. 6). There is a steep increase of adsorption rate constants with cluster size up to *i* = 7, followed by a much shallower increase above. A likely explanation for the initial steep rise of the first step rates with increasing cluster size is an increase of heat capacity and thus more effective redistribution of the released N₂ adsorption energy into the internal heat bath with increasing cluster size [68]. Otherwise desorption rates would remain high. This steep increase reflects also in the sticking probabilities of Rh₅⁺ to Rh₇⁺ (Tables 1-3; Fig. S13 and Table S6 in the supplement). Previous studies revealed the steep rise before: Zakin et al. also observed an

increase of reaction rates for Rh_i^0 clusters around $i = 5$ [37]. Anderson *et al.* found an increase of sticking probabilities for $i > 12$ for Rh_i^0 clusters at liquid N_2 temperatures without effective thermalizing of the clusters [35].

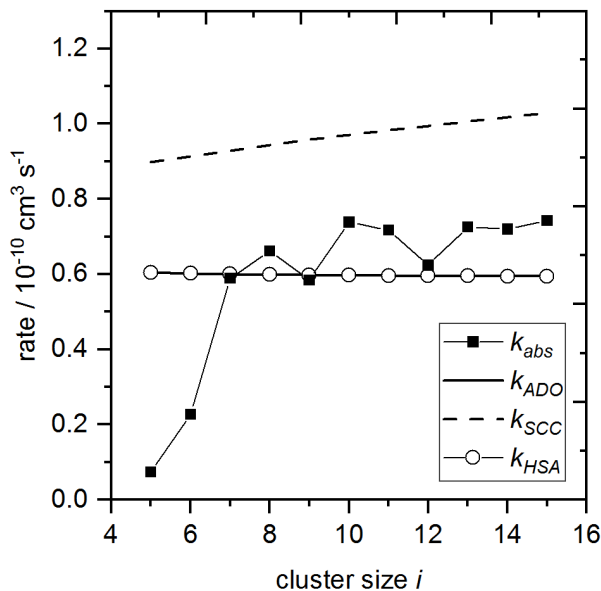


Fig. 5 Experimental absolute rate constants for the first adsorption step of Rh_i^+ with N_2 (filled squares) compared to classical ADO collision rates k_{coll} (solid line), the ‘Surface Charge Capture model’ k_{SCC} (dashed line), and the ‘Hard Sphere Average dipole orientation model’ k_{HSA} (open circles) [67].

The shallow rise in adsorption rates k_{abs} through $i = 7, \dots, 15$ seems to correlate with the geometric cluster size and its concomitant collision cross section. We compare our experimental absolute rate constants of the first N_2 adsorption step with the calculated ADO collision rate k_{ADO} , the ‘Surface Charge Capture Model’ k_{SCC} and the ‘Hard Sphere Average Dipole Orientation Model’ k_{HSA} from Kummerloewe and Beyer [67] (*cf.* Fig. 5 and Table S15). The k_{ADO} and k_{HSA} values coincide under the present conditions and fit quite well the experimental rate constants in the range from $i = 7 - 15$. A slight enhancement by the effects of the HSA model may contribute on top. The adsorption rate of $i = 5, 6$ clusters is reduced with respect to collision rate. Seemingly, the adsorption energy fails to redistribute in the cases of these small clusters, and the hot adsorbate complexes undergo desorption towards separate reactants by considerable amounts.

Subsequent stepwise N_2 adsorption. The trend of the relative and the absolute rate constants with increasing surface occupation is similar (Tables 1-4): The rate constants are high at the beginning, when the N_2 adsorption starts, implying that the adsorption proceeds fast. Upon

4. Cryokinetics and Spin Quenching in the N₂ Adsorption onto Rhodium-Cluster Cations

subsequent adsorption steps, when the cluster surface coverage is significant, the adsorption rate constants reduce. We observe significant desorption rates in the cases of the [Rh₆(N₂)₁₂]⁺ and [Rh₇(N₂)₁₃]⁺ cluster adsorbate complexes leading to an equilibrium between two isomers, as explained earlier.

Table 1 Relative Pseudo-First-Order rate constants, absolute rate constants, collision rates and sticking probabilities for the N₂ adsorption on [Rh₅(N₂)_m]⁺ clusters.

<i>m</i>	<i>k</i> _(5,<i>m</i>) (s ⁻¹)	<i>k</i> _{abs} (10 ⁻¹⁰ cm ³ s ⁻¹)	<i>k</i> _{coll} (10 ⁻¹⁰ cm ³ s ⁻¹)	<i>γ</i> _(5,<i>m</i>)
0	0.97	0.74	6.05	0.12
1	3.0	2.3	6.04	0.38
2	5.3	4.0	6.03	0.67
3	5.5	4.2	6.03	0.70
4	4.8	3.7	6.02	0.61
5	5.0	3.8	6.01	0.64
6	6.2	4.7	6.01	0.79
7	1.5	1.1	6.00	0.19
8	2.3	1.8	6.00	0.29
9	2.9	2.2	6.00	0.37

Table 2 Relative Pseudo-First-Order rate constants, absolute rate constants, collision rates and sticking probabilities for the N₂ adsorption on [Rh₆(N₂)_m]⁺ clusters.

<i>m</i>	<i>k</i> _(6,<i>m</i>) (s ⁻¹)	<i>k</i> _{abs} (10 ⁻¹⁰ cm ³ s ⁻¹)	<i>k</i> _{coll} (10 ⁻¹⁰ cm ³ s ⁻¹)	<i>γ</i> _(6,<i>m</i>)
0	3.0	2.3	6.0	0.38
1	6.8	5.2	6.02	0.86
2	8.5	6.6	6.01	1.1
3	9.0	6.9	6.01	1.2
4	8.7	6.7	6.00	1.1
5	8.5	6.5	6.00	1.1
6	7.4	5.7	5.99	0.94
7	6.3	4.8	5.99	0.81
8	2.8	2.2	5.99	0.36
9	5.4	4.1	5.98	0.69
10	3.4	2.6	5.98	0.44
11	0.23	0.17	5.98	0.03

Table 3 Relative Pseudo-First-Order rate constants, absolute rate constants, collision rates and sticking probabilities for the N₂ adsorption on [Rh₇(N₂)_m]⁺ clusters.

m	$k_{(7,m)} (s^{-1})$	$k_{abs} (10^{-10} \text{ cm}^3 \text{ s}^{-1})$	$k_{coll} (10^{-10} \text{ cm}^3 \text{ s}^{-1})$	$\gamma_{(7,m)}$
0	7.7	5.9	6.00	0.98
1	7.9	6.1	6.00	1.0
2	9.2	7.0	5.99	1.2
3	9.0	6.9	5.99	1.2
4	9.0	6.9	5.99	1.2
5	8.7	6.7	5.98	1.1
6	8.5	6.5	5.98	1.1
7	8.2	6.3	5.98	1.1
8	7.9	6.1	5.98	1.0
9	7.4	5.7	5.97	0.95
10	5.1	3.9	5.97	0.66
11	8.7	6.7	5.97	1.1
12	2.8	2.1	5.97	0.35

Table 4 Relative Pseudo-First-Order rate constants, absolute rate constants, collision rates and sticking probabilities for the N₂ adsorption on [Rh₉(N₂)_m]⁺ clusters.

m	$k_{(9,m)} (s^{-1})$	$k_{abs} (10^{-10} \text{ cm}^3 \text{ s}^{-1})$	$k_{coll} (10^{-10} \text{ cm}^3 \text{ s}^{-1})$	$\gamma_{(9,m)}$
0	7.6	5.9	5.98	0.98
1	7.9	6.1	5.98	1.0
2	8.4	6.5	5.97	1.1
3	9.1	7.0	5.97	1.2
4	9.2	7.1	5.97	1.2
5	8.9	6.8	5.97	1.1
6	8.9	6.9	5.96	1.2
7	8.7	6.7	5.96	1.1
8	8.5	6.5	5.96	1.1

4.5.3 The Gibbs energies

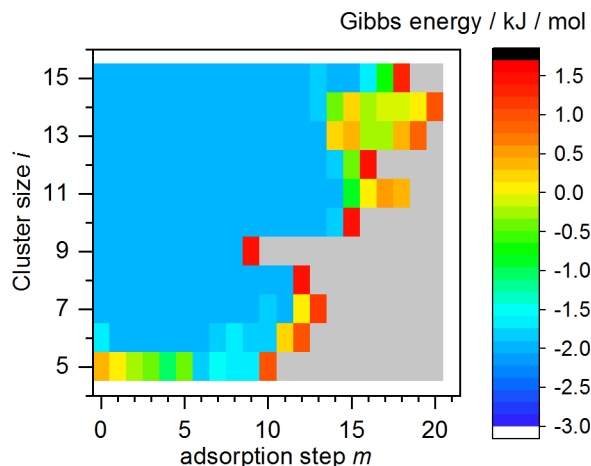
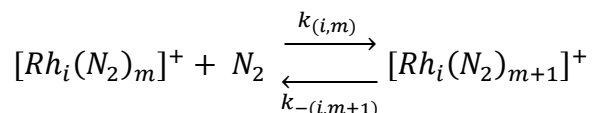


Fig. 6 Plot of Gibbs energies $\Delta_{\text{ads}}G^{26\text{K}}_{(i,m)}$ for the equilibria of N₂ adsorption onto $[\text{Rh}_i(\text{N}_2)_m]^+$ / desorption off $[\text{Rh}_i(\text{N}_2)_{m+1}]^+$. Note, that the $\Delta_{\text{ads}}G^{26\text{K}}_{(i,m)}$ values within the light blue plateau signify upper limits of otherwise unknown values. The last depicted step formally relates to the equilibrium of m_{max} with $m_{\text{max}}+1$. The positive Gibbs energies signify the last adsorption step towards m_{max} , with the only exception of Rh_5^+ . Its initial N₂ adsorption is hindered, and its subsequent steps become more spontaneous. $[\text{Rh}_i(\text{N}_2)_m]^+$, $i = 8, \dots, 10$ possess all negative $\Delta_{\text{ads}}G^{26\text{K}}_{(i,m)}$ values but m_{max} . The grey area signifies non-occurring processes.

We have included N₂ desorption steps into our kinetic fits whenever these steps improved the quality of fits – namely their χ^2 values – in a significant way. As a matter of fact, whenever invoked, these desorption steps were inevitable in order to achieve a fit of acceptable quality at all. Such desorption rates at hand, the according adsorption – desorption ratios of relative rate constants yield the equilibrium constant of the m^{th} N₂ adsorbate with the $(m+1)^{\text{th}}$ N₂ adsorbate, $k_{(i,m)}/k_{-(i,m+1)} =: K_m$ (Table S10), and its Gibbs free energy $\Delta_{\text{ads}}G^{26\text{K}}_{(i,m)} := -RT \ln K_m$ (Fig. 6, Table S11). Whenever our fits reveal negligible desorption, we set the corresponding rate constants $k_{-(i,m+1)}$ to an upper limit of 0.001 s^{-1} . We assume an according upper limit for the non-observable adsorption step $k_{(i,\text{max})}$.



In the cases of stepwise adsorption without observable desorption, $k_{-(i,m+1)} < 0.001 \text{ s}^{-1}$, our Gibbs energies take the value of an upper limit, $\Delta_{\text{ads}}G^{26\text{K}}_{(i,m)} \leq -1.7 \text{ kJ/mol}$ (cf. Fig. 6 and Table S11). Note, that we utilise upper limits for rate constants of the not observed desorption steps.

Beyond the general trend of an increase of total N₂ load (discussed above), we observe three 'features of reluctance' deserving special attention:

- (a) The low total N₂ load of Rh₉⁺
- (b) The N₂ adsorption reluctance of high N₂ loaded Rh₁₃⁺ and Rh₁₄⁺
- (c) The N₂ adsorption reluctance of naked and low N₂ loaded Rh₅⁺

The cases (b) and (c) are kinetic features that do not show in the m_{max} values; (a) is not kinetic/dynamic but static/structural and obvious by m_{max} (cf. Fig. 2). It likely reflects structure and indicates Langmuir type stoichiometric N₂ loading of each Rh atom, all of which are accessible.

Case (b): The adsorption of N₂ onto Rh₁₃⁺ and Rh₁₄⁺ is all spontaneous ($\Delta_{ads}G^{26K}_{(i,m)} < 0$) up to (13,14) and (14,15). This corresponds to a full loading with two geminal N₂s, depending on taking into account an inner, non-accessible Rh atom. The surface atoms of larger clusters are higher next neighbour coordinated and therefore less reactive towards adsorbates [76]. Additional N₂ molecules bind more loosely and likely form a second adsorbate shell. These loosely bound N₂s can easily desorb or roam about the surface of the cluster adsorbate complex. These processes will manifest themselves in the observed reversibility for large m up to m_{max} . Other than in the cases $i = 6,7$, the higher next neighbour coordination of $i = 13,14$ enhances the effect of desorption on the cryo N₂ adsorption kinetics. The m_{max}/i stoichiometries decrease (12/6, 13/7, 19/13, and 20/14) with cluster size i . It is beyond doubt that large Rh _{i} ⁺ clusters ($i > 10$) establish an N₂ adsorption - desorption equilibrium across multiple steps, a range of m values. In contrast, small Rhodium clusters hold tight to their N₂ adsorbates but for the very last one, an adsorption-desorption equilibrium at a single m value.

Case (c): The adsorption of a first N₂ onto Rh₅⁺ is not spontaneous. All subsequent adsorption steps up to $m_{max} = 10$ yield gradually more negative $\Delta_{ads}G^{26K}_{(5,m)}$ values. We had to consider desorption in each step up to $m = 5$, and negligible desorption rate constants < 0.001 for $m > 5$. Accordingly, the Gibbs energies decrease stepwise from $\Delta_{ads}G^{26K}_{(5,0)} = +0.4$ kJ/mol to $\Delta_{ads}G^{26K}_{(5,5)} = -0.5$ kJ/mol (cf. Table S11). This is in contrast to all other clusters Rh _{i} ⁺ ($i \neq 5$) where positive Gibbs energies occur towards (i, m_{max}). The desorption rate constants of $m > 5$ are negligible, the $\Delta_{ads}G^{26K}_{(5,m)}$ values have an upper limit of -1.6 kJ/mol, which is similar for all other investigated clusters (as emphasised by the colouring scheme in Fig 6).

In summary, the evaluation and mapping of Gibbs energies provided further information on the spontaneity of the adsorption desorption steps and consolidated our assumptions made before: Besides pure cluster geometry and stoichiometric N₂ adsorption, the coordination of the cluster surface atoms plays a crucial role in the adsorption process. Higher next neighbour coordination of Rh atoms impedes the adsorption of a second N₂ on a Rh atom. A desorption could precede easily. In these cases, we observe enhanced Gibbs energies. The case of N₂ adsorption to Rh₅⁺ bears strong evidence for spin and/or structural isomers and adsorption induced interconversion/relaxation.

4.5.4 DFT modelling

Rh₅⁺ geometry. The above discussion of experimental results received support from our previous DFT results [47] in the cases of Rh₆⁺, Rh₇⁺, and Rh₉⁺. Here, we performed additional DFT calculations on structures and multiplicities of the naked Rh₅⁺ cluster, in order to verify our previous structural speculations. We started from a square pyramid (**sp**) and a trigonal bipyramid (**tbp**) structure and checked for spin multiplicities $2S + 1 = 1, \dots, 15$ (Fig. 7). We found significant structural relaxation in the course of the optimization procedure. Low spin structures tend to relax into square pyramids. For septet and nonet spin states we observe coexisting and slightly distorted **sp** and **tbp** isomers, and some highly distorted geometries beyond simple classification. The geometries of these distorted clusters are 'in between'. For the quintet spin state, we obtain a square pyramid ⁵**sp** and a distorted structure. The total optimum - as of this survey - is a slightly distorted trigonal bipyramid with a nonet spin state. The second lowest isomer is a nonet square pyramid ⁹**sp** (+ 9 kJ/mol). The 11tet square pyramid ¹¹**sp** relaxed into a trigonal bipyramid ¹¹**tbp**.

Our results are in line with an earlier study by Hamilton et al. who reported similar stabilities of square-based pyramidal **sp** and trigonal bipyramidal **tbp** Rh₅ motifs in [Rh₅(N₂O)Ar]⁺ clusters [42]. Other studies on various levels of theory on neutral and anionic Rhodium clusters report similar results [27, 44, 48-51]: low energy differences of nonet square pyramid ⁹**sp** and trigonal bipyramid isomers **tbp**.

The Rhodium atoms in a square pyramid are on average less coordinated (four 3-fold, and one 4-fold coordinated Rh atom, 8 Rh-Rh bonds, and an average Rh-Rh next neighbour coordination number of 3.2) than in a trigonal bipyramid (three 4-fold, and two 3-fold coordinated Rh atoms, 9 Rh-Rh bonds, and an average Rh-Rh next neighbour coordination

number of 3.6), cf. Table S16 in the Supplement. We expect that a lower coordination of Rhodium atoms by adjacent metal atoms facilitates an enhanced N_2 adsorption.

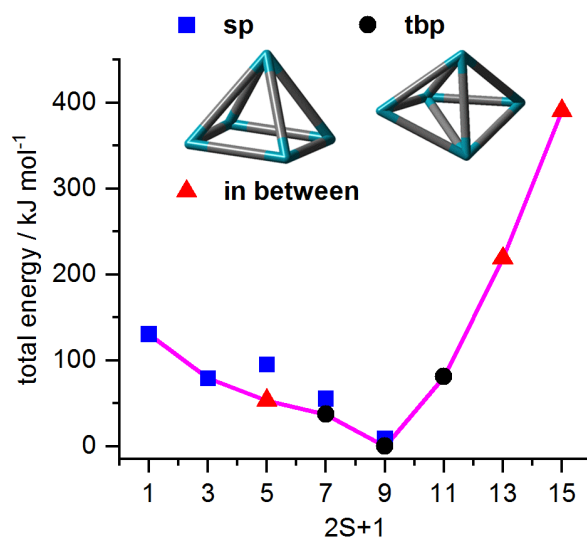


Fig. 7 Total energies of most stable Rh_5^+ cluster structures as a function of the spin multiplicity $2S + 1$, normalised to the most stable trigonal bipyramid nonet, ${}^9\mathbf{tbp}$. The second most stable isomer is a nonet square pyramid, ${}^9\mathbf{sp}$, + 9 kJ/mol. In the cases of high or low multiplicities, it is found a single stable isomer (as indicated) while others relax into these. The fully relaxed path of successive spin isomers connects to an asymmetric *spin valley* (indicated in pink).

A trigonal bipyramidal **tbp** structure of the Rh_5^+ cluster core facilitates the rationalization of our intermittent adsorption limit of (5,7): Three single N_2 molecules occupy each of the three highly coordinated equatorial Rh atoms, whereas the two apical, low coordinated Rh atoms receive two geminal N_2 molecules each.

Stepwise N_2 adsorption onto Rh_5^+ . To investigate the effects of stepwise N_2 adsorption on the cluster structure and possible spin relaxations, we optimised the cluster core together with the adsorbate shell of (5, m) in the cases of $m = 1, \dots, 4, 7, 10$. For each m , we started with several conceivable adsorption shell isomers around given **tbp** and **sp** cluster cores, and we obtained fully converged structures for singlet to tredecet multiplicities in most cases (Fig. 8). N_2 adsorption energies correspond to the offsets between the resulting curves – each of which resembles the *spin valley* of a single (5, m) complex.

The shape of the naked clusters' *spin valley* persists upon adsorption of a first and a second N_2 molecule. Nonet multiplicities are most stable. Higher multiplicities are most expensive,

lower ones are stepwise less stable by 37 – 11 kJ/mol per spin flip. Thus, spin pairing is more feasible than costly occupation of additional orbitals by additional single spins.

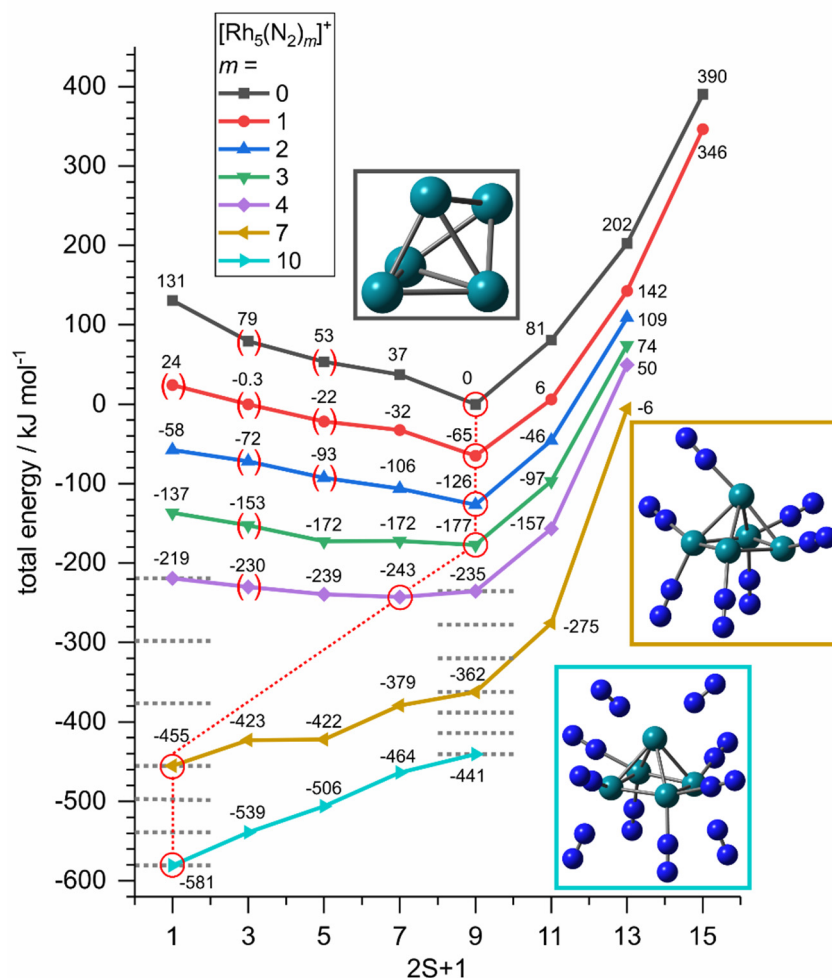


Fig. 8 Total energies of computed $[\text{Rh}_5(\text{N}_2)_m]^+$ cluster adsorbate complex structures $(5,m)$ as a function of the spin multiplicity $2S + 1$, normalised to the computed $(5,0)$ spin isomer (trigonal bipyramid, ⁹**tbp**, nonet). The calculated minimum structures for $(5,0)$, $(5,7)$ and $(5,10)$ are shown as insets. Spin contamination occurs in some low spin cases (red brackets). The horizontal grey dashed lines serve to interpolate singlet and nonet state energies where no computational data are available. Their offset against each other indicate the supposed average adsorption energy upon spin conservation. The red dashed lines connect the *spin valley curves'* minima as indicated by the red circles.

Here, and in the following, the low spin wing of *spin valleys* is more affected by N₂ adsorption than the high spin wing. The third N₂ adsorption reveals a more pronounced effect in this regard: Nonet, septet, and quintet become degenerate, and the fourth N₂ adsorption event widens the almost flat bottom of the spin valley by one more multiplicity towards the triplet

state, which locates merely 13 kJ/mol above the most stable septet. Even the singlet is only 24 kJ/mol higher than the septet.

The next calculated *spin valley* curve of (5,7) reveals even more relaxation of low spin multiplicities: The *spin valley* is continuously decreasing towards the most stable singlet state. The corresponding structure bases on a square pyramid **¹sp** cluster core: The spin relaxation is intertwined with a structural relaxation. However, **¹tbp** is found only 12 kJ/mol above **¹sp**.

We obtain comparable findings for the *spin valley* curve of (5,10): Once again, it is most stable a singlet square pyramid **¹sp** cluster core structure. It sustains a fully occupied first adsorbate layer of ten N₂ adsorbates, which locate pairwise on any of the five Rh core atoms. This is in full accord with the experimental adsorption limit and the recorded adsorption kinetics of Rh₅⁺ clusters.

It warrants to check for conceivable isomerism of adsorbate shells and cluster cores at this point. The second most stable isomer of (5,10) of +17 kJ/mol comprises of a tetrahedral core with a low coordinated extra Rh atom above one edge, labelled as a singly capped tetrahedral **¹sct** cluster core structure. The single twofold coordinated Rh atom might adsorb up to three N₂ molecules and suggest an adsorption limit at (5,11). The lowest **¹tbp** structure is 37 kJ/mol above **¹sp**, and it provides for two apical Rh atom, that might adsorb up to three N₂ molecules. This suggests a possible adsorption limit at (5,12). The observed limit at (5,10) is thus well in line with the calculate most stable **¹sp** cluster core, surrounded by a closed adsorbate layer and sustained by all doubly N₂ occupied Rh adsorption sites. The similar stabilities of **sp** and **tbp** isomers are well in line with literature as reported above.

Vertical and adiabatic N₂ adsorption. The total energies of each of the *spin valley curves* decrease stepwise with, and by the number of adsorbed N₂. These step sizes indicate the N₂ adsorption energies per step. We normalise absolute values to the energy of the minimum nonet **⁹tbp** (5,0) cluster. Both vertical and adiabatic adsorption energies (*cf.* Fig. S16 and Table S17) refer to this very starting point. The adiabatic and vertical (nonet) adsorption energies decline for the first three steps from -65 kJ/mol ($m = 0$) via -62 kJ/mol ($m = 1$) to -51 kJ/mol ($m = 2$). Vertical adsorption energies in the last observed step ($m = 9$) become as low as less than -30 kJ/mol ($m = 9$), whereas the adiabatic adsorption energies are somewhat higher, about -42 kJ/mol (interpolated).

In total, the vertical adsorption of 10 N₂ molecules stabilises the Rh₅⁺ cluster by 441 kJ/mol, and the adiabatic adsorption adds 140 kJ/mol of additional stabilization through spin relaxation on top. The effect of stepwise decreasing adsorption energies seems intuitive to us, and the red dashed lines in Fig. 8 serves to emphasise the actual course of concomitant adsorption and spin relaxation.

4.6 Conclusion

We have recorded the cryo kinetics of N₂ adsorption to cationic Rh_{*i*}⁺-clusters (*i* = 5-15). The adsorption limits m_{max} increase with cluster sizes *i*, and they range over $i \leq m_{max} \leq 2i$ with the Rh₉⁺ cluster providing for the lowest observed N₂ coverage of merely $m_{max}/i = 1$. In most cases, the intermittent adsorption limits m_x coincide with the adsorption limits m_{max} , which we take as an indication for a *smooth* cluster surface made of equal adsorption sites which stem from Rh cluster surface atoms with equal (or at least very similar) next neighbour coordination environments. We determine by kinetic fits relative rate constants for each N₂ adsorption and desorption step, which quantify the significant trends in adsorption behaviour in terms of rate constants. We obtain equilibrium constants and Gibbs free energies, and it is beyond doubt that large Rh_{*i*}⁺ clusters (*i* > 10) establish an N₂ adsorption - desorption equilibrium while small ones hold tight to their N₂ adsorbates but for the very last one. Our experimental absolute rate constants compare favourably to those from the 'Hard Sphere Average dipole orientation model'. We observed a significant reluctance towards N₂ adsorption for the Rh₅⁺ cluster, indicated by necessary desorption steps. By calculating the corresponding Gibbs energies for the adsorption – desorption equilibria and by first extensive DFT calculations, we gained information on the energetics of the N₂ adsorption onto Rh₅⁺ and postulate isomerization processes between a **tbp** and an **sp** cluster core type yielding a **sp** cluster core from an intermittent adsorption limit. A spin quench accompanies the N₂ adsorption and the isomerization. The course of the rate constants enabled us to tentatively assign a **tbp** cluster structure to Rh₅⁺. DFT calculations also support this assignment.

Further spectroscopic investigations accompanied by DFT modelling of each adsorption step (beyond our previous study, [47]) will deliver even more detailed insights into the cluster structures and the reorganization processes. Such studies are subject of ongoing work.

4.7 Acknowledgements/Funding

This work was supported by the DFG founded transregional collaborative research center SFB/TRR 88 'Cooperative effects in homo and heterometallic complexes' (3MET) and by the state research center OPTIMAS. We thank Annika Steiner for valuable discussions concerning data evaluation and nomenclature as well as Thomas Kolling for assistance on technical questions of any kind.

4.8 Conflicts of interest

There are no conflicts to declare.

4.9 References

- [1] S. Brunauer, P.H. Emmett and E. Teller, Adsorption of Gases in Multimolecular Layers, *J Am Chem Soc*, **60**, 309-319 (1938).
- [2] D.A. King and M.G. Wells, Reaction Mechanism in Chemisorption Kinetics: Nitrogen on the {100} Plane of Tungsten, *Proceedings of the Royal Society A: Mathematical, Physical and Engineering Sciences*, **339**, 245-269 (1974).
- [3] D.A. King and M.G. Wells, Molecular Beam Investigation of Adsorption Kinetics on Bulk Metal Targets: Nitrogen on Tungsten, *Surface Science*, **29**, 454-482 (1972).
- [4] G. Ertl, S.B. Lee and M. Weiss, Kinetics of Nitrogen Adsorption on Fe(111), *Surface Science*, **114**, 515-526 (1982).
- [5] M. Grunze, M. Golze, W. Hirschwald, H.J. Freund, H. Pulm, U. Seip, M.C. Tsai, G. Ertl and J. Küppers, π -Bonded N₂ on Fe(111): The Precursor for Dissociation, *Physical Review Letters*, **53**, 850-853 (1984).
- [6] D.K. Böhme and H. Schwarz, Gas-Phase Catalysis by Atomic and Cluster Metal Ions: The Ultimate Single-Site Catalysts, *Angewandte Chemie*, **44**, 2336-2354 (2005).
- [7] D.K. Bohme and H. Schwarz, Gas-phase Catalysis by Atomic and Cluster Metal Ions: the Ultimate Single-Site Catalysts, *Angew Chem Int Ed Engl*, **44**, 2336-2354 (2005).
- [8] D. Schröder and H. Schwarz, C-H and C-C Bond Activation by Bare Transition-Metal Oxide Cations in the Gas Phase, *Angewandte Chemie International Edition in English*, **34**, 1973-1995 (1995).
- [9] *Nanocatalysis*, edited by U. Heiz, U. Landman, (Springer-Verlag, Berlin Heidelberg, 2007).
- [10] S.M. Lang and T.M. Bernhardt, Gas Phase Metal Cluster Model Systems for Heterogeneous Catalysis, *Physical Chemistry Chemical Physics*, **14**, 9255-9269 (2012).
- [11] M.B. Knickelbein, Reactions of transition metal clusters with small molecules, *Annual Review of Physical Chemistry*, **50**, 79-115 (1999).
- [12] M.D. Morse, M.E. Geusic, J.R. Heath and R.E. Smalley, Surface Reactions of Metal Clusters. II. Reactivity Surveys with D₂, N₂, and CO, *The Journal of Chemical Physics*, **83**, 2293-2304 (1985).

- [13] A. Bérces, P.A. Hackett, L. Lian, S.A. Mitchell and D.M. Rayner, Reactivity of Niobium Clusters with Nitrogen and Deuterium, *The Journal of Chemical Physics*, **108**, 5476-5490 (1998).
- [14] F. Liu, M. Li, L. Tan and P.B. Armentrout, Guided Ion Beam Studies of the Reactions of Co_n⁺ (n=1-18) with N₂: Cobalt Cluster Mononitride and Dinitride Bond Energies, *J. Chem. Phys.*, **128**, 194313/194311-194313/194312 (2008).
- [15] J. Ho, E.K. Parks, L. Zhu and S.J. Riley, Reactions of Small Cobalt Clusters with N₂: Implications for Cluster Structure, *Chem. Phys.*, **201**, 245-261 (1995).
- [16] S.J. Riley, The Atomic Structure of Transition Metal Clusters, *Journal of Non-Crystalline Solids*, **205-207**, 781-787 (1996).
- [17] E.K. Parks, L. Zhu, J. Ho and S.J. Riley, The Structure of Small Nickel Clusters. I. Ni₃-Ni₁₅, *The Journal of Chemical Physics*, **100**, 7206-7222 (1994).
- [18] E.K. Parks, L. Zhu, J. Ho and S.J. Riley, The Structure of Small Nickel Clusters. II. Ni₁₆-Ni₂₈, *J. Chem. Phys.*, **102**, 7376-7389 (1995).
- [19] E.K. Parks and S.J. Riley, Nickel Cluster Structure Determined from the Adsorption of Molecular Nitrogen Ni₄₉-Ni₇₁, *Z. Phys. D: At., Mol. Clusters*, **33**, 59-70 (1995).
- [20] E.K. Parks, K.P. Kerns and S.J. Riley, The Structure of Nickel-Iron Clusters Probed by Adsorption of Molecular Nitrogen, *Chem. Phys.*, **262**, 151-167 (2000).
- [21] E.K. Parks, G.C. Nieman, K.P. Kerns and S.J. Riley, The Thermodynamics of Nitrogen Adsorption on Nickel Clusters: Ni₁₉-Ni₇₁, *J. Chem. Phys.*, **108**, 3731-3739 (1998).
- [22] L.-h. Mou, G.-d. Jiang, Z.-y. Li and S.-g. He, Activation of Dinitrogen by Gas-Phase Species, *Chinese Journal of Chemical Physics*, **33**, 507-520 (2020).
- [23] C. Berg, T. Schindler, G. Niedner-Schatteburg and V.E. Bondybey, Reactions of Simple Hydrocarbons with Nb_n⁺: Chemisorption and Physisorption on Ionized Niobium Clusters, *The Journal of Chemical Physics*, **102**, 4870-4884 (1995).
- [24] C. Berg, M. Beyer, T. Schindler, G. Niedner-Schatteburg and V.E. Bondybey, Reactions of Benzene with Rhodium Cluster Cations: Competition Between Chemisorption and Physisorption, *The Journal of Chemical Physics*, **104**, 7940-7946 (1996).
- [25] B. Pfeffer, S. Jaberg and G. Niedner-Schatteburg, Reactions of Simple Aromatic Heterocycles with Niobium Cluster Ions (n < 30), *Journal of Chemical Physics*, **131**, 194305 (2009).
- [26] C. Adlhart and E. Uggerud, C-H Activation of Alkanes on Rh_n⁺ (n=1-30) Clusters: Size Effects on Dehydrogenation, *J Chem Phys*, **123**, 214709 (2005).
- [27] Y. Ren, Y. Yang, Y.-X. Zhao and S.-G. He, Size-Dependent Reactivity of Rhodium Cluster Anions toward Methane, *The Journal of Physical Chemistry C*, **123**, 17035-17042 (2019).
- [28] Y.-X. Zhao, X.-G. Zhao, Y. Yang, M. Ruan and S.-G. He, Rhodium Chemistry: A Gas Phase Cluster Study, *Journal of Chemical Physics*, **in print**, (2021).
- [29] I. Balteanu, O.P. Balaj, M.K. Beyer and V.E. Bondybey, Size-Dependent Dehydrogenation of Ethane by Cationic Rhodium Clusters in the Gas Phase, *International Journal of Mass Spectrometry*, **255-256**, 71-75 (2006).
- [30] I. Balteanu, O.P. Balaj, B.S. Fox-Beyer, P. Rodrigues, M.T. Barros, A.M.C. Moutinho, M.L. Costa, M.K. Beyer and V.E. Bondybey, Size- and Charge-State-Dependent Reactivity of Azidoacetonitrile with Anionic and Cationic Rhodium Clusters Rh_n[±], *Organometallics*, **23**, 1978-1985 (2004).
- [31] G. Albert, C. Berg, M. Beyer, U. Achatz, S. Joos, G. Niedner-Schatteburg and V.E. Bondybey, Methane Activation by Rhodium Cluster Argon Complexes, *Chemical Physics Letters*, **268**, 235-241 (1997).

- [32] K. Koszinowski, M. Schlangen, D. Schröder and H. Schwarz, CH- and NH-Activation by Gaseous Rh_2^+ and PtRh^+ cluster ions, *International Journal of Mass Spectrometry*, **237**, 19-23 (2004).
- [33] C. Berg, M. Beyer, U. Achatz, S. Joos, G. Niedner-Schatteburg and V.E. Bondybey, Effect of Charge upon Metal Cluster Chemistry: Reactions of Nb_n and Rh_n Anions and Cations with Benzene, *The Journal of Chemical Physics*, **108**, 5398-5403 (1998).
- [34] F. Mafuné, Y. Tawaraya and S. Kudoh, Nitrogen Molecule Adsorption on Cationic Tantalum Clusters and Rhodium Clusters and Desorption from Their Nitride Clusters Studied by Thermal Desorption Spectrometry, *The Journal of Physical Chemistry A*, **120**, 4089-4095 (2016).
- [35] M. Andersson, L. Holmgren and A. Rosén, Rhodium-Cluster Reactivity: Sticking Probabilities of Some Diatomic Molecules, *Surf Rev Lett*, **3**, 683-686 (1996).
- [36] C. Cui, Y. Jia, H. Zhang, L. Geng and Z. Luo, Plasma-Assisted Chain Reactions of Rh_3^+ Clusters with Dinitrogen: $\text{N}\equiv\text{N}$ Bond Dissociation, *The journal of physical chemistry letters*, **11**, 8222-8230 (2020).
- [37] M.R. Zakin, D.M. Cox and A. Kaldor, Gas-Phase Rhodium Cluster Chemistry: Influence of Adsorbate Electronic Structure on Reaction Rate, *The Journal of Chemical Physics*, **89**, 1201-1202 (1988).
- [38] A. Fielicke, P. Gruene, G. Meijer and D.M. Rayner, The Adsorption of CO on Transition Metal Clusters: A Case Study of Cluster Surface Chemistry, *Surface Science*, **603**, 1427-1433 (2009).
- [39] A. Fielicke, G. von Helden, G. Meijer, D.B. Pedersen, B. Simard and D.M. Rayner, Size and Charge Effects on the Binding of CO to Small Isolated Rhodium Clusters, *The Journal of Physical Chemistry B*, **108**, 14591-14598 (2004).
- [40] A. Fielicke, G. von Helden, G. Meijer, D.B. Pedersen, B. Simard and D.M. Rayner, Size and Charge Effects on the Binding of CO to Late Transition Metal Clusters, *J Chem Phys*, **124**, 194305 (2006).
- [41] A. Fielicke, G. von Helden, G. Meijer, B. Simard, S. Dénommée and D.M. Rayner, Vibrational Spectroscopy of CO in Gas-Phase Rhodium Cluster-CO Complexes, *J Am Chem Soc*, **125**, 11184-11185 (2003).
- [42] S.M. Hamilton, W.S. Hopkins, D.J. Harding, T.R. Walsh, M. Haertelt, C. Kerpel, P. Gruene, G. Meijer, A. Fielicke and S.R. Mackenzie, Infrared-Induced Reactivity of N_2O on Small Gas-Phase Rhodium Clusters, *The journal of physical chemistry. A*, **115**, 2489-2497 (2011).
- [43] D.J. Harding, P. Gruene, M. Haertelt, G. Meijer, A. Fielicke, S.M. Hamilton, W.S. Hopkins, S.R. Mackenzie, S.P. Neville and T.R. Walsh, Probing the Structures of Gas-Phase Rhodium Cluster Cations by Far-Infrared Spectroscopy, *J Chem Phys*, **133**, 214304 (2010).
- [44] T.D. Hang, H.M. Hung, L.N. Thiem and H.M.T. Nguyen, Electronic Structure and Thermochemical Properties of Neutral and Anionic Rhodium Clusters Rh_n , $n = 2-13$. Evolution of Structures and Stabilities of Binary Clusters Rh_mM ($\text{M} = \text{Fe}, \text{Co}, \text{Ni}$; $m = 1-6$), *Computational and Theoretical Chemistry*, **1068**, 30-41 (2015).
- [45] J. Mohrbach, S. Dillinger and G. Niedner-Schatteburg, Cryo Kinetics and Spectroscopy of Cationic Nickel Clusters: Rough and Smooth Surfaces, *The Journal of Physical Chemistry C*, **121**, 10907-10918 (2017).
- [46] J. Mohrbach, S. Dillinger and G. Niedner-Schatteburg, Probing Cluster Surface Morphology by Cryo Kinetics of N_2 on Cationic Nickel Clusters, *J Chem Phys*, **147**, 184304 (2017).

- [47] M.P. Klein, A.A. Ehrhard, J. Mohrbach, S. Dillinger and G. Niedner-Schatteburg, Infrared Spectroscopic Investigation of Structures and N₂ Adsorption Induced Relaxations of Isolated Rhodium Clusters, *Topics in Catalysis*, **61**, 106-118 (2018).
- [48] C.-H. Chien, E. Blaisten-Barojas and M.R. Pederson, Magnetic and Electronic Properties of Rhodium Clusters, *Physical Review A*, **58**, 2196-2202 (1998).
- [49] J.H. Morkath and G.M. Pastor, Interplay between Chemical and Magnetic Order in FeRh Clusters, *The Journal of Physical Chemistry C*, **116**, 17228-17238 (2012).
- [50] B.V. Reddy, S.K. Nayak, S.N. Khanna, B.K. Rao and P. Jena, Electronic Structure and Magnetism of Rh_n (n=2–13) clusters, *Physical Review B*, **59**, 5214-5222 (1999).
- [51] Y. Jinlong, F. Toigo and W. Kelin, Structural, Electronic, and Magnetic Properties of Small Rhodium Clusters, *Physical review. B, Condensed matter*, **50**, 7915-7924 (1994).
- [52] D. Schroder, S. Shaik and H. Schwarz, Two-State Reactivity as a New Concept in Organometallic Chemistry, *Accounts of chemical research*, **33**, 139-145 (2000).
- [53] J.J. Melko, S.G. Ard, J.A. Fournier, N.S. Shuman, J. Troe and A.A. Viggiano, Exploring the Reactions of Fe⁺ and FeO⁺ with NO and NO₂, *The journal of physical chemistry. A*, **116**, 11500-11508 (2012).
- [54] J.J. Melko, S.G. Ard, J.A. Fournier, J. Li, N.S. Shuman, H. Guo, J. Troe and A.A. Viggiano, Iron Cation Catalyzed Reduction of N₂O by CO: Gas-Phase Temperature Dependent Kinetics, *Physical chemistry chemical physics : PCCP*, **15**, 11257-11267 (2013).
- [55] S.G. Ard, J.J. Melko, V.G. Ushakov, R. Johnson, J.A. Fournier, N.S. Shuman, H. Guo, J. Troe and A.A. Viggiano, Activation of Methane by FeO⁺: Determining Reaction Pathways Through Temperature-Dependent Kinetics and Statistical Modeling, *The journal of physical chemistry. A*, **118**, 2029-2039 (2014).
- [56] S.G. Ard, J.J. Melko, O. Martinez, Jr., V.G. Ushakov, A. Li, R.S. Johnson, N.S. Shuman, H. Guo, J. Troe and A.A. Viggiano, Further Insight Into the Reaction FeO⁺ + H₂ → Fe⁺ + H₂O: Temperature Dependent Kinetics, Isotope Effects, and Statistical Modeling, *The journal of physical chemistry. A*, **118**, 6789-6797 (2014).
- [57] S.G. Ard, R.S. Johnson, J.J. Melko, O. Martinez, N.S. Shuman, V.G. Ushakov, H. Guo, J. Troe and A.A. Viggiano, Spin-Inversion and Spin-Selection in the Reactions FeO⁺ + H₂ and Fe⁺ + N₂O, *Physical chemistry chemical physics : PCCP*, **17**, 19709-19717 (2015).
- [58] V.G. Ushakov, J. Troe, R.S. Johnson, H. Guo, S.G. Ard, J.J. Melko, N.S. Shuman and A.A. Viggiano, Statistical Modeling of the Reactions Fe⁺ + N₂O → FeO⁺ + N₂ and FeO⁺ + CO → Fe⁺ + CO₂, *Physical chemistry chemical physics : PCCP*, **17**, 19700-19708 (2015).
- [59] S. Dillinger, J. Mohrbach, J. Hewer, M. Gaffga and G. Niedner-Schatteburg, Infrared Spectroscopy of N₂ Adsorption on Size Selected Cobalt Cluster Cations in Isolation, *Physical Chemistry Chemical Physics*, **17**, 10358-10362 (2015).
- [60] D. Proch and T. Trickl, A High-Intensity Multi-Purpose Piezoelectric Pulsed Molecular Beam Source, *Review of Scientific Instruments*, **60**, 713-716 (1989).
- [61] P. Caravatti and M. Allemann, The 'Infinity Cell': A New Trapped-Ion Cell with Radiofrequency Covered Trapping Electrodes for Fourier Transform Ion Cyclotron Resonance Mass Spectrometry, *Org Mass Spectrom*, **26**, 514-518 (1991).
- [62] M. Graf, *Entwicklung eines auf Evolutionsstrategien basierenden Computerprogrammes zum optimierten Anpassen kinetischer Daten aus FT-ICR-Massenspektrometrie-Messungen*, (TU Kaiserslautern, September 2006).
- [63] T. Su and M.T. Bowers, Ion-Polar Molecule Collisions. Effect of Molecular Size on Ion-Polar Molecule Rate Constants, *J Am Chem Soc*, **95**, 7609-7610 (1973).

- [64] T. Su and M.T. Bowers, Ion-Polar Molecule Collisions. Proton Transfer Reactions of H_3^+ and CH_5^+ to the Geometric Isomers of Difluoroethylene, Dichloroethylene, and Difluorobenzene, *J Am Chem Soc*, **95**, 1370-1373 (1973).
- [65] T. Su and M.T. Bowers, Theory of Ion-Polar Molecule Collisions. Comparison with Experimental Charge Transfer Reactions of Rare Gas Ions to Geometric Isomers of Difluorobenzene and Dichloroethylene, *The Journal of Chemical Physics*, **58**, 3027-3037 (1973).
- [66] T. Su and M.T. Bowers, Ion-Polar Molecule Collisions: the Effect of Ion Size on Ion-Polar Molecule Rate Constants; the Parameterization of the Average-Dipole-Orientation Theory, *International Journal of Mass Spectrometry and Ion Physics*, **12**, 347-356 (1973).
- [67] G. Kummerlöwe and M.K. Beyer, Rate Estimates for Collisions of Ionic Clusters with Neutral Reactant Molecules, *International Journal of Mass Spectrometry*, **244**, 84-90 (2005).
- [68] I. Balteanu, U. Achatz, O.P. Balaj, B.S. Fox, M.K. Beyer and V.E. Bondybey, The Effect of Charge upon CO-Adsorption by Ionic Group 5 and Group 9 Transition Metal Clusters, *International Journal of Mass Spectrometry*, **229**, 61-65 (2003).
- [69] M.J. Frisch, G.W. Trucks, H.B. Schlegel, G.E. Scuseria, M.A. Robb, J.R. Cheeseman, G. Scalmani, V. Barone, B. Mennucci, G.A. Petersson, H. Nakatsuji, M. Caricato, X. Li, H.P. Hratchian, A.F. Izmaylov, J. Bloino, G. Zheng, J.L. Sonnenberg, M. Hada, M. Ehara, K. Toyota, R. Fukuda, J. Hasegawa, M. Ishida, T. Nakajima, Y. Honda, O. Kitao, H. Nakai, T. Vreven, J.A. Montgomery Jr., J.E. Peralta, F. Ogliaro, M.J. Bearpark, J. Heyd, E.N. Brothers, K.N. Kudin, V.N. Staroverov, R. Kobayashi, J. Normand, K. Raghavachari, A.P. Rendell, J.C. Burant, S.S. Iyengar, J. Tomasi, M. Cossi, N. Rega, N.J. Millam, M. Klene, J.E. Knox, J.B. Cross, V. Bakken, C. Adamo, J. Jaramillo, R. Gomperts, R.E. Stratmann, O. Yazyev, A.J. Austin, R. Cammi, C. Pomelli, J.W. Ochterski, R.L. Martin, K. Morokuma, V.G. Zakrzewski, G.A. Voth, P. Salvador, J.J. Dannenberg, S. Dapprich, A.D. Daniels, Ö. Farkas, J.B. Foresman, J.V. Ortiz, J. Cioslowski and D.J. Fox, Gaussian 09, Revision D.01, in, Gaussian, Inc., Wallingford, CT, USA, 2009.
- [70] C. Adamo and V. Barone, Toward Reliable Density Functional Methods without Adjustable Parameters: The PBE0 Model, *The Journal of Chemical Physics*, **110**, 6158-6170 (1999).
- [71] D. Andrae, U. Häußermann, M. Dolg, H. Stoll and H. Preuß, Energy-Adjusted Ab Initio Pseudopotentials for the Second and Third Row Transition Elements, *Theoretica chimica acta*, **77**, 123-141 (1990).
- [72] G. Niedner-Schatteburg, *Cooperative Effects in Clusters and Oligonuclear Complexes of Transition Metals in Isolation*, in *Clusters – Contemporary Insight in Structure and Bonding*, edited by S. Dehnen, (Springer International Publishing, Cham, 2017, 1-40).
- [73] G. Comelli, V.R. Dhanak, M. Kiskinova, K.C. Prince and R. Rosei, Oxygen and Nitrogen Interaction with Rhodium Single Crystal Surfaces, *Surface Science Reports*, **32**, 165-231 (1998).
- [74] T. Bligaard and J.K. Nørskov, *Chapter 4 - Heterogeneous Catalysis*, in *Chemical Bonding at Surfaces and Interfaces*, edited by, (Elsevier, Amsterdam, 2008, 255-321).
- [75] D. Harding, M.S. Ford, T.R. Walsh and S.R. Mackenzie, Dramatic Size Effects and Evidence of Structural Isomers in the Reactions of Rhodium Clusters, $\text{Rh}_n^{+/-}$, with Nitrous Oxide, *Physical Chemistry Chemical Physics*, **9**, 2130-2136 (2007).
- [76] J. Berwanger, S. Polesya, S. Mankovsky, H. Ebert and F.J. Giessibl, Atomically Resolved Chemical Reactivity of Small Fe Clusters, *Phys Rev Lett*, **124**, 096001 (2020).

4.10 Supplementary Information

Cryokinetics and spin quenching

in the N₂ Adsorption onto Rhodium-Cluster Cations

Amelie A. Ehrhard^{1,2}, Matthias P. Klein², Jennifer Mohrbach, Sebastian Dillinger,
and Gereon Niedner-Schatteburg

*Fachbereich Chemie and Forschungszentrum OPTIMAS
TU Kaiserslautern, 67663 Kaiserslautern, Germany*

I. Clarification of the used nomenclature

Text S1	Clarification of the used nomenclature
Table S1	Nomenclature of molecular adsorption onto and desorption off size selected elemental clusters

II. Data derived from kinetic measurements

a) Plots of adsorption kinetics and rate constants

Fig. S1 a	Isothermal kinetics of the stepwise N ₂ adsorption by isolated Rh ₅ ⁺
Fig. S1 b	Fitted values of relative rate constants for the N ₂ adsorption on Rh ₅ ⁺
Fig. S2 a	Isothermal kinetics of the stepwise N ₂ adsorption by isolated Rh ₅ ⁺ between 0.2 and 2.6 s storage time
Fig. S2 b	Fitted values of relative rate constants for the N ₂ adsorption on Rh ₅ ⁺ between 0.2 and 2.6 s
Fig. S3 a	Isothermal kinetics of the stepwise N ₂ adsorption by isolated Rh ₆ ⁺
Fig. S3 b	Fitted values of relative rate constants for the N ₂ adsorption on Rh ₆ ⁺
Fig. S4 a	Isothermal kinetics of the stepwise N ₂ adsorption by isolated Rh ₇ ⁺
Fig. S4 b	Fitted values of relative rate constants for the N ₂ adsorption on Rh ₇ ⁺
Fig. S5 a	Isothermal kinetics of the stepwise N ₂ adsorption by isolated Rh ₈ ⁺

¹ Present address: Max-Planck-Institut für Polymerforschung, 55128 Mainz, Germany

² These authors contributed equally

Fig. S5 b	Fitted values of relative rate constants for the N ₂ adsorption on Rh ₈ ⁺
Fig. S6 a	Isothermal kinetics of the stepwise N ₂ adsorption by isolated Rh ₉ ⁺
Fig. S6 b	Fitted values of relative rate constants for the N ₂ adsorption on Rh ₉ ⁺
Fig. S7 a	Isothermal kinetics of the stepwise N ₂ adsorption by isolated Rh ₁₀ ⁺
Fig. S7 b	Fitted values of relative rate constants for the N ₂ adsorption on Rh ₁₀ ⁺
Fig. S8 a	Isothermal kinetics of the stepwise N ₂ adsorption by isolated Rh ₁₁ ⁺
Fig. S8 b	Fitted values of relative rate constants for the N ₂ adsorption on Rh ₁₁ ⁺
Fig. S9 a	Isothermal kinetics of the stepwise N ₂ adsorption by isolated Rh ₁₂ ⁺
Fig. S9 b	Fitted values of relative rate constants for the N ₂ adsorption on Rh ₁₂ ⁺
Fig. S10 a	Isothermal kinetics of the stepwise N ₂ adsorption by isolated Rh ₁₃ ⁺
Fig. S10 b	Fitted values of relative rate constants for the N ₂ adsorption on Rh ₁₃ ⁺
Fig. S11 a	Isothermal kinetics of the stepwise N ₂ adsorption by isolated Rh ₁₄ ⁺
Fig. S11 b	Fitted values of relative rate constants for the N ₂ adsorption on Rh ₁₄ ⁺
Fig. S12 a	Isothermal kinetics of the stepwise N ₂ adsorption by isolated Rh ₁₅ ⁺
Fig. S12 b	Fitted values of relative rate constants for the N ₂ adsorption on Rh ₁₅ ⁺
Fig. S13	Sticking probabilities γ_i for the N ₂ adsorption first step on Rh _i ⁺ $i = 5, \dots, 15$

b) Values derived from the fits and for the N₂ adsorption onto each cluster (i,m)

Table S2	Calculated relative rate constants $k_{(i,m)}$ for the N ₂ adsorption onto [Rh _i (N ₂) _m] ⁺
Table S3	Drop of rate constants for the first adsorption after reaching the intermittent adsorption limit m_x
Table S4	Collision rates $k_{(i,m)}^{coll}$ (Langevin) for the N ₂ adsorption onto [Rh _i (N ₂) _m] ⁺
Table S5	Calculated absolute rate constants $k_{(i,m)}^{abs}$ for the N ₂ adsorption onto [Rh _i (N ₂) _m] ⁺
Table S6	Sticking probabilities $\gamma_{(i,m)}$ for the N ₂ adsorption onto [Rh _i (N ₂) _m] ⁺

c) Values derived from the fits and for the N₂ desorption off each cluster (i,m)

Table S7	Calculated relative rate constants $k_{-(i,m+1)}$ for the N ₂ desorption off [Rh _i (N ₂) _{m+1}] ⁺
Table S8	Calculated absolute rate constants $k_{-(i,m+1)}^{abs}$ for the N ₂ desorption off [Rh _i (N ₂) _{m+1}] ⁺
Table S9	Sticking probabilities $\gamma_{-(i,m+1)}$ for the N ₂ desorption off [Rh _i (N ₂) _{m+1}] ⁺

d) Values including N₂ adsorption onto and desorption off each cluster (i,m)

Table S10	Equilibrium constants for the N ₂ adsorption onto [Rh _i (N ₂) _m] ⁺ / desorption off [Rh _i (N ₂) _{m+1}] ⁺ at 26 K
Table S11	Gibbs free energies $\Delta_{\text{ads}}G^{26\text{K}}_{(i,m)}$ for the equilibrium reactions of N ₂ adsorption onto [Rh _i (N ₂) _m] ⁺ / desorption off [Rh _i (N ₂) _{m+1}] ⁺ at 26 K
Table S12	Relative rate constants for adsorption and desorption, equilibrium constants and Gibbs free energies for each adsorption step of Rh ₅ ⁺
Fig. S14	Plot of Gibbs energies $\Delta_{\text{ads}}G^{26\text{K}}_{(i,m)}$ for the equilibria of N ₂ adsorption onto [Rh _i (N ₂) _m] ⁺ / desorption off [Rh _i (N ₂) _{m+1}] ⁺

III. Comparison of absolute rate constants with Average Dipole Orientation (ADO), Hard-Sphere ADO and Surface Charge Capture theories

Table S13	Data used to calculate the radius of N ₂
Table S14	Input in program by Kummerloewe Beyer
Table S15	ADO, HSA and SCC Rates: Output of program by Kummerloewe/Beyer

IV. Computed structures

Table S16	Number of next neighbors and average coordination number for Rh atoms
Fig. S15	Pictures of the isomers mentioned in Table S16
Table S17	Energies of the isomers constituting the spin valley
Table S18	Vertical (nonet) and adiabatic adsorption energies
Fig. S16	Vertical (nonet) and adiabatic adsorption energies
Table S19	Effects of spin contamination in the calculated most stable isomers

I. Clarification of the used nomenclature

Text S1

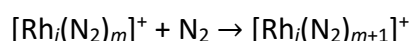
We are aware of possible confusion in the context of stepwise forward / backward kinetics of adsorption / desorption of multiple molecules onto size-selected clusters. In order to describe these processes systematically there are various schemes conceivable. None of these explains itself, and all of these bear residual potential of confusion.

We have chosen a systematic nomenclature, which leads to expression of species and processes as simple and as intuitive as possible.

Let us consider stepwise adsorption/desorption of multiple molecules M to a size-selected cluster $X_n^{+/o/-}$ which constitutes of n atoms of the element X , and which bears any or no charge. The adsorption of the $(m+1)^{\text{th}}$ molecule starts at a complex of this cluster which has attached m molecules before. This process reads as:

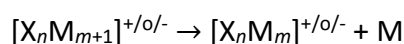


We describe its kinetics by **the adsorption rate constant k_m** . A particular case – e.g. Rhodium cluster cations and N_2 molecules – would read as follows:

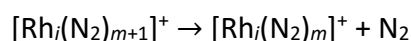


The change of cluster index n to i is void of significance and might occur for other reasons, e.g. when describing mixed clusters $Rh_i Fe_j^+$.

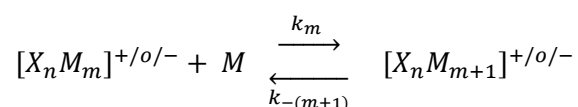
Likewise, we address the desorption of any single one of the $(m+1)$ molecules which starts at a complex of this cluster which has attached $m+1$ molecules before. This process reads as:



We describe its kinetics by **the desorption rate constant $k_{-(m+1)}$** . A particular case – e.g. Rhodium cluster cations and N_2 molecules – would read as follows:



Note, that the pair of rate constants k_m and $k_{-(m+1)}$ describes a pair of processes which we might write in a combined way as follows:

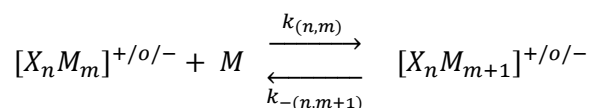


At first glance, it seems counterintuitive, that the indices of forward and backward reaction rate constants are different. Otherwise – when the same – they would lose their significance in ‘counting’ the ligands within the reacting complexes. This ‘counting’ seemed most important to us, and we took it as the imperative motivation for the stated nomenclature.

When dealing with size selected clusters, it is obvious to vary their size. Thus, we have extended our nomenclature as to incorporate the cluster size as follows:

(1) We abbreviate cluster adsorbate complexes $X_n^{+/0/-}$ as **(n,m)**, and we neglect indication of net charge as long as it is unique by context, *e.g.* when dealing with clusters of any single charge state. Once more, the running index of cluster size may vary, *e.g.* when dealing with heterogeneous clusters that are made of atoms from more than a single chemical element. *E.g.* an adsorbate complex of a mixed Rhodium Iron cluster $[Rh_iFe_j(N_2)_m]^+$ would abbreviate **(i,j,m)**.

(2) We denote rate constants of molecular adsorption and desorption k_m and $k_{-(m+1)}$ as $k_{(n,m)}$ and $k_{-(n,m+1)}$ when dealing with clusters made from n atoms of element X . The reaction scheme of a pair of adsorption / desorption reactions then reads as:



Thus n and m become most suitable indices for tabulating and plotting kinetic data of these reactions. Note, that the first and second adsorption steps are denoted k_0 or $k_{(n,0)}$, k_1 or $k_{(n,1)}$ etc., and the first and second desorption steps are denote k_{-1} or $k_{-(n,1)}$, k_{-2} or $k_{-(n,2)}$ etc.

Below, we summarize the chosen definitions according to our nomenclature.

Table S1 Nomenclature of molecular adsorption onto and desorption off size selected elemental clusters

Entity	Symbol	Exemplification
Indices	n, i, j	Atom count of one or two elements within the cluster
Naked clusters	$(n,0)$	<i>e.g.</i> : Ni_n^+, Fe_n^+ , but Rh_i^+
	$(i,j,0)$	<i>e.g.</i> : $Rh_iFe_j^+$, with $i+j=n$
Cluster adsorbate complexes	(n,m)	$[X_nM_m]^{+/o/-}$ when reactant in adsorption or product in desorption
	$(n,m+1)$	$[X_nM_{m+1}]^{+/o/-}$ when product in adsorption or reactant in desorption
	(i,j,m)	$[X_iY_jM_m]^{+/o/-}$ when reactant in adsorption or product in desorption
	$(i,j,m+1)$	$[X_iY_jM_{m+1}]^{+/o/-}$ when product in adsorption or reactant in desorption
Adsorption rate constants	$k_{(n,m)}$	Adsorption onto (n,m)
	$k_{(i,j,m)}$	Adsorption onto (i,j,m)
Desorption rate constants	$k_{-(n,m+1)}$	Desorption off $(n,m+1)$
	$k_{-(i,j,m+1)}$	Desorption off $(i,j,m+1)$
indices	$m = 0,1,2,\dots$	Ligand count within cluster adsorbate complex
	m_x	Intermittent adsorption limit ⁽¹⁾
	m_{max}	Maximum adsorption limit ⁽¹⁾

(1) For the definition of m_x and m_{max} , and for examples refer to the manuscript, section 3.1. of the main part of this publication.

To be consistent with our earlier papers and those in preparation, we choose i as counting index for the Rhodium atoms in clusters.

Differential rate laws relate the defined entities as follows:

- a) For the adsorption onto (i,m) : $-\frac{d[(i,m)]}{dt} = \frac{d[(i,m+1)]}{dt} = k_{(i,m)}[(i,m)]$ and
- b) For the desorption off $(i,m+1)$: $\frac{d[(i,m)]}{dt} = -\frac{d[(i,m+1)]}{dt} = k_{-(i,m+1)}[(i,m+1)]$
- or $-\frac{d[(i,m)]}{dt} = \frac{d[(i,m+1)]}{dt} = -k_{-(i,m+1)}[(i,m+1)]$

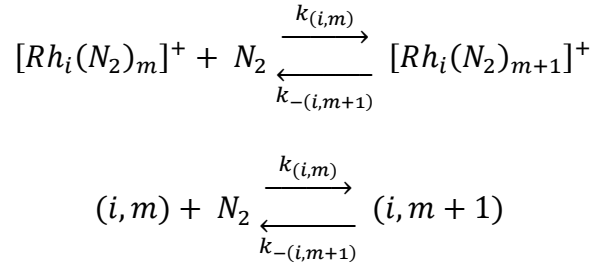
4. Cryokinetics and Spin Quenching in the N₂ Adsorption onto Rhodium-Cluster Cations

We emphasize that

- a) an adsorption rate constant $k_{(i,m)}$ describes the N₂ adsorption onto (i,m) forming $(i,m+1)$
- b) a desorption rate constant $k_{-(i,m+1)}$ describes the N₂ desorption off $(i,m+1)$ forming (i,m)

Keep in mind, that in the pseudo-first-order kinetic model, the available N₂ amount is assumed constant over time. Therefore, the process of adsorption does not change the N₂ pressure. The desorption processes are unimolecular decays and therefore they depend only on the number of cluster adsorbate complexes $(i,m+1)$ that may decay.

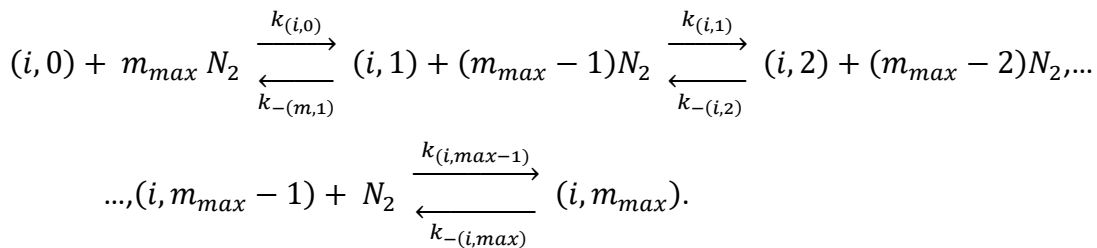
Altogether, this choice of nomenclature results in our applied adsorption/desorption scheme:



For the given adsorption-desorption equilibrium, we obtain

- a) An equilibrium constant $K_{(i,m)} = k_{(i,m)}/k_{-(i,m+1)}$ and
- b) A Gibbs energy $\Delta_{\text{ads}}G_{(i,m)} = -RT \cdot \ln(K_{(i,m)})$

Adsorption and desorption steps form a chain of reactions from $m = 0$ up to m_{max} :



Within a chain of sequential adsorption/desorption steps, the overall change rate of quantity of a species (i,m) is given:

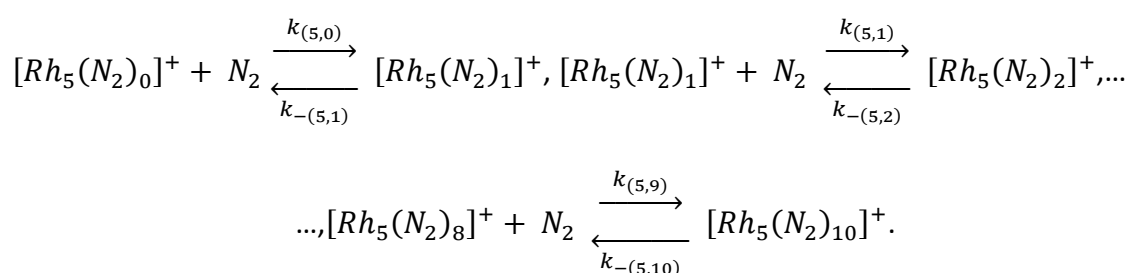
$$\frac{d[(i, m)]}{dt} = k_{(i,m-1)}[(i, m - 1)] - k_{-(i,m)}[(i, m)] - k_{(i,m)}[(i, m)] + k_{-(i,m+1)}[(i, m + 1)]$$

Note, that we define the equilibrium constants $K_{(i,m)}$ by the ratio of the rate constants relating (i,m) and $(i,m+1)$ $K_{(i,m)} = k_{(i,m)}/k_{-(i,m+1)}$. $K_{(i,m)}$ and $\Delta_{\text{ads}}G_{(i,m)}$ do not depend on concentrations but only on the experimental rate constants.

Example: (5,m)

We exemplify the impact of the chosen nomenclature on the description of our experimental results for $[\text{Rh}_5(\text{N}_2)_m]^+$ in Fig. S1. (Section II.a)

The equations of the adsorption/desorption steps are in this case



II. Data derived from kinetic measurements.

a) Plots of adsorption kinetics and rate constants

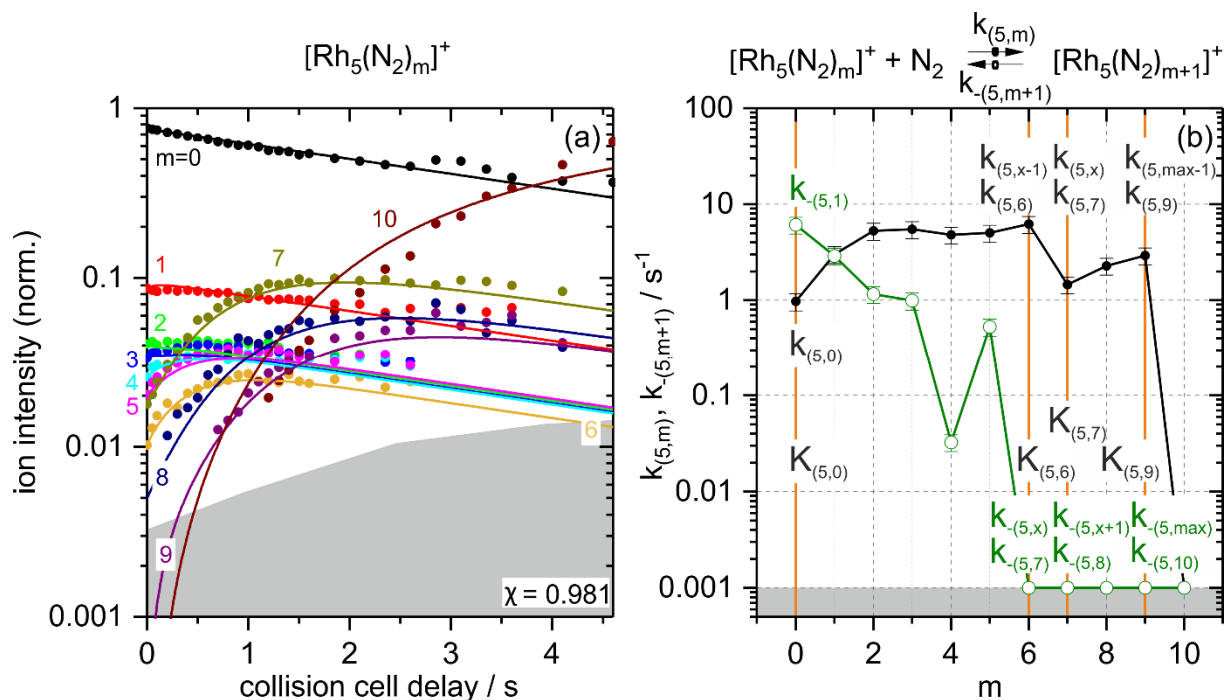


Fig. S1 (a) Isothermal kinetics of the stepwise N₂ adsorption by isolated Rh₅⁺ clusters at $p(\text{N}_2) = 3.1 \cdot 10^{-7}$ mbar within 26 K He buffer gas (solid symbols). The fits (solid lines) assume pseudo-first-order kinetics in an adsorption chain of up to 10 consecutive steps for Rh₅⁺ clusters. **(b)** Fitted values of relative rate constants of Rh₅⁺ as a function of the stepwise N₂ adsorption (level m). The grey shaded area indicates the approximate background noise level. Note, that the fitted rate constants for the adsorption ($k_{(5,m)}$, black filled circles) are nearly 4 orders of magnitude higher than those of the desorption ($k_{-(5,m+1)}$, green open circles, upper limits). The fit includes adsorption and desorption reaction for every step. The grey shaded area indicates the approximate background noise level.

In (b), we exemplify the used nomenclature for the adsorption $k_{(5,m)}$ (black) and desorption $k_{-(5,m+1)}$ (green) rate constants and the resulting equilibrium constants $K_{(5,m)}$. Related descriptors are connected by the orange lines. Note, that the nomenclature effects that the values of $k_{(i,m)}$ and $k_{(i,m+1)}$ lie on top of each other.

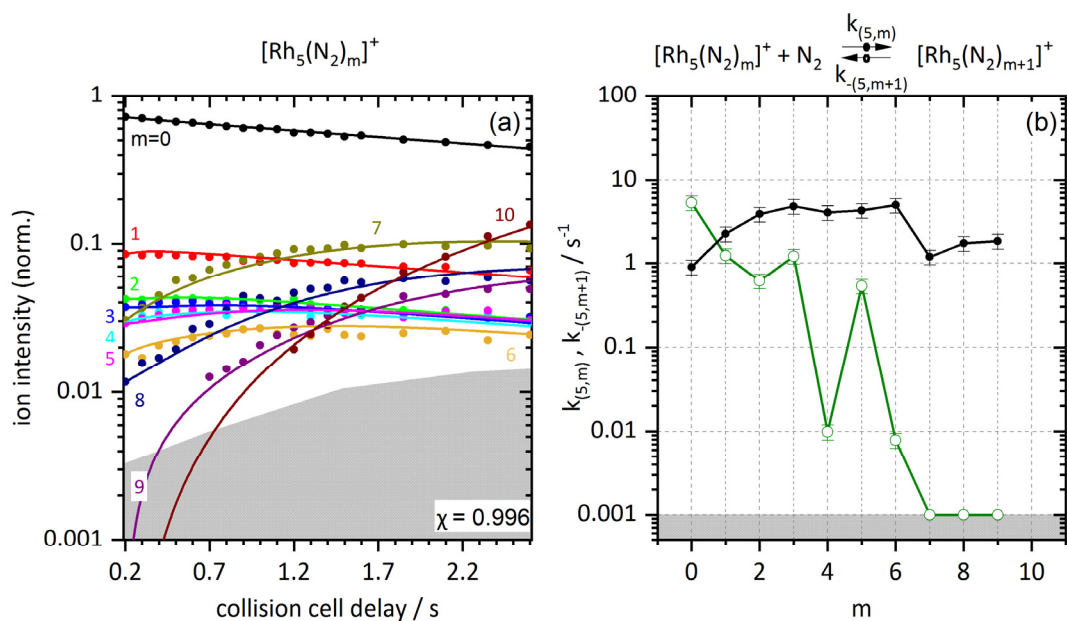


Fig. S2 (a) Isothermal kinetics of the stepwise N_2 adsorption by isolated Rh_5^+ clusters between 0.2 and 2.6 s storage time at $p(\text{N}_2) = 3.1 \cdot 10^{-7}$ mbar within 26 K He buffer gas (solid symbols). The fits (solid lines) assume pseudo-first-order kinetics in an adsorption chain of up to 10 consecutive steps. **(b)** Fitted values of relative rate constants from the kinetic fit for the N_2 adsorption on Rh_5^+ as a function of the stepwise N_2 adsorption (level m). The grey shaded area indicates the approximate background noise level.

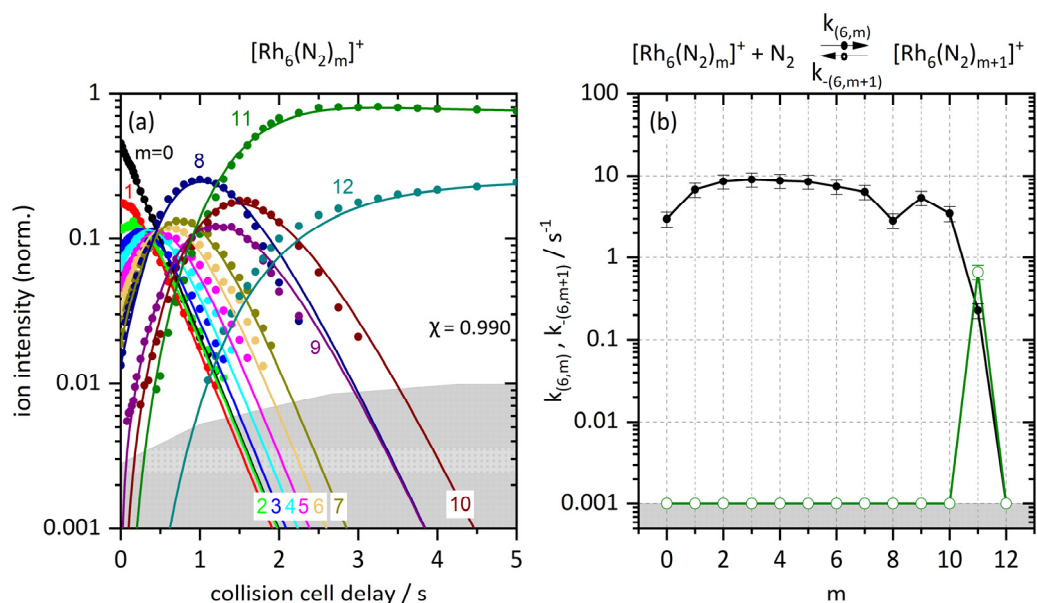


Fig. S3 (a) Isothermal kinetics of the stepwise N₂ adsorption by isolated Rh₆⁺ clusters at $p(\text{N}_2) = 3.1 \cdot 10^{-7}$ mbar within 26 K He buffer gas (solid symbols). The fits (solid lines) assume pseudo-first-order kinetics in an adsorption chain of up to 12 consecutive steps. **(b)** Fitted values of relative rate constants of Rh₆⁺ as a function of the stepwise N₂ adsorption (level m). The grey shaded area indicates the approximate background noise level. Note, that the adsorption rate constants ($k_{(6,m)}$, black filled circles) are nearly 4 orders of magnitude higher than those of the desorption ($k_{-(6,m+1)}$, green, upper limits) for $m \leq 10$. The fit includes adsorption and desorption for the last N₂ attachment step.

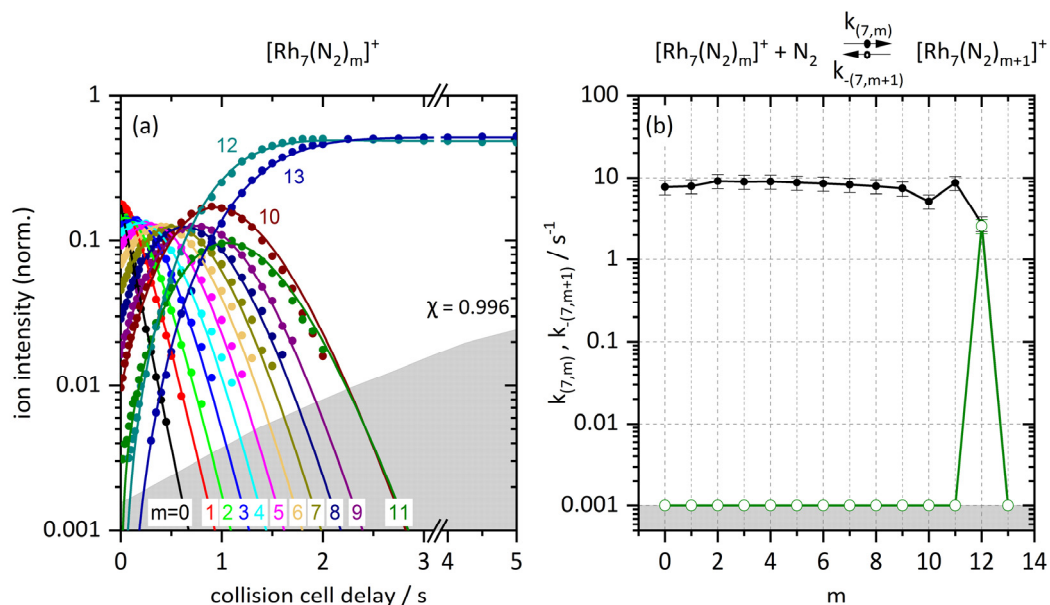


Fig. S4 (a) Isothermal kinetics of the stepwise N_2 adsorption by isolated Rh_7^+ clusters at $p(\text{N}_2) = 3.0 \cdot 10^{-7}$ mbar within 26 K He buffer gas (solid symbols). The fits (solid lines) assume pseudo-first-order kinetics in an adsorption chain of up to 13 consecutive steps. **(b)** Fitted values of relative rate constants of Rh_7^+ as a function of the stepwise N_2 adsorption (level m). The grey shaded area indicates the approximate background noise level. Note, that the adsorption rate constants ($k_{(7,m)}$, black filled circles) are nearly 4 orders of magnitude higher than those of the desorption ($k_{-(7,m+1)}$, green, upper limits) for $m \leq 11$. The fit includes adsorption and desorption for the last N_2 attachment step.

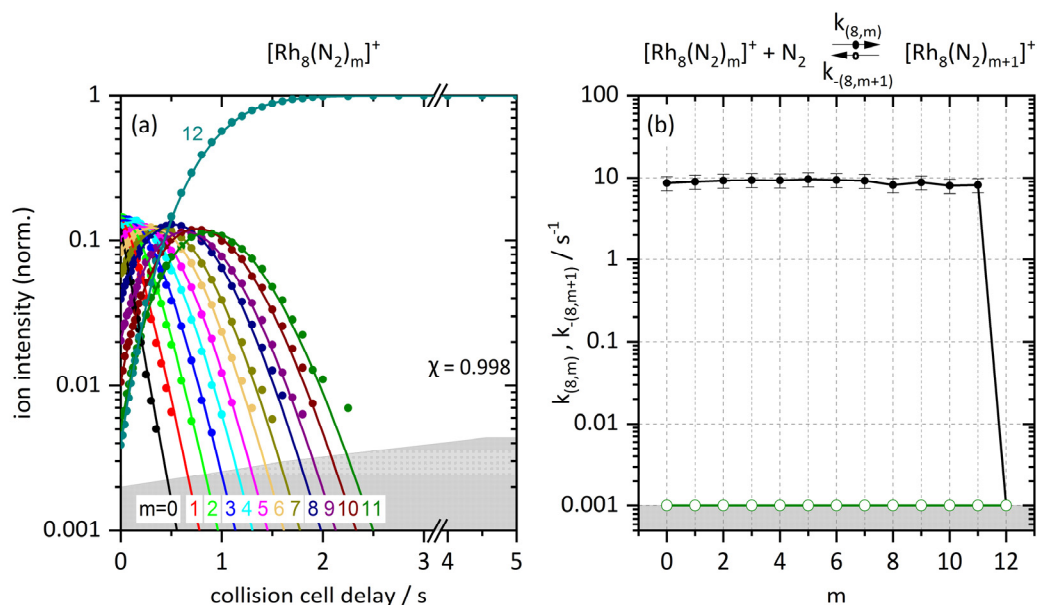


Fig. S5 (a) Isothermal kinetics of the stepwise N₂ adsorption by isolated Rh₈⁺ clusters at $p(\text{N}_2) = 3.0 \cdot 10^{-7}$ mbar within 26 K He buffer gas (solid symbols). The fits (solid lines) assume pseudo-first-order kinetics in an adsorption chain of up to 12 consecutive steps. **(b)** Fitted values of relative rate constants of Rh₈⁺ as a function of the stepwise N₂ adsorption (level m). The grey shaded area indicates the approximate background noise level. Note, that the adsorption rate constants ($k_{(8,m)}$, black filled circles) are nearly 4 orders of magnitude higher than those of the desorption ($k_{-(8,m+1)}$, green, upper limits). The fit includes only adsorption steps.

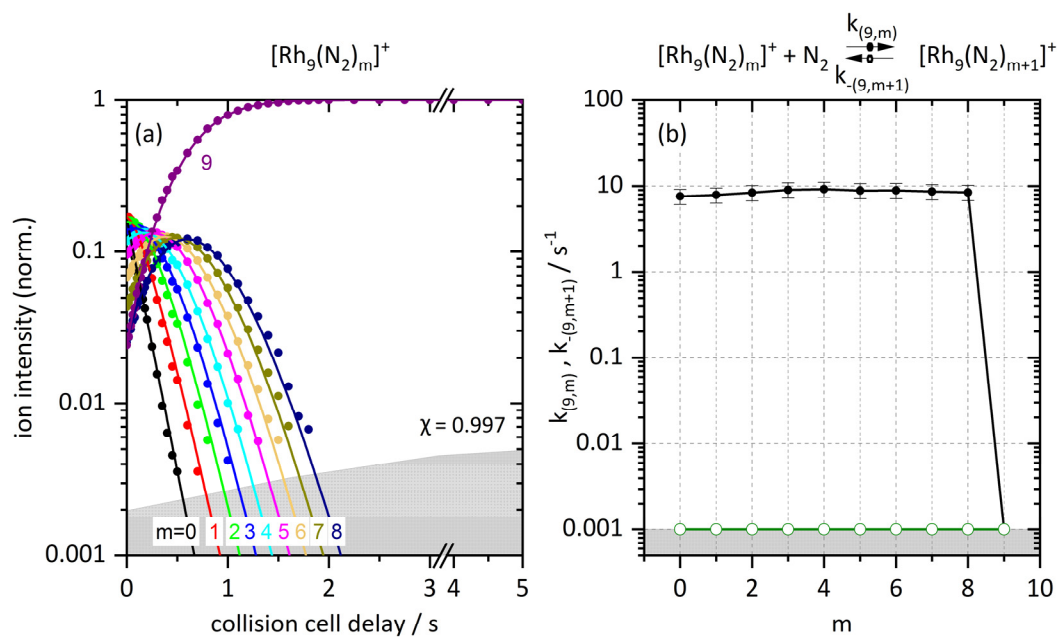


Fig. S6 (a) Isothermal kinetics of the stepwise N_2 adsorption by isolated Rh_9^+ clusters at $p(\text{N}_2) = 3.0 \cdot 10^{-7}$ mbar within 26 K He buffer gas (solid symbols). The fits (solid lines) assume pseudo-first-order kinetics in an adsorption chain of up to 9 consecutive steps. **(b)** Fitted values of relative rate constants of Rh_9^+ as a function of the stepwise N_2 adsorption (level m). The grey shaded area indicates the approximate background noise level. Note, that the adsorption rate constants ($k_{(9,m)}$, black filled circles) are nearly 4 orders of magnitude higher than those of the desorption ($k_{-(9,m+1)}$, green, upper limits). The fit includes only adsorption steps.

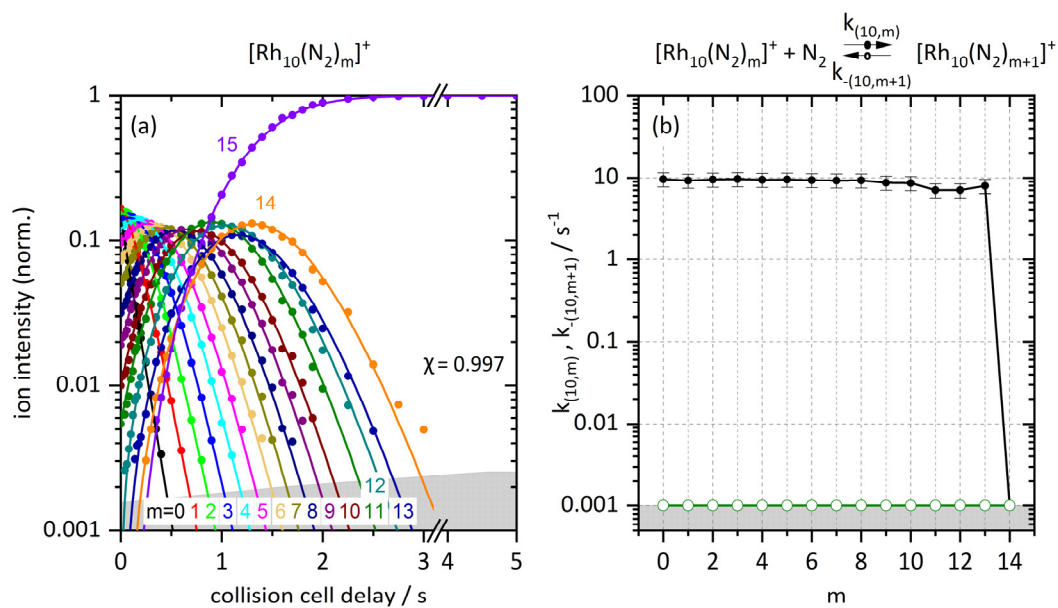


Fig. S7 (a) Isothermal kinetics of the stepwise N₂ adsorption by isolated Rh₁₀⁺ clusters at $p(\text{N}_2) = 3.0 \cdot 10^{-7}$ mbar within 26 K He buffer gas (solid symbols). The fits (solid lines) assume pseudo-first-order kinetics in an adsorption chain of up to 15 consecutive steps. **(b)** Fitted values of relative rate constants of Rh₁₀⁺ as a function of the stepwise N₂ adsorption (level m). The grey shaded area indicates the approximate background noise level. Note, that the adsorption rate constants ($k_{(10,m)}$, black filled circles) are nearly 4 orders of magnitude higher than those of the desorption ($k_{-(10,m+1)}$, green, upper limits). The fit includes only adsorption steps.

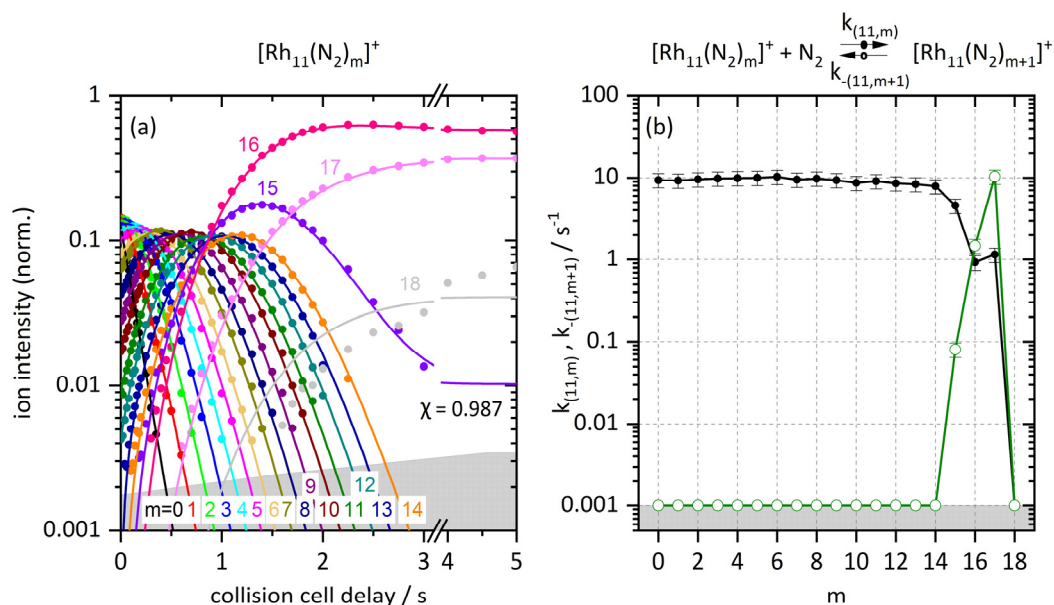


Fig. S8 (a) Isothermal kinetics of the stepwise N_2 adsorption by isolated Rh_{11}^+ clusters at $p(\text{N}_2) = 3.0 \cdot 10^{-7}$ mbar within 26 K He buffer gas (solid symbols). The fits (solid lines) assume pseudo-first-order kinetics in an adsorption chain of up to 18 consecutive steps. **(b)** Fitted values of relative rate constants of Rh_{11}^+ (b) as a function of the stepwise N_2 adsorption (level m). The grey shaded area indicates the approximate background noise level. Note, that the adsorption rate constants ($k_{(11,m)}$, black filled circles) are nearly 4 orders of magnitude higher than those of the desorption ($k_{-(11,m+1)}$, green, upper limits) for $m \leq 14$. The fit includes adsorption and desorption for the last three N_2 attachment steps.

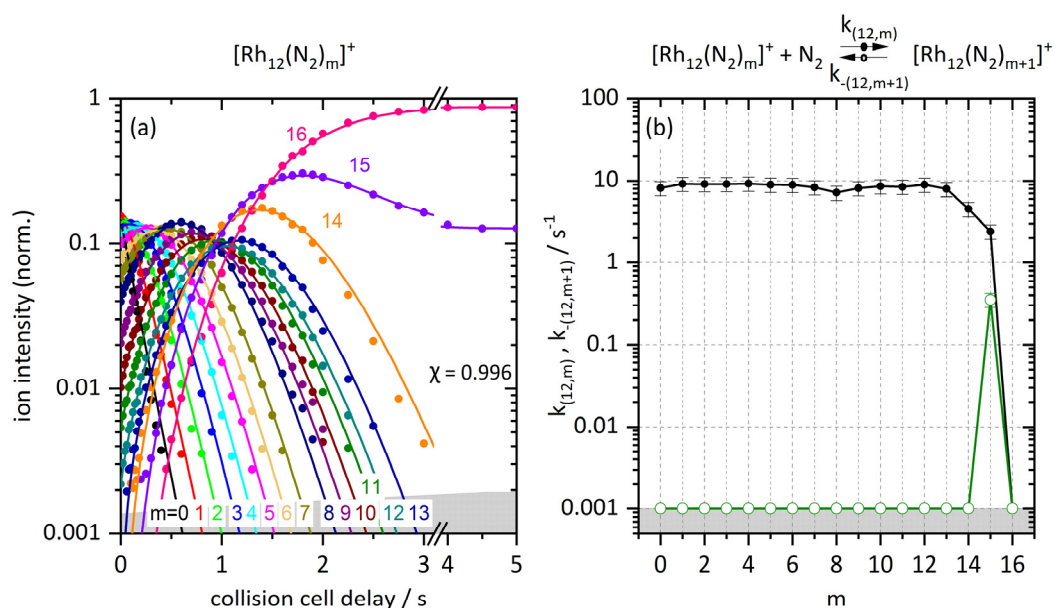


Fig. S9 (a) Isothermal kinetics of the stepwise N₂ adsorption by isolated Rh₁₂⁺ clusters at $p(\text{N}_2) = 3.0 \cdot 10^{-7}$ mbar within 26 K He buffer gas (solid symbols). The fits (solid lines) assume pseudo-first-order kinetics in an adsorption chain of up to 16 consecutive steps. **(b)** Fitted values of relative rate constants of Rh₁₂⁺ as a function of the stepwise N₂ adsorption (level m). The grey shaded area indicates the approximate background noise level. Note, that the adsorption rate constants ($k_{(12,m)}$, black filled circles) are nearly 4 orders of magnitude higher than those of the desorption ($k_{-(12,m+1)}$, green, upper limits) for $m \leq 14$. The fit includes adsorption and desorption for the last N₂ attachment step.

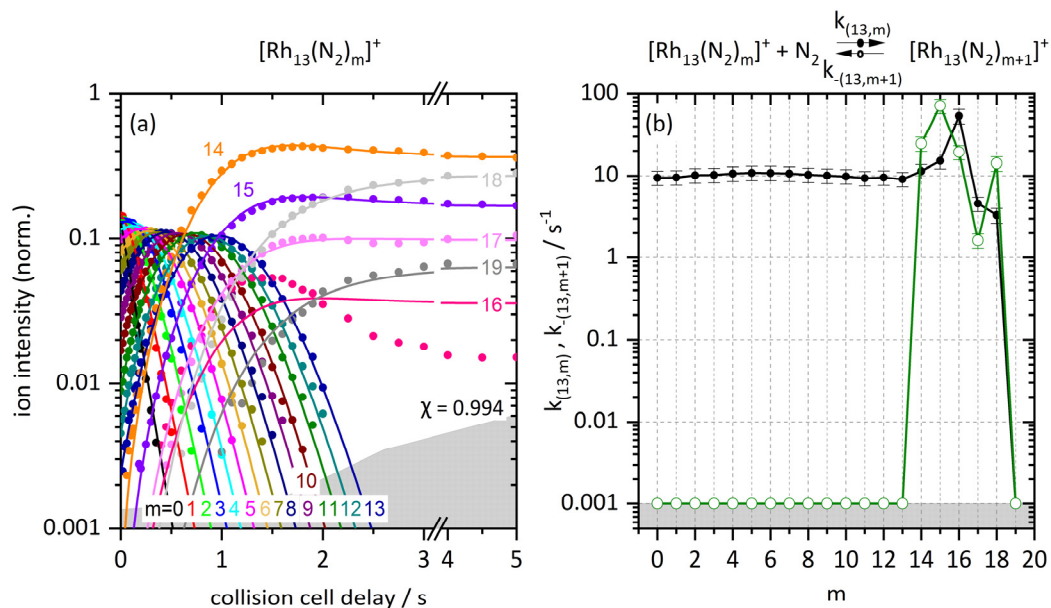


Fig. S10 (a) Isothermal kinetics of the stepwise N_2 adsorption by isolated Rh_{13}^+ clusters at $p(\text{N}_2) = 3.0 \cdot 10^{-7}$ mbar within 26 K He buffer gas (solid symbols). The fits (solid lines) assume pseudo-first-order kinetics in an adsorption chain of up to 19 consecutive steps. **(b)** Fitted values of relative rate constants of Rh_{13}^+ as a function of the stepwise N_2 adsorption (level m). The grey shaded area indicates the approximate background noise level. Note, that the adsorption rate constants ($k_{(13,m)}$, black filled circles) are nearly 4 orders of magnitude higher than those of the desorption ($k_{-(13,m+1)}$, green, upper limits) for $m \leq 13$. The fit includes adsorption and desorption for the last five N_2 attachment steps.

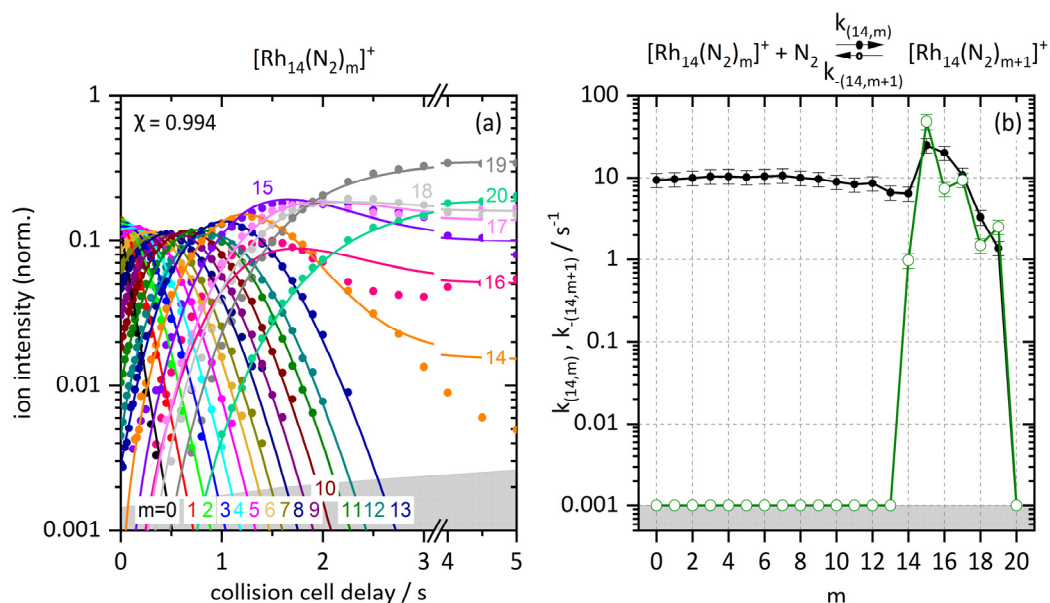


Fig. S11 (a) Isothermal kinetics of the stepwise N₂ adsorption by isolated Rh₁₄⁺ clusters at $p(\text{N}_2) = 3.0 \cdot 10^{-7}$ mbar within 26 K He buffer gas (solid symbols). The fits (solid lines) assume pseudo-first-order kinetics in an adsorption chain of up to 20 consecutive steps. **(b)** Fitted values of relative rate constants of Rh₁₄⁺ as a function of the stepwise N₂ adsorption (level m). The grey shaded area indicates the approximate background noise level. Note, that the adsorption rate constants ($k_{(14,m)}$, black filled circles) are nearly 4 orders of magnitude higher than those of the desorption ($k_{-(14,m+1)}$, green, upper limits) for $m \leq 13$. The fit includes adsorption and desorption for the last six N₂ attachment steps.

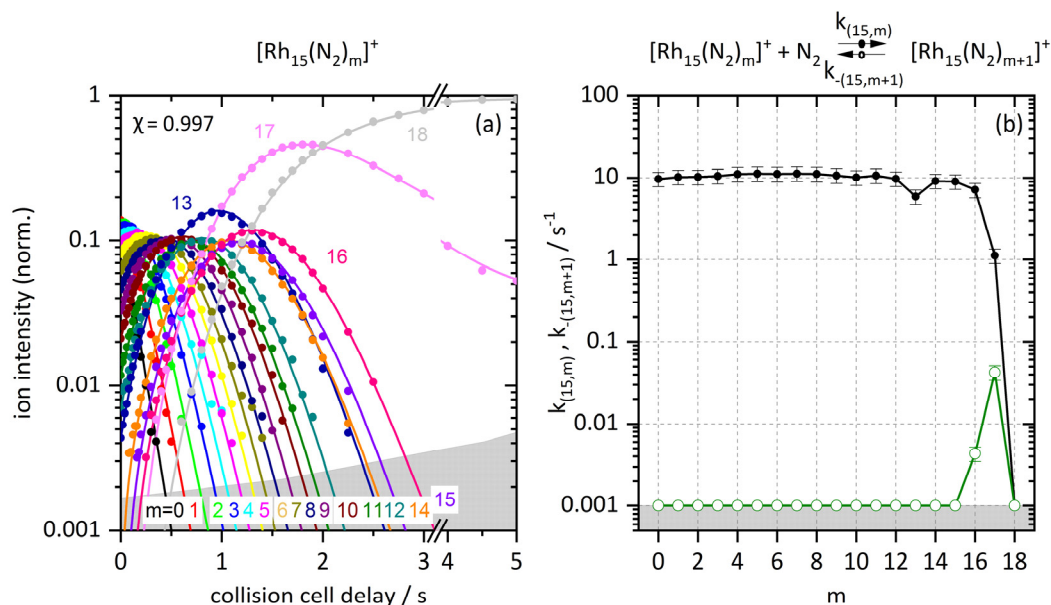


Fig. S12 (a) Isothermal kinetics of the stepwise N_2 adsorption by isolated Rh_{15}^+ clusters at $p(\text{N}_2) = 3.0 \cdot 10^{-7}$ mbar within 26 K He buffer gas (solid symbols). The fits (solid lines) assume pseudo-first-order kinetics in an adsorption chain of up to 18 consecutive steps. **(b)** Fitted values of relative rate constants of Rh_{15}^+ as a function of the stepwise N_2 adsorption (level m). The grey shaded area indicates the approximate background noise level. Note, that the adsorption rate constants ($k_{(15,m)}$, black filled circles) are nearly 4 orders of magnitude higher than those of the desorption ($k_{-(15,m+1)}$, green, upper limits) for $m \leq 15$. The fit includes adsorption and desorption for the last two N_2 attachment steps.

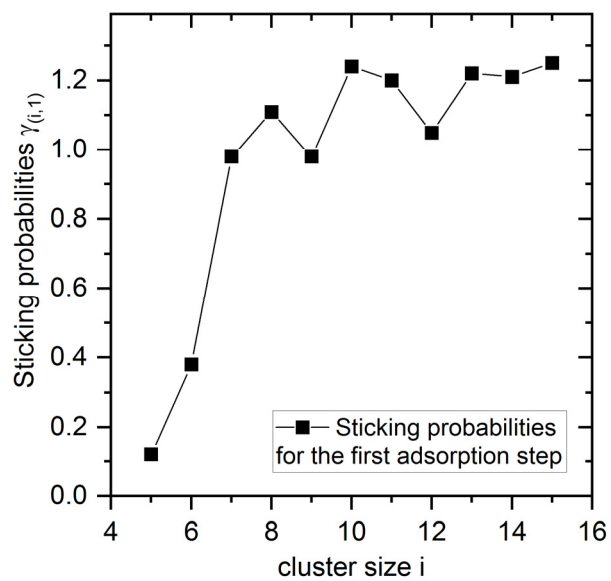


Fig. S13 Sticking probabilities $\gamma_{(i,1)}$ for the N₂ adsorption first step on Rh_{*i*}⁺ $i = 5, \dots, 15$. Relative uncertainties are + 20 % and – 30 % (conservative estimate).

b) Values derived from the fits and for the N₂ adsorption onto each cluster (i,m)

Table S2 Calculated relative rate constants $k_{(i,m)}$ for the N₂ adsorption onto $[\text{Rh}_i(\text{N}_2)_m]^+$. Relative uncertainties are $\pm 20\%$ (conservative estimate). Conversion to absolute rate constants is $k_{(i,m)}^{abs} = \frac{k_{(i,m)}}{\rho_{\text{N}_2}}$ and normalization to collision rate $k_{(i,m)}^{coll}$ (Langevin) yields sticking probabilities $\gamma_i = \frac{k_{abs,i}}{k_{coll,i}}$. The grey shaded fields contain the $k_{(i,m)}$ values exceeding m_{max} which are set to 0.001 for the forward reaction for each cluster size. Fields beyond this adsorption limit are left empty.

Relative rate constants $k_{(i,m)} / \text{s}^{-1}$	$m = 0$	1	2	3	4	5	6	7	8	9	10	11	12	13	14	15	16	17	18	19	20
$[\text{Rh}_5(\text{N}_2)_m]^+$	0.97	3.0	5.3	5.5	4.8	5.0	6.2	1.5	2.3	2.9	0.001										
$[\text{Rh}_6(\text{N}_2)_m]^+$	3.0	6.8	8.5	9.0	8.7	8.5	7.4	6.3	2.8	5.4	3.4	0.23	0.001								
$[\text{Rh}_7(\text{N}_2)_m]^+$	7.7	7.9	9.2	9.0	9.0	8.7	8.5	8.2	7.9	7.4	5.1	8.7	2.8	0.001							
$[\text{Rh}_8(\text{N}_2)_m]^+$	8.6	9.0	9.3	9.4	9.3	9.6	9.4	9.2	8.2	8.8	8.0	8.1	0.001								
$[\text{Rh}_9(\text{N}_2)_m]^+$	7.6	7.9	8.4	9.1	9.2	8.9	8.9	8.7	8.5	0.001											
$[\text{Rh}_{10}(\text{N}_2)_m]^+$	9.6	9.3	9.5	9.7	9.5	9.5	9.4	9.3	9.3	8.7	8.6	7.0	7.0	8.0	6.3	0.001					
$[\text{Rh}_{11}(\text{N}_2)_m]^+$	9.4	9.3	9.6	9.8	9.9	10.0	10.3	9.5	9.8	9.3	8.7	9.1	8.6	8.3	7.9	4.6	0.93	1.1	0.001		
$[\text{Rh}_{12}(\text{N}_2)_m]^+$	8.1	9.2	9.1	9.2	9.3	9.0	8.9	8.3	7.2	8.1	8.6	8.4	9.0	8.0	4.5	2.4	0.001				
$[\text{Rh}_{13}(\text{N}_2)_m]^+$	9.5	9.6	10	10	11	11	11	11	10	10	9.8	9.4	9.5	9.1	11	15	53	4.5	3.3	0.001	
$[\text{Rh}_{14}(\text{N}_2)_m]^+$	9.4	9.6	10	10	10	10	10	11	10	9.7	8.9	8.3	8.6	6.6	6.4	25	20	11	3.3	1.4	0.001
$[\text{Rh}_{15}(\text{N}_2)_m]^+$	9.7	10	10	10	11	11	11	11	11	11	10	11	9.7	5.9	9.2	9.0	7.1	1.1	0.001		

4. Cryokinetics and Spin Quenching in the N₂ Adsorption onto Rhodium-Cluster Cations

Table S3 Drop of rate constants for the first adsorption after reaching the intermittent adsorption limit m_x .

Cluster	$k_{(i,x-1)} / \text{s}^{-1}$	$k_{(i,x)} / \text{s}^{-1}$	Drop / s^{-1}	Ratio $k_{(i,x-1)} / k_{(i,x)}$
Rh ₅ ⁺	$k_{(5,6)}$ 6.2	$k_{(5,7)}$ 1.5	4.7	4.2
Rh ₆ ⁺	$k_{(6,7)}$ 6.3	$k_{(6,8)}$ 2.8	3.5	2.2
Rh ₇ ⁺	$k_{(7,9)}$ 7.4	$k_{(7,10)}$ 5.1	2.3	1.4

Table S4: Collision rates $k_{(i,m)}^{coll}$ (Langevin) for the N₂ adsorption onto [Rh_i(N₂)_m]⁺. Relative uncertainties are ± 40 % (conservative estimate). The grey shaded fields contain the $k_{(i,m)}^{coll}$ values exceeding m_{max} . Fields beyond this adsorption limit are left empty.

Collision rate (Langevin) $k_{(i,m)} / 10^{10} \text{ cm}^3 \text{ s}^{-1}$	$m=0$	1	2	3	4	5	6	7	8	9	10	11	12	13	14	15	16	17	18	19	20
[Rh ₅ (N ₂) _m] ⁺	6.05	6.04	6.03	6.03	6.02	6.01	6.01	6.00	6.00	6.00	5.99										
[Rh ₆ (N ₂) _m] ⁺	6.02	6.02	6.01	6.01	6.00	6.00	5.99	5.99	5.99	5.98	5.98	5.98	5.98								
[Rh ₇ (N ₂) _m] ⁺	6.00	6.00	5.99	5.99	5.99	5.98	5.98	5.98	5.98	5.97	5.97	5.97	5.97	5.97							
[Rh ₈ (N ₂) _m] ⁺	5.99	5.99	5.98	5.98	5.98	5.97	5.97	5.97	5.97	5.97	5.96	5.96	5.96								
[Rh ₉ (N ₂) _m] ⁺	5.98	5.98	5.97	5.97	5.97	5.97	5.96	5.96	5.96	5.96											
[Rh ₁₀ (N ₂) _m] ⁺	5.97	5.97	5.97	5.96	5.96	5.96	5.96	5.96	5.96	5.95	5.95	5.95	5.95	5.95	5.95	5.95					
[Rh ₁₁ (N ₂) _m] ⁺	5.96	5.96	5.96	5.96	5.96	5.95	5.95	5.95	5.95	5.95	5.95	5.95	5.95	5.94	5.94	5.94	5.94	5.94	5.94		
[Rh ₁₂ (N ₂) _m] ⁺	5.96	5.95	5.95	5.95	5.95	5.95	5.95	5.95	5.95	5.94	5.94	5.94	5.94	5.94	5.94	5.94	5.94				
[Rh ₁₃ (N ₂) _m] ⁺	5.95	5.95	5.95	5.95	5.95	5.95	5.94	5.94	5.94	5.94	5.94	5.94	5.94	5.94	5.94	5.94	5.94	5.93	5.93	5.93	5.93
[Rh ₁₄ (N ₂) _m] ⁺	5.95	5.95	5.94	5.94	5.94	5.94	5.94	5.94	5.94	5.94	5.94	5.94	5.94	5.94	5.93	5.93	5.93	5.93	5.93	5.93	5.93
[Rh ₁₅ (N ₂) _m] ⁺	5.94	5.94	5.94	5.94	5.94	5.94	5.94	5.94	5.94	5.93	5.93	5.93	5.93	5.93	5.93	5.93	5.93	5.93	5.93		

Table S5 Calculated absolute rate constants $k_{(i,m)}^{abs}$ for the N_2 adsorption onto $[Rh_i(N_2)_m]^+$. Relative uncertainties are $\pm 40\%$ (conservative estimate). We assume an effective geometry factor c_{app} of 1.8 as this provides realistic data for all our experiments [45] and is a viable value after comparison to experiments of Harding et al. [75]. Conversion to absolute rate constants is $k_{(i,m)}^{abs} = \frac{k_{(i,m)}}{\rho_{N_2}}$. The grey shaded fields contain the $k_{(i,m)}^{abs}$ values exceeding m_{max} . Fields beyond this adsorption limit are left empty.

Absolute rate constants $k_{(i,m)} / 10^{-10} \text{ cm}^3 \text{ s}^{-1}$	$m = 0$	1	2	3	4	5	6	7	8	9	10	11	12	13	14	15	16	17	18	19	20		
$[Rh_5(N_2)_m]^+$	0.74	2.3	4.0	4.2	3.7	3.8	4.7	1.1	1.8	2.2	0.77												
$[Rh_6(N_2)_m]^+$		2.3	5.2	6.5	6.9	6.7	6.5	5.7	4.8	2.2	4.1	2.6	0.17	0.77									
$[Rh_7(N_2)_m]^+$		5.9	6.1	7.0	6.9	6.9	6.7	6.5	6.3	6.1	5.7	3.9	6.7	2.1	0.77								
$[Rh_8(N_2)_m]^+$		6.6	6.9	7.1	7.2	7.1	7.4	7.2	7.1	6.3	6.8	6.1	6.2	0.77									
$[Rh_9(N_2)_m]^+$		5.8	6.1	6.5	7.0	7.1	6.8	6.8	6.7	6.5	0.77												
$[Rh_{10}(N_2)_m]^+$		7.4	7.1	7.3	7.4	7.3	7.3	7.2	7.1	7.1	6.7	6.6	5.4	5.4	6.1	4.8	0.77						
$[Rh_{11}(N_2)_m]^+$		7.2	7.1	7.3	7.5	7.6	7.7	7.9	7.3	7.5	7.2	6.7	7.0	6.6	6.4	6.0	3.5	0.71	0.9	0.77			
$[Rh_{12}(N_2)_m]^+$		6.2	7.1	7.0	7.0	7.1	6.9	6.8	6.4	5.5	6.2	6.6	6.5	6.9	6.1	3.4	1.8	0.77					
$[Rh_{13}(N_2)_m]^+$		7.3	7.3	7.8	7.8	8.2	8.3	8.3	8.2	7.9	7.7	7.5	7.2	7.3	7.0	8.7	12	41	3.5	2.5	0.77		
$[Rh_{14}(N_2)_m]^+$		7.2	7.4	7.7	8.0	8.0	7.8	8.0	8.2	7.7	7.4	6.8	6.4	6.6	5.1	4.9	19	15	8.3	2.5	1.1	0.77	
$[Rh_{15}(N_2)_m]^+$		7.4	7.8	7.9	8.0	8.5	8.6	8.5	8.6	8.5	8.2	7.7	8.2	7.5	4.5	7.0	6.9	5.5	0.9	0.77			

Table S6 Sticking probabilities $\gamma_{(i,m)} = \frac{k_{(i,m)}^{abs}}{k_{(i,m)}^{coll}}$ for the N_2 adsorption onto $[Rh_i(N_2)_m]^+$.

Relative uncertainties are $+20\%$ and -30% (conservative estimate). The grey shaded fields contain the $\gamma_{(i,m)}$ values exceeding m_{max} . In case of no entry, $\gamma_{(i,m)} \leq 0.004$.

Sticking probability $\gamma_{(i,m)}$	$m = 0$	1	2	3	4	5	6	7	8	9	10	11	12	13	14	15	16	17	18	19	20		
$[Rh_5(N_2)_m]^+$	0.12	0.38	0.67	0.70	0.61	0.64	0.79	0.19	0.29	0.37	$1.3 \cdot 10^{-4}$												
$[Rh_6(N_2)_m]^+$		0.38	0.86	1.09	1.2	1.1	1.1	0.94	0.81	0.36	0.69	0.44	0.03	$1.3 \cdot 10^{-4}$									
$[Rh_7(N_2)_m]^+$		0.98	1.0	1.2	1.1	1.2	1.1	1.1	1.1	1.0	0.95	0.66	1.1	0.35	$1.3 \cdot 10^{-4}$								
$[Rh_8(N_2)_m]^+$		1.1	1.1	1.2	1.2	1.2	1.2	1.2	1.2	1.0	1.1	1.0	1.0	$1.3 \cdot 10^{-4}$									
$[Rh_9(N_2)_m]^+$		0.98	1.0	1.1	1.2	1.2	1.1	1.1	1.1	1.1	$1.3 \cdot 10^{-4}$												
$[Rh_{10}(N_2)_m]^+$		1.2	1.2	1.2	1.2	1.2	1.2	1.2	1.2	1.2	1.1	1.1	0.91	0.90	1.0	0.81	$1.3 \cdot 10^{-4}$						
$[Rh_{11}(N_2)_m]^+$		1.2	1.2	1.2	1.3	1.3	1.3	1.3	1.2	1.3	1.2	1.1	1.2	1.1	1.1	1.0	0.59	0.12	0.15	$1.3 \cdot 10^{-4}$			
$[Rh_{12}(N_2)_m]^+$		1.0	1.2	1.2	1.2	1.2	1.2	1.2	1.1	0.9	1.0	1.1	1.1	1.2	1.0	0.58	0.31	$1.3 \cdot 10^{-4}$					
$[Rh_{13}(N_2)_m]^+$		1.2	1.2	1.3	1.3	1.4	1.4	1.4	1.4	1.3	1.3	1.3	1.2	1.2	1.2	1.5	1.9	6.9	0.59	0.43	$1.3 \cdot 10^{-4}$		
$[Rh_{14}(N_2)_m]^+$		1.2	1.2	1.3	1.3	1.3	1.3	1.3	1.4	1.3	1.3	1.1	1.1	1.1	0.85	0.83	3.2	2.6	1.4	0.42	0.18	$1.3 \cdot 10^{-4}$	
$[Rh_{15}(N_2)_m]^+$		1.3	1.3	1.3	1.4	1.4	1.4	1.4	1.5	1.4	1.4	1.3	1.4	1.3	0.76	1.2	1.2	0.92	0.14	$1.3 \cdot 10^{-4}$			

c) Values derived from the fits and for the N₂ desorption off each cluster (*i,m*)

Table S7 Calculated relative rate constants $k_{-(i,m+1)}$ for the N₂ desorption off [Rh_{*i*}(N₂)_{*m*+1}]⁺. Relative uncertainties are ± 20 % (conservative estimate). Conversion to absolute rate constants is $k_{(i,m)}^{abs} = \frac{k_{(i,m)}}{\rho_{N_2}}$ and normalization to collision rate k_{coll} (Langevin) yields sticking probabilities $\gamma_{(i,m)} = \frac{k_{(i,m)}^{abs}}{k_{(i,m)}^{coll}}$. * indicates values < 0.001 s⁻¹. The grey shaded fields contain the minimum $k_{-(i,max)}$ values exceeding m_{max} . These values were determined by comparing the intensity of [Rh_{*i*}(N₂)_{*m*+1}]⁺ with the noise level at [Rh_{*i*}(N₂)_{*m*+1}]⁺. Fields beyond this adsorption limit are left empty.

Relative rate constants $k_{-(i,m+1)} / s^{-1}$	<i>m</i> = 0	1	2	3	4	5	6	7	8	9	10	11	12	13	14	15	16	17	18	19	20
[Rh ₅ (N ₂) _{<i>m</i>}] ⁺	6.10	2.9	1.2	1.0	0.032	0.53	3.0·10 ⁻⁷	4.1·10 ⁻⁷	8.0·10 ⁻⁷	5.2·10 ⁻⁹	0.075										
[Rh ₆ (N ₂) _{<i>m</i>}] ⁺	*	*	*	*	*	*	*	*	*	*	*	0.67	0.075								
[Rh ₇ (N ₂) _{<i>m</i>}] ⁺	*	*	*	*	*	*	*	*	*	*	*	6.0·10 ⁻⁷	2.6	0.18							
[Rh ₈ (N ₂) _{<i>m</i>}] ⁺	*	*	*	*	*	*	*	*	*	*	*		0.75								
[Rh ₉ (N ₂) _{<i>m</i>}] ⁺	*	*	*	*	*	*	*	*	*	1.2											
[Rh ₁₀ (N ₂) _{<i>m</i>}] ⁺	*	*	*	*	*	*	*	*	*	*	*	*	*	*		0.75					
[Rh ₁₁ (N ₂) _{<i>m</i>}] ⁺	*	*	*	*	*	*	*	*	*	*	*	*	*	*		0.080	1.48	10.3	0.0060		
[Rh ₁₂ (N ₂) _{<i>m</i>}] ⁺	*	*	*	*	*	*	*	*	*	*	*	*	*	*		0.35	1.20				
[Rh ₁₃ (N ₂) _{<i>m</i>}] ⁺	*	*	*	*	*	*	*	*	*	*	*	*	*	*	25	71	19	1.6	14	0.050	
[Rh ₁₄ (N ₂) _{<i>m</i>}] ⁺	*	*	*	*	*	*	*	*	*	*	*	*	*	*	1.0	48	7.3	9.4	1.5	2.5	0.075
[Rh ₁₅ (N ₂) _{<i>m</i>}] ⁺	*	*	*	*	*	*	*	*	*	*	*	*	*	*	*		0.0	0.0	0.35		

Table S8 Calculated absolute rate constants $k_{-(i,m+1)}^{abs}$ for the N₂ desorption off [Rh_{*i*}(N₂)_{*m*+1}]⁺. Relative uncertainties are ± 40 % (conservative estimate). We assume an effective geometry factor C_{app} of 1.8 as this provides realistic data for all our experiments [45] and is a reliable/viable value after comparison to experiments of Harding et al [75]. Conversion to absolute rate constants is $k_{-(i,m+1)}^{abs} = \frac{k_{-(i,m+1)}}{\rho_{N_2}}$. * indicates values < 7.7 · 10¹⁴ cm³ s⁻¹. The grey shaded fields contain the minimum $k_{-(i,max+1)}$ values exceeding m_{max} . Fields beyond the respective adsorption limits are left empty.

Absolute rate constants $k_{-(i,m+1)} / 10^{-10} cm^3 s^{-1}$	<i>m</i> = 0	1	2	3	4	5	6	7	8	9	10	11	12	13	14	15	16	17	18	19	20
[Rh ₅ (N ₂) _{<i>m</i>}] ⁺	4.68	2.2	0.89	0.76	0.025	0.40	2.3·10 ⁻⁷	3.1·10 ⁻⁷	6.1·10 ⁻⁷	4.0·10 ⁻⁹	0.058										
[Rh ₆ (N ₂) _{<i>m</i>}] ⁺	*	*	*	*	*	*	*	*	*	*	*	0.51	0.058								
[Rh ₇ (N ₂) _{<i>m</i>}] ⁺	*	*	*	*	*	*	*	*	*	*	*	4.6·10 ⁻⁷	2.0	0.13							
[Rh ₈ (N ₂) _{<i>m</i>}] ⁺	*	*	*	*	*	*	*	*	*	*	*		0.58								
[Rh ₉ (N ₂) _{<i>m</i>}] ⁺	*	*	*	*	*	*	*	*	*	0.92											
[Rh ₁₀ (N ₂) _{<i>m</i>}] ⁺	*	*	*	*	*	*	*	*	*	*	*	*	*	*		0.58					
[Rh ₁₁ (N ₂) _{<i>m</i>}] ⁺	*	*	*	*	*	*	*	*	*	*	*	*	*	*		0.061	1.1	7.9	0.0046		
[Rh ₁₂ (N ₂) _{<i>m</i>}] ⁺	*	*	*	*	*	*	*	*	*	*	*	*	*	*		0.27	0.92				
[Rh ₁₃ (N ₂) _{<i>m</i>}] ⁺	*	*	*	*	*	*	*	*	*	*	*	*	*	*	19	54	15	1.2	11	0.038	
[Rh ₁₄ (N ₂) _{<i>m</i>}] ⁺	*	*	*	*	*	*	*	*	*	*	*	*	*	*	0.75	37	5.6	7.2	1.1	1.9	0.058
[Rh ₁₅ (N ₂) _{<i>m</i>}] ⁺	*	*	*	*	*	*	*	*	*	*	*	*	*	*	*		3.3·10 ⁻³	0.033	0.27		

Table S9 Sticking probabilities $\gamma_{-(i,m+1)}$ for the N_2 desorption off $[Rh_i(N_2)_{m+1}]^+$. Relative uncertainties are + 20 % and – 30 % (conservative estimate). * indicates values $\gamma_{-(i,m+1)} \leq 0.0002$. The grey shaded fields contain the $\gamma_{-(i,m_{max}+1)}$ values exceeding m_{max} . Fields beyond the respective adsorption limits are left empty.

Sticking probability $\gamma_{-(i,m+1)}$	$m = 0$	1	2	3	4	5	6	7	8	9	10	11	12	13	14	15	16	17	18	19	20		
$[Rh_5(N_2)_m]^+$	0.77	0.37	0.15	0.13	0.00	0.07	$3.8 \cdot 10^{-8}$	$5.2 \cdot 10^{-8}$	$1.0 \cdot 10^{-7}$	$6.6 \cdot 10^{-10}$	0.0096												
$[Rh_6(N_2)_m]^+$	*	*	*	*	*	*	*	*	*	*		0.09	0.0096										
$[Rh_7(N_2)_m]^+$	*	*	*	*	*	*	*	*	*	*		$7.7 \cdot 10^{-8}$	0.33	0.022									
$[Rh_8(N_2)_m]^+$	*	*	*	*	*	*	*	*	*	*			0.096										
$[Rh_9(N_2)_m]^+$	*	*	*	*	*	*	*	*	*	0.15													
$[Rh_{10}(N_2)_m]^+$	*	*	*	*	*	*	*	*	*	*	*	*	*	*	*	0.097							
$[Rh_{11}(N_2)_m]^+$	*	*	*	*	*	*	*	*	*	*	*	*	*	*	*	0.010	0.19	1.33	$7.7 \cdot 10^{-4}$				
$[Rh_{12}(N_2)_m]^+$	*	*	*	*	*	*	*	*	*	*	*	*	*	*	*	0.046	0.15						
$[Rh_{13}(N_2)_m]^+$	*	*	*	*	*	*	*	*	*	*	*	*	*	*	*	3.2	9.2	2.5	0.21	1.82	0.0065		
$[Rh_{14}(N_2)_m]^+$	*	*	*	*	*	*	*	*	*	*	*	*	*	*	0.13	6.2	0.95	1.2	0.19	0.33	0.0097		
$[Rh_{15}(N_2)_m]^+$	*	*	*	*	*	*	*	*	*	*	*	*	*	*	*	*	$5.6 \cdot 10^{-4}$	0.0055	0.045				

4. Cryokinetics and Spin Quenching in the N₂ Adsorption onto Rhodium-Cluster Cations

d) Values including N₂ adsorption onto and desorption off each cluster (i,m)

Table S10 Equilibrium constants for the N₂ adsorption onto [Rh_i(N₂)_m]⁺ / desorption off [Rh_i(N₂)_{m+1}]⁺ at 26 K. The equilibrium constants are calculated by the ratio of the relative adsorption and desorption rate constants $K_{(i,m)} = \frac{k_{(i,m)}}{k_{-(m+1)}}$.

* indicates values > 2970. The grey shaded fields contain the $K_{(i,max)}$ values exceeding m_{max} . Fields beyond the respective adsorption limits are left empty.

Equilibrium constants $K_{(i,m)}$	$m = 0$	1	2	3	4	5	6	7	8	9	10	11	12	13	14	15	16	17	18	19	20		
[Rh ₅ (N ₂) _m] ⁺	0.16	1.0	4.6	5.5	1.5·10 ²	9.5	2.1·10 ⁷	3.6·10 ⁶	2.9·10 ⁷	5.6·10 ⁷	0.013												
[Rh ₆ (N ₂) _m] ⁺	*	*	*	*	*	*	*	*	*	*	*	0.34	0.013										
[Rh ₇ (N ₂) _m] ⁺	*	*	*	*	*	*	*	*	*	*	*	1.4·10 ⁷	1.1	5.7·10 ⁻³									
[Rh ₈ (N ₂) _m] ⁺	*	*	*	*	*	*	*	*	*	*	*		1.3·10 ⁻³										
[Rh ₉ (N ₂) _m] ⁺	*	*	*	*	*	*	*	*	*	8.3·10 ⁻⁴													
[Rh ₁₀ (N ₂) _m] ⁺	*	*	*	*	*	*	*	*	*	*	*	*	*	*		1.3·10 ⁻³							
[Rh ₁₁ (N ₂) _m] ⁺	*	*	*	*	*	*	*	*	*	*	*	*	*	*	*		57	0.63	0.11	0.17			
[Rh ₁₂ (N ₂) _m] ⁺	*	*	*	*	*	*	*	*	*	*	*	*	*	*	*		6.8	8.3·10 ⁻⁴					
[Rh ₁₃ (N ₂) _m] ⁺	*	*	*	*	*	*	*	*	*	*	*	*	*	*	*		0.46	0.21	2.8	2.8	0.23	0.020	
[Rh ₁₄ (N ₂) _m] ⁺	*	*	*	*	*	*	*	*	*	*	*	*	*	*	*		6.6	0.51	2.7	1.2	2.2	0.55	0.013
[Rh ₁₅ (N ₂) _m] ⁺	*	*	*	*	*	*	*	*	*	*	*	*	*	*	*			1.7·10 ⁻³	26.3	2.9·10 ⁻³			

Table S11 Gibbs free energies $\Delta_{ads}G^{26K}_{(i,m)}$ for the equilibria of N₂ adsorption onto [Rh_i(N₂)_m]⁺ / desorption off [Rh_i(N₂)_{m+1}]⁺ at 26 K. * indicates values < -1.7 kJ/mol. The grey shaded fields contain the minimum $\Delta_{ads}G^{26K}_{(i,max)}$ values exceeding m_{max} . Fields beyond the respective adsorption limits are left empty.

$\Delta_{ads}G^{26K}_{(i,m)}$ / kJ/mol	$m = 0$	1	2	3	4	5	6	7	8	9	10	11	12	13	14	15	16	17	18	19	20		
[Rh ₅ (N ₂) _m] ⁺	0.40	-0.0081	-0.33	-0.37	-1.1	-0.49	-3.6	-3.3	-3.2	-4.4	0.93												
[Rh ₆ (N ₂) _m] ⁺	*	*	*	*	*	*	*	*	*	*	*	0.23	0.93										
[Rh ₇ (N ₂) _m] ⁺	*	*	*	*	*	*	*	*	*	*	*	-3.6	-0.013	1.1									
[Rh ₈ (N ₂) _m] ⁺	*	*	*	*	*	*	*	*	*	*	*		1.4										
[Rh ₉ (N ₂) _m] ⁺	*	*	*	*	*	*	*	*	*	1.5													
[Rh ₁₀ (N ₂) _m] ⁺	*	*	*	*	*	*	*	*	*	*	*	*	*	*	*		1.4						
[Rh ₁₁ (N ₂) _m] ⁺	*	*	*	*	*	*	*	*	*	*	*	*	*	*	*		-0.87	0.10	0.47	0.39			
[Rh ₁₂ (N ₂) _m] ⁺	*	*	*	*	*	*	*	*	*	*	*	*	*	*	*		-0.42	1.5					
[Rh ₁₃ (N ₂) _m] ⁺	*	*	*	*	*	*	*	*	*	*	*	*	*	*	*		0.17	0.33	-0.22	-0.22	0.31	0.85	
[Rh ₁₄ (N ₂) _m] ⁺	*	*	*	*	*	*	*	*	*	*	*	*	*	*	*		-0.41	0.14	-0.2	-0.031	-0.17	0.13	0.93
[Rh ₁₅ (N ₂) _m] ⁺	*	*	*	*	*	*	*	*	*	*	*	*	*	*	*			-1.6	-0.71	1.3			

Table S12 Relative rate constants for adsorption and desorption, equilibrium constants and Gibbs free energies for each adsorption step of Rh_5^+ . The grey shaded fields contain the values exceeding m_{max} for the reaction of $(5, m_{max})$ to $(5, m_{max}+1)$. We had to consider back reactions for each adsorption step and yielded negligible rate constants for the back reaction $k_{-(5, m+1)} < 0.001 \text{ s}^{-1}$ for some steps. We calculated $K_{(5, m)}$ and $\Delta_{ads}G^{26K}_{(i, m)}$ for the actually obtained rate constants and repeated the calculation after setting the negligible rate constants to an upper limit of 0.001 (K_m^* and $\Delta_{ads}G^{26K}_{(i, m)^*}$).

m	$k_{(5, m)} / \text{s}^{-1}$	$k_{-(5, m+1)} / \text{s}^{-1}$	Fitted constants $k_{-(5, m+1)}$		Upper limit for $k_{-(5, m+1)} < 0.001$	
			$K_{(5, m)}$	$\Delta_{ads}G^{26K}_{(5, m)} / \text{kJ/mol}$	$K_{(5, m)}^*$	$\Delta_{ads}G^{26K}_{(5, m)}^* / \text{kJ/mol}$
0	0.97	6.1	0.16	0.40	0.16	0.40
1	3.0	2.9	1.0	-0.0081	1.0	-0.0081
2	5.3	1.2	4.6	-0.33	4.6	-0.33
3	5.5	1.0	5.5	-0.37	5.5	-0.37
4	4.8	0.032	150	-1.1	150	-1.1
5	5.1	0.53	9.5	-0.49	9.5	-0.49
6	6.2	$3.0 \cdot 10^{-7}$	$2.1 \cdot 10^7$	-3.64	$6.2 \cdot 10^3$	-1.9
7	1.5	$4.1 \cdot 10^{-7}$	$3.6 \cdot 10^6$	-3.26	$1.5 \cdot 10^3$	-1.6
8	2.3	$7.9 \cdot 10^{-7}$	$2.9 \cdot 10^6$	-3.21	$2.3 \cdot 10^3$	-1.7
9	2.9	$5.2 \cdot 10^{-7}$	$5.6 \cdot 10^8$	-4.35	$2.9 \cdot 10^3$	-1.7
10	$1.0 \cdot 10^{-3}$	0.075	0.013	0.93	0.013	0.93

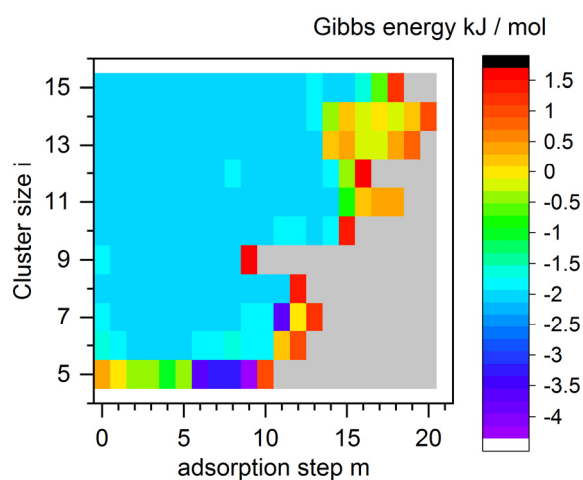


Fig. S14 Plot of Gibbs energies $\Delta_{\text{ads}}G^{26\text{K}}_{(i,m)}$ for the equilibria of N₂ adsorption onto $[\text{Rh}_i(\text{N}_2)_m]^+$ / desorption off $[\text{Rh}_i(\text{N}_2)_{m+1}]^+$. Note, that the $\Delta_{\text{ads}}G^{26\text{K}}_{(i,m)}$ values within the light blue plateau signify upper limits of otherwise unknown values. The last depicted step formally relates to the equilibrium of m_{max} with $m_{\text{max}}+1$. The positive Gibbs energies signify the last adsorption step towards m_{max} , with the only exception of Rh_5^+ . Its initial N₂ adsorption is hindered, and its subsequent steps become more spontaneous. $[\text{Rh}_i(\text{N}_2)_m]^+$, $i = 8, \dots, 10$ possess all negative $\Delta_{\text{ads}}G^{26\text{K}}_{(i,m)}$ values but m_{max} . If the fit yielded rate constants $k_{(i,m+1)} < 0.001 \text{ s}^{-1}$, we considered the actual obtained value, as given in Table S12 instead of an upper limit. The grey area signifies non-occurring processes. Note the striking similarity to the data of Fig. 6 in the main text.

III. Comparison of absolute rate constants with Average Dipole Orientation (ADO), Hard-Sphere ADO and Surface Charge Capture theories

We compared our absolute rate constants with the three models employed by Kummerloewe and Beyer and used the software presented in this work [67]. We first calculated the radius of N_2 according to Equation 19 therein. We used the viscosity of N_2 at 300 K.

Table S13 Data used to calculate the radius of N_2

Entity (unit)	value
$m(N_2) / 10^{-26} \text{ kg}$	4.65
$k_B / 10^{-23} \text{ J K}^{-1}$	1.38
T / K	300
$\eta / 10^{-6} \text{ Pa}\cdot\text{s}$ [77]	17.9
$r(N_2) / 10^{-10} \text{ m}$	1.85
$d(N_2) / 10^{-10} \text{ m}$	3.70

Table S14 Input data

Entity (unit)	value
$\alpha(N_2) / 10^{-40} \text{ C m}^2 \text{ V}^{-1}$ [78]	1.97
$\mu(N_2) / 10^{-30} \text{ C m}$	0
Dipole locking constant	0
$m(N_2) / \text{amu}$	28
$r(N_2) / 10^{-10} \text{ m}$	1.85
Maximum cluster size	15
Monomer mass / amu	103
ρ (cubic Rh) / g cm^{-3} [77]	12.4
Temperature / K used in ADO/HSA	26
Cluster charge state	1

Table S15 Output data: ADO, HSA and SCC Rates

i	HSA Rate	Capture	ADO Rate	Geometric	SCC Rate
1	6.6418	1.0000	6.6418	0.5534	8.4203
2	6.2769	1.0000	6.2769	0.6512	8.4286
3	6.1504	1.0000	6.1504	0.7345	8.5907
4	6.0862	1.0000	6.0862	0.8075	8.7672
5	6.0473	1.0000	6.0474	0.8733	8.9379
6	6.0212	1.0000	6.0213	0.9338	9.0992
7	6.0027	1.0000	6.0026	0.9901	9.2510
8	5.9886	0.9999	5.9886	1.0430	9.3941
9	5.9776	0.9997	5.9777	1.0931	9.5295
10	5.9689	0.9994	5.9689	1.1409	9.6582
11	5.9618	0.9989	5.9617	1.1867	9.7808
12	5.9557	0.9981	5.9557	1.2306	9.8980
13	5.9507	0.9970	5.9506	1.2731	10.0104
14	5.9464	0.9955	5.9463	1.3141	10.1185
15	5.9426	0.9935	5.9425	1.3539	10.2227

IV. Computed structures

Table S16 Number of next neighbors and average coordination number for Rh atoms in several isomers of Rh_i^+ $i = 5,6,7,9$ clusters. For each isomer, we give the number of Rh atoms that has a distinct number of next neighbors.

<i>i</i>	isomer	Next neighbors					average
		3	4	5	6	7	
5	sp	4	1	-	-	-	3.2
	tbp	2	3	-	-	-	3.6
6	oct	-	6	-	-	-	4
	boat	2	2	2	-	-	4
	csp	3	2	1	-	-	3.7
	tp	6	-	-	-	-	3
7	pbp	-	5	2	-	-	4.3
	coh	1	3	3	-	-	4.3
	ctp	2	5	-	-	-	3.7
9	ac-top	-	5	4	-	-	4.4
	dc-pbp	2	2	3	1	1	4.7
	dc-pbp2	2	1	4	2	-	4.7
	tc-oh	3	1	2	2	1	4.7
	tri	-	3	6	-	-	4.7
	trig-ap	-	6	-	3	-	4.7

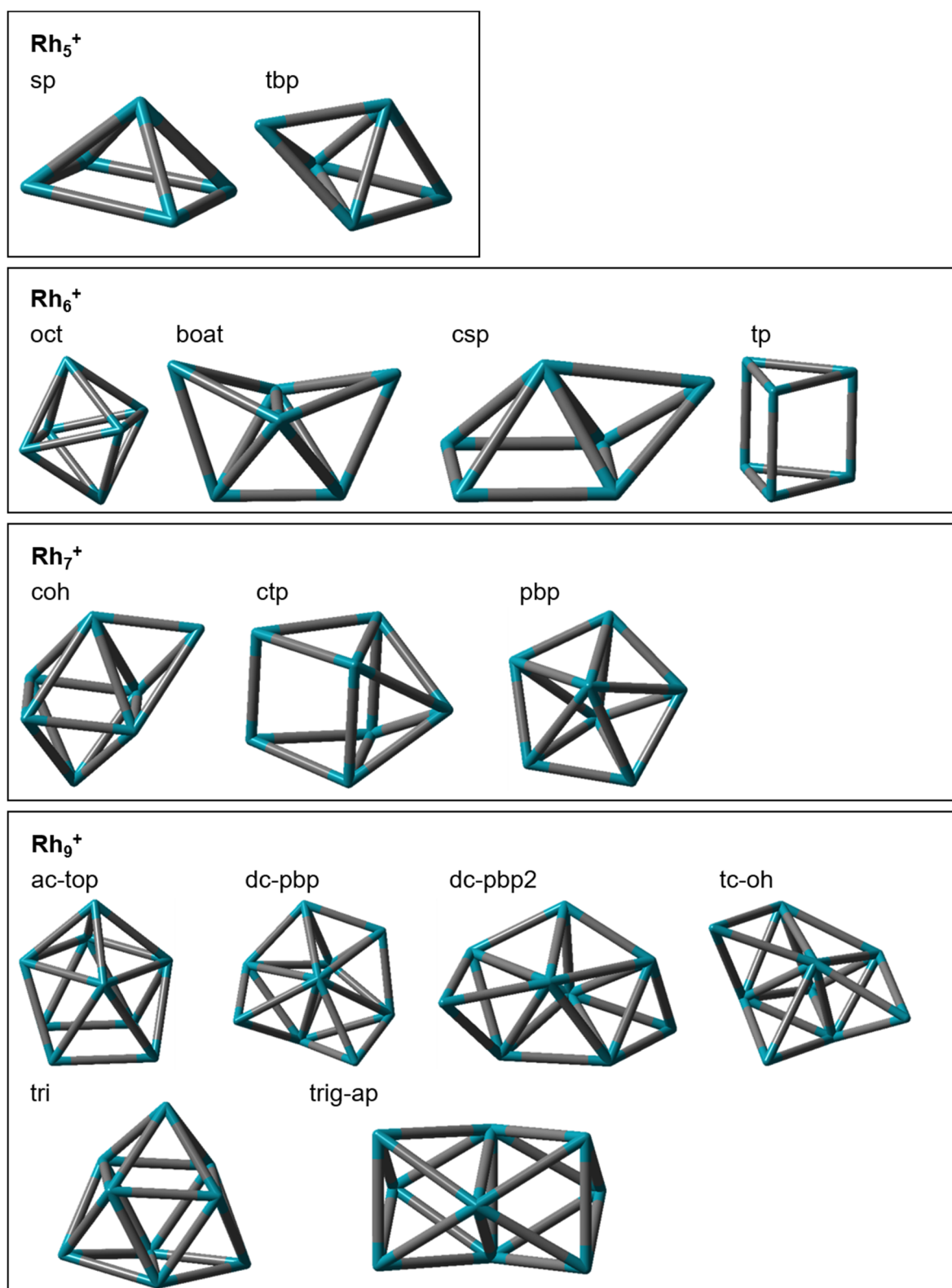


Fig. S15 Pictures of the isomers mentioned in Table S15.

Table S17 Energies of the isomers constituting the spin valley: (a) Absolute energies of the cluster adsorbate complexes, (b) absolute energies of the “(5, *m*) + (10-*m*) N₂” systems, and (c) the relative energies of the “(5, *m*) + (10-*m*) N₂” systems. The grey shaded fields denote the most stable isomer for each *m*.

(a) E_{abs} ([Rh₅(N₂)_{*m*})⁺ / a.u.

2S+1	m							
	0	1	2	3	4	7	10	
1	-552.324382	-661.806351	-771.279022	-880.750489	-990.223295	-1318.637443	-1647.009482	
3	-552.344011	-661.815712	-771.284350	-880.756571	-990.227460	-1318.625181	-1646.993510	
5	-552.353882	-661.823865	-771.292257	-880.764099	-990.230954	-1318.624827	-1646.981157	
7	-552.360020	-661.827949	-771.297434	-880.763994	-990.232293	-1318.608583	-1646.964998	
9	-552.374188	-661.840278	-771.305183	-880.765844	-990.229442	-1318.602058	-1646.956100	
11	-552.343408	-661.813327	-771.274470	-880.735389	-990.199585	-1318.568974		
13	-552.297148	-661.761362	-771.215497	-880.670122	-990.120918	-1318.466357		
15	-552.225494	-661.683707						

(b) E_{abs} ([Rh₅(N₂)_{*m*})⁺ + (10-*m*) N₂ / a.u.

2S+1	m							
	0	1	2	3	4	7	10	
1	-1646.738478	-1646.779038	-1646.810299	-1646.840356	-1646.871753	-1646.961672	-1647.009482	
3	-1646.758108	-1646.788399	-1646.815627	-1646.846439	-1646.875918	-1646.949410	-1646.993510	
5	-1646.767979	-1646.796552	-1646.823534	-1646.853966	-1646.879412	-1646.949056	-1646.981157	
7	-1646.774116	-1646.800636	-1646.828711	-1646.853862	-1646.880751	-1646.932812	-1646.964998	
9	-1646.788285	-1646.812965	-1646.836461	-1646.855711	-1646.877899	-1646.926287	-1646.956100	
11	-1646.757505	-1646.786014	-1646.805747	-1646.825257	-1646.848043	-1646.893203		
13	-1646.711245	-1646.734048	-1646.746775	-1646.759990	-1646.769376	-1646.790586		
15	-1646.639590	-1646.656394						

(c) E_{rel} ([Rh₅(N₂)_{*m*})⁺ + (10-*m*) N₂ / kJ/mol

2S+1	m							
	0	1	2	3	4	7	10	
1	130.77	24.28	-57.80	-136.71	-219.15	-455.23	-580.75	
3	79.23	-0.30	-71.79	-152.68	-230.08	-423.03	-538.82	
5	53.31	-21.71	-92.55	-172.45	-239.25	-422.10	-506.39	
7	37.20	-32.43	-106.14	-172.17	-242.77	-379.46	-463.96	
9	0.00	-64.80	-126.49	-177.03	-235.28	-362.32	-440.60	
11	80.81	5.96	-45.85	-97.07	-156.90	-275.46		
13	202.27	142.40	108.99	74.29	49.65	-6.04		
15	390.40	346.28						

Table S18 Vertical (nonet) and adiabatic adsorption energies as derived from our calculated (5,*m*) *m* = 0,...,4,7,10 isomers. The values represent the steps 0,...,3 as well as the values for triple adsorption (5,4)→(5,7) and (5,7)→(5,10). For the latter two larger steps, we also present interpolated values in an additional column (grey shaded).

step <i>m</i>	Adsorption energy / kJ/mol			
	vertical nonet	adiabatic		
0	-64.8			-64.8
1	-61.7			-61.7
2	-50.5			-50.5
3	-58.3			-65.7
4		-42.3		-70.8
5	-127.0	-42.3	-212.5	-70.8
6		-42.3		-70.8
7		-26.1		-41.8
8	-78.3	-26.1	-125.5	-41.8
9		-26.1		-41.8

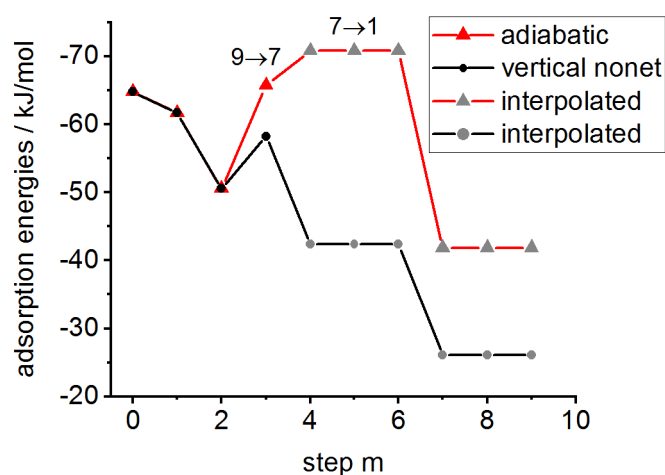


Fig. S16 Vertical (nonet) and adiabatic adsorption energies $\Delta_{\text{ads}}E$ of the adsorption steps *m* = 0 through *m*_{max} = 10. The grey points represent interpolated values between (5,4) – (5,7) and (5,7) – (5,10), respectively. The labelling indicates transition between spin states.

Table S19 Effects of spin contamination in the calculated most stable isomers. The grey shaded fields indicate S^2 values that are increased by at least 0.25.

(a) expected and obtained S^2 values for each spin state and number of N_2

2S+1	S^2	m						
		0	1	2	3	4	7	10
1	0	0.00	9.71	0.00	0.00	0.00	0.00	0.00
3	2	4.61	7.83	3.50	4.05	2.60	2.00	2.00
5	6	6.62	6.87	6.41	6.03	6.01	6.01	6.01
7	12	12.11	12.04	12.01	12.00	12.01	12.00	12.00
9	20	20.01	20.01	20.01	20.01	20.01	20.00	20.00
11	30	30.00	30.00	30.00	30.00	30.00	30.00	
13	42	42.00	42.00	42.00	42.00	42.00	42.00	
15	56	56.00	56.00					

(b) deviations from the expected S^2 values for each spin state and number of N_2

2S+1	S^2	m						
		0	1	2	3	4	7	10
1	0	0.00	9.71	0.00	0.00	0.00	0.00	0.00
3	2	2.61	5.83	1.50	2.05	0.60	0.00	0.00
5	6	0.62	0.87	0.41	0.03	0.01	0.01	0.01
7	12	0.11	0.04	0.01	0.00	0.01	0.00	0.00
9	20	0.01	0.01	0.01	0.01	0.01	0.00	0.00
11	30	0.00	0.00	0.00	0.00	0.00	0.00	
13	42	0.00	0.00	0.00	0.00	0.00	0.00	
15	56	0.00	0.00					

References

- [1] J. Mohrbach, S. Dillinger and G. Niedner-Schatteburg, Cryo Kinetics and Spectroscopy of Cationic Nickel Clusters: Rough and Smooth Surfaces, *The Journal of Physical Chemistry C*, **121**, 10907-10918 (2017).
- [2] D. Harding, M.S. Ford, T.R. Walsh and S.R. Mackenzie, Dramatic Size Effects and Evidence of Structural Isomers in the Reactions of Rhodium Clusters, Rh_n^{+/-}, with Nitrous Oxide, *Physical Chemistry Chemical Physics*, **9**, 2130-2136 (2007).
- [3] G. Kummerlöwe and M.K. Beyer, Rate Estimates for Collisions of Ionic Clusters with Neutral Reactant Molecules, *International Journal of Mass Spectrometry*, **244**, 84-90 (2005).
- [4] *CRC Handbook of Chemistry and Physics*, edited by D.R. Lide, 90 ed., (CRC Press, Boca Raton, 2010).
- [5] P.W. Atkins and J. De Paula, *Physical Chemistry*, 8th ed., (Oxford University Press, Oxford ; New York, 2006).

5. Cryospectroscopy and Spin Quenching in the N₂ Adsorption onto a Rh₆⁺ Cluster Cation

Matthias P. Klein, Annika Straßner, Maximilian E. Huber, Daniela V. Fries
and Gereon Niedner-Schatteburg¹

*Fachbereich Chemie and Forschungszentrum OPTIMAS,
Technische Universität Kaiserslautern, 67663 Kaiserslautern, Germany*

5.1 Preamble

An experimental team consisting of A. Straßner, M. Huber, D. V. Fries, and me conducted the experiments. I conducted and evaluated the quantum chemical calculations. Data evaluation was closely accompanied by discussions with G. Niedner-Schatteburg. I wrote the manuscript.

5.2 Abstract

The investigation of cryo IR-PD spectra of [Rh₆(N₂)_m]⁺ (6,*m*) *m* = 1,...,12 cluster adsorbate complexes up to saturation in combination with DFT modelling serves to address assumptions and observations that were made in the course of our earlier publications on Rh clusters: (a) possible cluster core reorganization with increasing amount of adsorbate molecules, (b) either a gradual or sharp spin quench, (c) decreasing adsorption energies from the first to the ultimate step, and (d) a possible N₂ monolayer at an *intermittent adsorption limit*. The spectra reveal a continuous redshift of the N-N stretching band upon adsorption of the first N₂ adsorbate. An analysis of the first five adsorption steps enables us to rationalize the continuous vibrational redshift throughout the first adsorption steps. We expand the known charge dilution model from a metal number centered approach to a correlation of charge density and size of adsorbate shell.

¹ Corresponding author: Prof. Dr. Gereon Niedner-Schatteburg, Erwin-Schrödinger-Straße 52, 67663 Kaiserslautern, gns@chemie.uni-kl.de

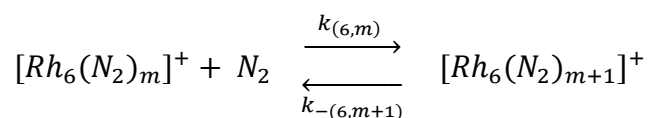
5.3 Introduction

The dinitrogen molecule has proven to be a suitable probe for catalytically active surface sites throughout the last 90 years.[1-4] Transition metal clusters serve as model systems for these heterogeneous catalysts and their interaction with N₂ adsorbate molecules has become a vivid field of research.[5-16]

Our group employed cryo conditions to investigate the adsorption kinetics of molecular nitrogen onto clusters and to characterize the resulting cluster adsorbate complexes by the infrared spectra of the adsorbate molecules.[17] For Ni clusters, we could identify rough and smooth cluster surfaces [18] and N₂/H₂ co-adsorption provided information on the mobility of different adsorbate molecules on the cluster surface of Ru₈⁺ [19]. Finally we were able to investigate a double N₂ dissociation on a Ta₄⁺ cluster and clearly identify IR signatures of an intermediate on the dissociation pathway.[20]

In our earlier publications on cationic Rh clusters, we investigated N₂ adsorption kinetics of [Rh_i(N₂)_m]⁺ [21] and the IR signatures of their selected adsorbates [22]. We found that the N₂ adsorption proceeds in a sequential chain of adsorption steps. In some cases, desorption lead to dynamic equilibrium.

The adsorption kinetics reveal an N₂ adsorption up to a *maximum adsorption limit* of $m_{max} = 12$ and a co-acting of adsorption/desorption for the last step $m = 11$. This results in an equilibrium between (6,11) and (6,12). We observed an additional *intermittent adsorption limit* at $m_x = 8$. For ease of reference we will utilize in the following the abbreviating nomenclature [Rh₆(N₂)_m]⁺ = (6,*m*). We clarified the used nomenclature in more detail before in [21] (Supplement Text S1 therein).



In the course of our analyses, we found evidence for the following effects:

- a) Isomerization of the adsorbate shell in particular at large N₂ loads and isomerization of the cluster core
- b) Spin quench of the cluster adsorbate complex in the course of N₂ adsorption (stepwise or gradual?)

- c) Decreasing adsorption energies for each sequential N₂ and thus low binding energies for large N₂ loads
- d) The intermittent adsorption limit (6,8) was interpreted as a formation of a monolayer. This step delays the formation of the subsequent adsorbates

Points c) and d) were assumptions made to support the interpretation of our adsorption kinetic studies.

In the present paper, we strive to verify these observations for the Rh₆⁺ cluster. Thus, we measured cryo IR-PD spectra of each [Rh₆(N₂)_m] (6,m) $m = 1, \dots, 12$ cluster adsorbate complex up to the *maximum adsorption limit* $m = 12$. We use extensive DFT modelling in order to find appropriate isomers for each number of N₂ molecules m and assign optimized structures to each cluster adsorbate complex. By this comparison of the IR signatures of DFT modelled candidate structures (with $M = 2S+1 = 2, \dots, 12$) with cryo IR-PD spectra we find a conclusive adsorption chain for the first five adsorption steps. We use natural population analysis to evaluate electronic properties like charge and spin distribution for these initial steps. NLMO analysis serves to describe the interacting Rh and N centered orbitals.

5.4 Experimental and theoretical methods

A customized 7 T Fourier Transform-Ion Cyclotron Resonance (FT-ICR)-mass spectrometer (Apex Ultra Bruker Daltonics) serves to produce and isolate the metal clusters, and to perform N₂ adsorption, mass analysis, and InfraRed Photodissociation (IR-PD) spectroscopy. The detailed construction has been described elsewhere [17]. In short, the second harmonic of a Nd:YAG laser is guided into the home-built laser vaporization cluster ion source chamber as described before [23, 24]. The laser beam is focused on a rotating Rh-target (99.8%, *Alfa Aesar*, 0.1 mm thick) and produces a plasma, consisting of atoms and ions. A Helium gas pulse (40 μs, 10-15 bar) is generated and induced into the vaporization chamber by using a homemade piezoelectric valve [25] operating in synchronization with the laser at 20 Hz. The gas pulse entrains the plasma through a 69 mm long channel (2 mm diameter) and allows for the atoms and ions to cool down and aggregate to clusters in the subsequent jet expansion into vacuum (3.5×10^{-7} mbar).

The ions in the skimmed cluster beam are guided through a 90° ion beam bender and a quadruple mass filter into a cryogenic hexapole ion trap which is cooled to 26 K by a closed cycle He cryostat. We introduce collision gas and reaction gas in the ion trap by a continuous gas inlet.

The attachment of nitrogen is achieved by maintaining a constant N₂ pressure of about 2.0 - 4.0 × 10⁻⁷ mbar N₂. We increase the pressure in the ion trap to roughly 3.0 × 10⁻⁶ mbar by adding helium gas to accomplish efficient trapping and cooling of the ions. The ions are stored for a variable time (0.05-1.5 s). Subsequently, the cluster ions are steered into the ICR-cell, using various electrostatic ion lenses. Our ICR-cell of the so-called infinity-type [26] is cooled down to 10 K by a closed cycle He cryostat to prevent heating of the clusters by black body radiation.

To study the selected [Rh₆(N₂)_m]⁺ cluster adsorbate complexes within the ICR cell, we first isolate the [Rh₆]⁺ metal cluster in the quadrupole mass filter and afterwards the cluster adsorbate complex of interest in the ICR cell and remove all other ions by correlated frequency sweeps and shots. We control the number *m* of adsorbed N₂ on the cluster by varying the storage time in the hexapole collision cell. For high storage time the amount of adsorbed N₂ can reach a *maximum adsorption limit* $m_{max} = 12$ [21, 22].

A tunable IR laser system coupled to the ICR cell and serves to excite and to dissociate the stored ions. This laser is a KTP/KTA optical parametric oscillator/amplifier (OPO/A, *LaserVision*) system pumped by a pulsed 10 Hz injection seeded Nd:YAG laser (PL8000, *Continuum*) followed by an AgGaSe₂ crystal to generate the difference frequency (DF) between signal and idler waves [27]. This method can generate IR radiation in the range of 1000 – 2400 cm⁻¹. Each trapped and isolated package of ions is irradiated by 7 - 10 laser pulses to yield a sufficient amount of fragment ions. A typical pulse energy spectrum is given in Fig. S1. The IR spectra were recorded as ion chromatograms while continuously scanning the IR wavelength. We evaluated the IR-PD signal as $\sum_n F_n / (\sum_n F_n + \sum_x P_x)$, where *F_n* and *P_x* indicate fragment and the parent ion signals, respectively. Plotting the fragmentation efficiency as a function of laser frequency yields an IR-PD spectrum. We employed the IR-PD spectroscopy in the 2140 – 2300 cm⁻¹ range on the [Rh₆(N₂)_m]⁺ *m* = 1, ..., 12 cluster adsorbate complexes. In this range, we expected the end-on N₂ stretching frequencies of the species. We expanded this range to 1160 – 2400 cm⁻¹ in selected cases to check for non-end-on N₂ ligands. For all complexes, the loss of the N₂ was the only observed fragmentation channel.

Geometry optimizations and vibrational analysis were performed by the Gaussian 09 package [28] at PBE0/ECP(Rh); cc-pVTZ(N) level of theory [29, 30] as proven suitable for cobalt, nickel and rhodium clusters [17, 18, 21, 22, 31]. We utilize Stuttgart RSC 1997 ECP(Rh) basis sets of double zeta quality.[32] We had to tolerate relaxed SCF convergence criteria of 10^{-6} (as compared to 10^{-8} in 'standard' DFT calculations) to achieve SCF convergence. Natural Population Analysis was performed using NBO 5.9 as implemented in Gaussian 09 [33].

5.5 Results and discussion

5.5.1 IR-PD spectroscopy

We have recorded cryo IR-PD spectra of $[\text{Rh}_6(\text{N}_2)_m]^+$ ($6,m$) $m = 1, \dots, 12$ cluster adsorbate complexes up to saturation (Fig. 1). We have reported the IR-PD spectra of (6,1), (6,8), and (6,11) in an earlier publication.[22] For single N_2 adsorption $m = 1$ we found a single band at 2266 cm^{-1} which is red shifted by 64 cm^{-1} with respect to the free N_2 stretching vibration at 2330 cm^{-1} [34]. An interpretation of this general redshift in terms of the Blyholder model [35] as N-N bond softening by σ -donor and π -acceptor synergism has proven helpful in our previous studies.

Upon further N_2 adsorption up to $m = 5$, we observe a redshift and broadening of a single band as indicated by the gray shaded area (Fig. 1). The broadening corresponds with the existence of an increasing number of oscillators on different but similar adsorption sites in these cluster adsorbate complexes.

The sequential increasing redshift is tentatively explained by polarization effects: I reminds of the charge dilution model that considers an increase of the number of metal atoms with constant charge and size of adsorption shell, e.g. one single adsorbate molecule [36]: The constant charge distributes over more metal atoms and the net charge at each metal atom decreases. The thus increased electron density on adsorbing metal atoms is available for π -backbonding and facilitates softening of the N-N bond. We utilized this model before to interpret sequential redshifts of a single N_2 adsorbed onto Co, Ni, Fe and Rh cluster adsorbate complexes [17, 18, 22, 31, 37]. This explanation may hold for the first few N_2 ligands. The spectra of less electronegative tantalum clusters do not reveal this effect.[20, 38]

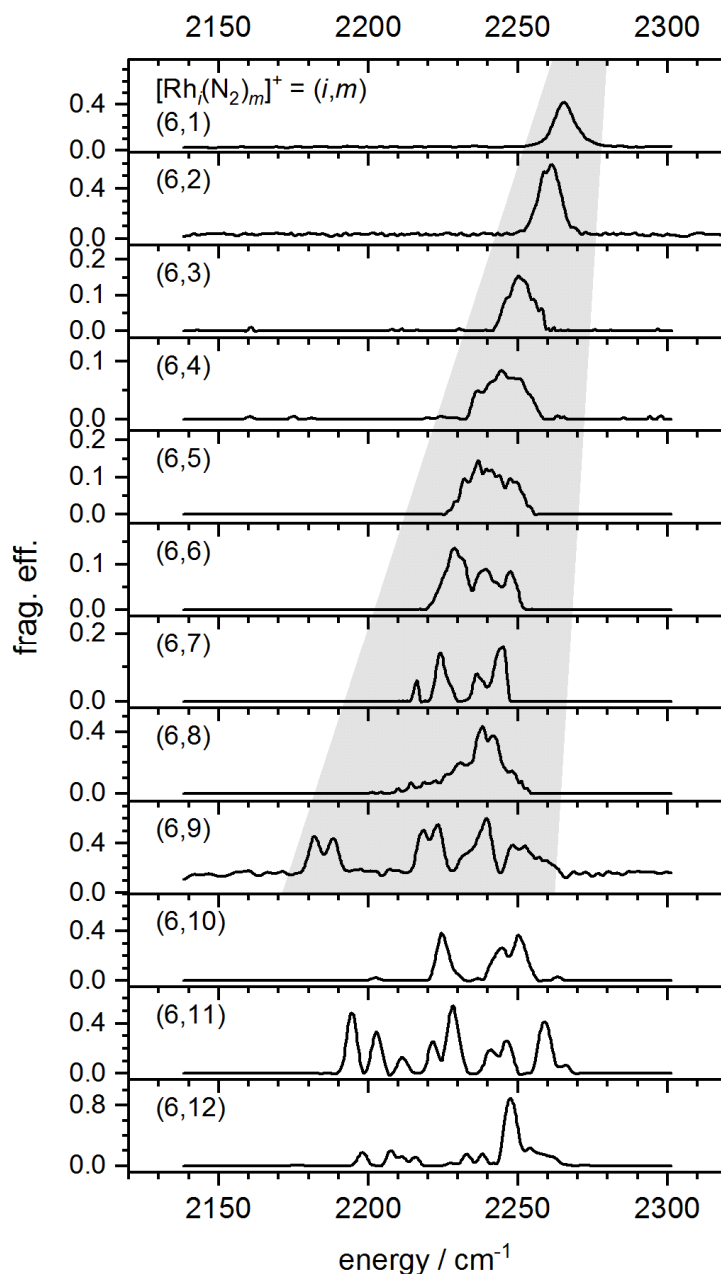


Fig. 1 IR-PD spectra of sequential N₂ adsorption steps onto Rh₆⁺ cluster cations [Rh₆(N₂)_m]⁺, $m = 1-12$ as recorded after 26 K He buffer gas cooling. The grey shaded area serves to guide the eye indicating a redshift and broadening of the absorption range with the number m of adsorbed N₂.

This model applies to systems with constant charge and size of adsorbate shell and varying number of metal atoms. In the present case, charge and number of metal atoms are constant and the size of the adsorbate shells varies. We apply a different kind of charge dilution model/model including charge dilution. The increase of ligands on a fixed size metal cluster core may have a similar effect as for the increase of metal atoms: The cluster adsorbate complex increases by stepwise adsorption of N₂ molecules that each donate electron density

into the fixed size Rh_6^+ metal cluster core and decrease the net charge on each metal atom. The enhanced electron density on the metal cluster core facilitates back donation into the N_2 π -orbitals effecting an additional softening of the N-N bond. The positive charge is in part transferred to the adsorbate shell and therewith diluted. The positive charge distributes towards the adsorbate shell.

This explanation may hold for the first few N_2 ligands. At a certain point, the cluster core cannot serve as an electron acceptor anymore and the continuous redshift ceases. This may be the case above $m = 7$. A validation of this hypothesis of charge dilution by distribution towards the adsorbate shell is part of our theoretical analyses.

The (6,2) band at 2261 cm^{-1} is by 5 cm^{-1} more red shifted than the single (6,1) band but it is similarly broad ($\sim 9\text{ cm}^{-1}$). This band comprises a shoulder at 2259 cm^{-1} on the red slope indicating a second N_2 adsorbate molecule with similar electronic properties or adsorption sites.

The (6,3) band at 2250 cm^{-1} is further red shifted by 9 cm^{-1} and its width has increased (11 cm^{-1} fwhm). The band seems to consist of a central feature accompanied by shoulders on the red and on the blue slope, each resembling the three vibrational modes of the three adsorbed N_2 molecules.

The IR-PD spectra of (6,4) and (6,5) comprise of one single broad absorption pattern (20 cm^{-1} fwhm) around 2245 cm^{-1} and 2240 cm^{-1} , respectively.

The (6,6) IR-PD spectrum consists of a broad band pattern (26 cm^{-1} fwhm) where three peaks at 2229 , 2239 , and 2248 cm^{-1} stand out.

The four (6,7) bands at 2216 , 2224 , 2236 , and 2245 cm^{-1} are further red shifted. We could assume a geminal coupling of N_2 oscillators that are adsorbed onto the same Rh atom for $m > 6$. Such a coupling does not clearly manifest in the spectrum as additional broadening or double bands.

The sequential redshift ceases with (6,8), where two peaks at 2238 and 2242 cm^{-1} stick out of a broad, barely separate absorption pattern between 2207 and 2255 cm^{-1} . Such a broad pattern with only few defined bands may indicate a flexible adsorbate shell with facile transitions between adsorbate shell isomers.

The (6,9) spectrum exhibits a significant broadening over the range 2180 – 2270 cm⁻¹ as compared to the smaller cluster adsorbate complexes. A double band at 2182/2188 cm⁻¹ appears red shifted by 30 cm⁻¹ with respect to a second double band at 2218/2223 cm⁻¹. An intense band at 2240 cm⁻¹ has a pronounced shoulder on its red slope. An additional broad band around 2255 cm⁻¹ comprises a double peak and a broad adsorption to its blue slope. The multitude of bands and the occurrence of two narrow band pairs arise from the multitude of N₂ oscillators and their couplings, in particular if adsorbed to the same adsorption site.

The three most intense bands of (6,10) (at 2224, 2245 and 2250 cm⁻¹) spread over a smaller range between 2219 and 2257 cm⁻¹, similar to the (6,8) spectrum. Two very weak features appear at 2202 and 2263 cm⁻¹.

The bands of (6,11) and (6,12) are spread widely between 2190 and 2270 cm⁻¹. (6,11) reveals nine clearly separate and narrow (4 – 5 cm⁻¹ fwhm) bands which would imply equivalent N₂ oscillators. The (6,12) spectrum comprises one strong band at 2247 cm⁻¹ with a broad absorption pattern to its blue and up to seven weak peaks between 2190 and 2240 cm⁻¹. The single strong band may arise from a multitude of similar N₂ oscillators, the weak bands from coexisting isomers differing in the relative orientation of the N₂ adsorbate molecules. We would also expect a high number of coupling N₂ modes arising from multiple adsorptions onto each Rh atom.

5.5.2 DFT calculations

5.5.2.1 Stabilities and adsorption energies for each $m = 0, \dots, 12$

Our experimental IR-PD spectra provide the basis for an assignment of structures obtained by extensive DFT modelling. We chose as a starting point an octahedral Rh₆⁺ cluster structure that has proven most stable in our previous studies.[22] In the course of our theoretical analyses, we considered a multitude of adsorption shell isomers for each number of N₂ adsorbates m . In a first step, we evaluated the relative stabilities of the obtained relaxed minimum structures in dependence on their multiplicities. Doing this, we obtain *spin valley curves* for each amount of adsorbed N₂ (Fig. 2). This procedure proved useful to investigate spin relaxations in the case of Rh₅⁺ clusters.[21] For low multiplicities, we observe significant spin contamination as indicated by enhanced S² values (red parentheses in Fig. 2, S² at least 0.25 higher than expected, values given in Table S2). The extent of contamination ceases with

increasing adsorbate shell. In the following we denote the spin isomers of each cluster adsorbate complex as $^{2S+1}(6,m)$

As reported before, the (6,0) curve reveals a minimum 10tet. We chose the energy of this most stable $^{10}(6,0)$ isomer as reference for all other calculated minimum energies by calculating the energies of each $[\text{Rh}_6(\text{N}_2)_m]^+ + (12-m) \text{N}_2^{(\text{free})}$ system. The resulting offset between the spin valley curves with increasing N_2 amount m is a measure for the adsorption energy (Fig. 4).

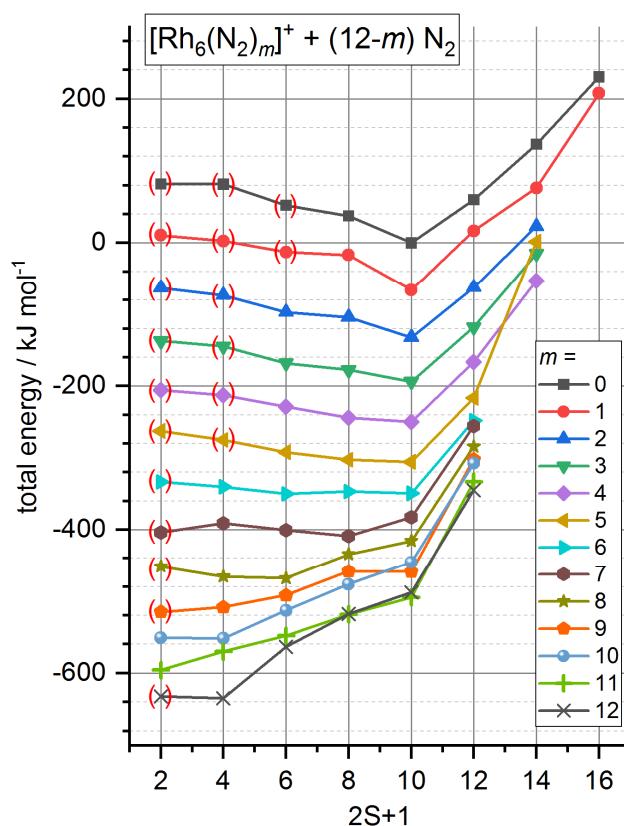


Fig. 2 Total energies of $[\text{Rh}_6(\text{N}_2)_m]^+$ cluster adsorbate complexes as a function of the spin multiplicity $2S+1$, normalized to the computed (6,0) spin isomer (octahedron, $^{10}(6,0)$, dectet). The energies correspond to the systems $[\text{Rh}_6(\text{N}_2)_m]^+ + (12-m) \text{N}_2^{(\text{free})}$. Each data point represents the lowest energy isomer of $[\text{Rh}_6(\text{N}_2)_m]^+$ at the respective spin state. The lines connect the data points for each number of adsorbed N_2 . The offsets between the curves represent the respective adsorption energy for each adsorption step. The red parentheses indicate a spin contamination for the respective cluster isomer: The obtained S^2 value is at least 0.25 higher than expected for the defined/given spin state. For detailed number values of each point refer to Table S1.

The shape of the naked clusters (6,0) *spin valley* persists upon adsorption of a first N₂ molecule. Dectet multiplicities are most stable. Higher multiplicities are most expensive, formation of a dodectet requires 60 kJ/mol. Lower multiplicities are stepwise less stable by up to 39 kJ/mol per spin flip. Thus, spin pairing becomes more feasible than costly occupation of additional orbitals by additional single spins. In any case, the high spin wing stays steeper than the low spin wing. Here and in the following, N₂ adsorption affects mainly the low spin wing of the *spin valleys*. With the second N₂ adsorbate molecule, the spin valley flattens: (6,2) octet and sextet states are only 28 and 35 kJ/mol above the dectet.

The low spin states stabilize further with the following adsorption step: ⁸(6,3) is only 16 kJ/mol less stable than ¹⁰(6,3). For (6,4) and (6,5) octet and dectet are nearly degenerate (<6 kJ/mol). The bottom of the valley has widened from (6,3) to (6,4). Cluster adsorbate complex ⁶(6,4) is 21 kJ/mol less stable than ¹⁰(6,4), ⁶(6,5) is 14 kJ/mol less stable than ¹⁰(6,5). At (6,6), the range of degenerate states has extended from dectet ¹⁰(6,6) to quartet ⁴(6,6), where the quartet state is only 10 kJ/mol above the most stable sextet. In the case of (6,7), the octet is most stable with the sextet 8 kJ/mol above. With further adsorption of N₂ up to $m_{max} = 12$, the low spin states stabilize continuously: For $m = 8, 10$, and 12 , there are two spin states each that are almost degenerate, denoted by the superscript: ^{4,6}(6,8), ^{2,4}(6,10), and ^{2,4}(6,12). For (6,9) and (6,11), doublet states are most stable.

Our investigations revealed that a spin quench proceeds from the most stable ¹⁰(6,0) towards ^{2,4}(6,12) in the course of the adsorption process. This spin quench is mainly continuous without significant steps, e.g. at the intermittent maximum $m_x = 8$.

The energetic differences between the most stable isomers in Fig. 2 measure the adsorption energies for each adsorption step. Note, that in an adsorption step m one N₂ molecule is adsorbed onto a cluster adsorbate complex (6, m) and the complex (6, $m+1$) forms. We consider the energies of an adsorption process with relaxation towards most stable spin isomers (adiabatic) (Fig. 3). The adsorption energies of the first two steps $m = 0$ and $m = 1$ are both -66 kJ/mol and decrease continuously towards -45 kJ/mol at step $m = 5$, where the (6,6) cluster adsorbate complex forms. The continuous decrease is reduced at step $m = 4$, where the spin valley starts to extend towards low spin states. The adsorption of the 7th N₂ and the 8th N₂ molecule is with -59 kJ/mol more favorable. We identified (6,8) as intermittent adsorption limit in our kinetic studies, which does not show clearly in the calculated

adsorption energies [21]. The next two adsorption steps $m = 8$ and 9 are more unfavorable again (-47 and -36 kJ/mol). In the penultimate step $m = 10$, the adsorption energy rises again to -44 kJ/mol and decreases back to -39 kJ/mol in the last step $m = 12$. The obtained adsorption energies for the first steps agree well with the reported -56 kJ/mol for stepped Rhodium surfaces.[39, 40] We observe a tendency of the adsorption energies to decrease with proceeding adsorption but we do not find a correlation between the course of the adsorption energies and the rate constants of adsorption, except for a decrease of both for step $m = 8$ after reaching the intermittent adsorption limit.

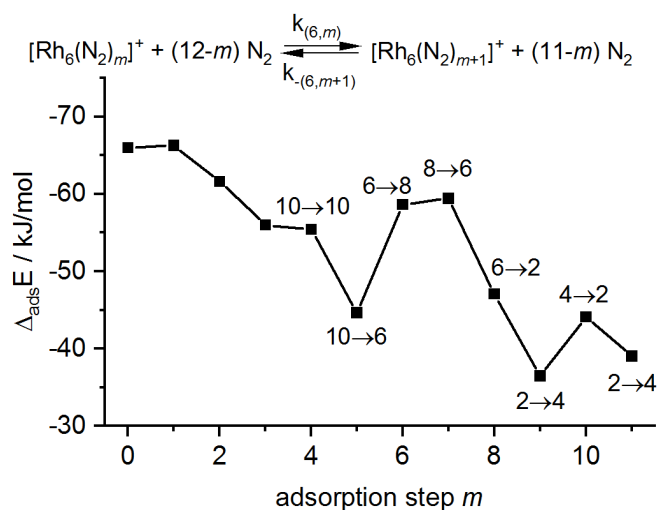


Fig. 3 Adiabatic adsorption energies $\Delta_{\text{ads}}E$ of the adsorption steps $m = 0, \dots, 11$. The numbers indicate spin transitions that accompany the respective adsorption steps.

A two-dimensional plot serves to emphasize the relative stabilities of the spin states and the effects of spin relaxation in the course of consecutive N_2 adsorption (Fig. 4). The relative energies for each amount of adsorbed N_2 are plotted in dependence on the spin states. Each column represents an adsorption step. The minimum of each spin valley curve is set to zero, thus each column contains a zero value (dark blue). The energies in each column are scaled to their minimum. The rows represent the spin states.

The dectet is stable from $m = 0$ to $m = 6$. At $m = 4$, the range of stable spin states widens towards octet state. At $m = 6$ the range of stable states extends to the doublet and starting from $m = 7$, dectet, octet, and sextet lose stability. From $m = 9$ through $m_{\text{max}} = 12$, doublet and quartet states are by far more stable than the higher spin states.

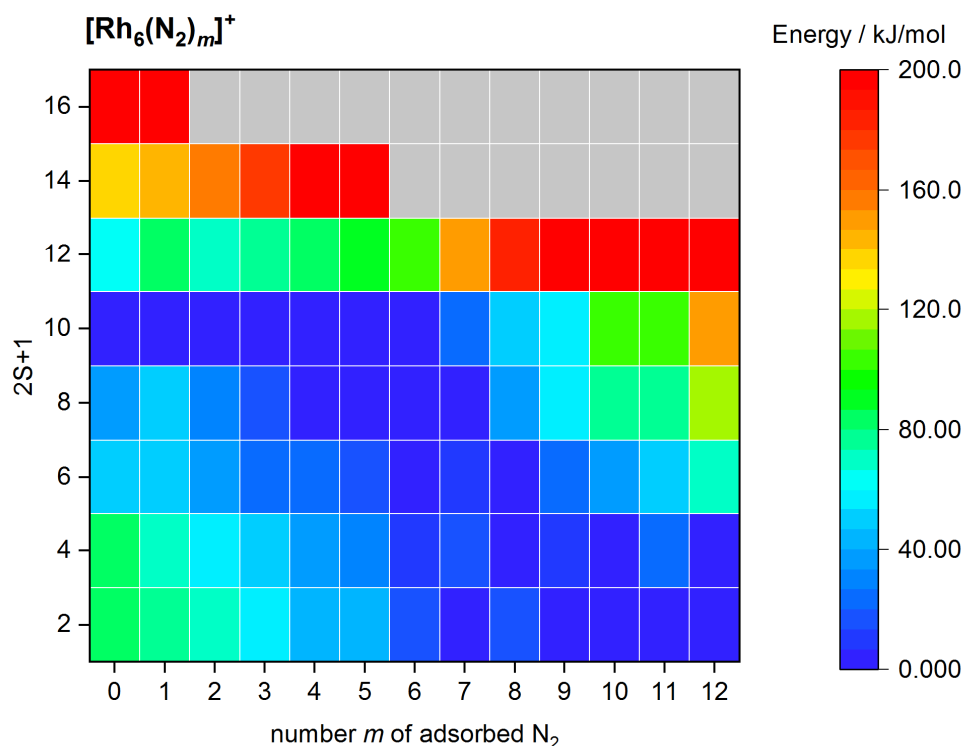


Fig. 4 Relative energies for each adsorption step $(6,m)$ dependent on the spin multiplicities. The energies of each column are normalized to their minimum. This minimum is set to zero for each adsorption step $(6,m)$. Blue color denotes low energies, red color high energies. The darkest blue denotes a zero value.

5.5.2.2 Isomer assignment to the spectra

We investigated the cluster adsorbate complexes $(6,m)$ $m = 1, \dots, 5$ in further detail in order to assign isomers for these steps. Note that for the larger adsorbate complexes, many isomers reveal a similar stability and proper annealing towards the correct local minimum is crucial for a definite assignment. In the view of various relative orientations of the N_2 oscillators, the effort of optimization applied in this paper reaches its limits. We encourage able colleagues to address this issue based on the provided experimental IR-PD spectra and the electronic properties reported here. For $m = 2, \dots, 5$, we yield reasonable assignments (Fig.s 5 and 6, and Fig.s S3, ..., S28):

(6,1) For the $(6,1)$ cluster adsorbate complex, the vibrational band of the single N_2 oscillator does not help assign isomers. Thus, we assign the most stable isomer $^{10}(6,2)_a$.

(6,2) The narrow splitting (6 cm^{-1}) of the second most stable $(6,2)$ isomer $^{10}(6,2)_d$ resembles the single band with a shoulder better than the most stable isomer $^{10}(6,2)_c$ (9 cm^{-1}). The N_2

molecules in both isomers are adsorbed to neighbored Rh atoms and differ in their relative angle. The energy difference is only 2 kJ/mol. We assign isomer $^{10}(6,2)_c$.

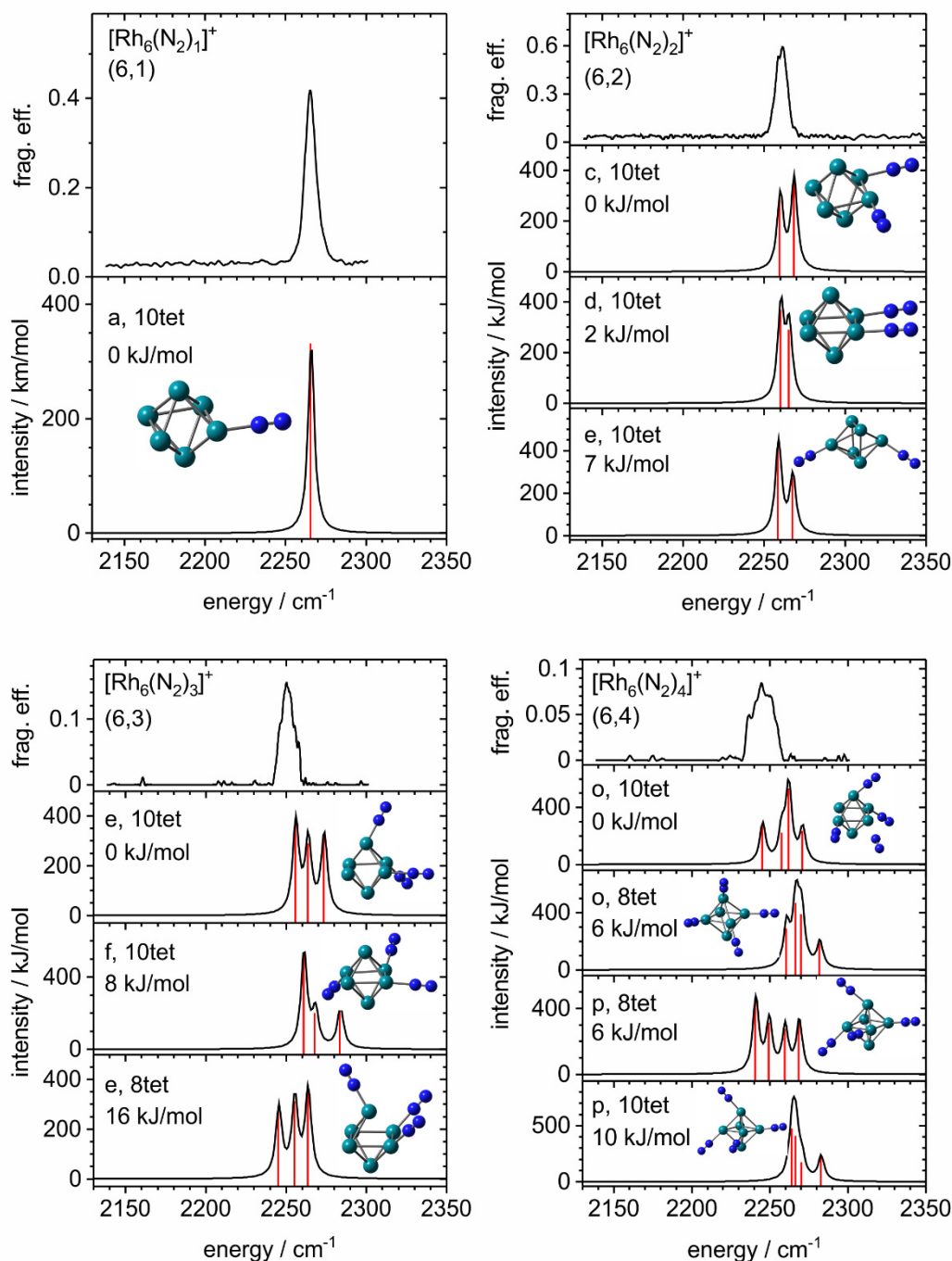


Fig. 5 Experimental IR-PD spectra and calculated linear absorption spectra of most stable isomers for $[\text{Rh}_6(\text{N}_2)_m]^+$, $m = 1, \dots, 4$ cluster adsorbate complex. The calculated spectra are scaled by 0.9519. The corresponding isomers are shown as insets. The structures of the assigned isomers are shown in Fig. 7.

(6,3) The three bands of the most stable $^{10}(6,3)_e$ resemble the experimental spectrum best. The octet $^8(6,3)_e$ has relaxed into a minimum structure with different relative angles

between the N₂ molecules and is 16 kJ/mol less stable. In both cases, the N₂ molecules are located on three neighbored Rh atoms that form a triangle at the cluster surface. The intensity of the three bands of ¹⁰(6,3)_f (8 kJ/mol) differs more and would yield a less symmetric absorption pattern which fits the experimental spectrum worse. However, we consider both ¹⁰(6,3)_e and ¹⁰(6,3)_f in the further discussion.

(6,4) Four isomers ^{8,10}(6,4)_o and ^{8,10}(6,4)_p have similar stabilities within 10 kJ/mol. The relative position of N₂ adsorption sites are the same. The isomers differ in spin state and the relative orientation of the N₂ molecules. These relative orientations lead to clearly different absorption patterns. This exemplifies the important role of annealing towards the right local minimum.

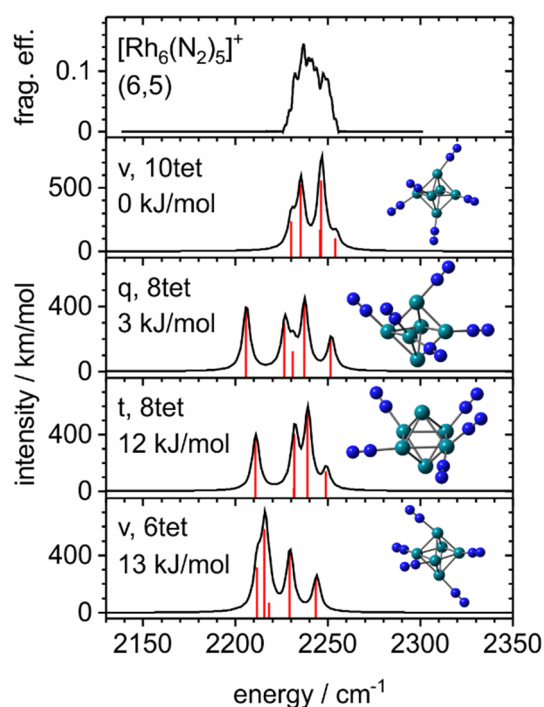


Fig. 6 Experimental IR-PD spectrum and calculated linear absorption spectra of most stable isomers for the [Rh₆(N₂)₅]⁺ cluster adsorbate complex. The calculated spectra are scaled by 0.9385. The corresponding isomers are shown as insets. The structure of the assigned isomer ¹⁰(6,5)_v is shown in Fig. 7.

(6,5) The ⁶(6,5)_v is 13 kJ/mol less stable than the most stable ¹⁰(6,5)_v isomer. Both comprise five single N₂ occupied Rh atoms. Again, the spectra differ due to different orientations of the N₂ adsorbates. The ⁸(6,5)_q and ⁸(6,5)_t isomers comprise both one double occupied Rh atom, but the relative position of the adsorption sites differs. The most stable isomer ¹⁰(6,5)_v provides the best spectral fit.

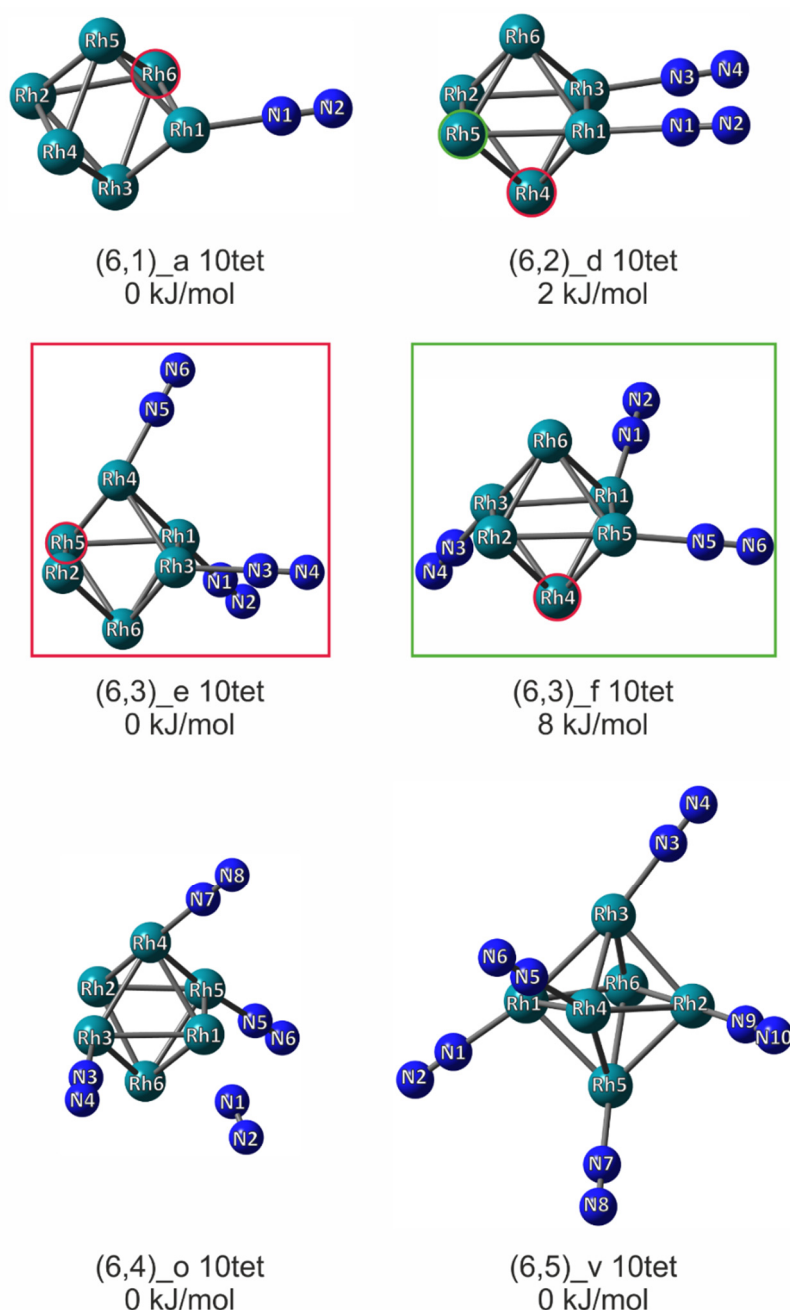


Fig. 7 Assigned isomers for the $[\text{Rh}_6(\text{N}_2)_m]^+$ $m = 1, \dots, 5$ cluster adsorbate complexes. Note, that for (6,3) two isomers are presented and marked with a red and green box. The isomers are formed by addition of one N_2 molecule to the accordingly red and green circled Rh atom in (6,2). An addition of one N_2 molecule onto the red circled Rh atoms of each of the (6,3) isomers forms the same (6,4) isomer $^{10}(6,4)_o$.

The structural assignments allow reconstructing the course of adsorption for the first five steps starting from a Rh_6^+ octahedron (Fig. 7). The first N_2 molecule is adsorbed onto the Rh1 atom. The second N_2 is adsorbed in parallel to the first one. Note, that low barriers between different relative orientations of the N_2 adsorbates allow for isomerization. Annealing into the right potential well is difficult to accomplish. The adsorption of an additional N_2 molecule may

change the orientation of the already adsorbed ones. Therefore, we use the relative position of the adsorption sites for description of the isomers. Starting from ¹⁰(6,2)_d, there are two possible adsorption sites. The third N₂ may adsorb onto Rh5 (green) or Rh4 (red). The respective products ¹⁰(6,3)_e and ¹⁰(6,3)_f are marked with a red and green box. Starting from these two (6,3) isomers, the assigned ¹⁰(6,4)_o isomer can form by N₂ adsorption onto the red marked Rhodium atoms Rh5 (¹⁰(6,3)_e) or Rh4 (¹⁰(6,3)_f). The assigned ¹⁰(6,5)_v isomer may form by N₂ adsorption onto either of the two remaining free Rh sites Rh2 and Rh6.

Thus, our theoretical calculations allowed for a reasonable chain of the first five cluster adsorbate complexes based on an octahedral cluster core that corresponds in most cases to the minima of the spin valley curves.

5.5.2.3 Electronic properties of the assigned isomers

We used the assigned isomers to investigate trends in charge and spin distribution of the above assigned isomers by the help of natural population analysis, in addition to the observed spin quench (Fig. 8, Table S4). All isomers taken into account in this section have dectet multiplicity and thus an excess of nine alpha spin electrons as compared to the beta spin electrons.

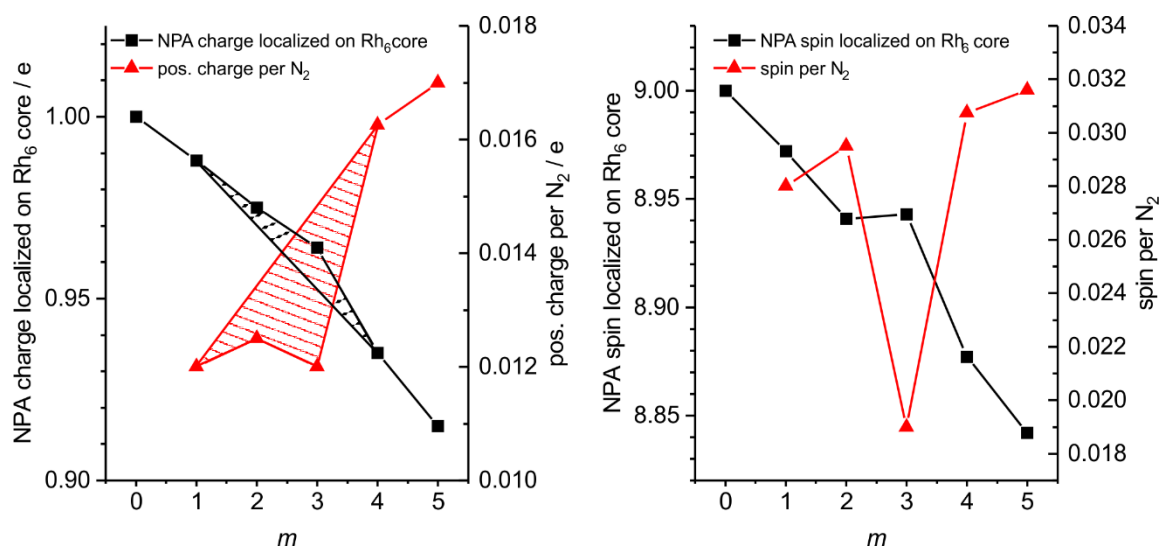


Fig. 8 (a) Positive charge localized on the Rh₆ cluster core dependent on adsorbed N₂ molecules m (black) and the corresponding charge per adsorbed N₂ molecule (black) for the assigned isomers. The black and red shaded areas correspond to non-proportional charge shifts towards N₂ adsorbate shell with respect to m . (b) Spin localized on the Rh₆ cluster core dependent on adsorbed N₂ molecules m (black) and the corresponding spin per adsorbed N₂ molecule (black) for the assigned isomers.

The charge located on the cluster core continuously decreases with increasing N₂ coverage and is transferred to the N₂ adsorbate molecules (Fig. 8a). The electron density on the cluster core increases. The charge on the cluster core is reduced to 0.988 e by adsorption of the first N₂ molecule and then continuously decreases towards 0.15 e at (6,*m*). This charge shift from the cluster core towards the adsorbate shell would support the charge dilution hypothesis we used to explain the observed redshift of the IR absorption. This shift is not proportional as indicated by the shaded area.

A normalization of the charge shift to the number *m* of adsorbed N₂ molecules reveals a deviation from an increasing trend for *m* = 3. The averaged charge per N₂ increases from 0.012 e (*m* = 1) to 0.0125 e (*m* = 2) and then decreases to 0.012 e (*m* = 3). The adsorption of the 4th N₂ molecule effects a significant increase in charge shift to 0.01625 e per N₂. The charge per N₂ molecule reaches a maximum of 0.017 e at (6,5).

The spin on the cluster core decreases corresponding to the charge from 9 (*m* = 0) to 8.842 (*m* = 5) (Fig. 8b). The (6,3) cluster adsorbate complex stands out of the approximately linear trend (dashed dotted line). The spin on Rh₆ increases slightly from 8.941 for (6,2) to 8.943 for (6,3). After a steep decrease to 8.877 for (6,4), the linear trend continues towards 8.842 for (6,5). As for the development of the charge distribution, we observe a discontinuity around *m* = 3.

This discontinuity becomes more apparent in the course of the average spin per N₂ molecule: Corresponding to the roughly linear decrease of spin on the cluster core, the spin per N₂ molecule increases hyperbolically. A single adsorbed N₂ molecule receives a spin density of 0.028, that increases towards the (6,5) cluster adsorbate complex to 0.0316 per N₂. The single deviation from the trend occurs as a break down at (6,3): the spin located at each N₂ molecule drops to 0.019. The adsorption step from (6,3) to (6,4) yields the steepest increase of spin per N₂ (from 0.019 to 0.03075), similar as observed for the charge per N₂ before.

In the course of sequential adsorption, charge and spin continuously dissipate from the cluster core over the whole cluster adsorbate complex. A deviation from the trend is (6,3) where the decrease of charge and spin on the cluster core is non-proportional.

The general trend supports our charge dilution approach to the explanation of the spectral redshifts in the course of the first adsorption steps. It warrants checking which orbitals are involved in the charge and spin shifts.

5.5.2.4 Orbital analysis of (6,1)

To investigate the orbitals involved in the interaction between cluster core and the adsorbed N₂, we performed NBO calculations. We chose the most simple ¹⁰(6,1)_a cluster adsorbate complex. The NBOs do not indicate a binding interaction between the cluster core and N₂ and treats them as separate units. However, single electron NLMOs provide insight into the interaction between N₂ and the cluster core. They include the interaction of the NBOs localized on N₂ with hybrid orbitals localized on the Rh atoms and vice versa. The NPA analysis reveals an excess of nine alpha spin electrons compared to beta spin electrons (Table S4, Fig. S29). Rh-Rh bonding NLMOs are only among the beta spin orbitals. For further analysis, we consider NLMOs with more than 1% contribution of the N atoms and focus on the NLMOs that reveal an interaction between the N₂ unit and the cluster core (Fig. 9). The other orbitals with N₂ contribution are given in the Supplement (Fig. S32). The NBO output is presented in (Fig.s S30,...,S36).

The discussed orbitals are depicted in Fig.s 9 and 10. The chosen nomenclature consists of four lines that resemble (1) the running number of the orbital and its spin (2), the principal character/location of the NLMO, (3) the minor contributing component interacting with the NLMO, and (d) the nature of the interaction between the two components.

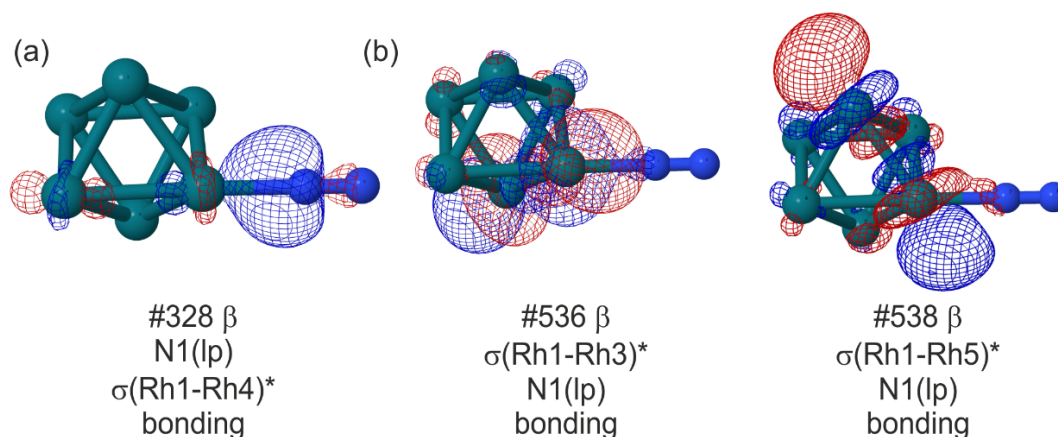


Fig. 9 NLMOs of ¹⁰(6,1)_a consisting of (a) a lone NBO located on N1 with considerable Rh contribution and (b) of Rh-Rh antibonding NBOs with considerable contributions of a N1 lone orbital. The numbering of NLMOs follows the output of the NBO program. The labels consist of the number and spin of the orbital, the principal component as given by NBO program, the minor contributing orbital and the kind of interaction between both contributing orbitals.

In a first step, we focus on the neutral N₂ adsorbate molecule as an electron donor towards the positively charged/electron deficient Rhodium cluster core. The N₂ molecule possesses ten valence electrons, four of which are part of the lone pairs. Each electron is represented by one NLMO (Fig. 9 and Fig. S31 and S32). Only the β spin NLMO located on N1 contains a significant contribution of orbitals located on Rh atoms (Fig. 9): The lone electron NBO overlaps with Rh1-Rh4 σ^* antibonding like orbital and is able to donate electron density into the Rh cluster core. In our analysis, the bonding N₂ orbitals do not interact with the Rh cluster core.

We expect to find accepting orbitals within the virtual NLMOs: Out of the virtual orbitals, two σ -antibonding Rh-Rh (Rh1-Rh and Rh1-Rh5) orbitals reveal positive overlap with an N1 lone electron that is directed towards the metal cluster core. The σ -bond between N₂ and the Rh cluster core establishes by donation of the N1 lone β electron into Rh-Rh antibonding orbitals. This is conceivable in terms of the deficit of β electrons within the cluster core and the fact, that the bonds between the Rh atoms constitute by only 14 β orbitals (Fig. S35). There are only beta Rh-Rh antibonding orbitals (Fig. S36). A transfer of a β electron would lower the charge as well as the spin inside the cluster core, in line with our previous results that predict a charge and spin dissipation over the cluster adsorbate complex.

A second kind of interaction between Rhodium and N₂ centered orbitals involves Rh1 lone pairs and π -antibonding N₂ orbitals (Fig. 10). The lone electrons are not involved in any Rh-Rh bond and they are suitable electron donors. The 39 lone electrons of the Rhodium cluster core are listed in the supplement (Fig. S33 and S34). Note the excess of 31 α lone electrons over eight β lone electrons, which compensates the 14 β bonding electrons and leaves an excess of nine α electrons to yield an overall dectet.

We observe a π -like overlap of four such lone electrons with $\pi^*(N_2)$ orbitals (2x α and 2x β). A fifth orbital reveals a weak σ interaction with an N-hybrid orbital. A look at the N-N antibonding orbitals which may be acceptors of the back donation, reveals that the back donation seems not only to affect $\pi^*(N_2)$ orbitals but also the $\sigma^*(N_2)$ orbital. Preferably, beta orbitals are accessible by electron donation from the cluster core, which counteracts the beta donation from N₂ towards the metal cluster core. Such an interaction is well known as π -backbonding and constitutes the often-observed σ donor- π acceptor synergism that is also core of the Blyholder model. An inspection of the six antibonding N₂ orbitals (Fig. 10) reveals

that only two beta orbitals are interacting with the cluster core: a π^* NBO and the σ^* NBO interact with d orbitals of Rh1 due to asymmetry along the bonding axis.

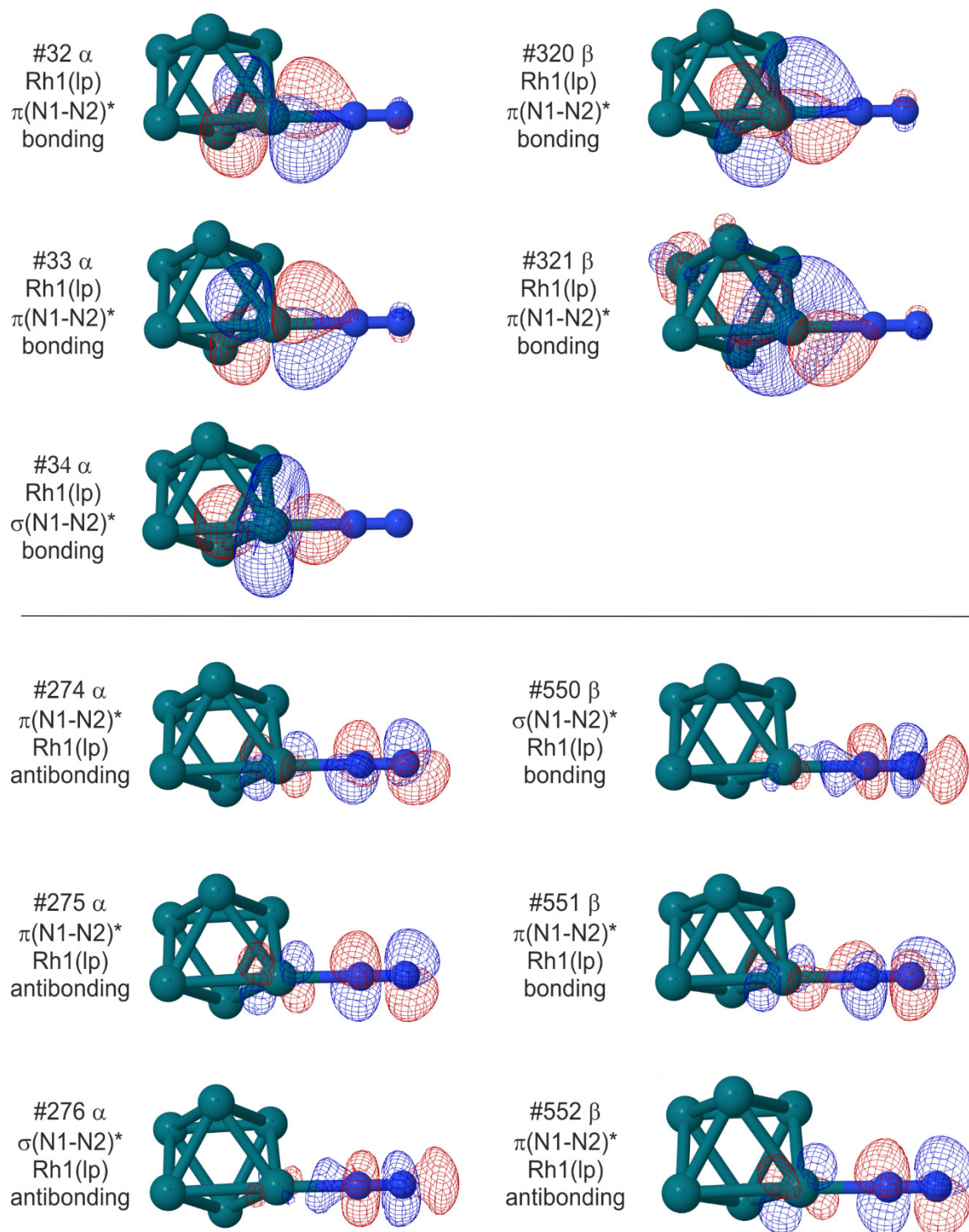


Fig. 10 NLMOs of ¹⁰(6,1)_a consisting of a Rh lone NBO with considerable antibonding N₂ contribution (top) and antibonding N₂ NBOs with considerable Rh contribution (bottom). The labels consist of the number and spin of the orbital, the principal component as given by NBO program, the minor contributing orbital and the kind of interaction between both contributing orbitals.

Our results confirm the σ -donor π -acceptor synergism as predicted by the Blyholder model with additional contribution of a σ -donation from Rh into a σ^* (N_2) orbital.

The observed σ -donation from N_2 into the cluster core is consistent with the calculated spin and charge shifts: beta electron density is transferred into cluster core (Fig. 9) resulting in an alpha excess on N_2 as indicated in earlier chapters. Our results confirm in principle a σ - π synergism. Not the N-N sigma bond donates but seemingly the lone electron, in contrary to preliminary assumptions. In order to study the effect of charge dilution and the orbital interactions for an increasing number of adsorbed N_2 molecules, the (6,2) cluster has to be examined in the same way.

5.6 Conclusions

We have recorded cryo IR-PD spectra of $[Rh_6(N_2)_m]^+$ ($6,m$) $m = 1, \dots, 12$ cluster adsorbate complexes up to saturation. The spectra reveal a redshift of the N-N stretching band upon adsorption of the first N_2 adsorbates and multiple bands for high amounts of adsorbed N_2 that indicate geminal N_2 adsorption. A continuous vibrational redshift throughout the first seven adsorption steps is interpreted as a result of an adsorbate dependent charge dilution effect. By help of DFT modelling, we could assign isomers with an octahedral cluster core for the first five adsorption steps. From a multitude of calculated isomers, we evaluated the most stable isomers in terms of *spin valley curves* up to saturation. Our analysis addressed the assumptions of our earlier publications: (a) Starting from a (6,0) octahedral cluster core structure, we observed no cluster core reorganization with increasing amount of adsorbate molecules. (b) We found a dectet cluster adsorbate complex for $m = 1, \dots, 4$. With the 5th adsorbed N_2 , a gradual spin quench sets in and continues to yield degenerate doublet and quartet isomers. (c) The adsorption energies between the (6, m) cluster adsorbate complexes decrease from the first to the ultimate step (65-35 kJ/mol). In between, we observe an increase for $m = 4$ and 5, right where the spin quench sets in. (d) At the intermittent adsorption limit (6,8), the narrow spectrum indicates a symmetric cluster with similar N_2 oscillators. The search of a suitable isomer is work in progress.

A population analysis of the naked clusters and the first five assigned cluster adsorbate complexes revealed a gradual shift of charge and spin density towards the adsorbate shell. This dissipation of charge and spin density from the metal cluster core over the whole cluster

adsorbate complex confirms our charge dilution hypothesis. An orbital analysis confirmed a σ -bonding π -back bonding synergism.

In the course of this work, we addressed the open questions of our earlier publications and were able to expand the known charge dilution model: Not only an increase of the number of metal atoms but also an increase of the adsorbate shell effects a charge dilution resulting in a softened N₂ stretching vibration.

5.7 Acknowledgement

This work was supported by the German research foundation DFG within the transregional collaborative research center SFB/TRR 88 'Cooperative effects in homo and heterometallic complexes' (3MET.de) and by the state research center OPTIMAS. We thank Thomas Kolling for assistance on technical questions of any kind.

5.8 References

1. Brunauer, S., Emmett, P.H., and Teller, E., *Adsorption of Gases in Multimolecular Layers*. J. Am. Chem. Soc. **1938**, *60*, 309-319.
2. King, D.A. and Wells, M.G., *Reaction Mechanism in Chemisorption Kinetics: Nitrogen on the {100} Plane of Tungsten*. Proceedings of the Royal Society A: Mathematical, Physical and Engineering Sciences **1974**, *339*, 245-269.
3. King, D.A. and Wells, M.G., *Molecular beam investigation of adsorption kinetics on bulk metal targets: Nitrogen on tungsten*. Surf. Sci. **1972**, *29*, 454-482.
4. Ertl, G., Lee, S.B., and Weiss, M., *Kinetics of nitrogen adsorption on Fe(111)*. Surf. Sci. **1982**, *114*, 515-526.
5. Knickelbein, M.B., *Reactions of transition metal clusters with small molecules*. Ann. Rev. Phys. Chem. **1999**, *50*, 79-115.
6. Morse, M.D., Geusic, M.E., Heath, J.R., and Smalley, R.E., *Surface reactions of metal clusters. II. Reactivity surveys with D₂, N₂, and CO*. J. Chem. Phys. **1985**, *83*, 2293-2304.
7. Bérces, A., Hackett, P.A., Lian, L., Mitchell, S.A., and Rayner, D.M., *Reactivity of niobium clusters with nitrogen and deuterium*. J. Chem. Phys. **1998**, *108*, 5476-5490.
8. Liu, F., Li, M., Tan, L., and Armentrout, P.B., *Guided ion beam studies of the reactions of Co_n⁺ (n=1-18) with N₂: Cobalt cluster mononitride and dinitride bond energies*. J. Chem. Phys. **2008**, *128*, 194313.
9. Ho, J., Parks, E.K., Zhu, L., and Riley, S.J., *Reactions of small cobalt clusters with N₂: implications for cluster structure*. Chem. Phys. **1995**, *201*, 245-261.
10. Riley, S.J., *The atomic structure of transition metal clusters*. Journal of Non-Crystalline Solids **1996**, *205-207*, 781-787.
11. Parks, E.K., Zhu, L., Ho, J., and Riley, S.J., *The structure of small nickel clusters. I. Ni₃–Ni₁₅*. J. Chem. Phys. **1994**, *100*, 7206-7222.

12. Parks, E.K., Zhu, L., Ho, J., and Riley, S.J., *The structure of small nickel clusters. II. Ni₁₆-Ni₂₈*. J. Chem. Phys. **1995**, *102*, 7377-7389.
13. Parks, E.K. and Riley, S.J., *Nickel cluster structure determined from the adsorption of molecular nitrogen Ni₄₉-Ni₇₁*. Zeitschrift für Physik D Atoms, Molecules and Clusters **1995**, *33*, 59-70.
14. Parks, E.K., Kerns, K.P., and Riley, S.J., *The structure of nickel-iron clusters probed by adsorption of molecular nitrogen*. Chem. Phys. **2000**, *262*, 151-167.
15. Parks, E.K., Nieman, G.C., Kerns, K.P., and Riley, S.J., *The thermodynamics of nitrogen adsorption on nickel clusters: Ni₁₉-Ni₇₁*. J. Chem. Phys. **1998**, *108*, 3731-3739.
16. Mou, L.-H., Jiang, G.-D., Li, Z.-Y., and He, S.-G., *Activation of dinitrogen by gas-phase species*. Chinese Journal of Chemical Physics **2020**, *33*, 507-520.
17. Dillinger, S., Mohrbach, J., Hewer, J., Gaffga, M., and Niedner-Schatteburg, G., *Infrared spectroscopy of N₂ adsorption on size selected cobalt cluster cations in isolation*. Phys. Chem. Chem. Phys. **2015**, *17*, 10358-10362.
18. Mohrbach, J., Dillinger, S., and Niedner-Schatteburg, G., *Cryo Kinetics and Spectroscopy of Cationic Nickel Clusters: Rough and Smooth Surfaces*. J. Phys. Chem. C **2017**, *121*, 10907-10918.
19. Dillinger, S., Klein, M.P., Steiner, A., McDonald, D.C., Duncan, M.A., Kappes, M.M., and Niedner-Schatteburg, G., *Cryo IR Spectroscopy of N₂ and H₂ on Ru₈⁺: The Effect of N₂ on the H-Migration*. J. Phys. Chem. Lett. **2018**, *9*, 914-918.
20. Fries, D.V., Klein, M.P., Steiner, A., Prosenc, M.H., and Niedner-Schatteburg, G., *Observation and Mechanism of Cryo N₂ Cleavage by a Tantalum Cluster*. Phys. Chem. Chem. Phys. **2021**, *23*, 11345-11354.
21. Ehrhard, A.A., Klein, M.P., Mohrbach, J., Dillinger, S., and Niedner-Schatteburg, G., *Cryokinetics and spin quenching in the N₂ adsorption onto rhodium cluster cations*. Mol. Phys. **2021**, e1953172.
22. Klein, M.P., Ehrhard, A.A., Mohrbach, J., Dillinger, S., and Niedner-Schatteburg, G., *Infrared Spectroscopic Investigation of Structures and N₂ Adsorption Induced Relaxations of Isolated Rhodium Clusters*. Top. Catal. **2018**, *61*, 106-118.
23. Berg, C., Schindler, T., Niedner-Schatteburg, G., and Bondybey, V.E., *Reactions of Simple Hydrocarbons with Nb_n⁺: Chemisorption and Physisorption on Ionized Niobium Clusters*. J. Chem. Phys. **1995**, *102*, 4870-4884.
24. Maruyama, S., Anderson, L.R., and Smalley, R.E., *Direct injection supersonic cluster beam source for FT-ICR studies of clusters*. Rev. Sci. Instrum. **1990**, *61*, 3686-3693.
25. Proch, D. and Trickl, T., *A high-intensity multi-purpose piezoelectric pulsed molecular beam source*. Rev. Sci. Instrum. **1989**, *60*, 713-716.
26. Caravatti, P. and Allemann, M., *The 'infinity cell': A new trapped-ion cell with radiofrequency covered trapping electrodes for fourier transform ion cyclotron resonance mass spectrometry*. Org. Mass Spectrom. **1991**, *26*, 514-518.
27. Gerhards, M., *High energy and narrow bandwidth mid IR nanosecond laser system*. Opt. Commun. **2004**, *241*, 493-497.
28. Frisch, M.J., Trucks, G.W., Schlegel, H.B., Scuseria, G.E., Robb, M.A., Cheeseman, J.R., Scalmani, G., Barone, V., Mennucci, B., Petersson, G.A., Nakatsuji, H., Caricato, M., Li, X., Hratchian, H.P., Izmaylov, A.F., Bloino, J., Zheng, G., Sonnenberg, J.L., Hada, M., Ehara, M., Toyota, K., Fukuda, R., Hasegawa, J., Ishida, M., Nakajima, T., Honda, Y., Kitao, O., Nakai, H., Vreven, T., Montgomery Jr., J.A., Peralta, J.E., Ogliaro, F., Bearpark, M.J., Heyd, J., Brothers, E.N., Kudin, K.N., Staroverov, V.N., Kobayashi, R., Normand, J., Raghavachari, K., Rendell, A.P., Burant, J.C., Iyengar, S.S., Tomasi, J., Cossi, M., Rega,

- N., Millam, N.J., Klene, M., Knox, J.E., Cross, J.B., Bakken, V., Adamo, C., Jaramillo, J., Gomperts, R., Stratmann, R.E., Yazyev, O., Austin, A.J., Cammi, R., Pomelli, C., Ochterski, J.W., Martin, R.L., Morokuma, K., Zakrzewski, V.G., Voth, G.A., Salvador, P., Dannenberg, J.J., Dapprich, S., Daniels, A.D., Farkas, Ö., Foresman, J.B., Ortiz, J.V., Cioslowski, J., and Fox, D.J., *Gaussian 09, Revision D.01*. 2009, Gaussian, Inc.: Wallingford, CT, USA.
29. Adamo, C. and Barone, V., *Toward reliable density functional methods without adjustable parameters: The PBE0 model*. J. Chem. Phys. **1999**, *110*, 6158-6170.
 30. Dunning, T.H., *Gaussian basis sets for use in correlated molecular calculations. I. The atoms boron through neon and hydrogen*. J. Chem. Phys. **1989**, *90*, 1007-1023.
 31. Dillinger, S., Mohrbach, J., and Niedner-Schatteburg, G., *Probing cluster surface morphology by cryo spectroscopy of N₂ on cationic nickel clusters*. J. Chem. Phys. **2017**, *147*, 184305.
 32. Andrae, D., Häußermann, U., Dolg, M., Stoll, H., and Preuß, H., *Energy-adjusted ab initio pseudopotentials for the second and third row transition elements*. Theor. Chim. Acta **1990**, *77*, 123-141.
 33. Glendening, E.D., Badenhoop, J.K., Reed, A.E., Carpenter, J.E., Bohmann, J.A., Morales, C.M., and Weinhold, F., *NBO 5.9*. 2009, Theoretical Chemistry Institute, University of Wisconsin: Madison, WI.
 34. Bendtsen, J., *The rotational and rotation-vibrational Raman spectra of ¹⁴N₂, ¹⁴N¹⁵N and ¹⁵N₂*. J. Raman Spectrosc. **1974**, *2*, 133-145.
 35. Blyholder, G., *Molecular Orbital View of Chemisorbed Carbon Monoxide*. J. Phys. Chem. **1964**, *68*, 2772-2777.
 36. Fielicke, A., von Helden, G., Meijer, G., Pedersen, D.B., Simard, B., and Rayner, D.M., *Size and charge effects on the binding of CO to late transition metal clusters*. J. Chem. Phys. **2006**, *124*, 194305.
 37. Straßner, A., Wiehn, C., Klein, M.P., Fries, D.V., Dillinger, S., Mohrbach, J., Armentrout, P.B., and Niedner-Schatteburg, G., *Cryo spectroscopy of N₂ on cationic iron clusters*. under review at J. Chem. Phys.
 38. Klein, M.P., Fries, D.V., Straßner, A., Huber, M.E., and Niedner-Schatteburg, G., *N₂ Adsorption onto Ta_n⁺ n = 4,5 Clusters: IR-PD Spectroscopy, Cryo-Kinetics, and DFT Modelling*. unpublished.
 39. Bligaard, T. and Nørskov, J.K., *Chapter 4 - Heterogeneous Catalysis*, in *Chemical Bonding at Surfaces and Interfaces*. **2008**, Elsevier: Amsterdam. 255-321.
 40. Comelli, G., Dhanak, V.R., Kiskinova, M., Prince, K.C., and Rosei, R., *Oxygen and nitrogen interaction with rhodium single crystal surfaces*. Surface Science Reports **1998**, *32*, 165-231.

5.9 Supplementary Information

I. IR spectroscopy

Fig. S1 Laser pulse energy in dependence of photon energy

Fig. S2 IR-PD spectra of sequential N₂ adsorption steps onto Rh₆⁺ cluster cations [Rh₆(N₂)_m]⁺, $m = 1, \dots, 12$, extended range

II. Stabilities and adsorption energies

Table S1 Energies of the isomers constituting the spin valley

Table S2 Effects of spin contamination in the calculated most stable isomers

Table S3 Vertical (dectet) and adiabatic adsorption energies

III. Isomer assignment and calculated linear absorption spectra

Fig.s S3-S28 Experimental IR-PD spectrum of the [Rh₆(N₂)_m]⁺ cluster adsorbate complexes and calculated linear absorption spectra

Text S1 Coordinates of the assigned isomers

V. Electronic properties

Table S3 Positive charge and spin localized on the Rh₆ cluster core dependent on adsorbed N₂ molecules m

Fig. S29 Total Charges and spins from Natural Population Analysis of ¹⁰(6,1)_a

VI. Orbital analysis

Fig. S30 Composition of the NLMOs depicted in Fig.s 9 and 10

Fig. S31 Composition of the NLMOs depicted in Fig. S32

Fig. S32 NLMOs of ¹⁰(6,1)_a that are centered on N₂

Fig. S33 α-NLMOs of ¹⁰(6,1)_a consisting of a Rh lone NBO

Fig. S34 β-NLMOs of ¹⁰(6,1)_a consisting of a Rh lone NBO

Fig. S34 NLMOs of ¹⁰(6,1)_a consisting of a Rh-Rh bonding NBO

Fig. S3 NLMOs of ¹⁰(6,1)_a consisting of a Rh-Rh antibonding NBO

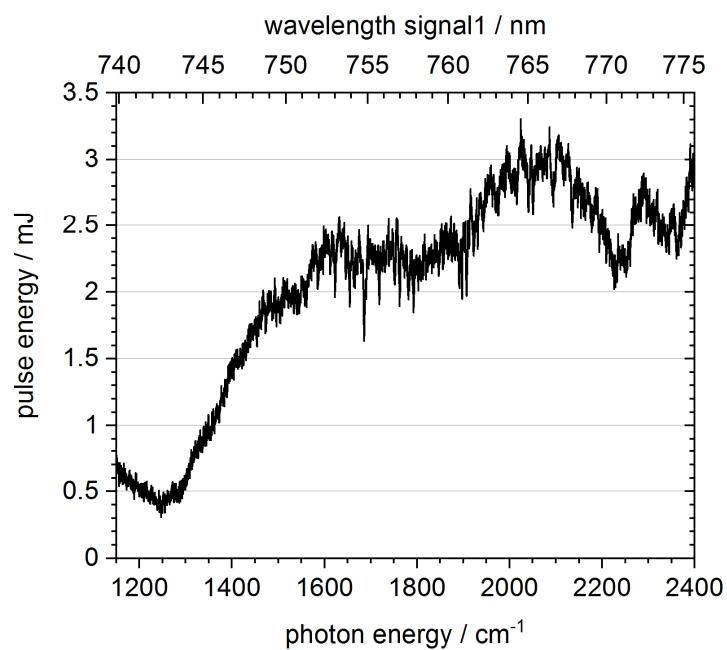


Fig. S1 Laser pulse energy in dependence of photon energy in the complete measured range.

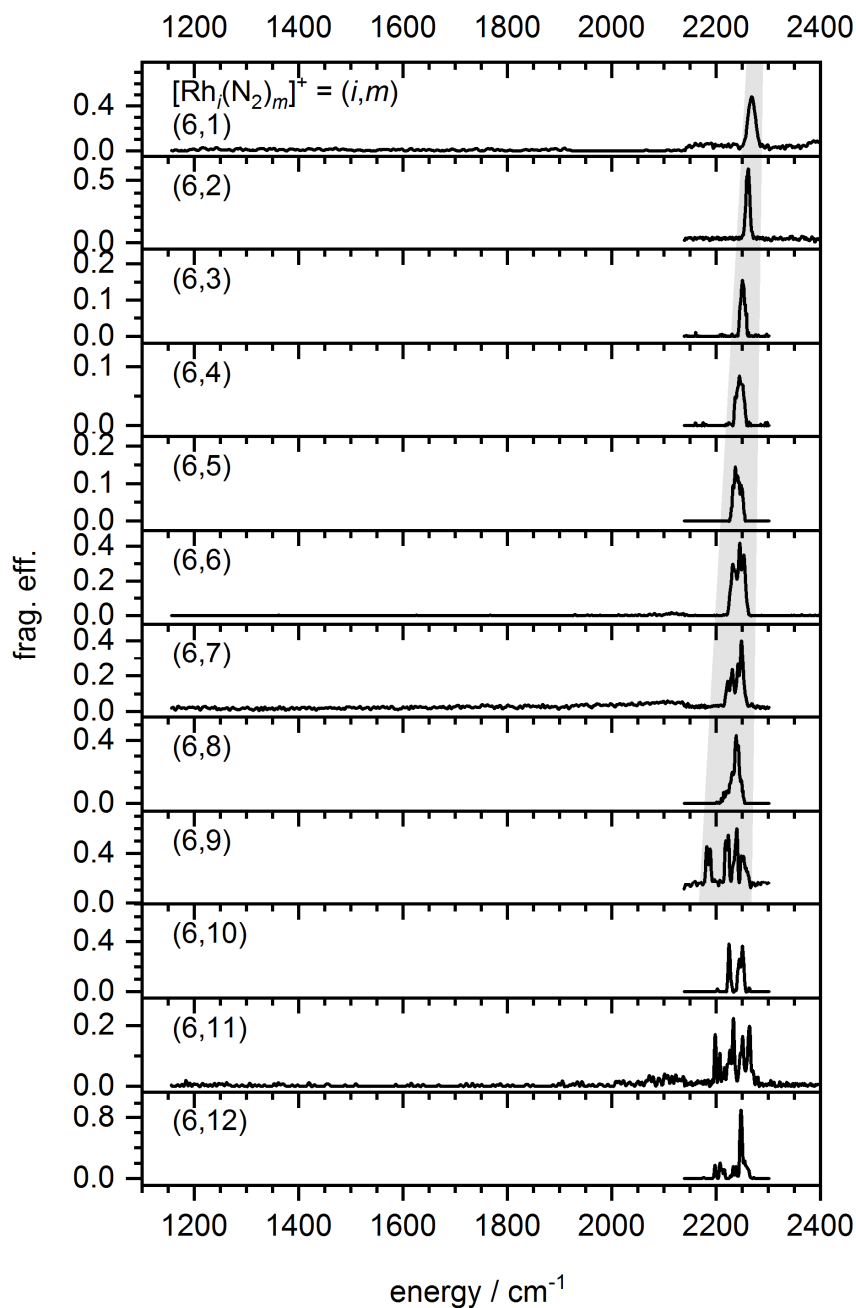


Fig. S2 IR-PD spectra of sequential N_2 adsorption steps onto Rh_6^+ cluster cations $[Rh_6(N_2)_m]^+$, $m = 1-12$ as recorded after 26 K He buffer gas cooling. The grey shaded area serves to guide the eye indicating a redshift and broadening of the absorption range with number m of adsorbed N_2 . In some cases, the measuring range is expanded in order to observe possible side-on N_2 adsorption.

Table S1 Energies of the isomers constituting the spin valley: (a) Absolute energies of the cluster adsorbate complexes, (b) absolute energies of the '(6, *m*) + (12-*m*) N₂' systems, and (c) the relative energies of these systems. The gray shaded fields denote the most stable isomer for each *m*.

(a) $E_{\text{abs}} ([\text{Rh}_6(\text{N}_2)_m]^+) / \text{a.u.}$													
	m												
	0	1	2	3	4	5	6	7	8	9	10	11	12
2S+1													
2	-662.913907	-772.382375	-881.851945	-991.321546	-1100.789024	-1210.252165	-1319.720523	-1429.188684	-1538.648421	-1648.114008	-1757.569016	-1867.027531	-1976.482797
4	-662.914063	-772.385516	-881.855861	-991.324473	-1100.791708	-1210.256829	-1319.723093	-1429.183765	-1538.653776	-1648.111424	-1757.569911	-1867.017724	-1976.483807
6	-662.925132	-772.391346	-881.864817	-991.333341	-1100.797908	-1210.263336	-1319.726860	-1429.187545	-1538.654659	-1648.105062	-1757.554607	-1867.009363	-1976.456670
8	-662.930725	-772.392917	-881.867492	-991.336917	-1100.803643	-1210.267374	-1319.725722	-1429.190615	-1538.641869	-1648.092423	-1757.540681	-1866.998120	-1976.439238
10	-662.945081	-772.411628	-881.878289	-991.343163	-1100.805909	-1210.268436	-1319.726574	-1429.180708	-1538.634760	-1648.092673	-1757.528888	-1866.989899	-1976.427757
12	-662.922141	-772.380124	-881.851663	-991.314185	-1100.774135	-1210.234531	-1319.688072	-1429.132246	-1538.584545	-1648.032728	-1757.476220	-1866.927461	-1976.373248
14	-662.892881	-772.357410	-881.819005	-991.274979	-1100.730893	-1210.151478							
16	-662.857331	-772.307365											
18	-662.726411	-772.176882											
(b) $E_{\text{abs}} ([\text{Rh}_6(\text{N}_2)_m]^+ + (12-m) \text{N}_2) / \text{a.u.}$													
	m												
	0	1	2	3	4	5	6	7	8	9	10	11	12
2S+1													
2	-1976.210823	-1976.237882	-1976.266042	-1976.294233	-1976.320301	-1976.342033	-1976.368981	-1976.395732	-1976.414060	-1976.438237	-1976.451836	-1976.468941	-1976.482797
4	-1976.210979	-1976.241022	-1976.269958	-1976.297160	-1976.322985	-1976.346697	-1976.371551	-1976.390813	-1976.419415	-1976.435653	-1976.452130	-1976.459133	-1976.483807
6	-1976.222048	-1976.246852	-1976.271891	-1976.306028	-1976.329186	-1976.353204	-1976.375318	-1976.394593	-1976.420298	-1976.429291	-1976.4337426	-1976.450772	-1976.456670
8	-1976.227641	-1976.248423	-1976.281588	-1976.309604	-1976.334920	-1976.357242	-1976.374180	-1976.397663	-1976.407508	-1976.416652	-1976.423500	-1976.439530	-1976.439238
10	-1976.241997	-1976.267134	-1976.292386	-1976.315850	-1976.337187	-1976.358304	-1976.375032	-1976.387756	-1976.400399	-1976.416902	-1976.411708	-1976.430399	-1976.427757
12	-1976.219056	-1976.235630	-1976.265760	-1976.286872	-1976.305412	-1976.324398	-1976.336530	-1976.339295	-1976.350184	-1976.356957	-1976.359039	-1976.368871	-1976.373248
14	-1976.189797	-1976.212916	-1976.233101	-1976.247665	-1976.262170	-1976.241346							
16	-1976.154247	-1976.162871											
18	-1976.023327	-1976.032388											
(c) $E_{\text{rel}} ([\text{Rh}_6(\text{N}_2)_m]^+ + (12-m) \text{N}_2) / \text{kJ/mol}$													
	m												
	0	1	2	3	4	5	6	7	8	9	10	11	12
2S+1													
2	81.85	10.80	-63.13	-137.14	-205.59	-262.64	-333.40	-403.63	-451.75	-515.23	-550.93	-595.84	-632.22
4	81.44	2.56	-73.41	-144.83	-212.63	-274.89	-340.14	-390.72	-465.81	-508.44	-551.71	-570.09	-634.87
6	52.38	-12.75	-96.92	-168.11	-228.91	-291.97	-350.03	-400.64	-468.13	-491.74	-513.10	-548.14	-563.62
8	37.69	-16.87	-103.95	-177.50	-243.97	-302.58	-347.05	-408.70	-434.55	-458.56	-476.54	-518.62	-517.86
10	0.00	-66.00	-132.30	-193.90	-249.92	-305.36	-349.28	-382.69	-415.88	-459.21	-445.58	-494.65	-487.71
12	60.23	16.72	-62.39	-117.82	-166.50	-216.34	-248.20	-255.46	-284.04	-301.83	-307.29	-333.11	-344.60
14	137.05	76.35	23.36	-14.88	-52.96	1.71							
16	230.39	207.75											
18	574.12	550.33											

Table S2 Effects of spin contamination in the calculated most stable isomers. The gray shaded fields indicate S^2 values that are increased by at least 0.25.

(a) expected and obtained S^2 values for each spin state and number of N_2														
		m												
$2S+1$	S^2	0	1	2	3	4	5	6	7	8	9	10	11	12
2	0.75	11.39	11.91	9.14	9.12	7.69	3.08	2.65	1.18	1.11	1.08	0.98	0.75	1.16
4	3.75	6.59	6.27	5.74	5.16	4.57	5.40	3.83	3.77	3.75	3.75	3.75	3.76	3.75
6	8.75	9.29	9.07	8.86	8.80	8.79	8.76	8.75	8.79	8.76	8.75	8.76	8.76	8.76
8	15.75	15.76	15.76	15.79	15.77	15.76	15.75	15.76	15.75	15.76	15.76	15.76	15.76	15.76
10	24.75	24.76	24.76	24.76	24.76	24.76	24.76	24.76	24.76	24.76	24.76	24.76	24.76	24.76
12	35.75	35.76	35.76	35.75	35.75	35.75	35.75	35.75	35.75	35.75	35.75	35.75	35.75	35.75
14	48.75	48.75	48.75	48.75	48.75	48.75	48.75							
16	63.75	63.75	63.75											
18	80.75	80.75	80.75											
(b) deviations from the expected S^2 values for each spin state and number of N_2														
		m												
$2S+1$	S^2	0	1	2	3	4	5	6	7	8	9	10	11	12
2	0.75	10.64	11.16	8.39	8.37	6.94	2.33	1.90	0.43	0.36	0.33	0.23	0.00	0.41
4	3.75	2.84	2.52	1.99	1.41	0.82	1.65	0.08	0.02	0.00	0.00	0.00	0.01	0.00
6	8.75	0.54	0.32	0.11	0.05	0.04	0.01	0.00	0.04	0.01	0.00	0.01	0.01	0.01
8	15.75	0.01	0.01	0.04	0.02	0.01	0.00	0.01	0.00	0.01	0.01	0.01	0.01	0.01
10	24.75	0.01	0.01	0.01	0.01	0.01	0.01	0.01	0.01	0.01	0.01	0.01	0.01	0.01
12	35.75	0.01	0.01	0.00	0.00	0.00	0.00	0.00	0.00	0.00	0.00	0.00	0.00	0.00
14	48.75	0.00	0.00	0.00	0.00	0.00	0.00							
16	63.75	0.00	0.00											
18	80.75	0.00	0.00											

Table S3 Vertical (dectet) and adiabatic adsorption energies as derived from our calculated $(6,m)$ $m = 0, \dots, 12$ isomers.

step m	Adsorption energy / kJ/mol	
	vertical dectet	adiabatic
0	-66.0	-66.0
1	-66.3	-66.3
2	-61.6	-61.6
3	-56.0	-56.0
4	-55.4	-55.4
5	-43.9	-44.7
6	-33.4	-58.7
7	-33.2	-59.4
8	-43.3	-47.1
9	13.6	-36.5
10	-49.1	-44.1
11	6.9	-39.0

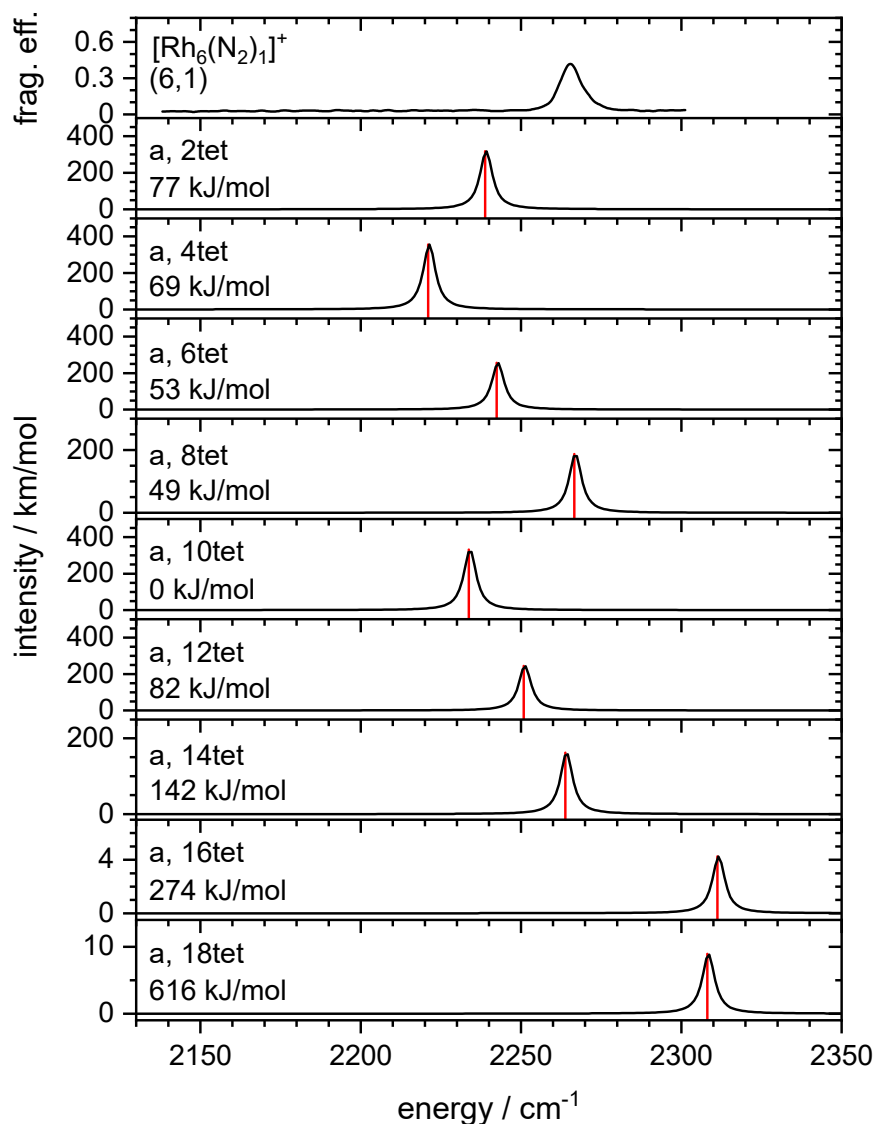


Fig. S3 Experimental IR-PD spectrum of the $[\text{Rh}_6(\text{N}_2)_1]^+$ cluster adsorbate complex and calculated linear absorption spectra (scaled by 0.9385). The line spectra were convoluted with a 5 cm^{-1} FWHM Lorentzian. The letter indicates the arrangement of the N_2 molecules on the octahedral cluster core and is followed by spin multiplicity and the relative energy with respect to the most stable isomer.

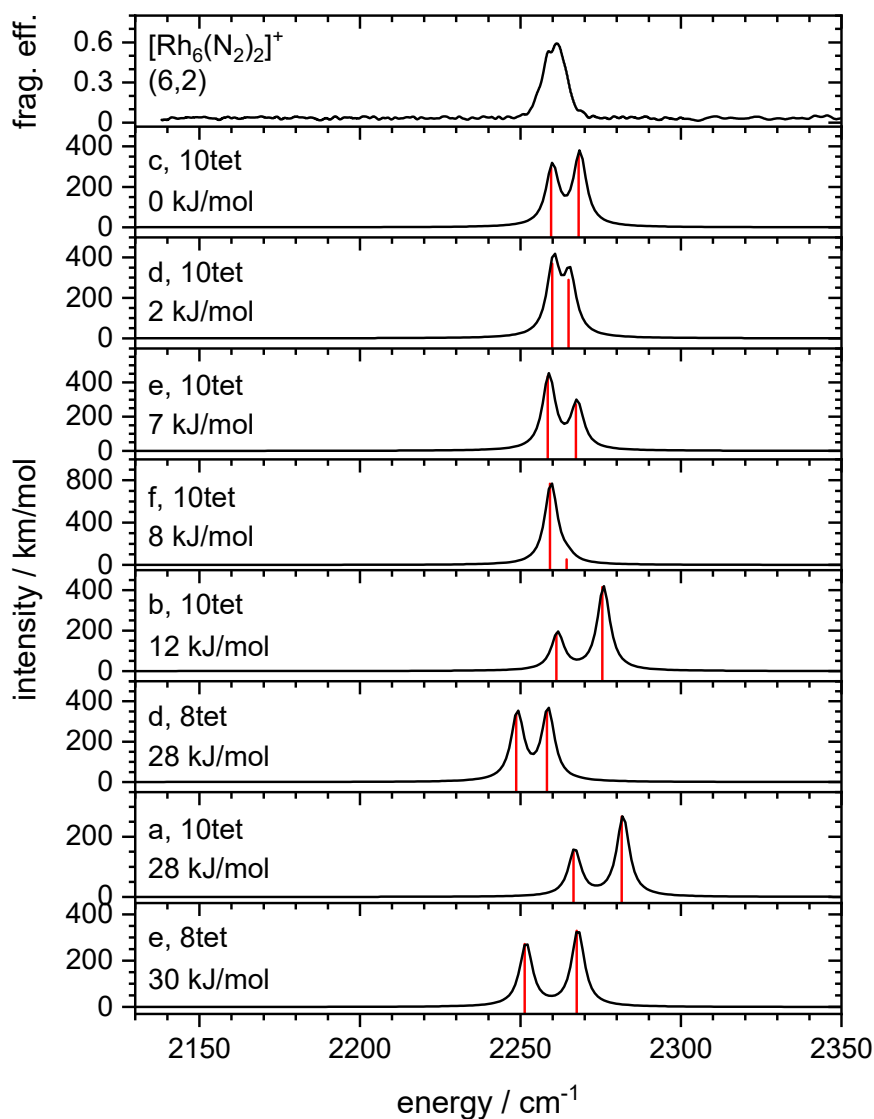


Fig. S4 Experimental IR-PD spectrum of the $[\text{Rh}_6(\text{N}_2)_2]^+$ cluster adsorbate complex and calculated linear absorption spectra of the isomers up to 30 kJ/mol above the most stable one (scaled by 0.9385). The line spectra were convoluted with a 5 cm^{-1} FWHM Lorentzian. The letter indicates the arrangement of the N_2 molecules and is followed by spin multiplicity and the relative energy with respect to the most stable isomer.

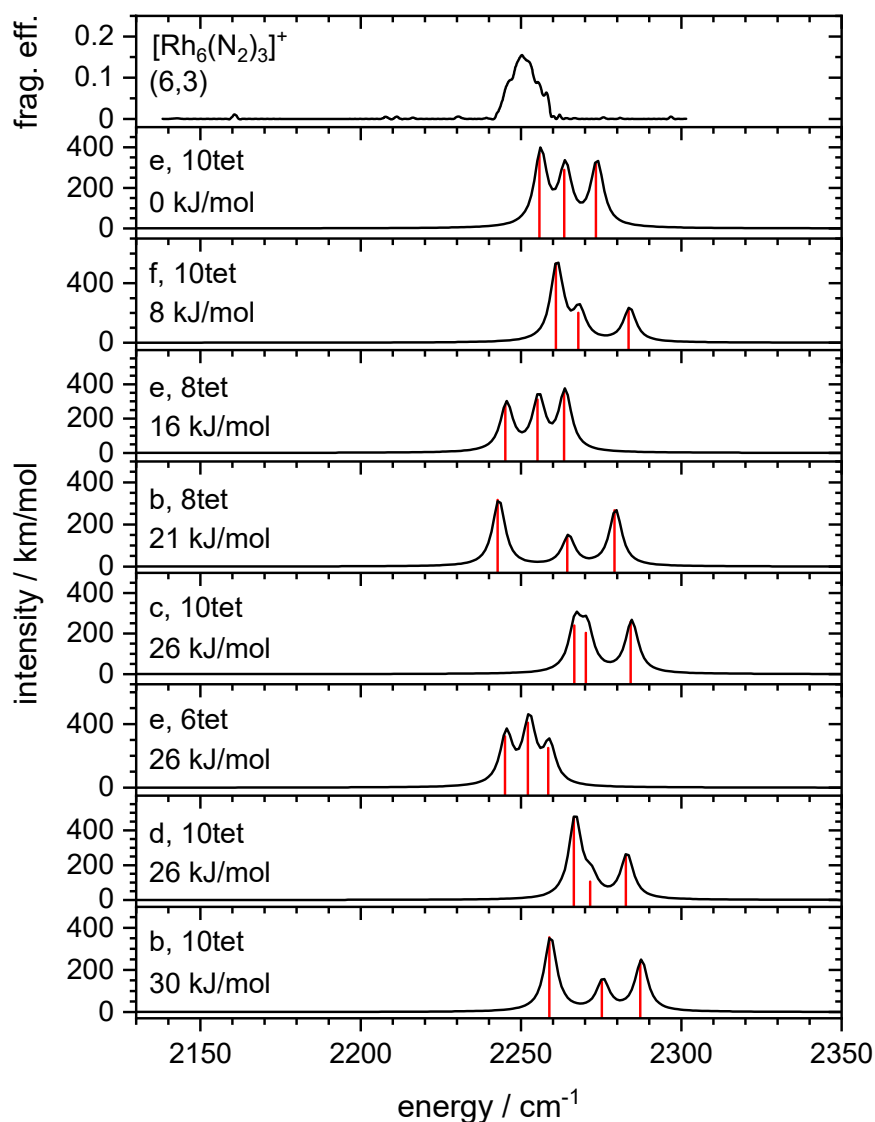


Fig. S5 Experimental IR-PD spectrum of the [Rh₆(N₂)₃]⁺ cluster adsorbate complex and calculated linear absorption spectra of the isomers up to 30 kJ/mol above the most stable one (scaled by 0.9385). The line spectra were convoluted with a 5 cm⁻¹ FWHM Lorentzian. The letter indicates the arrangement of the N₂ molecules and is followed by spin multiplicity and the relative energy with respect to the most stable isomer.

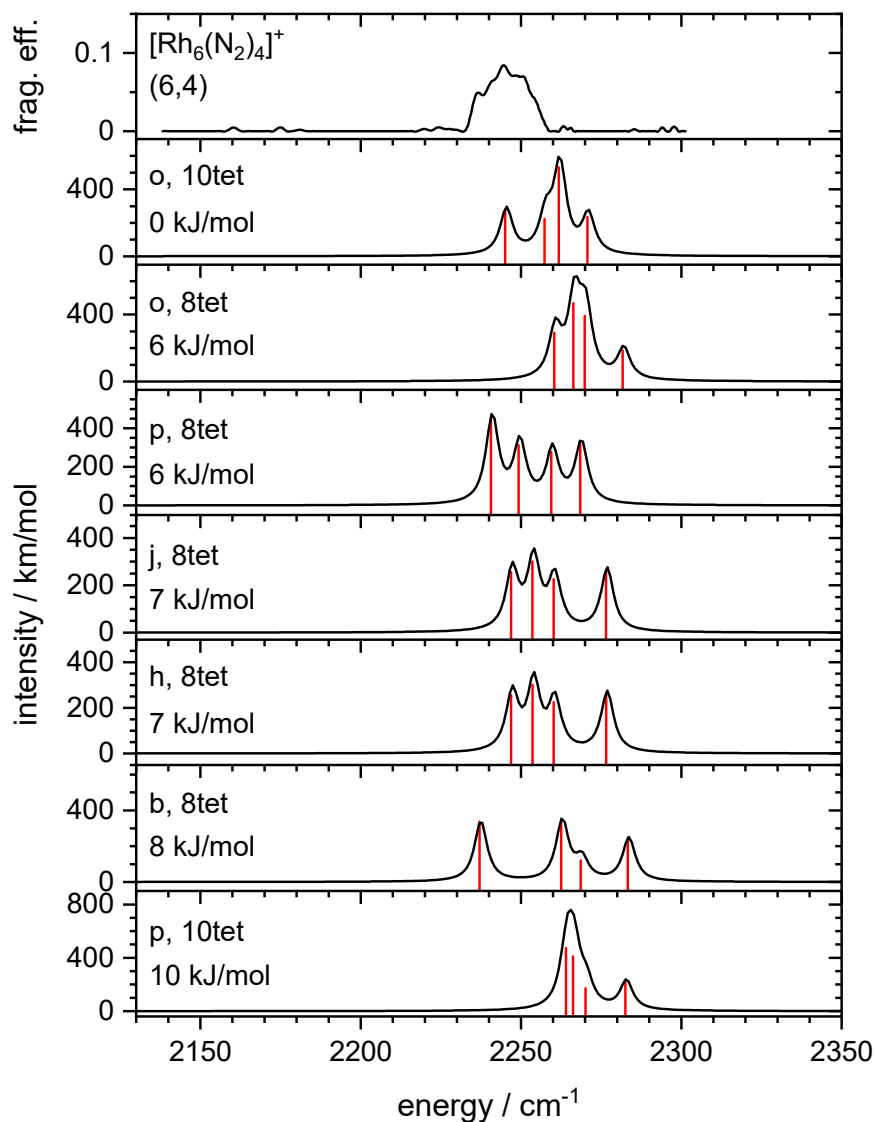


Fig. S6 Experimental IR-PD spectrum of the $[\text{Rh}_6(\text{N}_2)_4]^+$ cluster adsorbate complex and calculated linear absorption spectra of the isomers up to 10 kJ/mol above the most stable one (scaled by 0.9385). The line spectra were convoluted with a 5 cm^{-1} FWHM Lorentzian. The letter indicates the arrangement of the N_2 molecules and is followed by spin multiplicity and the relative energy with respect to the most stable isomer.

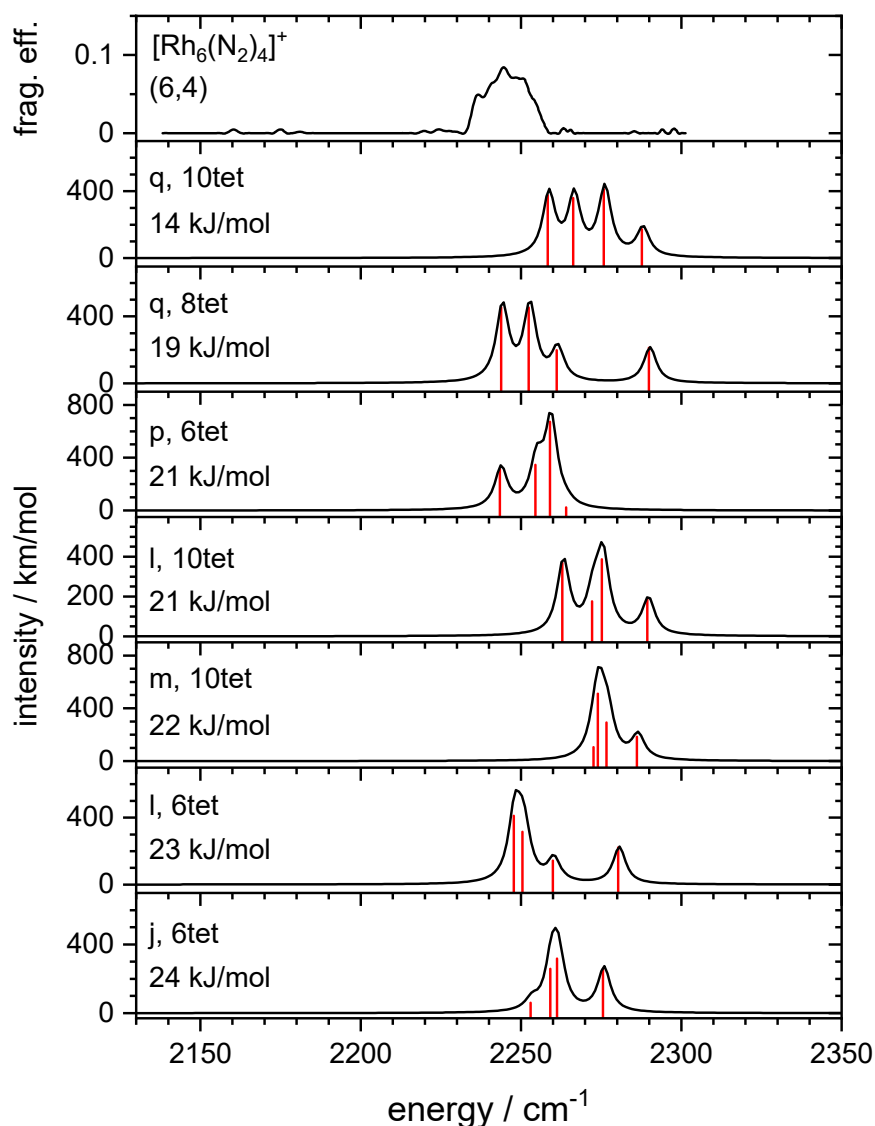


Fig. S7 Experimental IR-PD spectrum of the [Rh₆(N₂)₄]⁺ cluster adsorbate complex and calculated linear absorption spectra of the isomers between 10 and 24 kJ/mol above the most stable one (scaled by 0.9385). The line spectra were convoluted with a 5 cm⁻¹ FWHM Lorentzian. The letter indicates the arrangement of the N₂ molecules and is followed by spin multiplicity and the relative energy with respect to the most stable isomer.

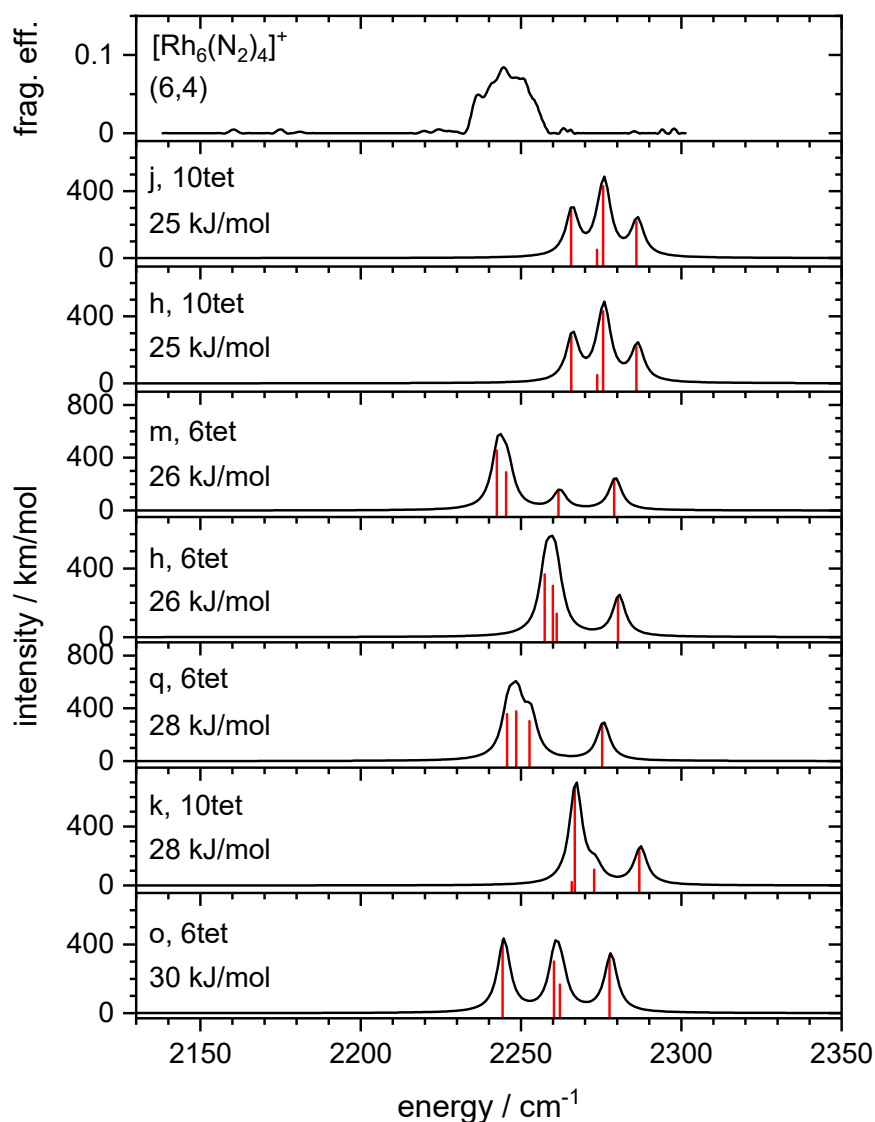


Fig. S8 Experimental IR-PD spectrum of the $[\text{Rh}_6(\text{N}_2)_4]^+$ cluster adsorbate complex and calculated linear absorption spectra of the isomers between 25 and 30 kJ/mol above the most stable one (scaled by 0.9385). The line spectra were convoluted with a 5 cm^{-1} FWHM Lorentzian. The letter indicates the arrangement of the N_2 molecules and is followed by spin multiplicity and the relative energy with respect to the most stable isomer.

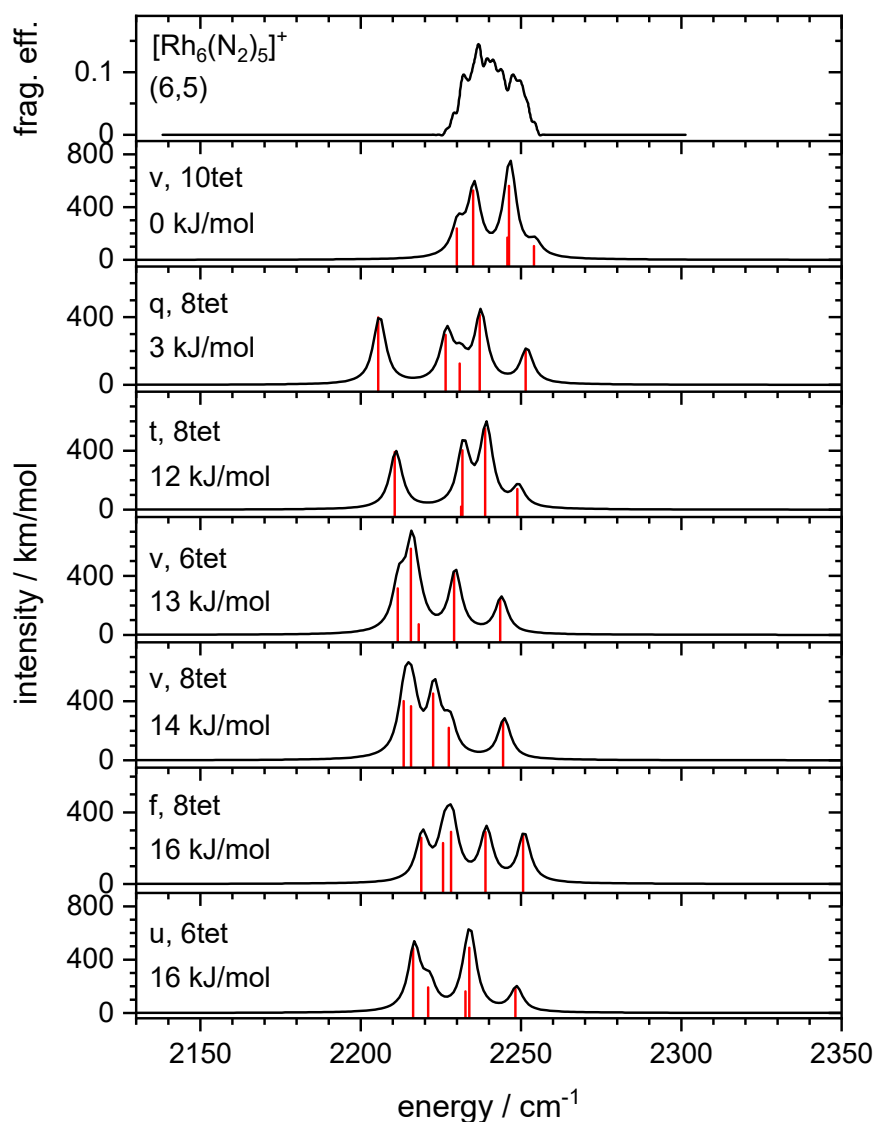


Fig. S9 Experimental IR-PD spectrum of the [Rh₆(N₂)₅]⁺ cluster adsorbate complex and calculated linear absorption spectra of the isomers between 0 and 16 kJ/mol above the most stable one (scaled by 0.9385). The line spectra were convoluted with a 5 cm⁻¹ FWHM Lorentzian. The letter indicates the arrangement of the N₂ molecules and is followed by spin multiplicity and the relative energy with respect to the most stable isomer.

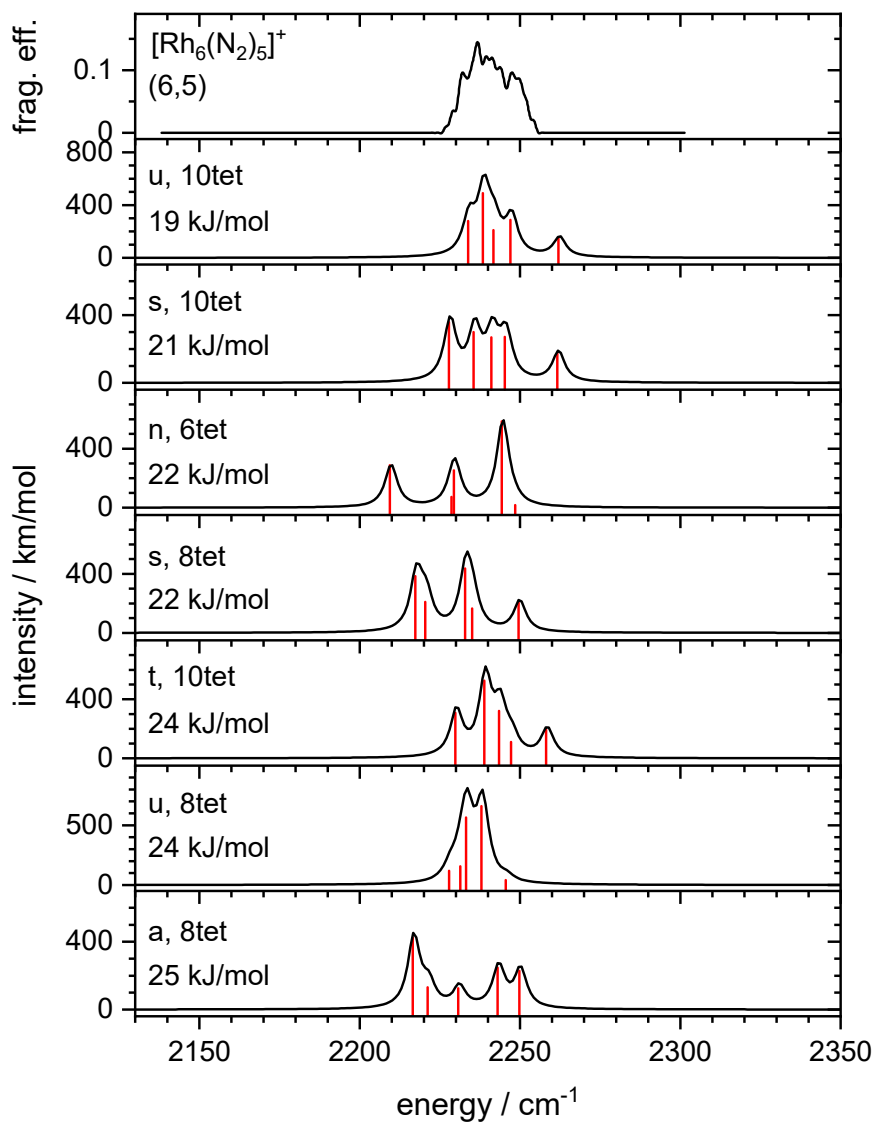


Fig. S10 Experimental IR-PD spectrum of the $[\text{Rh}_6(\text{N}_2)_5]^+$ cluster adsorbate complex and calculated linear absorption spectra of the isomers between 19 and 25 kJ/mol above the most stable one (scaled by 0.9385). The line spectra were convoluted with a 5 cm^{-1} FWHM Lorentzian. The letter indicates the arrangement of the N_2 molecules and is followed by spin multiplicity and the relative energy with respect to the most stable isomer.

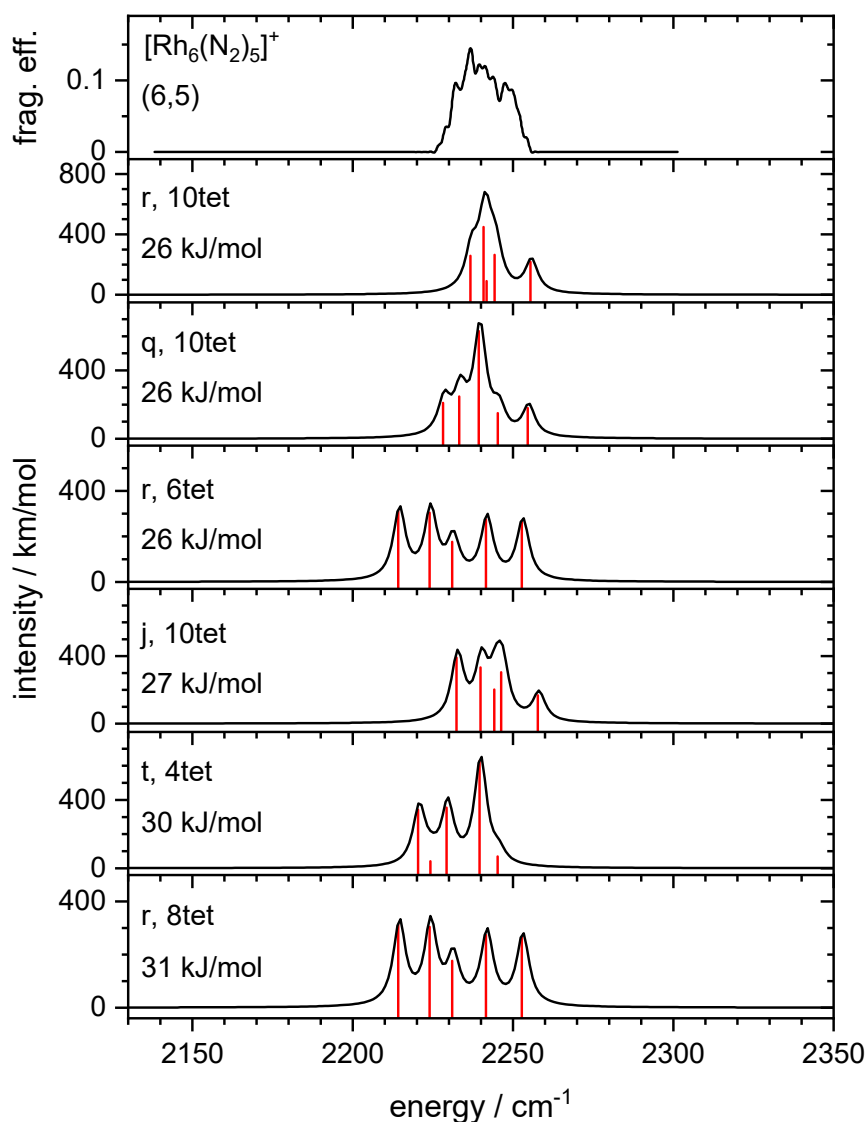


Fig. S11 Experimental IR-PD spectrum of the [Rh₆(N₂)₅]⁺ cluster adsorbate complex and calculated linear absorption spectra of the isomers between 26 and 31 kJ/mol above the most stable one (scaled by 0.9385). The line spectra were convoluted with a 5 cm⁻¹ FWHM Lorentzian. The letter indicates the arrangement of the N₂ molecules and is followed by spin multiplicity and the relative energy with respect to the most stable isomer.

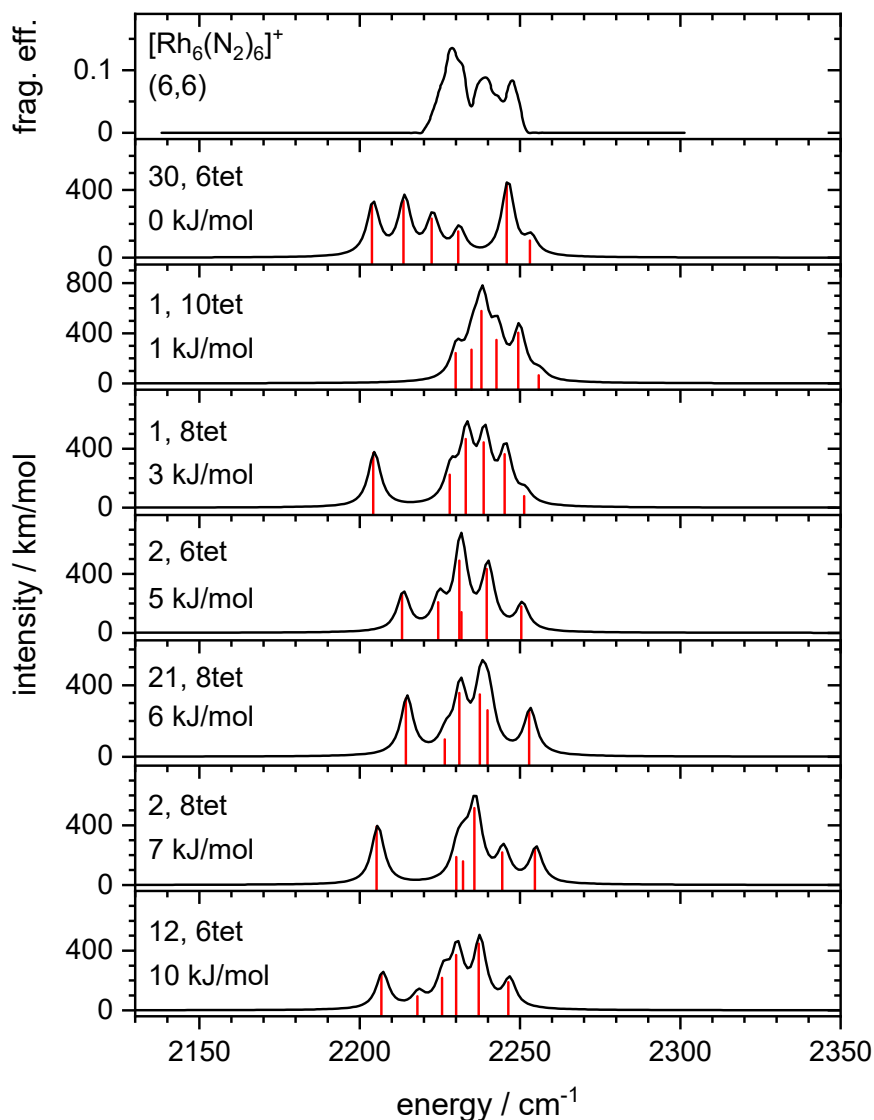


Fig. S12 Experimental IR-PD spectrum of the $[\text{Rh}_6(\text{N}_2)_6]^+$ cluster adsorbate complex and calculated linear absorption spectra of the isomers between 0 and 10 kJ/mol above the most stable one (scaled by 0.9385). The line spectra were convoluted with a 5 cm^{-1} FWHM Lorentzian. The letter indicates the arrangement of the N_2 molecules and is followed by spin multiplicity and the relative energy with respect to the most stable isomer.

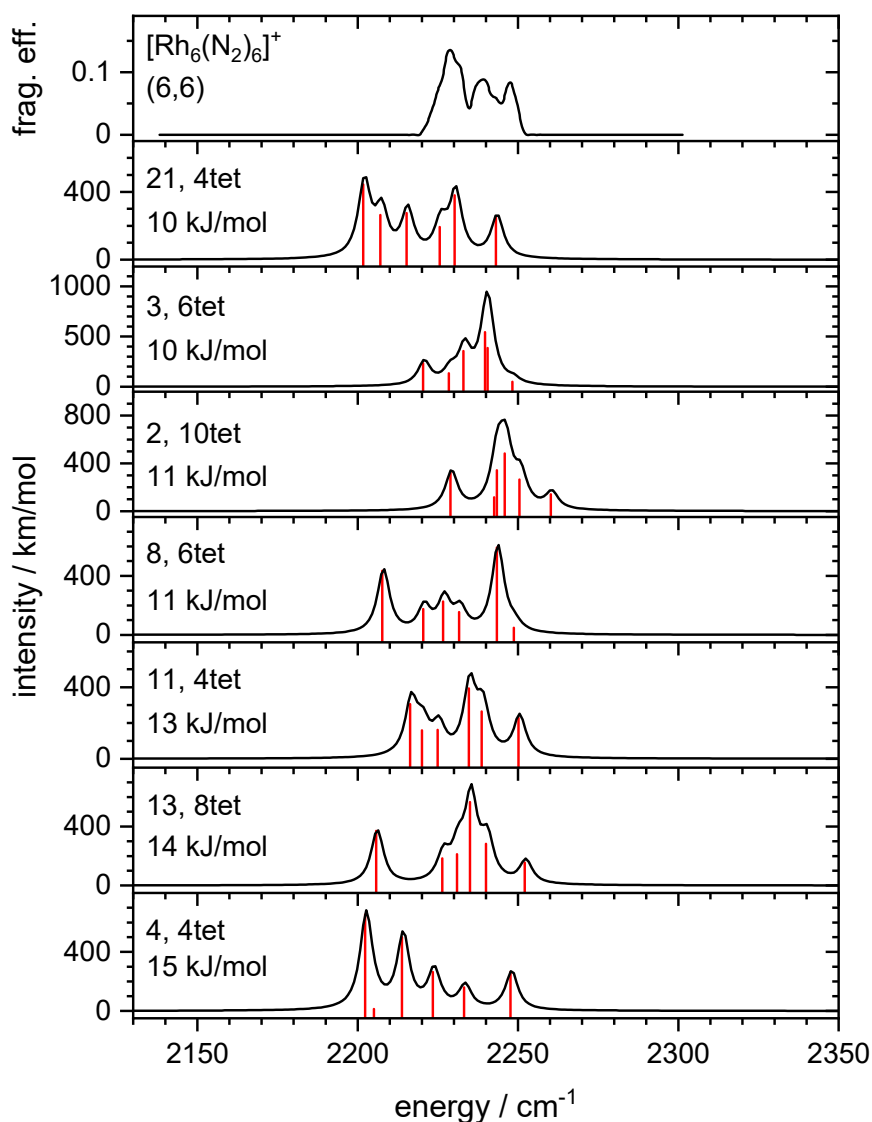


Fig. S13 Experimental IR-PD spectrum of the [Rh₆(N₂)₆]⁺ cluster adsorbate complex and calculated linear absorption spectra of the isomers between 10 and 15 kJ/mol above the most stable one (scaled by 0.9385). The line spectra were convoluted with a 5 cm⁻¹ FWHM Lorentzian. The letter indicates the arrangement of the N₂ molecules and is followed by spin multiplicity and the relative energy with respect to the most stable isomer.

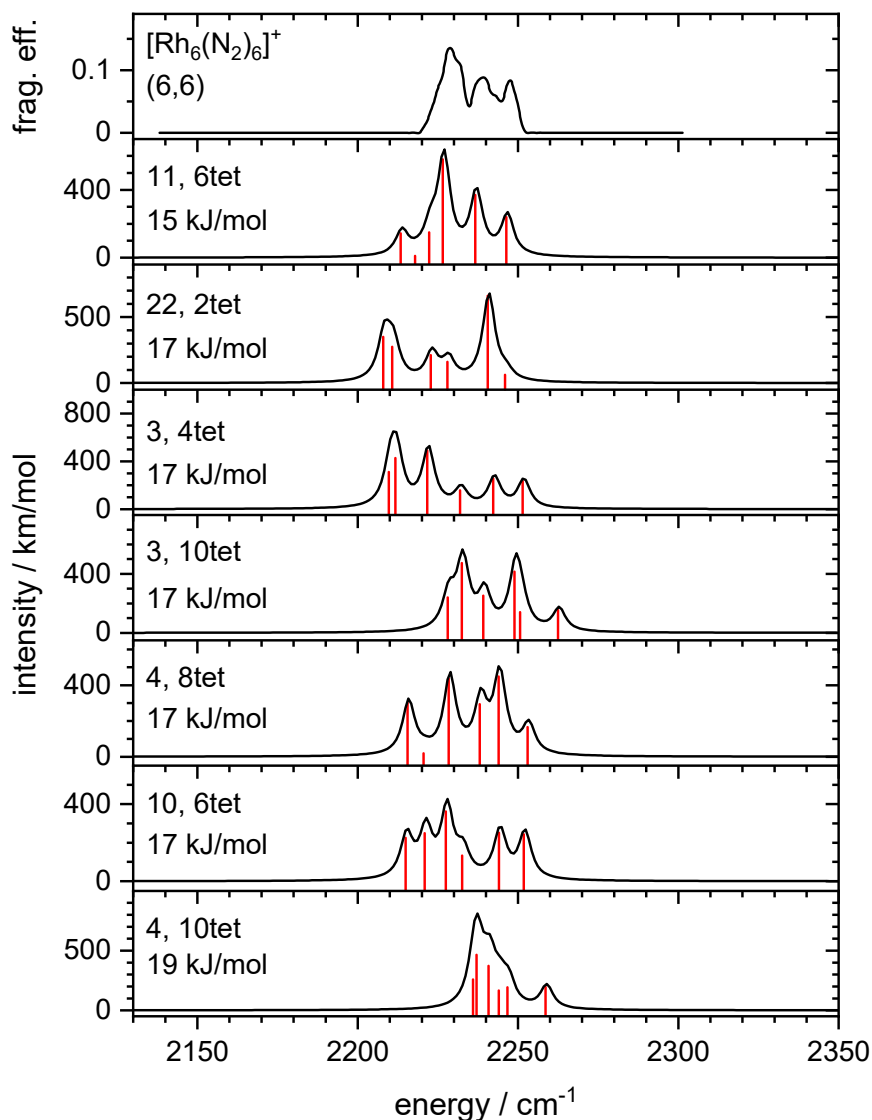


Fig. S14 Experimental IR-PD spectrum of the $[\text{Rh}_6(\text{N}_2)_6]^+$ cluster adsorbate complex and calculated linear absorption spectra of the isomers between 15 and 19 kJ/mol above the most stable one (scaled by 0.9385). The line spectra were convoluted with a 5 cm^{-1} FWHM Lorentzian. The letter indicates the arrangement of the N_2 molecules and is followed by spin multiplicity and the relative energy with respect to the most stable isomer.

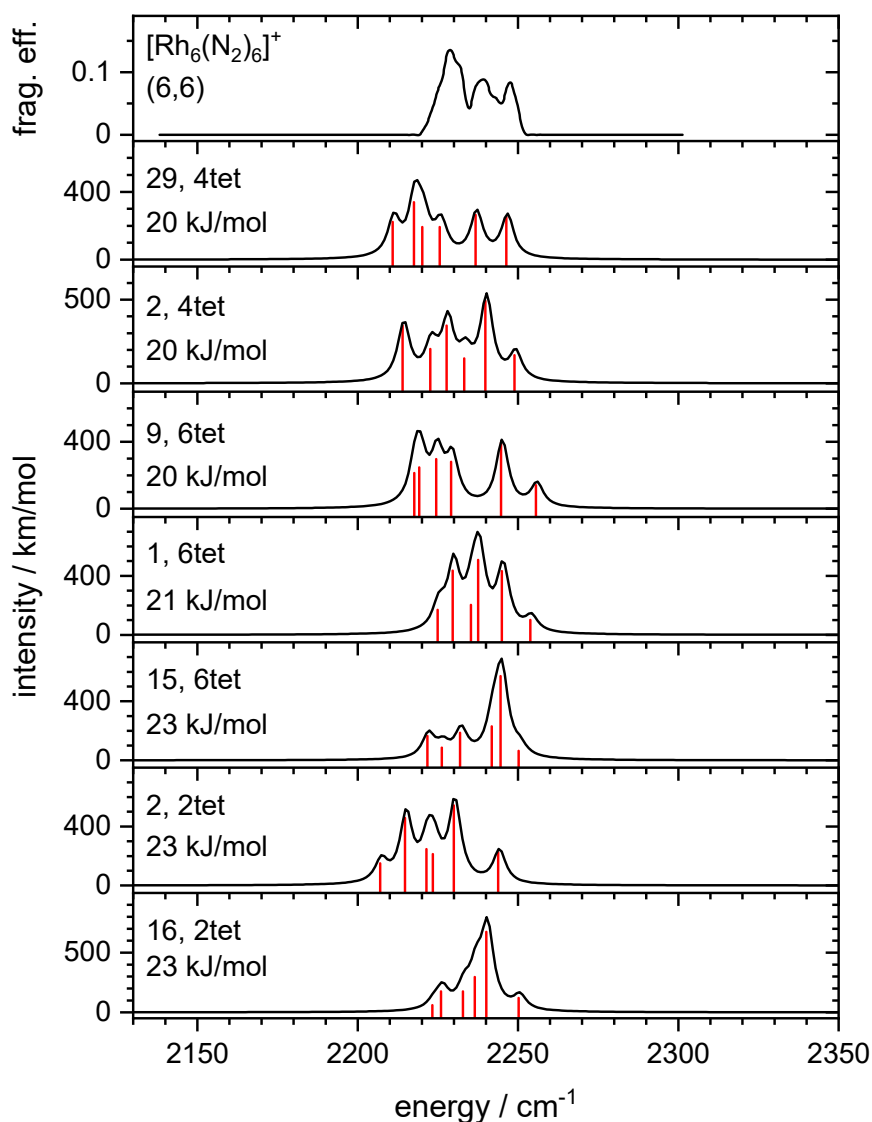


Fig. S15 Experimental IR-PD spectrum of the [Rh₆(N₂)₆]⁺ cluster adsorbate complex and calculated linear absorption spectra of the isomers between 20 and 23 kJ/mol above the most stable one (scaled by 0.9385). The line spectra were convoluted with a 5 cm⁻¹ FWHM Lorentzian. The letter indicates the arrangement of the N₂ molecules and is followed by spin multiplicity and the relative energy with respect to the most stable isomer.

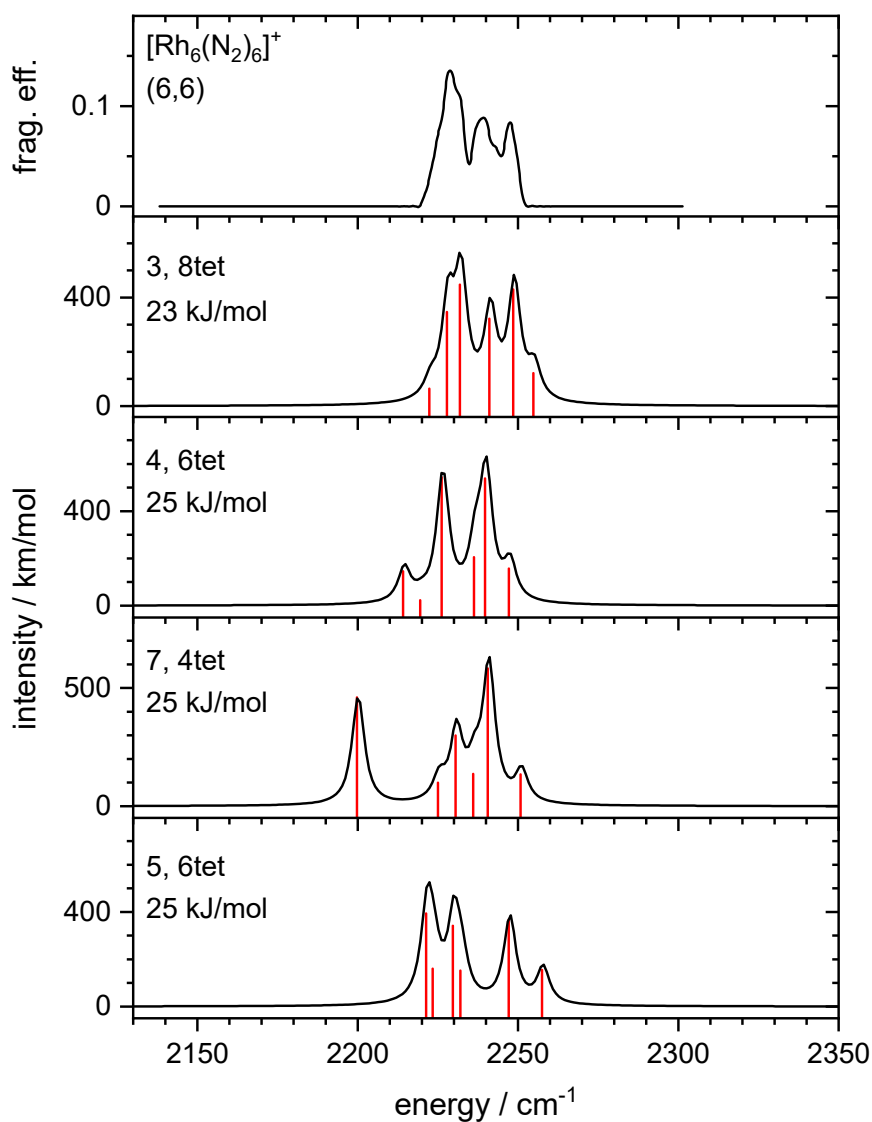


Fig. S16 Experimental IR-PD spectrum of the $[\text{Rh}_6(\text{N}_2)_6]^+$ cluster adsorbate complex and calculated linear absorption spectra of the isomers between 23 and 25 kJ/mol above the most stable one (scaled by 0.9385). The line spectra were convoluted with a 5 cm^{-1} FWHM Lorentzian. The letter indicates the arrangement of the N_2 molecules and is followed by spin multiplicity and the relative energy with respect to the most stable isomer.

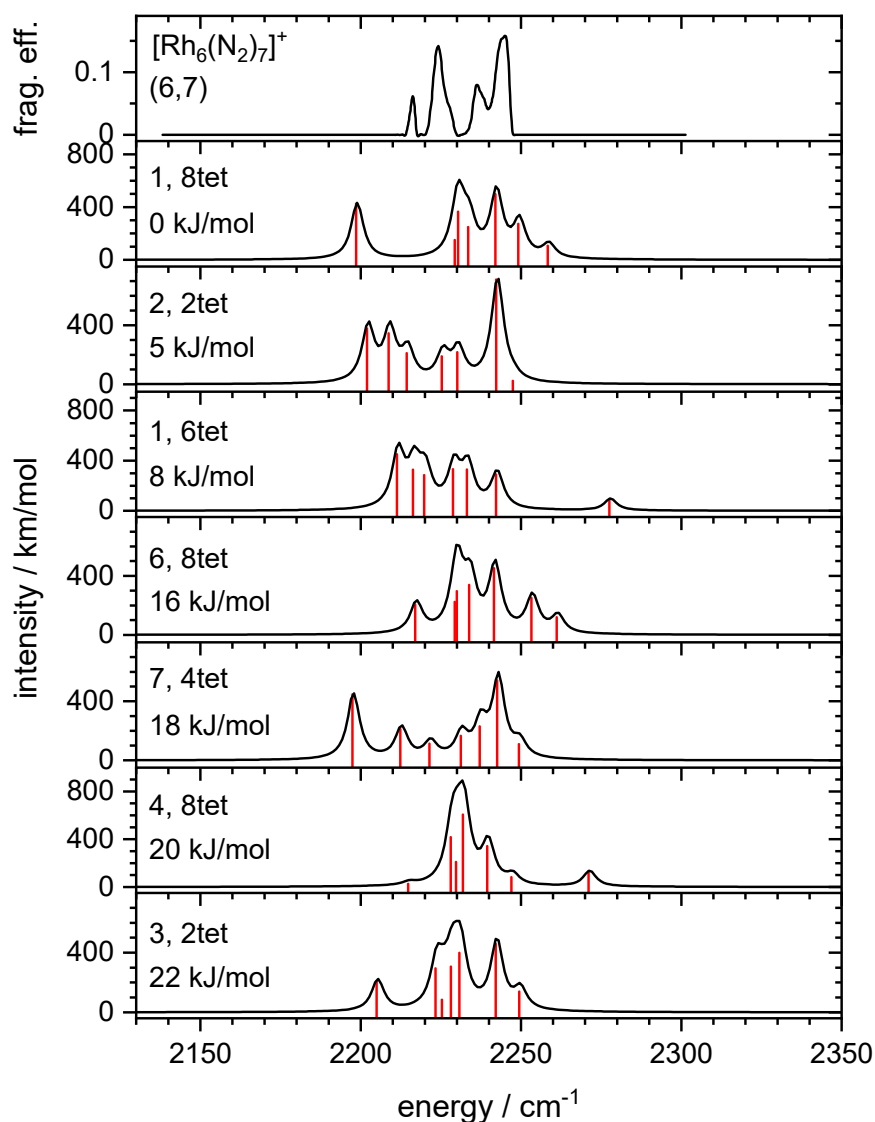


Fig. S17 Experimental IR-PD spectrum of the [Rh₆(N₂)₇]⁺ cluster adsorbate complex and calculated linear absorption spectra of the isomers between 0 and 22 kJ/mol above the most stable one (scaled by 0.9385). The line spectra were convoluted with a 5 cm⁻¹ FWHM Lorentzian. The letter indicates the arrangement of the N₂ molecules and is followed by spin multiplicity and the relative energy with respect to the most stable isomer.

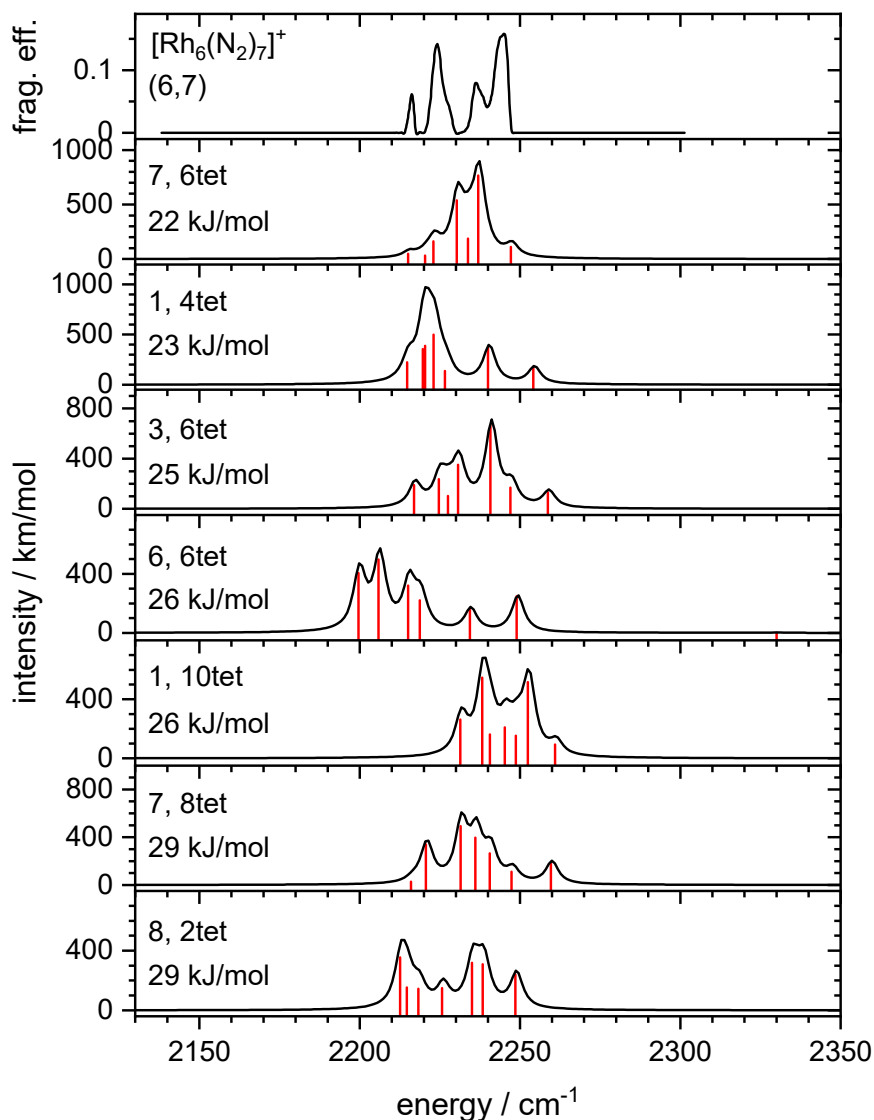


Fig. S18 Experimental IR-PD spectrum of the $[\text{Rh}_6(\text{N}_2)_7]^+$ cluster adsorbate complex and calculated linear absorption spectra of the isomers between 22 and 29 kJ/mol above the most stable one (scaled by 0.9385). The line spectra were convoluted with a 5 cm^{-1} FWHM Lorentzian. The letter indicates the arrangement of the N_2 molecules and is followed by spin multiplicity and the relative energy with respect to the most stable isomer.

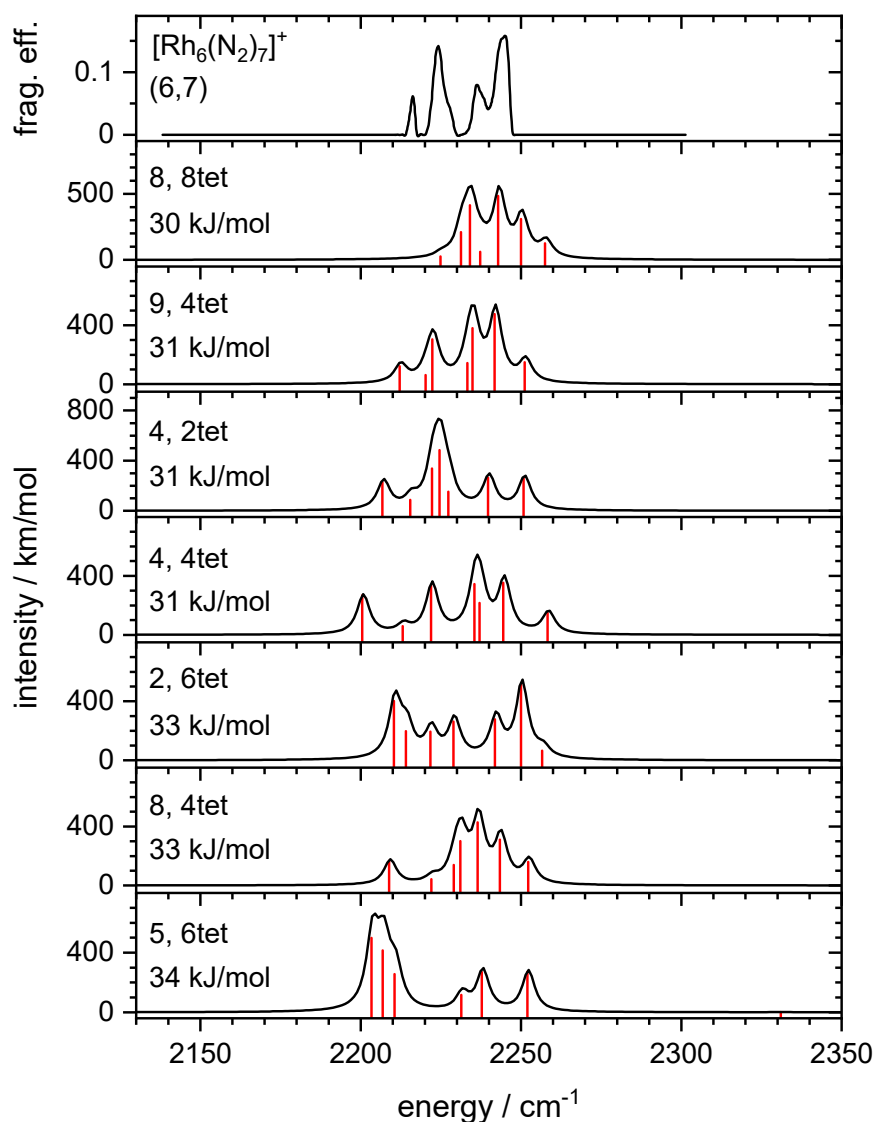


Fig. S19 Experimental IR-PD spectrum of the [Rh₆(N₂)₇]⁺ cluster adsorbate complex and calculated linear absorption spectra of the isomers between 30 and 34 kJ/mol above the most stable one (scaled by 0.9385). The line spectra were convoluted with a 5 cm⁻¹ FWHM Lorentzian. The letter indicates the arrangement of the N₂ molecules and is followed by spin multiplicity and the relative energy with respect to the most stable isomer.

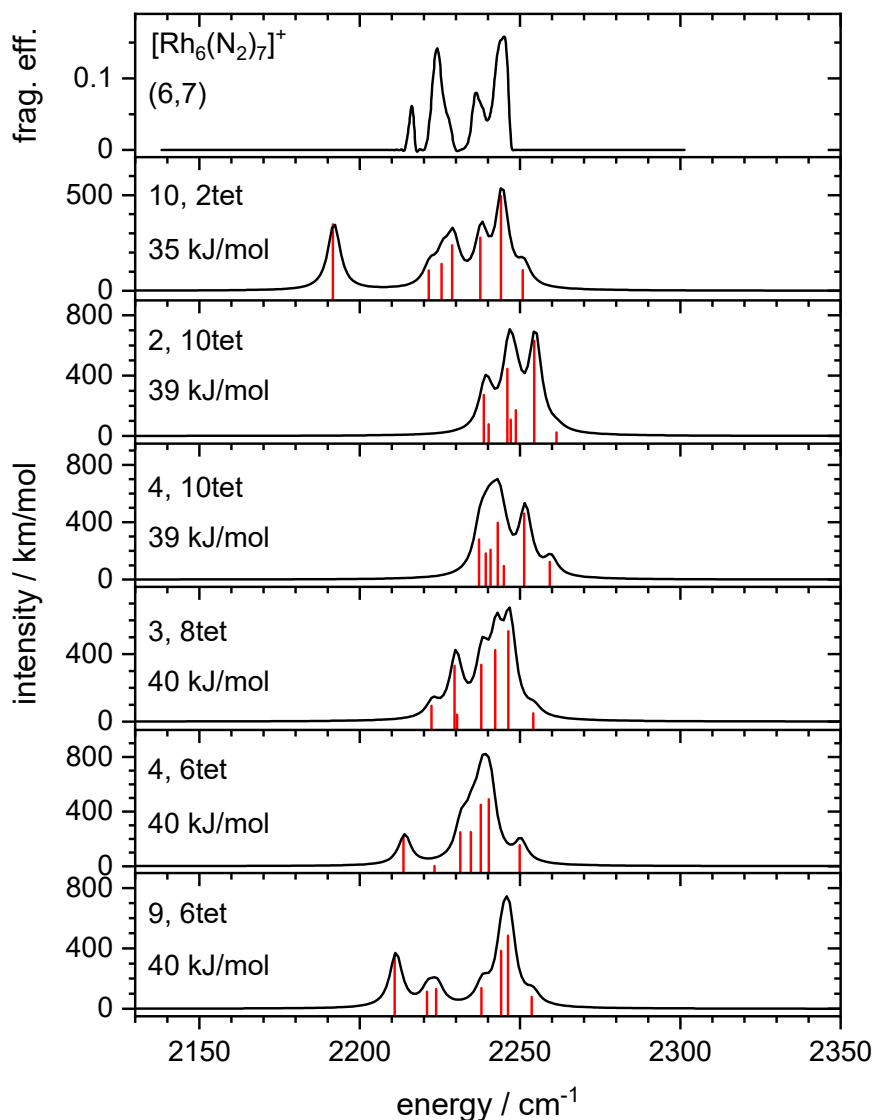


Fig. S20 Experimental IR-PD spectrum of the $[\text{Rh}_6(\text{N}_2)_7]^+$ cluster adsorbate complex and calculated linear absorption spectra of the isomers between 35 and 40 kJ/mol above the most stable one (scaled by 0.9385). The line spectra were convoluted with a 5 cm^{-1} FWHM Lorentzian. The letter indicates the arrangement of the N_2 molecules and is followed by spin multiplicity and the relative energy with respect to the most stable isomer.

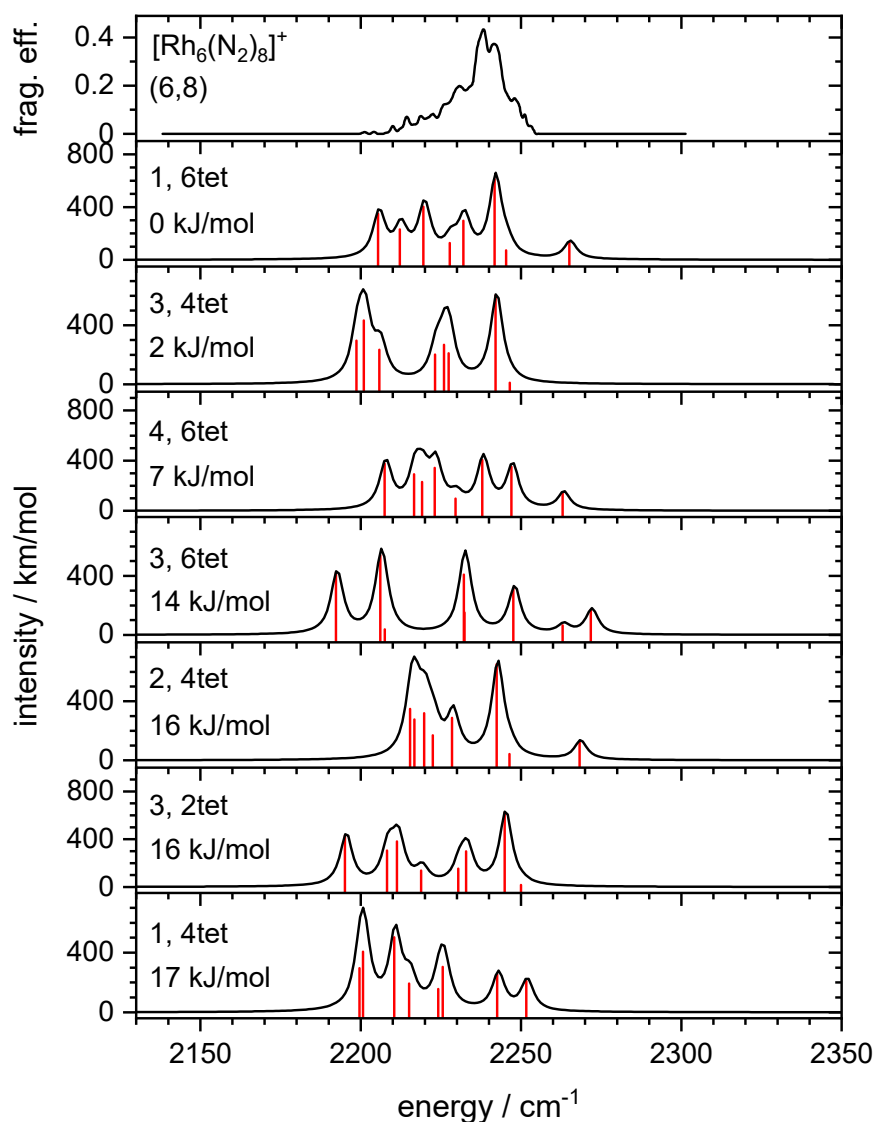


Fig. S21 Experimental IR-PD spectrum of the [Rh₆(N₂)₈]⁺ cluster adsorbate complex and calculated linear absorption spectra of the isomers between 0 and 17 kJ/mol above the most stable one (scaled by 0.9385). The line spectra were convoluted with a 5 cm⁻¹ FWHM Lorentzian. The letter indicates the arrangement of the N₂ molecules and is followed by spin multiplicity and the relative energy with respect to the most stable isomer.

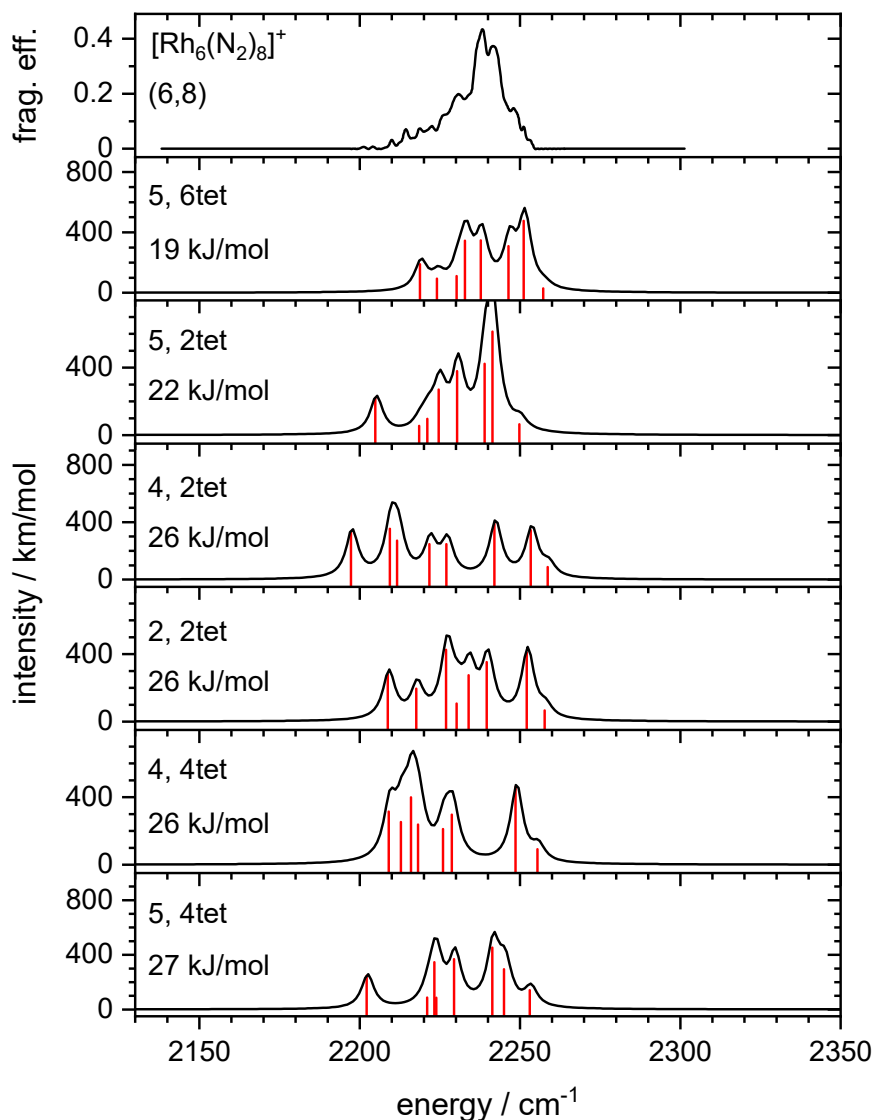


Fig. S22 Experimental IR-PD spectrum of the $[\text{Rh}_6(\text{N}_2)_8]^+$ cluster adsorbate complex and calculated linear absorption spectra of the isomers between 19 and 27 kJ/mol above the most stable one (scaled by 0.9385). The line spectra were convoluted with a 5 cm^{-1} FWHM Lorentzian. The letter indicates the arrangement of the N_2 molecules and is followed by spin multiplicity and the relative energy with respect to the most stable isomer.

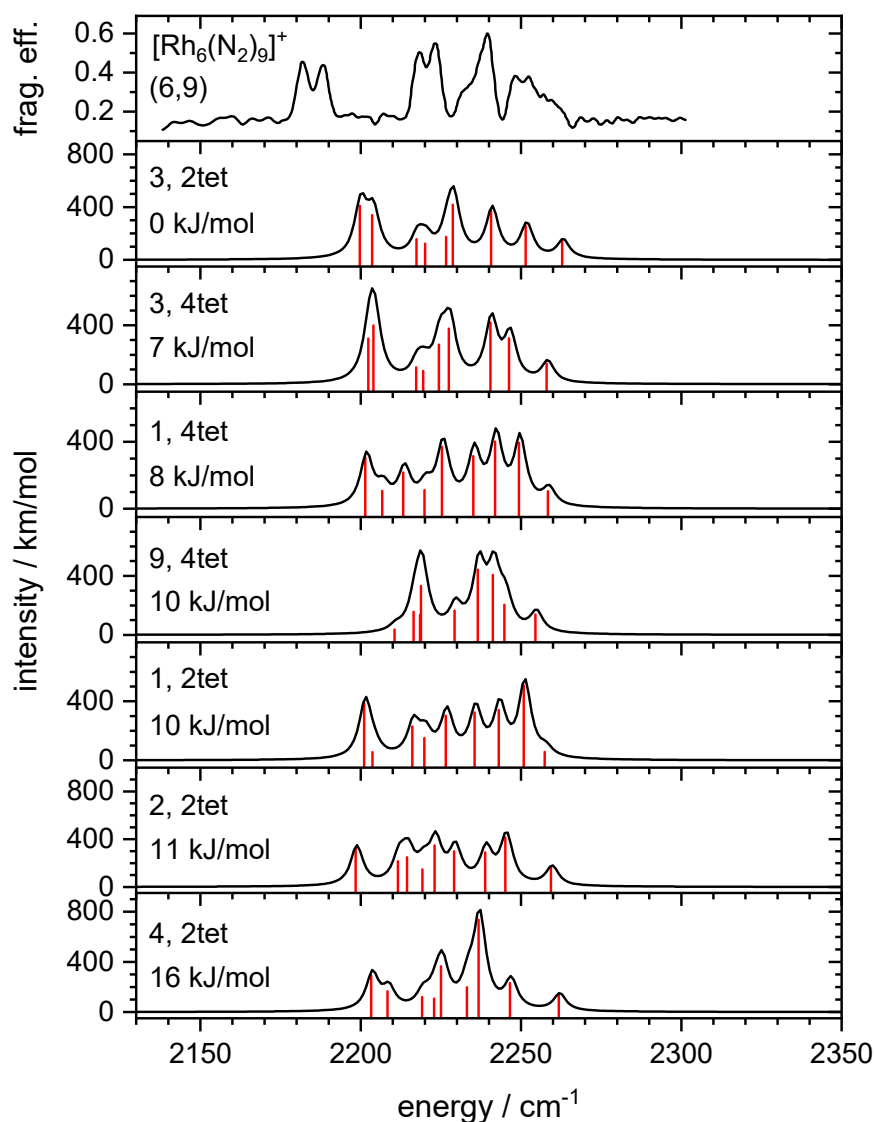


Fig. S23 Experimental IR-PD spectrum of the [Rh₆(N₂)₉]⁺ cluster adsorbate complex and calculated linear absorption spectra of the isomers between 0 and 16 kJ/mol above the most stable one (scaled by 0.9385). The line spectra were convoluted with a 5 cm⁻¹ FWHM Lorentzian. The letter indicates the arrangement of the N₂ molecules and is followed by spin multiplicity and the relative energy with respect to the most stable isomer.

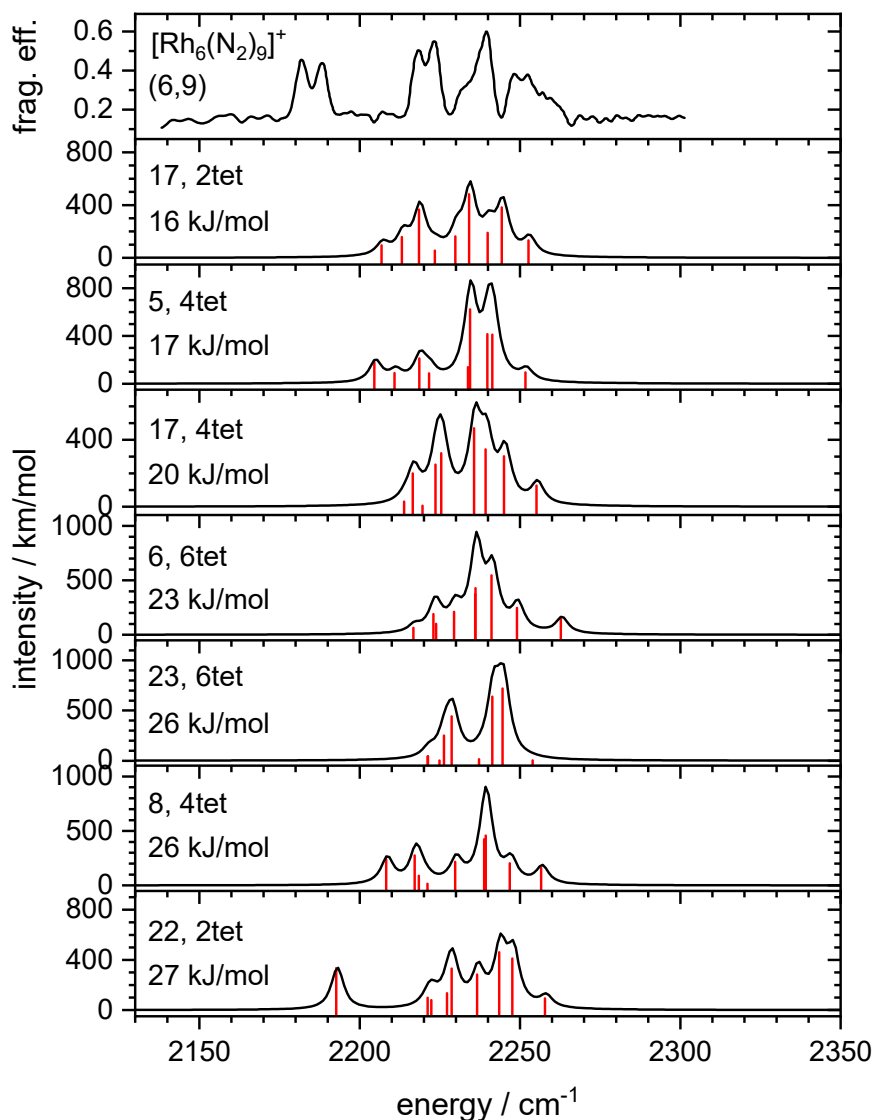


Fig. S24 Experimental IR-PD spectrum of the $[\text{Rh}_6(\text{N}_2)_9]^+$ cluster adsorbate complex and calculated linear absorption spectra of the isomers between 16 and 27 kJ/mol above the most stable one (scaled by 0.9385). The line spectra were convoluted with a 5 cm^{-1} FWHM Lorentzian. The letter indicates the arrangement of the N_2 molecules and is followed by spin multiplicity and the relative energy with respect to the most stable isomer.

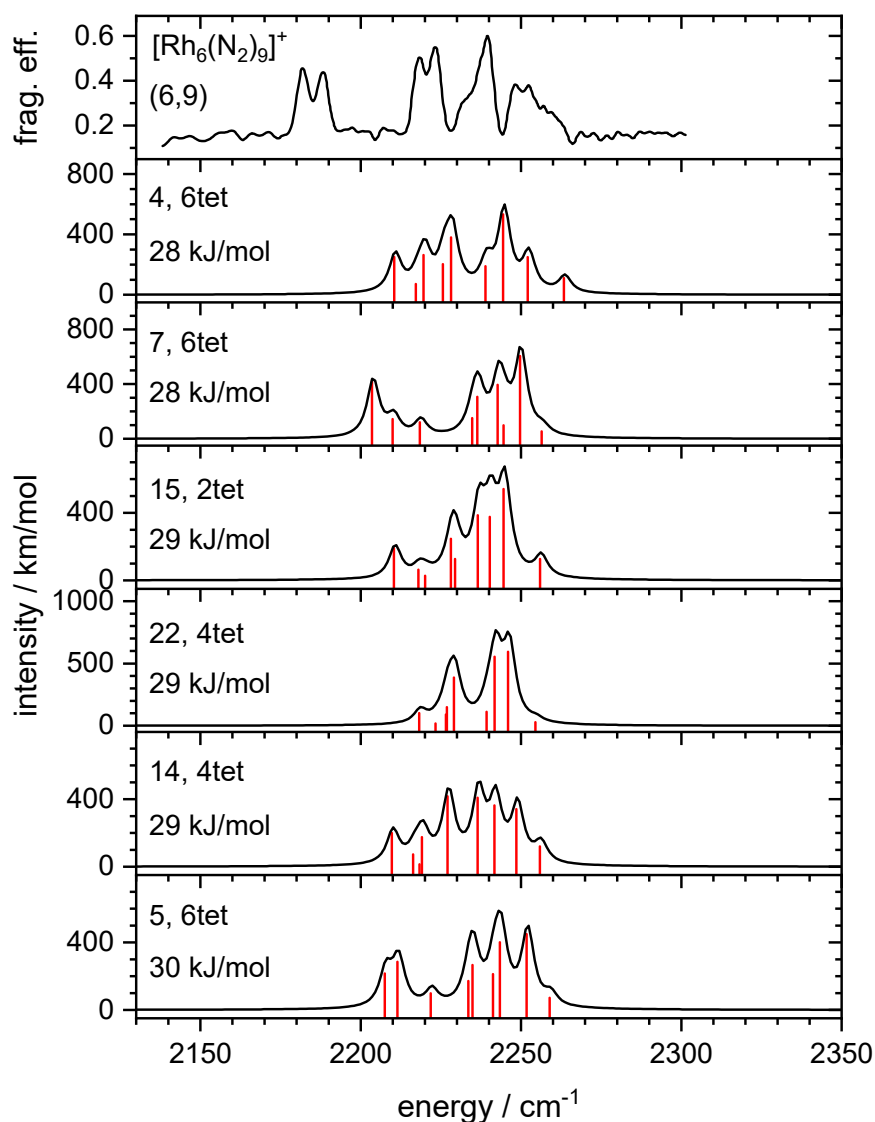


Fig. S25 Experimental IR-PD spectrum of the [Rh₆(N₂)₉]⁺ cluster adsorbate complex and calculated linear absorption spectra of the isomers between 28 and 30 kJ/mol above the most stable one (scaled by 0.9385). The line spectra were convoluted with a 5 cm⁻¹ FWHM Lorentzian. The letter indicates the arrangement of the N₂ molecules and is followed by spin multiplicity and the relative energy with respect to the most stable isomer.

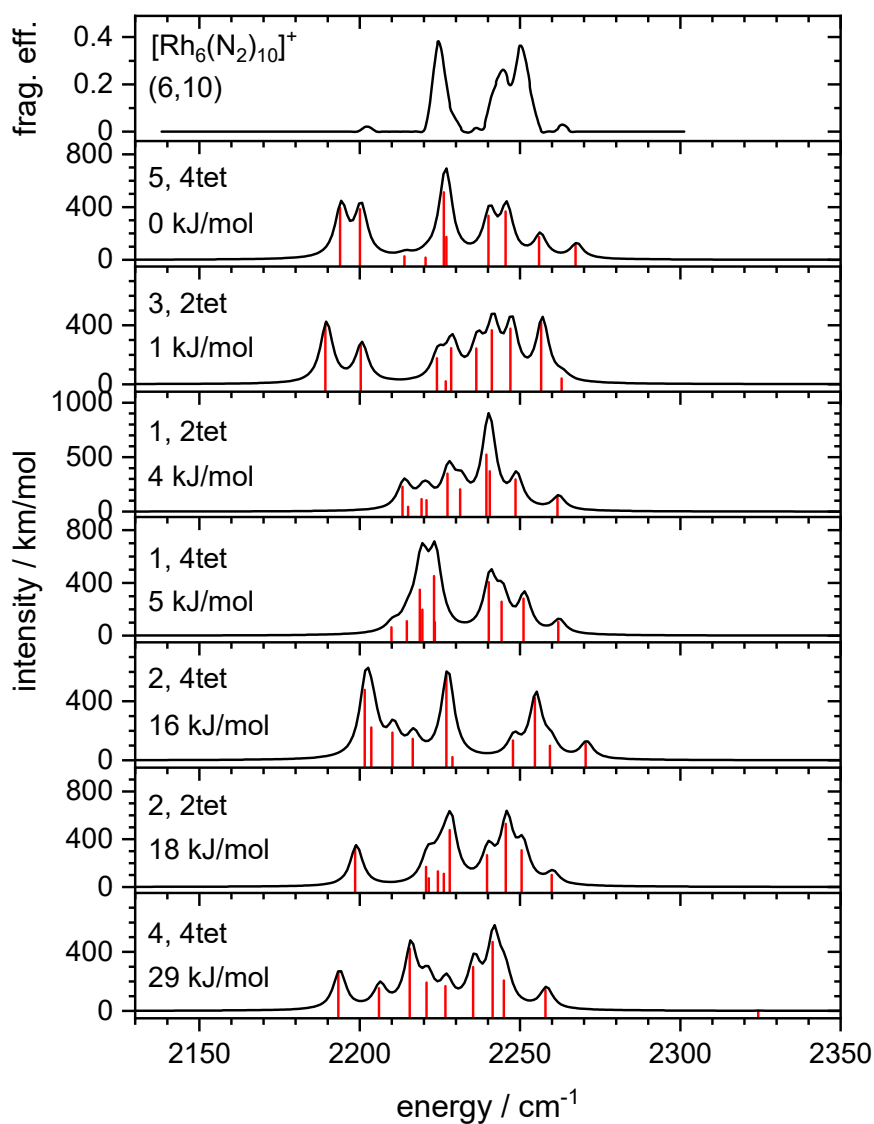


Fig. S26 Experimental IR-PD spectrum of the $[\text{Rh}_6(\text{N}_2)_{10}]^+$ cluster adsorbate complex and calculated linear absorption spectra of the isomers between 0 and 29 kJ/mol above the most stable one (scaled by 0.9385). The line spectra were convoluted with a 5 cm^{-1} FWHM Lorentzian. The letter indicates the arrangement of the N_2 molecules and is followed by spin multiplicity and the relative energy with respect to the most stable isomer.

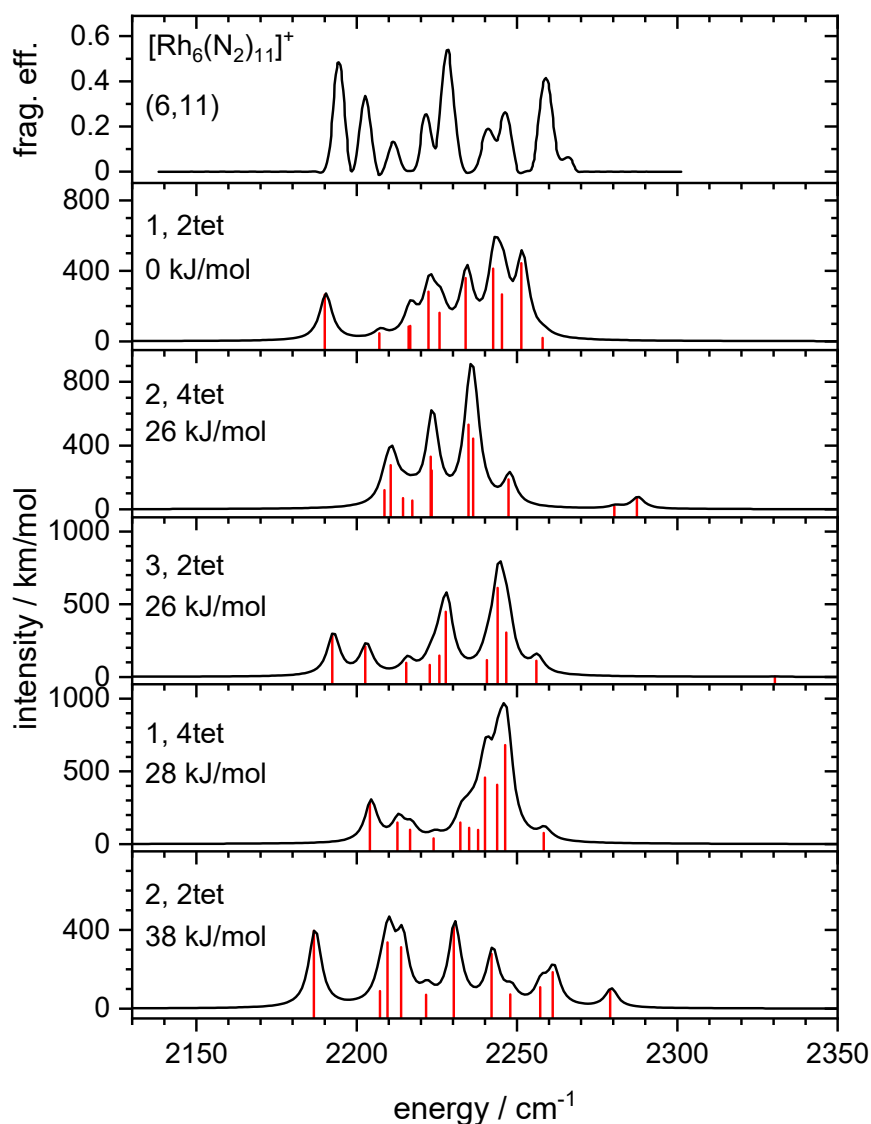


Fig. S27 Experimental IR-PD spectrum of the [Rh₆(N₂)₁₁]⁺ cluster adsorbate complex and calculated linear absorption spectra of the isomers between 0 and 38 kJ/mol above the most stable one (scaled by 0.9385). The line spectra were convoluted with a 5 cm⁻¹ FWHM Lorentzian. The letter indicates the arrangement of the N₂ molecules and is followed by spin multiplicity and the relative energy with respect to the most stable isomer.

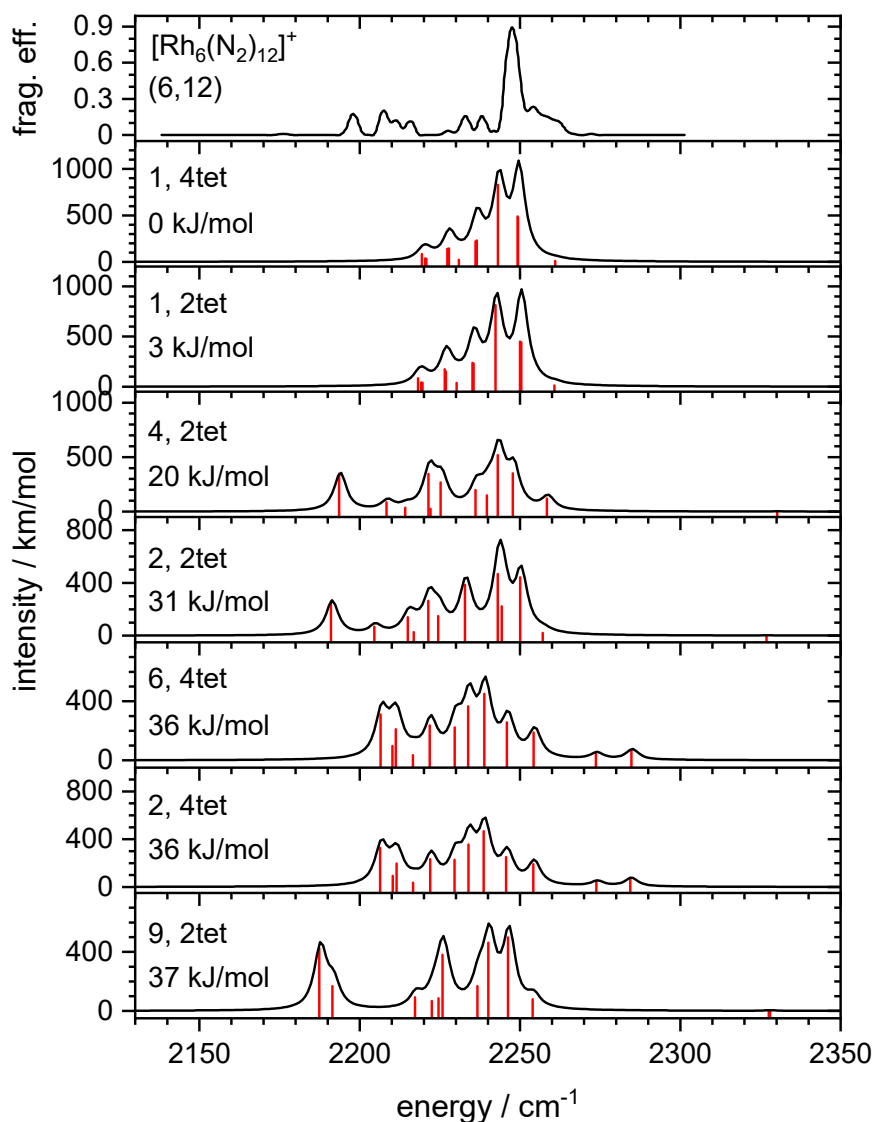


Fig. S28 Experimental IR-PD spectrum of the $[\text{Rh}_6(\text{N}_2)_{12}]^+$ cluster adsorbate complex and calculated linear absorption spectra of the isomers between 0 and 37 kJ/mol above the most stable one (scaled by 0.9385). The line spectra were convoluted with a 5 cm^{-1} FWHM Lorentzian. The letter indicates the arrangement of the N_2 molecules and is followed by spin multiplicity and the relative energy with respect to the most stable isomer.

Text S1 Coordinates of the assigned isomers**¹⁰(6,0)**

scf done: -662.945081

Rh	0.739432	-1.110562	-1.003755
Rh	-0.353738	-0.686303	2.454242
Rh	0.263606	0.929208	0.500110
Rh	-1.548854	-0.929320	0.236788
Rh	0.115323	-2.687683	0.978060
Rh	1.957221	-0.861220	1.255095

¹⁰(6,1)_a

scf done: -772.411628

Rh	1.234736	0.753996	-0.357270
Rh	-1.500978	-1.828946	-0.001732
Rh	-0.870068	0.038582	-1.655187
Rh	0.819524	-1.783507	-1.202269
Rh	0.654665	-1.175946	1.243522
Rh	-1.112018	0.638087	0.828092
N	1.620163	2.646177	0.218463
N	1.826320	3.676656	0.532874

¹⁰(6,2)_c

scf done: -881.878289

Rh	0.997415	0.652165	0.406436
Rh	-1.130253	-2.372745	0.341113
Rh	-0.889309	-0.241172	-1.121063
Rh	1.215232	-1.693094	-0.735815
Rh	0.777599	-1.607958	1.808392
Rh	-1.239423	-0.125815	1.480634
N	1.097179	2.434956	-0.521863
N	1.155627	3.412882	-1.015927
N	3.042868	-1.311937	-1.494629
N	4.037963	-1.107882	-1.908478

¹⁰(6,2)_d

scf done: -881.877387

Rh	0.937586	0.632803	0.686626
Rh	-0.988715	-2.502468	-0.121657
Rh	-0.643032	-0.166927	-1.267242
Rh	1.341934	-1.632134	-0.539698
Rh	0.647958	-1.691501	1.913892
Rh	-1.413220	-0.382094	1.177511
N	1.193249	2.419012	-0.203320
N	1.339246	3.396247	-0.680362
N	1.845905	-1.111542	3.413546
N	2.500392	-0.801598	4.237905

¹⁰(6,3)_e

scf done: -991.343163

Rh	0.655995	1.439079	-0.002119
Rh	-0.574977	-2.012454	0.713098
Rh	-0.094346	-0.590154	-1.479052
Rh	1.793499	-0.909652	0.262012
Rh	0.196415	-0.062224	2.116261
Rh	-1.638006	0.258932	0.415437
N	-0.104767	3.310610	0.001356
N	-0.509217	4.330174	0.008932
N	0.087449	0.396768	-3.236284
N	0.187814	0.928424	-4.189876
N	3.593167	-0.068661	0.044213
N	4.589574	0.373858	-0.084178

¹⁰(6,4)_o

scf done: -1100.805909

Rh	0.464793	0.707362	-0.128922
Rh	-0.403773	-2.618286	0.856643
Rh	-1.539952	-0.852078	-0.770548
Rh	0.954088	-1.598085	-1.084278
Rh	1.488035	-1.029948	1.487806
Rh	-1.052109	-0.332431	1.741730
N	-0.212689	2.653371	-0.304859
N	-0.585819	3.677545	-0.409492
N	-2.557331	0.458629	-1.952039
N	-3.093137	1.172219	-2.589009
N	2.413874	-0.936685	-2.303804
N	3.224009	-0.588706	-2.956483
N	2.093876	-0.469557	3.354959
N	2.418434	-0.165751	4.356896

¹⁰(6,5)_v

scf done: -1210.268436

Rh	1.563776	1.491527	-0.834326
Rh	-1.113287	-0.701631	0.597092
Rh	-0.365492	-0.208009	-1.859083
Rh	1.363370	-0.959312	-0.130065
Rh	0.697455	0.893509	1.558898
Rh	-0.899152	1.742148	-0.350813
N	3.012091	2.878793	-0.390138
N	3.772783	3.623643	-0.132139
N	-1.741571	-1.308496	-2.914882
N	-2.491009	-1.893701	-3.458846
N	2.781746	-1.869143	-1.291586
N	3.534835	-2.335547	-1.936027
N	1.859989	0.244075	3.089111
N	2.478635	-0.125438	3.915913
N	-1.314272	-2.552299	1.402971
N	-1.407194	-3.548719	1.851721

Table S4 Positive charge and spin localized on the Rh₆ cluster core dependent on adsorbed N₂ molecules m and the corresponding charge and spin per adsorbed N₂ molecule for the assigned isomers.

m	charge				spin			
	total	on Rh6 core	on m N ₂	per N ₂	total	on Rh6 core	on m N ₂	per N ₂
0	1	1	--	--	9	9	--	--
1	1	0.988	0.012	0.012	9	8.972	-7.972	0.028
2	1	0.975	0.025	0.0125	9	8.941	-7.941	0.0295
3	1	0.964	0.036	0.012	9	8.943	-7.943	0.019
4	1	0.935	0.065	0.01625	9	8.877	-7.877	0.03075
5	1	0.915	0.085	0.017	9	8.842	-7.842	0.0316

Summary of Natural Population Analysis:**Sum of alpha and beta spin orbitals**

Atom	No	Natural Charge	Natural Population				Natural Spin Density	
			Core	Valence	Rydberg	Total		
Rh	1	0.05687	35.98949	8.88348	0.07016	44.94313	1.24862	
Rh	2	0.17038	35.99154	8.78103	0.05706	44.82962	1.59815	
Rh	3	0.1869	35.99083	8.76147	0.0608	44.8131	1.54088	
Rh	4	0.15247	35.9907	8.80145	0.05537	44.84753	1.50594	
Rh	5	0.18654	35.99082	8.76174	0.0609	44.81346	1.541	
Rh	6	0.23531	35.99183	8.72005	0.05282	44.76469	1.53706	
N	7	-0.10875	1.99959	5.04104	0.06812	7.10875	0.02811	
N	8	0.1203	1.9997	4.83905	0.04096	6.8797	0.00023	
* Total *			1	219.94449	62.58932	0.46619	283	9

Alpha spin orbitals

Atom	No	Natural Charge	Natural Population				
			Core	Valence	Rydberg	Total	
Rh	1	-0.59588	17.9955	5.0707	0.02969	23.09588	
Rh	2	-0.71389	17.99698	5.19342	0.02349	23.21389	
Rh	3	-0.67699	17.99658	5.15572	0.0247	23.17699	
Rh	4	-0.67673	17.99639	5.15648	0.02387	23.17673	
Rh	5	-0.67723	17.99657	5.15592	0.02474	23.17723	
Rh	6	-0.65088	17.99693	5.13245	0.0215	23.15088	
N	7	-0.06843	0.9998	2.53139	0.03724	3.56843	
N	8	0.06003	0.99985	2.41948	0.02064	3.43997	
* Total *			-4	109.97859	35.81555	0.20586	146

Beta spin orbitals

Atom	No	Natural Charge	Natural Population				
			Core	Valence	Rydberg	Total	
Rh	1	0.65274	17.994	3.81278	0.04048	21.84726	
Rh	2	0.88427	17.99456	3.5876	0.03357	21.61573	
Rh	3	0.86389	17.99425	3.60575	0.03611	21.63611	
Rh	4	0.82921	17.99432	3.64498	0.0315	21.67079	
Rh	5	0.86377	17.99425	3.60582	0.03616	21.63623	
Rh	6	0.88618	17.99489	3.5876	0.03132	21.61382	
N	7	-0.04032	0.99979	2.50965	0.03088	3.54032	
N	8	0.06026	0.99985	2.41958	0.02031	3.43974	
* Total *			5	109.96591	26.77377	0.26033	137

Fig. S29 Total charges and spins from Natural Population Analysis of $^{10}(6,1)_a$.

5. Cryospectroscopy and Spin Quenching in the N₂ Adsorption onto a Rh₆⁺ Cluster Cation

alpha		beta	
#328	52. (1.00000) 88.1340% LP (1) N 7	8.547% Rh 1 s(26.93%)p 0.01(0.32%)d 2.70(72.74%)	
		0.316% Rh 2 s(35.57%)p 0.03(0.92%)d 1.79(63.51%)	
		0.188% Rh 3 s(16.94%)p 0.39(6.62%)d 4.51(76.45%)	
		2.014% Rh 4 s(14.48%)p 0.20(2.89%)d 5.71(82.63%)	
		0.196% Rh 5 s(18.27%)p 0.36(6.60%)d 4.11(75.12%)	
		0.367% Rh 6 s(22.14%)p 0.06(1.32%)d 3.46(76.55%)	
		88.139% N 7 s(58.57%)p 0.71(41.40%)d 0.00(0.01%)	
		f 0.00(0.02%)	
		0.234% N 8 s(65.60%)p 0.47(30.91%)d 0.04(2.65%)	
		f 0.01(0.83%)	
#32	32. (1.00000) 96.3530% LP (3)Rh 1	#320	44. (1.00000) 96.3522% LP (1)Rh 1
	96.361% Rh 1 s(0.13%)p 0.35(0.04%)d99.99(99.83%)		96.357% Rh 1 s(0.00%)p 1.00(0.01%)d99.99(99.99%)
	0.050% Rh 2 s(93.65%)p 0.04(3.61%)d 0.03(2.74%)		0.017% Rh 2 s(0.08%)p 6.54(0.53%)d99.99(99.39%)
	0.014% Rh 3 s(12.00%)p 2.47(29.71%)d 4.86(58.29%)		0.036% Rh 3 s(3.24%)p10.52(34.04%)d19.39(62.73%)
	0.255% Rh 4 s(87.76%)p 0.06(5.46%)d 0.08(6.78%)		0.034% Rh 4 s(0.01%)p 1.00(39.44%)d 1.54(60.55%)
	0.015% Rh 5 s(13.02%)p 2.20(28.70%)d 4.48(58.28%)		0.037% Rh 5 s(2.93%)p11.67(34.19%)d21.46(62.88%)
	0.112% Rh 6 s(79.78%)p 0.11(8.98%)d 0.14(11.24%)		0.018% Rh 6 s(0.27%)p99.99(55.90%)d99.99(43.83%)
	1.543% N 7 s(2.50%)p38.60(96.64%)d 0.32(0.80%)		1.608% N 7 s(0.00%)p 1.00(99.03%)d 0.01(0.92%)
	f 0.02(0.05%)		f 0.00(0.06%)
	1.650% N 8 s(0.14%)p99.99(99.81%)d 0.13(0.02%)		1.894% N 8 s(0.00%)p 1.00(99.93%)d 0.00(0.04%)
	f 0.22(0.03%)		f 0.00(0.03%)
#33	33. (1.00000) 95.8841% LP (4)Rh 1	#321	45. (1.00000) 89.7592% LP (2)Rh 1
	95.884% Rh 1 s(0.00%)p 1.00(0.08%)d99.99(99.92%)		89.822% Rh 1 s(1.90%)p 0.01(0.01%)d51.75(98.09%)
	0.333% Rh 2 s(91.33%)p 0.02(2.05%)d 0.07(6.62%)		4.043% Rh 2 s(23.93%)p 0.01(0.28%)d 3.17(75.79%)
	0.023% Rh 3 s(0.65%)p48.44(31.44%)d99.99(67.91%)		1.050% Rh 3 s(0.91%)p 1.06(0.97%)d99.99(98.12%)
	0.341% Rh 4 s(91.70%)p 0.02(1.94%)d 0.07(6.36%)		0.480% Rh 4 s(1.30%)p 1.30(1.69%)d74.46(97.00%)
	0.012% Rh 5 s(1.94%)p 2.31(4.47%)d48.22(93.59%)		0.989% Rh 5 s(1.51%)p 0.65(0.99%)d64.55(97.50%)
	1.607% N 7 s(0.00%)p 1.00(99.19%)d 0.01(0.75%)		0.410% Rh 6 s(2.83%)p 1.21(3.41%)d33.17(93.76%)
	f 0.00(0.05%)		1.537% N 7 s(1.52%)p64.32(97.46%)d 0.64(0.98%)
	1.792% N 8 s(0.00%)p 1.00(99.96%)d 0.00(0.01%)		f 0.03(0.05%)
	f 0.00(0.03%)		1.668% N 8 s(0.03%)p99.99(99.91%)d 0.93(0.03%)
			f 0.82(0.03%)
#34	34. (1.00000) 95.3847% LP (5)Rh 1		
	95.396% Rh 1 s(5.30%)p 0.04(0.22%)d17.83(94.48%)		
	0.698% Rh 2 s(95.88%)p 0.04(3.40%)d 0.01(0.71%)		
	0.118% Rh 3 s(80.17%)p 0.17(13.89%)d 0.07(5.94%)		
	0.765% Rh 4 s(93.73%)p 0.02(2.19%)d 0.04(4.09%)		
	0.110% Rh 5 s(78.86%)p 0.18(14.54%)d 0.08(6.60%)		
	1.898% Rh 6 s(95.31%)p 0.04(3.70%)d 0.01(0.99%)		
	0.847% N 7 s(65.31%)p 0.50(32.88%)d 0.03(1.76%)		
	f 0.00(0.05%)		
	0.168% N 8 s(14.03%)p 6.11(85.74%)d 0.01(0.17%)		

Fig. S30 Composition of the NLMOs depicted in Figs 9 and 10.

		alpha	beta
#1	1. (1.00000)	99.9300% BD (1) N 7- N 8 0.034% Rh 1 s(15.51%)p 2.40(37.27%)d 3.04(47.21%) 0.010% Rh 4 s(93.32%)p 0.04(3.36%)d 0.04(3.32%) 0.016% Rh 6 s(72.63%)p 0.28(20.20%)d 0.10(7.17%) 53.629% N 7 s(5.92%)p15.84(93.79%)d 0.04(0.25%) f 0.01(0.04%) 46.307% N 8 s(5.21%)p18.09(94.24%)d 0.10(0.52%) f 0.01(0.03%)	#291 15. (1.00000) 99.8847% BD (1) N 7- N 8 0.071% Rh 1 s(48.75%)p 0.47(22.82%)d 0.58(28.43%) 0.018% Rh 6 s(38.91%)p 0.56(21.67%)d 1.01(39.41%) 51.810% N 7 s(34.79%)p 1.86(64.82%)d 0.01(0.31%) f 0.00(0.09%) 48.083% N 8 s(31.80%)p 2.13(67.66%)d 0.02(0.48%) f 0.00(0.06%)
#2	2. (1.00000)	99.9166% BD (2) N 7- N 8 0.036% Rh 1 s(0.00%)p 1.00(46.28%)d 1.16(53.72%) 0.023% Rh 3 s(89.80%)p 0.08(7.43%)d 0.03(2.76%) 0.023% Rh 5 s(89.77%)p 0.08(7.48%)d 0.03(2.75%) 53.800% N 7 s(0.00%)p 1.00(99.74%)d 0.00(0.23%) f 0.00(0.03%) 46.117% N 8 s(0.00%)p 1.00(99.45%)d 0.01(0.53%) f 0.00(0.03%)	#292 16. (1.00000) 99.7710% BD (2) N 7- N 8 0.105% Rh 1 s(18.90%)p 0.82(15.45%)d 3.47(65.64%) 0.020% Rh 2 s(23.91%)p 0.05(1.14%)d 3.14(74.96%) 0.032% Rh 3 s(7.00%)p 0.18(1.27%)d13.10(91.73%) 0.028% Rh 4 s(19.82%)p 0.34(6.68%)d 3.71(73.51%) 0.013% Rh 5 s(4.59%)p 0.74(3.37%)d20.06(92.04%) 0.022% Rh 6 s(69.95%)p 0.19(13.36%)d 0.24(16.69%) 53.388% N 7 s(7.43%)p12.43(92.29%)d 0.03(0.24%) f 0.01(0.04%) 46.392% N 8 s(7.13%)p12.95(92.32%)d 0.07(0.51%) f 0.00(0.03%)
#3	3. (1.00000)	99.8743% BD (3) N 7- N 8 0.080% Rh 1 s(54.48%)p 0.43(23.24%)d 0.41(22.28%) 0.025% Rh 6 s(83.61%)p 0.10(8.03%)d 0.10(8.35%) 51.686% N 7 s(36.11%)p 1.76(63.48%)d 0.01(0.32%) f 0.00(0.09%) 48.196% N 8 s(33.88%)p 1.94(65.58%)d 0.01(0.48%) f 0.00(0.06%)	#293 17. (1.00000) 99.7636% BD (3) N 7- N 8 0.122% Rh 1 s(0.51%)p30.33(15.43%)d99.99(84.07%) 0.038% Rh 3 s(32.86%)p 0.15(4.86%)d 1.90(62.29%) 0.063% Rh 5 s(23.90%)p 0.13(3.05%)d 3.06(73.05%) 54.035% N 7 s(0.24%)p99.99(99.50%)d 0.96(0.23%) f 0.14(0.03%) 45.729% N 8 s(0.23%)p99.99(99.21%)d 2.27(0.53%) f 0.11(0.03%)
#61	61. (1.00000)	91.3072% LP (1) N 7 7.424% Rh 1 s(90.43%)p 0.00(0.45%)d 0.10(9.12%) 0.147% Rh 2 s(94.98%)p 0.05(4.64%)d 0.00(0.38%) 0.049% Rh 3 s(80.12%)p 0.17(13.25%)d 0.08(6.63%) 0.210% Rh 4 s(78.64%)p 0.25(19.65%)d 0.02(1.70%) 0.046% Rh 5 s(78.61%)p 0.19(15.04%)d 0.08(6.35%) 0.560% Rh 6 s(96.54%)p 0.03(2.57%)d 0.01(0.89%) 91.310% N 7 s(58.92%)p 0.70(41.05%)d 0.00(0.01%) f 0.00(0.01%) 0.255% N 8 s(66.70%)p 0.45(29.83%)d 0.04(2.62%) f 0.01(0.85%)	
#62	62. (1.00000)	98.8991% LP (1) N 8 0.464% Rh 1 s(78.77%)p 0.05(4.32%)d 0.21(16.91%) 0.033% Rh 2 s(94.17%)p 0.05(4.40%)d 0.02(1.43%) 0.011% Rh 3 s(53.89%)p 0.43(23.20%)d 0.43(22.91%) 0.053% Rh 4 s(70.42%)p 0.19(13.12%)d 0.23(16.46%) 0.011% Rh 5 s(54.88%)p 0.42(22.99%)d 0.40(22.13%) 0.033% Rh 6 s(81.27%)p 0.12(9.82%)d 0.11(8.92%) 0.495% N 7 s(45.06%)p 1.18(53.12%)d 0.01(0.53%) f 0.03(1.29%) 98.899% N 8 s(62.45%)p 0.60(37.45%)d 0.00(0.10%) f 0.00(0.00%)	#329 53. (1.00000) 98.8886% LP (1) N 8 0.457% Rh 1 s(53.68%)p 0.08(4.09%)d 0.79(42.23%) 0.015% Rh 2 s(73.81%)p 0.08(5.98%)d 0.27(20.21%) 0.018% Rh 3 s(30.20%)p 0.44(13.35%)d 1.87(56.45%) 0.069% Rh 4 s(38.36%)p 0.23(8.99%)d 1.37(52.65%) 0.019% Rh 5 s(31.61%)p 0.43(13.53%)d 1.74(54.85%) 0.031% Rh 6 s(62.18%)p 0.13(8.36%)d 0.47(29.46%) 0.501% N 7 s(43.16%)p 1.28(55.10%)d 0.01(0.46%) f 0.03(1.28%) 98.889% N 8 s(62.49%)p 0.60(37.41%)d 0.00(0.09%) f 0.00(0.00%)

Fig. S31 Composition of the NLMOs depicted in Fig. S32.

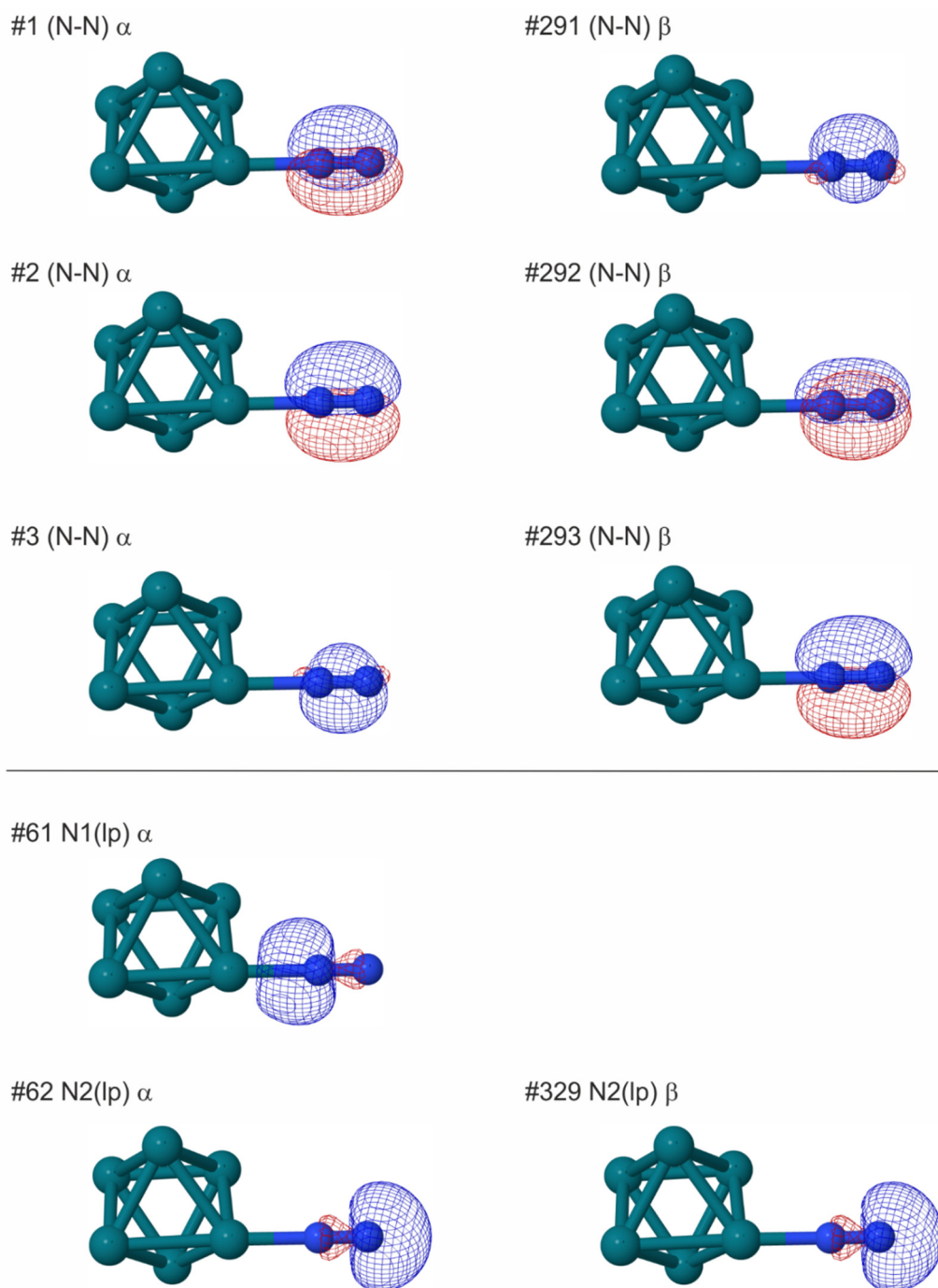


Fig. S32 NLMOs of ¹⁰(6,1)_a that are centered on N₂.

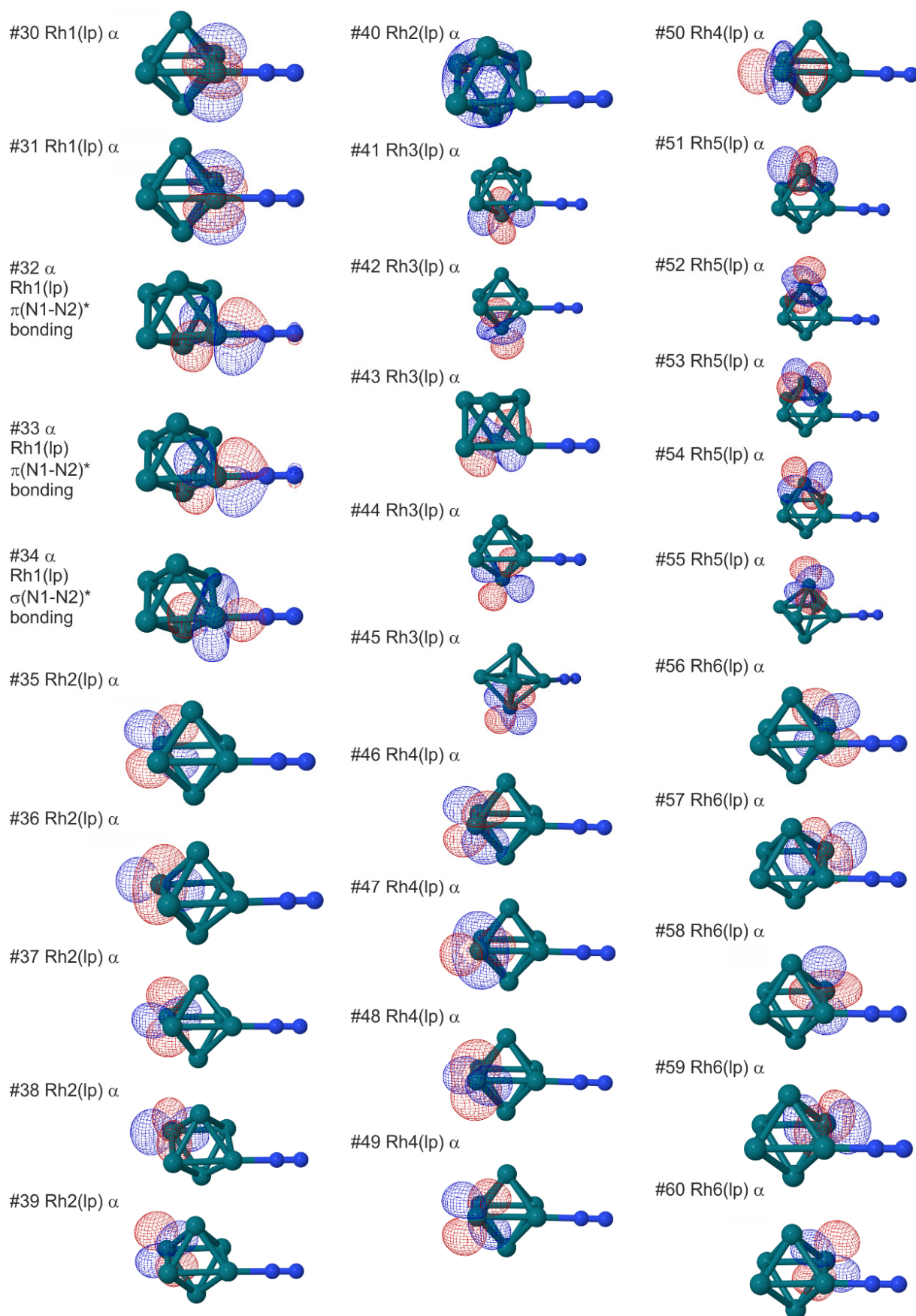


Fig. S33 α -NLMOs of $^{10}(6,1)_a$ consisting of a Rh lone NBO.

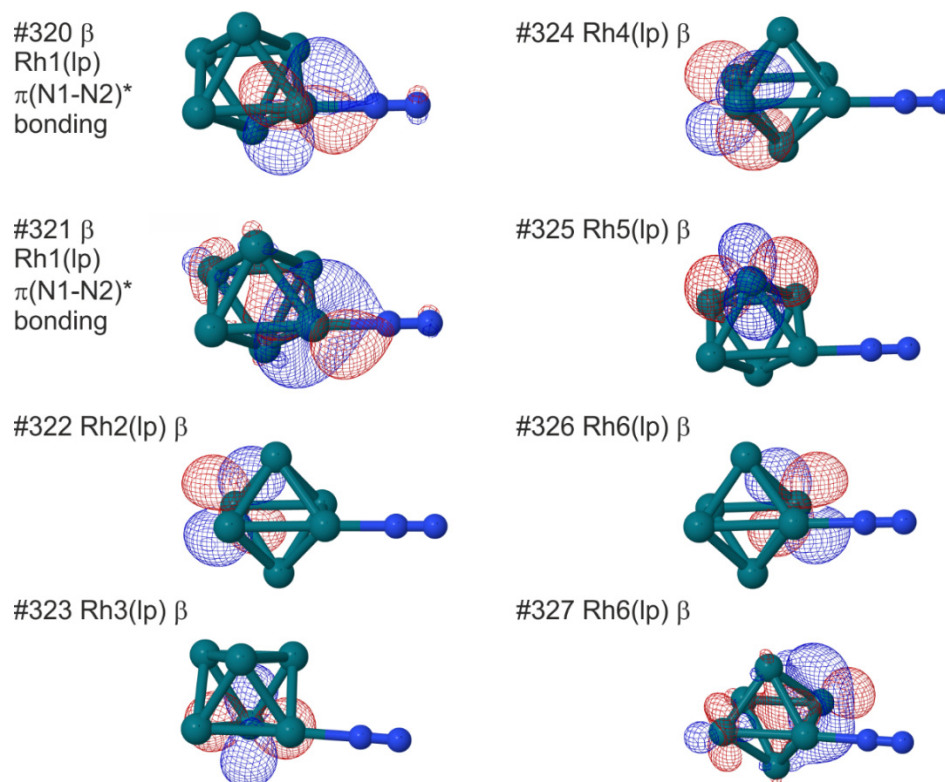


Fig. S34 β -NLMOs of ¹⁰(6,1)_a consisting of a Rh lone NBO.

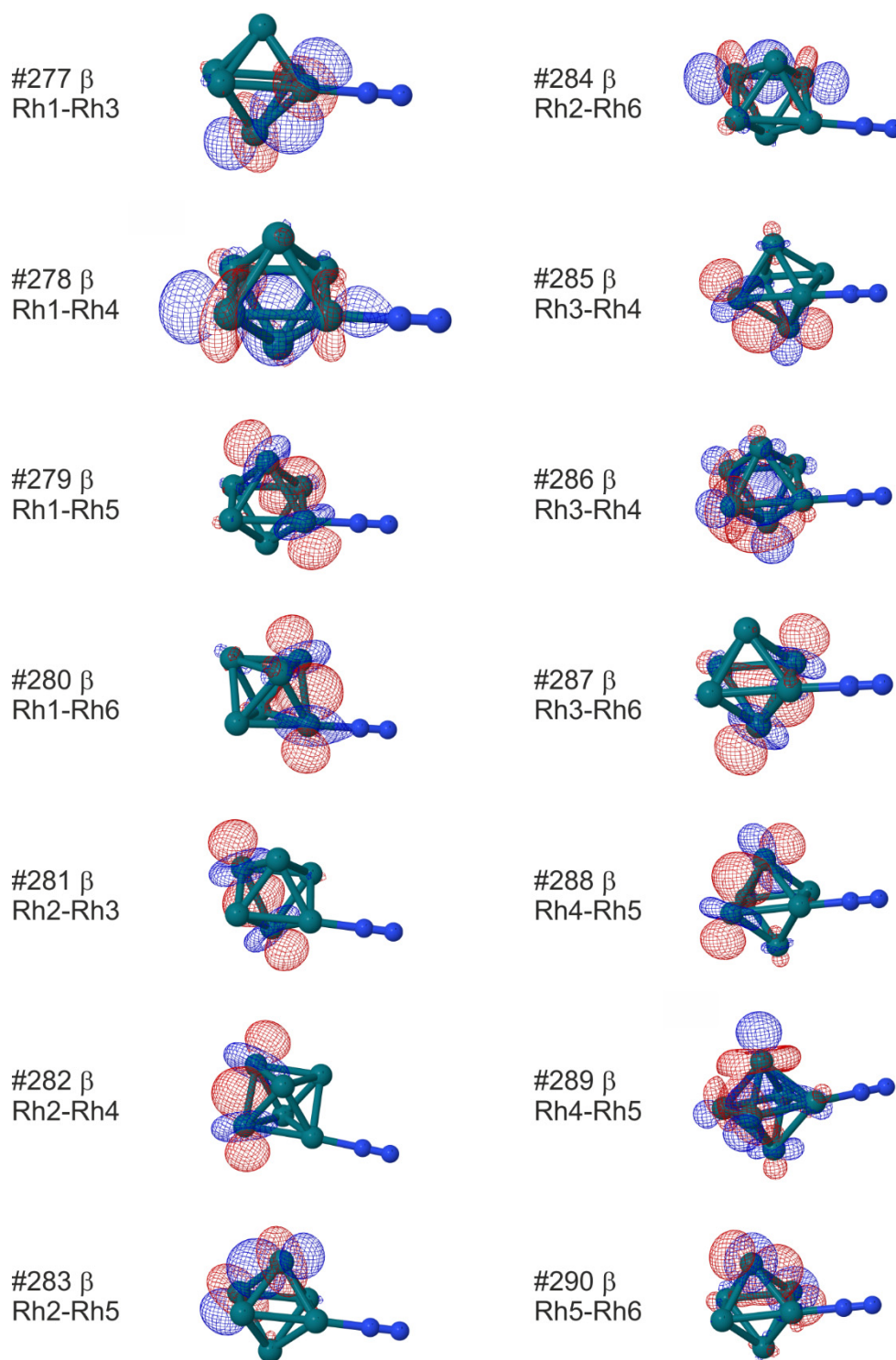


Fig. S35 NLMOs of $^{10}(6,1)_a$ consisting of a Rh-Rh bonding NBO.

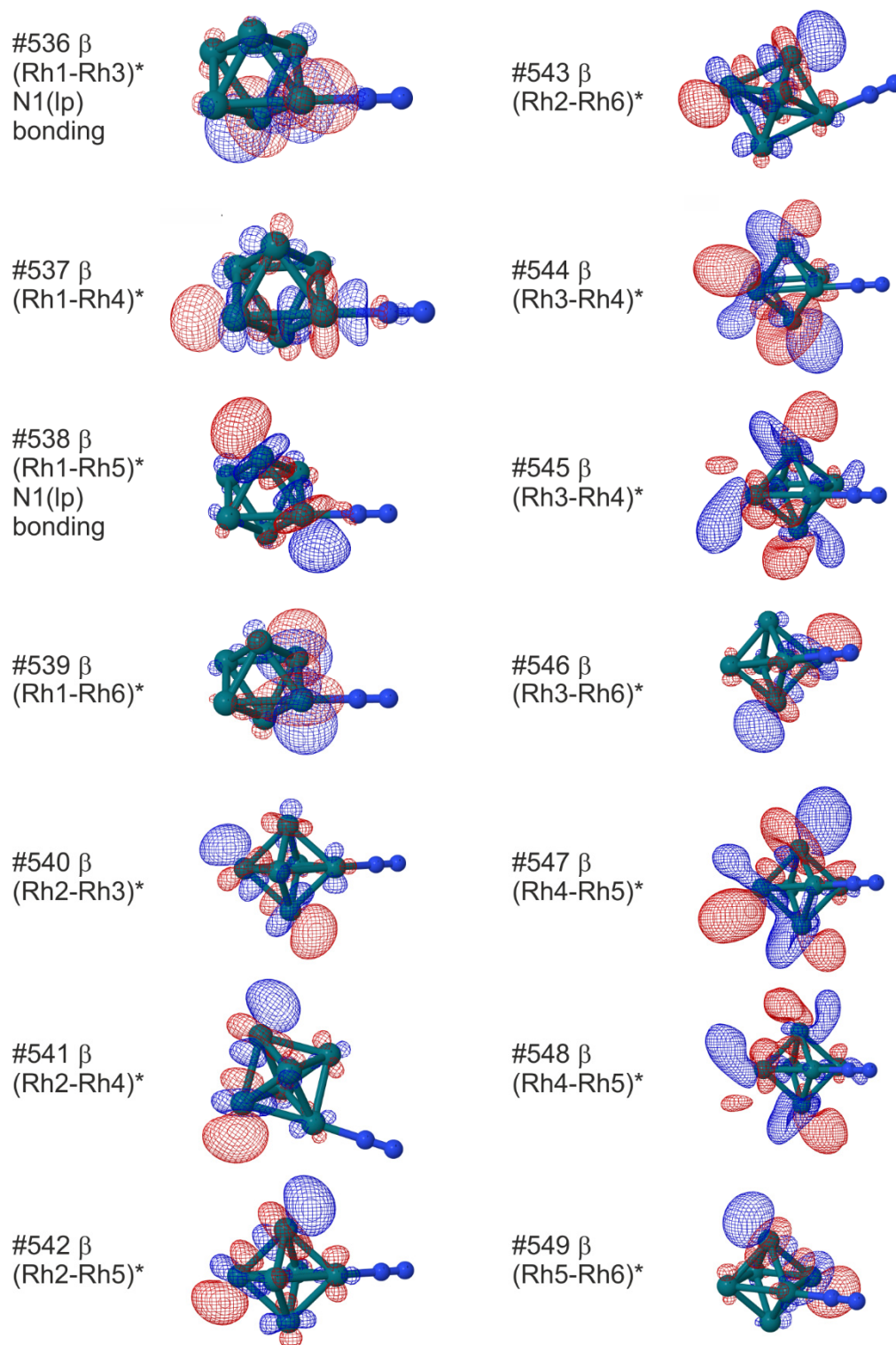


Fig. S36 NLMOs of ¹⁰(6,1)_a consisting of a Rh-Rh antibonding NBO.

6. Cryo Kinetics of N₂ Adsorption onto Bimetallic Rhodium-Iron Clusters in Isolation

Amelie A. Ehrhard¹, Matthias P. Klein, Jennifer Mohrbach, Sebastian Dillinger,
and Gereon Niedner-Schatteburg²

*Fachbereich Chemie and Forschungszentrum OPTIMAS,
Technische Universität Kaiserslautern, 67663 Kaiserslautern, Germany*

6.1 Preamble

An experimental team consisting of A. A. Ehrhard, S. Dillinger, J. Mohrbach, and me conducted the experiments. A. A. Ehrhard and I conducted the data evaluation. A. A. Ehrhard wrote the initial manuscript, and I revised it with the help of A. A. Ehrhard, and G. Niedner-Schatteburg. I prepared the manuscript for final publication.

A preliminary version of this manuscript is part of the Diploma thesis of A. A. Ehrhard.

This manuscript is **under review** at *The Journal of Chemical Physics* as part 1 of 2 of a back-to-back submission (for part 2 cf. chapter 7).

6.2 Abstract

We report the N₂ cryo adsorption kinetics of gas phase mixed Rhodium-Iron clusters [Rh_{*i*}Fe_{*j*}]⁺ (*i* = 3 – 8 and *j* = 3 – 8; *i* + *j* = *n*) of the three particular cases [Rh_{*n*/2}Fe_{*n*/2}]⁺, [Rh_{(*n*-1)/2}Fe_{(*n*+1)/2}]⁺, and [Rh_{(*n*+1)/2}Fe_{(*n*-1)/2}]⁺ in 26 K He buffer gas by the use of a cryo tandem RF-hexapole trap - Fourier transform ion cyclotron resonance (FT-ICR) mass spectrometer. From kinetic data and fits, we extract relative rate constants for each N₂ adsorption step and possible desorption steps. We find significant trends in adsorption behavior, which reveals adsorption limits, intermittent adsorption limits and equilibrium reactions. For those steps, which are in equilibrium, we determine the Gibbs free energies. We conclude on likely ligand shell reorganization and some

¹ Present address: Max-Planck-Institut für Polymerforschung, 55128 Mainz, Germany

² Corresponding author: Prof. Dr. Gereon Niedner-Schatteburg, Erwin-Schrödinger-Straße 52, 67663 Kaiserslautern, gns@chemie.uni-kl.de

weakly bound N₂ ligands for clusters, where multiple N₂ adsorbates are in equilibrium. The relative rate constants are transferred to absolute rate constants, which are slightly smaller than the collision rate constants calculated by the Average Dipole Orientation (ADO, Langevin) theory. The calculated sticking probabilities increase in general with size of the clusters and decrease with the level of N₂ adsorption, in particular when reaching an adsorption/desorption equilibrium. We receive further evidence on cluster size dependent properties, such as cluster geometries and metal atom distributions within the clusters through the accompanying spectroscopic and computational study on the equiatomic clusters [M. P. Klein, A. A. Ehrhard, J. Mohrbach, S. Dillinger, and G. Niedner-Schatteburg [MPK]].

6.3 Introduction

Transition metal clusters had been the focus of intensive studies for many years owing to their catalytic and size dependent properties. There are complex correlations between the size of a metal cluster and the reactivity to small molecules.[1-3] Their reactivity is determined by geometric and by electronic factors. Small metal clusters are frequently used as tractable model system in fundamental studies with outreach towards catalysis, since they are well accessible to experimental and computational studies.[1, 4]

There are different ways to classify catalytic reactions. One approach divides catalytic reactions into structure sensitive ones and structure insensitive ones. A structure sensitive reaction would change its rate constant with the size of the cluster, while the rate constant of a structure insensitive reaction would remain constant when changing size of the cluster.[5] One widely applied structure sensitive reaction is the ammonia synthesis. The close packed (110) crystal face of body centered cubic iron is several orders of magnitude less active, than the open (111) and (211) surfaces.[6, 7]

Another important metal for catalytic reactions is rhodium. This is attributed to the fact, that it belongs to the group of the platinum metals.[8] One of the most important applications of rhodium is in automobile catalytic converters, where it reduces nitrous oxides to N₂, selectively. Simultaneously, hydrocarbons are oxidized to CO₂ and H₂O.[9-11] Compared to platinum or palladium, it is advantageous, that Rhodium does no further reduce N₂ [9]. Hence, a rhodium-platinum alloy was found to lower the reducing effect of pure platinum.[11] N₂O chemistry on rhodium clusters showed sensitive to coadsorbates and modulates by IR

excitation.[12-14] Kinetic studies in an ICR cell confirmed these findings for Rh_n^\pm $n < 30$ clusters and indicate multiple isomers and collisional activation.[15] In addition, Rh_5O^+ clusters reveal an enhanced activity in CO oxidation.[16]

Rhodium clusters. Rhodium owns a naturally monoisotopic character, which made it popular for experimental studies of mass spectrometric techniques.[17] Noteworthy are the reactions of rhodium clusters with CO [18], as *e.g.* those of $n \leq 5$ are almost unreactive towards CO, while larger ones react faster by at least three orders of magnitude. Rhodium clusters Rh_n^\pm with $n = 3 - 28$ activate/dehydrogenate hydrocarbons like benzene, and the reactivity strongly depends on cluster shape and geometry [19]. Acidoacetonitrile decomposes upon adsorption onto cationic Rh_n^+ clusters forming $\text{Rh}_n\text{C}_x\text{N}_y^+$ products; for clusters $n < 3$ the formation of nitrides and carbides dominates [20]. The reactivity studies of small rhodium clusters with NO revealed a competition of dissociative and molecular adsorption.[21, 22] Studies of Rh_n^+ clusters, $n = 1 - 23$, with ethane revealed single and double hydrogenation with remarkable size dependencies.[23] Neutral Rh_n clusters revealed significantly lower sticking probabilities of the first N_2 adsorbate than of D_2 , O_2 , CO or NO.[24]

Cryo IR-PD spectroscopy and adsorption kinetics of N_2 on rhodium clusters by ourselves has provided evidence of octahedral geometric motifs ($n = 6, 7$) and of a remarkable high spin electronic structure, which changes upon sequential N_2 adsorption, in line with our 'spin valley' concept.[25-27]

Iron clusters. Several guided ion beam studies investigated the thermochemistry of the reactions of small iron clusters with O_2 [28], D_2 [29], CH_4 [30], CO_2 [31], NH_3 [32], ND_3 [32], and N_2 [33]. The reactivities of H_2 , NH_3 , and H_2O with Fe_n clusters has been used as a probe for cluster structures, and they were utilized to deduce cluster structures and adsorption induced relaxations.[34] The hydrogen adsorption rates onto Fe_n clusters are strongly size dependent and vary with temperature.[35] For $n < 30$ the H_2 adsorption was found to happen dissociatively and it seems to form a hydride monolayer.[36] A correspondence of Fe cluster ionization threshold and the adsorption rates is understood as an indication for charge transfer in the H_2 bond activation.[37] DFT calculations predict a change of the magnetic moment and anisotropy upon the successive addition of H atoms to small Fe_n clusters $n \leq 4$. [38] The bonding energy of N_2 on the atomic Fe cation was determined as 0.56 eV.[39] DFT calculations on N_2 adsorbate complexes of Fe atoms and small Fe_n clusters revealed a preference of an end-on N_2 coordination to Fe centers.[40, 41] The side-on coordination of

the two N₂ molecules in the [Fe(N₂)₂] complex is an exception. FT-IR studies of co-deposited [Fe_n(N₂)_x]^{0,+} clusters reveal evidence for both end-on and side-on adsorption motifs.[41]

Ongoing studies of N₂ adsorption by cationic iron clusters reveal particularly strong size dependencies, and our exploratory DFT studies indicate very high spin states.[42, 43]

Mixed metal clusters. Nano alloys have been extensively studied in the past and four structural prototypes have been discussed in the context of an exhaustive review [44]: (1) core-shell clusters, (2) Janus-type clusters, (3) ordered or randomly mixed clusters, and (4) multi-shell nanoalloys. Isolated Ni-Fe clusters have revealed a reduced N₂ adsorption as compared to pure Ni clusters, suggesting a reluctance of Fe sites to adsorb N₂. [45, 46]

The addition of cobalt and nickel to ferromagnetic rhodium clusters may lead to spin polarization effects.[47-50] Indeed, there is a size dependent distribution of cobalt and Rhodium atoms to the surface: small mixed clusters prefer to locate rhodium atoms to the surface, whereas larger clusters prefer cobalt atoms at the surface.[51-53] Adding rhodium to nickel clusters yields enhanced magnetic moments as compared to the pure cluster.[54] X-Ray absorption spectroscopy applied to mixed cobalt-rhodium clusters on a nickel surface revealed strong influence of size and composition on reactivity towards oxygen and on the magnetic couplings.[55] DFT calculations of TiO₂ supported Rh-Au clusters suggest adsorption enthalpies of CO and O₂ that increase with the size of the cluster. The Rh sites seem to adsorb N₂ tighter than the Au sites. For such Janus type mixed Rh-Au clusters, the effective adsorption strength onto the Rh sites thus seems reduced with respect to pure Rh clusters.[56]

Magnetism. Published DFT modelling data of bimetallic Rh-Fe clusters $7 \leq n \leq 19$ predict ferromagnetic alloy-like, compact clusters that tend to maximize the number of nearest neighbor Fe-Rh contacts.[57] Bulk iron-rhodium alloys reveal interesting magnetic properties. In the ground state, they possess an antiferromagnetic order with a first-order metamagnetic transition to the ferromagnetic state (at 340-350 K) and another transition occurs at 675 K to the paramagnetic state.[58, 59] Pure rhodium and pure iron clusters differ for their magnetic properties. Rhodium clusters did reveal ferromagnetic ordering, even though the bulk is nonmagnetic.[49, 50] Clusters of non-ferromagnetic materials as rhodium are expected to reveal the large magnetic moments due to their reduced dimensionality and a high degree of symmetry.[60, 61] Molecular beam deflection measurements reveal that Iron clusters show large magnetic moments, which decrease with increasing cluster size towards the bulk

value.[62, 63] With increasing temperature a transition from high to low magnetic moment occurs, probably due to a crystallographic phase transition. XMCD spectroscopy of isolated Fe_n^+ cluster ions reveals ferromagnetic coupling between Fe atoms (except for Fe_{13}^+ where the central Fe atom in the icosahedron couples antiferromagnetically to the surface atoms) and a quench of orbital angular momenta by formation of Fe-Fe bonds.[64] A similar study by ourselves reveals about 10% lower magnetic moments than reported previously.[65]

Prior cryo adsorption studies. We have been successful in probing structures of cationic cobalt [66], nickel [67-69], iron [42, 43], and rhodium [25-27] clusters by means of N_2 cryo adsorption kinetics and IR-PD spectroscopy, and we confirmed the existence of N_2 cleavage and identified intermediates on a Ta_4^+ cluster [70]. We also introduced gas phase XMCD investigations and recorded XMCD spectra of iron, cobalt and nickel clusters.[65, 71] For a better understanding of structural properties and of the size-dependence of physical properties, we have studied some reactions of N_2 adsorption to cationic rhodium-iron clusters $[\text{Rh}_i\text{Fe}_j]^+$ under cryo conditions.[72] The present study investigates the N_2 adsorption kinetics and the cluster size-dependent rate constants of these reactions in a systematic way. It is complemented by an accompanying cryo IR spectroscopic study that focuses on the equiatomic mixed $[\text{Rh}_i\text{Fe}_j]^+$ $i = j$ clusters [MPK] [72]. Therein, we refer to the present paper as [AAE].

6.4 Experimental Methods, Data Evaluation, and Computational Approach

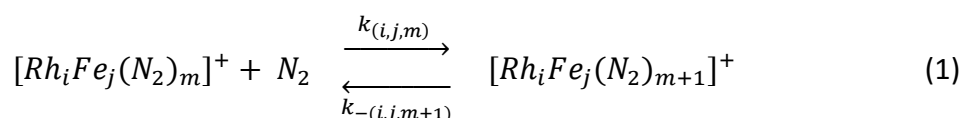
6.4.1 Experimental Methods

The experiments were performed in a customized 7 T Fourier Transform-Ion Cyclotron Resonance (FT-ICR)-mass spectrometer (Apex Ultra Bruker Daltonics). The particular construction of this heavily modified instrument has been described in detail before.[68] In short, we utilize intense pulses from the second harmonic of a Nd:YAG laser, which is guided in the home-built laser vaporization cluster ion source chamber as described before.[66, 73] The laser beam is focused on a rotating RhFe-target (Rh: ^{56}Fe , stoichiometry 1:1, *MaTeck*). The resulting plasma is entrained in a helium gas pulse (40 μs , 10 - 15 bar), which was generated by using a homemade piezoelectric valve [74], operating in synchronization with the laser at 20 Hz. The plasma contains atoms and ions and while they cool down, they aggregate to clusters in the subsequent jet expansion through a 69 mm long channel (2 mm diameter) into vacuum (3.0×10^{-7} mbar). The cluster beam is skimmed, and the isolated cluster ions are

accelerated and proceed through a 90 degrees ion beam bender and a quadruple mass filter into a cryogenic RF hexapole ion trap, which is cooled to 26 K by a closed cycle He cryostat. We admit continuous steams of He buffer gas (3.0×10^{-6} mbar) and N₂ ($2.0 - 3.0 \times 10^{-7}$ mbar) to the ion trap. The ions are stored for variable reaction times (0 – 10 s). Subsequently, the cluster ions gently extracted and steered into the ICR cell of the so-called infinity-type [75], which is cooled down to 10 K by another closed cycle He cryostat thus preventing an uptake of heating of black body radiation by the clusters.

6.4.2 Data evaluation

In order to study the reaction between [Rh_iFe_j]⁺ clusters and nitrogen we isolate the desired parent cluster ion in the quadrupole and record formed product ions throughout a stepwise scan of reaction delays as given by ion trapping times. The kinetic data can be achieved by analysis of the mass spectra obtained after various reaction times by storing the cluster ions with N₂ in the hexapole collision cell for different storage times. We obtain pseudo-first-order kinetic fits to the measured data by applying a genetic algorithm procedure.[76] This yields relative rate constants $k_{(i,j,m)}$ for each N₂ adsorption step $m \rightarrow m + 1$, and $k_{-(i,j,m+1)}$ for each N₂ desorption step $m+1 \rightarrow m$ alike:



We determine the relative rate constants for each adsorption (Table S1) and desorption step (Table S4) with an estimated uncertainty of $\pm 20\%$. With the relative rate constants, we obtain the absolute rate constants, with the number density $\rho_{N_2}(T)$ serving as the conversion factor:

$$k_{(i,j,m)}^{abs} = k_{(i,j,m)} / \rho_{N_2}(T) \quad (2)$$

Where the number density $\rho_{N_2}(T)$ is approximated by

$$\rho_{N_2}(26\text{ K}) = \frac{c_{app} p_c^{300\text{ K}}}{k_B T_{300\text{ K}}} \quad (3)$$

The geometry factor c_{app} reveals a non-negligible temperature dependence. We have evaluated this factor before by numerous kinetic studies to 1.8 at 26 K with an uncertainty of $\pm 50\%$. [26, 67, 68] With the thus determined collision rates, we transform the absolute rate constants to the sticking probabilities. We estimate the collision rates by the average dipole orientation theory [77-80] (ADO), which assumes a classical trajectory of a linear dipole in the

field of a point charge. ADO collision rates reduce to the Langevin rate in the case of a negligible dipole moment.

$$\gamma_{(i,j,m)} = \frac{k_{(i,j,m)}^{abs}}{k_{(i,j,m)}^{coll}} \quad (4)$$

The measured reaction rates for charged metal clusters may exceed the ADO collision rates [20], and Kummerlöwe and Beyer presented two models to determine collision rates of ionic clusters with neutral molecules accordingly [81]. Cluster and neutral reaction partners are treated as hard spheres in both models. The charge is treated as point charge and the attraction between point charge and the neutral molecule is represented by the interaction potential from ADO theory. The Surface Charge Capture (SCC) model is in good agreement with the experimental rate constants of the reaction of charged metal clusters with small molecules. In this model, we assume an ideally conducting cluster, so the point charge is free to move within the geometric boundaries of the cluster. The charge will migrate to the surface of the cluster, because of the attractive interaction with the neutral molecule. This model shows significantly increased collision rates compared to Langevin or ADO theory and provides sometimes more realistic data in case of the reaction of charged metal clusters with small molecules. Nevertheless, even the SCC collision rates are exceeded by our experiments in some cases, for instance in the reaction of Rh_n^\pm with CO.[18, 81]

We calculated the Gibbs free energies $\Delta_{ads} G_{m \rightarrow m+1}^{T_{trap}=26 K}$ for the equilibrium reactions of N_2 adsorption onto $[Rh_i Fe_j (N_2)_m]^+$ / desorption off $[Rh_i Fe_j (N_2)_{m+1}]^+$ at 26 K from the relative rate constants:

$$\Delta_{ads} G_{m \rightarrow m+1}^{T_{trap}} = - R T_{trap} \ln \left(\frac{k_{(i,j,m)}}{k_{-(i,j,m)}} \right) \quad (5)$$

For the calculation of equilibrium constants and Gibbs energies we set all obtained relative rate constants below a value of 0.001 s^{-1} (noise level) to this value as an upper limit and used it for the further evaluation. We obtained upper limits for ΔG in these cases.

6.4.3 Computational Approach

We performed geometry optimizations and vibrational analysis based on density functional theory (DFT). We chose the PBE0 hybrid functional and ECP(Rh, Fe); cc-pVTZ(N) basis sets as level of theory. These calculations are presented and discussed at length in the accompanying paper on the IR spectroscopy of N_2 adsorbates to rhodium-iron clusters and shall not be

reproduced here in duplicate. For details on the obtained results refer to that paper [MPK] [72].

6.4.4 Nomenclature

We choose our nomenclature carefully such that n denotes the total number of atoms in the reacting cluster. The number of Rhodium and Iron atoms in the cluster is given by i and j , respectively ($i + j = n$). The number of adsorbed N₂ molecules is indicated as m . The cluster adsorbate species $[Rh_iFe_j(N_2)_m]^+$ is abbreviated as (i,j,m) .

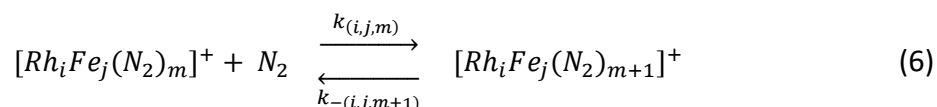
To describe the rate constants of the observed adsorption and desorption processes, we use the descriptors $k_{(i,j,m)}$ and $k_{-(i,j,m+1)}$. These descriptors contain the species where the described adsorption or desorption step starts from. For a more detailed description of the nomenclature refer to [26] (Supplement Text S1 therein).

6.5 Results and Discussion

6.5.1 The Limits of N₂ Adsorption and the Cluster Size Dependences

We have chosen to investigate the cryo adsorption of N₂ to a selected subset of $[Rh_iFe_j]^+$ clusters, namely $[Rh_{n/2}Fe_{n/2}]^+$ with $i = j = n/2 = 3, \dots, 8$ and $[Rh_{(n-1)/2}Fe_{(n+1)/2}]^+$ with $n = 7, 9, \dots, 15$ and $[Rh_{(n+1)/2}Fe_{(n-1)/2}]^+$ with $n = 7, 9, \dots, 15$ by recording its cryogenic mass spectra at a temperature of 26 Kelvin. This subset contains clusters with $i - j = 0$ and ± 1 .

We find two patterns of the temporal evolution ($t = 0 - 10$ s) of $[Rh_3Fe_3(N_2)_m]^+$ and $[Rh_3Fe_4(N_2)_m]^+$ intensities during the exposure to 2.8×10^{-7} mbar N₂ (Fig. 1). We use these clusters to demonstrate the key features, representative for the other investigated cluster sizes. For clusters of all sizes studied, there are taking place apparently dominating, sequential steps of N₂ adsorption onto and desorption off the clusters:



Plain inspection of the recorded mass spectra does not reveal any evidence for further reactions going on. Some desorption steps are not obvious at first sight. Nevertheless, they are identified by the explicit kinetic fits.

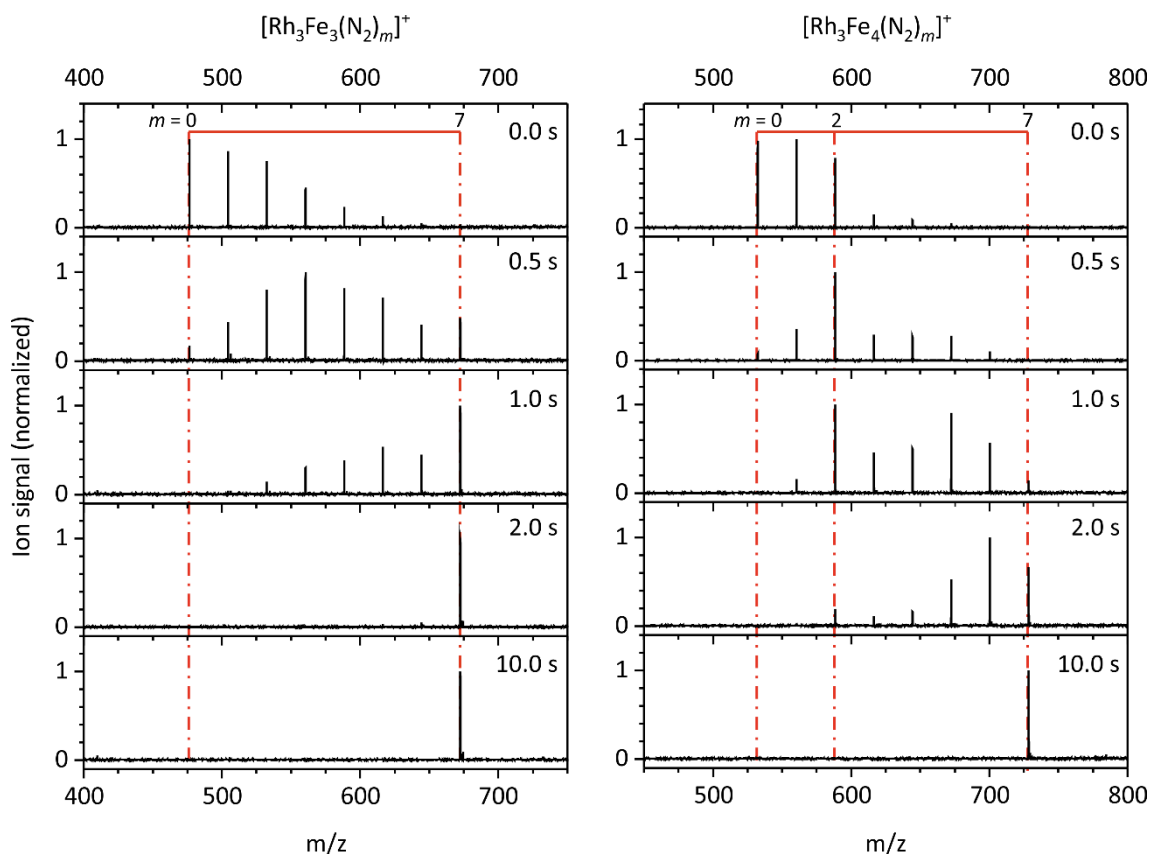


Fig. 1 FT-ICR mass-spectra of $[\text{Rh}_3\text{Fe}_3]^+$ and $[\text{Rh}_3\text{Fe}_4]^+$ exposed to 2.8×10^{-7} mbar N_2 at a temperature of 26 K at various storage times in the cryogenic hexapole ion trap. Note, that in both cases the N_2 adsorption stops after the adsorption of 7 N_2 .

Obviously, the displayed mass spectra reveal strong evidence, that both $[\text{Rh}_3\text{Fe}_3]^+$ and $[\text{Rh}_3\text{Fe}_4]^+$ attach seven N_2 at maximum, and no further N_2 adsorbates beyond (Fig. 1). These largest observable cluster adsorbate complexes $[\text{Rh}_3\text{Fe}_3(\text{N}_2)_7]^+$ and $[\text{Rh}_3\text{Fe}_4(\text{N}_2)_7]^+$ seem to mark some point of saturation. We define these values of m as the N_2 *maximum adsorption limit* m_{max} of such clusters, and we find an according adsorption limit in the mass spectra of all investigated $[\text{Rh}_i\text{Fe}_j]^+$ clusters.

On the way towards m_{max} , we observe some significantly slower adsorption steps, as e.g. for $k_{(3,4,1)}$ towards $(3,4,2)$, the $[\text{Rh}_3\text{Fe}_4(\text{N}_2)_2]^+$ complex. We define such an adsorbate species, where the sequential adsorption decelerates amidst the otherwise fast adsorption chain, as an *intermittent adsorption limit* m_x . Albeit, several adsorption chains of other $[\text{Rh}_i\text{Fe}_j]^+$ clusters proceed without any such intermittent adsorption limit.

We evaluate our recorded adsorption limits of the $[\text{Rh}_{n/2}\text{Fe}_{n/2}]^+$ clusters in comparison to those of pure $[\text{Rh}_n]^+$ and $[\text{Fe}_n]^+$ clusters (Fig. 2). It is one of the key findings of our study, that the N_2 maximum adsorption limits fluctuate with the cluster sizes, and they do so in an element

specific manner. We find that [Fe_{*n*}]⁺ clusters adsorb N₂ molecules up to $m_{max} < n$ (sub stoichiometric). In contrast, [Rh_{*n*}]⁺ clusters adsorb N₂ up to $n \leq m_{max} \leq 2n$ (super stoichiometric). The magnitudes of [Rh_{*n/2*}Fe_{*n/2*}(N₂)_{*m(max)*}]⁺ adsorption limits m_{max} lie somewhat in between. In the case of [Fe_{*n*}]⁺ and [Rh_{*n*}]⁺ clusters, we find remarkable cluster size dependent fluctuations of the maximum adsorption limits, which are only present to a minor extent in the case of mixed [Rh_{*n/2*}Fe_{*n/2*}]⁺ clusters.

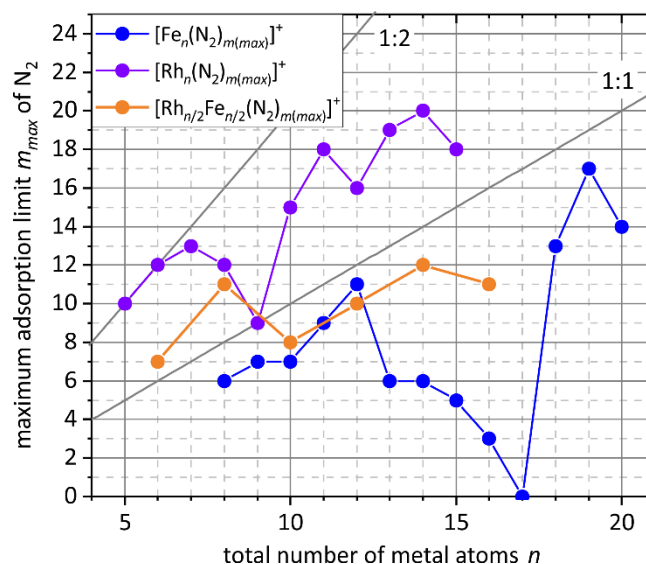


Fig. 2 The observed maximum adsorption limits m_{max} of N₂ adsorbates onto [Fe_{*n*}]⁺ clusters (blue circles) [42], onto [Rh_{*n*}]⁺ clusters (purple circles) [26] and to the equiatomic ($i = j$) [Rh_{*n/2*}Fe_{*n/2*}]⁺ clusters (orange circles). The grey lines indicate stoichiometries of $n : m_{max} = (1 : 1)$, $(1 : 2)$, which would imply one or two ‘monolayers’ of adsorbates to a cluster with all surface atoms, respectively.

In the particular case of the [Rh₉]⁺ clusters, there is an adsorption limit of $m_{max} = 9$, which implies a stoichiometry of $n : m_{max} = 1 : 1$. In small clusters ($n \leq 12$), we expect that all metal atoms are easily accessible from the outside, commonly termed ‘surface atoms’.[82] Hence, it is likely that the [Rh₉]⁺ cluster attaches one N₂ to each rhodium atom, so we can envision something like a single ‘monolayer’ of N₂ on the ‘surface’ of this cluster.

The situation for [Fe_{*n*}]⁺ clusters is more complex and somewhat perplexing, as discussed elsewhere [42]: With small clusters ($n \leq 12$), we recognize a trend in N₂ adsorption limits towards a stoichiometry of $n : m_{max} = 1 : 1$. There is a huge reluctance in N₂ adsorption, starting at the [Fe₁₃]⁺ cluster and reaching the minimum at the [Fe₁₇]⁺ cluster. The interpretation of this finding is subject of ongoing work.[42]

In remarkable contrast, we find much less fluctuations in the magnitudes of adsorption limits of the mixed equiatomic $[\text{Rh}_i\text{Fe}_j]^+ i = j$ clusters: The clusters consisting of 6 and 8 metal atoms in total reveal a super stoichiometric adsorption behavior, which rises up to (4,4,11). Beyond these two cluster adsorbate complexes, the m_{max} values decline towards $m_{max} = 8$ in (5,5,8), and all larger clusters adsorb a substoichiometric amount of N_2 , albeit steadily increasing. The stoichiometries $n : m_{max}$ approximate unity, but for (8,8,11).

An exceedingly large amount of N_2 adsorbates on the (4,4,11) cluster comes along with extensive desorption steps and equilibria at the adsorption maximum, which we will elaborate further below. Ultimately, at very long storage times, it is (4,4,8) which stays most intense. Observed dynamic equilibria at the end of the adsorption chain for all investigated cluster adsorbate complexes are denoted in Fig. 3, and adsorption kinetics are discussed in more detail below.

In complement to the equiatomic clusters $[\text{Rh}_{n/2}\text{Fe}_{n/2}]^+$ (n even) we also investigated odd n type clusters. These are the rhodium deficient clusters $[\text{Rh}_{(n-1)/2}\text{Fe}_{(n+1)/2}]^+$, denoted $((n-1)/2, (n+1)/2)$, and the rhodium excess clusters $[\text{Rh}_{(n+1)/2}\text{Fe}_{(n-1)/2}]^+$, denoted $((n+1)/2, (n-1)/2)$, both of which comprise a total metal atom count n (Fig. 3). We find that the maximum adsorption limits of all three classes of clusters vary little; their values fall within a narrow range, as indicated by the grey shaded area in Fig. 3: The adsorbate layer grows with cluster size less than proportional. This may imply the existence of highly coordinated subsurface atoms inside the cluster, which are not accessible to N_2 adsorption. It is also conceivable and likely that there is some preference of N_2 adsorption to Rh sites. This assumption is supported by the finding that Rh excess $((n+1)/2, (n-1)/2, m)$ adsorb more N_2 than Rh deficient clusters $((n-1)/2, (n+1)/2, m)$ of same size n in the cases of $n = 7, 9, 15$.

This is different in the cases of $n = 11, 13$ – which are $[\text{Rh}_5\text{Fe}_6]^+$, $[\text{Rh}_6\text{Fe}_5]^+$ and $[\text{Rh}_6\text{Fe}_7]^+$, $[\text{Rh}_7\text{Fe}_6]^+$: The rhodium deficient clusters adsorb one more N_2 than the rhodium excess clusters. Remarkable is the fact, that there is nearly no cluster size dependent fluctuation and no drop of the maximum adsorption limit with increasing cluster size for $n > 10$ – other than in the case of the pure $[\text{Rh}_n]^+$ and $[\text{Fe}_n]^+$ clusters. There may be somewhat of an exceptional high maximum adsorption limit in the case of the $[\text{Rh}_5\text{Fe}_4]^+$ cluster that resembles the behavior of the $[\text{Rh}_4\text{Fe}_4]^+$ cluster. For sure, all of these recorded data are closely related to structural and electronic features that change with and critically depend on size and composition of the adsorbing clusters.

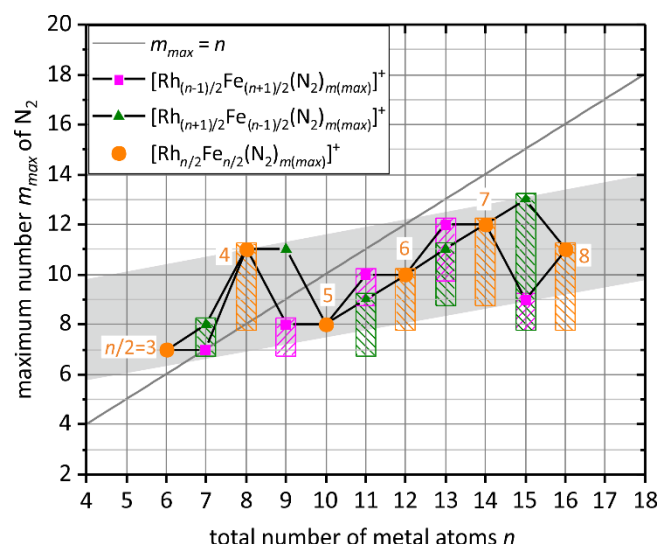


Fig. 3 The observed maximum adsorption limits m_{\max} of N₂-adsorbates to equiatomic $[\text{Rh}_{n/2}\text{Fe}_{n/2}]^+$ clusters (orange circles), to $[\text{Rh}_{n/2+1}\text{Fe}_{n/2}]^+$ clusters (green triangles), and to $[\text{Rh}_{n/2}\text{Fe}_{n/2+1}]^+$ clusters (red squares). The grey line indicates a stoichiometry of $n : m_{\max} = (1 : 1)$ namely one hypothetical ‘monolayer’ of adsorbates, respectively. Note, that the ‘trend’ in m_{\max} (grey shading) deviates significant from a $m_{\max} : n_{\text{total}} = 1 : 1$ behavior. The colored striped rectangles emphasize the ranges of equilibria at the end of consecutive adsorption chains.

We also find first evidence of likely desorption steps from cluster adsorbate complexes with high N₂ loads. We emphasize the according adsorption/desorption equilibria by the colored striped rectangles in Fig. 3. The color coring resembles the corresponding cluster composition (i, j) . The boxes indicate the adsorption steps $m < m_{\max}$ and desorption steps $m+1 \rightarrow m$ that are in equilibrium. Most of the clusters in the investigated size range $n = 6, \dots, 16$ show these equilibria, except for the small clusters $(i, j) = (3, 3), (3, 4), (5, 4),$ and $(5, 5)$. Every cluster larger than $(5, 5)$ has at least two pairs of adsorption/desorption steps in equilibrium. In the case of the cluster $(8, 7)$ there is a remarkably large range of adsorption/desorption steps $m = 8, \dots, 13$ acting in parallel which causes the according complexes $(8, 7, m)$ to coexist for long storage times.

The number of co-acting adsorption/desorption steps m varies for $((n-1)/2, (n+1)/2, m)$ between 2 ($n = 9, 11, 15$) and 3 ($n = 13$) and for $((n+1)/2, (n-1)/2, m)$ between 2 ($n = 7$), 3 ($n = 11, 13$), and 6 ($n = 15$). In the cases of $n = 11$ and 15, the ranges of these co-acting adsorption/desorption steps is larger for the rhodium excess clusters than that for the rhodium deficient clusters. The former ones seem to have a more volatile or a more flexible adsorbate shell.

We emphasize that in all cases the term *adsorption limit* m_{max} denotes the species with the most adsorbed N_2 . It does not necessarily coincide with the ultimately most intense species. *E.g.* we observe (4,4,8) most intense at $t = 10$ s and (4,4,11) as largest complex, $m_{max} = 11$ (*cf.* Fig. 6).

6.5.2 Reaction kinetics and rate constants

Following up the determination of adsorption limits, we have recorded in more detail the individual reaction kinetics of each investigated cluster within the three classes discussed above. By assuming pseudo-first order kinetics, it is possible to fit the temporal evolution of the kinetic data. From these fits, we extract the relative rate constants for each adsorption step. We have chosen to utilize relative values at this point, with relative uncertainties of as low as $\pm 20\%$. Conversion to absolute rate constants by pressure normalization does imply somewhat higher absolute uncertainties of $\pm 50\%$. For the latter values refer to the supplement (Table S4). In the following we will present and discuss the recorded kinetic data, the kinetic fits, and the obtained rate constants for each reactant cluster individually:

6.5.2.1 $[Rh_3Fe_3]^+$

The experimental kinetic data reveal seven consecutive steps of N_2 adsorption which allow for a kinetic fit with a very good quality (Fig. 4a). These consecutive reaction steps develop rather smoothly with no particular exception occurring up to a single final product species, which is $[Rh_3Fe_3(N_2)_7]^+$. This species constitutes some form of a saturation point at given conditions (p, T), which we have specified as adsorption limit $m_{max} = 7$. The kinetic data reveal no intermittent adsorption limit. We conclude that $[Rh_3Fe_3]^+$ provides for a *smooth* cluster surface which implies equal (or at least similar) coordination of all metal atoms to its nearest neighbors within the cluster. There is no evidence for any preferred adsorption site.

The relative adsorption rate constants (Fig. 4b) are constant within their small uncertainties. This finding lends additional support to the above stated equivalence of adsorption sites in $[Rh_3Fe_3]^+$. One may speculate about a conceivable octahedral structure, which will serve as a starting point for further computational studies in the accompanying IR Paper [MPK] [72]. The kinetic fit does not reveal any evidence of N_2 desorption at any step. Any such rate constant $k_{-(i,j,m+1)}$ would amount at least 4 orders of magnitude less than the relative rate constants of the forward reaction, $k_{(i,j,m)}$. The vanishing adsorption rate constants $k_{(3,3,7)}$ indicates the adsorption limit $m_{max} = 7$. We do not observe any adsorption beyond.

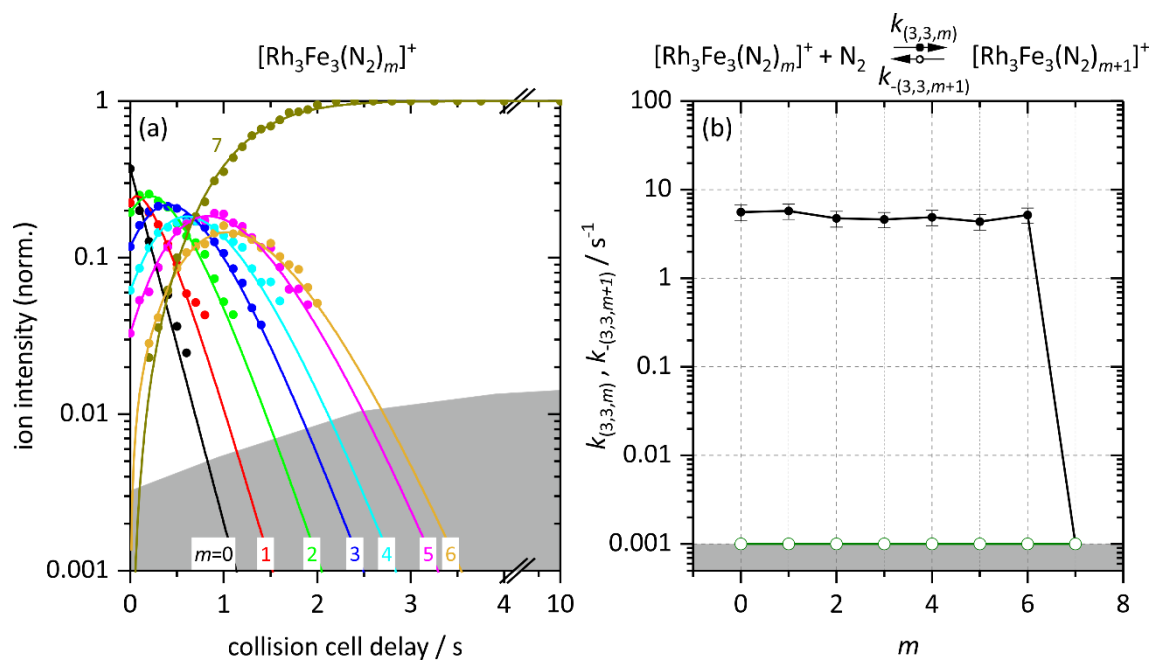


Fig. 4 (a) Isothermal kinetics of the stepwise N₂ adsorption onto isolated [Rh₃Fe₃(N₂)_m]⁺ clusters at 26 K (colored data points). The fits (solid colored lines) assume pseudo-first-order kinetics in an adsorption chain of up to 7 consecutive steps. (b) Fitted values of relative rate constants for N₂ adsorption ($k_{(3,3,m)}$, black filled circles) and desorption ($k_{-(3,3,m+1)}$, green open circles, upper limits) as a function of the stepwise N₂ adsorption level m . The grey shaded areas indicate the approximate background noise level. Values of 0.001 s⁻¹ represent an upper limit.

6.5.2.2 [Rh₃Fe₄]⁺ and [Rh₄Fe₃]⁺

We have recorded the experimental kinetic data of the clusters [Rh₄Fe₃]⁺ (Fig. 5a) and [Rh₃Fe₄]⁺ (Fig. 5b), both of which comprise of a total of 7 metal atoms ($n = 7$). Both data sets allow for a fit with good overall quality. The adsorption limits are $m_{max} = 7$ and 8 in the case of [Rh₄Fe₃]⁺ and [Rh₃Fe₄]⁺, respectively. There are one and two intermittent adsorption limits at $m_x = 2$, and at $m_x = 3$ and 6 in these two cases. We deduce that both clusters provide for *rough* cluster surfaces, which implies some variation of nearest neighbor coordination within the cluster. This may indicate preferred and less preferred adsorption sites – to some extent.

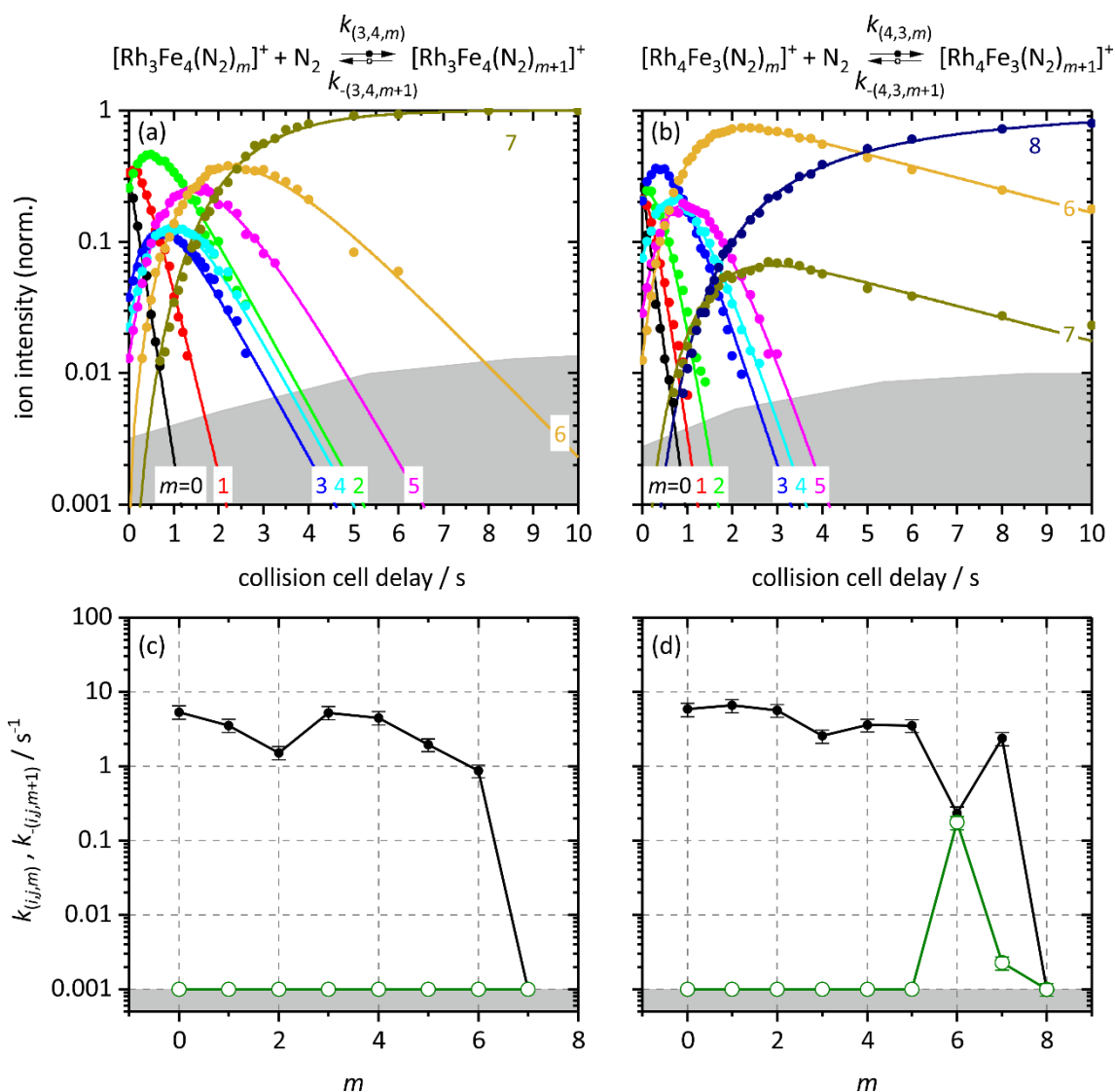


Fig. 5 Isothermal kinetics of the stepwise N₂ adsorption onto (a) isolated [Rh₃Fe₄]⁺ clusters and (b) [Rh₄Fe₃]⁺ clusters at 26 K (colored data points). The fits (solid colored lines) assume pseudo-first-order kinetics in an adsorption chain of up to 7 consecutive steps for [Rh₃Fe₄]⁺ and 8 for [Rh₄Fe₃]⁺ clusters. Fitted values of relative rate constants from the kinetic fit for the N₂ adsorption ($k_{(i,j,m)}$, black filled circles) and desorption ($k_{-(i,j,m+1)}$, green open circles, upper limits) on (c) [Rh₃Fe₄]⁺ clusters and (d) [Rh₄Fe₃]⁺ clusters as a function of the stepwise N₂ adsorption level m . The grey shaded areas indicate the approximate background noise level. Values of 0.001 s⁻¹ represent an upper limit.

The stepwise relative rate constants of N₂ adsorption onto [Rh₃Fe₄]⁺ (Fig. 5c) and onto [Rh₄Fe₃]⁺ (Fig. 5d) reveal further insights. The two sets of rate constants show drops at $m = 2$ and 3, respectively – confirming the above presumed intermittent adsorption limits. Consequently, stable species that adsorb additional N₂ molecules only slowly manifest in a reduction of the rate constants. The drop at $m = 3$ is more pronounced in the case of [Rh₃Fe₄]⁺

and it is one adsorption step earlier than in the case of [Rh₄Fe₃]⁺. It corresponds in both cases to the amount of Rh-atoms, which are present in the cluster. This indicates a likely preference of N₂ adsorption to Rh atoms in disfavor to the competing Fe adsorption sites. This observation might be a first hint that the enhanced propensity of [Rh_{*n*}]⁺ clusters to adsorb N₂ compared to [Fe_{*n*}]⁺ applies also to the metal atoms in an alloy cluster. An alternative explanation such as adsorbate induced relaxation at $m = 2$ and $m = 3$, 6 in [Rh₃Fe₄]⁺ and [Rh₄Fe₃]⁺, seems less likely. In the case of [Rh₃Fe₄]⁺, the rate constants $k_{(3,4,5)}$ and $k_{(3,4,6)}$ have diminished with respect to $k_{(3,4,3)}$ and $k_{(3,4,4)}$. The subsequent chain of adsorption proceeds in a decelerated way towards the last adsorption step $k_{(3,4,6)}$ which leads to $m_{max} = 7$ (3,4,7). In contrast, the [Rh₄Fe₃]⁺ cluster does not only reveal a deceleration. The kinetic fit also reveals significant N₂ desorption for the last two steps. The second but last adsorption step $m = 6$ proceeds with a reduced relative rate constant that is reduced by one order of magnitude as compared to the preceding adsorption rate constants.

The corresponding desorption rate constant has a similar value, which is two orders of magnitude above noise level. In the last step $m = 7$, the adsorption constant has recovered to a higher value and the desorption is only slightly above noise level. This makes for a low intensity of (4,3,7) and a high intensity of (4,3,6) and (4,3,8) as elucidated in the kinetic curves in Fig. 5b. These findings support the hypothesis of non-equivalent adsorption sites of [Rh₃Fe₄]⁺ and [Rh₄Fe₃]⁺. We suggest a stiff and somewhat rigid first solvation shell. In case of the [Rh₃Fe₄]⁺ this would be a stiff monolayer of 1:1 stoichiometry on the surface of the cluster.

6.5.2.3 [Rh₄Fe₄]⁺

The experimental kinetic data (Fig. 6a) reveal 11 consecutive steps of N₂ adsorption and desorption, and these data allow for a fit with good overall quality. The terminal four product species (4,4, m) $m = 8, \dots, 11$ are in equilibrium with each other in favor of (4,4,8) and at the expense of the three minor species (4,4, m) $m = 9, 10, 11$. Note, that N₂ desorption off (4,4, m) $m = 9, \dots, 11$ is statistically significant. There is an intermittent adsorption limit at $m = 4$, and we deduce a *rough* cluster surface on [Rh₄Fe₄]⁺.

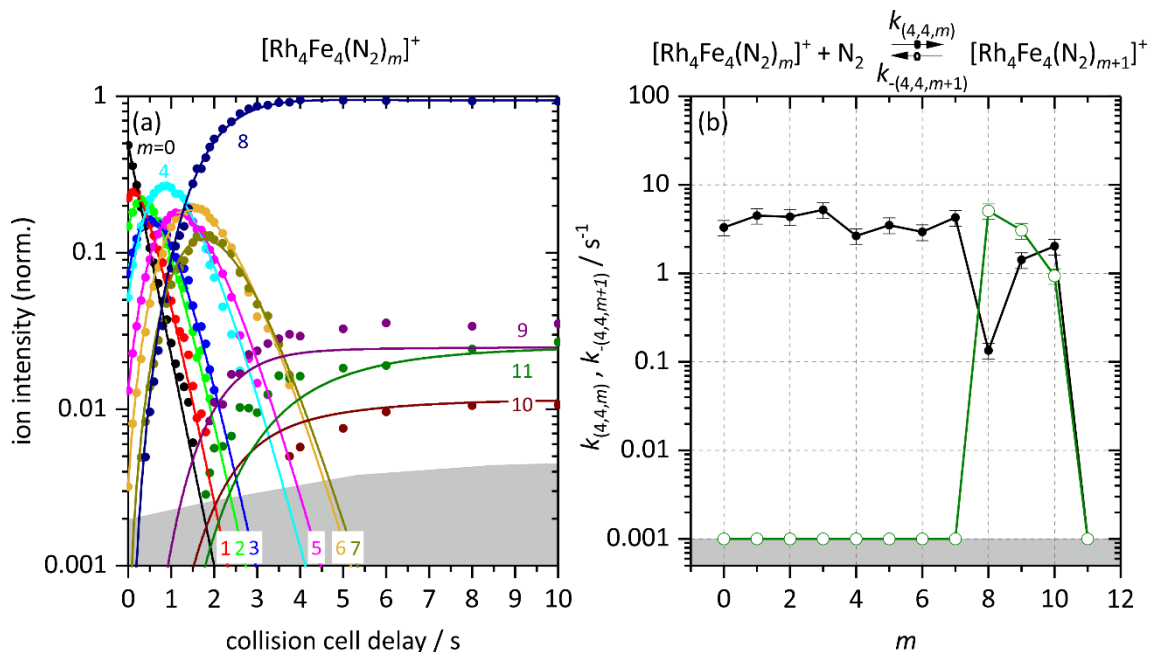


Fig. 6 (a) Isothermal kinetics of the stepwise N_2 adsorption onto isolated $[\text{Rh}_4\text{Fe}_4]^+$ clusters at 26 K (colored data points). The fits (solid colored lines) assume pseudo-first-order kinetics in an adsorption chain of up to 11 consecutive steps. (b) Fitted values of relative rate constants from the kinetic fit for the N_2 adsorption ($k_{(4,4,m)}$, black filled circles) and desorption ($k_{-(4,4,m+1)}$, green open circles, upper limits) as a function of the stepwise N_2 adsorption level m . The grey shaded areas indicate the background noise level. Values of 0.001 s^{-1} represent an upper limit.

The obtained relative adsorption rate constants (Fig. 6b) reveal subtle details. Rate constants $k_{(4,4,5)}$ and $k_{(4,4,9)}$ are particularly slow, which relates to the intermittent adsorption limits for $m_x = 4$ and $m_x = 8$. Subsequent desorption rate constants $k_{-(4,4,m+1)}$ $m = 8$ and 9 are somewhat and significantly faster than pseudo first order adsorption rate constants $k_{(4,4,8)}$ and $k_{(4,4,9)}$, respectively. Note, that $k_{(4,4,9)}$ and $k_{(4,4,10)}$ are significantly faster than $k_{(4,4,8)}$. It seems possible that the $m = 9$ step ($k_{(4,4,9)}$) induces a structural change in either the adsorbate layer or in the underlying $[\text{Fe}_4\text{Rh}_4]^+$ cluster structure whereby subsequent adsorption is facilitated. We conceive N_2 -adsorbate layer isomers with comparable stability. Beyond $m = 8$, we observe pronounced equilibria that indicate a somewhat flexible adsorbate layer which facilitates further isomerization and fluctuations. Perhaps these N_2 molecules are roaming in a second adsorbate shell.

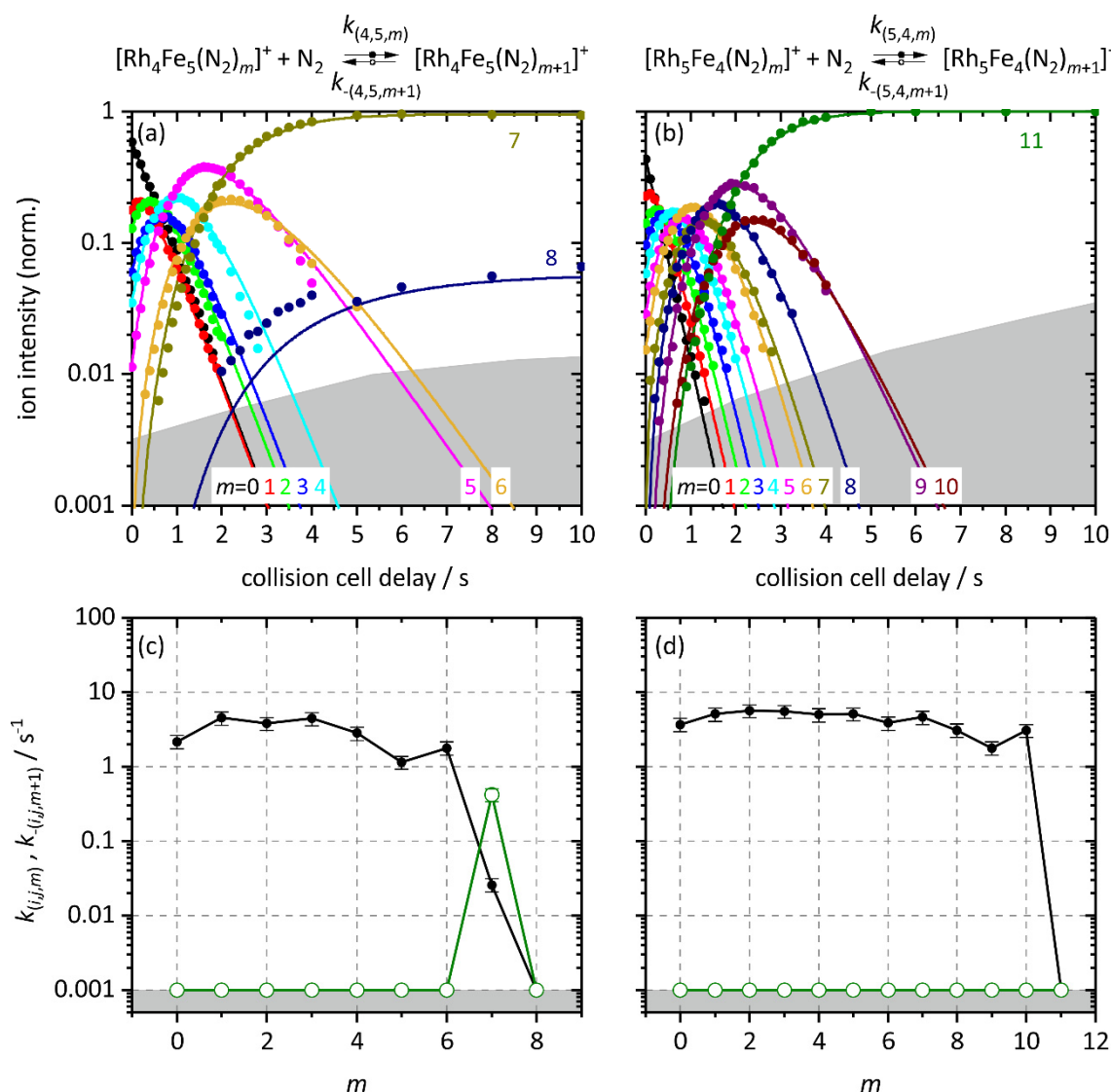
6.5.2.4 [Rh₄Fe₅]⁺ and [Rh₅Fe₄]⁺

Fig. 7 Isothermal kinetics of the stepwise N₂ adsorption onto (a) isolated [Rh₄Fe₅]⁺ clusters and (b) [Rh₅Fe₄]⁺ clusters at 26 K (colored data points). The fits (solid colored lines) assume pseudo-first-order kinetics in an adsorption chain of up to 8 consecutive steps for [Rh₄Fe₅]⁺ and 11 for [Rh₅Fe₄]⁺ clusters. Fitted values of relative rate constants from the kinetic fit for the N₂ adsorption ($k_{(i,j,m)}$, black filled circles) and desorption ($k_{-(i,j,m+1)}$, green open circles, upper limits) on (c) [Rh₄Fe₅]⁺ clusters and (d) [Rh₅Fe₄]⁺ clusters as a function of the stepwise N₂ adsorption level m . The grey shaded areas indicate the background noise level. Values of 0.001 s⁻¹ represent an upper limit.

We have recorded kinetic data for the clusters [Rh₄Fe₅]⁺ (Fig. 7a) and [Rh₅Fe₄]⁺ (Fig. 7b). Either set of kinetic curves allows for a fit with very good overall quality. The data reveal very different maximum and intermittent adsorption limits. For [Rh₄Fe₅]⁺ there is a pronounced intermittent adsorption limit at $m_x = 5$ and the last two cluster adsorbate complexes

$m = 7$ and 8 run into equilibrium, and the maximum adsorption limit is at $m_{max} = 8$. In contrast, the $[\text{Rh}_5\text{Fe}_4]^+$ cluster adsorbs N_2 up to a maximum adsorption limit $m_{max} = 11$. The $[\text{Rh}_5\text{Fe}_4]^+$ cluster reveals a somewhat weakly pronounced intermittent adsorption limit at $m_x = 9$. In consequence of all these findings, we conclude in a somewhat *rough* cluster surface in both of these cases. For sure, the cluster surfaces of both $[\text{Rh}_4\text{Fe}_5]^+$ and $[\text{Rh}_5\text{Fe}_4]^+$ are less *smooth* than that of *e.g.* $[\text{Rh}_3\text{Fe}_3]^+$ (*cf.* Fig. 4).

The stepwise N_2 adsorption rate constants of $[\text{Rh}_4\text{Fe}_5]^+$ (Fig. 7c) and of $[\text{Rh}_5\text{Fe}_4]^+$ (Fig. 7d) are somewhat similar, some differences prevailing: There are slow adsorption rate constants of $[\text{Rh}_4\text{Fe}_5]^+$ past the intermittent adsorption limits $m_x = 5$ and of $[\text{Rh}_5\text{Fe}_4]^+$ past $m_x = 9$. $[\text{Rh}_4\text{Fe}_5]^+$ runs into an equilibrium of (4,5,7) and (4,5,8) cluster adsorbate complexes, *cf.* rate constants $k_{(4,5,7)}$ and $k_{-(4,5,8)}$, whereas $[\text{Rh}_5\text{Fe}_4]^+$ ultimately forms a single cluster adsorbate complex (5,4,11) without discernible evidence for any desorption.

6.5.2.5 $[\text{Rh}_5\text{Fe}_5]^+$

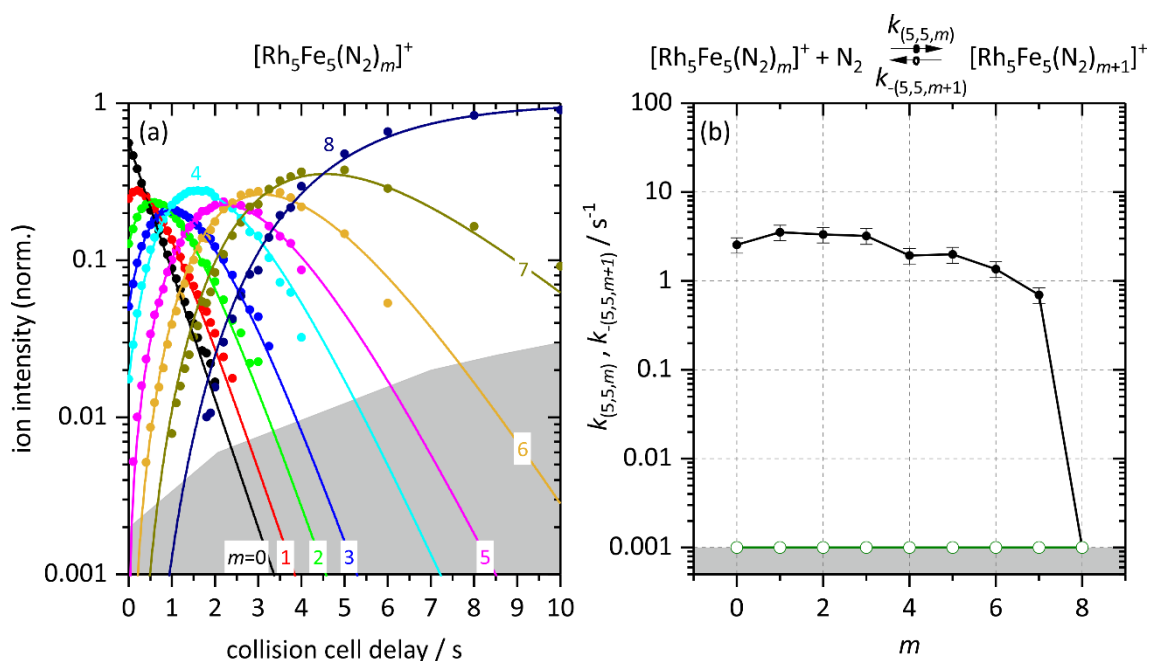


Fig. 8 (a) Isothermal kinetics of the stepwise N_2 adsorption onto isolated $[\text{Rh}_5\text{Fe}_5]^+$ clusters at 26 K (colored data points). The fits (solid colored lines) assume pseudo-first-order kinetics in an adsorption chain of up to 8 consecutive steps. (b) Fitted values of relative rate constants from the kinetic fit for the N_2 adsorption ($k_{(5,5,m)}$, black filled circles) and desorption ($k_{-(5,5,m+1)}$, green open circles, upper limits) as a function of the stepwise N_2 adsorption level m . The grey shaded areas indicate the background noise level. Values of 0.001 s^{-1} represent an upper limit.

The kinetic data disclose merely eight consecutive N₂ adsorption steps up to the adsorption limit at $m_{max} = 8$ – with no indication of any adsorption beyond. The data allow for a fit with good overall quality (Fig. 8a). It reveals a weak intermittent adsorption limit at (5,5,4), which may indicate a somewhat *rough* cluster surface.

The relative rate constants of [Rh₅Fe₅]⁺ (Fig. 8b) drop at $k_{(5,5,5)}$, which is due to the intermittent adsorption limit at $m_x = 4$. The fit reveals no evidence for N₂ desorption at any step. [Rh₅Fe₅]⁺ is the largest cluster without an equilibrium of at least two species at the end of the adsorption chain. We will see in the following that all the larger cluster do experience N₂ desorption at some point.

6.5.2.6 [Rh₅Fe₆]⁺ and [Rh₆Fe₅]⁺

We obtained kinetic data for the stepwise N₂ adsorption to [Rh₅Fe₆]⁺ (Fig. 9a) and [Rh₆Fe₅]⁺ (Fig. 9b), and we find a similarity of the recorded intensity pattern of [Rh₆Fe₅]⁺ to that of [Rh₄Fe₃]⁺. The cluster [Rh₅Fe₆]⁺ reveals an adsorption limit of $m_{max} = 10$, and two very weak intermittent adsorption limits at $m_x = 4$ and 7. The (5,6,10) cluster adsorbate complex, at the maximum adsorption limit $m_{max} = 10$, is in equilibrium with its precursor (5,6,9). The N₂ adsorption onto [Rh₆Fe₅]⁺ runs into an equilibrium amongst the cluster adsorbate complexes (6,5, m), $m = 7, \dots, 9$, and it reveals an intermittent adsorption limit at $m_x = 6$. The kinetic curves of [Rh₆Fe₅]⁺ reveal a particularly fast N₂ adsorption up to $m = 6$, followed by a significantly slower addition of further N₂ adsorbates up to $m = 9$. Note, that the N₂ uptake beyond $m_x = 6$ proceeds beyond 10 s, and an ultimate equilibrium falls outside our current kinetic window.

The stepwise relative rate constants of [Rh₅Fe₆]⁺ (Fig. 9c) and of [Rh₆Fe₅]⁺ (Fig. 9d) reveal some differences: N₂ adsorption on [Rh₅Fe₆]⁺ runs into equilibrium of the two terminal products (5,6,9) and (5,6,10), *cf.* rate constants $k_{(5,6,9)}$ and $k_{-(5,6,10)}$. While overall slightly decreasing, the rate constants of [Rh₅Fe₆]⁺ reveal weak drops at $k_{(5,6,4)}$ and $k_{(5,6,7)}$, corresponding to the intermittent adsorption limits at $m_x = 4$ and 7.

In contrast, the rate constants of [Rh₆Fe₅]⁺ reveal a much more significant drop by one order of magnitude at $k_{(6,5,6)}$ and $k_{(6,5,7)}$, all prior steps proceeding equally fast. Most noteworthy, the subsequent adsorption rate $k_{(6,5,8)}$ is almost as fast as the initial ones, $k_{(6,5,m)}$ $m = 0, \dots, 5$. Obviously, the N₂ adsorption step $m = 7$ induces some severe changes in the [Rh₆Fe₅(N₂)₈]⁺ product complex which makes it more receptive for acceptance of its terminal ninth N₂ adsorbate. The non-zero desorption rate constants $k_{-(6,5,7)}$ and $k_{-(6,5,9)}$ reveal evidence for two

desorption steps, a likely $k_{-(6,5,8)}$ desorption step being uncertain due to some deficiencies in the recorded intensities of $m = 8$, which fall short of the noise level. We thus refrain from drawing further conclusion at this point. For sure, there are multiple cluster adsorbate complexes in adsorption/desorption equilibrium, and we conclude in a flexible and soft N_2 coverage of the cluster surface, where reorganization and interconversion is likely.

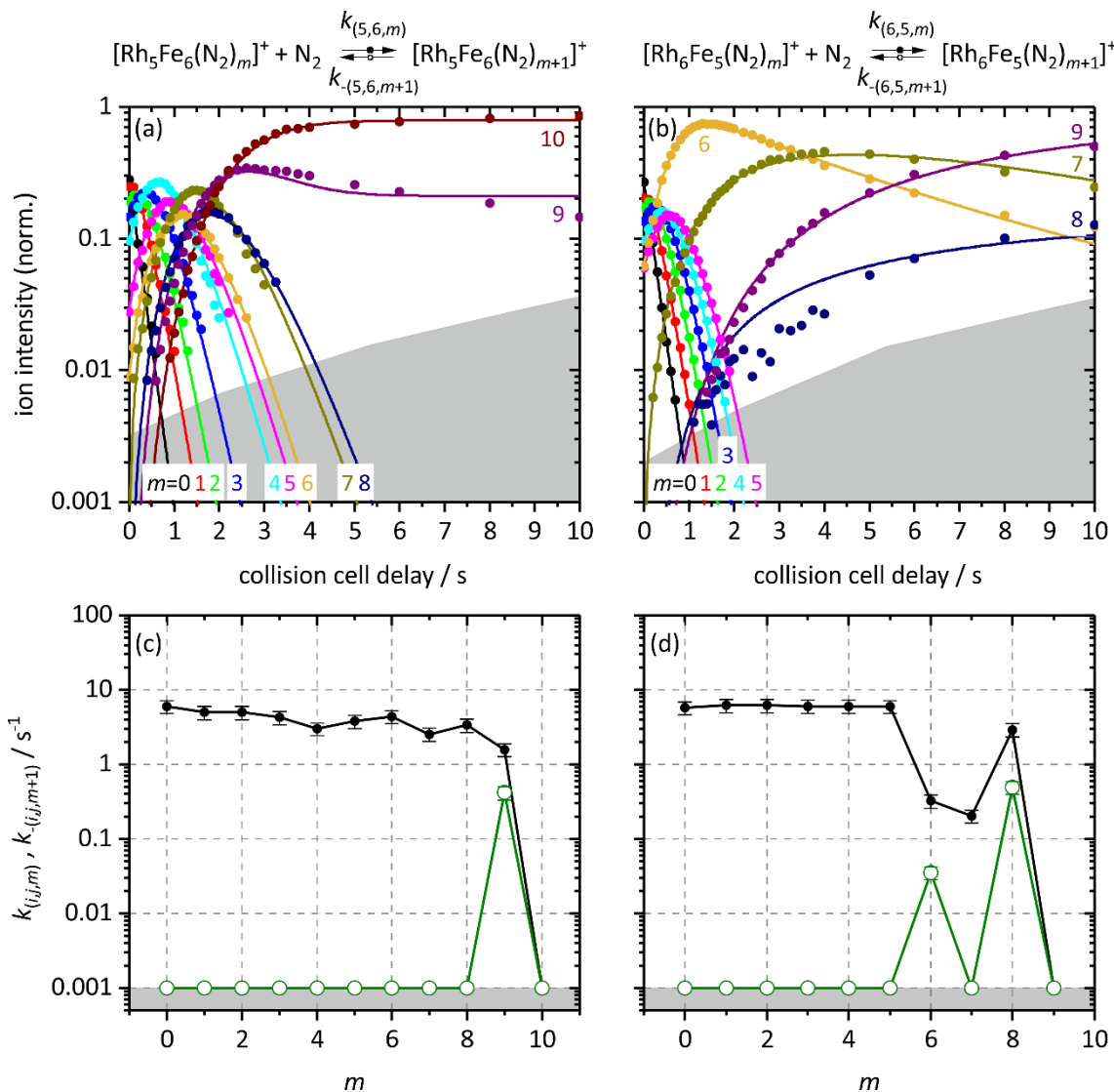


Fig. 9 Isothermal kinetics of the stepwise N_2 adsorption onto (a) isolated $[Rh_5Fe_6]^+$ clusters and (b) $[Rh_6Fe_5]^+$ clusters at 26 K (colored data points). The fits (solid colored lines) assume pseudo-first-order kinetics in an adsorption chain of up to 10 consecutive steps for $[Rh_5Fe_6]^+$ and 9 for $[Rh_6Fe_5]^+$ clusters. Fitted values of relative rate constants from the kinetic fit for the N_2 adsorption ($k_{(i,j,m)}$, black filled circles) and desorption ($k_{-(i,j,m+1)}$, green open circles, upper limits) on (c) $[Rh_5Fe_6]^+$ clusters and (d) $[Rh_6Fe_5]^+$ clusters as a function of the stepwise N_2 adsorption level m . The grey shaded areas indicate the background noise level. Values of $0.001 s^{-1}$ represent an upper limit.

In general, an unexpectedly high adsorption rate constant with a corresponding high desorption rate constant likely indicates a facile N₂ attachment and facile desorption. This very N₂ molecule is loosely bound and likely attached in a second adsorption layer – maybe roaming around. We will elaborate further on the evidence of such behavior in the following. Moreover, IR-PD spectroscopy may help to characterize and identify such loosely bound N₂ molecules [MPK].

6.5.2.7 [Rh₆Fe₆]⁺

The experimental kinetic data reveal ten consecutive steps of N₂ adsorption onto [Rh₆Fe₆]⁺ (Fig. 10a), which allow for a fit with very good overall quality. The stepwise adsorption runs up to three final species (6,6,*m*), *m* = 8, ..., 10, which are in equilibrium within 10 s (at 26 K buffer gas temperature). The adsorption limit is *m*_{max} = 10, and there is no evidence for an intermittent adsorption limit. We interpret this finding in terms of a *smooth* cluster surface of equivalent binding sites.

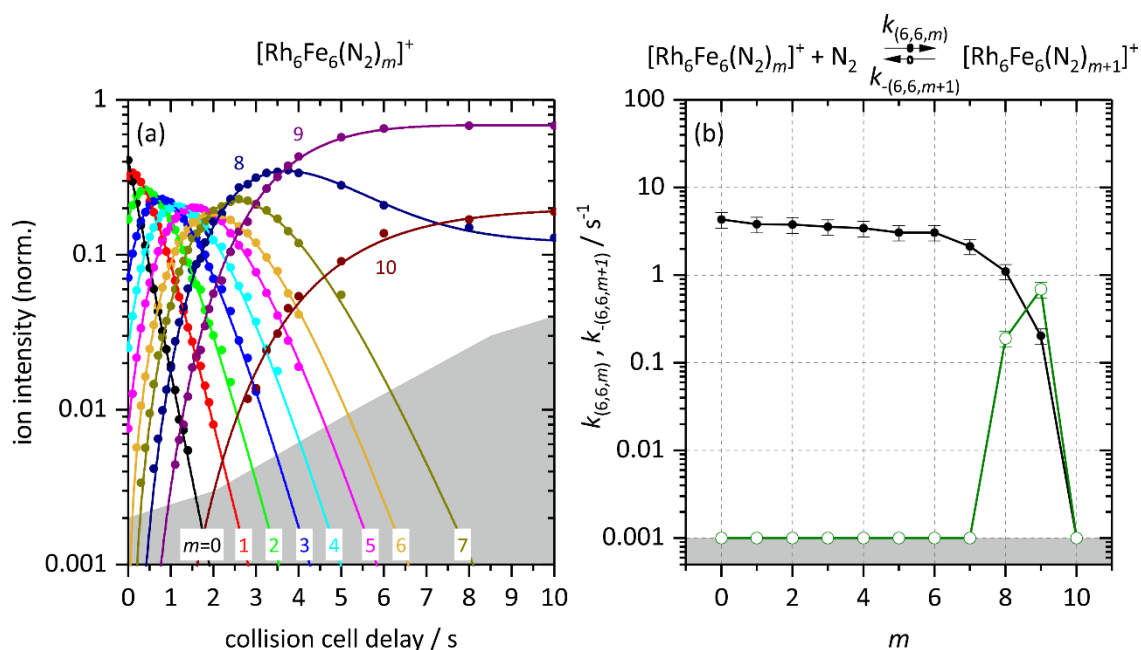


Fig. 10 (a) Isothermal kinetics of the stepwise N₂ adsorption onto isolated [Rh₆Fe₆]⁺ clusters at 26 K (colored data points). The fits (shown as solid colored lines) assume pseudo-first-order kinetics in an adsorption chain of up to 10 consecutive steps. (b) Fitted values of relative rate constants from the kinetic fit for the N₂ adsorption (*k*_(6,6,*m*), black filled circles) and desorption (*k*_{-(6,6,*m*+1)}, green open circles, upper limits) as a function of the stepwise N₂ adsorption level *m*. The grey shaded areas indicate the background noise level. Values of 0.001 s⁻¹ represent an upper limit.

The relative adsorption rates (Fig. 10b) decrease slightly and steadily upon stepwise N₂ adsorption up to $k_{(6,6,6)}$. Above, they reduce by nearly an order of magnitude up to $k_{(6,6,9)}$. For the last two steps, there is an additional desorption with increasing rates $k_{-(6,6,9)}$ and $k_{-(6,6,10)}$.

The high desorption rate constant $k_{-(6,6,10)}$ of the last step $m = 9$ might indicate a loosely attached N₂ molecule that roams around within an otherwise empty second layer.

An N₂ adsorption step to highly covered complexes (at high m , such as $m = 8,9$) might attach the incoming N₂ into a local, metastable second layer adsorption site which does – or does not – relax by migration of the second shell N₂ into a remote first shell vacancy. If not, it encounters high rate of desorption. In this regard, the observed and adsorption–desorption equilibria – here at $m = 8$ and $m = 9$ – fingerprint a significant degree of fluxionality within and amongst the adsorbate layers. In short, we summarize this behavior as ligand shell reorganization.

6.5.2.8 [Rh₆Fe₇]⁺ and [Rh₇Fe₆]⁺

We have recorded the experimental kinetic data of N₂ adsorption to the clusters [Rh₆Fe₇]⁺ (Fig. 11a) and [Rh₇Fe₆]⁺ (Fig. 11b), both of which reveal somewhat similar kinetic curves. In both cases, the stepwise N₂ adsorption develops rather smoothly up to the adsorption limit of $m_{max} = 12$ and $m_{max} = 11$, respectively.

The kinetic curves of [Rh₆Fe₇]⁺ reveal a swift N₂ adsorption up to (6,7,10) without a clear indication of any *intermittent adsorption limit*. The (6,7,10) cluster adsorbate complex is in dynamic equilibrium with the less intense (6,7,11) and (6,7,12) complexes. In contrast, [Rh₇Fe₆]⁺ reveals an undisputable intermittent adsorption limit at $m_x = 9$. For both clusters, the kinetics reveal multiple terminal N₂ adsorption products in equilibrium, which are (6,7, m), $m = 10, \dots, 12$, and (7,6, m), $m = 9, \dots, 11$, respectively.

In the course of N₂ adsorption onto the [Rh₇Fe₆]⁺ cluster, the cluster adsorbate complex (7,6,9) becomes the dominating product species at 2 s before it starts to diminish into equilibrium with larger products (7,6, m), $m = 10, 11$, by further N₂ uptake. This might be interpreted in terms of a reorganization of the N₂ adsorbate shell and / or of an N₂ induced reorganization of the metallic cluster core. If indeed so, the kinetic fits would need to involve at least two isomer specific rate constants $k_{(7,6,9(1))} < k_{(7,6,9(2))}$. The present fit of good quality does not require this treatment. It is work in progress to check for such isomerism.

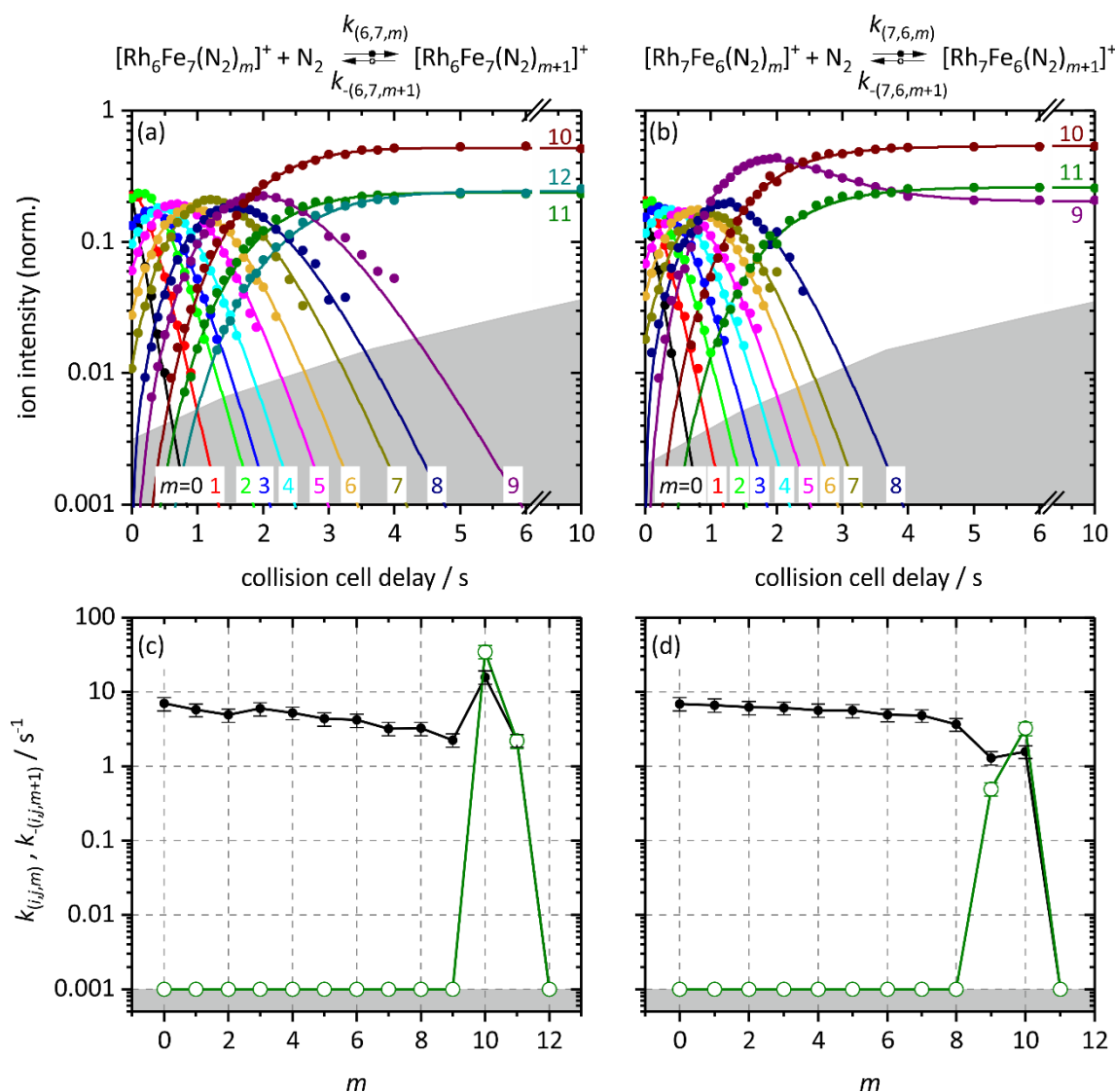


Fig. 11 Isothermal kinetics of the stepwise N₂ adsorption onto (a) isolated [Rh₆Fe₇]⁺ clusters and (b) [Rh₇Fe₆]⁺ clusters at 26 K (colored data points). The fits (solid colored lines) assume pseudo-first-order kinetics in an adsorption chain of up to 12 consecutive steps for [Rh₆Fe₇]⁺ and 11 for [Rh₇Fe₆]⁺ clusters. Fitted values of relative rate constants from the kinetic fit for the N₂ adsorption ($k_{(i,j,m)}$, black filled circles) and desorption ($k_{-(i,j,m+1)}$, green open circles, upper limits) on (c) [Rh₆Fe₇]⁺ clusters and (d) [Rh₇Fe₆]⁺ clusters as a function of the stepwise N₂ adsorption level m . The grey shaded areas indicate the background noise level. Values of 0.001 s⁻¹ represent an upper limit.

There are striking similarities in the relative rate constants of [Rh₆Fe₇]⁺ (Fig. 11c) and [Rh₇Fe₆]⁺ (Fig. 11d). The two sets of rate constants decrease steadily up to $k_{(6,7,9)}$ and $k_{(7,6,8)}$, respectively. In the case of [Rh₇Fe₆]⁺, there is a drop in stepwise N₂ adsorption at $k_{(7,6,9)}$, clearly related to the proposed intermittent adsorption limit at $m_x = 9$ (7,6,9). In the case of [Rh₆Fe₇]⁺ it sticks out, that the rate constants $k_{(6,7,10)}$ and $k_{-(6,7,11)}$ are surprisingly large. The fits reveal evidence

for desorption in both cases, namely $k_{-(6,7,10)}$, $k_{-(6,7,11)}$ and $k_{-(7,6,9)}$, $k_{-(7,6,10)}$, respectively. The magnitudes of adsorption and desorption rates differ in a non-predictable manner: In the case of $[\text{Rh}_6\text{Fe}_7]^+$ $k_{(6,7,10)} < k_{-(6,7,11)}$ and $k_{(6,7,11)} \sim k_{-(6,7,12)}$. In the case of $[\text{Rh}_7\text{Fe}_6]^+$ $k_{(7,6,9)} > k_{-(7,6,10)}$ and $k_{(7,6,10)} < k_{-(7,6,11)}$. In both cases, we suggest a likely flexible and soft surface coverage, where interconversion is possible for the last three N_2 adsorbates. In both cases, $m = 10$ desorption rates constants exceed adsorption rates and may indicate the onset of facile N_2 adsorption in a second shell that easily desorbs.

6.5.2.9 $[\text{Rh}_7\text{Fe}_7]^+$

The experimental kinetic data of $[\text{Rh}_7\text{Fe}_7]^+$ reveal twelve consecutive steps of N_2 adsorption (Fig. 12a) up to four final adsorption products, $(7,7,m)$, $m = 9, \dots, 12$, which are in equilibrium. The N_2 maximum adsorption limit is at $m_{\max} = 12$ and there is an intermittent adsorption limit $m_x = 9$. Note, that in equilibrium it is not the product $m_{\max} = 12$, which is most abundant, but $m = 10$ instead.

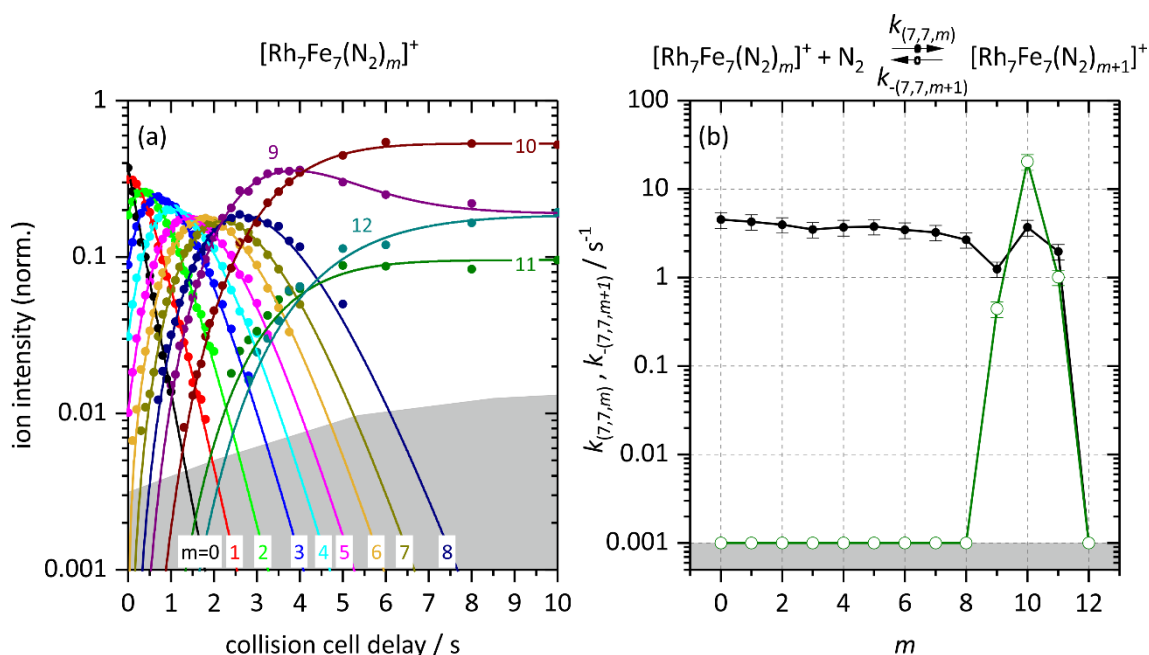


Fig. 12 (a) Isothermal kinetics of the stepwise N_2 adsorption onto isolated $[\text{Rh}_7\text{Fe}_7]^+$ clusters at 26 K (colored data points). The fits (solid colored lines) assume pseudo-first-order kinetics in an adsorption chain of up to 12 consecutive steps. (b) Fitted values of relative rate constants from the kinetic fit for the N_2 adsorption ($k_{(7,7,m)}$, black filled circles) and desorption ($k_{-(7,7,m+1)}$, green open circles, upper limits) as a function of the stepwise N_2 adsorption level m . The grey shaded areas indicate the background noise level. Values of 0.001 s^{-1} represent an upper limit.

The relative adsorption rate constants $k_{(7,7,m)}$ are constant within their small uncertainties up to a drop at $k_{(7,7,9)}$ (Fig. 12b), where the desorption $k_{-(7,7,10)}$ sets in. The magnitudes of adsorption and desorption rates of $(7,7,m)$ with large m – at high N₂ coverage - differ in a non-predictable manner: $k_{(7,7,9)} > k_{-(7,7,10)}$ and $k_{(7,7,10)} < k_{-(7,7,11)}$, and $k_{(7,7,11)} > k_{-(7,7,12)}$. We suggest a likely flexible and soft surface N₂ coverage on the likely *smooth* surface of [Rh₇Fe₇]⁺, where interconversion is possible for the last three N₂ adsorbates. As for [Rh₆Fe₇]⁺ and [Rh₇Fe₆]⁺, $m = 10$ adsorption and desorption rate constants are significantly enhanced, which may indicate the onset of facile N₂ adsorption in a second shell that easily desorbs.

6.5.2.10 [Rh₇Fe₈]⁺ and [Rh₈Fe₇]⁺

Obviously, there are striking differences in the recorded kinetic data of the clusters [Rh₇Fe₈]⁺ (Fig. 13a) and [Rh₈Fe₇]⁺ (Fig. 13b) and in their fits. In both cases, there is a rather smooth and stepwise N₂ adsorption up to both $(i,j,7)$ without any desorption steps. Beyond, differences set in: In the case of [Rh₇Fe₈]⁺ adsorption proceeds continuously to form $(7,8,8)$ as most intense species. One more N₂ is adsorbed and yields a low intensity of $(7,8,9)$. This last step is the only one where a corresponding desorption step is likely, yielding an equilibrium between the dominant $m = 8$ $(7,8,8)$ (85%) and $m_{max} = 9$ $(7,8,9)$ (15%). We may assume a stiff N₂ surface coverage, where merely a single surface site allows for some additional N₂ adsorption/desorption, giving rise to a bilateral equilibrium between $(7,8,8)$ and $(7,8,9)$. In the case of [Rh₈Fe₇]⁺, the $(8,7,m)$, $m = 8$ and 9, products are mere intermediates or precursors for further adsorption of four additional N₂ molecules up to $m_{max} = 13$. The last six adsorbate species $(8,7,m)$, $m = 8, \dots, 13$, are in equilibrium, including ‘intermediates’ within the time scale of our experiments, 10 s. This equilibrium takes longer to stabilize than the two-species-equilibrium in the $(7,8,m)$ case. In the case of the $(8,7,m)$ cluster adsorbate complexes, we may assume a soft surface coverage, where multiple sites of swift N₂-adsorption/desorption operate independently which gives rise to the observed broad equilibrium of six species.

The two products [Rh₈Fe₇(N₂)_{8,9}]⁺ become the dominating product species after less than 1 s reaction delay before they start to diminish into equilibrium with larger products ($m = 10, \dots, 13$) by further N₂ adsorption. This might be interpreted once more in terms of a reorganization of the N₂ adsorbate shell and / or of an N₂ induced reorganization of the metallic cluster core. If indeed so the kinetic fits would need to involve at least two isomer specific rate constants $k_{(8,7,9(1))} < k_{(8,7,9(2))}$, similar to $(7,6,9)$. The present fit of good quality does not need to do so for $(8,7,m)$, $m = 8, \dots, 10, 12$, and 13. Note, however, that the $m = 11$ product

intensity is significantly off from any such fit. Here, we find clear evidence for such a possible reorganization, and the analysis of this feature is subject of current work in progress.

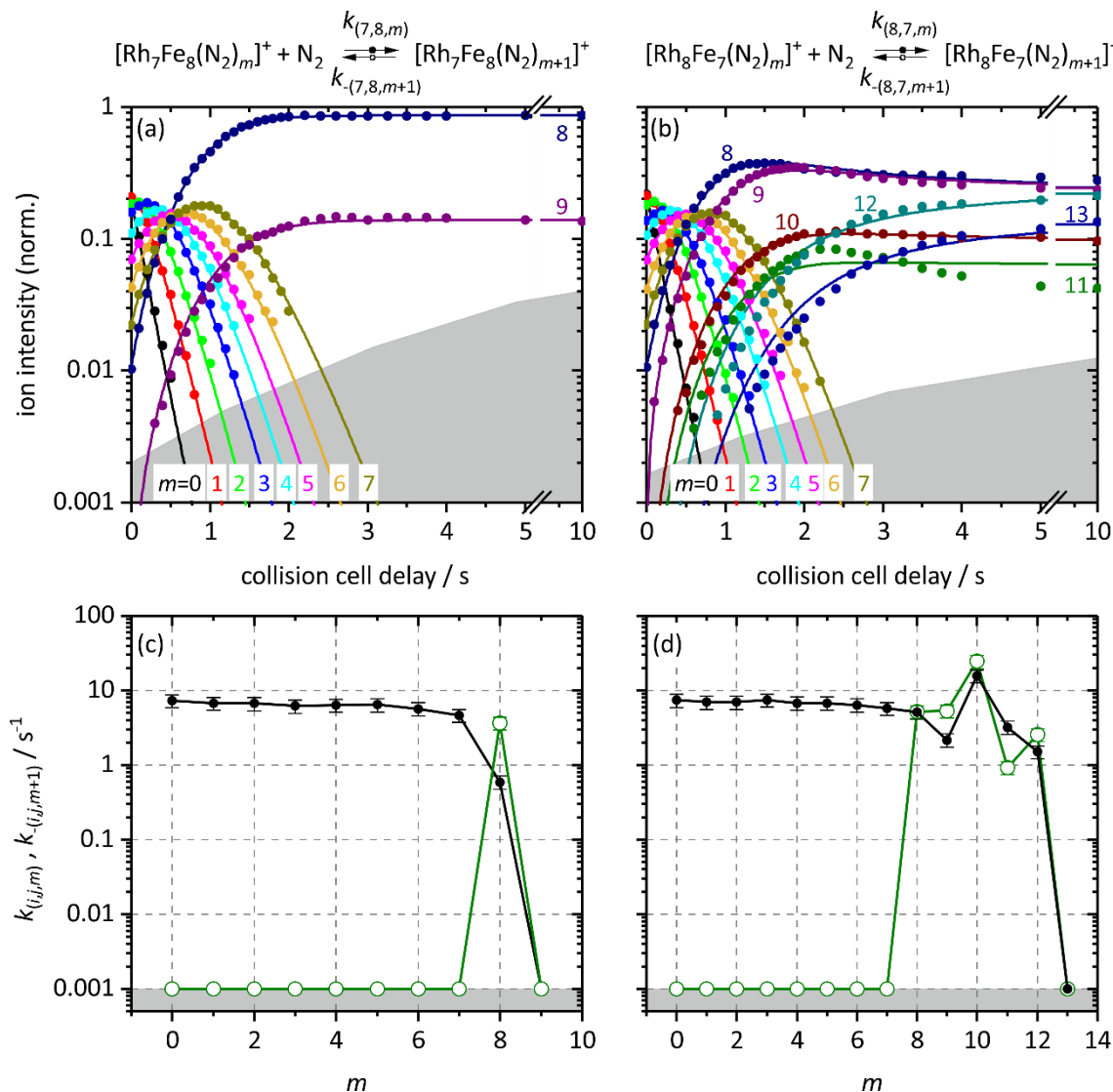


Fig. 13 Isothermal kinetics of the stepwise N₂ adsorption onto (a) isolated [Rh₇Fe₈]⁺ clusters and (b) [Rh₈Fe₇]⁺ clusters at 26 K (colored data points). The fits (solid colored lines) assume pseudo-first-order kinetics in an adsorption chain of up to 9 consecutive steps for [Rh₇Fe₈]⁺ and 13 for [Rh₈Fe₇]⁺ clusters. Fitted values of relative rate constants from the kinetic fit for the N₂ adsorption ($k_{(i,j,m)}$, black filled circles) and desorption ($k_{-(i,j,m+1)}$, green open circles, upper limits) on (c) [Rh₇Fe₈]⁺ clusters and (d) [Rh₈Fe₇]⁺ clusters as a function of the stepwise N₂ adsorption level m . The grey shaded areas indicate the background noise level. Values of 0.001 s⁻¹ represent an upper limit.

At the bottom line, the above discussed kinetic data and fits of Fig. 13a,b provide for the rate constants of stepwise N₂ adsorption and desorption to [Rh₇Fe₈]⁺ (Fig. 13c) and [Rh₈Fe₇]⁺ (Fig. 13d), respectively. In both cases, the rate constants $k_{(7,8,m)}$ and $k_{(8,7,m)}$ are constant within

their small uncertainties up to $m = 7,8$. With $k_{(7,8,8)}$ desorption $k_{-(7,8,9)}$ sets in and terminates the stepwise N₂ addition. In the case of [Rh₈Fe₇]⁺ there are non-vanishing adsorption and desorption rate constants up to $k_{(8,7,12)}$ and $k_{-(8,7,13)}$, respectively. Note, that the $k_{(8,7,10)}$ and $k_{-(8,7,11)}$ pair of constants significantly exceeds the magnitudes of all prior adsorption steps, which might indicate the onset of facile N₂ adsorption in a second shell that easily desorbs. We strive to incorporate into the fitting procedure a two-step, isomer sensitive mechanism in the near future – work in progress.

6.5.2.11 [Rh₈Fe₈]⁺

Finally, we have recorded the experimental kinetics of [Rh₈Fe₈]⁺ (Fig. 14a), which comprise a maximum adsorption limit of $m_{max} = 11$. There are multiple N₂ adsorbates in equilibrium, which are the four largest (8,8, m), $m = 8, \dots, 11$, and there is no evidence for an intermittent adsorption limit.

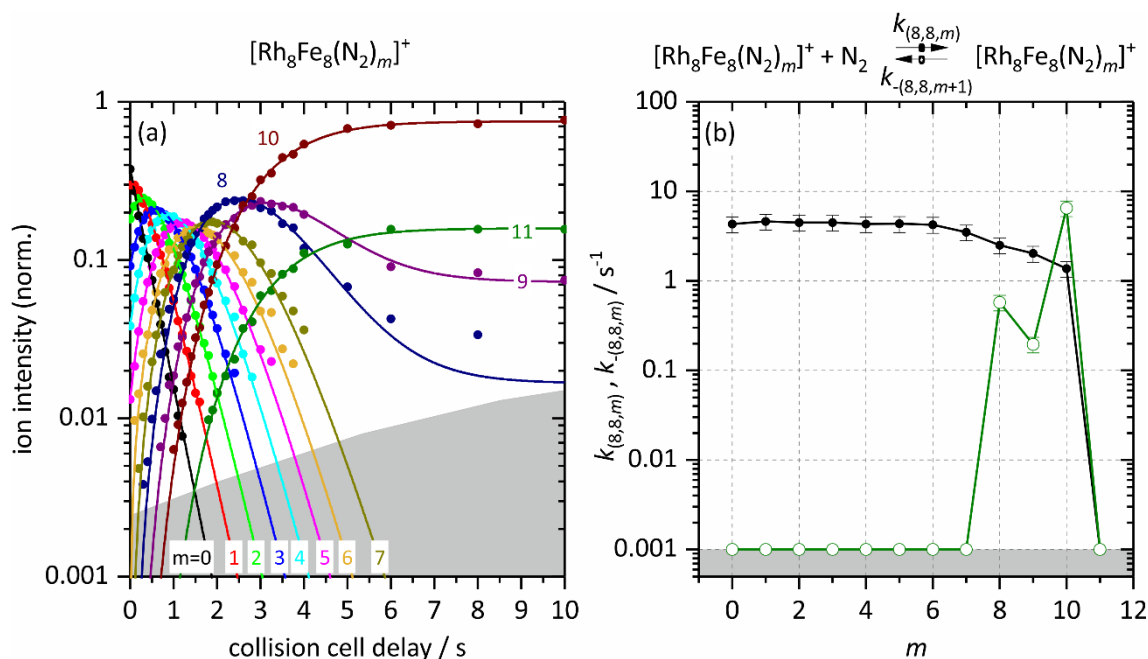


Fig. 14 (a) Isothermal kinetics of the stepwise N₂ adsorption onto isolated [Rh₈Fe₈]⁺ clusters at 26 K (colored data points). The fits (solid colored lines) assume pseudo-first-order kinetics in an adsorption chain of up to 11 consecutive steps. (b) Fitted values of relative rate constants from the kinetic fit for the N₂ adsorption ($k_{(8,8,m)}$, black filled circles) and desorption ($k_{-(8,8,m+1)}$, green open circles, upper limits) as a function of the stepwise N₂ adsorption (level m). The grey shaded areas indicate the background noise level. Values of 0.001 s⁻¹ represent an upper limit.

The rate constants $k_{(8,8,m)}$ remain constant up to $k_{(8,8,6)}$ where a steady decrease sets in (Fig. 14b). Our fit predicts significant desorption steps $k_{-(8,8,m+1)}$, $m = 8, \dots, 10$ which put (8,8, m)

$m = 8, \dots, 11$ into equilibrium and confirm the discussion of the kinetic curves. We interpret our findings in terms of a flexible surface N_2 coverage on the likely *smooth* surface of $[Rh_8Fe_8]^+$, where interconversion is possible for the last three N_2 adsorbates. For $[Rh_8Fe_8]^+$ $m = 10$ adsorption and desorption rate constants exceed the previous values and may indicate – once more – the onset of facile N_2 adsorption in a second shell that easily desorbs.

The adsorption of N_2 is the only observable product channel for all investigated cases. There might be N_2 activation by these $[Rh_iFe_j]^+$ clusters. If so, it does not reflect in the present kinetic data on their own. Any statement in this regard would take spectroscopic structure elucidation as pursued in parallel **[MPK]** [72].

The above documented and discussed stoichiometry variation plus 1 reveals that addition of an extra Fe atom may promote N_2 uptake, *e.g.* in cases (5,5) and (6,6), or it may quench the maximum N_2 uptake, as *e.g.* in the cases of (4,4) and (7,7). In remarkable contrast, the addition of a single Rh atom does not make a difference in the case of (4,4) but promotes N_2 uptake by one in the cases of (5,5), (6,6) and (7,7).

6.5.3 Determination of sticking probabilities $\gamma_{(i,j,m)}$ and Gibbs free energies ΔG_{ad}

6.5.3.1 Sticking probabilities

Calculation of absolute rate constants (Table S2) and their comparison with the Langevin collision rates (Table S3) enables us to evaluate sticking probabilities for each adsorption step (Table 1). The explicit evaluation for each desorption step is given in the Supplement. (*cf.* Tables S4, S5, S6).

We found sticking probabilities up to $\gamma_{(i,j,m)} = 0.96$ at low N_2 coverages ($m < 6$), and few values up to $\gamma_{(i,j,m)} = 2$ at high N_2 coverage (*cf.* values in Table 1 with orange background). Two of these exceptionally high sticking probabilities are $\gamma_{(6,7,10)}$ and $\gamma_{(8,7,10)}$ of $[Rh_6Fe_7]^+$ and $[Rh_8Fe_7]^+$. In principal, the absolute rate constants k_{abs} might exceed the theoretical collision rates k_{coll} [81]. However, we regard this unlikely in the present cases. Note, that the corresponding desorption rate constants are exceedingly high as well (*cf.* Table 2). These findings might thus indicate the onset of facile N_2 adsorption and desorption in a second shell with low binding energy, reminiscent of a physisorption.

Table 1 Sticking probabilities $\gamma_{(i,j,m)}$ of N₂ adsorption to $[\text{Rh}_i\text{Fe}_j(\text{N}_2)_m]^+$. Relative uncertainties are +20 % and -30 % (conservative estimate). In case of no entry, $\gamma_{(i,j,m)} \leq 0.004$. Light blue shading marks the observation of adsorption to the $[\text{Rh}_i\text{Fe}_j(\text{N}_2)_m]^+$ species, dark blue shading marks the species $(i,j,m+1)$ with highest abundance at long storage times. Blue frames mark some high adsorption rates, and light orange shading indicates two cases of very high rates; for further discussion, refer to the text.

Sticking probabilities													
$\gamma_{(i,j,m)}$	$m = 0$	1	2	3	4	5	6	7	8	9	10	11	12
[Rh₃Fe₃(N₂)_m]⁺	0.71	0.73	0.60	0.59	0.62	0.56	0.66						
[Rh ₃ Fe ₄ (N ₂) _m] ⁺	0.68	0.45	0.19	0.67	0.57	0.25	0.11						
[Rh ₄ Fe ₃ (N ₂) _m] ⁺	0.74	0.83	0.72	0.32	0.46	0.45	0.03	0.30					
[Rh₄Fe₄(N₂)_m]⁺	0.42	0.57	0.56	0.66	0.34	0.45	0.37	0.54	0.02	0.18	0.26		
[Rh ₄ Fe ₅ (N ₂) _m] ⁺	0.28	0.58	0.49	0.56	0.36	0.15	0.23	3E-3					
[Rh ₅ Fe ₄ (N ₂) _m] ⁺	0.47	0.65	0.72	0.71	0.64	0.65	0.49	0.59	0.39	0.23	0.39		
[Rh₅Fe₅(N₂)_m]⁺	0.33	0.45	0.43	0.41	0.25	0.25	0.17	0.09					
[Rh ₅ Fe ₆ (N ₂) _m] ⁺	0.77	0.64	0.64	0.54	0.39	0.49	0.56	0.32	0.43	0.20			
[Rh ₆ Fe ₅ (N ₂) _m] ⁺	0.74	0.79	0.79	0.78	0.77	0.77	0.04	0.03	0.37				
[Rh₆Fe₆(N₂)_m]⁺	0.55	0.49	0.48	0.46	0.44	0.39	0.39	0.27	0.14	0.03			
[Rh ₆ Fe ₇ (N ₂) _m] ⁺	0.90	0.74	0.63	0.76	0.67	0.56	0.54	0.41	0.41	0.29	2.03	0.29	
[Rh ₇ Fe ₆ (N ₂) _m] ⁺	0.89	0.86	0.80	0.79	0.73	0.72	0.63	0.62	0.47	0.17	0.20		
[Rh₇Fe₇(N₂)_m]⁺	0.58	0.55	0.51	0.45	0.47	0.49	0.44	0.42	0.35	0.16	0.47	0.25	
[Rh ₇ Fe ₈ (N ₂) _m] ⁺	0.94	0.87	0.86	0.80	0.82	0.83	0.73	0.60	0.08				
[Rh ₈ Fe ₇ (N ₂) _m] ⁺	0.95	0.89	0.90	0.96	0.87	0.88	0.82	0.74	0.66	0.28	2.03	0.41	0.19
[Rh₈Fe₈(N₂)_m]⁺	0.55	0.59	0.58	0.58	0.56	0.56	0.55	0.45	0.32	0.26	0.18		

A sticking probability of 96% as in the case of $\gamma_{(8,7,3)}$ implies that nearly every collision leads to an adsorption. The initial five first N₂ adsorption steps occur with equal sticking probabilities, within given uncertainties, for all clusters (i,j) investigated. Beyond, we see a general tendency of decreasing sticking probabilities with increasing N₂ adsorption m . Upon gradual saturation of available adsorption sites, the stepwise sticking probabilities decline.

6.5.3.2 Desorption rates

The applied fitting procedures invoked desorption wherever necessary, and the fitted unimolecular rate constants are collected in Table 2, with small values beyond significance

omitted (for a full compilation refer to Table S4). Desorption rate constants above 0.001 s^{-1} indicate the onset of adsorption/desorption equilibria. There are some very high desorption rates, $k_{-(i,j,m+1)} > 4 \text{ s}^{-1}$, which are $k_{-(4,4,9)}$, $k_{-(6,7,11)}$, $k_{-(7,7,11)}$, $k_{-(8,7,9)}$, $k_{-(8,7,10)}$, $k_{-(8,7,11)}$ and $k_{-(8,8,11)}$. All of these imply a high volatility of the $(m+1)^{\text{th}}$ N_2 adsorbate as *e.g.* through second shell adsorption. In any case, it leads to high intensities of the previous N_2 adsorbate species (i,j,m) .

Table 2 Fitted relative rate constants $k_{-(i,j,m+1)}$ $m = 6, \dots, 12$ for the N_2 desorption off $[\text{Rh}_i\text{Fe}_j(\text{N}_2)_{m+1}]^+$. Relative uncertainties are $\pm 20\%$ (conservative estimate). In case of no entry, $k_{-(i,j,m+1)} \leq 0.001 \text{ s}^{-1}$, which holds in particular for all cases of $m < 6$. Exceedingly high values are marked in red. Light blue shading marks pure observation of the (i,j,m) species, dark blue shading marks the species $(i,j,m+1)$ with highest abundance at long storage times.

Relative rate constants	$m = 6$	7	8	9	10	11	12
$k_{-(i,j,m+1)} / \text{s}^{-1}$							
[Rh₃Fe₃]⁺							
[Rh ₃ Fe ₄] ⁺							
[Rh ₄ Fe ₃] ⁺	0.18	0.0023					
[Rh₄Fe₄]⁺			5.1	3.1	0.94		
[Rh ₄ Fe ₅] ⁺		0.42					
[Rh ₅ Fe ₄] ⁺							
[Rh₅Fe₅]⁺							
[Rh ₅ Fe ₆] ⁺				0.42			
[Rh ₆ Fe ₅] ⁺	0.035		0.49				
[Rh₆Fe₆]⁺			0.19	0.69			
[Rh ₆ Fe ₇] ⁺						35	2.2
[Rh ₇ Fe ₆] ⁺				0.50	3.2		
[Rh₇Fe₇]⁺				0.44	20	1.0	
[Rh ₇ Fe ₈] ⁺			3.7				
[Rh ₈ Fe ₇] ⁺			5.2	5.3	24	0.92	2.56
[Rh₈Fe₈]⁺			0.58	0.20	6.5		

6.5.3.3 Gibbs energies

We have managed to observe adsorption/desorption equilibria in numerous cases, and in particular when reaching the N_2 adsorption limit. Such equilibria – established under isothermal buffer gas conditions – allow for further thermochemical considerations by evaluating Gibbs energies for every such equilibrium (*cf.* Table S8). We depict these values in

Fig. 15 with one row for each investigated cluster of size (i,j) . The data reveal a blue marked plateau at low N₂ coverages m with negative Gibbs energies (upper limits of -1.5 to -2.0 kJ/mol) from swift adsorption without any significant desorption (set to upper limits of $k_{-(i,j,m+1)} < 0.001 \text{ s}^{-1}$). The adsorption step m that forms the most intense species $(i,j,m+1)$ after 10 s storage is highlighted by a black box.

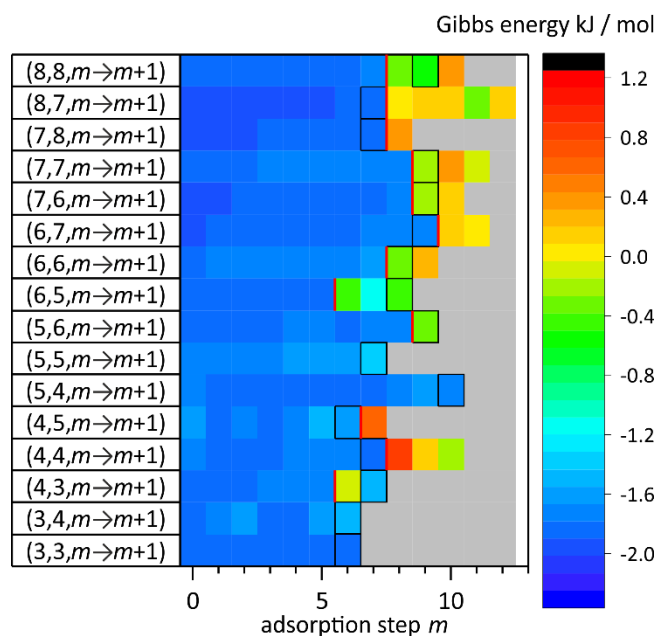


Fig. 15 Plot of Gibbs energies $\Delta_{\text{ads}}G^{26 \text{ K}}_{(i,j,m)}$ for the equilibria of N₂ adsorption onto $[\text{Rh}_i\text{Fe}_j(\text{N}_2)_m]^+$ / desorption off $[\text{Rh}_i\text{Fe}_j(\text{N}_2)_{m+1}]^+$. Note, that the $\Delta_{\text{ads}}G^{26 \text{ K}}_{(i,j,m)}$ values within the blue plateau signify upper limits of otherwise unknown values. Note, that deviations from this plateau indicating swift adsorption steps which occur only for high N₂ coverages towards m_{max} . The adsorption becomes less spontaneous towards the end of the chain. The red lines indicate the onset of desorption steps. The grey area signifies non-occurring processes. The black boxes denote the most intense species $(i,j,m+1)$ after 10 s. The $\Delta_{\text{ads}}G^{26 \text{ K}}_{(i,j,m)}$ values hold for the corrected chamber pressure of $p = 5.4 \times 10^{-7} \text{ mbar}$.

With increasing m , the Gibbs energies gradually increase and become less negative. Adsorption becomes less spontaneous towards m_{max} , in parallel to desorption steps becoming significant. The onset of desorption steps is marked by the red lines in Fig. 15. In a few cases desorption is faster than adsorption, and we obtain Gibbs energies of up to +0.78 kJ/mol (4,4,8). In general, the range of adsorption/desorption equilibrium becomes broader in m with increasing cluster size n . Seemingly, high N₂ coverages on large clusters allow for swift N₂ ligand shell reorganization.

The obtained values of the Gibbs energies are remarkably small in view of single N₂ adsorption enthalpies on surfaces, which are -0.35 eV (= 34 kJ/mol) (Fe) and -0.56 eV (= 54 kJ/mol) (Rh), respectively [82]. Values for N₂ adsorption onto cationic Rh clusters are in the same range as for the bimetallic clusters.[25, 27, 72]

Upon closer inspection of the 16 individual cases in the investigated size range $(i,j) = (3,3) - (8,8)$, we observe two classes of clusters with a similar behavior, and a single, remarkable exception:

Firstly, we find four cases ($[\text{Rh}_3\text{Fe}_3(\text{N}_2)_7]^+$, $[\text{Rh}_4\text{Fe}_4(\text{N}_2)_8]^+$, $[\text{Rh}_7\text{Fe}_8(\text{N}_2)_8]^+$, $[\text{Rh}_8\text{Fe}_7(\text{N}_2)_8]^+$), which are most abundant species $(i,j,m+1)$, $m = 6, 7$, provide for high adsorption rates $k_{(i,j,6 \text{ or } 7)} > 4.0 \text{ s}^{-1}$ and vanishing desorption rates $k_{-(i,j,7 \text{ or } 8)} < 0.001 \text{ s}^{-1}$ (cf. kinetic plots in section 6.5.2 and Table S1, Table 2 for values). We take these cases as evidences for a filling of the first or second N₂ ligand shell at step $m = 7$ or 8 . These most abundant species are not part of adsorption – desorption equilibria. In three out of four cases, however, there are subsequent N₂ adsorption/desorption processes which do equilibrate – in line with some weakly bound N₂ ligands beyond the first shell closure.

Secondly, there are six cases ($[\text{Rh}_5\text{Fe}_6(\text{N}_2)_{10}]^+$, $[\text{Rh}_6\text{Fe}_5(\text{N}_2)_9]^+$, $[\text{Rh}_6\text{Fe}_6(\text{N}_2)_9]^+$, $[\text{Rh}_7\text{Fe}_6(\text{N}_2)_{10}]^+$, $[\text{Rh}_7\text{Fe}_7(\text{N}_2)_{10}]^+$, $[\text{Rh}_8\text{Fe}_8(\text{N}_2)_{10}]^+$), where (i,j,m) , $m = 9, 10$, become most abundant while being part of adsorption/desorption equilibria – reminiscent of a ligand shell reorganization and the occurrence of weakly bound N₂ ligands.

There is one remarkable exception occurring: $[\text{Rh}_5\text{Fe}_4]^+$ reveals a swift N₂ adsorption onto seemingly equivalent adsorption sites up to N₂ coverages, which are surprisingly high, in particular when compared to $[\text{Rh}_4\text{Fe}_5]^+$ and $[\text{Rh}_5\text{Fe}_5]^+$. In this particular case, there seems to be a high likelihood for either double N₂ occupation of Rh sites or for additional adsorption to the less preferred Fe sites, or a combination of both. It is striking, that the fit of good quality provides for no evidence of any desorption.

The equiatomic clusters $(i,j,m) = (3,3,m), \dots, (8,8,m)$ are in the focus of the accompanying cryo infrared spectroscopic study [MPK] [72].

6.6 Conclusions

We have recorded the cryo kinetics of N₂ adsorption onto cationic mixed [Rh_iFe_j]⁺ clusters. The adsorption limits of equiatomic clusters [Rh_{*n*/2}Fe_{*n*/2}]⁺ reveal less adsorbed N₂ than the [Rh_{*n*}]⁺ clusters, but more adsorbed N₂ than the [Fe_{*n*}]⁺ clusters. In the cases of the clusters [Rh_{*(n-1)/2*}Fe_{*(n+1)/2*}]⁺ and [Rh_{*(n+1)/2*}Fe_{*(n-1)/2*}]⁺ with stoichiometries out of balance, we observe an increase of the adsorption limits with their sizes. From the kinetic fits, we extract relative rate constants for each N₂ adsorption step and possible desorption steps. We find significant trends in adsorption behavior, which reveals adsorption limits, intermittent adsorption limits and equilibrium reactions. For those steps, which are in equilibrium, we determine the Gibbs free energies. We conclude on likely ligand shell reorganization and some weakly bound N₂ ligands for clusters, where multiple N₂ adsorbates are in equilibrium. The relative rate constants are transferred to absolute rate constants, which are slightly smaller than the collision rates calculated by the Average Dipole Orientation (ADO, Langevin) theory. The calculated sticking probabilities increase in general with cluster size. We observe in most cases a decrease in the sticking probability with increasing amount *m* of adsorbed N₂ onto a specific cluster, in particular when reaching an adsorption/desorption equilibrium. For such equilibria we observe significant desorption rates in several cases. Despite these indications for cluster size dependent properties, we cannot conclude on the particular structures, *e.g.* their geometries and the metal atom distributions within the clusters. A spectroscopic study on the equiatomic cluster will provide further insight in this regard.

6.7 Acknowledgements

This work was supported by the German research foundation DFG within the transregional collaborative research center SFB/TRR 88 'Cooperative effects in homo and heterometallic complexes' (3MET.de) and by the state research center OPTIMAS. We thank Thomas Kolling for technical support.

6.8 References

1. Knickelbein, M.B., *Reactions of transition metal clusters with small molecules*. Annual Review of Physical Chemistry **1999**, *50*, 79-115.

2. O'Hair, R.A.J. and Khairallah, G.N., *Gas Phase Ion Chemistry of Transition Metal Clusters: Production, Reactivity, and Catalysis*. Journal of Cluster Science **2004**, *15*, 331-363.
3. Somorjai, G.A. and McCrea, K., *Roadmap for catalysis science in the 21st century: a personal view of building the future on past and present accomplishments*. Applied Catalysis A: General **2001**, *222*, 3-18.
4. Armentrout, P., *Reactions and thermochemistry of small transition metal cluster ions*. Annu Rev Phys Chem **2001**, *52*, 423-61.
5. Boudart, M., *Catalysis by Supported Metals*, in *Advances in Catalysis*, D.D. Eley, H.P. and Paul, B.W., editors. **1969**, Academic Press. 153-166.
6. Boudart, M. and Djega-Mariadassou, G., *Kinetics Of Heterogenous Catalytic Reactions*. **1984**: Princeton University Press.
7. Strongin, D.R., Carrazza, J., Bare, S.R., and Somorjai, G.A., *Importance of C_7 sites and surface roughness in the ammonia synthesis reaction over iron*. J. Catal.; (United States) **1987**, 213-215.
8. Selman, G.L. and Bourne, A.A., *Dispersion-Strengthened Rhodium-Platinum*. Platinum Metals Rev. **1976**, *20*.
9. Votsmeier, M., Kreuzer, T., Gieshoff, J., and Lepperhoff, G., *Automobile Exhaust Control*, in *Ullmann's Encyclopedia of Industrial Chemistry*. **2009**.
10. Ertl, G., *Reactions at Surfaces: From Atoms to Complexity (Nobel Lecture)*. Angewandte Chemie International Edition **2008**, *47*, 3524-3535.
11. Harrison, B., Cooper, B.J., and Wilkins, A.J.J., *Control of Nitrogen Oxide Emissions from Automobile Engines*. Platinum Metals Rev **1981**, *25*, 14-22.
12. Hermes, A.C., Hamilton, S.M., Hopkins, W.S., Harding, D.J., Kerpel, C., Meijer, G., Fielicke, A., and Mackenzie, S.R., *Effects of Coadsorbed Oxygen on the Infrared Driven Decomposition of N_2O on Isolated Rh_5^+ Clusters*. The Journal of Physical Chemistry Letters **2011**, *2*, 3053-3057.
13. Hamilton, S.M., Hopkins, W.S., Harding, D.J., Walsh, T.R., Haertelt, M., Kerpel, C., Gruene, P., Meijer, G., Fielicke, A., and Mackenzie, S.R., *Infrared-induced reactivity of N_2O on small gas-phase rhodium clusters*. Journal of Physical Chemistry A **2011**, *115*, 2489-2497.
14. Hamilton, S.M., Hopkins, W.S., Harding, D.J., Walsh, T.R., Gruene, P., Haertelt, M., Fielicke, A., Meijer, G., and Mackenzie, S.R., *Infrared induced reactivity on the surface of isolated size-selected clusters: dissociation of N_2O on rhodium clusters*. Journal of the American Chemical Society **2010**, *132*, 1448-1449.
15. Harding, D., Ford, M.S., Walsh, T.R., and Mackenzie, S.R., *Dramatic size effects and evidence of structural isomers in the reactions of rhodium clusters, $Rh_n^{+/-}$, with nitrous oxide*. Physical Chemistry Chemical Physics **2007**, *9*, 2130-2136.
16. Parry, I.S., Kartouzian, A., Hamilton, S.M., Balaj, O.P., Beyer, M.K., and Mackenzie, S.R., *Collisional activation of N_2O decomposition and CO oxidation reactions on isolated rhodium clusters*. Journal of Physical Chemistry A **2013**, *117*, 8855-8863.
17. Zhao, Y.-X., Zhao, X.-G., Yang, Y., Ruan, M., and He, S.-G., *Rhodium chemistry: A gas phase cluster study*. The Journal of Chemical Physics **2021**, *154*, 180901.
18. Balteanu, I., Achatz, U., Balaj, O.P., Fox, B.S., Beyer, M.K., and Bondybey, V.E., *The effect of charge upon CO-adsorption by ionic group 5 and group 9 transition metal clusters*. International Journal of Mass Spectrometry **2003**, *229*, 61-65.

19. Berg, C., Beyer, M., Achatz, U., Joos, S., Niedner-Schatteburg, G., and Bondybey, V.E., *Effect of charge upon metal cluster chemistry: Reactions of Nb_n and Rh_n anions and cations with benzene*. Journal of Chemical Physics **1998**, *108*, 5398-5403.
20. Balteanu, I., Balaj, O.P., Fox-Beyer, B.S., Rodrigues, P., Barros, M.T., Moutinho, A.M.C., Costa, M.L., Beyer, M.K., and Bondybey, V.E., *Size- and Charge-State-Dependent Reactivity of Azidoacetonitrile with Anionic and Cationic Rhodium Clusters Rh_n[±]*. Organometallics **2004**, *23*, 1978-1985.
21. Ford, M.S., Anderson, M.L., Barrow, M.P., Woodruff, D.P., Drewello, T., Derrick, P.J., and Mackenzie, S.R., *Reactions of nitric oxide on Rh₆⁺ clusters: abundant chemistry and evidence of structural isomers*. Physical Chemistry Chemical Physics **2005**, *7*, 975-980.
22. Anderson, M.L., Ford, M.S., Derrick, P.J., Drewello, T., Woodruff, D.P., and Mackenzie, S.R., *Nitric Oxide Decomposition on Small Rhodium Clusters, Rh_n⁺*. The Journal of Physical Chemistry A **2006**, *110*, 10992-11000.
23. Balteanu, I., Balaj, O.P., Beyer, M.K., and Bondybey, V.E., *Size-dependent dehydrogenation of ethane by cationic rhodium clusters in the gas phase*. International Journal of Mass Spectrometry **2006**, *255-256*, 71-75.
24. Andersson, M., Holmgren, L., and Rosén, A., *Rhodium-cluster reactivity: Sticking probabilities of some diatomic molecules*. Surface Review and Letters **1996**, *3*, 683-686.
25. Klein, M.P., Ehrhard, A.A., Mohrbach, J., Dillinger, S., and Niedner-Schatteburg, G., *Infrared Spectroscopic Investigation of Structures and N₂ Adsorption Induced Relaxations of Isolated Rhodium Clusters*. Topics in Catalysis **2018**, *61*, 106-118.
26. Ehrhard, A.A., Klein, M.P., Mohrbach, J., Dillinger, S., and Niedner-Schatteburg, G., *Cryokinetics and Spin Quenching in the N₂ Adsorption onto Rhodium-Cluster Cations*. Molecular Physics **2021**, accepted.
27. Klein, M.P., Straßner, A., Huber, M.E., and Niedner-Schatteburg, G., *IR spectroscopy of sequential N₂ adsorption onto Rh₆⁺ clusters*. unpublished.
28. Griffin, J.B. and Armentrout, P.B., *Guided ion beam studies of the reactions of Fe_n⁺ (n=2–18) with O₂: Iron cluster oxide and dioxide bond energies*. The Journal of Chemical Physics **1997**, *106*, 4448-4462.
29. Conceição, J., Loh, S.K., Lian, L., and Armentrout, P.B., *Guided ion beam studies of the reactions of Fe_n⁺ (n=2–15) with D₂: Cluster–deuteride bond energies as a chemical probe of cluster structures*. The Journal of Chemical Physics **1996**, *104*, 3976-3988.
30. Liyanage, R., Zhang, X.-G., and Armentrout, P.B., *Activation of methane by size-selected iron cluster cations, Fe_n⁺ (n=2–15): Cluster-CH_x (x=0–3) bond energies and reaction mechanisms*. The Journal of Chemical Physics **2001**, *115*, 9747-9763.
31. Griffin, J.B. and Armentrout, P.B., *Guided ion-beam studies of the reactions of Fe_n⁺ (n=1–18) with CO₂: Iron cluster oxide bond energies*. The Journal of Chemical Physics **1997**, *107*, 5345-5355.
32. Liyanage, R., Griffin, J.B., and Armentrout, P.B., *Thermodynamics of ammonia activation by iron cluster cations: Guided ion beam studies of the reactions of Fe_n⁺ (n=2–10,14) with ND₃*. The Journal of Chemical Physics **2003**, *119*, 8979.
33. Tan, L., Liu, F., and Armentrout, P.B., *Thermochemistry of the activation of N₂ on iron cluster cations: Guided ion beam studies of the reactions of Fe_n⁺ (n = 1-19) with N₂*. J. Chem. Phys. **2006**, *124*, 084302.
34. Parks, E.K., Weiller, B.H., Bechthold, P.S., Hoffman, W.F., Nieman, G.C., Pobo, L.G., and Riley, S.J., *Chemical probes of metal cluster structure: Reactions of iron clusters with hydrogen, ammonia, and water*. The Journal of Chemical Physics **1988**, *88*, 1622-1632.

35. Richtsmeier, S.C., Parks, E.K., Liu, K., Pobo, L.G., and Riley, S.J., *Gas phase reactions of iron clusters with hydrogen. I. Kinetics*. The Journal of Chemical Physics **1985**, *82*, 3659-3665.
36. Parks, E.K., Liu, K., Richtsmeier, S.C., Pobo, L.G., and Riley, S.J., *Reactions of iron clusters with hydrogen. II. Composition of the fully hydrogenated products*. The Journal of Chemical Physics **1985**, *82*, 5470-5474.
37. Whetten, R.L., Cox, D.M., Trevor, D.J., and Kaldor, A., *Correspondence between electron binding energy and chemisorption reactivity of iron clusters*. Phys Rev Lett **1985**, *54*, 1494-1497.
38. Jones, N.O., Beltran, M.R., Khanna, S.N., Baruah, T., and Pederson, M.R., *Hydrogen adsorption and magnetic behavior of Fe_n and Co_n clusters: Controlling the magnetic moment and anisotropy one atom at a time*. Physical Review B **2004**, *70*, 165406.
39. Tjelta, B.L. and Armentrout, P.B., *Gas-Phase Metal Ion Ligation: Collision-Induced Dissociation of $Fe(N_2)_x^+$ ($x=1-5$) and $Fe(CH_2O)_x^+$ ($x=1-4$)*. The Journal of Physical Chemistry A **1997**, *101*, 2064-2073.
40. Duarte, H.A., Salahub, D.R., Haslett, T., and Moskovits, M., *$Fe(N_2)_n$ ($n=1-5$): Structure, Bonding, and Vibrations from Density Functional Theory*. Inorganic Chemistry **1999**, *38*, 3895-3903.
41. Haslett, T.L., Fedrigo, S., Bosnick, K., Moskovits, M., Duarte, H.A., and Salahub, D., *Binary Iron–Dinitrogen Compounds Synthesized by Co-deposition of Mass-Selected Fe, Fe_2 , and Fe_3 with N_2* . Journal of the American Chemical Society **2000**, *122*, 6039-6044.
42. Straßner, A., Wiehn, C., Klein, M.P., Fries, D.V., Dillinger, S., Mohrbach, J., Armentrout, P.B., and Niedner-Schatteburg, G., *Kinetic nitrophobia of size selected iron clusters*. unpublished.
43. Straßner, A., Wiehn, C., Klein, M.P., Fries, D.V., Dillinger, S., Mohrbach, J., Armentrout, P.B., and Niedner-Schatteburg, G., *Cryo spectroscopy of N_2 on cationic iron clusters*.
44. Ferrando, R., Jellinek, J., and Johnston, R.L., *Nanoclusters: from theory to applications of alloy clusters and nanoparticles*. Chem Rev **2008**, *108*, 845-910.
45. Parks, E.K., Kerns, K.P., and Riley, S.J., *The structure of nickel-iron clusters probed by adsorption of molecular nitrogen*. Chem. Phys. **2000**, *262*, 151-167.
46. Parks, E.K. and Riley, S.J., *Nickel cluster structure determined from the adsorption of molecular nitrogen Ni_{49-71}* . Z. Phys. D: At., Mol. Clusters **1995**, *33*, 59-70.
47. Muñoz-Navia, M., Villaseñor-González, P., Dorantes-Dávila, J., and Pastor, G.M., *Surface and interface magnetic effects in Co_nRh_m clusters*. Computational Materials Science **2006**, *35*, 302-306.
48. Dennler, S., Morillo, J., and Pastor, G.M., *Calculation of magnetic and structural properties of small Co–Rh clusters*. Surface Science **2003**, *532-535*, 334-340.
49. Cox, A.J., Louderback, J.G., and Bloomfield, L.A., *Experimental observation of magnetism in rhodium clusters*. Physical Review Letters **1993**, *71*, 923-926.
50. Cox, A.J., Louderback, J.G., Apsel, S.E., and Bloomfield, L.A., *Magnetism in 4d-transition metal clusters*. Physical Review B **1994**, *49*, 12295-12298.
51. Díaz-Ortiz, A., Aguilera-Granja, F., Michaelian, K., Berlanga-Ramírez, E.O., Montejano-Carrizales, J.M., and Vega, A., *Tight-binding and evolutionary search approach for nanoscale CoRh alloys*. Physica B: Condensed Matter **2005**, *370*, 200-214.
52. Fromen, M.C., Lecante, P., Casanove, M.J., Guillemaud, P.B., Zitoun, D., Amiens, C., Chaudret, B., Respaud, M., and Benfield, R.E., *Structural study of bimetallic Co_xRh_{1-x} nanoparticles: Size and composition effects*. Physical Review B **2004**, *69*, 235416.

53. Fromen, M.C., Morillo, J., Casanove, M.J., and Lecante, P., *Structure and chemical order in Co–Rh nanoparticles*. Europhysics Letters (EPL) **2006**, *73*, 885-891.
54. Sondón, T., Guevara, J., and Saúl, A., *Study of the structure, segregation, and magnetic properties of Ni-Rh clusters*. Physical Review B **2007**, *75*, 104426.
55. Beeck, T., Baev, I., Chen, K., Palutke, S., Wurth, W., and Martins, M., *Quantum size effects of small, size-selected and deposited CoRh clusters on Ni*. New Journal of Physics **2016**, *18*, 113007.
56. Demiroglu, I., Li, Z.Y., Piccolo, L., and Johnston, R.L., *A DFT study of molecular adsorption on titania-supported AuRh nanoalloys*. Computational and Theoretical Chemistry **2017**, *1107*, 142-151.
57. Mokkath, J.H. and Pastor, G.M., *Interplay between Chemical and Magnetic Order in FeRh Clusters*. The Journal of Physical Chemistry C **2012**, *116*, 17228-17238.
58. Polesya, S., Mankovsky, S., Ködderitzsch, D., Minár, J., and Ebert, H., *Finite-temperature magnetism of FeRh compounds*. Physical Review B **2016**, *93*, 024423.
59. Kouvel, J.S. and Hartelius, C.C., *Anomalous Magnetic Moments and Transformations in the Ordered Alloy FeRh*. Journal of Applied Physics **1962**, *33*, 1343-1344.
60. Dunlap, B.I., *Symmetry and ferromagnetic clusters*. Zeitschrift für Physik D Atoms, Molecules and Clusters **1991**, *19*, 255-257.
61. Liu, F., Khanna, S.N., and Jena, P., *Magnetism in small vanadium clusters*. Physical Review B **1991**, *43*, 8179-8182.
62. Billas, I.M.L., Châtelain, A., and de Heer, W.A., *Magnetism of Fe, Co and Ni clusters in molecular beams*. Journal of Magnetism and Magnetic Materials **1997**, *168*, 64-84.
63. Billas, I.M.L., Châtelain, A., and de Heer, W.A., *Magnetism from the Atom to the Bulk in Iron, Cobalt, and Nickel Clusters*. Science **1994**, *265*, 1682-1684.
64. Niemeyer, M., Hirsch, K., Zamudio-Bayer, V., Langenberg, A., Vogel, M., Kossick, M., Ebrecht, C., Egashira, K., Terasaki, A., Möller, T., v. Issendorff, B., and Lau, J.T., *Spin Coupling and Orbital Angular Momentum Quenching in Free Iron Clusters*. Physical Review Letters **2012**, *108*, 057201.
65. Meyer, J., Tombers, M., van Wüllen, C., Niedner-Schatteburg, G., Peredkov, S., Eberhardt, W., Neeb, M., Palutke, S., Martins, M., and Wurth, W., *The spin and orbital contributions to the total magnetic moments of free Fe, Co, and Ni clusters*. The Journal of Chemical Physics **2015**, *143*, 104302.
66. Dillinger, S., Mohrbach, J., Hewer, J., Gaffga, M., and Niedner-Schatteburg, G., *Infrared spectroscopy of N₂ adsorption on size selected cobalt cluster cations in isolation*. Physical Chemistry Chemical Physics **2015**, *17*, 10358-10362.
67. Mohrbach, J., Dillinger, S., and Niedner-Schatteburg, G., *Probing cluster surface morphology by cryo kinetics of N₂ on cationic nickel clusters*. The Journal of Chemical Physics **2017**, *147*, 184304.
68. Mohrbach, J., Dillinger, S., and Niedner-Schatteburg, G., *Cryo Kinetics and Spectroscopy of Cationic Nickel Clusters: Rough and Smooth Surfaces*. The Journal of Physical Chemistry C **2017**, *121*, 10907-10918.
69. Dillinger, S., Mohrbach, J., and Niedner-Schatteburg, G., *Probing cluster surface morphology by cryo spectroscopy of N₂ on cationic nickel clusters*. The Journal of Chemical Physics **2017**, *147*, 184305.
70. Fries, D.V., Klein, M.P., Steiner, A., Prosenc, M.H., and Niedner-Schatteburg, G., *Observation and Mechanism of Cryo N₂ Cleavage by a Tantalum Cluster*. Phys Chem Chem Phys **2021**, *23*, 11345-11354.

-
71. Peredkov, S., Savci, A., Peters, S., Neeb, M., Eberhardt, W., Kampschulte, H., Meyer, J., Tombers, M., Hofferberth, B., Menges, F., and Niedner-Schatteburg, G., *X-ray absorption spectroscopy of mass-selected transition metal clusters using a cyclotron ion trap: An experimental setup for measuring XMCD spectra of free clusters*. Journal of Electron Spectroscopy and Related Phenomena **2011**, *184*, 113-118.
 72. Klein, M.P., Ehrhard, A.A., Huber, M.E., Dillinger, S., Mohrbach, J., and Niedner-Schatteburg, G., *Cryo Infrared Spectroscopy of N₂ Adsorption onto Bimetallic Rhodium-Iron Clusters in Isolation*. unpublished.
 73. Berg, C., Schindler, T., Niedner-Schatteburg, G., and Bondybey, V.E., *Reactions of simple hydrocarbons with Nb_n⁺: chemisorption and physisorption on ionized niobium clusters*. The Journal of Chemical Physics **1995**, *102*, 4870-4884.
 74. Proch, D. and Trickl, T., *A high-intensity multi-purpose piezoelectric pulsed molecular beam source*. Review of Scientific Instruments **1989**, *60*, 713-716.
 75. Caravatti, P. and Allemann, M., *The 'infinity cell': A new trapped-ion cell with radiofrequency covered trapping electrodes for fourier transform ion cyclotron resonance mass spectrometry*. Organic Mass Spectrometry **1991**, *26*, 514-518.
 76. Graf, M., *Entwicklung eines auf Evolutionsstrategien basierenden Computerprogrammes zum optimierten Anpassen kinetischer Daten aus FT-ICR-Massenspektrometrie-Messungen*. September 2006, TU Kaiserslautern.
 77. Su, T. and Bowers, M.T., *Ion-polar molecule collisions. Effect of molecular size on ion-polar molecule rate constants*. Journal of the American Chemical Society **1973**, *95*, 7609-7610.
 78. Su, T. and Bowers, M.T., *Ion-polar molecule collisions. Proton transfer reactions of H₃⁺ and CH₅⁺ to the geometric isomers of difluoroethylene, dichloroethylene, and difluorobenzene*. Journal of the American Chemical Society **1973**, *95*, 1370-1373.
 79. Su, T. and Bowers, M.T., *Theory of ion-polar molecule collisions. Comparison with experimental charge transfer reactions of rare gas ions to geometric isomers of difluorobenzene and dichloroethylene*. The Journal of Chemical Physics **1973**, *58*, 3027-3037.
 80. Su, T. and Bowers, M.T., *Ion-Polar molecule collisions: the effect of ion size on ion-polar molecule rate constants; the parameterization of the average-dipole-orientation theory*. International Journal of Mass Spectrometry and Ion Physics **1973**, *12*, 347-356.
 81. Kummerlöwe, G. and Beyer, M.K., *Rate estimates for collisions of ionic clusters with neutral reactant molecules*. International Journal of Mass Spectrometry **2005**, *244*, 84-90.
 82. Bergmann and Schäfer, *Lehrbuch der Experimentalphysik-Gase, Nanosysteme, Flüssigkeiten*. Band 5 **2006**.

6.9 Supplementary Information

Cryo Kinetics of N₂ Adsorption onto Bimetallic Rhodium-Iron Clusters in Isolation

Amelie A. Ehrhard¹, Matthias P. Klein, Jennifer Mohrbach, Sebastian Dillinger,
and Gereon Niedner-Schatteburg²

*Fachbereich Chemie and Forschungszentrum OPTIMAS,
Technische Universität Kaiserslautern, 67663 Kaiserslautern, Germany*

Table S4	Calculated relative rate constants $k_{(i,j,m)}$ for the N ₂ <i>adsorption</i> onto [Rh _i Fe _j (N ₂) _m] ⁺
Table S5	Calculated absolute rate constants $k_{(i,j,m)}^{abs}$ for the N ₂ <i>adsorption</i> onto [Rh _i Fe _j (N ₂) _m] ⁺
Table S6	Collision rates $k_{(i,j,m)}^{coll}$ (Langevin) for the N ₂ <i>adsorption</i> onto [Rh _i Fe _j (N ₂) _m] ⁺
Table S4	Calculated relative rate constants $k_{-(i,j,m+1)}$ for the N ₂ <i>desorption</i> off [Rh _i Fe _j (N ₂) _{m+1}] ⁺
Table S5	Calculated absolute rate constants $k_{-(i,j,m+1)}^{abs}$ for the N ₂ <i>desorption</i> off [Rh _i Fe _j (N ₂) _{m+1}] ⁺
Table S6	Sticking probabilities $\gamma_{-(i,j,m+1)}$ for the N ₂ <i>desorption</i> off [Rh _i Fe _j (N ₂) _{m+1}] ⁺
Table S7	Equilibrium constants for the N ₂ <i>adsorption</i> onto [Rh _i Fe _j (N ₂) _m] ⁺ / <i>desorption</i> off [Rh _i Fe _j (N ₂) _{m+1}] ⁺ at 26 K
Table S8	Gibbs free energies $\Delta_{ads}G^{26K}_{(i,j,m)}$ for the equilibria of N ₂ <i>adsorption</i> onto [Rh _i Fe _j (N ₂) _m] ⁺ / <i>desorption</i> off [Rh _i Fe _j (N ₂) _{m+1}] ⁺ at 26 K

¹ Present address: Max-Planck-Institut für Polymerforschung, 55128 Mainz, Germany

² Corresponding author: Prof. Dr. Gereon Niedner-Schatteburg, Erwin-Schrödinger-Straße 52, 67663 Kaiserslautern, gns@chemie.uni-kl.de

Table S1 Calculated relative rate constants $k_{(i,j,m)}$ for the N_2 adsorption onto $[Rh_iFe_j(N_2)_m]^+$. Relative uncertainties are $\pm 20\%$ (conservative estimate). Conversion to absolute rate constants is $k_{(i,j,m)}^{abs} = \frac{k_{(i,j,m)}}{\rho_{N_2}}$ and normalization to collision rate $k_{(i,j,m)}^{coll}$ (Langevin) yields sticking probabilities $\gamma_{(i,j,m)} = \frac{k_{abs,(i,j,m)}}{k_{coll,(i,j,m)}}$. Fields above the respective adsorption limit are left empty.

Relative rate constants $k_{(i,j,m)} / s^{-1}$	$m = 0$	1	2	3	4	5	6	7	8	9	10	11	12
$[Rh_3Fe_3(N_2)_m]^+$	5.6	5.8	4.7	4.6	4.9	4.4	5.2						
$[Rh_3Fe_4(N_2)_m]^+$	5.4	3.5	1.5	5.3	4.5	2.0	0.87						
$[Rh_4Fe_3(N_2)_m]^+$	5.8	6.5	5.7	2.6	3.6	3.5	0.23	2.4					
$[Rh_4Fe_4(N_2)_m]^+$	3.3	4.5	4.4	5.2	2.7	3.5	2.9	4.3	0.14	1.4	2.0		
$[Rh_4Fe_5(N_2)_m]^+$	2.2	4.5	3.8	4.4	2.8	1.2	1.8	0.026					
$[Rh_5Fe_4(N_2)_m]^+$	3.7	5.1	5.6	5.5	5.0	5.1	3.8	4.6	3.1	1.8	3.1		
$[Rh_5Fe_5(N_2)_m]^+$	2.6	3.5	3.3	3.2	1.9	2.0	1.4	0.70					
$[Rh_5Fe_6(N_2)_m]^+$	6.0	5.0	5.0	4.3	3.0	3.8	4.4	2.5	3.4	1.6			
$[Rh_6Fe_5(N_2)_m]^+$	5.8	6.2	6.2	6.0	6.0	6.0	0.32	0.20	2.9				
$[Rh_6Fe_6(N_2)_m]^+$	4.3	3.8	3.8	3.6	3.4	3.1	3.1	2.1	1.1	0.20			
$[Rh_6Fe_7(N_2)_m]^+$	7.0	5.8	4.9	5.9	5.2	4.3	4.2	3.2	3.2	2.3	16	2.2	
$[Rh_7Fe_6(N_2)_m]^+$	6.9	6.7	6.2	6.1	5.7	5.6	4.9	4.8	3.7	1.3	1.6		
$[Rh_7Fe_7(N_2)_m]^+$	4.5	4.3	4.0	3.5	3.7	3.8	3.5	3.2	2.7	1.2	3.7	2.0	
$[Rh_7Fe_8(N_2)_m]^+$	7.3	6.7	6.7	6.2	6.4	6.4	5.7	4.6	0.59				
$[Rh_8Fe_7(N_2)_m]^+$	7.4	7.0	7.0	7.4	6.8	6.8	6.4	5.8	5.1	2.2	16	3.2	1.5
$[Rh_8Fe_8(N_2)_m]^+$	4.3	4.6	4.5	4.5	4.3	4.4	4.3	3.5	2.5	2.0	1.4		

6. Cryo Kinetics of N₂ Adsorption onto Bimetallic Rhodium-Iron Clusters in Isolation

Table S2 Calculated absolute rate constants $k_{(i,j,m)}^{abs}$ for the N₂ adsorption onto [Rh_iFe_j(N₂)_m]⁺. Relative uncertainties are ± 40% (conservative estimate). We assume an instrument constant of 1.8 as this provides realistic data for all our experiments [68] and is a viable value after comparison to experiments of Harding *et al.* [15] for Rh clusters. Conversion to absolute rate constants is $k_{(i,j,m)}^{abs} = \frac{k_{(i,j,m)}}{\rho_{N_2}}$. Fields above the respective adsorption limit are left empty.

Absolute rate constants $k_{(i,j,m)} / 10^{-10} \text{ cm}^3 \text{ s}^{-1}$	$m = 0$	1	2	3	4	5	6	7	8	9	10	11	12
[Rh ₃ Fe ₃ (N ₂) _m] ⁺	4.3	4.4	3.6	3.5	3.8	3.4	4.0						
[Rh ₃ Fe ₄ (N ₂) _m] ⁺	4.1	2.7	1.2	4.0	3.4	1.5	0.67						
[Rh ₄ Fe ₃ (N ₂) _m] ⁺	4.5	5.0	4.3	2.0	2.8	2.7	0.18	1.8					
[Rh ₄ Fe ₄ (N ₂) _m] ⁺	2.5	3.4	3.3	4.0	2.0	2.7	2.3	3.3	0.10	1.1	1.6		
[Rh ₄ Fe ₅ (N ₂) _m] ⁺	1.7	3.5	2.9	3.4	2.2	0.88	1.4	0.020					
[Rh ₅ Fe ₄ (N ₂) _m] ⁺	2.8	3.9	4.3	4.3	3.8	3.9	2.9	3.5	2.4	1.4	2.4		
[Rh ₅ Fe ₅ (N ₂) _m] ⁺	2.0	2.7	2.6	2.5	1.5	1.5	1.0	0.5					
[Rh ₅ Fe ₆ (N ₂) _m] ⁺	4.6	3.8	3.8	3.3	2.3	2.9	3.4	1.9	2.6	1.2			
[Rh ₆ Fe ₅ (N ₂) _m] ⁺	4.4	4.7	4.7	4.6	4.6	4.6	0.25	0.16	2.2				
[Rh ₆ Fe ₆ (N ₂) _m] ⁺	3.3	2.9	2.9	2.7	2.6	2.4	2.4	1.6	0.85	0.16			
[Rh ₆ Fe ₇ (N ₂) _m] ⁺	5.4	4.4	3.7	4.5	4.0	3.3	3.2	2.5	2.5	1.7	12	1.7	
[Rh ₇ Fe ₆ (N ₂) _m] ⁺	5.3	5.1	4.8	4.7	4.4	4.3	3.8	3.7	2.8	1.0	1.2		
[Rh ₇ Fe ₇ (N ₂) _m] ⁺	3.5	3.3	3.0	2.7	2.8	2.9	2.6	2.5	2.1	1.0	2.8	1.5	
[Rh ₇ Fe ₈ (N ₂) _m] ⁺	5.6	5.2	5.1	4.8	4.9	4.9	4.4	3.6	0.45				
[Rh ₈ Fe ₇ (N ₂) _m] ⁺	5.7	5.3	5.3	5.7	5.2	5.2	4.9	4.4	3.9	1.7	12	2.5	1.2
[Rh ₈ Fe ₈ (N ₂) _m] ⁺	3.3	3.5	3.5	3.4	3.3	3.3	3.3	2.7	1.9	1.6	1.1		

Table S3 Collision rates $k_{(i,j,m)}^{coll}$ (Langevin) for the N_2 adsorption onto $[Rh_iFe_j(N_2)_m]^+$. Relative uncertainties are $\pm 40\%$ (conservative estimate). Fields above the respective adsorption limit are left empty.

collision rate (Langevin) $k_{(i,j,m)} / 10^{-10} \text{ cm}^3 \text{ s}^{-1}$	$m = 0$	1	2	3	4	5	6	7	8	9	10	11	12	13
$[Rh_3Fe_3(N_2)_m]^+$	6.06	6.05	6.04	6.03	6.03	6.02	6.02							
$[Rh_3Fe_4(N_2)_m]^+$	6.04	6.04	6.03	6.03	6.02	6.02	6.01							
$[Rh_4Fe_3(N_2)_m]^+$	6.03	6.03	6.03	6.03	6.03	6.03	6.03	6.03						
$[Rh_4Fe_4(N_2)_m]^+$	6.02	6.02	6.02	6.02	6.02	6.02	6.02	6.02	6.02	6.02	6.02	6.02		
$[Rh_4Fe_5(N_2)_m]^+$	6.01	6.01	6.01	6.01	6.01	6.01	6.01	6.01						
$[Rh_5Fe_4(N_2)_m]^+$	6.00	6.00	6.00	6.00	6.00	6.00	6.00	6.00	6.00	6.00	6.00	6.00		
$[Rh_5Fe_5(N_2)_m]^+$	5.99	5.99	5.99	5.99	5.99	5.99	5.99	5.99						
$[Rh_5Fe_6(N_2)_m]^+$	5.99	5.99	5.99	5.99	5.99	5.99	5.99	5.99	5.99	5.99	5.99			
$[Rh_6Fe_5(N_2)_m]^+$	5.98	5.98	5.98	5.98	5.98	5.98	5.98	5.98	5.98	5.98				
$[Rh_6Fe_6(N_2)_m]^+$	5.98	5.98	5.98	5.98	5.98	5.98	5.98	5.98	5.98	5.98	5.98			
$[Rh_6Fe_7(N_2)_m]^+$	5.97	5.97	5.97	5.97	5.97	5.97	5.97	5.97	5.97	5.97	5.97	5.97	5.97	
$[Rh_7Fe_6(N_2)_m]^+$	5.97	5.97	5.97	5.97	5.97	5.97	5.97	5.97	5.97	5.97	5.97	5.97		
$[Rh_7Fe_7(N_2)_m]^+$	5.96	5.96	5.96	5.96	5.96	5.96	5.96	5.96	5.96	5.96	5.96	5.96	5.96	
$[Rh_7Fe_8(N_2)_m]^+$	5.96	5.96	5.96	5.96	5.96	5.96	5.96	5.96	5.96	5.96				
$[Rh_8Fe_7(N_2)_m]^+$	5.96	5.96	5.96	5.96	5.96	5.96	5.96	5.96	5.96	5.96	5.96	5.96	5.96	5.96
$[Rh_8Fe_8(N_2)_m]^+$	5.95	5.95	5.95	5.95	5.95	5.95	5.95	5.95	5.95	5.95	5.95	5.95		

6. Cryo Kinetics of N₂ Adsorption onto Bimetallic Rhodium-Iron Clusters in Isolation

Table S4 Calculated relative rate constants $k_{-(i,j,m+1)}$ for the N₂ *desorption* off [Rh_iFe_j(N₂)_{m+1}]⁺. Relative uncertainties are ± 20 % (conservative estimate). Conversion to absolute rate constants is $k_{-(i,j,m)}^{abs} = \frac{k_{-(i,j,m)}}{\rho_{N_2}}$ and normalization to collision rate k_{coll} (Langevin) yields sticking probabilities $\gamma_{-(i,j,m+1)} = \frac{k_{-(i,j,m)}^{abs}}{k_{coll}^{-(i,j,m)}}$. * indicates values < 0.001 s⁻¹. Fields above the respective adsorption limit are left empty.

Relative rate constants $k_{-(i,j,m+1)} / s^{-1}$	$m = 0$	1	2	3	4	5	6	7	8	9	10	11	12
[Rh ₃ Fe ₃ (N ₂) _m] ⁺	*	*	*	*	*	*	*						
[Rh ₃ Fe ₄ (N ₂) _m] ⁺	*	*	*	*	*	*	*						
[Rh ₄ Fe ₃ (N ₂) _m] ⁺	*	*	*	*	*	*	0.18	0.0023					
[Rh ₄ Fe ₄ (N ₂) _m] ⁺	*	*	*	*	*	*	*	8.1E-06	5.1	3.1	0.94		
[Rh ₄ Fe ₅ (N ₂) _m] ⁺	*	*	*	*	*	*	*	0.42					
[Rh ₅ Fe ₄ (N ₂) _m] ⁺	*	*	*	*	*	*	*	*	*	*			
[Rh ₅ Fe ₅ (N ₂) _m] ⁺	*	*	*	*	*	*	*	*					
[Rh ₅ Fe ₆ (N ₂) _m] ⁺	*	*	*	*	*	*	*	*	*	0.42			
[Rh ₆ Fe ₅ (N ₂) _m] ⁺	*	*	*	*	*	*	0.035	1.5E-05	0.49				
[Rh ₆ Fe ₆ (N ₂) _m] ⁺	*	*	*	*	*	*	*	*	0.19	0.69			
[Rh ₆ Fe ₇ (N ₂) _m] ⁺	*	*	*	*	*	*	*	*	*	*	35	2.2	
[Rh ₇ Fe ₆ (N ₂) _m] ⁺	*	*	*	*	*	*	*	*	*	0.50	3.2		
[Rh ₇ Fe ₇ (N ₂) _m] ⁺	*	*	*	*	*	*	*	*	*	0.44	20	1.0	
[Rh ₇ Fe ₈ (N ₂) _m] ⁺	8.8E-07	7.4E-07	7.8E-06	3.8E-07	5.5E-07	1.6E-07	7.9E-08	1.7E-08	3.7				
[Rh ₈ Fe ₇ (N ₂) _m] ⁺	*	*	*	*	*	*	*	*	5.2	5.3	24	0.92	2.56
[Rh ₈ Fe ₈ (N ₂) _m] ⁺	*	*	*	*	*	*	*	*	0.58	0.20	6.5		

Table S5 Calculated absolute rate constants $k_{-(i,j,m+1)}^{abs}$ for the N₂ desorption off [Rh_iFe_j(N₂)_{m+1}]⁺. Relative uncertainties are ± 40 % (conservative estimate). We assume an instrument constant of 1.8 as this provides realistic data for all our experiments [68] and is a viable value after comparison to experiments of Harding *et al.* [15] for Rh clusters. Conversion to absolute rate constants is $k_{-(i,j,m+1)}^{abs} = \frac{k_{-(i,j,m+1)}}{\rho_{N_2}}$. * indicates values < 7.7 · 10⁻¹⁴ cm³ s⁻¹. Fields above the respective adsorption limit are left empty.

Absolute rate constants $k_{-(i,j,m+1)} / 10^{-10} \text{ cm}^3 \text{ s}^{-1}$	$m = 0$	1	2	3	4	5	6	7	8	9	10	11	12
[Rh ₃ Fe ₃ (N ₂) _m] ⁺	*	*	*	*	*	*	*						
[Rh ₃ Fe ₄ (N ₂) _m] ⁺	*	*	*	*	*	*	*						
[Rh ₄ Fe ₃ (N ₂) _m] ⁺	*	*	*	*	*	*	0.13	1.7E-03					
[Rh ₄ Fe ₄ (N ₂) _m] ⁺	*	*	*	*	*	*	*	*	3.9	2.3	0.72		
[Rh ₄ Fe ₅ (N ₂) _m] ⁺	*	*	*	*	*	*	*	0.32					
[Rh ₅ Fe ₄ (N ₂) _m] ⁺	*	*	*	*	*	*	*	*	*	*	*		
[Rh ₅ Fe ₅ (N ₂) _m] ⁺	*	*	*	*	*	*	*	*					
[Rh ₅ Fe ₆ (N ₂) _m] ⁺	*	*	*	*	*	*	*	*	*	0.32			
[Rh ₆ Fe ₅ (N ₂) _m] ⁺	*	*	*	*	*	*	0.027	*	0.38				
[Rh ₆ Fe ₆ (N ₂) _m] ⁺	*	*	*	*	*	*	*	*	0.15	0.53			
[Rh ₆ Fe ₇ (N ₂) _m] ⁺	*	*	*	*	*	*	*	*	*	*	27	1.7	
[Rh ₇ Fe ₆ (N ₂) _m] ⁺	*	*	*	*	*	*	*	*	*	0.38	2.5		
[Rh ₇ Fe ₇ (N ₂) _m] ⁺	*	*	*	*	*	*	*	*	*	0.34	16	0.78	
[Rh ₇ Fe ₈ (N ₂) _m] ⁺	*	*	*	*	*	*	*	*	2.8				
[Rh ₈ Fe ₇ (N ₂) _m] ⁺	*	*	*	*	*	*	*	*	4.0	4.1	19	0.71	2.0
[Rh ₈ Fe ₈ (N ₂) _m] ⁺	*	*	*	*	*	*	*	*	0.44	0.15	5.0		

6. Cryo Kinetics of N₂ Adsorption onto Bimetallic Rhodium-Iron Clusters in Isolation

Table S6 Sticking probabilities $\gamma_{-(i,j,m+1)}$ for the N₂ *desorption* off [Rh_iFe_j(N₂)_{m+1}]⁺. Relative uncertainties are + 20 % and – 30 % (conservative estimate). * indicates values $\gamma_{-(i,j,m+1)} \leq 0.00013$. Fields above the respective adsorption limit are left empty.

Sticking probabilities $\gamma_{-(i,j,m+1)}$	<i>m</i> = 0	1	2	3	4	5	6	7	8	9	10	11	12
[Rh ₃ Fe ₃ (N ₂) _{<i>m</i>}] ⁺	*	*	*	*	*	*	*						
[Rh ₃ Fe ₄ (N ₂) _{<i>m</i>}] ⁺	*	*	*	*	*	*	*						
[Rh ₄ Fe ₃ (N ₂) _{<i>m</i>}] ⁺	*	*	*	*	*	*	0.022	2.9E-04					
[Rh ₄ Fe ₄ (N ₂) _{<i>m</i>}] ⁺	*	*	*	*	*	*	*	*	0.65	0.39	0.12		
[Rh ₄ Fe ₅ (N ₂) _{<i>m</i>}] ⁺	*	*	*	*	*	*	*	0.053					
[Rh ₅ Fe ₄ (N ₂) _{<i>m</i>}] ⁺	*	*	*	*	*	*	*	*	*	*	*		
[Rh ₅ Fe ₅ (N ₂) _{<i>m</i>}] ⁺	*	*	*	*	*	*	*	*					
[Rh ₅ Fe ₆ (N ₂) _{<i>m</i>}] ⁺	*	*	*	*	*	*	*	*	*	0.053			
[Rh ₆ Fe ₅ (N ₂) _{<i>m</i>}] ⁺	*	*	*	*	*	*	4.5E-03	*	0.063				
[Rh ₆ Fe ₆ (N ₂) _{<i>m</i>}] ⁺	*	*	*	*	*	*	*	*	0.024	0.088			
[Rh ₆ Fe ₇ (N ₂) _{<i>m</i>}] ⁺	*	*	*	*	*	*	*	*	*	*	4.5	0.28	
[Rh ₇ Fe ₆ (N ₂) _{<i>m</i>}] ⁺	*	*	*	*	*	*	*	*	*	0.064	0.41		
[Rh ₇ Fe ₇ (N ₂) _{<i>m</i>}] ⁺	*	*	*	*	*	*	*	*	*	0.057	2.6	0.13	
[Rh ₇ Fe ₈ (N ₂) _{<i>m</i>}] ⁺	*	*	*	*	*	*	*	*	0.47				
[Rh ₈ Fe ₇ (N ₂) _{<i>m</i>}] ⁺	*	*	*	*	*	*	*	*	0.67	0.68	3.2	0.12	0.33
[Rh ₈ Fe ₈ (N ₂) _{<i>m</i>}] ⁺	*	*	*	*	*	*	*	*	0.074	0.025	0.84		

Table S7 Equilibrium constants for the N_2 adsorption onto $[Rh_iFe_j(N_2)_m]^+$ / desorption off $[Rh_iFe_j(N_2)_{m+1}]^+$ at 26 K. The equilibrium constants are calculated by the ratio of the relative adsorption and desorption rate constants $K_{(i,j,m)} = \frac{k_{(i,j,m)}}{k_{-(i,j,m+1)}}$. * indicates values > 600. Fields above the respective adsorption limit are left empty.

Equilibrium constants $K_{(i,j,m)}$	$m = 0$	1	2	3	4	5	6	7	8	9	10	11	12
$[Rh_3Fe_3(N_2)_m]^+$	*	*	*	*	*	*	*						
$[Rh_3Fe_4(N_2)_m]^+$	*	*	*	*	*	*	*						
$[Rh_4Fe_3(N_2)_m]^+$	*	*	*	*	*	*	1.33	1041					
$[Rh_4Fe_4(N_2)_m]^+$	*	*	*	*	*	*	*		0.027	0.47	2.2		
$[Rh_4Fe_5(N_2)_m]^+$	*	*	*	*	*	*	*	0.062					
$[Rh_5Fe_4(N_2)_m]^+$	*	*	*	*	*	*	*	*	*	*	*		
$[Rh_5Fe_5(N_2)_m]^+$	*	*	*	*	*	*	*	*					
$[Rh_5Fe_6(N_2)_m]^+$	*	*	*	*	*	*	*	*	*	3.8			
$[Rh_6Fe_5(N_2)_m]^+$	*	*	*	*	*	*	9.17	*	5.9				
$[Rh_6Fe_6(N_2)_m]^+$	*	*	*	*	*	*	*	*	5.8	0.29			
$[Rh_6Fe_7(N_2)_m]^+$	*	*	*	*	*	*	*	*	*	*	0.46	1.0	
$[Rh_7Fe_6(N_2)_m]^+$	*	*	*	*	*	*	*	*	*	2.6	0.49		
$[Rh_7Fe_7(N_2)_m]^+$	*	*	*	*	*	*	*	*	*	2.8	0.18	1.9	
$[Rh_7Fe_8(N_2)_m]^+$	*	*	*	*	*	*	*	*	0.16				
$[Rh_8Fe_7(N_2)_m]^+$	*	*	*	*	*	*	*	*	0.99	0.41	0.64	3.5	0.59
$[Rh_8Fe_8(N_2)_m]^+$	*	*	*	*	*	*	*	*	4.4	10	0.21		

6. Cryo Kinetics of N₂ Adsorption onto Bimetallic Rhodium-Iron Clusters in Isolation

Table S8 Gibbs free energies $\Delta_{\text{ads}}G^{26\text{K}}_{(i,j,m)}$ for the equilibria of N₂ adsorption onto $[\text{Rh}_i\text{Fe}_j(\text{N}_2)_m]^+$ / desorption off $[\text{Rh}_i\text{Fe}_j(\text{N}_2)_{m+1}]^+$ at 26 K. * indicates values < -1.5 kJ/mol. Fields above the respective adsorption limit are left empty.

$\Delta_{\text{ads}}G^{26\text{K}}_{(i,j,m)} /$ kJ/mol	$m = 0$	1	2	3	4	5	6	7	8	9	10	11	12
$[\text{Rh}_3\text{Fe}_3(\text{N}_2)_m]^+$	*	*	*	*	*	*	*						
$[\text{Rh}_3\text{Fe}_4(\text{N}_2)_m]^+$	*	*	*	*	*	*	*						
$[\text{Rh}_4\text{Fe}_3(\text{N}_2)_m]^+$	*	*	*	*	*	*	-0.062	-1.5					
$[\text{Rh}_4\text{Fe}_4(\text{N}_2)_m]^+$	*	*	*	*	*	*	*	*	0.78	0.17	-0.17		
$[\text{Rh}_4\text{Fe}_5(\text{N}_2)_m]^+$	*	*	*	*	*	*	*	0.60					
$[\text{Rh}_5\text{Fe}_4(\text{N}_2)_m]^+$	*	*	*	*	*	*	*	*	*	*	*		
$[\text{Rh}_5\text{Fe}_5(\text{N}_2)_m]^+$	*	*	*	*	*	*	*	*					
$[\text{Rh}_5\text{Fe}_6(\text{N}_2)_m]^+$	*	*	*	*	*	*	*	*	*	-0.29			
$[\text{Rh}_6\text{Fe}_5(\text{N}_2)_m]^+$	*	*	*	*	*	*	-0.48	*	-0.38				
$[\text{Rh}_6\text{Fe}_6(\text{N}_2)_m]^+$	*	*	*	*	*	*	*	*	-0.38	0.26			
$[\text{Rh}_6\text{Fe}_7(\text{N}_2)_m]^+$	*	*	*	*	*	*	*	*	*	*	0.17	-0.01	
$[\text{Rh}_7\text{Fe}_6(\text{N}_2)_m]^+$	*	*	*	*	*	*	*	*	*	*	-0.21	0.16	
$[\text{Rh}_7\text{Fe}_7(\text{N}_2)_m]^+$	*	*	*	*	*	*	*	*	*	*	-0.22	0.37	-0.14
$[\text{Rh}_7\text{Fe}_8(\text{N}_2)_m]^+$	*	*	*	*	*	*	*	*	0.39				
$[\text{Rh}_8\text{Fe}_7(\text{N}_2)_m]^+$	*	*	*	*	*	*	*	*	3.1E-03	0.19	0.095	-0.27	0.11
$[\text{Rh}_8\text{Fe}_8(\text{N}_2)_m]^+$	*	*	*	*	*	*	*	*	-0.32	-0.51	0.34		

7. Cryo Infrared Spectroscopy of N₂ Adsorption onto Bimetallic Rhodium-Iron Clusters in Isolation

Matthias P. Klein, Amelie A. Ehrhard¹, Maximilian E. Huber, Annika Straßner, Daniela V. Fries, Sebastian Dillinger, Jennifer Mohrbach, and Gereon Niedner-Schatteburg²

*Fachbereich Chemie and Forschungszentrum OPTIMAS,
Technische Universität Kaiserslautern, 67663 Kaiserslautern, Germany*

7.1 Preamble

An experimental team consisting of A. A. Ehrhard, M. E. Huber, A. Straßner, D. V. Fries, S. Dillinger, J. Mohrbach, and me conducted the experiments. I conducted the data evaluation. A. A. Ehrhard and I conducted and evaluated the quantum chemical calculations. I wrote the initial manuscript and revised it with the help of A. A. Ehrhard, S. Dillinger, and G. Niedner-Schatteburg. I prepared the manuscript for final publication.

Preliminary versions of this manuscript are part of the Diploma theses of A. A. Ehrhard and myself.

This manuscript is **under review** at *The Journal of Chemical Physics* as part 2 of 2 of a back-to-back submission (for part 1 cf. chapter 6).

7.2 Abstract

We investigated the N₂ adsorption behavior of bimetallic Rhodium-Iron cluster cations ([Rh_iFe_j(N₂)_m]⁺) by means of InfraRed PhotoDissociation (IR-PD) spectroscopy in comparison with DFT modelling. This approach allows us to refine our kinetic results [A. A. Ehrhard, M. P. Klein, J. Mohrbach, S. Dillinger, and G. Niedner-Schatteburg **[AAE]**] to enhance our conclusions. We focus on a selection of cluster adsorbate complexes within the ranges of $i = j = 3 - 8$ and $m = 1 - 10$. For $i = j = 3, 4$, DFT suggests alloy structures, in case of $i = j = 4$ of

¹ Present address: Max-Planck-Institut für Polymerforschung, 55128 Mainz, Germany

² Corresponding author: Prof. Dr. Gereon Niedner-Schatteburg, Erwin-Schrödinger-Straße 52, 67663 Kaiserslautern, gns@chemie.uni-kl.de

high (D_{2d}) symmetry: Rh-Fe bonds are preferred instead of Fe-Fe bonds or Rh-Rh bonds. N₂ adsorption and IR-PD studies reveals strong evidence for preferential adsorption to Rh sites and mere secondary adsorption to Fe. In some cases, we observe adsorption isomers. By help of modelling the cluster adsorbate complex $[\text{Rh}_3\text{Fe}_3(\text{N}_2)_7]^+$, we find clear evidence that the position of IR bands allows for an element specific assignment of an adsorption site. We transfer these findings to the $[\text{Rh}_4\text{Fe}_4(\text{N}_2)_m]^+$ cluster adsorbate complex where the first four N₂ molecules are adsorbed exclusively to the Rh atoms. The spectra of the larger adsorbates reveal N₂ adsorption onto the Fe atoms. Thus, the spectroscopic findings are well interpreted for the smaller clusters in terms of the computed structures, and both compare well to those of our accompanying kinetic study. In contrast to our own studies of bare rhodium clusters, the present investigations do not provide any indication for a spin quench in $[\text{Rh}_i\text{Fe}_j(\text{N}_2)_m]^+$ upon stepwise N₂ adsorption.

7.3 Introduction

Surfaces and small molecules. Transition metal clusters may serve as model systems for elemental processes that are of relevance in the context of heterogeneous catalysis.[1, 2] Such catalysts may consist of several metal components, either separated or as alloy, that provide for catalytic activity for various reactions [3]: In the automobile three way catalyst a combination of precious metals catalyzes oxidation hydrocarbons as well as reduction of CO and of nitrous oxides.[4] The latter takes place on Rhodium sites and effects the production of N₂ and CO₂. [5, 6] Iron is well known as a catalyst for dinitrogen activation, especially in the Haber-Bosch process. In this case N₂ activation is considered as the rate limiting step; In the course of the activation, physisorption of N₂ is the precursor state.[7] Apart from this, the adsorption of N₂ on surfaces to study the surface properties was an early research field.[8, 9]

N₂ on surfaces. Surface studies also provided information about the binding states of N₂ on Fe surfaces: α -N₂ (side-on) and γ -N₂ (end-on) adsorption motifs were identified.[10] Upon adsorption onto rhodium surfaces, N₂ is polarized and the otherwise IR inactive N₂ stretching vibration becomes IR active.[11] Thus chemisorbed as well as physisorbed N₂ species were identified where the physisorbed ones reveal no shift of the N₂ stretching vibration and are only very weakly bound (adsorption heat only 1.6 kcal/mol). The adsorption state as well as the adsorption site determine the stretching frequency. Recently, spectroscopic investigations

of N₂ adsorption on zirconia supported Rh nanoparticles were used to investigate step-edge sites that are required to dissociate CO [12]. IR bands of N₂ adsorbed onto an oxidized or reduced Rh layer appear at 2293 cm⁻¹ or 2205 cm⁻¹, respectively. The π-backbonding effect could be instrumentalized to selectively adsorb N₂ onto exposed vanadium centers in a metal organic framework.[13]

N₂ on gaseous atoms and clusters. Also isolated transition metal clusters like neutral Ru_n clusters polarize and activate N₂ and make it accessible to infrared spectroscopy.[14] The vibrational bands were observed red shifted with respect to the free N₂ vibration. For cases of N₂ adsorbed to cobalt cluster cations, we found similar red shifts of the N₂ stretching frequencies.[15] The interaction between metal atoms at surfaces and adsorbates containing π-bonds can be explained in terms of the Blyholder model.[16] This model refers to the same σ-donor, π-acceptor synergism as the Dewar-Chatt-Duncanson model for coordination compounds.[17, 18] The dependence of CO stretching frequencies on the number of metal atoms within the cluster can be nicely explained by Fielickes charge dilution model.[19]

In addition, IR-PD spectra of CO and N₂ adsorbed to a rhodium cation (Rh(N₂/CO)_m⁺) reveal a red shift of the N-N vibration and a blue shift of the CO vibration in the case of $m = 4$. [20] By help of DFT calculations, this result could be explained by a combination of σ-donation and an electrostatic polarization of the ligand. Up to now, we published cryo spectroscopic investigations on N₂ adsorption on Co [15], Ni [21, 22], Ru [14, 23], and Rh [24] clusters. A combination of IR studies with N₂ adsorption kinetics proved useful to investigate cluster surface morphologies and to discriminate *rough* and *smooth* cluster surfaces in the case of Ni.[21, 22, 25] IR-PD spectroscopy of [Rh_i(N₂)_m]⁺ clusters revealed coexisting isomers and a spin quench upon N₂ adsorption.[24] It is necessary to support the experimental work with theoretical models but in the case of clusters these often reach their limits.[26]

Rhodium-iron alloy clusters. Rhodium-iron alloys were found to reveal interesting magnetic properties such as transitions between antiferromagnetic and ferromagnetic states [27-40]. Especially theoretical studies have been performed to determine structures and magnetism of neutral [Rh_iFe_j] clusters and they provide for a set of initial structures for our own modelling and a basis of comparison with obtained data.[41] In particular for small clusters Rh-Fe bonds are stronger than Fe-Fe and Rh-Rh bonds.[40] These differences diminish with an increase of the size of the cluster.

Our approach. Together with the accompanying kinetic paper [AAE] [42], we present a combined spectroscopic and kinetic approach to investigate the N₂ adsorption steps and the cluster adsorbate complexes themselves. This approach has proven successful in the case of Ni clusters before [22, 25]. To facilitate readability, we use the short notation (i,j,m) for the cluster adsorbate complexes $[\text{Rh}_i\text{Fe}_j(\text{N}_2)_m]^+$. The kinetic study presents extensive adsorption kinetic data for all cluster adsorbate complexes (i,j,m) with $i = j$, $i = j + 1$ and $i + 1 = j$ for $i = 3, \dots, 8$ and $j = 3, \dots, 8$, in the range of $(3,3,m), \dots, (8,8,m)$.

In our present study, we investigated a selection of cationic $[\text{Rh}_i\text{Fe}_j(\text{N}_2)_m]^+$ cluster adsorbate complexes by means of infrared photodissociation spectroscopy (IR-PD). Single and maximum adsorption as well as special intermittent sizes are of special interest. We interpret the obtained spectra in conjunction with according DFT calculations. We chose to select for investigation the equiatomic $[\text{Rh}_i\text{Fe}_j(\text{N}_2)_m]^+$ clusters with single N₂ adsorption ($m = 1$), intermittent and high coverages, where the high load cases do not necessarily represent the maximum adsorption limit as defined in [AAE]. We compare our recorded IR-PD spectra to those of pure Rhodium and Iron clusters.[24, 43] In the present study, we focused on N₂ adsorbates of the equiatomic (i,j,m) clusters $i = j = 3, \dots, 8$.

For a description of the chosen (i,j,m) nomenclature and for a detailed discussion of the adsorption kinetics, refer to the accompanying kinetics paper [AAE] [42], and to the SI Text S1 of [44].

7.4 Experimental Methods and Computational Approach

In a customized 7 T Fourier Transform-Ion Cyclotron Resonance (FT-ICR)-mass spectrometer (Apex Ultra Bruker Daltonics) the metal clusters were produced and isolated. We let N₂ adsorb, and performed InfraRed PhotoDissociation (IR-PD) and mass analysis. The detailed construction has been described elsewhere [15]. In short, the second harmonic of a Nd:YAG laser is guided into the home-built laser vaporization cluster ion source chamber as described before [45, 46]. The laser beam is focused on a rotating RhFe-target (¹⁰³Rh:⁵⁶Fe stoichiometry 1:1, *MaTeck*) and produces a plasma, consisting of atoms and ions. A helium gas pulse (40 μs, 10 – 15 bar) is generated and induced into the vaporization chamber by using a homemade piezoelectric valve [47] operating in synchronization with the laser at 20 Hz. The gas pulse entrains the plasma through a 69 mm long channel (2 mm diameter) and allows for the atoms

and ions to cool down and aggregate to clusters in the subsequent jet expansion into vacuum (3.5×10^{-7} mbar). The ions in the skimmed cluster beam are guided through a 90° ion beam bender and a quadrupole mass filter into a cryogenic hexapole ion trap, which is cooled to 26 K by a closed cycle He cryostat. We introduce collision gas and reaction gas in the ion trap by a continuous gas inlet. The attachment of nitrogen is achieved by introducing N_2 and we maintain the requested constant pressure of about $2.2 - 3.2 \times 10^{-7}$ mbar N_2 . We increase the pressure in the ion trap to roughly 3.0×10^{-6} mbar by adding helium gas to accomplish efficient trapping and cooling of the ions. The ions are stored for a variable time (0.0 - 3.0 s). Subsequently, the cluster ions are steered into the ICR-cell, using various electrostatic ion lenses. Our ICR-cell of the so-called infinity-type [48] is cooled down to 10 K by a closed cycle He cryostat to prevent heating of the clusters by black body radiation.

To study the N_2 adsorbates of the selected $[Rh_i/Fe_j]^+$ clusters within the ICR cell, we first isolate the metal cluster of interest in the quadrupole mass filter and afterwards the cluster adsorbate complex of interest in the ICR cell and remove all other ions by correlated frequency sweeps and shots.

The number m of adsorbed N_2 on the cluster can be controlled by varying the storage time in the hexapole collision cell. The storage time can be increased until the amount of N_2 adsorbed reaches a maximum limit and at higher storage times no further N_2 adsorption is observed as is shown for $[Rh_3Fe_3]^+$ (Fig. 1). The $[Rh_3Fe_3]^+$ and $[Rh_4Fe_4]^+$ cluster can adsorb up to 7 and 8 N_2 molecules respectively. We can observe an additional *intermittent adsorption limit* for some metal cluster cores, e.g. $[Rh_4Fe_4(N_2)_4]^+$. Detailed kinetic investigations have confirmed that this behavior correlates with a slower rate of additional N_2 adsorption above this intermittent limit [AAE] [42]. Upon closer inspection, the $[Rh_4Fe_4(N_2)_4]^+$ mass spectra reveal further but very weak adsorption peaks as discussed in the accompanying kinetic study. For the following spectroscopic investigations, we chose single N_2 adsorbed clusters and clusters at *intermittent* and *maximum adsorption limit*. The adsorption limits are given in [AAE] [42], Fig. 2 therein.

A tunable IR laser system is coupled to the ICR cell to effect fragmentation of the stored ions. This laser is a KTP/KTA optical parametric oscillator/amplifier (OPO/A, *LaserVision*) system pumped by a pulsed 10 Hz injection seeded Nd:YAG laser (PL8000, *Continuum*) followed by an AgGaSe₂ crystal to generate the difference frequency (DF) between signal and idler waves [49]. This method can generate IR radiation in the range of $1200 - 2400 \text{ cm}^{-1}$. Each trapped and isolated package of ions is irradiated by 7 – 10 laser pulses to yield a sufficient amount of

7. Cryo Infrared Spectroscopy of N₂ Adsorption onto Bimetallic Rhodium-Iron Clusters in Isolation

fragment ions. A typical pulse energy spectrum is given in Fig. S1. The IR spectra were recorded as ion chromatograms while continuously scanning the IR wavelength. We evaluated the IR-PD signal as $\sum_n F_n / (\sum_n F_n + \sum_x P_x)$, where F_n and P_x indicate fragment and the parent ion signals, respectively. An IR-PD spectrum as depicted in this work arises out of plot of the fragmentation efficiency as a function of laser frequency. We employed the IR-PD spectroscopy in the 2140 – 2350 cm⁻¹ range on the $[\text{Rh}_i\text{Fe}_j(\text{N}_2)_m]^+$ species ($i = j = 3, \dots, 8$ and $m = 1, \dots, 10$). In this range, we expected the end-on N₂ stretching frequencies of the species. We expanded this range to 1160 – 2400 cm⁻¹ in selected cases to check for non-end-on N₂ ligands. For all complexes, the loss of the N₂ was the only observed fragmentation channel.

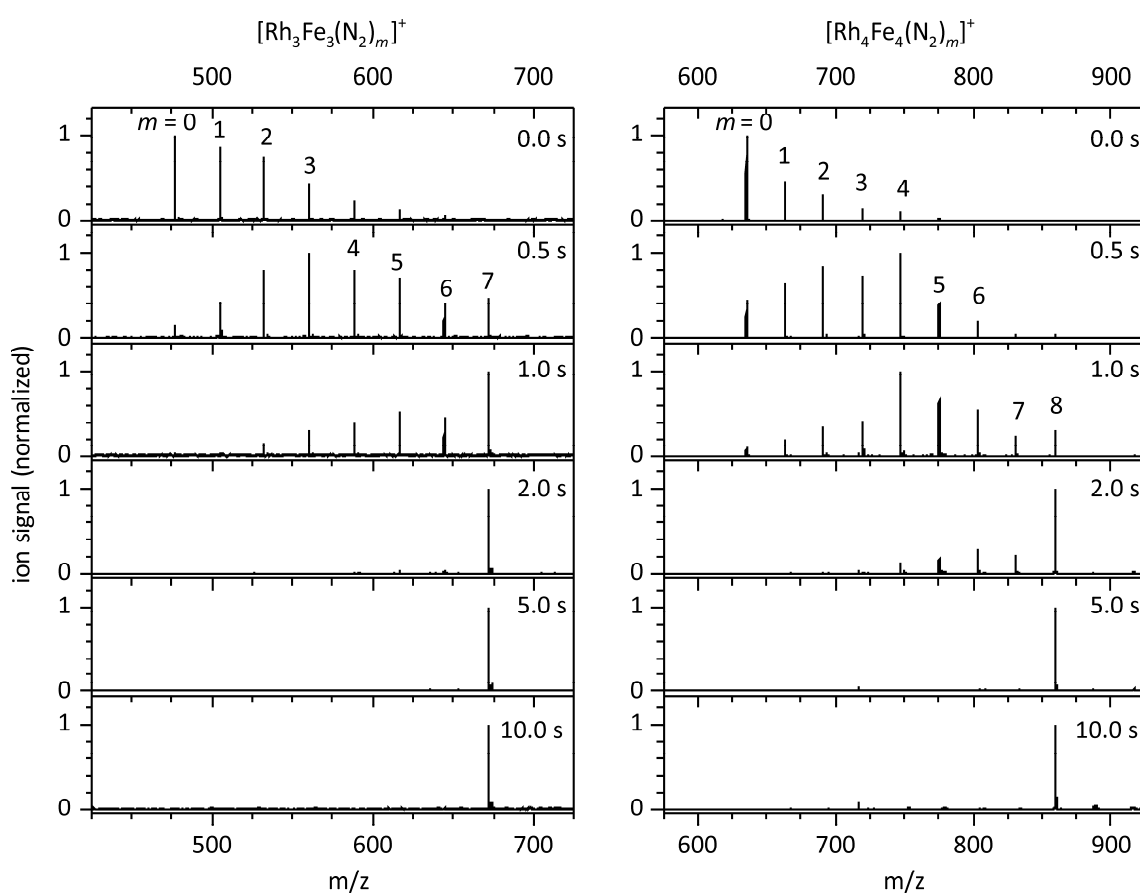


Fig. 16 FT-ICR mass spectra of $[\text{Rh}_3\text{Fe}_3]^+$ and $[\text{Rh}_4\text{Fe}_4]^+$ exposed to 2.8×10^{-7} mbar N₂ at a temperature of 26 K with various storage times in the cryogenic hexapole ion trap. $[\text{Rh}_3\text{Fe}_3]^+$ reveals a *smooth* adsorption behavior up to a limit of 7 N₂ whereas measurements on the $[\text{Rh}_4\text{Fe}_4]^+$ cluster show in addition to an adsorption limit of 8 N₂ an *intermittent* limit of 4 N₂ *i.e.* after a distinct number of N₂ is adsorbed additional adsorption of N₂ happens with a slower rate (confirmed by detailed kinetic investigations done by [AAE] [42]).

Geometry optimizations and vibrational analysis were performed by the Gaussian 09 package [50] at PBE0/ECP(Rh, Fe); cc-pVTZ(N) level of theory [51, 52] as proven suitable for cobalt,

nickel and rhodium clusters [15, 21, 22, 24, 44, 53]. We utilize Stuttgart RSC 1997 ECP(Rh) basis sets of double zeta quality [54]. We had to tolerate relaxed SCF convergence criteria of 10^{-5} (as compared to 10^{-8} in ‘standard’ DFT calculations) to achieve SCF convergence.

7.5 Results and Discussion

7.5.1 The computed structures and spin states of bare $[\text{Rh}_3\text{Fe}_3]^+$ and $[\text{Rh}_4\text{Fe}_4]^+$ clusters

We take as a starting point for our studies of bimetallic cluster adsorbate complexes $[\text{Rh}_i\text{Fe}_j(\text{N}_2)_m]^+$, abbreviated as (i,j,m) , the modelling the minimum structures of the bare (3,3,0) and (4,4,0) clusters. The optimization towards a minimum energy structure is more involved for bimetallic clusters than for monometallic clusters: One needs to take into account several mixing topologies, which imply various topologic isomers.

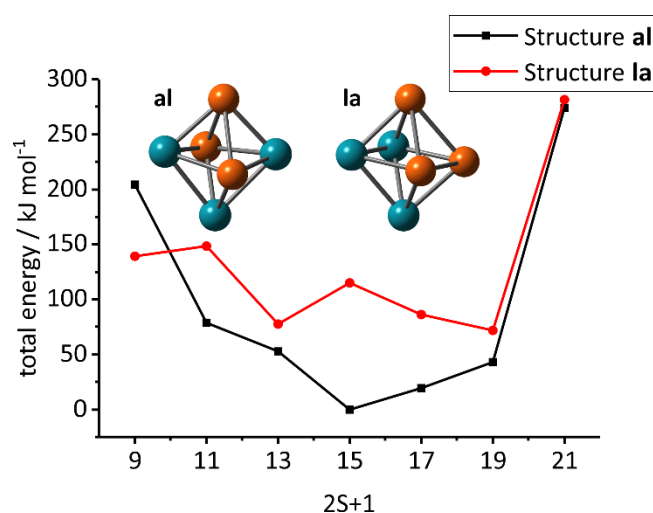


Fig. 17 Total energies of alloy like $[\text{Rh}_3\text{Fe}_3]^+$ clusters (black squares) and of layered $[\text{Rh}_3\text{Fe}_3]^+$ clusters (red circles) as a function of the spin multiplicity $2S+1$, relative to the 15tet of structure **(a)**. The insets display the two possible isomers in near octahedral geometry (details see text; Fe: orange; Rh: turquoise).

The Rh_3Fe_3 cluster was found to assume an octahedral structure [41]. We took these findings as a basis for our calculations on the cationic $[\text{Rh}_3\text{Fe}_3]^+$ cluster. Within the octahedral geometry there are exactly two possible distributions of 3+3 equivalent atoms: An intermixed ‘alloy’ structure **(a)** and a segregated ‘layered’ structure **(b)**. Pairwise permutation of any two non-equivalent atoms would interconvert these two isomers into each other (*cf.* insets to Fig. 2). Within the two possible octahedral isomers, the rhodium and iron atoms find themselves to

7. Cryo Infrared Spectroscopy of N₂ Adsorption onto Bimetallic Rhodium-Iron Clusters in Isolation

form two alternative triangular arrangements, respectively (Fig. 2). These triangles are perpendicular orientated to each other in the alloy like structure **(al)** (meridional) and are parallel to each other in the layered structure **(la)** (facial).

In order to model such conceivable isomers we had to explore their possible spin multiplicities in parallel. It showed that both isomers are stable in all multiplicities explored ($2S+1 = 9, \dots, 21$), and that their geometries do relax to a minor extent by some symmetry lowering. The alloy structure **(al)** is most stable when in a 15tet. This value fits well to the average spin moment per atom ($\bar{\mu}_N = 2.50 \mu_B$ of the neutral cluster 16tet) calculated by Mokkath *et al.* for structure **(al)** [41]. All of **(al)**'s multiplet states are more stable than those of the layered structure **(la)** – but the 9tet. The most favourable layered multiplet, the 19tet of **(la)**, is 72 kJ mol⁻¹ less stable than the most favorable alloy multiplet, which is the 15tet of **(al)**.

Table 3 Calculated atomic distances (in Å) of nearest neighbors within the two [Rh₃Fe₃]⁺ cluster isomers **(al)** and **(la)** (15tet) in comparison with sums of atomic radii, with experimental data and with calculations on an **(al)**-like structure.

Species	Sums of atomic radii		PW91 ^a	PBE0 ^{tw}	PBE0 ^{tw}
	dimer	bulk	(al)	(al)	(la)
Rh-Rh	Theo 2.21 ^a Theo 2.27 ^b Exp 2.3855 ^c Exp 2.28 ^d	2.69 ^f	2.61	2.737	2.725
Rh-Fe	-	2.586 ^f 2.581 ^g	2.38	2.643 – 2.666	2.65
Fe-Fe	Exp 2.198(2) – 2.2318(8) ^f	α Fe 2.482 ^f	2.62	2.580	2.584

a Ref. [41]; b [55]; c [56]; d [57]; e [58]; f [59], distance of next neighbors in fcc crystal, lattice parameter $a = 3.8032 \text{ \AA}$; g [60]; tw this work

We compare the atomic distances to the next neighbors of each atom in the previously shown structures **(al)** and **(la)** with the bulk values and the previously calculated neutral cluster distances [41] (Table 1, Table S1, and Table S2). Our calculated [Rh₃Fe₃]⁺ cluster values come closer to the ones known from crystal data. The PW91 functional used by Mokkath *et al.* [41] overbinds the Rh-Rh and the Rh-Fe distances in an **(la)** type cluster and yields longer Fe-Fe contacts, compared to this work. Only the Rh-Fe contacts appear to form a bond. The range of Rh-Fe bond length in structure **(la)** reflects that there are two different coordination geometries for each element and thus the symmetry is lower than in structure **(al)**. Structure

(al) provides for eight Rh-Fe bonds, structure **(la)** only for six Rh-Fe bonds at the expense of additional Fe-Fe and Rh-Rh interaction, exclusive Rh-Fe interaction is not possible or too small.

We started our survey for $[\text{Rh}_4\text{Fe}_4]^+$ minimum structures with bicapped octahedral structures **(h)** [41], and we added cubic **(e)**, and quadratic antiprismatic **(ab, ae)** structures, inspired by earlier investigations of pure Rh clusters by Harding *et al.* [61]. In all these cases we found a geometry relaxation towards a distorted bicapped octahedral structure (most stable when $2S+1 = 22$), which consist of two Rh dimers that are separated by central four Fe atoms in a distorted tetrahedral conformation (Table S3, Table S4, Table S5, and Table S6). The Rh-Fe-Rh coordination angles are obtuse (larger than 90°) and the Fe-Rh-Fe coordination angles are acute (smaller than 90°). Thus, the rhodium atoms provide more space for adsorption of N_2 . The PW91 functional predicts less Rh-Rh relaxation in distances relative to bulk values than our PBE0 modelling (Table 2).

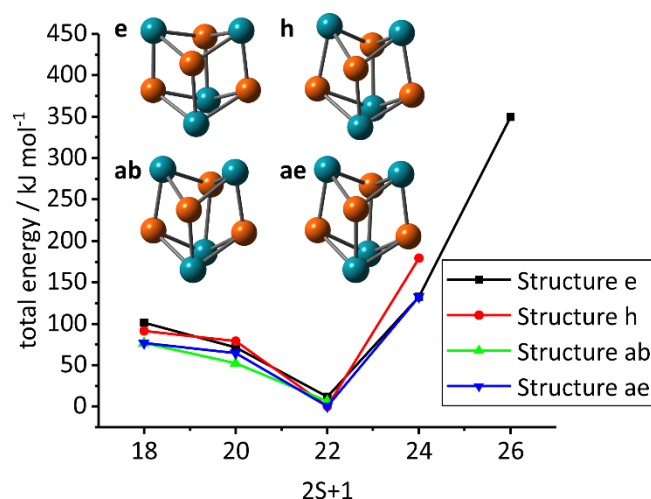


Fig. 18 Total energies of alloy like $[\text{Rh}_4\text{Fe}_4]^+$ clusters as a function of the spin multiplicity $2S+1$, relative to the 22tet of structure **(h)**. The structures **(e)**, **(h)**, **(ab)**, **(ae)** originate from distinct starting geometries by relaxation in the course of optimization; they converge to a single structural type that comes close to D_{2d} symmetry. Note, that only Rh-Fe bonds exist, and the Rh atoms are separated by the Fe atoms. (more details see text; Fe: orange; Rh: turquoise).

Computed Rh-Rh distances range between 2.706 \AA and 2.737 \AA , which is slightly but significantly larger than bond distances in the bulk. Our computed Rh-Rh and Fe-Fe distances are far off the ones from the dimer data. In the case of structure **(e)** one distance between neighbored Rh atoms (Rh2-Rh3, *cf.* Table S3) is much too long to indicate a bond. For $[\text{Rh}_4\text{Fe}_4]^+$ the Fe-Fe and Rh-Rh distances are too long for a binding interaction. This allows for large-scale

7. Cryo Infrared Spectroscopy of N₂ Adsorption onto Bimetallic Rhodium-Iron Clusters in Isolation

flexibility at little enthalpic penalty. In contrast, all computed Rh-Fe distances are short indicating binding, for sure a stronger interaction than for Rh-Rh and Fe-Fe.

That means that in the [Rh₄Fe₄]⁺ cluster Rh-Fe bonds are dominant and each Rh atom is coordinated by three Fe atoms and vice versa. Moreover, within this [Rh₄Fe₄]⁺ cluster the Fe-Fe and Rh-Rh interactions seem negligible, and no such bonds exist in favor of dominant Fe-Rh bonding. This cluster is sufficiently large to avoid the unfavorable interactions and to allow for optimized mixing. Structure **(e)** has relaxed to C_{2v}, and it is somewhat less stable (by ~ 6 kJ/mol) than **(e)**, **(ab)**, and **(ae)** all of which resume almost perfect D_{2d} symmetry.

Table 4 Calculated atomic distances (in Å) for nearest neighbors for the [Rh₄Fe₄]⁺ clusters (22tet) in comparison with sum of atomic radii, experimental data and calculations on a bicapped octahedral structure.

Species	Sums of atomic radii		PW91 ^a	PBE0 ^{tw} (e)	PBE0 ^{tw} (h)	PBE0 ^{tw} (ab)	PBE0 ^{tw} (ae)
	dimer	bulk					
Rh-Rh	Theo.	2.69 ^f	2.70	2.751 –	2.715 –	2.706 –	2.715 –
	2.21 ^a			3.307	2.737	2.716	2.737
	Theo.						
	2.27 ^b						
	Exp.						
	2.3855 ^c						
	Exp. 2.28 ^d						
Rh-Fe	-	2.586 ^f	2.42	2.332 –	2.361 –	2.375 –	2.362 –
		2.581 ^g		2.412	2.537	2.433	2.715
Fe-Fe	Exp.	αFe	2.45	2.839 –	2.826 –	2.615 –	2.766 –
	2.198(2) –	2.482 ^f		2.842	2.779	2.839	2.827
	2.2318(8) ^f						

a Ref. [41]; b [55]; c [56]; d [57]; e [58]; f [59], distance of next neighbors in fcc crystal, lattice parameter a = 3.8032 Å; g [60]; tw this work

7.5.2 IR spectroscopy of N₂ adsorption onto [Rh_iFe_j]⁺ i = j = 3, ..., 8 clusters

We recorded IR-PD spectra of N₂ adsorbed onto equiatomic Rhodium - Iron cluster cations (Figs 4 and 5), and we found multitudes of bands which are red shifted with respect to the free N₂ stretching vibration at 2330 cm⁻¹ [62]. The obtained band positions range from 2175 to 2315 cm⁻¹. This is to compare to N₂ adsorbate spectra of cobalt clusters (2170 – 2290 cm⁻¹) [15] as well as to those of nickel (2175 – 2280 cm⁻¹) [21, 22], tantalum (2180 – 2325 cm⁻¹) [63,

64], iron ($2270 - 2310 \text{ cm}^{-1}$) [43] and rhodium clusters ($2180 - 2270 \text{ cm}^{-1}$) [24, 53]. The red and green shaded areas in the present spectra (Figs 4,5) mark the previously found ranges of the band positions of single N_2 when adsorbed to pure rhodium and iron clusters, respectively.

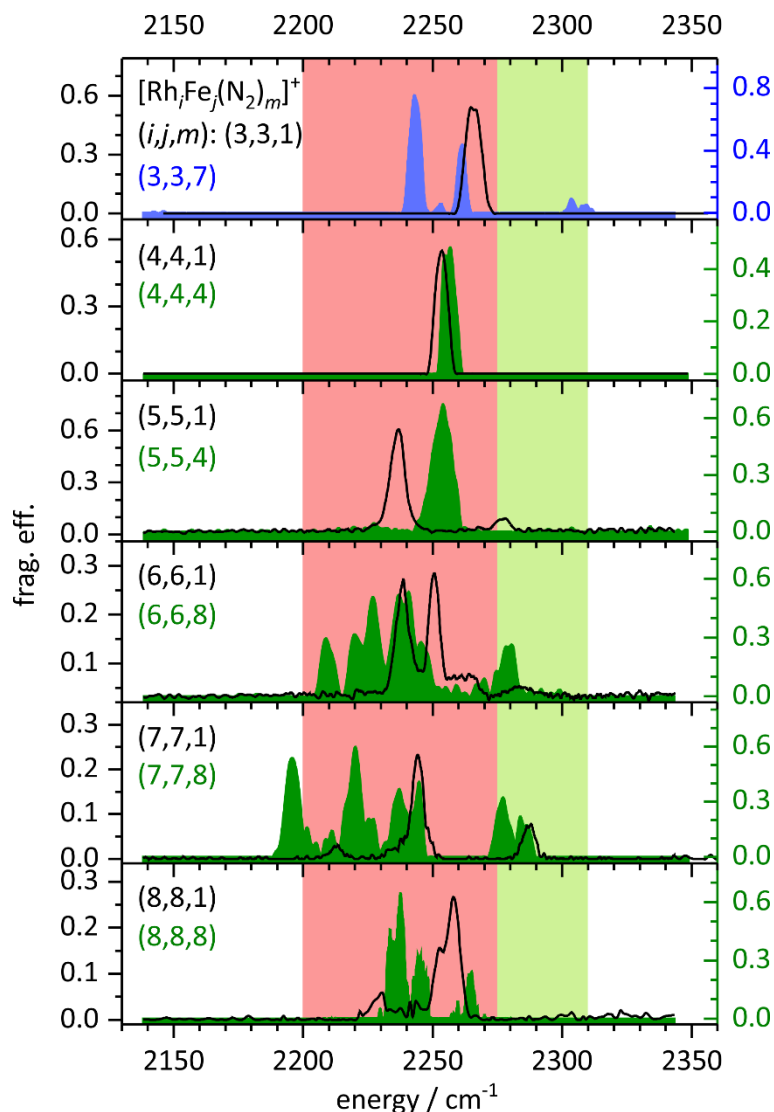


Fig. 19 IR-PD spectra of single N_2 adsorption (black line) and of first intermittent N_2 adsorption (see exptl. part.; green shaded) on equiatomic alloy cluster cations $[\text{Rh}_i\text{Fe}_j(\text{N}_2)_m]^+$ as a function of the size of the cluster core $i = j$. In the case of $i = j = 3$ the blue color denotes the absence of any intermittent adsorption limit. Instead we provide for the spectrum of the maximum N_2 adsorption limit at $m = 7$. The red and green shaded background indicate the known spectral ranges of the single N_2 vibrations on pure Rh and Fe cluster cations, respectively (for further details see text).

In our present study we took IR-PD spectra of equiatomic $[\text{Rh}_i\text{Fe}_j(\text{N}_2)_m]^+$ clusters at three values of m : single N_2 adsorption $m = 1$ (black line in Figs 4 and 5), intermittent coverage state (green shaded areas in Fig. 4) and high amounts of adsorbed N_2 (blue shaded areas in Figs 4 and 5).

7. Cryo Infrared Spectroscopy of N₂ Adsorption onto Bimetallic Rhodium-Iron Clusters in Isolation

For (3,3,*m*) we recorded IR-PD spectra of *m* = 1 and 7 omitting the case of intermittent coverage. For exemplary measurements down to below 1200 cm⁻¹, and further recorded spectra of some more cluster adsorbate complexes (*i,j,m*) refer to the Supplement.

7.5.2.1 The cases of single N₂ adsorption

In the cases of single and of intermittent N₂ adsorption (Fig. 4) onto [Fe_{*i*}Rh_{*j*}]⁺ clusters we observe vibrational bands around 2250 ± 50 cm⁻¹, which coincides with the range of previously found vibrational bands of pure Rh cluster N₂ adsorbates [24]. This implies red shifts of about 30 to 130 cm⁻¹ with respect to the IR inactive stretching vibration of free N₂ (2330 cm⁻¹) [62]. Encouraged by this coincidence we assume that a single N₂ adsorbs preferentially to a rhodium atom rather than to an iron atom. We find support for this assumption by previously calculated adsorption energy of N₂ on rhodium surfaces (- 54 kJ/mol) which are considerably lower than those on Fe surfaces (- 34 kJ/mol).[1]

[Rh₃Fe₃(N₂)₁]⁺ to [Rh₅Fe₅(N₂)₁]⁺: In all cases up to *i* = *j* = 5 there are single strong bands of single N₂ adsorbates (*m* = 1) at 2266, 2253, and 2237 cm⁻¹. These single bands gradually red shift by 29 cm⁻¹. Such a red shift was observed before in the case of N₂ adsorption to pure cobalt and rhodium cluster cations and it was interpreted in terms of a cooperative polarization effect [15, 24]: the (likely) metallic nature of the cluster cations allows for electron density back donation to molecular adsorbate acceptors (*e.g.* antibinding π*). This would weaken the N–N bond and increase the redshift of the N₂ stretching frequency with the number of metal atoms. The further weak IR-PD band of (5,5,1) at 2277 cm⁻¹ likely stems from a combination band of N-N stretching plus Rh-N-N wagging character, plus 40 cm⁻¹ with respect to the pure N-N stretching band.

[Rh₆Fe₆(N₂)₁]⁺: The *i* = *j* = 6 case is special in revealing two strong IR-PD bands at 2239 and 2251 cm⁻¹ by a mere single N₂ adsorbate, *m* = 1 (black line in Fig. 4). This may likely indicate two distinguishable N₂ binding sites, less likely two cluster isomers, and even less likely, two spin state isomers. If indeed so, one may tentatively conclude on the presence of Rh atoms in two different coordination geometries, which vary either by number or by nature of nearest neighbors. Elucidation remains to future DFT modelling. Above the second strong band, we find some more absorption around 2265 and 2285 cm⁻¹. Both may originate as well from some combination band of N-N stretching plus Rh-N-N wagging character, the latter contributing by about 25 and 35 cm⁻¹, respectively.

[Rh₇Fe₇(N₂)₁]⁺ and [Rh₈Fe₈(N₂)₁]⁺: When inspecting the IR spectra of these larger clusters the $m = 1$ cases reveal a remarkable blue shift of the observed single strong N₂ vibrational bands of 5 cm⁻¹ from $i = j = 6$ to 7 (2244 cm⁻¹), and of 14 cm⁻¹ from $i = j = 7$ to 8 (2258 cm⁻¹). This is surprising at first sight. If we assume an alloy like structure, that is only Rh-Fe bonds and no Rh-Rh or Fe-Fe bonds within these clusters, the number of iron atoms coordinating to each Rh atom will increase with the size of the cluster. Since Fe is more electronegative than Rh more electron density is shifted from Rh to Fe, and the vibrational frequency of Rh attached N₂ will decrease, which is due to less π -back bonding. The known charge dilution effect [19] may also contribute to some extent, which would be minor for clusters of this size, however. The (8,8,1) cluster adsorbate complex has an additional shoulder on the red slope of the strong band at 2253 cm⁻¹ that may indicate a second N₂ binding site. Both clusters, (7,7,1) and (8,8,1), show an additional band about 30 cm⁻¹ to the red of the strong bands at 2213 and 2231 cm⁻¹, respectively. We observed these bands only upon exposure to high IR photon fluxes, and we assume these to represent combination bands of the N-N stretching band with some populated Rh-N-N wagging modes. The spectrum (7,7,1) cluster adsorbate complex reveals an additional band red shifted by 43 cm⁻¹ at 2287 cm⁻¹ which may arise from a combination mode of N-N stretching and Rh-N-N wagging mode as assumed above for the cases of (5,5,1) and (6,6,1).

7.5.2.2 The cases of the 'intermittent adsorption limits'

As outlined in the experimental section, we have defined as an intermittent adsorption limit those cluster adsorbate complexes where we find enhanced amounts of N₂ adsorption and delayed kinetics for further adsorption. Note, that in all of the investigated cases of $i = j = 4, \dots, 8$ there are such intermittent adsorption limits – but for the smallest cluster case $i = j = 3$ where N₂ adsorption proceeds towards its maximum limit without any intermittent delay.

[Rh₃Fe₃(N₂)₇]⁺: We observe two strong bands (at 2243 and 2261 cm⁻¹), one weak band (in between at 2253 cm⁻¹) and a couple of very weak, near degenerate bands around 2305 cm⁻¹ (blue spectrum indicated as (3,3,7) in Fig. 4). The former three of these bands fall within the red shaded area, and they likely stem from the stretching vibrations of those N₂ adsorbates, which adsorb onto Rh sites. The super-stoichiometric composition of a 6 : 7 metal : adsorbate ratio requires at least one metal site with geminal N₂ adsorption. We assume a monolayer

7. Cryo Infrared Spectroscopy of N₂ Adsorption onto Bimetallic Rhodium-Iron Clusters in Isolation

with single adsorption of the first six N₂ molecules onto the [Rh₃Fe₃]⁺ cluster and the 7th N₂ adsorbs onto an already singly occupied site.

Symmetric/asymmetric couplings of those equivalent N₂ oscillators are expected to induce significant splittings. Further insights will arise from the DFT modelling of such vibrations (*cf.* below, chapter 7.5.3). The weak bands around 2305 cm⁻¹ fall into the green shaded area of Fe-N₂ stretching vibrations, and they likely arise from such N₂ adsorptions to Iron sites. Note, that this IR-PD spectrum does not provide any discernible evidence for isomerization of any type, which well coincides with the swift adsorption kinetics up to the maximum adsorption limit as reported in [AAE][42].

[Rh₄Fe₄(N₂)₄]⁺: This cluster shows a single band at 2257 cm⁻¹, slightly blue shifted with respect to single N₂ adsorption by about 4 cm⁻¹, and well within the red shaded area of N₂ adsorption to Rh sites. This occurrence of a single band by numerous IR active N₂ oscillators is indicative of a high cluster symmetry. The computations of [Rh₄Fe₄]⁺ structures have suggested such a high symmetry in a D_{2d} like structure (*cf.* inset to Fig. 3). All Rh atoms and all Fe atoms have the same coordination geometry, respectively; all Rh sites and all Fe sites are equivalent, respectively. An exclusive N₂ adsorption to Rh sites finds further support by structural and enthalpic reasons: The Rh atoms are coordinated by Fe with acute Fe-Rh-Fe angles, and they protrude from the cluster surface. This reduces steric hindrance by next neighbors and provides for open space. Multiple N₂ adsorbates may share a single Rh site. For Fe sites, the opposite holds. Enthalpic reasoning arises from the computed N₂ adsorption enthalpies of pure Fe and Rh surfaces – which are stronger for Rh than for Fe.

[Rh₅Fe₅(N₂)₄]⁺: The IR-PD spectrum of this cluster shows a single band at 2254 cm⁻¹ which falls into the red area, and it almost coincides with the single band of the [Rh₄Fe₄(N₂)₄]⁺ cluster adsorbate complex. Note the difference to the (4,4,1) and (5,5,1) cases, where the two single bands are displaced against each other by about 17 cm⁻¹. Once more, we take the occurrence of a single absorption band by multiple N₂ adsorbates as strong evidence for a cluster structure of high symmetry. However, its very nature is yet unexplored. A very weak band at 2227 cm⁻¹ might indicate either a hot band or a second isomer. According DFT calculations would have been beyond the scope of the present study.

[Rh₆Fe₆(N₂)₈]⁺ and [Rh₇Fe₇(N₂)₈]⁺: In contrast to the IR-PD spectra of the smaller clusters these clusters provide for spectra with numerous bands within the red shaded area of N₂ adsorption

to Rh sites; they spread out over a range of up to 75 cm^{-1} . This likely points out that the Rh coordination sites are distinguishable, and that these clusters are of low symmetry. There are bands at 2209, 2220, 2227, 2237, 2241, and 2245 cm^{-1} of the (6,6,8) cluster adsorbate complex and at 2175, 2210, 2220, 2226, 2237, and 2244 cm^{-1} of the (7,7,8) cluster adsorbate complex. There are some additional bands in the range of $2270 - 2290\text{ cm}^{-1}$ that fall into the green shaded area of likely N_2 adsorption to Fe sites. Such adsorption is indeed conceivable in cases where the amount of N_2 adsorbates exceeds the adsorbing Rh sites within the cluster. The excess of N_2 molecules may choose to accept the less favorable Fe sites. Of course, it is conceivable to adsorb multiple N_2 to a single Rh, which might induce further splittings by symmetric/asymmetric coupling. Given the high total amount of metal atoms in these clusters (12 and 14, respectively), it is likely that some atoms are not at the cluster surface. They may assume high coordination to the inside and form bulk like bonding motifs. This remains to verify.

$[\text{Rh}_8\text{Fe}_8(\text{N}_2)_8]^+$: In this intermittent adsorption limit case, the amount of adsorbed N_2 molecules is the same as the number of Rh and Fe atoms, each. The IR-PD spectrum reveals several bands within the red shaded area of preferential N_2 adsorption to Rh sites (at 2233, 2238, 2245, and 2265 cm^{-1}); there are no bands in the range of single Fe- N_2 adsorption. In view of the previous findings, all N_2 molecules seem to adsorb to Rh sites only – albeit to distinguishable ones. We observe two weak bands about $+20\text{ cm}^{-1}$ off, which we tentatively assign to stretch/wag combinations. All of this indicates a cluster structure of some symmetry that is slightly distorted. These findings may serve as a valuable starting point for further elucidation by future DFT modelling.

7.5.2.3 The cases of ‘maximum adsorption limits’

We recorded IR-PD spectra of highly abundant clusters with high N_2 coverages, (4,4,8), (6,6,9), (8,8,10), and of maximum adsorption limits (5,5,8) and (7,7,12). For all of these cluster adsorbate complexes, $m > i$. The (3,3,7) case is discussed above.

$[\text{Rh}_4\text{Fe}_4(\text{N}_2)_8]^+$: Despite the high level of N_2 adsorption, $m = 8$, we observe a single band at 2226 cm^{-1} with a shoulder at 2231 cm^{-1} . The center of this double band is red shifted by 25 cm^{-1} with respect to single N_2 adsorption, $m = 1$, and by 28 cm^{-1} with respect to the intermittent N_2 adsorption, $m = 4$. By virtue of the red and green shaded areas, all of the N_2 molecules likely adsorb onto Rh sites. This is conceivable based on the structural and enthalpic reasons

7. Cryo Infrared Spectroscopy of N₂ Adsorption onto Bimetallic Rhodium-Iron Clusters in Isolation

discussed above. Closer inspection of the observed band reveals a small splitting of about 5 cm⁻¹. This likely results from symmetric/antisymmetric coupling of stretching vibrations of two N₂ on the same Rh site. A weak band around 2297 cm⁻¹ likely arises from some N₂ adsorption to Fe sites. Some splitting on the order of 4 cm⁻¹ is discernible, but close to the noise level. Note, that higher levels of N₂ coverage up to $m_{max} = 11$ are in equilibrium but their abundances are almost 2 orders of magnitude lower than that of $m = 8$ [42]. We find no indication of isomerization or swift adsorption/desorption equilibria in the recorded IR-PD spectra of (4,4, m).

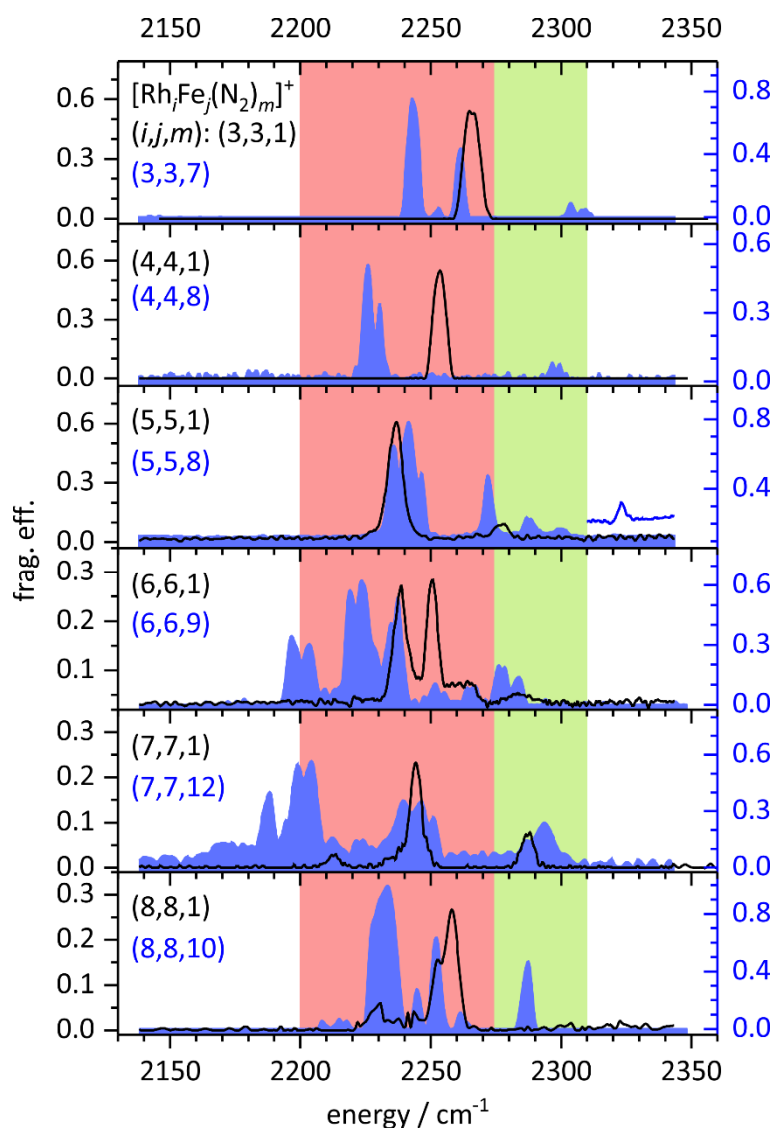


Fig. 20 IR-PD spectra of single (black line) and high N₂ adsorption (blue shaded) on equiatomic cationic Rh-Fe alloy cluster cations as a function of the size of the cluster core $i=j$. The red and green shaded backgrounds indicate the known spectral ranges of the single N₂ vibrations on pure Rh and Fe cluster cations, respectively (details see text).

[Rh₅Fe₅(N₂)₈]⁺: The strong band of the (5,5,8) cluster at 2241 cm⁻¹ appears blue shifted by 4 cm⁻¹ from the according band of the (5,5,1) cluster at 2237 cm⁻¹ and reveals some triple splitting by 4 – 6 cm⁻¹. There is an additional set of three weaker bands to the blue at 2272 cm⁻¹ and above. We tentatively assign these to other N₂ adsorption sites. The two bands at 2288 and 2299 cm⁻¹ are in the green area of N₂ adsorbed likely to Fe clusters.

We may note in passing that in both cases of $i = j = 4$ and 5 the investigated levels of N₂ adsorption are $m = 4$ and $m = 8$. Both IR-PD bands of $m = 4$ occur around 2254 – 2257 cm⁻¹, both IR-PD bands of $m = 8$ shift considerably to the red (12 – 32 cm⁻¹). Despite these similarities, the single N₂ adsorption cases (4,4,1) and (5,5,1) are remarkably different: The found single IR-PD bands of $i = j = 4$ and 5 are shifted with respect to each other by 17 cm⁻¹.

There is an additional band at 2323 cm⁻¹ which appears only upon application of maximum laser power (2.5 mJ/pulse as opposed to 1 mJ/pulse else). It likely originates from a merely bound and weakly polarized N₂ molecule, roaming around or locating close to other strongly bound N₂ adsorbates. The adsorption rates continuously decrease towards $m_{max} = 8$ (cf. **[AAE]**) and support such weak interaction of the last N₂ ligand with the cluster [42]. Thus, there may be indeed a loosely bound second shell N₂ adsorbate. For all of the least red shifted bands, 2299 cm⁻¹ and above, we need to keep in mind the general possibility of stretching wagging combination modes.

[Rh₆Fe₆(N₂)₉]⁺ and [Rh₇Fe₇(N₂)₁₂]⁺ and [Rh₈Fe₈(N₂)₁₀]⁺: In these three cases of $i = j = 6, 7,$ and 8 we recorded the IR-PD spectra of the cluster adsorbate complexes with $m = 9, 12,$ and 10, respectively. We found bands for (6,6,9) at 2196, 2203, 2219, 2223, 2237, 2251, 2265, 2276, 2284 cm⁻¹; and for (8,8,10) at 2233, 2245, 2252, 2261, and 2287 cm⁻¹. The bands of the (7,7,12) spectrum separate in two sets: One in the red shaded Rh range at 2188, 2199, 2204, 2213, 2223, 2240, 2247, and 2251 cm⁻¹, and one weaker set of overlapping bands in the green shaded Fe range around 2294 cm⁻¹. The spectra resemble closely those of the lower coverage intermittent adsorption limits discussed above. All spectral features prevail, with some minor shifts and intensity variations occurring. There is one remarkable exception: In the $i = j = 8$ cases there is an additional band at 2287 cm⁻¹ in the $m = 10$ spectrum which does not show in the $m = 8$ spectrum. This additional band is indicative of N₂ adsorption to Fe sites; it falls into the green shaded spectral area. Thus we find evidence that the $i = j = 8$ cluster [Rh₈Fe₈]⁺ adsorbs up to eight N₂ to Rh sites, and two more N₂ adsorbates onto Fe sites thereafter. In all three cases, we did not observe any bands around 2330 cm⁻¹.

7. Cryo Infrared Spectroscopy of N₂ Adsorption onto Bimetallic Rhodium-Iron Clusters in Isolation

With (7,7,12), we were able to record an IR-PD spectrum of a maximum adsorption limit, despite an adsorption/desorption equilibrium between four species at long storage times [42]. The spectrum shows broad bands, which are in line with a flexible adsorbate shell. The recorded bands exhibit narrow splittings of 4 – 10 cm⁻¹ which indicate couplings as expected for double N₂ occupation of metal sites.

In addition, we recorded the spectrum of the (7,7,10) intermittent adsorption limit (*cf.* Fig S11 in the Supplement), which reveals remarkably sharp and widely spaced bands – void of the above mentioned small couplings.

Upon closer inspection, some of the properties of the (6,6,9) and the (7,7,12) spectra warrant some more attention: Firstly, for (6,6,9) the three strongest bands reveal a splitting up to 7 cm⁻¹ which does not show up to the first intermittent N₂ adsorption. Such splittings are likely indicative of symmetric/antisymmetric couplings of two N₂ at the same Rh site, see above. In this case, they show only at high N₂ loads. Even the weak bands in the green shaded area reveal a splitting. We conclude on some Rh and Fe atoms that are more exposed and others that are higher coordinated and thus do adsorb at most a single N₂. Secondly, the (6,6,9) and the (7,7,12) spectra spread out over a range of up to 120 cm⁻¹. We assume that the most red shifted bands arise from N₂ adsorption onto a class of Rh atoms that provide for a weak σ -acceptor and strong π -donor character. The less red shifted bands arise from N₂ adsorbed onto a class of Rh atoms with a strong σ -acceptor and weak π -donor character. In the case of (8,8,10) cluster adsorbate complex these separate classes seem to vanish.

The IR-PD spectra of (6,6,9) and (8,8,10) document intermittent species which are in equilibrium with the maximum adsorption limit, and which constitute the most abundant species within these equilibria [42] [AAE]. In both cases, the adsorption rate constants drop continuously with increasing number of adsorbed N₂ molecules, the adsorption becomes slower, step for step. Investigation of their true maximum adsorption limits would probably also show weakly bound and weakly activated N₂ ligands as revealed for (5,5,8). However, the low abundance of these maximum adsorption limits (6,6,10) and (8,8,11) as well as their involvement in swift adsorption/desorption equilibria have impeded their spectroscopic investigation so far.

Quantum chemical modelling of all investigated species and their recorded spectra is far out of reach. Instead, we chose one case of limited complexity for exemplary DFT modelling in

order to achieve some better understanding of the adsorption behavior and the structural properties of such an alloy cluster.

7.5.3 Modelling of the $[\text{Rh}_3\text{Fe}_3(\text{N}_2)_7]^+$ vibrational spectra

We chose the case of the maximum N_2 adsorption limit of $m_{\text{max}} = 7$ to the $i = j = 3$ alloy cluster as a test case for vibrational analysis by further DFT modelling. The most stable (3,3,7) isomers base on a metal cluster core (3,3,0) of most stable type **(a)**. Each of the Rh and Fe sites serves to adsorb a single N_2 , the seventh remaining N_2 to locate as a second adsorbate on one of four optional and distinguishable sites (*cf.* Fig. 21 for atom labeling): at the Rh site (two Rh next neighbors, labeled Rh1), at either of two equivalent Rh sites (one Rh next neighbor, labeled Rh2 and Rh3), at the Fe site (two Fe next neighbors, labeled Fe1), or at the two equivalent Fe site (one Fe next neighbor, labeled Fe2 and Fe3). It shows that such tiny differences in adsorption do induce remarkable enthalpic consequences, namely in terms of the preferred spin multiplets. Adsorption of the seventh N_2 at either of the Rh sites favors the cluster in a 15tet, at any of the Fe sites in a 13tet.

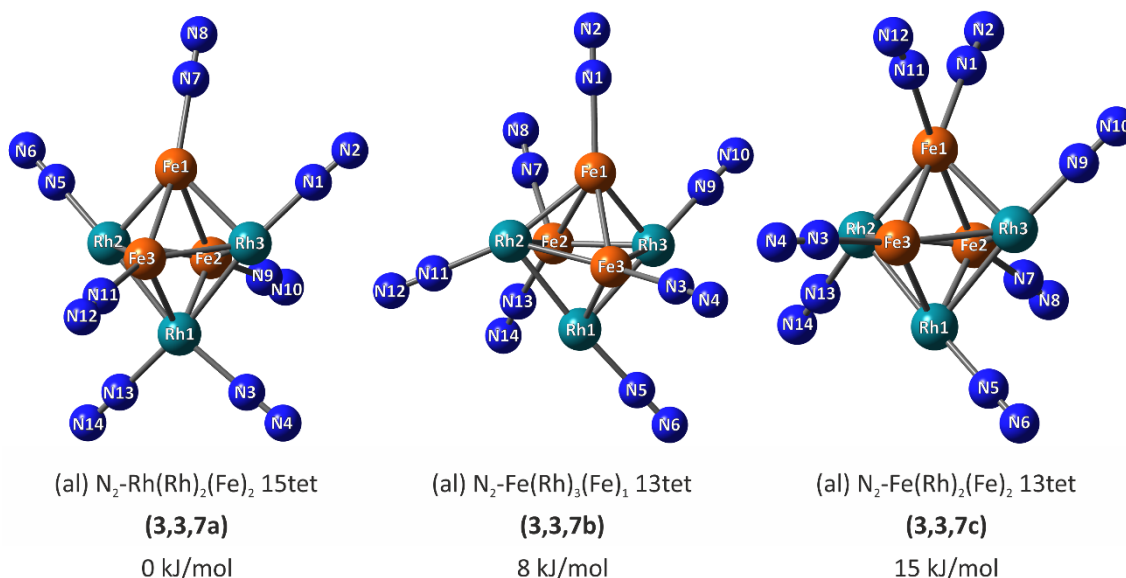


Fig. 21 DFT optimized structures of three most stable $[\text{Rh}_3\text{Fe}_3(\text{N}_2)_7]^+$ clusters. All isomers derive from the cluster core type **(a)**. All N_2 s chose to adsorb by μ_1 type end-on coordination. The most stable case **(3,3,7a)** reveals single N_2 adsorbates at each Rh and Fe site but Rh1, which reveals two geminal N_2 adsorbates. This Rh site is unique by its two Rh next neighbors. Cases **(3,3,7b)** and **(3,3,7c)** reveal two geminal N_2 adsorbates at sites Fe2 and Fe1, respectively. The xyz coordinates are provided in the supplement (Table S9-Table S11).

7. Cryo Infrared Spectroscopy of N₂ Adsorption onto Bimetallic Rhodium-Iron Clusters in Isolation

We compare the recorded IR-PD spectra to our computed IR absorption spectra, where the computed spectra are scaled by 0.9385 [24] to match experimental and calculated fundamentals of free N₂ (Fig. 7). It shows that the experimental IR-PD spectrum matches best to the calculated absorption spectrum of the cluster in a 15tet with the seventh N₂ adsorbed to the sole Rh site with two Rh next neighbors (structures as displayed in Fig. 6, spectrum as in Fig. 7, second to the top). We provide for a compilation of assigned vibrational bands by Table 3. Note, that the calculated and observed bands are slightly shifted in their frequency against each other. However, the overall pattern and the IR intensities agree remarkably well when considering the most stable case of the DFT modelling. The other calculated isomers are at least 46 kJ/mol higher in energy and their spectra are documented by Fig. S14.

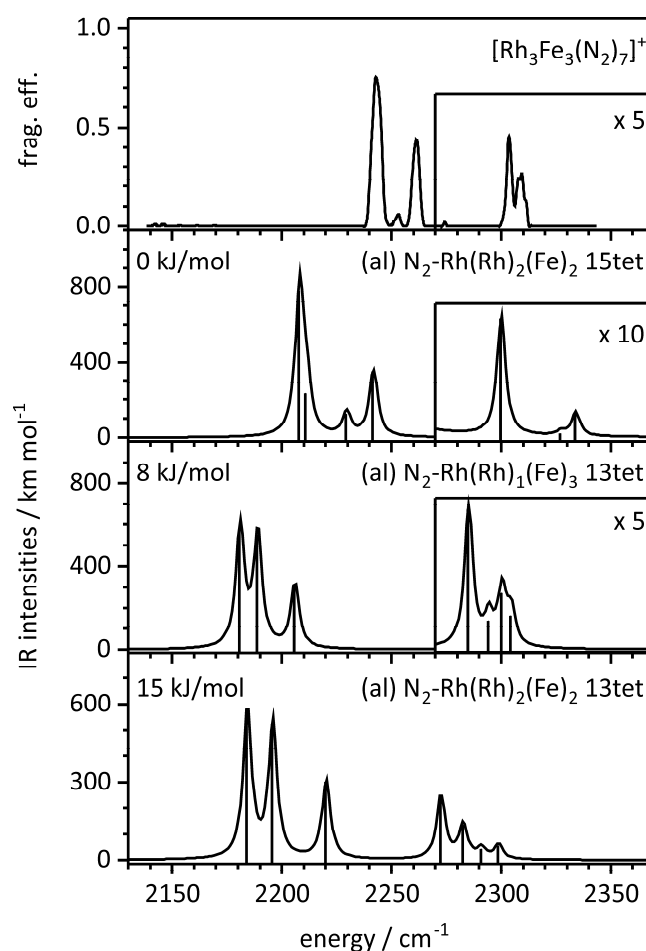


Fig. 22 Experimental IR-PD spectrum (top trace) and calculated IR absorption spectra of some $[\text{Rh}_3\text{Fe}_3(\text{N}_2)_7]^+$ coordination and spin isomers. The calculated spectra (scaled by 0.9385) represent the three preferential coordination and spin isomers from Fig. 6. Note, the slightly shifted and otherwise matching pattern of vibrational modes in the topmost computed spectrum of the most stable isomer (**3,3,7a**) which comes along in a 15tet spin state.

The twofold occupation of a Rh site causes a symmetric/antisymmetric coupling and allows for an assignment of the recorded bands at 2253 cm^{-1} (antisymmetric) and 2261 cm^{-1} (symmetric) (N3/N4 and N13/N14). It is remarkable that there is a significant shift between the bands of N_2 adsorbed on Fe and on Rh. Indeed, all bands around 2250 cm^{-1} can be assigned to stretching vibrations of N_2 on rhodium – in line with our working hypothesis, that spectral findings from pure Rh and pure Fe clusters may serve to guide for a classification of spectral feature in the mixed alloy type Rh-Fe clusters (visualized by the red and green shaded areas in Fig. 4 and 5).

Table 5 Vibrational data for the lowest lying $[\text{Rh}_3\text{Fe}_3(\text{N}_2)_7]^+$ structure. The scaling factor for the N_2 stretching frequencies is 0.9385. The low frequency modes are strongly coupling.

Mode	Type	Freq. / cm^{-1}	Scaled freq. / cm^{-1}	IR intensity / km mol^{-1}
1 – 18	Wagging modes	9.3 – 77	8.7 – 72	0.009 – 11
19 – 32	Internal cluster vibrations	99 – 231	93 – 217	0.044 – 5.3
33 – 47	Bending modes	249 – 343	234 – 322	0.39 – 32
48	Asymm. stretch N1-N2/N5-N6	2352	2207	778
49	Symm. stretch N1-N2/N5-N6	2356	2211	233
50	Asymm. stretch N3-N4/N13-N14	2375	2229	124
51	Symm. stretch N3-N4/N13-N14	2388	2241	351
52	Stretch N7-N8	2450	2299	63
53	Stretch N11-N14	2479	2327	2.3
54	Stretch N9-N10	2487	2334	13

The calculations indicate a symmetric/antisymmetric N_2 -Rh-Rh-Rh- N_2 coupling between the stretching vibrations of N1/N2 and N5/N6. The coupling of these two distant but equivalent N_2 ligands is very weak (calculated as $3 - 4\text{ cm}^{-1}$) and does not necessarily manifest in separate bands. The weak recorded bands above 2300 cm^{-1} can be assigned to N_2 adsorbed to Fe. Calculations indicate no vibrational coupling between these Fe bound N_2 adsorbates. The calculated IR spectra of less stable coordination isomers (the two lower traces in Fig. 7) do not fit to the experimental IR-PD spectrum. These results are in line with our kinetic

7. Cryo Infrared Spectroscopy of N₂ Adsorption onto Bimetallic Rhodium-Iron Clusters in Isolation

measurements that exhibit swift adsorption to a single maximum adsorption limit without any equilibrium at the end of the adsorption chain.[42]

In (3,3,7), the first six N₂ molecules adsorb onto a free metal site such that each metal site is singly occupied, independent of the metal (Rh or Fe). We observe a Langmuir type of stoichiometric adsorption. The 7th N₂ molecule has no choice but to adsorb onto an occupied site and finds itself as geminal adsorbate, preferentially at a Rh site. The adsorption kinetics reveal a swift stepwise adsorption without any indication of an intermittent adsorption limit.[42] The IR bands of the N₂ molecules adsorbed onto the Rh sites are in the range as observed for pure Rh clusters; those of N₂ adsorbed onto Fe sites are in the range as observed for pure Fe clusters, and these IR bands are by at least one order of magnitude less intense than the N₂ stretching IR bands at Rh sites. The polarization of N₂ by adsorption to Fe sites seems weaker than that by adsorption to Rh sites. Note, that these results indicate a conservation of the 15tet spin state at the maximum adsorption limit (3,3,7) rather than a spin quench as observed for pure rhodium clusters before.[24, 44]

The modelling of the (3,3,7) cluster adsorbate complex, the thereby achieved assignment of recorded IR bands, and further insights above thus allow to support the interpretation of the (4,4,8) spectrum:

The IR-PD spectrum of the (4,4,8) cluster adsorbate complex reveals a strong doublet band in the Rh range and a weak set of bands in the Fe range. Such a sparse spectrum by eight chromophores strongly suggests a single type of Rh adsorption sites and of Fe adsorption sites, which implies high symmetry. The recorded band in the Rh range is split by about 4 cm⁻¹ which likely indicates symmetric/antisymmetric coupling of a distant pair of N₂ molecules whose adsorption sites are separated by another metal atom, as revealed in the (3,3,7) case above. In the IR-PD spectrum of (4,4,8), there is no indication of a splitting in the order of 12 cm⁻¹ and therefore no indication for double adsorption onto a single metal site. The IR-PD spectrum thus indicates stoichiometric adsorption onto each of the eight metal sites. The IR-PD spectrum of the (4,4,4) cluster adsorbate complex has not revealed any evidence for N₂ occupation of Fe sites, and the recorded single band indicates a highly symmetric cluster. The adsorption kinetics reveal an intermittent adsorption limit for this complex. We conclude on a highly symmetric cluster core that likely resembles the computed most stable D_{2d} structural type. The first four N₂ molecules likely adsorb onto the equivalent Rh atoms whereas the

remaining four adsorption steps yield at the equivalent Fe sites. The final product is a highly symmetric cluster adsorbate complex (4,4,8) with a Langmuir type stoichiometric first adsorption shell.

7.6 Conclusion

We have recorded IR-PD spectra of size selected N₂ adsorbates on equiatomic Rh-Fe cluster cations. These spectra show a multitude of bands within ranges that coincide with spectra of N₂ adsorbates on Rh and Fe cluster cations recorded before. The sparse spectra of the cluster adsorbate complexes of [Rh₄Fe₄]⁺ and of [Rh₅Fe₅]⁺ indicate high symmetries of these.

We have modelled geometries of [Rh₃Fe₃]⁺ and [Rh₄Fe₄]⁺ clusters as well as IR spectra of the [Rh₃Fe₃(N₂)₇]⁺ cluster which confirm the propensity of the clusters to form as much Rh-Fe bonds as possible and which allows for high symmetry and an alloy like character. Comparison with our adsorption kinetics yields a conclusive description of spectral phenomena like weakly adsorbed N₂ ligands. By assignment of the blue shifted bands to Fe adsorption sites, we validate the element sensitivity of the N₂ stretching vibration with respect to adsorption to Fe or Rh sites. In the case of the [Rh₃Fe₃]⁺ cluster, we conclude on a formation of an N₂ monolayer on all metal atoms. The next N₂ molecule adsorbs onto a Rh atom in a geminal manner. The spectrum of the [Rh₄Fe₄]⁺ cluster indicates an adsorption of the first four N₂ molecules solely/exclusively onto the rhodium atoms. The spectrum of [Rh₄Fe₄(N₂)₈]⁺ indicates additional stoichiometric adsorption onto iron atoms. In contrast to bare rhodium clusters, our investigations do not provide any indication for a spin quench upon N₂ adsorption.

The present IR-PD studies in conjunction with the DFT modelling thus allow relating recorded IR bands to element specific adsorption sites. We thereby find strong evidence for preferential adsorption to rhodium sites and merely secondary adsorption to iron.

7.7 Acknowledgement

This work was supported by the German research foundation DFG within the transregional collaborative research center SFB/TRR 88 'Cooperative effects in homo and heterometallic complexes' (3MET.de) and by the state research center OPTIMAS. We thank Thomas Kolling for assistance on technical questions of any kind.

7.8 References

1. Bligaard, T. and Nørskov, J.K., *Chapter 4 - Heterogeneous Catalysis*, in *Chemical Bonding at Surfaces and Interfaces*. **2008**, Elsevier: Amsterdam. 255-321.
2. Somorjai, G.A., *Introduction to Surface Chemistry and Catalysis*. **1994**: John Wiley & Sons.
3. Deutschmann, O., Knözinger, H., Kochloefl, K., and Turek, T., *Heterogeneous Catalysis and Solid Catalysts*, in *Ullmann's Encyclopedia of Industrial Chemistry*. **2000**, Wiley-VCH Verlag GmbH & Co. KGaA.
4. Votsmeier, M., Kreuzer, T., Gieshoff, J., and Lepperhoff, G., *Automobile Exhaust Control*, in *Ullmann's Encyclopedia of Industrial Chemistry*. **2009**.
5. Ertl, G., *Reactions at Surfaces: From Atoms to Complexity (Nobel Lecture)*. *Angewandte Chemie International Edition* **2008**, *47*, 3524-3535.
6. Harrison, B., Cooper, B.J., and Wilkins, A.J.J., *Control of Nitrogen Oxide Emissions from Automobile Engines*. *Platinum Metals Rev* **1981**, *25*, 14-22.
7. Ertl, G., *Surface Science and Catalysis—Studies on the Mechanism of Ammonia Synthesis: The P. H. Emmett Award Address*. *Catalysis Reviews* **1980**, *21*, 201-223.
8. Brunauer, S., Emmett, P.H., and Teller, E., *Adsorption of Gases in Multimolecular Layers*. *Journal of the American Chemical Society* **1938**, *60*, 309-319.
9. Langmuir, I., *The Adsorption of Gases on Plane Surfaces of Glass, Mica and Platinum*. *Journal of the American Chemical Society* **1918**, *40*, 1361-1403.
10. Freund, H.J., Bartos, B., Messmer, R.P., Grunze, H., Kühlenbeck, H., and Neumann, M., *The adsorption of N₂ on Fe(111): Angle resolved photoemission and theoretical model studies*. *Surface Science* **1987**, *185*, 187-202.
11. Wang, H.P. and Yates, J.T., *Infrared spectroscopic study of molecular nitrogen chemisorption on rhodium surfaces*. *The Journal of Physical Chemistry* **1984**, *88*, 852-856.
12. Lighthart, D.A.J.M., Pilot, I.A.W., Almutairi, A.A.H., and Hensen, E.J.M., *Identification of step-edge sites on Rh nanoparticles for facile CO dissociation*. *Catalysis Communications* **2016**, *77*, 5-8.
13. Jaramillo, D.E., Reed, D.A., Jiang, H.Z.H., Oktawiec, J., Mara, M.W., Forse, A.C., Lussier, D.J., Murphy, R.A., Cunningham, M., Colombo, V., Shuh, D.K., Reimer, J.A., and Long, J.R., *Selective nitrogen adsorption via backbonding in a metal-organic framework with exposed vanadium sites*. *Nat Mater* **2020**, *19*, 517-521.
14. Kerpál, C., Harding, D.J., Lyon, J.T., Meijer, G., and Fielicke, A., *N₂ Activation by Neutral Ruthenium Clusters*. *The Journal of Physical Chemistry C* **2013**, *117*, 12153-12158.
15. Dillinger, S., Mohrbach, J., Hewer, J., Gaffga, M., and Niedner-Schatteburg, G., *Infrared spectroscopy of N₂ adsorption on size selected cobalt cluster cations in isolation*. *Physical Chemistry Chemical Physics* **2015**, *17*, 10358-10362.
16. Blyholder, G., *Molecular Orbital View of Chemisorbed Carbon Monoxide*. *Journal of Physical Chemistry* **1964**, *68*, 2772-2777.
17. Chatt, J. and Duncanson, L.A., *586. Olefin co-ordination compounds. Part III. Infra-red spectra and structure: attempted preparation of acetylene complexes*. *Journal of the Chemical Society (Resumed)* **1953**, 2939-2947.
18. Dewar, J.S., *A Review of the Pi-Complex Theory*. *Bulletin De La Societe Chimique De France* **1951**, *18*, C71-C79.

19. Fielicke, A., von Helden, G., Meijer, G., Pedersen, D.B., Simard, B., and Rayner, D.M., *Size and charge effects on the binding of CO to late transition metal clusters*. Journal of Chemical Physics **2006**, *124*, 194305.
20. Brathwaite, A.D., Abbott-Lyon, H.L., and Duncan, M.A., *Distinctive Coordination of CO vs N₂ to Rhodium Cations: An Infrared and Computational Study*. The Journal of Physical Chemistry A **2016**, *120*, 7659-7670.
21. Mohrbach, J., Dillinger, S., and Niedner-Schatteburg, G., *Cryo Kinetics and Spectroscopy of Cationic Nickel Clusters: Rough and Smooth Surfaces*. The Journal of Physical Chemistry C **2017**, *121*, 10907-10918.
22. Dillinger, S., Mohrbach, J., and Niedner-Schatteburg, G., *Probing cluster surface morphology by cryo spectroscopy of N₂ on cationic nickel clusters*. The Journal of Chemical Physics **2017**, *147*, 184305.
23. Dillinger, S., Klein, M.P., Steiner, A., McDonald, D.C., Duncan, M.A., Kappes, M.M., and Niedner-Schatteburg, G., *Cryo IR Spectroscopy of N₂ and H₂ on Ru₈⁺: The Effect of N₂ on the H-Migration*. The Journal of Physical Chemistry Letters **2018**, *9*, 914-918.
24. Klein, M.P., Ehrhard, A.A., Mohrbach, J., Dillinger, S., and Niedner-Schatteburg, G., *Infrared Spectroscopic Investigation of Structures and N₂ Adsorption Induced Relaxations of Isolated Rhodium Clusters*. Topics in Catalysis **2018**, *61*, 106-118.
25. Mohrbach, J., Dillinger, S., and Niedner-Schatteburg, G., *Probing cluster surface morphology by cryo kinetics of N₂ on cationic nickel clusters*. The Journal of Chemical Physics **2017**, *147*, 184304.
26. Nilsson, A., Pettersson, L.G.M., and Nørskov, J.K., *Chemical bonding at surfaces and interfaces*. 1st ed. **2008**, Amsterdam ; Boston Mass.: Elsevier.
27. Paduani, C., *Magnetic properties of Fe-Rh alloys*. Journal of Applied Physics **2001**, *90*, 6251-6254.
28. Hernando, A., Rojo, J.M., Yavari, R., Navarro, E., Barandiaran, J.M., and Ibarra, M.R., *On the antiferromagnetism of Fe-Rh*. Mater. Sci. Forum **1997**, *235-238*, 675-683.
29. Kashyap, A., Skomski, R., Solanki, A.K., Xu, Y.F., and Sellmyer, D.J., *Magnetism of L1₀ compounds with the composition MT (M=Rh, Pd, Pt, Ir and T=Mn, Fe, Co, Ni)*. J. Appl. Phys. **2004**, *95*, 7480-7482.
30. Gu, R.Y. and Antropov, V.P., *Magnetic phase transition in FeRh*. Los Alamos Natl. Lab., Prepr. Arch., Condens. Matter **2005**, 1-7, arXiv:cond-mat/0501701.
31. Lu, W., Wang, Y., Yan, B., and Suzuki, T., *Magnetic properties and first-order magnetic phase transition in single crystal FeRh thin film*. J. Mater. Sci. **2010**, *45*, 4919-4923.
32. Ohtake, K., Onodera, R., Mitsui, Y., Takahashi, K., Kimura, S., Watanabe, K., and Koyama, K., *High magnetic field magnetization measurements of FeRh at high temperatures*. Tohoku Daigaku Kinzoku Zairyo Kenkyusho Kyojiba Chodendo Zairyo Kenkyu Senta Nenji Hokoku **2013**, 71-72.
33. Marti, X., Fina, I., Frontera, C., Liu, J., Wadley, P., He, Q., Paull, R.J., Clarkson, J.D., Kudrnovsky, J., Turek, I., Kunes, J., Yi, D., Chu, J.H., Nelson, C.T., You, L., Arenholz, E., Salahuddin, S., Fontcuberta, J., Jungwirth, T., and Ramesh, R., *Room-temperature antiferromagnetic memory resistor*. Nat. Mater. **2014**, *13*, 367-374.
34. Heidarian, A., Bali, R., Grenzer, J., Wilhelm, R.A., Heller, R., Yildirim, O., Lindner, J., and Potzger, K., *Tuning the antiferromagnetic to ferromagnetic phase transition in FeRh thin films by means of low-energy/low fluence ion irradiation*. Nucl. Instrum. Methods Phys. Res., Sect. B **2015**, *358*, 251-254.
35. Wakisaka, Y., Uemura, Y., Yokoyama, T., Asakura, H., Morimoto, H., Tabuchi, M., Ohshima, D., Kato, T., and Iwata, S., *Anomalous structural behavior in the*

- metamagnetic transition of FeRh thin films from a local viewpoint.* Phys. Rev. B: Condens. Matter Mater. Phys. **2015**, *92*, 184408/1-184408/7.
36. Clarkson, J., Frontera, C., Liu, Z.Q., Lee, Y., Kim, J., Cordero, K., Wizotsky, S., Sanchez, F., Sort, J., Hsu, S.L., Ko, C., Wu, J., Christen, H.M., Heron, J.T., Schlom, D.G., Salahuddin, S., Kioussis, N., Fontcuberta, J., Fina, I., Ramesh, R., and Marti, X., *An "invisible" non-volatile solid-state memory.* arXiv.org, e-Print Arch., Condens. Matter **2016**, 1-14.
37. Odkhuu, D., *Magnetization reversal of giant perpendicular magnetic anisotropy at the magnetic-phase transition in FeRh films on MgO.* Phys. Rev. B **2016**, *93*, 064412/1-064412/6.
38. Witte, R., Kruk, R., Gruner, M.E., Brand, R.A., Wang, D., Schlabach, S., Beck, A., Provenzano, V., Pentcheva, R., Wende, H., and Hahn, H., *Tailoring magnetic frustration in strained epitaxial FeRh films.* Phys. Rev. B **2016**, *93*, 104416/1-104416/9.
39. Chaboy, J., Bartolomé, F., Ibarra, M., Marquina, C., Algarabel, P., Rogalev, A., and Neumann, C., *X-ray magnetic circular dichroism probe of the Rh magnetic moment instability in Fe_{1-x}Rh_x alloys near the equiatomic concentration.* Physical Review B **1999**, *59*, 3306-3309.
40. Mokkath, J.H. and Pastor, G.M., *First-principles study of structural, magnetic, and electronic properties of small Fe-Rh alloy clusters.* Physical Review B **2012**, *85*, 054407.
41. Mokkath, J.H. and Pastor, G.M., *Interplay between Chemical and Magnetic Order in FeRh Clusters.* The Journal of Physical Chemistry C **2012**, *116*, 17228-17238.
42. Ehrhard, A.A., Klein, M.P., Mohrbach, J., Dillinger, S., and Niedner-Schatteburg, G., *Cryo Kinetics of N₂ Adsorption onto Bimetallic Rhodium-Iron Clusters in Isolation.* unpublished.
43. Straßner, A., Wiehn, C., Klein, M.P., Fries, D.V., Dillinger, S., Mohrbach, J., Armentrout, P.B., and Niedner-Schatteburg, G., *Cryo spectroscopy of N₂ on cationic iron clusters.*
44. Ehrhard, A.A., Klein, M.P., Mohrbach, J., Dillinger, S., and Niedner-Schatteburg, G., *Cryokinetics and Spin Quenching in the N₂ Adsorption onto Rhodium-Cluster Cations.* Molecular Physics **2021**, accepted.
45. Berg, C., Schindler, T., Niedner-Schatteburg, G., and Bondybey, V.E., *Reactions of Simple Hydrocarbons with Nb_n⁺: Chemisorption and Physisorption on Ionized Niobium Clusters.* The Journal of Chemical Physics **1995**, *102*, 4870-4884.
46. Maruyama, S., Anderson, L.R., and Smalley, R.E., *Direct injection supersonic cluster beam source for FT-ICR studies of clusters.* Review of Scientific Instruments **1990**, *61*, 3686-3693.
47. Proch, D. and Trickl, T., *A high-intensity multi-purpose piezoelectric pulsed molecular beam source.* Review of Scientific Instruments **1989**, *60*, 713-716.
48. Caravatti, P. and Allemann, M., *The 'infinity cell': A new trapped-ion cell with radiofrequency covered trapping electrodes for fourier transform ion cyclotron resonance mass spectrometry.* Organic Mass Spectrometry **1991**, *26*, 514-518.
49. Gerhards, M., *High energy and narrow bandwidth mid IR nanosecond laser system.* Optics Communications **2004**, *241*, 493-497.
50. Frisch, M.J., Trucks, G.W., Schlegel, H.B., Scuseria, G.E., Robb, M.A., Cheeseman, J.R., Scalmani, G., Barone, V., Mennucci, B., Petersson, G.A., Nakatsuji, H., Caricato, M., Li, X., Hratchian, H.P., Izmaylov, A.F., Bloino, J., Zheng, G., Sonnenberg, J.L., Hada, M., Ehara, M., Toyota, K., Fukuda, R., Hasegawa, J., Ishida, M., Nakajima, T., Honda, Y., Kitao, O., Nakai, H., Vreven, T., Montgomery Jr., J.A., Peralta, J.E., Ogliaro, F., Bearpark, M.J., Heyd, J., Brothers, E.N., Kudin, K.N., Staroverov, V.N., Kobayashi, R., Normand, J., Raghavachari, K., Rendell, A.P., Burant, J.C., Iyengar, S.S., Tomasi, J., Cossi, M., Rega,

- N., Millam, N.J., Klene, M., Knox, J.E., Cross, J.B., Bakken, V., Adamo, C., Jaramillo, J., Gomperts, R., Stratmann, R.E., Yazyev, O., Austin, A.J., Cammi, R., Pomelli, C., Ochterski, J.W., Martin, R.L., Morokuma, K., Zakrzewski, V.G., Voth, G.A., Salvador, P., Dannenberg, J.J., Dapprich, S., Daniels, A.D., Farkas, Ö., Foresman, J.B., Ortiz, J.V., Cioslowski, J., and Fox, D.J., *Gaussian 09, Revision D.01*. 2009, Gaussian, Inc.: Wallingford, CT, USA.
51. Adamo, C. and Barone, V., *Toward reliable density functional methods without adjustable parameters: The PBE0 model*. The Journal of Chemical Physics **1999**, *110*, 6158-6170.
 52. Dunning, T.H., *Gaussian basis sets for use in correlated molecular calculations. I. The atoms boron through neon and hydrogen*. The Journal of Chemical Physics **1989**, *90*, 1007-1023.
 53. Klein, M.P., Straßner, A., Huber, M.E., and Niedner-Schatteburg, G., *IR spectroscopy of sequential N₂ adsorption onto Rh₆⁺ clusters*. unpublished.
 54. Andrae, D., Häußermann, U., Dolg, M., Stoll, H., and Preuß, H., *Energy-adjusted ab initio pseudopotentials for the second and third row transition elements*. Theoretica chimica acta **1990**, *77*, 123-141.
 55. Beltran, M.R., Zamudio, F.B., Chauhan, V., Sen, P., Wang, H., Ko, Y.J., and Bowen, K., *Ab initio and anion photoelectron studies of Rh_n (n = 1-9) clusters*. Eur. Phys. J. D **2013**, *67*, 63.
 56. Cotton, F.A., DeBoer, B.G., LaPrade, M.D., Pipal, J.R., and Ucko, D.A., *The crystal and molecular structures of dichromium tetraacetate dihydrate and dirhodium tetraacetate dihydrate*. Acta Crystallographica Section B **1971**, *27*, 1664-1671.
 57. Gingerich, K.A. and Cocke, D.L., *Thermodynamic confirmation for the high stability of gaseous TiRh as predicted by the Brewer-Engel metallic theory and the dissociation energy of diatomic rhodium*. Journal of the Chemical Society, Chemical Communications **1972**, 536-536.
 58. Murillo, C.A., *An Iron Complex with an Unsupported Fe-Fe Bond*. Angewandte Chemie International Edition **2009**, *48*, 5076-5077.
 59. *CRC Handbook of Chemistry and Physics*. 90 ed, ed. Lide, D.R. **2010**, Boca Raton: CRC Press.
 60. Zakharov, A.I., Kadomtseva, A.M., Levitin, P.Z., and Ponyatovskii, E.G., *Magnetic and Magnetoelastic Properties of a Metamagnetic Iron-Rhodium Alloy*. Journal of Experimental and Theoretical Physics **1964**, *19*, 1348-1353.
 61. Harding, D.J., Gruene, P., Haertelt, M., Meijer, G., Fielicke, A., Hamilton, S.M., Hopkins, W.S., Mackenzie, S.R., Neville, S.P., and Walsh, T.R., *Probing the structures of gas-phase rhodium cluster cations by far-infrared spectroscopy*. Journal of Chemical Physics **2010**, *133*, 214304.
 62. Bendtsen, J., *The rotational and rotation-vibrational Raman spectra of ¹⁴N₂, ¹⁴N¹⁵N and ¹⁵N₂*. Journal of Raman Spectroscopy **1974**, *2*, 133-145.
 63. Fries, D.V., Klein, M.P., Steiner, A., Prosenc, M.H., and Niedner-Schatteburg, G., *Observation and Mechanism of Cryo N₂ Cleavage by a Tantalum Cluster*. Phys Chem Chem Phys **2021**, *23*, 11345-11354.
 64. Klein, M.P., Fries, D.V., Straßner, A., Huber, M.E., and Niedner-Schatteburg, G., *N₂ Adsorption onto Ta_n⁺ n = 4,5 Clusters: IR-PD Spectroscopy, Cryo-Kinetics, and DFT Modelling*. unpublished.

7.9 Supplementary Information

Cryo Infrared Spectroscopy of N₂ Adsorption onto Bimetallic Rhodium-Iron Clusters in Isolation

Matthias P. Klein, Amelie A. Ehrhard¹, Maximilian E. Huber, Sebastian Dillinger,
Jennifer Mohrbach, and Gereon Niedner-Schatteburg²

*Fachbereich Chemie and Forschungszentrum OPTIMAS,
Technische Universität Kaiserslautern, 67663 Kaiserslautern, Germany*

I. Laser power curve

Fig. S1 Laser pulse energy in dependence of photon energy

II. Structures of the bare clusters

- Table S1** Atomic distances in the [Rh₃Fe₃]⁺ cluster a
Table S2 Atomic distances in the [Rh₃Fe₃]⁺ cluster b
Fig. S2 Relaxed structures of the [Rh₃Fe₃]⁺ cluster isomers a and b
Table S3 Atomic distances in the [Rh₄Fe₄]⁺ cluster e
Fig. S3 Relaxed structure of the [Rh₄Fe₄]⁺ cluster e
Table S4 Atomic distances in the [Rh₄Fe₄]⁺ cluster h
Fig. S4 Relaxed structure of the [Rh₄Fe₄]⁺ cluster h
Table S5 Atomic distances in the [Rh₄Fe₄]⁺ cluster ab
Fig. S5 Relaxed structure of the [Rh₄Fe₄]⁺ cluster ab
Table S5 Atomic distances in the [Rh₄Fe₄]⁺ cluster ae
Fig. S6 Relaxed structure of the [Rh₄Fe₄]⁺ cluster ae

III. The measured IR-PD spectra

Fig.s S7-S12 IR-PD spectra of [Rh_iFe_j(N₂)_m]⁺ $i = j = 3, \dots, 8$ cluster adsorbate complexes with varying numbers m of adsorbed N₂

¹ Present address: Max-Planck-Institut für Polymerforschung, 55128 Mainz, Germany

² Corresponding author: Prof. Dr. Gereon Niedner-Schatteburg, Erwin-Schrödinger-Straße 52, 67663 Kaiserslautern, gns@chemie.uni-kl.de

IV. Modelling of the (3,3,1) and (3,3,7) cluster adsorbate complexes

Table S7	XYZ coordinates of the assigned lowest energy $[\text{Rh}_3\text{Fe}_3(\text{N}_2)_1]^+$ isomer
Fig. S13	Relaxed structure of the lowest energy $[\text{Rh}_3\text{Fe}_3(\text{N}_2)_1]^+$ isomer
Table S8	Vibrational data for the lowest energy $[\text{Rh}_3\text{Fe}_3(\text{N}_2)_1]^+$ isomer
Fig. S14	Experimental IR-PD spectrum (top trace) and calculated IR absorption spectra of some $[\text{Rh}_3\text{Fe}_3(\text{N}_2)_7]^+$ coordination and spin isomers
Table S9	XYZ coordinates of the assigned most stable $[\text{Rh}_3\text{Fe}_3(\text{N}_2)_7]^+$ isomer (al) (3,3,7a) $\text{N}_2\text{-Rh}(\text{Rh})_2(\text{Fe})_2$ 15tet
Table S10	XYZ coordinates of the $[\text{Rh}_3\text{Fe}_3(\text{N}_2)_7]^+$ isomer (al) $\text{N}_2\text{-Fe}(\text{Rh})_3(\text{Fe})_1$ (3,3,7b) 13tet
Table S10	XYZ coordinates of the $[\text{Rh}_3\text{Fe}_3(\text{N}_2)_7]^+$ isomer (al) $\text{N}_2\text{-Fe}(\text{Rh})_2(\text{Fe})_2$ (3,3,7c) 13tet

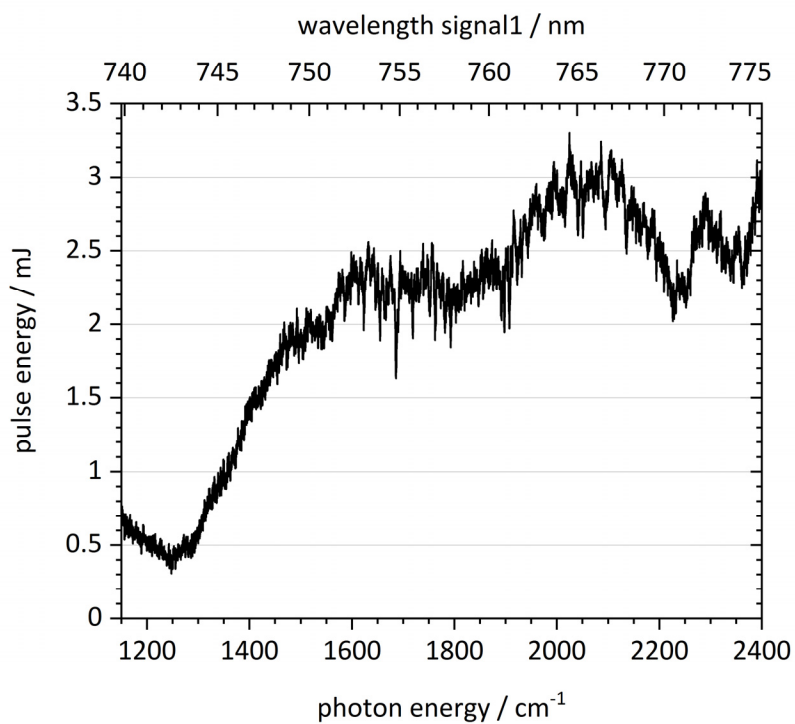


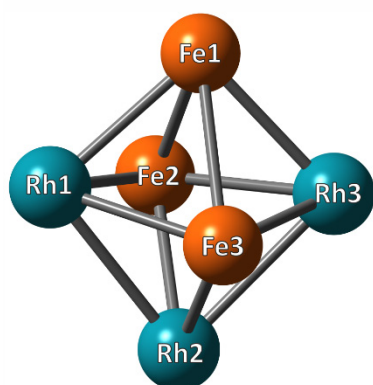
Fig. S4 Laser pulse energy in dependence of photon energy in the complete measured range.

Table S1 Atomic distances in the $[\text{Rh}_3\text{Fe}_3]^+$ cluster (**al**) 15tet.

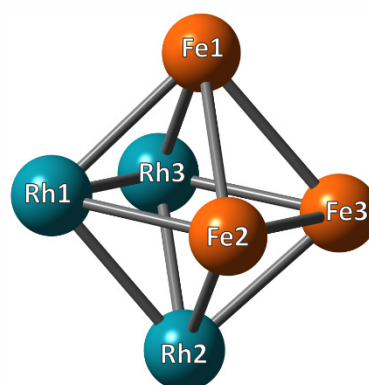
R / Å	Rh1	Rh2	Rh3	Fe1	Fe2	Fe3
Rh1	0	2.612	3.476	2.400	2.538	2.441
Rh2		0	2.612	3.601	2.479	2.407
Rh3			0	2.399	2.536	2.442
Fe1				0	2.560	2.636
Fe2					0	3.525
Fe3						0

Table S2 Atomic distances in the $[\text{Rh}_3\text{Fe}_3]^+$ cluster (**la**) 19tet.

R / Å	Rh1	Rh2	Rh3	Fe1	Fe2	Fe3
Rh1	0	2.580	2.581	2.504	2.505	3.631
Rh2		0	2.579	3.626	2.504	2.504
Rh3			0	2.502	3.635	2.509
Fe1				0	2.681	2.672
Fe2					0	2.678
Fe3						0

 $[\text{Rh}_3\text{Fe}_3]^+$ al 15tet

0 kJ/mol

 $[\text{Rh}_3\text{Fe}_3]^+$ la 19tet

72 kJ/mol

Fig. S2 Relaxed structures of the $[\text{Rh}_3\text{Fe}_3]^+$ cluster isomers (**al**) and (**la**).

Table S3 Atomic distances in the [Rh₄Fe₄]⁺ cluster **(e)** 22tet.

R / Å	Rh1	Rh2	Rh3	Rh4	Fe1	Fe2	Fe3	Fe4
Rh1	0	3.839	3.838	2.751	2.427	2.412	2.413	3.798
Rh2		0	3.307	3.839	2.390	2.332	4.157	2.390
Rh3			0	3.837	2.390	4.155	2.332	2.390
Rh4				0	3.796	2.413	2.413	2.426
Fe1					0	2.839	2.841	3.100
Fe2						0	3.579	2.839
Fe3							0	2.842
Fe4								0

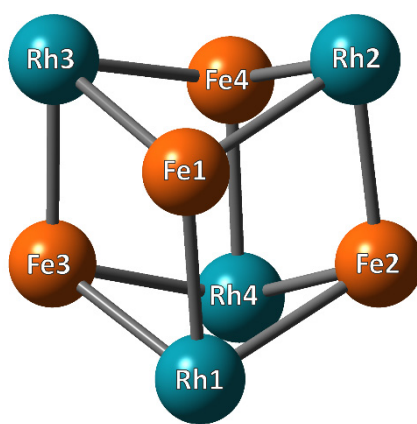
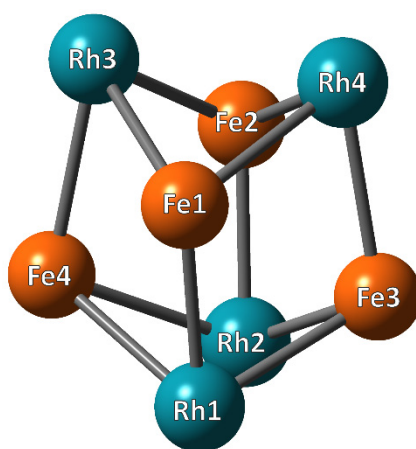


Fig. S3 Relaxed structure of the [Rh₄Fe₄]⁺ cluster **(e)** 22tet.

Table S4 Atomic distances in the $[\text{Rh}_4\text{Fe}_4]^+$ cluster (**h**) 22tet.

R / Å	Rh1	Rh2	Rh3	Rh4	Fe1	Fe2	Fe3	Fe4
Rh1	0	2.715	3.973	3.832	2.361	3.834	2.379	2.537
Rh2		0	3.974	3.832	3.830	2.364	2.382	2.528
Rh3			0	2.737	2.401	2.405	3.999	2.482
Rh4				0	2.414	2.412	2.407	3.948
Fe1					0	3.353	2.826	2.779
Fe2						0	2.831	2.773
Fe3							0	3.587
Fe4								0

**Fig. S4** Relaxed structure of the $[\text{Rh}_4\text{Fe}_4]^+$ cluster (**h**) 22tet.

7. Cryo Infrared Spectroscopy of N₂ Adsorption onto Bimetallic Rhodium-Iron Clusters in Isolation

Table S5 Atomic distances in the [Rh₄Fe₄]⁺ cluster (**ab**) 22tet.

R / Å	Rh1	Rh2	Rh3	Rh4	Fe1	Fe2	Fe3	Fe4
Rh1	0	3.839	3.841	2.716	2.418	2.433	3.908	2.401
Rh2		0	2.706	4.094	2.370	3.900	2.559	2.375
Rh3			0	3.926	3.747	2.365	2.502	2.395
Rh4				0	2.428	2.376	2.495	4.001
Fe1					0	3.343	2.615	2.839
Fe2						0	2.834	2.818
Fe3							0	3.563
Fe4								0

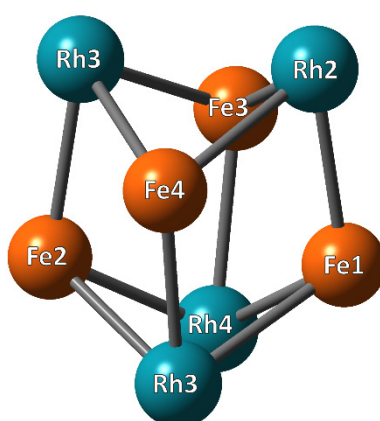
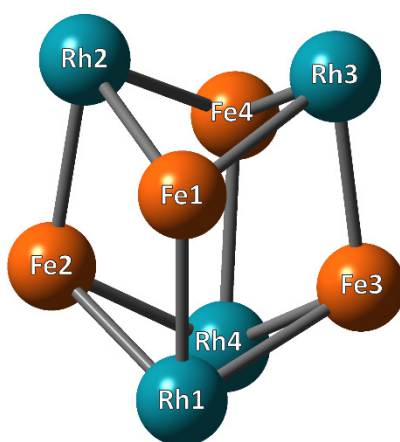


Fig. S5 Relaxed structure of the [Rh₄Fe₄]⁺ cluster (**ab**) 22tet.

Table S6 Atomic distances in the $[\text{Rh}_4\text{Fe}_4]^+$ cluster (**ae**) 22tet.

R / Å	Rh1	Rh2	Rh3	Rh4	Fe1	Fe2	Fe3	Fe4
Rh1	0	3.832	3.836	2.737	2.407	2.412	2.416	3.950
Rh2		0	2.715	3.979	2.379	2.363	3.835	2.532
Rh3			0	3.967	2.380	3.828	2.362	2.535
Rh4				0	3.995	2.407	2.400	2.481
Fe1					0	2.827	2.823	3.585
Fe2						0	3.353	2.766
Fe3							0	2.786
Fe4								0

**Fig. S6** Relaxed structure of the $[\text{Rh}_4\text{Fe}_4]^+$ cluster (**ae**) 22tet.

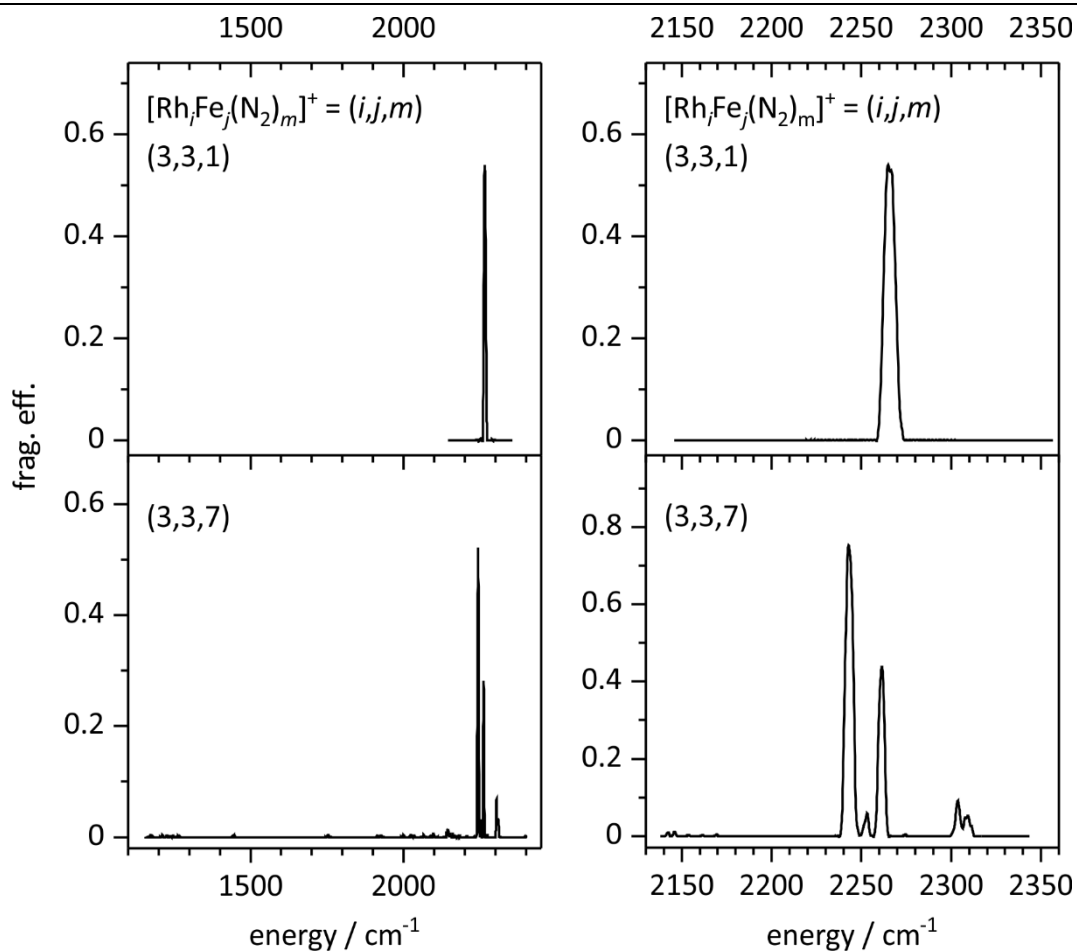


Fig. S7 IR-PD spectra of $[\text{Rh}_3\text{Fe}_3(\text{N}_2)_m]^+$ cluster adsorbate complexes with varying number m of adsorbed N₂. We recorded spectra for $m = 1$ and $m = 7$. On the right side spectra over a range from 2140 to 2340 cm⁻¹ are depicted. In this range, we expect only end-on N₂ ligands. Other N₂ binding motifs that could indicate activation precursors would evoke vibrational bands with lower wavenumbers. We chose (3,3,7) to look for these other binding motifs. Therefore, we checked for IR induced fragmentation in a larger range from 1156 to 2400 cm⁻¹. These spectra are shown on the left side and contain no indication for non-end-on N₂.

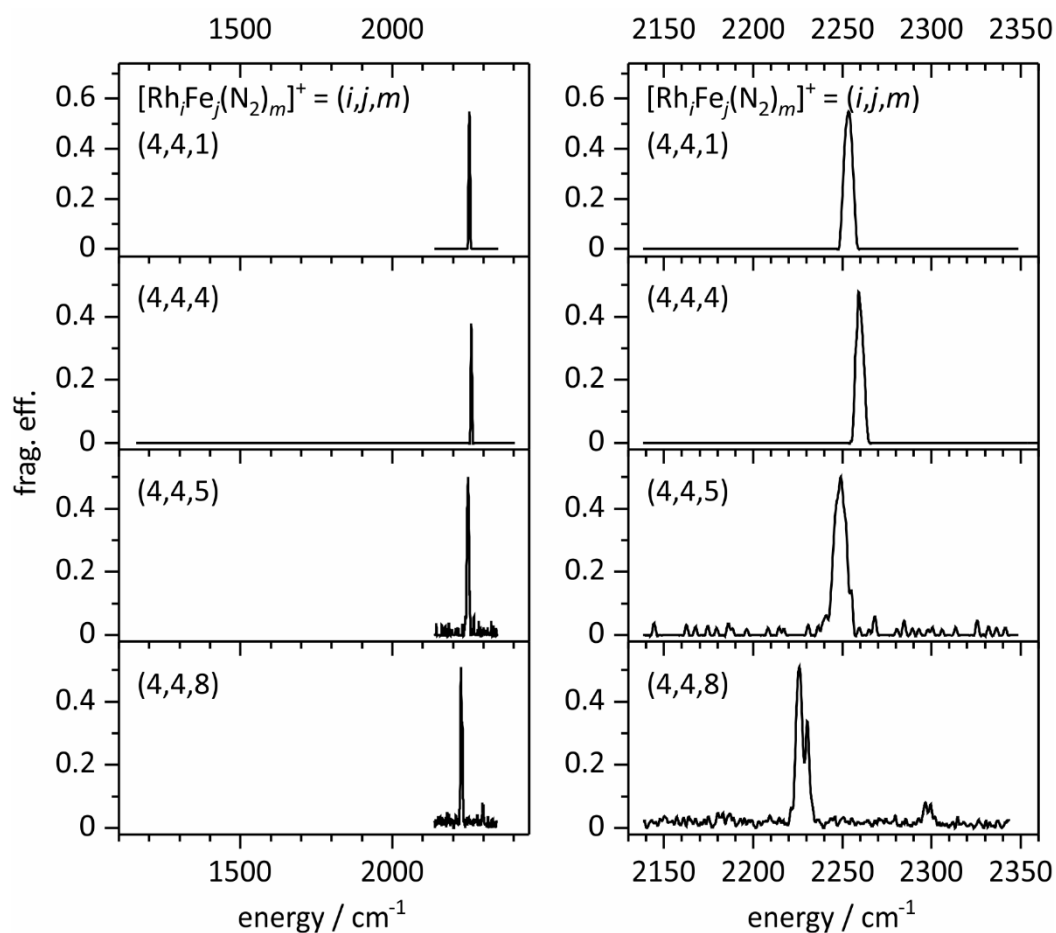


Fig. S8 IR-PD spectra of $[\text{Rh}_4\text{Fe}_4(\text{N}_2)_m]^+$ cluster adsorbate complexes with varying number m of adsorbed N_2 . We recorded spectra for $m = 1, 4, 5$ and $m = 8$. On the right side spectra over a range from 2140 to 2340 cm^{-1} are depicted. In this range, we expect only end-on N_2 ligands. Other N_2 binding motifs that could indicate activation precursors would evoke vibrational bands with lower wavenumbers. We chose (4,4,4) to look for these other binding motifs. Therefore, we checked for IR induced fragmentation in a larger range from 1156 to 2400 cm^{-1} . These spectra are shown on the left side and contain no indication for non-end-on N_2 .

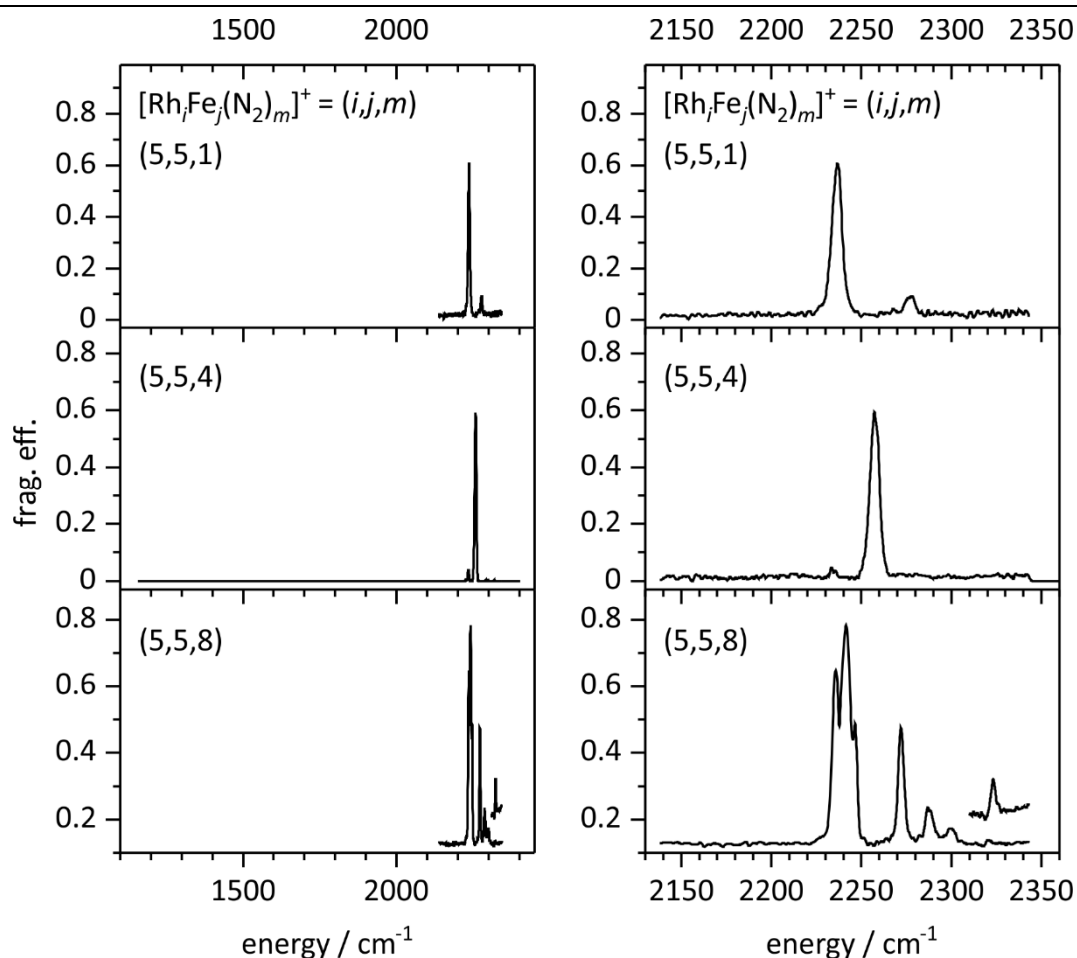


Fig. S9 IR-PD spectra of $[\text{Rh}_5\text{Fe}_5(\text{N}_2)_m]^+$ cluster adsorbate complexes with varying number m of adsorbed N₂. We recorded spectra for $m = 1, 4$, and $m = 5$. On the right side spectra over a range from 2140 to 2340 cm^{-1} are depicted. In this range, we expect only end-on N₂ ligands. Other N₂ binding motifs that could indicate activation precursors would evoke vibrational bands with lower wavenumbers. We chose (5,5,4) to look for these other binding motifs. Therefore, we checked for IR induced fragmentation in a larger range from 1156 to 2400 cm^{-1} . These spectra are shown on the left side and contain no indication for non-end-on N₂.

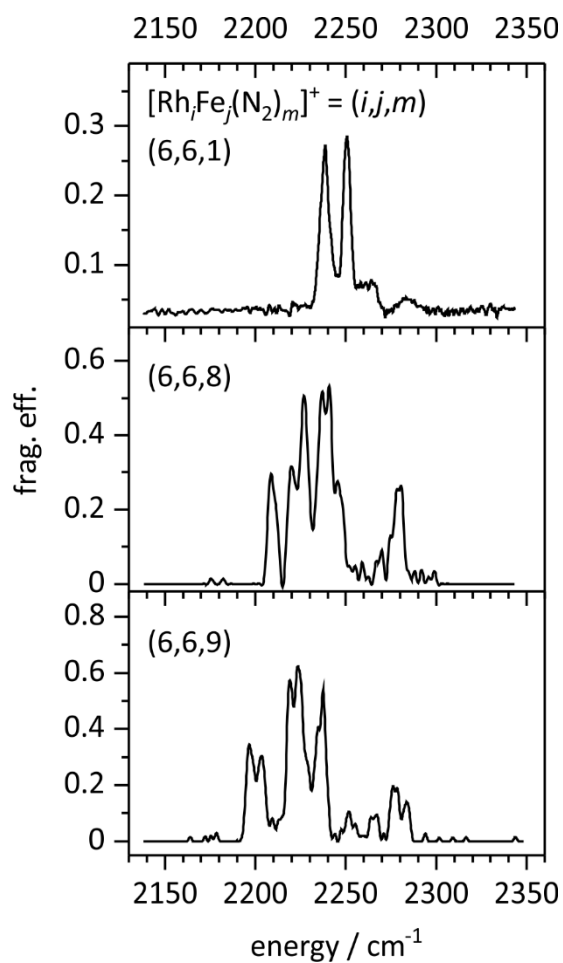


Fig. S10 IR-PD spectra of $[\text{Rh}_6\text{Fe}_6(\text{N}_2)_m]^+$ cluster adsorbate complexes with varying number m of adsorbed N_2 . We recorded spectra for $m = 1, 8,$ and $m = 9$. On the right side spectra over a range from 2140 to 2340 cm^{-1} are depicted. In this range, we expect only end-on N_2 ligands.

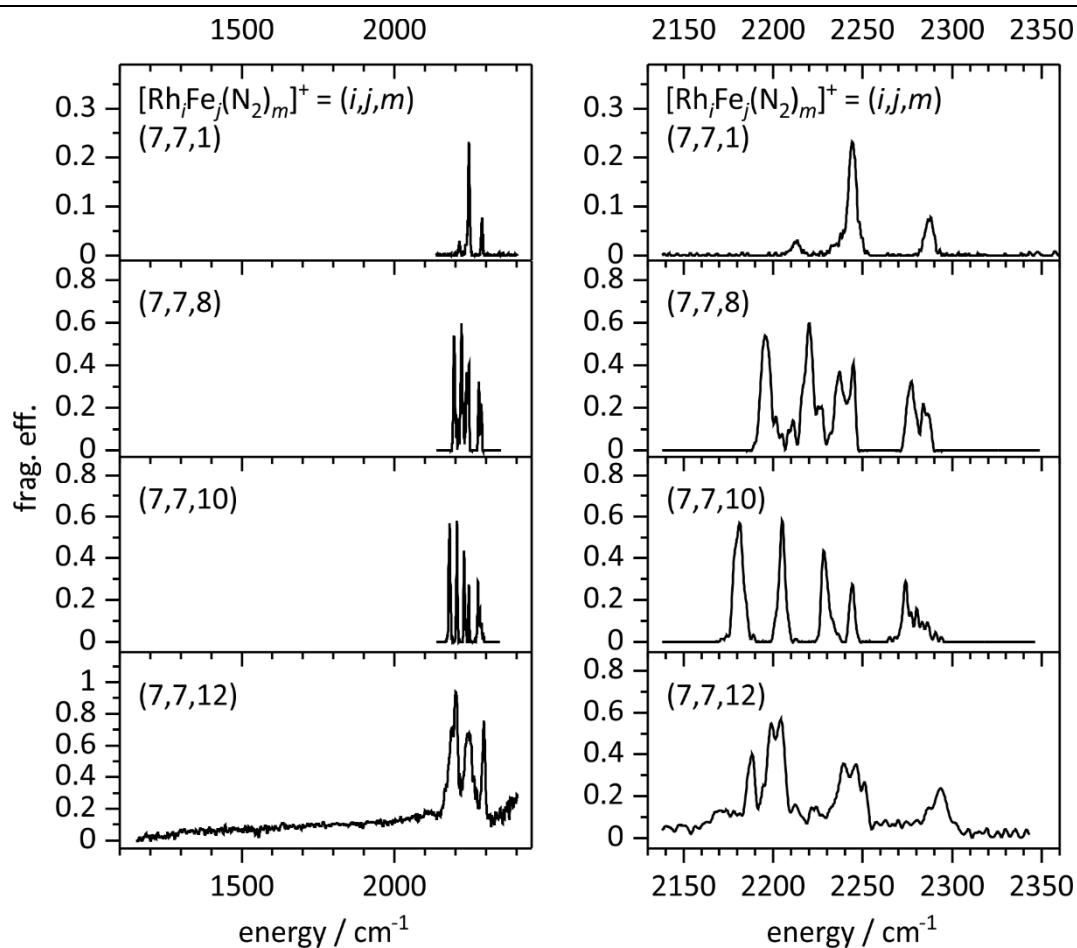


Fig. S11 IR-PD spectra of $[\text{Rh}_7\text{Fe}_7(\text{N}_2)_m]^+$ cluster adsorbate complexes with varying number m of adsorbed N_2 . We recorded spectra for $m = 1, 8, 10$ and $m = 12$. On the right side spectra over a range from 2140 to 2340 cm^{-1} are depicted. In this range, we expect only end-on N_2 ligands. Other N_2 binding motifs that could indicate activation precursors would evoke vibrational bands with lower wavenumbers. We chose (7,7,12) to look for these other binding motifs. Therefore, we checked for IR induced fragmentation in a larger range from 1156 to 2400 cm^{-1} . These spectra are shown on the left side and contain no indication for non-end-on N_2 .

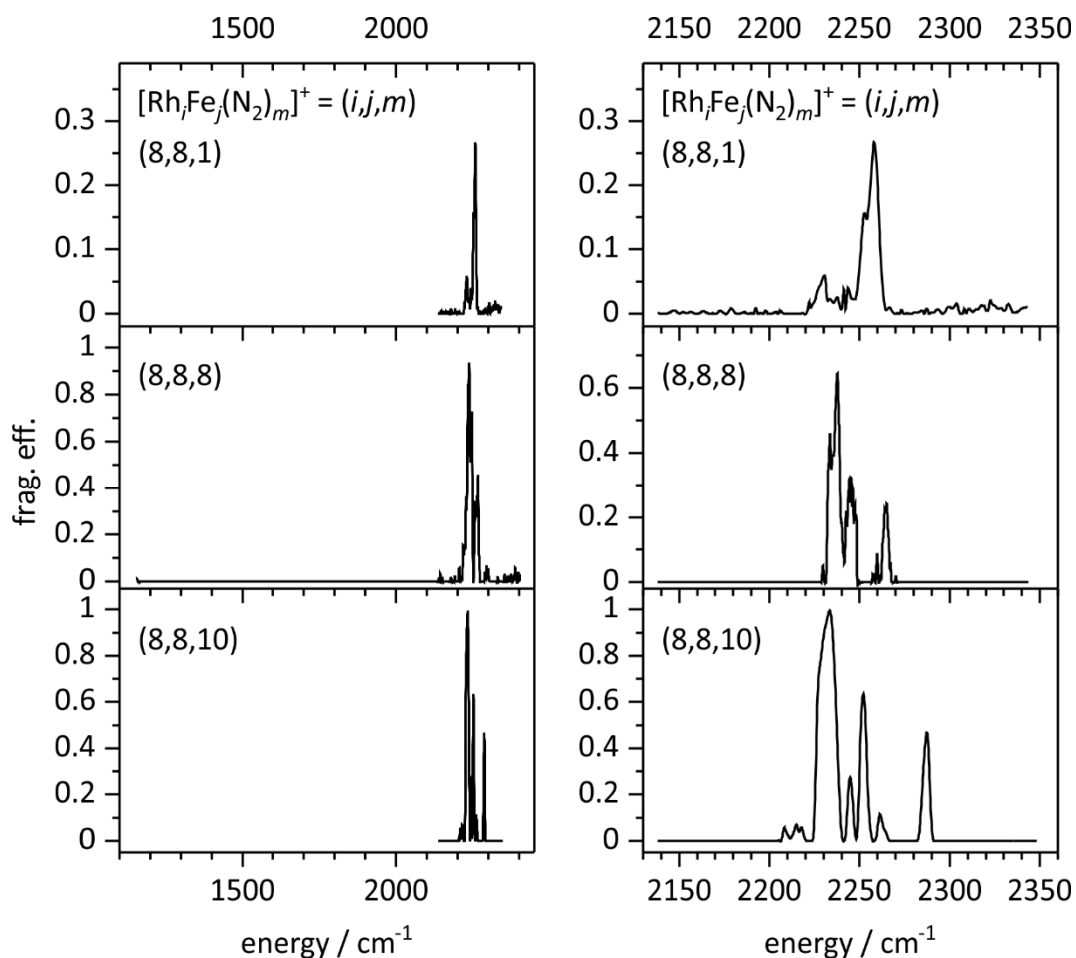


Fig. S12 IR-PD spectra of $[\text{Rh}_8\text{Fe}_8(\text{N}_2)_m]^+$ cluster adsorbate complexes with varying number m of adsorbed N_2 . We recorded spectra for $m = 1, 8$, and $m = 10$. On the right side spectra over a range from 2140 to 2340 cm^{-1} are depicted. In this range, we expect only end-on N_2 ligands. Other N_2 binding motifs that could indicate activation precursors would evoke vibrational bands with lower wavenumbers. We chose (8,8,8) to look for these other binding motifs. Therefore, we checked for IR induced fragmentation in a larger range from 1156 to 2400 cm^{-1} . These spectra are shown on the left side and contain no indication for non-end-on N_2 .

7. Cryo Infrared Spectroscopy of N₂ Adsorption onto Bimetallic Rhodium-Iron Clusters in Isolation

Table S7 Xyz coordinates of the assigned lowest energy [Rh₃Fe₃(N₂)₁]⁺ isomer.

	X	Y	Z
Rh1	2.96	2.3002	1.44
Rh2	1.3006	0.7109	2.7245
Rh3	2.1839	1.0981	-0.5755
Fe1	0.421	0.0015	0.6435
Fe2	3.0313	-0.3222	1.3044
Fe3	0.5774	2.5236	0.9796
N1	0.2137	-0.5005	3.8284
N2	-0.3943	-1.1509	4.473

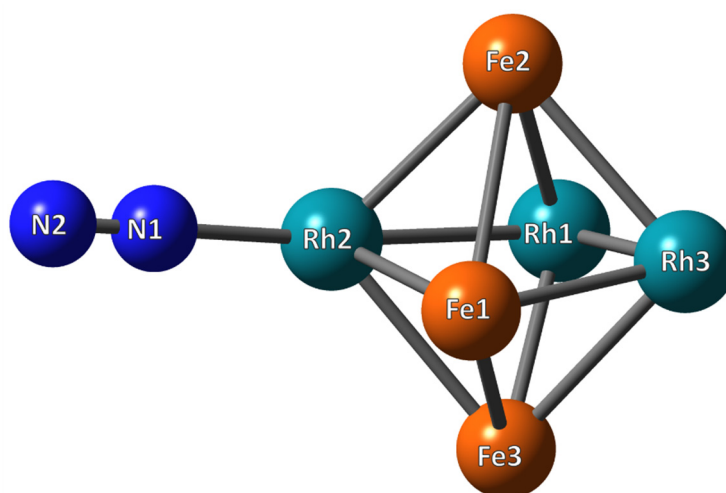


Fig. S13 Relaxed structure of the lowest energy [Rh₃Fe₃(N₂)₁]⁺ isomer.

Table S8 Vibrational data for the lowest energy [Rh₃Fe₃(N₂)₁]⁺ isomer. The scaling factor for the N₂ stretching frequencies is 0.9385.

Mode	Type	Freq. / cm ⁻¹	Scaled freq. / cm ⁻¹	IR intensity / km mol ⁻¹
1-2	Wagging	47-68	44-64	0.12-0.39
3-14	internal cluster vibrations	78-286	73-267	0.10-6.3
15-17	bending	328-374	308-351	2.0-9.6
18	N ₂ stretch	2361	2216	357

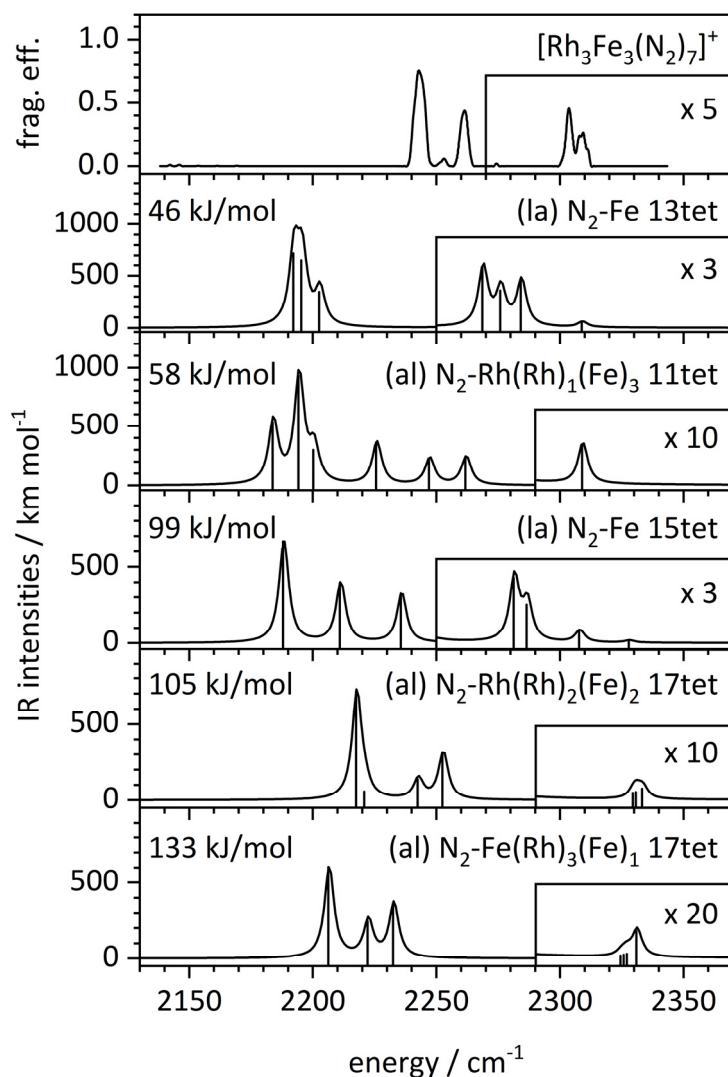


Fig. S14 Experimental IR-PD spectrum (top trace) and calculated IR absorption spectra of some $[\text{Rh}_3\text{Fe}_3(\text{N}_2)_7]^+$ coordination and spin isomers. The calculated spectra (scaled by 0.9385) represent coordination and spin isomers of higher energy, out of eight conceivable ones (work in progress). Most of the shown modelled spectra originate from metal cluster cores of structure **(al)** and N_2 is adsorbed to Rh. The coordination of the adsorbing Rh atom is given in parentheses, for the two spin isomers of structure **(la)** N_2 is adsorbed to Fe.

7. Cryo Infrared Spectroscopy of N₂ Adsorption onto Bimetallic Rhodium-Iron Clusters in Isolation

Table S9 Xyz coordinates of the assigned most stable energy [Rh₃Fe₃(N₂)₇]⁺ isomer **(a)** N₂-Rh(Rh)₂(Fe)₂ (**3,3,7a**) 15tet.

	X	Y	Z
Rh1	3.180866	2.814957	1.632428
Rh2	0.781631	1.896088	2.390068
Rh3	2.684986	1.205181	-0.449373
Fe1	0.46155	0.662917	0.333577
Fe2	2.694734	0.495294	1.871043
Fe3	1.174397	3.154958	0.207788
N1	2.617496	-0.150468	-1.927088
N2	2.630868	-0.895215	-2.735596
N3	5.062701	3.156239	0.880068
N4	6.068163	3.326278	0.476255
N5	-0.85087	1.109633	3.253474
N6	-1.723143	0.689762	3.774427
N7	-0.627819	-1.187367	0.056502
N8	-1.155622	-2.134395	-0.063183
N9	4.23802	-1.345731	3.32269
N10	4.883083	-2.023606	3.880596
N11	0.76004	5.403887	-0.592885
N12	0.65527	6.443849	-0.900486
N13	3.348801	3.777118	3.441246
N14	3.431371	4.282669	4.411079

Table S10 Xyz coordinates of the $[\text{Rh}_3\text{Fe}_3(\text{N}_2)_7]^+$ isomer **(a)** $\text{N}_2\text{-Fe}(\text{Rh})_3(\text{Fe})_1$ (**3,3,7b**) 13tet.

	X	Y	Z
Rh1	2.378374	2.464857	1.734572
Rh2	0.217534	1.272694	2.671132
Rh3	2.617295	0.286879	0.274282
Fe1	0.377567	-0.38625	0.824641
Fe2	2.352019	0.064757	2.695735
Fe3	0.616398	2.05166	0.227069
N1	-0.505596	-2.388882	0.729855
N2	-0.947397	-3.385653	0.696239
N3	0.338933	2.994083	-1.642843
N4	0.261386	3.525762	-2.593224
N5	3.862403	3.325581	0.853207
N6	4.696412	3.827857	0.336485
N7	2.321457	-1.979422	3.517019
N8	2.209552	-3.018908	3.830107
N9	3.025913	-1.373285	-0.645561
N10	3.289784	-2.312793	-1.159224
N11	0.383897	1.768043	4.597537
N12	0.443042	2.051384	5.658466
N13	3.939388	0.456327	4.226803
N14	4.724169	0.808278	4.897774

7. Cryo Infrared Spectroscopy of N₂ Adsorption onto Bimetallic Rhodium-Iron Clusters in Isolation

Table S11 Xyz coordinates of the [Rh₃Fe₃(N₂)₇]⁺ isomer **(al)** N₂-Fe(Rh)₂(Fe)₂ **(3,3,7c)** 13tet.

	X	Y	Z
Rh1	2.505697	2.066958	2.387861
Rh2	0.103028	1.048332	2.856616
Rh3	2.371504	0.667456	0.116344
Fe1	0.043381	0.09076	0.524482
Fe2	1.963664	-0.387292	2.292488
Fe3	0.774608	2.52904	0.850944
N1	-0.655736	-2.023527	0.197964
N2	-0.872205	-3.092938	0.17915
N3	-0.451018	4.217925	0.638484
N4	-1.057245	5.126368	0.618946
N5	4.20269	2.851901	1.876659
N6	5.158854	3.303976	1.569489
N7	3.180428	-1.716307	3.388065
N8	3.845642	-2.355511	3.971888
N9	2.439744	-0.423057	-1.498655
N10	2.500052	-1.04452	-2.407118
N11	-1.456838	0.515701	-1.107171
N12	-2.148322	0.881962	-1.868426
N13	0.283297	1.111869	4.874379
N14	0.354934	1.139174	5.96984

8. Observation and mechanism of cryo N₂ cleavage by a tantalum cluster

Daniela V. Fries, Matthias P. Klein, Annika Steiner, Marc H. Prosenc,
and Gereon Niedner-Schatteburg

*Fachbereich Chemie and Forschungszentrum OPTIMAS,
Technische Universität Kaiserslautern, 67663 Kaiserslautern, Germany*

8.1 Preamble

The following chapter is a reprint of a publication in the journal „Phys. Chem. Chem. Phys.“.

An experimental team consisting of D. V. Fries, A. Steiner, and me conducted the experiments. D. V. Fries and I conducted the data evaluation. D. V. Fries., M. H. Prosenc, and I conducted the quantum chemical calculations. D. V. Fries, M. H. Prosenc and G. Niedner-Schatteburg, and I wrote and revised the manuscript. All authors evaluated and discussed the results.

Full Reference:

Observation and mechanism of cryo N₂ cleavage by a tantalum cluster

D. V. Fries, **M. P. Klein**, A. Steiner, M. H. Prosenc, and Gereon Niedner-Schatteburg, *Phys. Chem. Chem. Phys.* **2021**, 23, 11345-11354.

<https://doi.org/10.1039/DOCP06208A>

Reproduced with permission from the PCCP Owner Societies.

8.2 Reprint

Observation and mechanism of cryo N₂ cleavage by a tantalum cluster

D. V. Fries, M. P. Klein, A. Steiner, M. H. Prosenc and G. Niedner-Schatteburg,
Phys. Chem. Chem. Phys., 2021, **23**, 11345 DOI: 10.1039/D0CP06208A

To request permission to reproduce material from this article, please go to the [Copyright Clearance Center request page](#).

If you are **an author contributing to an RSC publication, you do not need to request permission** provided correct acknowledgement is given.

If you are **the author of this article, you do not need to request permission to reproduce figures and diagrams** provided correct acknowledgement is given. If you want to reproduce the whole article in a third-party publication (excluding your thesis/dissertation for which permission is not required) please go to the [Copyright Clearance Center request page](#).

Read more about [how to correctly acknowledge RSC content](#).

Cite this: *Phys. Chem. Chem. Phys.*, 2021, 23, 11345

Observation and mechanism of cryo N₂ cleavage by a tantalum cluster†

Daniela V. Fries,[†] Matthias P. Klein,[†] Annika Steiner,[†] Marc H. Prosenč[†] and Gereon Niedner-Schatteburg^{†*}

We explore the cryogenic kinetics of N₂ adsorption to Ta₄⁺ and the infrared signatures of [Ta₄(N₂)_m]⁺ complexes, *m* = 1–5. This is accomplished by N₂ exposure of isolated ions within a cryogenic ion trap. We find stepwise addition of numerous N₂ molecules to the Ta₄⁺ cluster. Interestingly, the infrared signatures of the [Ta₄(N₂)₁]⁺ and [Ta₄(N₂)₂]⁺ products are special: there are no NN stretching bands. This is consistent with cleavage of the first two adsorbed dinitrogen molecules. DFT calculations reveal intermediates and barriers along reaction paths of N₂ cleavage in support of these experimental findings. We indicate the identified multidimensional path of N₂ cleavage as an across edge-above surface (AEAS) mechanism: initially end-on coordinated N₂ bends towards a neighboring Ta-atom which yields a second intermediate, with a μ₂ bonded N₂ across an edge of the Ta₄⁺ tetrahedron core. Further rearrangement above a Ta–Ta–Ta surface of the Ta₄⁺ tetrahedron results in a μ₃ bonded N₂ ligand. This intermediate relaxes swiftly by ultimate NN cleavage unfolding into the final dinitrido motif. Submerged activation barriers below the entrance channel confirm spontaneous cleavage of the first two dinitrogen molecules (–59 and –33 kJ mol^{–1}, respectively), while cleavage of the third N₂ ligand is kinetically hindered (+55 kJ mol^{–1}). We recognize that substoichiometric N₂ exposure allows for spontaneous activation by Ta₄⁺, while higher N₂ exposure causes self-poisoning.

Received 30th November 2020,
Accepted 5th April 2021

DOI: 10.1039/d0cp06208a

rsc.li/pccp

Introduction

Life on earth relies on the essential element nitrogen.¹ High temperature, high pressure Haber–Bosch synthesis managed to couple the ubiquitous reservoir of inert dinitrogen, N₂, from the biosphere on a large scale. Biotic low temperature N₂ hydration by metallo-enzymatic complexes^{2,3} – amazing as it is – takes place by an apparent waste of metabolic energy (16 ATP per N₂ molecule).⁴ Likewise inefficient, the Haber–Bosch process as well as other industrial processes take place only at the expense of high pressure and high temperature.^{5–7} An energetically optimized technical protocol of inert N≡N triple bond activation is still to be found^{8,9} – despite all of the high effort and award winning research as of now.^{10–12} This is the more so as heterogeneous N₂ activation at high temperatures is entropically disfavored and thus is often presumed to become rate limiting.

Obviously, there is a quest for an enhanced understanding at the molecular level of heterogeneous catalytic N₂ activation and functionalization. Such insight would allow for an able interpretation of the ground-breaking empirical survey of prospective

Haber–Bosch catalysts by Mittasch *et al.*¹³ It seems certain that multi-metallic cooperativity is a prerequisite for N₂ activation prior to further cleavage and functionalization.¹⁴ For example, the DFT modeling of experimental ammonia synthesis by supported Ru catalyst¹⁵ managed to predict elementary steps along a feasible reaction path. Step sites are found much more reactive than terrace sites – and alkali adatoms act as promoters.¹⁶

The synthesis of seemingly appropriate mononuclear transition metal complexes received inspiration from enzymatic N₂ cleavage. It showed that N₂ may coordinate in an activating M–NN–M motif through aggregation of mononuclear W and Mo complexes.^{17–19} Dissociation kinetics of a Mo–NN–Mo complex reveal activation barriers as low as 100 kJ mol^{–1} and thereby confirm considerable N₂ activation within the complex.²⁰ Alkaline promotion in turn reached out towards synthesized TM complexes. In this regard, a synthetic Fe-phenoxide-K complex provides for a flexible di-iron core and rapid formation of di-iron-N₂ products. Modeling suggests N₂ preorientation by K and subsequent N≡N activation by Fe–Fe cooperativity which together creates a low-energy pathway towards N₂ reactions.²¹ Variation of alkali promoters (Na, K, Rb, Cs) suggests that it might take at least three Fe centers to cleave N≡N.^{22,23} Ti_{3,4}-imide and Ti_{3,4}-hydride frameworks enable N₂ activation and hydrogenation through a partly reversible interplay among hydride, imide, and nitride ligands. A precursor complex showed to encompass an N₂

Fachbereich Chemie and Forschungszentrum OPTIMAS, Technische Universität Kaiserslautern, 67663 Kaiserslautern, Germany. E-mail: gns@chemie.uni-kl.de

† Electronic supplementary information (ESI) available. See DOI: 10.1039/d0cp06208a

molecule bonded to three Ti atoms in a $\mu\text{-}\eta^1\text{:}\eta^2\text{:}\eta^2$ -end-on/side-on fashion to give a $\mu_2\text{-N}/\mu_3\text{-N}$ dinitrido species.^{24,25}

In the gas phase, further mechanistic insights at the molecular level were provided by studying well defined model systems and their characterization by advanced methods. In this regard TM clusters and complexes were recognized to unravel elementary processes of relevance to heterogeneous catalysis.^{26–31} Naked transition metal dimers of Gd,³² Sc,³³ and Ta³⁴ are known to activate N₂ spontaneously. Also, small Ta-nitride cations are able to activate NH₃.³⁵

Early surveys of larger transition metal (Fe, Co, Ni, Cu, Nb) clusters included some studies of N₂ adsorption and introduced the concept of cluster surface reactivity.³⁶ In another early study, size-selected clusters of Nb and Ta exhibited bi-exponential reaction kinetics for N₂ adsorption.³⁷ Larger clusters of Fe and Al revealed convincing, yet indirect, evidence for N₂ activation without explicit structural characterization.^{38,39} Larger Ta clusters received attention in the context of various oxidation reactions.^{40–44} Size-selected anion clusters of V and Ta-nitrides and of Co-hydrides showed N₂ adsorption kinetics, and concomitant *ab initio* modeling^{45–47} pointed to N₂ activation. More recently, the gas phase chemistry of metal clusters received renewed attention;⁴⁸ in part, this is motivated by advances in cryogenic ion trapping and IR vibrational spectroscopy.⁴⁹ Quantum chemical modeling proved extremely helpful towards a better understanding of N₂ activation at bare metal atoms, and the findings relate to corresponding processes at organometallic complexes, clusters and surfaces up to enzymatic nitrogenase catalysis.⁵⁰

Raman spectra of Ta_n⁺ clusters confirmed a tetrahedral geometry for the ground state.⁵¹ Infrared-induced multiple photon dissociation (IR-MPD) spectra of Ta_n⁺ clusters ($6 \leq n \leq 20$)⁵² received structural interpretation by DFT modeling⁵³ and were in line with previous studies.⁵⁴ Ta₄⁺ clusters were found to dehydrogenate CH₄ while Ta₅⁺ does not.⁵⁵

DFT modeling predicted dissociative adsorption of the very first N₂ molecule when reacted with small Ta_n⁺ clusters ($n \leq 4$).⁵⁶ Combined DFT and experimental studies of Ta₆⁺ confirmed single N₂ activation under slightly hyperthermal conditions.⁵⁷ Subsequent DFT studies focused on reverse catalysis modeling, namely on ammonia activation, by Ta_n⁺ ($n = 2\text{--}10$) cluster complexes.⁵⁸

In the present contribution we present a detailed mechanism of N₂ activation by the model system Ta₄⁺. This choice was motivated by an increase of the electron reservoir with respect to the well-studied Ta₂⁺.³⁴ We combine kinetic and IR-PD spectroscopic cryo ion trap investigations with DFT modeling; this is a continuation of a series of related studies on model systems.^{59–61} Here, we provide an elucidation of a detailed across edge-above surface (AEAS) mechanism for the cleavage of first and second N₂ adsorbates.

Experimental and computational methods

All experiments were performed by a customized Fourier transform ion cyclotron resonance (FT-ICR) mass spectrometer

(Apex Ultra, Bruker Daltonics). Using this instrument, we were able to produce the Ta_n⁺ clusters, to isolate the generated cluster ions and adsorb N₂ to them prior to examination by infrared multi photon dissociation (IR-PD) spectroscopy and mass spectrometry of the adsorbate complexes. A home built laser evaporation source (LVAP)^{62,63} was used for cluster generation from a rotating Ta-target (99.95%, 0.5 mm thick, Alfa Aesar). The respective cluster ions were mass isolated and stored in the cryogenic hexapole ion trap (26 K) where the reaction gas (N₂; 2.6×10^{-7} mbar) is introduced continuously. In addition, collision gas (He; up to 6.8×10^{-6} mbar) ensures efficient trapping and cooling of the ions in the hexapole. After trapping in the hexapole for various storage times (reaction delays: 0–20 s), the cluster complexes were guided by electrostatic lenses into the FT-ICR cell (~ 10 K).

In order to investigate adsorption kinetics, reaction delay scans were recorded. Subsequently, the obtained mass spectra were evaluated by the program *evofit*⁶⁴ yielding pseudo-first-order kinetics and relative rate constants for each N₂ adsorption and desorption step. Absolute rate constants originate from normalization of relative rate constants to the absolute N₂ number densities.

In the IR-PD experiments, the chosen complexes of interest are trapped in the ICR cell and irradiated by a tunable OPO IR-laser. Thus, every isolated ion packet was treated by 7–10 laser pulses with an energy of 0.3–4.0 mJ per pulse within a wavelength range of 1200 to 2400 cm⁻¹. The obtained IR-PD signals of the fragment F_i and the parent ion P_i are evaluated as $\sum_i F_i / \left(\sum_i F_i + \sum_i P_i \right)$. To obtain an IR-PD spectra, the determined fragmentation efficiency is plotted as a function of laser frequency.

All quantum chemical calculations are carried out by the Gaussian 09⁶⁵ and the Gaussian 16 suite of programs.⁶⁶ We employed the PBE0 functional^{67,68} and the def2-TZVP basis set.^{69,70} We did so in continuation of previous studies which have succeeded to model N₂ adsorption before, as *e.g.* in the cases of Rhodium clusters⁷¹ and Nickel clusters.^{60,61} Moreover, we verified our choice of method by employing a multitude of available exchange correlation functionals, and CC2 calculations on top (*cf.* Fig. S8, ESI†) along some part of the reaction path of initial N₂ activation along three local minima (**I2**_(4,1) and **I3**_(4,1) and **P**_{vic(4,1)}) and both intermediate transition states (**TS23**_(4,1) and **TS3P**_{vic(4,1)}). It shows that the optimized minimum structures and transition states are robust (for a survey of some critical geometric parameters refer to Tables S15 and S16 in the ESI†), as well as the relative energies by less than 30 kJ mol⁻¹ (*cf.* Table S14, ESI†). We take this as a valid gauge of the chosen level of theory, PBE0/def2-TZVP. All stationary points were checked by second derivative calculations revealing no and one imaginary frequency in cases of minima and transition states, respectively. Reaction paths were searched for by QST2/3⁷² or linear transit methods⁷³ and after location and optimization of the transition states calculated along the IRC (Intrinsic Reaction Coordinate).⁷⁴ Orbital and charge analysis were performed using molecular orbitals as well as Natural Bonding Orbitals (NBO) as employed in the Gaussian 16 program.^{75,76}

Results and discussion

N₂ adsorption limits

We have facilitated the investigation of the N₂ adsorption kinetics to Ta₄⁺ clusters at a cryo temperature of 26 K. The recorded mass spectra (*cf.* Fig. S1 in the ESI†) show a series of N₂ adsorbates (+28 *m/z*) which increase at extended storage time. Ultimately, we find an apparent adsorption limit of 13 N₂ molecules onto Ta₄⁺ at storage times of up to 20 s where the further adsorbate growth ceases (*cf.* Fig. S1, ESI†).

Cryo kinetics and rate constants of N₂ adsorption to the Ta₄⁺ cluster

The measurement of the temporal evolution of the adsorbate intensities for each N₂ adsorption step onto Ta₄⁺ reveals their adsorption kinetics (Fig. 1, Fig. S2 and Table S1, ESI†). We opt for fitting the recorded intensities to pseudo-first-order kinetics by the genetic algorithm routine *evofit*.⁶⁴ The resulting fit confirms the model of consecutive adsorption/desorption steps.

The first and second N₂ molecules adsorb differently than subsequent ones, up to the 7th N₂ molecule: the first and second fitted relative rate constants ($k_0 = 9.58 \text{ s}^{-1}$ and $k_1 = 1.88 \text{ s}^{-1}$) deviate significantly from k_2 to k_6 of around 5 s^{-1} . We tentatively assign equivalent adsorption sites for [Ta₄(N₂)₂]⁺ through [Ta₄(N₂)₆]⁺, and different sites (or processes) in the cases of [Ta₄(N₂)₀]⁺ and [Ta₄(N₂)₁]⁺. The fitted intensities of [Ta₄(N₂)₇]⁺ to [Ta₄(N₂)₁₁]⁺ deviate somewhat from the recorded ones; this implies the occurrence of further species and/or processes beyond our simple stepwise adsorption model.

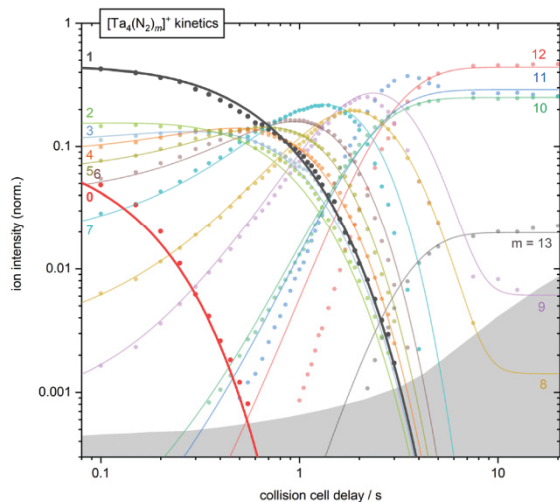


Fig. 1 Double logarithmic plot of isothermal kinetics of N₂ adsorption by mass-selected Ta₄⁺ clusters at 26 K, He buffer gas (6.8×10^{-6} mbar) and an exposure of 2.6×10^{-7} mbar N₂. The experimental data (solid dots) and the fits (solid lines) assume pseudo-first order kinetics for the N₂ adsorption in up to 13 consecutive steps. The kinetics of first and second N₂ adsorption are highlighted. The gray-shaded area indicates the background noise level. Corresponding rate constants of the pseudo-first order fits for each adsorption/desorption is shown in the ESI† (*cf.* Fig. S2).

Such processes might involve adsorbate shell reorganization and/or adsorbate induced cluster relaxation both of which may induce some N₂ ligand desorption. While such desorption is taken into account in the form of a “backwards reaction” it is the conceivable – and likely – isomerism of multiple participating structures which hampers a more effective fitting. Further elucidation is subject of ongoing studies and beyond the scope of the current study.

The kinetic curves at storage times beyond 8 s reveal horizontal and parallel curves for the generation of the ultimate products [Ta₄(N₂)_{*m*}]⁺, *m* = 9–13. This clearly indicates that these five adsorbate complexes are in a dynamic equilibrium. Our fitting supports this conclusion by non-vanishing rate constants for the desorption.

Cryogenic IR-PD spectra

We recorded infrared-photo dissociation (IR-PD) spectra of [Ta₄(N₂)_{*m*}]⁺ adsorbate complexes, *m* = 1–5, under adiabatic conditions in the ICR ion trap (Fig. 2), and we annotate these complexes in a short notation as (*m*,*n*). For the first two N₂ adsorptions onto Ta₄⁺, *i.e.* for the product complexes (4,1) and (4,2), we observe no resonant IR induced fragmentation. However, for (4,3) to (4,5) one notes multiple IR bands in two spectral regions. We observe broad vibrational bands in the range of 2200 cm⁻¹ to 2300 cm⁻¹ for (4,4) and (4,5). We tentatively assign all of these bands to N–N stretching vibrations of N₂ adsorbates which bind end-on to single Ta centers – in line with previously reported cases of Co, Ni, Rh and Ru.^{59–61,71} Starting with (4,3), vibrational bands in the range of 1400 cm⁻¹ to 1500 cm⁻¹ shift to the red by 21 cm⁻¹ and 11 cm⁻¹ per additionally adsorbed N₂ molecule.

The absence of vibrational bands in the cases of (4,1) and (4,2), and the deviating adsorption rate constants k_0 and k_1 raised our interest. The following DFT calculations shall gain further insights into these processes and the species involved.

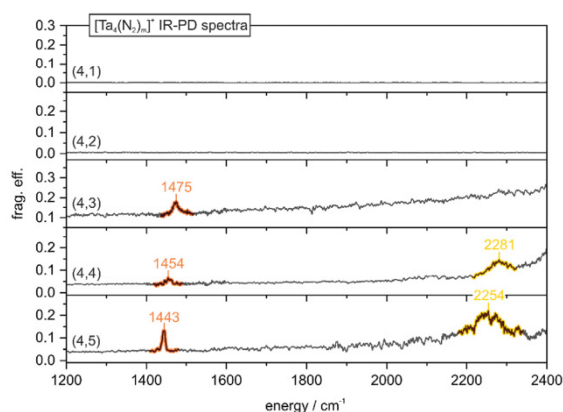


Fig. 2 IR-PD spectra of [Ta₄(N₂)_{*m*}]⁺ (simplified nomenclature: (*m*,*n*)), *m* = 1–5 in the range of 1200 cm⁻¹ to 2400 cm⁻¹. Note the absence of vibrational bands in the cases of (4,1) and (4,2). The gradual rise of baseline in cases (4,3) to (4,5) may originate either from auto-dissociation or from multi-photon absorptions into low lying electronic states.

DFT modeling of consecutive N₂ activations by Ta₄⁺ clusters

Recalling the lack of any vibrational bands in the recorded IR-PD spectra of [Ta₄(N₂)₁]⁺ and [Ta₄(N₂)₂]⁺, it seems possible that the bare Ta₄⁺ cluster activates and cleaves the first and second N₂ adsorbates. This would be analogous to the dinitride formation by Ta₂⁺, as described by Geng *et al.*,³⁴ and for Ta₆⁺ by Mafuné *et al.*⁵⁷ In order to verify this suggestion, we undertook DFT modeling for conceivable N₂ adsorption, activation and nitride formation pathways. We chose as a starting point Jahn Teller distorted, near tetrahedral geometries of the Ta₄⁺ bare cluster in doublet and quartet states (Fig. 3, in blue for doublet state and in red for quartet state). It showed that the excited quartet state pathway runs in parallel to the ground doublet state with an energy gap of about 50 kJ mol⁻¹ without intersecting each other. In the following, we therefore focus on the doublet ground state.

The initial N₂ adsorption to Ta₄⁺ leads to the cation **I1**_(4,1). The optimized structure reveals distances of $d(\text{Ta1-N1}) = 2.13 \text{ \AA}$ and $d(\text{N1-N2}) = 1.11 \text{ \AA}$. This indicates a σ -bonded N₂ molecule that coordinates to a single Ta center (Fig. 3). Adopting the

notation scheme of IUPAC and Salzer,⁷⁷ this coordination is denoted as $\mu_1:\kappa\text{N1}$ with the N₂ molecule almost perpendicular to the (Ta1-Ta2-Ta3) plane.

A facile tilting of the N₂ ligand in **I1**_(4,1) leads to **TS12**_(4,1) with $d(\text{Ta2-N1}) = 2.51 \text{ \AA}$ (-0.61 \AA with respect to **I1**_(4,1)) and requires merely an activation of $+5 \text{ kJ mol}^{-1}$. The adjacent intermediate **I2**_(4,1) is significantly more stable than **I1**_(4,1), by 52 kJ mol^{-1} . Note, that this $\mu_2:\kappa\text{N1}:\kappa\text{N1},\text{N2}$ coordination motif corresponds to a tantalum complex with a bridging N₂ unit that is coordinated both side-on and end-on.^{78,79} Related complexes with **I2** type bonding motifs were reported for Gd,³² Sc,³³ and V.⁴⁵

A transformation from μ_2 to μ_3 coordination takes some activation, and it takes place by further decrease the Ta2-N1 and Ta2-N2 distances while bending the N₂ unit sideways towards the Ta3 center. This torsional reorganization of initially in-plane $\mu_2:\kappa\text{N}:\kappa\text{N},\text{N}$ coordination across an intact Ta-Ta edge in **I2**_(4,1) towards a perpendicular $\mu_3:\kappa\text{N}:\kappa\text{N},\text{N}:\kappa\text{N},\text{N}$ coordination above a Ta-Ta-Ta surface in **I3**_(4,1) will prove to be crucial for N₂ cleavage. It is this transition from a structural motif **I2** via a transition state **TS23** to a structural motif **I3**

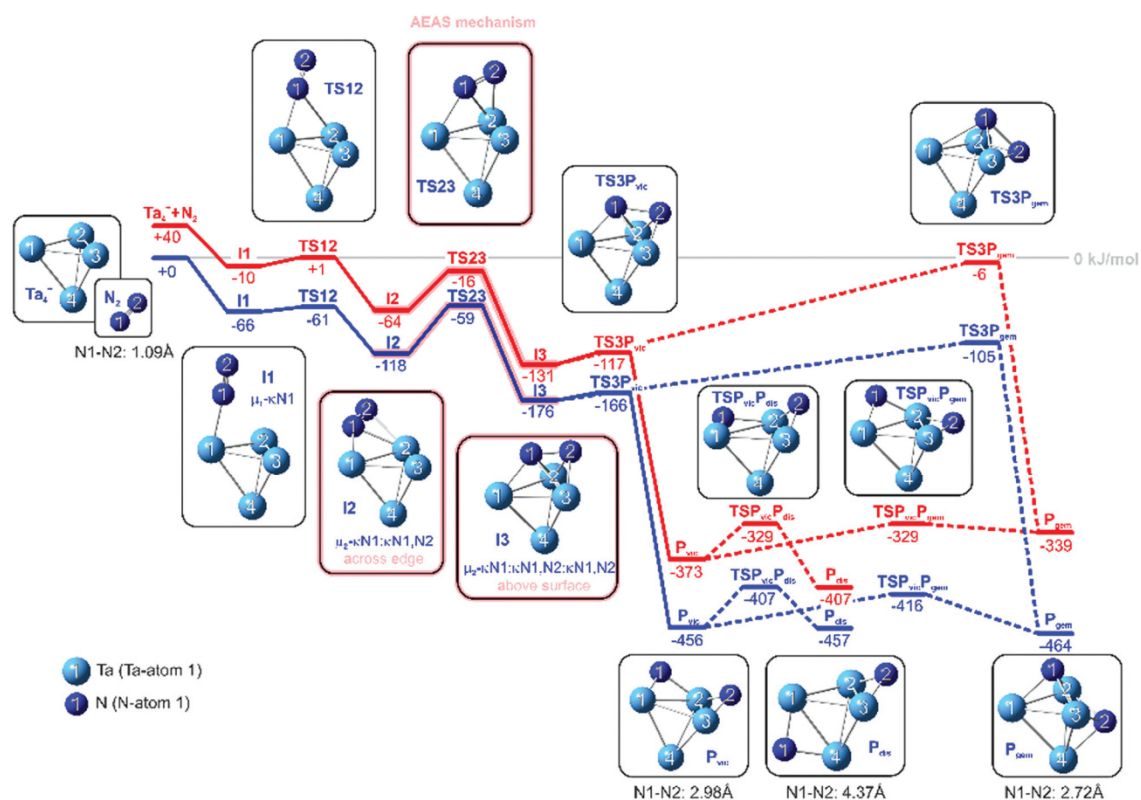


Fig. 3 Reaction pathway of N₂ activation by Ta₄⁺ (blue: doublet, red: quartet). Three submerged transition states allow for facile stepwise activation, which ultimately leads to the μ_2 or μ_3 bridging nitrido product structures **P_{vic}** or **P_{gem}**. Transition state **TSP_{vic}P_{dis}(4,1)** gives rise to a third isomer **P_{dis}(4,1)**. The subscript abbreviations gem, vic, and dis indicate geminal, vicinal, and distal, respectively, and they are more explicitly described in the supplement. Relative Energies are in kJ mol⁻¹. The torsional reorganization of the AEAS mechanism from an initial in-plane $\mu_2:\kappa\text{N}:\kappa\text{N},\text{N}$ coordination across an intact Ta-Ta edge towards perpendicular $\mu_3:\kappa\text{N}:\kappa\text{N},\text{N}:\kappa\text{N},\text{N}$ coordination above a Ta-Ta-Ta surface is highlighted. For reasons of clarity, the nomenclature is presented in an abbreviated form (e.g. **I1** stands for **I1**_(4,1)).

which we shall label as an across edge-above surface (AEAS) mechanism. The transition state $\text{TS23}_{(4,1)}$ is located merely 59 kJ mol^{-1} above $\text{I2}_{(4,1)}$, it is thus almost isoenergetic to $\text{TS12}_{(4,1)}$. The subsequent intermediate $\text{I3}_{(4,1)}$ engages a stabilization of 58 kJ mol^{-1} below $\text{I2}_{(4,1)}$. Note, that an AEAS mechanism requires four atomic centers at minimum. It operates significantly more likely on small clusters, and on highly corrugated and open surfaces.

$\text{I3}_{(4,1)}$ proves metastable against further activation. We find facile N–N bond cleavage which requires a shallow barrier of mere $+10 \text{ kJ mol}^{-1}$. The concomitant increase of the N–N bond length from 1.43 \AA , $\text{I3}_{(4,1)}$, to 1.67 \AA in the transition state $\text{TS3P}_{\text{vic}(4,1)}$ is decisive for product formation.

There is a steep decline of the computed energy surface along the reaction coordinate towards the conceivable product $\text{P}_{\text{vic}(4,1)}$ of as much as -280 kJ mol^{-1} below intermediate $\text{I3}_{(4,1)}$. This vicinal (vic) di-nitride structure comprises a Ta_4 -tetrahedron with two vicinal μ_2 -bridged nitrido ligands. The total decline of -456 kJ mol^{-1} is along the line of the previously published value of -550 kJ mol^{-1} in the case of Ta_6 .⁵⁷ Most of this energy decline is due to the final N_2 cleavage from $\text{I3}_{(4,1)}$ to $\text{P}_{\text{vic}(4,1)}$ and to an actual transfer of electron density from Ta to N atoms as evidenced by NPA charges from the DFT calculations (*cf.* Table S4, ESI[†]).

We found an alternative, second pathway for the N–N bond cleavage starting at the intermediate $\text{I3}_{(4,1)}$. There is a transition state $\text{TS3P}_{\text{gem}(4,1)}$, which lies 71 kJ mol^{-1} above $\text{I3}_{(4,1)}$, and 61 kJ mol^{-1} above $\text{TS3P}_{\text{vic}(4,1)}$. In $\text{TS3P}_{\text{gem}(4,1)}$, the pre-activated N_2 ligand, $d(\text{N1-N2}) = 1.83 \text{ \AA}$, coordinates perpendicular to the Ta2-Ta3 bond, as found before for the N_2 activation by Ta_2 .³⁴ This reaction path from $\text{I3}_{(4,1)}$ to $\text{TS3P}_{\text{gem}(4,1)}$ continues to an alternative product $\text{P}_{\text{gem}(4,1)}$, which comprises of two μ_3 -bridging geminal nitrido ligands with $d(\text{N1-N2}) = 2.72 \text{ \AA}$. It is almost isoenergetic to $\text{P}_{\text{vic}(4,1)}$ (-8 kJ mol^{-1}) and connected by a transition state $\text{TSP}_{\text{vic}\text{P}_{\text{gem}(4,1)}}$ *via* a barrier of 40 kJ mol^{-1} above $\text{P}_{\text{vic}(4,1)}$. There is a third isomer, the dinitrido Ta_4^+ cation with a distal configuration of the two nitrido ligands ($\text{P}_{\text{dis}(4,1)}$) and it is almost isoenergetic with $\text{P}_{\text{vic}(4,1)}$ by -1 kJ mol^{-1} and connected by a barrier of 49 kJ mol^{-1} *via* transition state $\text{TSP}_{\text{vic}\text{P}_{\text{dis}(4,1)}}$. Product $\text{P}_{\text{vic}(4,1)}$ forms directly from $\text{I3}_{(4,1)}$ whereas $\text{P}_{\text{dis}(4,1)}$ and $\text{P}_{\text{gem}(4,1)}$ would form only *via* slow isomerization from $\text{P}_{\text{vic}(4,1)}$.

In summary, the DFT modeling suggests a considerably exothermic cleavage along an all-over declining reaction path (-456 kJ mol^{-1}). Cleavage of the dinitrogen molecule by the bare Ta_4^+ takes place across three subsequent transition states, and it leads either to μ_2 or μ_3 bridging nitrido structures. The highest barrier of 59 kJ mol^{-1} ($\text{I2}_{(4,1)}$ to $\text{I3}_{(4,1)}$) is surmountable as it is submerged with respect to the entrance channel. Thus, N_2 cleavage by Ta_4^+ is a fast thermal process. These findings nicely agree with the observation of a fast initial N_2 adsorption process (*cf.* Fig. 1), and with the lack of vibrational N_2 fingerprints in the IR-PD spectra of (4,1), (*cf.* Fig. 2).

Obviously, one wonders if a second N_2 cleavage is feasible, subsequent to the thermal cleavage of the first N_2 molecule. The IR-PD spectra revealed no fingerprint of a coordinated and

intact N_2 molecule in the readily formed $[\text{Ta}_4(\text{N}_2)_2]^+$ complex (*cf.* Fig. 2). This observation provides strong evidence for the cleavage of a second N_2 molecule.

Indeed, the DFT modeling revealed energetically accessible pathways for second N \equiv N cleavage (Fig. 4, Fig. S5 and Fig. S6, ESI[†]). Starting from the likely product complex $\text{P}_{\text{vic}(4,1)}$ (Fig. 3), all four Ta centers may act as coordination sites for a second N_2 adsorbate. This results in four conceivable intermediates $\text{I1}^{\text{Ta1}}_{(4,2)}$, $\text{I1}^{\text{Ta2}}_{(4,2)}$, $\text{I1}^{\text{Ta3}}_{(4,2)}$, or $\text{I1}^{\text{Ta4}}_{(4,2)}$. Initial N_2 coordination through $\text{I1}^{\text{Ta2}}_{(4,2)}$ proves not suitable for the second N_2 activation due to sterical congestion (*cf.* Fig. S6, ESI[†]). Two of the other initial intermediates are equivalent, $\text{I1}^{\text{Ta1}}_{(4,2)}$, $\text{I1}^{\text{Ta3}}_{(4,2)}$ and $\text{I1}^{\text{Ta4}}_{(4,2)}$ is slightly less stable. Both subsequent reaction pathways towards full N_2 cleavage evolve in a mechanically related manner, and the corresponding energetics of stationary points and minima are likewise. We refer to the ESI[†] (Fig. S5 and Table S6) for the pathway of second N_2 activation, which starts at $\text{I1}^{\text{Ta3}}_{(4,2)}$.

In the following, we discuss in more detail the pathway which starts at $\text{I1}^{\text{Ta4}}_{(4,2)}$. In analogy to the path for the first N_2 cleavage (Fig. 3) the second N_2 ligand at the complex $\text{I1}_{(4,2)}$ (-41 kJ mol^{-1}) bends *via* transition state $\text{TS12}_{(4,2)}$ (-25 kJ mol^{-1}) into $\text{I2}_{(4,2)}$ (-100 kJ mol^{-1}) and subsequently *via* $\text{TS23}_{(4,2)}$ (-33 kJ mol^{-1}) towards $\text{I3}_{(4,2)}$ (-157 kJ mol^{-1} , Fig. 4). Note the remarkable similarity of the coordination motif of N_2 in $\text{I3}_{(4,1)}$ (Fig. 3). This implies the capability of the Ta_4^+ cluster to achieve N_2 cleavage twice *via* comparable intermediate geometries. In particular, there is considerable similarity of the N3–N4 distances of stationary points along the reaction path of the second activation and the respective values of N1–N2 distances along the reaction path of first activation (*cf.* Table S2 and S7, ESI[†]). Note that similar to the first N_2 activation path, the path of the 2nd activation also follows an AEAS mechanism at this point: torsional reorganization of initial in plane μ_2 - $\kappa\text{N}:\kappa\text{N},\text{N}$ coordination across an intact Ta–Ta edge towards μ_3 - $\kappa\text{N}:\kappa\text{N},\text{N}:\kappa\text{N},\text{N}$ coordination above a Ta–Ta–Ta surface. Ultimately, a transition state $\text{TS3P}_{(4,2)}$, located 37 kJ mol^{-1} above $\text{I3}_{(4,2)}$ leads to the product $\text{P}_{(4,2)}$, -222 kJ mol^{-1} below $\text{I3}_{(4,2)}$.

All activation barriers along the second N_2 cleavage path are submerged with respect to the entrance channel $[\text{Ta}_4\text{NN}]^+ + \text{N}_2$. The decisive step for the activation of the second N_2 , which proceeds from $\text{I3}_{(4,2)}$ across $\text{TS3P}_{(4,2)}$ to $\text{P}_{(4,2)}$, takes $+37 \text{ kJ mol}^{-1}$ activation, while the cleavage of the first N_2 molecule from $\text{I3}_{(4,1)}$ across $\text{TS3P}_{\text{vic}(4,1)}$ to $\text{P}_{\text{vic}(4,1)}$ requires less activation, namely $+10 \text{ kJ mol}^{-1}$. Nevertheless, both processes are facile. Thus, the modeling is in line with our spectroscopic findings.

Note, that $\text{P}_{\text{dis}(4,1)}$ cannot serve as a starting point for a second N_2 activation *via* an AEAS mechanism. A second N_2 activation which starts at $\text{P}_{\text{gem}(4,1)}$ leads to some $\text{P}_{(4,2)}$ like isomer in as much as starting from $\text{P}_{\text{vic}(4,1)}$ would do.

The facile activation of two N_2 molecules raises the question whether the cleavage of a third N_2 molecule is also accessible. We calculated the initial coordination and reaction paths of a third N_2 reactant to possible Ta sites of the $\text{P}_{(4,2)}$ structure of Fig. 4. Other starting points, namely $\text{P}_{(4,2)}$ of Fig. S5 and S6 (ESI[†]), are less likely. They would inevitably run into steric

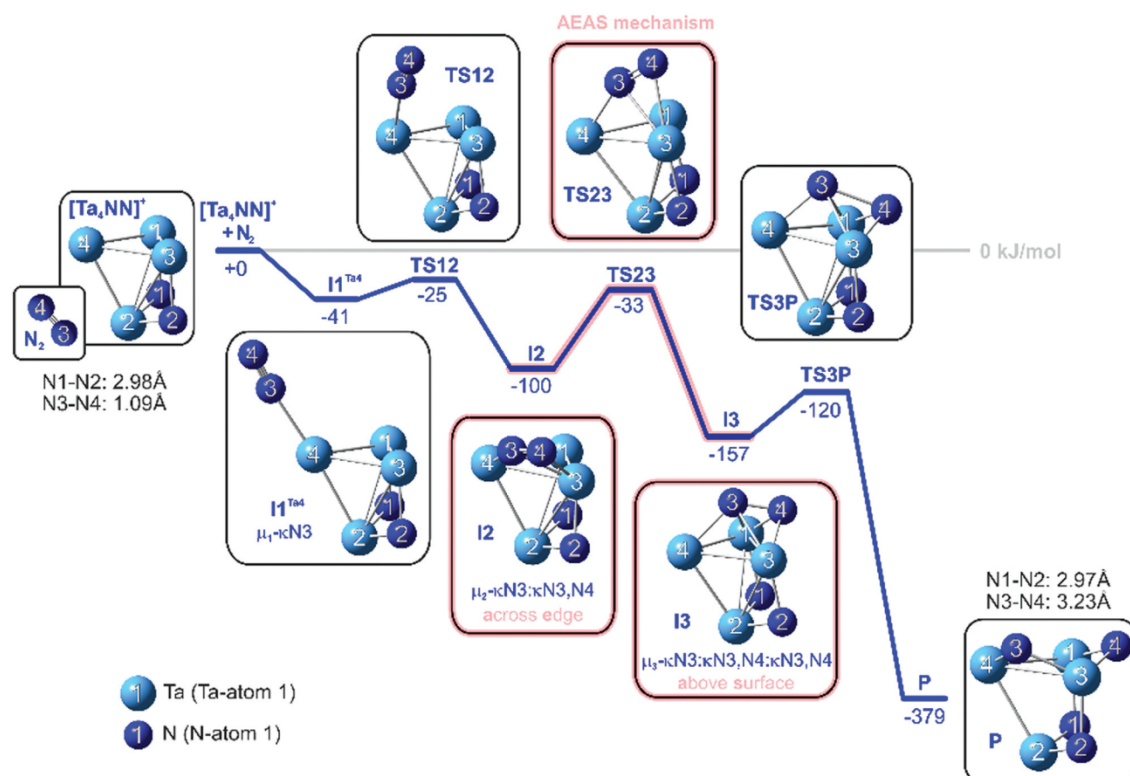


Fig. 4 A reaction pathway of second N₂ cleavage on a [Ta₄NN]¹⁺ cluster complex. There is a striking similarity to the first cleavage pathway, cf. Fig. 3, including the highlighted AEAS mechanism. Note, that the prior dissociated N1–N2 couple remains activated (at least 2.97 Å apart) in the course of the second activation, as compared to the free N₂ bond length of 1.09 Å.

congestion by the unavoidable proximity of the third N₂ ligand and the adjacent μ₂ nitrido ligands.

Thus, a conceivable AEAS mechanism might start by coordination of a third N₂ molecule to Ta1 of P_(4,2) (Fig. 5). This leads to the [Ta₄NNNN(N₂)]¹⁺ complex **I1**^{Ta1}_(4,3) with a stabilization of –64 kJ mol^{–1}. As revealed in the previous two cases of N₂ reorganization this third N₂ molecule bends over *via* transition state **TS12**_(4,3), +42 kJ mol^{–1}, into the intermediate **I2**_(4,3), –23 kJ mol^{–1} below **I1**_(4,3), which exhibit a μ₂-κN5:κN5,N6 coordination as in both previous cases. Further reorganization would take place *via* a transition state **TS23**_(4,2) which turns out to hamper such a process by virtue of its remarkable barrier of +142 kJ mol^{–1}, and towards the intermediate **I3**_(4,3); the latter is by +11 kJ mol^{–1} higher in energy than intermediate **I2**_(4,3). Note, that this barrier locates +55 kJ mol^{–1} above the starting point which prevents any thermal reaction process at this point. While the corresponding **I3**_(4,1) and **I3**_(4,2) states of the first and second N₂ activation stabilize with respect to the according **I2**_(4,1) and **I2**_(4,2) states, the **I3**_(4,3) state for the third N₂ activation is destabilized with respect to **I2**_(4,3). Further rearrangements from **I3**_(4,3) towards a product **P**_(4,3) would lead *via* a transition state **TS3P**_(4,3), +82 kJ mol^{–1}, to the product complex cation **P**_(4,3); the latter is stabilized by –176 kJ mol^{–1} with respect to **I3**_(4,3).

In the third N₂ activation, there are striking similarities of mechanisms at work with respect to those of first and second N₂ activation. The energetics, however, are quite unfavorable for the third N₂ activation step. Initial coordination of a third N₂ molecule to sites other than the structurally equivalent sites Ta1 and Ta2, namely Ta3 and Ta4, would lead to highly congested transition states which come along with even higher barriers.

The conclusions for the 3rd N₂ activation, based on the modeling, are twofold: firstly, we note, that the reaction path reveals a chain of rearranging steps which invoke the AEAS mechanisms in salient analogy to the reaction paths for activation of the prior two N₂ molecules. We take this sturdiness of N₂ activation by Ta₄⁺ as strong indication for a more general concept that might operate on highly corrugated surfaces at sub stoichiometric N₂ load under moderate operation conditions.

While the first two N₂ cleavages are facile, there are two subsequent activation barriers, which work against thermal cleavage of a 3rd N₂ adsorbate. We find evidence for this lack of 3rd N₂ activation in the IR-PD spectra: there is an undisputable presence of N₂ vibrations in the case of the cluster cations (4,*m*), *m* ≥ 3. The obtained frequencies clearly indicate the

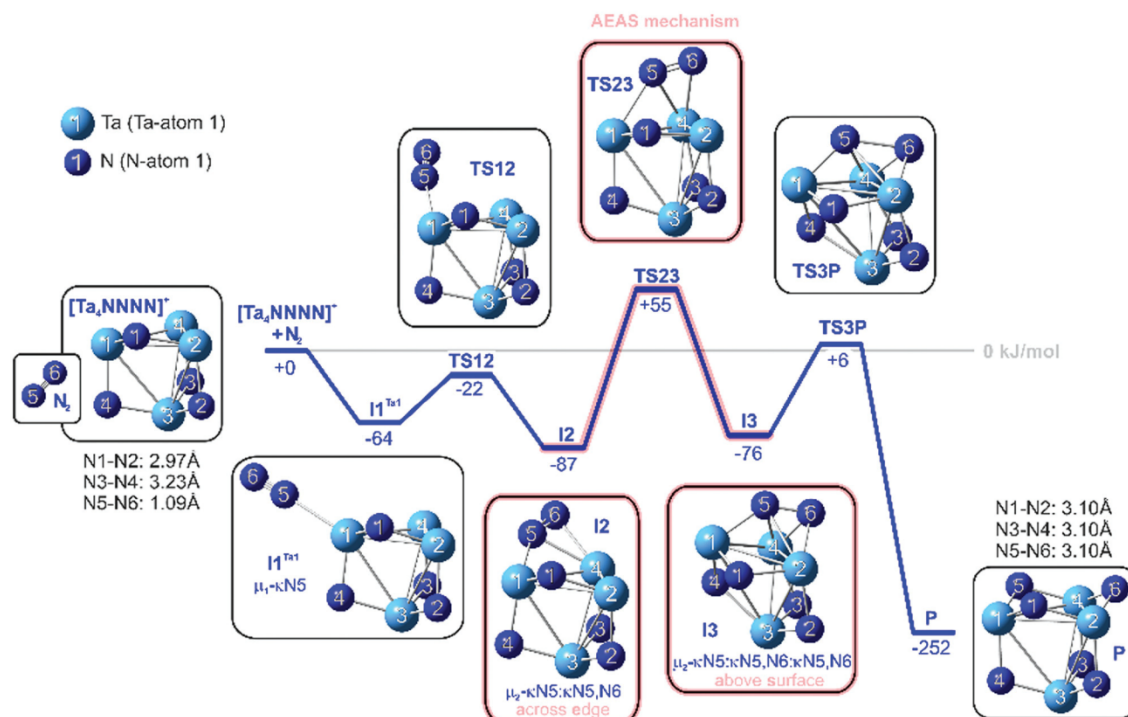


Fig. 5 A reaction pathway of 3rd N_2 cleavage on a $[\text{Ta}_4\text{NNNN}]^+$ cluster complex. The facile and highlighted AEAS mechanism across **TS23** of first and second N_2 activation becomes demanding in this case.

presence of at least one polarized but otherwise intact N_2 ligand. We will assign these vibrational bands in the following to structures in analogy to $\text{I}_{2(4,3)}$, and we will assume unsurmountable activation barriers for any further activation.

In the course of the discussion of the reaction paths, a multitude of model structures were presented, and they possess vibrational frequencies within the regions of 2200 cm^{-1} to 2310 cm^{-1} (cf. Fig. S7, ESI†). They serve to interpret the experimental IR-PD spectra of $[\text{Ta}_4(\text{N}_2)_m]^+$ labeled as $(4,m)$, $m = 1-5$, (Fig. 2) in some more detail. In addition we identified conceivable $[\text{Ta}_4(\text{N})_4(\text{N}_2)_j]^+$ species, with $j = 1-3$ starting from $\text{I}_{2(4,3)}$ (cf. Tables S11–S13, ESI†). The optimized structures reveal some noticeable findings:

(a) Numerous isomers (cf. Fig. S7, ESI†) suggest a likely coexistence of species which feature IR-PD absorptions within ranges of the observed broad bands of $(4,4)$ and $(4,5)$ (Fig. 2, 2200 cm^{-1} to 2300 cm^{-1}).

(b) Calculated IR-PD bands of $\text{I}_{2(4,3)}$ type core structures without or with additional end-on coordinated N_2 ligands (cf. Table S11, ESI†) nicely correspond to IR-PD band(s) around 1475 cm^{-1} , $(4,3)$, up to 1443 cm^{-1} , $(4,5)$. This spectral evidence of $\text{I}_{2(4,3)}$ indicates the absence of a third AEAS type N_2 cleavage in $(4,3)$. The flow of reaction stops at $\text{I}_{2(4,3)}$ in front of the unsurmountable **TS23** $_{(4,3)}$ barrier – subsequent N_2 uptake prevailing.

(c) Addition of end-on N_2 ligands to I_2 type structures shifts the calculated vibration of the $\mu_2\text{-}\kappa\text{N}:\kappa\text{N,N}$ N_2 ligand up to

40 cm^{-1} to the red depending on the coordination site. This agrees with the observed shifts per additional N_2 ligand of 21 cm^{-1} , $(4,3)$ to $(4,4)$, and 11 cm^{-1} , $(4,4)$ to $(4,5)$. NPA-calculations revealed an increase of the positive charge at the π -coordinated Ta4 atom by ca. $+0.02\text{ e}$ and an increase of the corresponding N–N bond distance by ca. 0.01 \AA upon coordination of an end-on coordinated N_2 molecule to an adjacent Ta atom (Ta1, Ta2, Ta3). Similar effects are reported in the correlation of charge density shifts with IR-PD vibration band shifts in transition metal π -coordinated benzene complexes.⁸⁰ It has also been reported that the decrease of IR-PD stretching frequencies of $\mu\text{-N}_2$ ligands correlates with the N_2 bond length activation.²⁰ By further addition of a second end-on coordinated N_2 molecule the positive charge at Ta4 increases along with a slight increase of the N–N bond distance. Thus, stepwise addition of N_2 molecules to the Ta_4^+ cluster result in a softening of the $\mu_2\text{-}\kappa\text{N}:\kappa\text{N,N}$ N_2 coordinated ligand and manifests in a redshift of the corresponding IR-PD band.

Conclusions

The cryogenic kinetics of N_2 adsorption to Ta_4^+ reveal stepwise addition of numerous N_2 molecules, with peculiar details for the first and second adsorptions. The infrared signatures of $[\text{Ta}_4(\text{N}_2)_1]^+$ and $[\text{Ta}_4(\text{N}_2)_2]^+$ are special: there are no NN

stretching bands. This is consistent with cleavage of the first two adsorbed dinitrogen molecules. The cleavage of N₂ molecules proceeds *via* a novel across edge-above surface (AEAS) mechanism: the reaction path proceeds *via* an initial end-on coordination of N₂. Bending of the N₂ ligand towards a neighboring Ta atom yields a second intermediate, with a μ_2 N₂ bonding motif across an edge of the Ta₄⁺ tetrahedron core. Further rearrangement above a Ta–Ta–Ta surface of the Ta₄⁺ tetrahedron results in a μ_3 bonded N₂ ligand that relaxes swiftly by ultimate NN bond cleavage, and it unfolds into the final dinitrido species. Calculated activation barriers confirm spontaneous cleavage of the first two dinitrogen molecules. Cleavage of the third N₂ ligand is kinetically hindered. Substoichiometric N₂ exposure allows for spontaneous activation, whereas higher exposure imposes self-poisoning.

The found AEAS mechanism provides for a mechanistic understanding of facile N₂ cleavage by a sub nano structure with a highly curved surface. It shall serve as an inspiration for the knowledge inspired design of future tailor made catalyst materials that might invoke highly corrugated surfaces and operate under moderate conditions.

Author contributions

D. V. F., M. P. K. and A. S. performed the experiments. D. V. F. and M. P. K. evaluated the data. D. V. F., M. P. K. and M. H. P. performed the calculations. D. V. F., M. P. K., M. H. P. and G. N. S. wrote and revised the manuscript. All authors evaluated and discussed the results.

Conflicts of interest

There are no conflicts to declare.

Acknowledgements

This work was supported by the German research foundation DFG within the transregional collaborative research center SFB/TRR 88 “Cooperative effects in homo and heterometallic complexes” (3MET.de) and by the state research center OPTIMAS. We thank Helmut Schwarz for valuable and critical comments and for his ongoing support. We thank Thomas Kolling for technical assistance and valuable discussions. Quantum chemical modeling took place at the “Regionales Hochschulrechenzentrum Kaiserslautern (RHRK)”.

References

- 1 D. E. Canfield, A. N. Glazer and P. G. Falkowski, *Science*, 2010, **330**, 192–196.
- 2 B. K. Burgess and D. J. Lowe, *Chem. Rev.*, 1996, **96**, 2983–3012.
- 3 D. Sippel and O. Einsle, *Nat. Chem. Biol.*, 2017, **13**, 956–960.
- 4 B. M. Hoffman, D. Lukoyanov, Z.-Y. Yang, D. R. Dean and L. C. Seefeldt, *Chem. Rev.*, 2014, **114**, 4041–4062.
- 5 M. Appl, *Ammonia: Principles and Industrial Practice*, Wiley-VCH, 2007.
- 6 R. Schlögl, *Ammonia Synthesis in Handbook of Heterogeneous Catalysis*, Wiley-VCH, 2008, pp. 2501–2575.
- 7 H. Liu, *Ammonia Synthesis Catalysts*, World Scientific, Singapore, 2013.
- 8 R. Schlögl, *Angew. Chem., Int. Ed.*, 2003, **42**, 2004–2008.
- 9 H. Liu and Cuihua Xuebao, *Chin. J. Catal.*, 2014, **35**, 1619–1640.
- 10 G. Ertl, *Catal. Rev.*, 1980, **21**, 201–223.
- 11 G. Ertl, S. B. Lee and M. Weiss, *Surf. Sci.*, 1982, **114**, 515–526.
- 12 G. Ertl, *Angew. Chem., Int. Ed.*, 2008, **47**, 3524–3535.
- 13 A. Mittasch, *Geschichte der Ammoniaksynthese*, Verlag Chemie, Berlin-Weinheim, 1951.
- 14 S. Gambarotta and J. Scott, *Angew. Chem., Int. Ed.*, 2004, **43**, 5298–5308.
- 15 K. Honkala, A. Hellman, I. N. Remediakis, A. Logadottir, A. Carlsson, S. Dahl, C. H. Christensen and J. K. Nørskov, *Science*, 2005, **307**, 555–558.
- 16 Á. Logadottir and J. K. Nørskov, *J. Catal.*, 2003, **220**, 273–279.
- 17 C. E. Laplaza and C. C. Cummins, *Science*, 1995, **268**, 861–863.
- 18 C. E. Laplaza, A. R. Johnson and C. C. Cummins, *J. Am. Chem. Soc.*, 1996, **118**, 709–710.
- 19 B. Schluschaß, J. Abbenseth, S. Demeshko, M. Finger, A. Franke, C. Herwig, C. Würtele, I. Ivanovic-Burmazovic, C. Limberg, J. Telsler and S. Schneider, *Chem. Sci.*, 2019, **10**, 10275–10282.
- 20 C. E. Laplaza, M. J. A. Johnson, J. C. Peters, A. L. Odom, E. Kim, C. C. Cummins, G. N. George and I. J. Pickering, *J. Am. Chem. Soc.*, 1996, **118**, 8623–8638.
- 21 K. P. Chiang, S. M. Bellows, W. W. Brennessel and P. L. Holland, *Chem. Sci.*, 2014, **5**, 267–274.
- 22 K. Grubel, W. W. Brennessel, B. Q. Mercado and P. L. Holland, *J. Am. Chem. Soc.*, 2014, **136**, 16807–16816.
- 23 S. F. McWilliams and P. L. Holland, *Acc. Chem. Res.*, 2015, **48**, 2059–2065.
- 24 T. Shima, S. Hu, G. Luo, X. Kang, Y. Luo and Z. Hou, *Science*, 2013, **340**, 1549–1552.
- 25 T. Shima, G. Luo, S. Hu, Y. Luo and Z. Hou, *J. Am. Chem. Soc.*, 2019, **141**, 2713–2720.
- 26 E. L. Muetterties, *Bull. Soc. Chim. Belg.*, 1975, **84**, 959–986.
- 27 D. K. Böhme and H. Schwarz, *Angew. Chem., Int. Ed.*, 2005, **44**, 2336–2354.
- 28 A. W. Castleman and P. Jena, *Proc. Natl. Acad. Sci. U. S. A.*, 2006, **103**, 10552–10553.
- 29 Z. Luo, A. W. Castleman and S. N. Khanna, *Chem. Rev.*, 2016, **116**, 14456–14492.
- 30 S. M. Lang and T. M. Bernhardt, *Phys. Chem. Chem. Phys.*, 2012, **14**, 9255–9269.
- 31 O. Hübner and H.-J. Himmel, *Chem. – Eur. J.*, 2018, **24**, 8941–8961.
- 32 M. Zhou, X. Jin, Y. Gong and J. Li, *Angew. Chem., Int. Ed.*, 2007, **46**, 2911–2914.
- 33 Y. Gong Zhao and M. Zhou, *J. Phys. Chem. A*, 2007, **111**, 6204–6207.

- 34 C. Geng, J. Li, T. Weiske and H. Schwarz, *Proc. Natl. Acad. Sci. U. S. A.*, 2018, **115**, 11680–11687.
- 35 C. Geng, J. Li, T. Weiske and H. Schwarz, *Proc. Natl. Acad. Sci. U. S. A.*, 2019, **116**, 21416–21420.
- 36 M. D. Morse, M. E. Geusic, J. R. Heath and R. E. Smalley, *J. Chem. Phys.*, 1985, **83**, 2293–2304.
- 37 Y. M. Hamrick and M. D. Morse, *J. Phys. Chem.*, 1989, **93**, 6494–6501.
- 38 B. Cao, A. K. Starace, O. H. Judd, I. Bhattacharyya and M. F. Jarrold, *J. Chem. Phys.*, 2014, **141**, 204304.
- 39 P. B. Armentrout, *Catal. Sci. Technol.*, 2014, **4**, 2741–2755.
- 40 K. Lange, B. Visser, D. Neuwirth, J. F. Eckhard, U. Boesl, M. Tschurl, K. H. Bowen and U. Heiz, *Int. J. Mass Spectrom.*, 2015, **375**, 9–13.
- 41 D. Neuwirth, J. F. Eckhard, B. R. Visser, M. Tschurl and U. Heiz, *Phys. Chem. Chem. Phys.*, 2016, **18**, 8115–8119.
- 42 J. F. Eckhard, D. Neuwirth, C. Panosetti, H. Oberhofer, K. Reuter, M. Tschurl and U. Heiz, *Phys. Chem. Chem. Phys.*, 2017, **19**, 5985–5993.
- 43 J. F. Eckhard, D. Neuwirth, M. Tschurl and U. Heiz, *Phys. Chem. Chem. Phys.*, 2017, **19**, 10863–10869.
- 44 T. Masubuchi, J. F. Eckhard, G. Goddard, M. Tschurl and U. Heiz, *Phys. Chem. Chem. Phys.*, 2019, **21**, 20743–20749.
- 45 X. Cheng, Z.-Y. Li, L.-H. Mou, Y. Ren, Q.-Y. Liu, X.-L. Ding and S.-G. He, *Chem. – Eur. J.*, 2019, **25**, 16523–16527.
- 46 Y. Zhao, J.-T. Cui, M. Wang, D. Y. Valdivielso, A. Fielicke, L.-R. Hu, X. Cheng, Q.-Y. Liu, Z.-Y. Li, S.-G. He and J.-B. Ma, *J. Am. Chem. Soc.*, 2019, **141**, 12592–12600.
- 47 L.-H. Mou, Z.-Y. Li, Q.-Y. Liu and S.-G. He, *J. Am. Soc. Mass Spectrom.*, 2019, **30**, 1956–1963.
- 48 R. A. J. O’Hair and G. N. Khairallah, *J. Cluster Sci.*, 2004, **15**, 331–363.
- 49 H. Schwarz and K. R. Asmis, *Chem. – Eur. J.*, 2019, **25**, 2112–2126.
- 50 H.-J. Himmel and M. Reiher, *Angew. Chem., Int. Ed.*, 2006, **45**, 6264–6288.
- 51 H. Wang, R. Craig, H. Haouari, J.-G. Dong, Z. Hu, A. Vivoni, J. R. Lombardi and D. M. Lindsay, *J. Chem. Phys.*, 1995, **103**, 3289–3292.
- 52 P. Gruene, A. Fielicke and G. Meijer, *J. Chem. Phys.*, 2007, **127**, 234307.
- 53 J. Du, X. Sun and G. Jiang, *J. Chem. Phys.*, 2012, **136**, 094311.
- 54 F. Wei, C. Luo and J. Dong, *J. Chem. Phys.*, 2006, **125**, 114305.
- 55 J. F. Eckhard, T. Masubuchi, M. Tschurl, R. N. Barnett, U. Landman and U. Heiz, *J. Phys. Chem. C*, 2018, **122**, 25628–25637.
- 56 M. Kumar Yadav and A. Mookerjee, *Phys. B*, 2010, **405**, 3940–3942.
- 57 F. Mafuné, Y. Tawaraya and S. Kudoh, *J. Phys. Chem. A*, 2016, **120**, 4089–4095.
- 58 M. Arakawa, K. Ando, S. Fujimoto, S. Mishra, G. N. Patwari and A. Terasaki, *Phys. Chem. Chem. Phys.*, 2018, **20**, 13974–13982.
- 59 S. Dillinger, J. Mohrbach, J. Hewer, M. Gaffga and G. Niedner-Schatteburg, *Phys. Chem. Chem. Phys.*, 2015, **17**, 10358–10362.
- 60 J. Mohrbach, S. Dillinger and G. Niedner-Schatteburg, *J. Phys. Chem. C*, 2017, **121**, 10907–10918.
- 61 S. Dillinger, M. P. Klein, A. Steiner, D. C. McDonald, M. A. Duncan, M. M. Kappes and G. Niedner-Schatteburg, *J. Phys. Chem. Lett.*, 2018, **9**, 914–918.
- 62 C. Berg, T. Schindler, G. Niedner-Schatteburg and V. E. Bondybey, *J. Chem. Phys.*, 1995, **102**, 4870–4884.
- 63 V. E. Bondybey and J. H. English, *J. Chem. Phys.*, 1981, **74**, 6978–6979.
- 64 M. Graf, Diploma thesis, TU Kaiserslautern, 2006.
- 65 M. J. Frisch, G. W. Trucks, H. B. Schlegel, G. E. Scuseria, M. A. Robb, J. R. Cheeseman, G. Scalmani, V. Barone, B. Mennucci, G. A. Petersson, H. Nakatsuji, M. Caricato, X. Li, H. P. Hratchian, A. F. Izmaylov, J. Bloino, G. Zheng, J. L. Sonnenberg, M. Hada, M. Ehara, K. Toyota, R. Fukuda, J. Hasegawa, M. Ishida, T. Nakajima, Y. Honda, O. Kitao, H. Nakai, T. Vreven, J. A. Montgomery Jr., J. E. Peralta, F. Ogliaro, M. J. Bearpark, J. Heyd, E. N. Brothers, K. N. Kudin, V. N. Staroverov, R. Kobayashi, J. Normand, K. Raghavachari, A. P. Rendell, J. C. Burant, S. S. Iyengar, J. Tomasi, M. Cossi, N. Rega, N. J. Millam, M. Klene, J. E. Knox, J. B. Cross, V. Bakken, C. Adamo, J. Jaramillo, R. Gomperts, R. E. Stratmann, O. Yazyev, A. J. Austin, R. Cammi, C. Pomelli, J. W. Ochterski, R. L. Martin, K. Morokuma, V. G. Zakrzewski, G. A. Voth, P. Salvador, J. J. Dannenberg, S. Dapprich, A. D. Daniels, Ö. Farkas, J. B. Foresman, J. V. Ortiz, J. Cioslowski and D. J. Fox, *Gaussian 09, Revision D.01*, Gaussian, Inc., Wallingford, CT, USA, 2009.
- 66 M. J. Frisch, G. W. Trucks, H. B. Schlegel, G. E. Scuseria, M. A. Robb, J. R. Cheeseman, G. Scalmani, V. Barone, G. A. Petersson, H. Nakatsuji, X. Li, M. Caricato, A. V. Marenich, J. Bloino, B. G. Janesko, R. Gomperts, B. Mennucci, H. P. Hratchian, J. V. Ortiz, A. F. Izmaylov, J. L. Sonnenberg, F. Ding Williams, F. Lipparini, F. Egidi, J. Goings, B. Peng, A. Petrone, T. Henderson, D. Ranasinghe, V. G. Zakrzewski, J. Gao, N. Rega, G. Zheng, W. Liang, M. Hada, M. Ehara, K. Toyota, R. Fukuda, J. Hasegawa, M. Ishida, T. Nakajima, Y. Honda, O. Kitao, H. Nakai, T. Vreven, K. Throssell, J. A. Montgomery Jr., J. E. Peralta, F. Ogliaro, M. J. Bearpark, J. J. Heyd, E. N. Brothers, K. N. Kudin, V. N. Staroverov, T. A. Keith, R. Kobayashi, J. Normand, K. Raghavachari, A. P. Rendell, J. C. Burant, S. S. Iyengar, J. Tomasi, M. Cossi, J. M. Millam, M. Klene, C. Adamo, R. Cammi, J. W. Ochterski, R. L. Martin, K. Morokuma, O. Farkas, J. B. Foresman and D. J. Fox, *Gaussian 16, Revision C.01*, Gaussian, Inc., Wallingford, CT, USA, 2016.
- 67 C. Adamo and V. Barone, *J. Chem. Phys.*, 1999, **110**, 6158–6170.
- 68 J. P. Perdew, K. Burke and M. Ernzerhof, *Phys. Rev. Lett.*, 1996, **77**, 3865.
- 69 D. Andrae, U. Häußermann, M. Dolg, H. Stoll and H. Preuß, *Theor. Chim. Acta*, 1990, **77**, 123–141.
- 70 F. Weigend and R. Ahlrichs, *Phys. Chem. Chem. Phys.*, 2005, **7**, 3297–3305.

Paper

PCCP

- 71 M. P. Klein, A. A. Ehrhard, J. Mohrbach, S. Dillinger and G. Niedner-Schatteburg, *Top. Catal.*, 2018, **61**, 106–118.
- 72 C. Peng and H. Bernhard Schlegel, *Isr. J. Chem.*, 1993, **33**, 449–454.
- 73 L. Fan, D. Harrison, L. Deng, T. K. Woo, D. Swerhone and T. Ziegler, *Can. J. Chem.*, 1995, **73**, 989–998.
- 74 K. Fukui, *Acc. Chem. Res.*, 1981, **14**, 363–368.
- 75 F. Weinhold and J. E. Carpenter, in *The Structure of Small Molecules and Ions*, ed. R. Naaman and Z. Vager, Springer US, Boston, MA, 1988, DOI: 10.1007/978-1-4684-7424-4_24, pp. 227–236.
- 76 E. D. Glendening, C. R. Landis and F. Weinhold, *J. Comput. Chem.*, 2013, **34**, 1429–1437.
- 77 A. Salzer, *J. Pure Appl. Chem.*, 1999, **71**, 1557.
- 78 M. D. Fryzuk, S. A. Johnson and S. J. Rettig, *J. Am. Chem. Soc.*, 1998, **120**, 11024–11025.
- 79 M. D. Fryzuk, S. A. Johnson, B. O. Patrick, A. Albinati, S. A. Mason and T. F. Koetzle, *J. Am. Chem. Soc.*, 2001, **123**, 3960–3973.
- 80 T. D. Jaeger, D. van Heijnsbergen, S. J. Klippenstein, G. von Helden, G. Meijer and M. A. Duncan, *J. Am. Chem. Soc.*, 2004, **126**, 10981–10991.

8.3 Supplementary Information

Electronic Supplementary Information

Observation and Mechanism of Cryo N₂ Cleavage by a Tantalum Cluster

Daniela V. Fries, Matthias P. Klein, Annika Steiner, Marc H. Prosenc and Gereon Niedner-Schatteburg

Fachbereich Chemie and Forschungszentrum OPTIMAS,

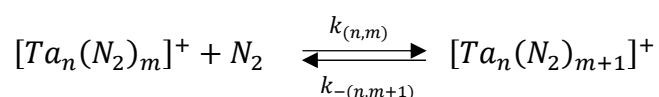
Technische Universität Kaiserslautern, 67663 Kaiserslautern, Germany

Text 1: Detailed Experimental and Computational Methods

The experiments were performed with a customized Fourier transform ion cyclotron resonance (FT-ICR) mass spectrometer (Apex Ultra, Bruker Daltonics). This specific apparatus configuration allows us to generate cluster ions and isolate required mass complexes. Furthermore, we are able to adsorb reaction gases while trapping the ions in the hexapole cell and record mass spectra of the adsorbate complexes. Finally, we can examine the ions in the ICR cell by adsorption kinetics and infrared (multi) photon dissociation (IR-PD) spectroscopy.

First, we generate required cluster ions using a home-built laser vaporization (LVAP) source as described before.^{1, 2} The second harmonic of a pulsed Nd:YAG laser (Spitlight300, Innolas, 20 Hz) was used to evaporate tantalum atoms from a rotating tantalum foil (0.5 mm thick, 99.95 %, Alfa Aesar). Next, a gas pulse created from a piezoelectric valve³ captures the hot plasma. While guided subsequently through the expansion channel (69 mm long, 2 mm diameter) the atoms and ions cool down and aggregate. Passing electrostatic lenses, the resulting cluster size distribution reaches the 90° ion beam bender. The bare clusters can be mass selected by a quadrupole mass filter and reach the cryogenic hexapole cell (10 K) subsequently. Therein, we are able to trap required mass complexes and introduce buffer or reaction gases. This can be done continuously or in pulses. For our investigations on tantalum clusters we only used continuously injection of up to $2.6 \cdot 10^{-7}$ mbar N₂. To achieve sufficient cluster signal and thermalization, additional collision gas (He; up to $6.8 \cdot 10^{-6}$ mbar) was introduced into the hexapole. After trapping the clusters and cluster adsorbates for various storage times (0 - 20 s), the ions are guided by electrostatic lenses into the FT-ICR cell for detection. If required, it is possible to isolate ion complexes within and introduce further reaction gas into this infinity cell.⁴

Reaction delay scans were recorded in order to investigate adsorption kinetics of nitrogen molecules to tantalum clusters. From this, we obtain a temporal evolution of mass spectra, which is evaluated by the program DataAnalysis 4.0 (Bruker Daltonics). The outcoming signal intensities and assigned storage times of each adsorbate complexes are input data for evaluation by evofit⁵. This program performs pseudo-first-order fits, from which we receive relative rate constants for adsorption ($k_{(n,m)}$) and desorption steps ($k_{-(n,m+1)}$), respectively.



The relative rate constants ($k_{(n,m)}$, $k_{-(n,m+1)}$) determine the absolute rate constants ($k_{(n,m)}^{abs}$, $k_{-(n,m+1)}^{abs}$), the absolute collision gas number densities $\rho_{N_2}(T)$ serving as the conversion factor.

$$k_{(n,m)}^{abs} = \frac{k_{(n,m)}}{\rho_{N_2}(T)} \quad k_{-(n,m+1)}^{abs} = \frac{k_{-(n,m+1)}}{\rho_{N_2}(T)}$$

Approximate values for $\rho_{N_2}(T)$ are indirectly given by the pressure in the surrounding chamber p_c^{300K} and an effective geometry factor c_{app} .

$$\rho_{N_2}(T) = \frac{c_{app} \cdot p_c^{300K}}{k_B \cdot T_{300K}}$$

This geometry factor c_{app} shows a significant dependency on the temperature of the hexapole ion trap. We evaluated this factor to 1.8 at 26 K (uncertainty of $\pm 50\%$) by numerous of previous kinetic studies of transition metal cluster cations with neutral reactants at cryo temperatures. Three models are used for determination of collision rates. The average dipole orientation (ADO) theory is based on a concept of a classical trajectory of a linear dipole in the field of a point charge.

$$k_{coll} = \frac{q}{2\varepsilon_0\sqrt{\mu}} \cdot \left(\sqrt{\alpha} + c\mu_D \sqrt{\frac{2}{\pi k_B T}} \right)$$

Whereby μ is the reduced mass of the cluster adsorbate complex, μ_D stands for the dipole moment and α is the polarizability. The parameter c can take values from 0 to 1 and can be expressed by the polarizability of the neutral reactant, here N_2 . The volume α' and μ_D .⁶ It simplifies to the Langevin rate in the case of a negligible dipole moment. The ADO theory often underestimates the reaction rates for charged clusters with small molecules. Nevertheless, it is frequently used to calculate reaction rates for charged clusters with small molecules.⁷ Therefore, Kummerlöwe and Beyer⁸ devised two new models to determine collision rates of ionic clusters with neutral molecules. While the hard sphere average dipole orientation (HSA) model assumes a point charge in the center of the ionic cluster, the charge in the surface charge capture (SSC) theory is able to migrate to the cluster surface by its attractive interaction with the neutral collision partner.

For performing IR-PD experiments, a tunable IR laser ($\delta t = 7$ ns) is coupled into the ICR cell. This laser is comprised of a KTP/KTA optical parametric oscillator/amplifier (OPO/OPA. LaserVision) system pumped by a pulsed injection seeded Nd:YAG laser (10 Hz, PL8000,

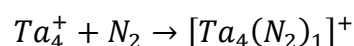
Continuum). To obtain IR radiation (1100 – 2400 cm⁻¹), an AgGaSe₂ crystal is used to generate the difference frequency (DF) between the OPA signal and idler waves. During irradiation with the IR laser, the ions are isolated and trapped in the ICR cell. Subsequently, every ion package is treated by 7 – 10 laser pulses (0.3 – 4.0 mJ/pulse) to yield sufficient fragment ions. A series of fragmentation mass spectra is recorded while continuously scanning the IR wavelength. The measured IR-PD signal is evaluated as $\sum_I F_I / (\sum_I F_I + \sum_I P_I)$, where F_I and P_I represent fragment and parent ion signal, respectively. Finally, the determined fragmentation efficiency is plotted as a function of laser frequency in order to obtain an IR-PD spectrum.

All quantum chemical calculations are carried out by the program package Gaussian 09⁹ and the Gaussian 16 suite¹⁰. We employed the PBE0 functional^{11, 12} for nonlocal corrections and the def2-TZVP basis set^{13, 14} for all atoms. We did so in continuation previous studies which have succeeded to model N₂ adsorption before, as e.g. in the cases of Rhodium clusters¹⁵ and Nickel clusters^{16, 17}. We did so in continuation of previous studies which have succeeded to model N₂ adsorption before, as e.g. in the cases of Rhodium clusters¹⁵ and Nickel clusters^{16, 17}. Moreover, we verified our choice of method by employing a multitude of available exchange correlation functionals, and CC2 calculations on top (cf. Fig. S8) along some part of the reaction path of initial N₂ activation along three local minima (I2_(4,1) and I3_(4,1) and P_{vic(4,1)}) and both intermediate transition states (TS23_(4,1) and TS3P_{vic(4,1)}). It shows that the optimized minimum structures and transition states are robust (for a survey of some critical geometric parameters refer to Table S15 in the supplement), as well as the relative energies by less than 30 kJ/mol (cf. Table S14). We take this as a valid gauge of the chosen level of theory, PBE0/def2-TZVP. All stationary states were checked by second derivative calculations revealing no (minima) and only one (transition state) imaginary frequency. Reaction paths were searched by QST2/3¹⁸ or linear transit methods¹⁹ and after location and optimization of the transition states scanned by IRC calculations.²⁰ Orbital analyses were performed using Molecular Orbitals as well as Natural Bonding Orbitals as employed in the Gaussian 16 program.^{21, 22}

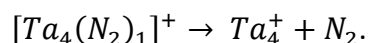
Text 2: Nomenclature for the Ta₄⁺ cluster and its adsorbates

There are 14 complexes of the form [Ta₄(N₂)_m]⁺, where *m* stands for the number of N₂ molecules attached to the cluster. The index *m* ranges from 0 to 13. For ease of reference, we use the notation (4,*m*). The 14 complexes are interlinked by 13 processes, respectively, in the form of adsorption and desorption reactions. The rate constants for these adsorption and desorption processes are labelled as *k_m* and *k_{-(m+1)}*. Therefore, *m* can assume values from 0 to 12.

We use e.g. *k₀* := *k_{0→1}* for the adsorption step:



and *k₋₁* := *k_{1→0}* for the desorption step:



To simplify the description of the products, we use the following subscript abbreviations for the relative positions of the resulting nitride ligands: gem (geminal, on the same Ta-Ta edge), vic (vicinal, on neighbored Ta-Ta edges), and dis (distal, on opposite edges of the Ta₄⁺ tetrahedron).

Text 3: Detailed discussion of the intermediate I1_(4,1)

According to an NBO analysis, there are minor contributions from 6s and 6p orbitals which we omit in further discussion. The Ta1 atom provides for five 5d electrons. It utilizes three of these to form three σ-bonds to the remaining three Ta atoms of the cluster. The Ta1 atom thereby experiences a local weak ML3 ligand field splitting of the 5d orbitals which destabilizes the thus empty d_{z²} orbital.²³ The remaining two d electrons fill the d_{xz} orbital. This d_{xz} orbital is a lone pair orbital at the Ta1 atom within the NBO framework. The N₂ ligand's lone pair donates towards the empty d_{z²} orbital which locates perpendicular to the (Ta1 Ta2 Ta3) plane. The bonding of the N₂ ligand to the Ta1 atom seems to increase the Ta1-Ta4 bond length from 2.52 Å in Ta₄⁺ to 2.72 Å in I1_(4,1), and the N₂ binding energy amounts to 66 kJ/mol (in the doublet state).

Text 4: Detailed discussion of the intermediate I_{2(4,1)}

The stabilization of I_{2(4,1)} with respect to I_{1(4,1)} is accompanied by a reduction of d(Ta1-N1) to 2.02 Å (-0.11 Å with respect to I_{1(4,1)}), an elongation of d(N1-N2) to 1.19 Å (+0.08 Å), and a tilting of the N₂ ligand towards Ta2. The result is a bridged μ_2 - κ N1: κ N1, κ N2 structure with d(Ta2-N1) = 2.12 Å (-1.00 Å with respect to I_{1(4,1)}) and d(Ta2-N2) = 2.18 Å (-1.80 Å). Note, that this coordination motif corresponds to a tantalum complex with a bridging N₂ unit that is coordinated both side on and end on^{23, 24}. Related complexes with I2 type bonding motifs were reported for Gd²⁵, Sc²⁶, and V²⁷. By the tilting, the distance d(Ta1-Ta4) in I_{2(4,1)} decreases to 2.56 Å (-0.16 Å with respect to I_{1(4,1)}) due to the diminished donation of the coordinating nitrogen lone pair electron density into the Ta1 T4 σ^* -antibonding orbital. In effect, the Ta1-Ta4 bond strengthens and the distance between the Ta atoms shrinks. Note, that at this point there are no Ta3-N1 and Ta3-N2 interactions.

Text 5: Detailed discussion of the intermediate I_{3(4,1)}

The structure of I_{3(4,1)} reveals the bridged μ_3 - κ N1: κ N1,N2: κ N1,N2 bonded nitrogen ligand which comprises an elongated N1-N2 bond of 1.43 Å (+0.24 Å with respect to I_{2(4,1)}). The Ta1-N1 distance has decreased to 1.92 Å (-0.10 Å), as well as the Ta2-N2 distances of 2.00 Å (-0.17 Å) and Ta3-N2 distance of 1.96 Å (-2.29 Å). The Ta2-Ta3 bond has elongated from 2.57 Å, I_{2(4,1)}, to 2.87 Å, I_{3(4,1)}, (+0.30 Å), and the Ta1-Ta3 bond from 2.56 Å, I_{2(4,1)}, to 2.92 Å, I_{3(4,1)}, (+0.36 Å); the charge density of both bonds dilutes significantly. In parallel, the N1-N2 bond elongates from 1.19 Å, I_{2(4,1)}, to 1.43 Å, I_{3(4,1)}, (+0.24 Å). Note, that this points to a mere N-N single bond distance as e.g. found in hydrazine²⁸ and related complexes (1.45 Å). Thus, the adaptive Ta₄⁺ cluster enables a bridged μ_3 coordination of N₂ (cf. I3 in Figure 3). The concomitant cleavage of the N₂ triple bond is accompanied by a relaxation of the Ta₄⁺ scaffold.

Text 6: Detailed discussion of the product P_{vic(4,1)}

The four Ta N bonds in P_{vic(4,1)} possess almost equal bond length on the order of 1.84 - 1.90 Å. Minor variations might originate from partial double and single bond characters. Accordingly, the two N bridged Ta1-Ta2 and Ta2-Ta3 bonds are equally elongated to 2.81 Å as compared to the non bridged Ta-Ta bonds, e.g. d(Ta1 Ta3) = 2.69 Å.

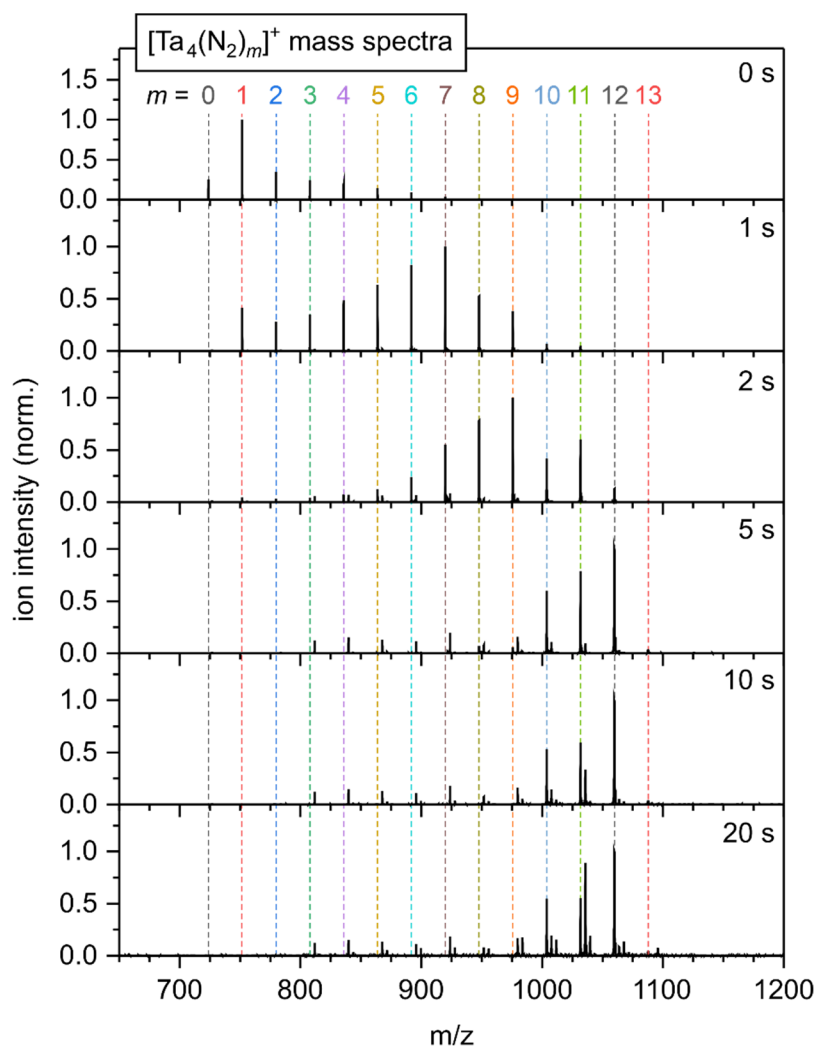


Fig. S1. Temporal evolution of the FT-ICR mass spectra of Ta_4^+ cluster complexes at 26 K and various storage times in the cryogenic hexapole ion trap exposed to an N_2 pressure of $2.6 \cdot 10^{-7}$ mbar. The least quantifiable maximum of N_2 adsorption to Ta_4^+ clusters from the carried-out measurement is 13 N_2 .

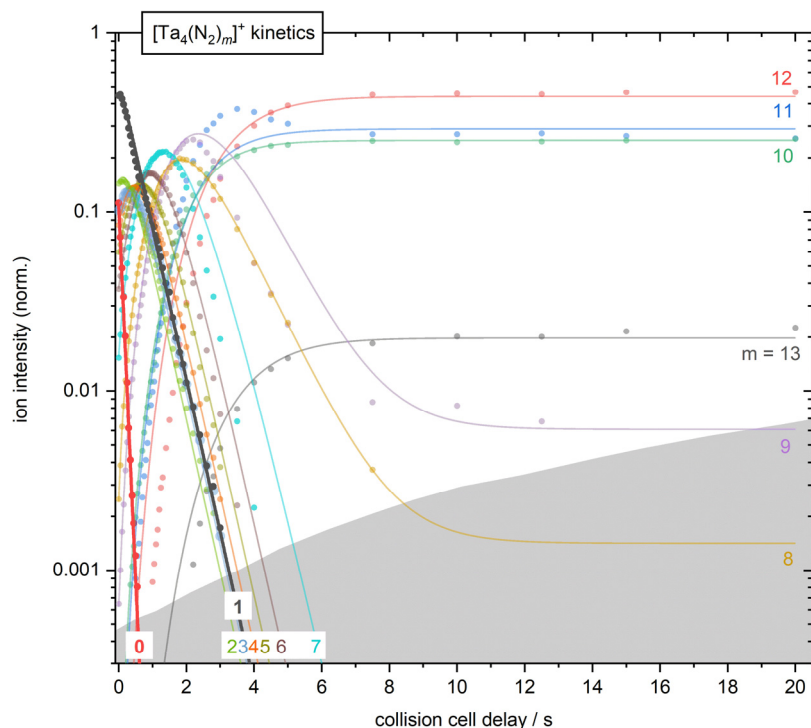


Fig. S2. Isothermal kinetics of N₂ adsorption by mass-selected Ta₄⁺ clusters at 26 K, He buffer gas ($6.8 \cdot 10^{-6}$ mbar) and an exposure of $2.6 \cdot 10^{-7}$ mbar N₂. The experimental data (solid dots) and the fits (solid lines) assume pseudo-first order kinetics for the N₂ adsorption in up to 13 consecutive steps. The kinetics of first and second N₂ adsorption are highlighted. The grey-shaded area indicates the background noise level. Corresponding rate constants of the pseudo-first order fits for each adsorption/desorption is shown in the Supporting Information (cf. Fig. S3)

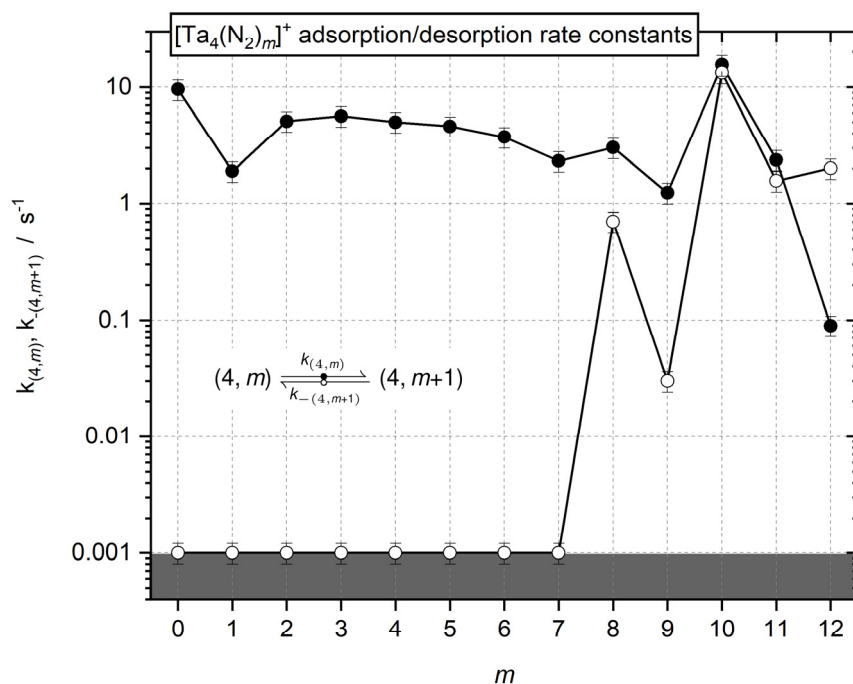


Fig. S3. Observed rate constants resulting from pseudo-first-order fits of measured kinetic data of the Ta_4^+ cluster complex as a function of stepwise N_2 adsorption. Filled circles show the rate of adsorption ($k_{(4,m)}$). Desorption rates ($k_{-(4,m+1)}$) are represented by open circles. The gray shaded area indicates the background noise level.

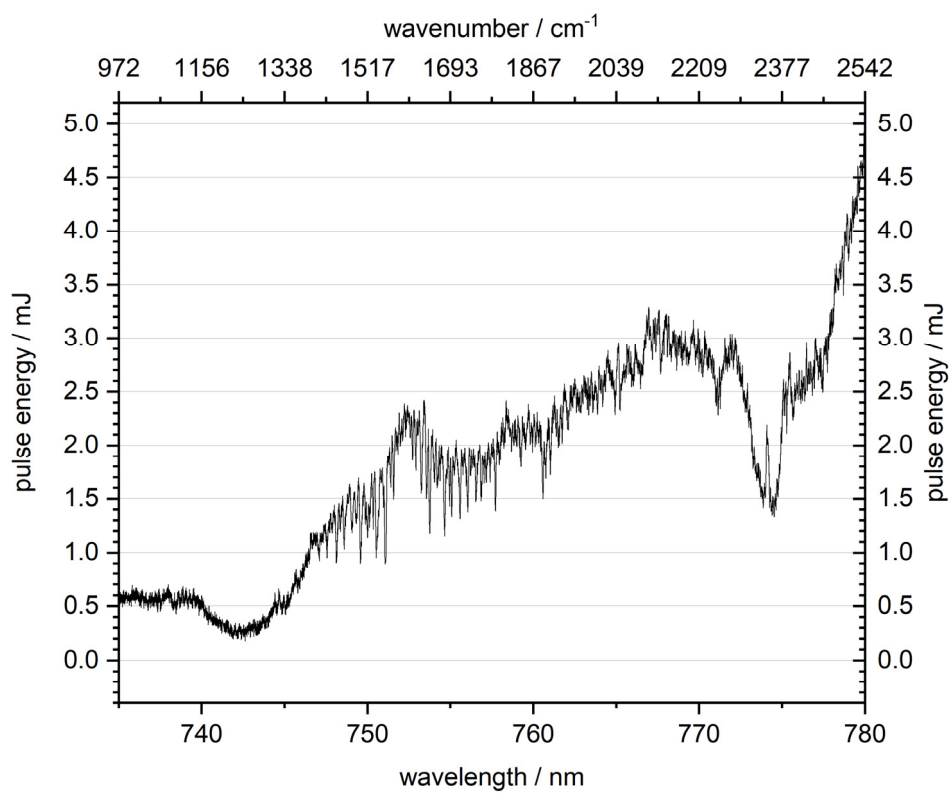


Fig. S4. Laser pulse energy in dependency of wavelength and wavenumber.

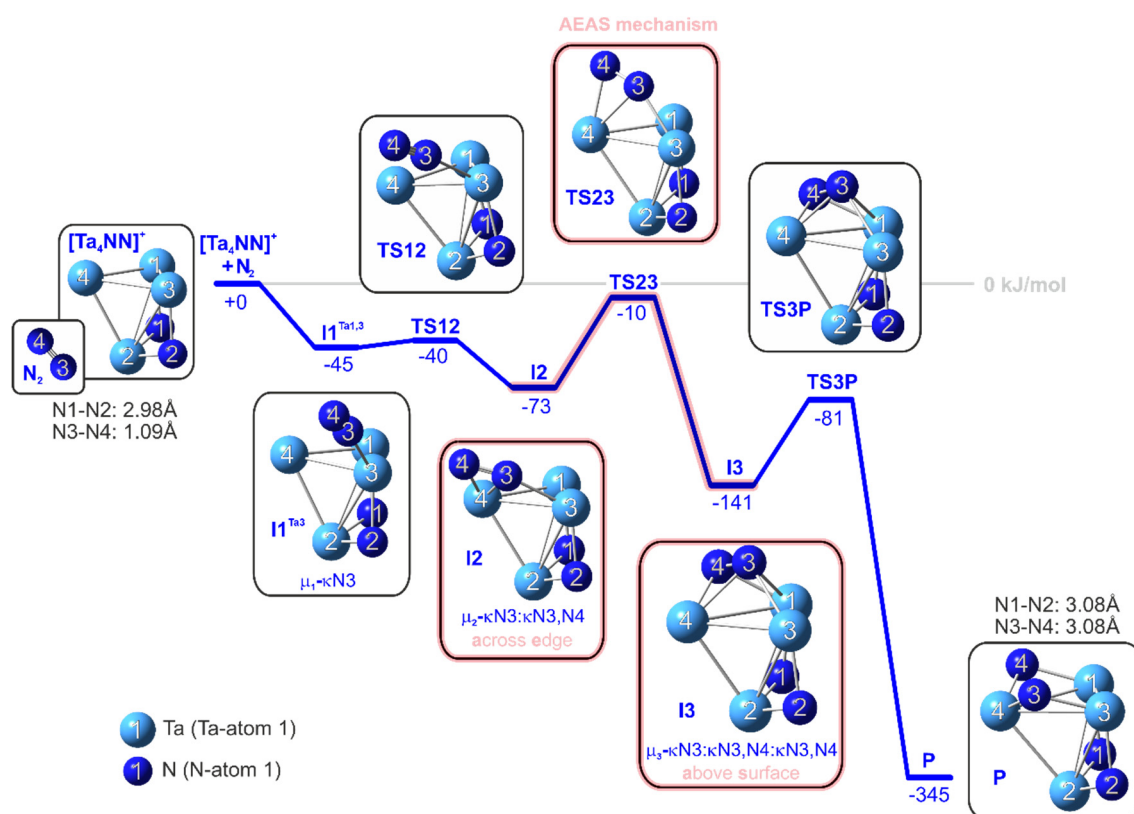


Fig. S5. A reaction pathway of second N₂ cleavage on a [Ta₄NN]⁺ cluster complex (adsorption site: Ta3). The torsional reorganization of the AEAS mechanism is highlighted. For reasons of clarity, the nomenclature is presented in a shortened form (e.g. here I1 stands for I1_(4,2) or rather I1^{Ta3}_(4,2)).

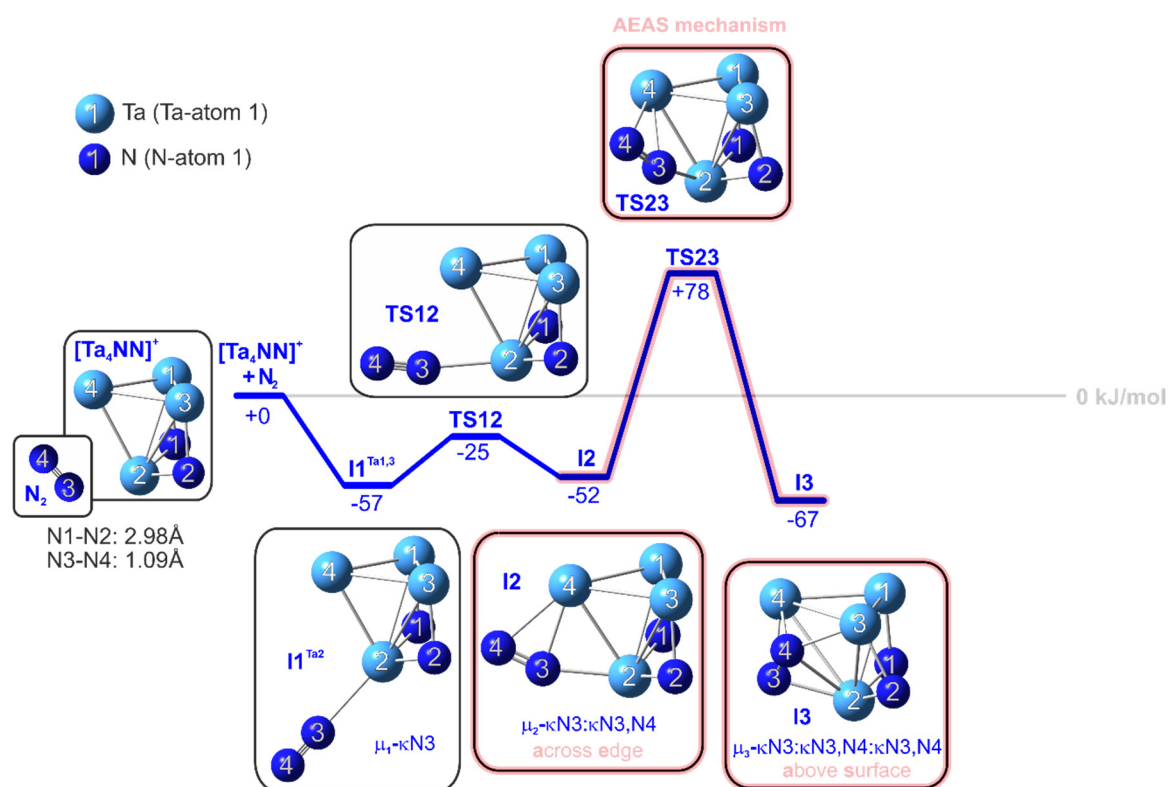


Fig. S6. A reaction pathway of second N₂ cleavage on a [Ta₄NN]⁺ cluster complex (adsorption site: Ta2). The torsional reorganization of the AEAS mechanism is highlighted. For reasons of clarity, the nomenclature is presented in a shortened form (e.g. here I1 stands for I1_(4,2) or rather I1^{Ta2}_(4,2)).

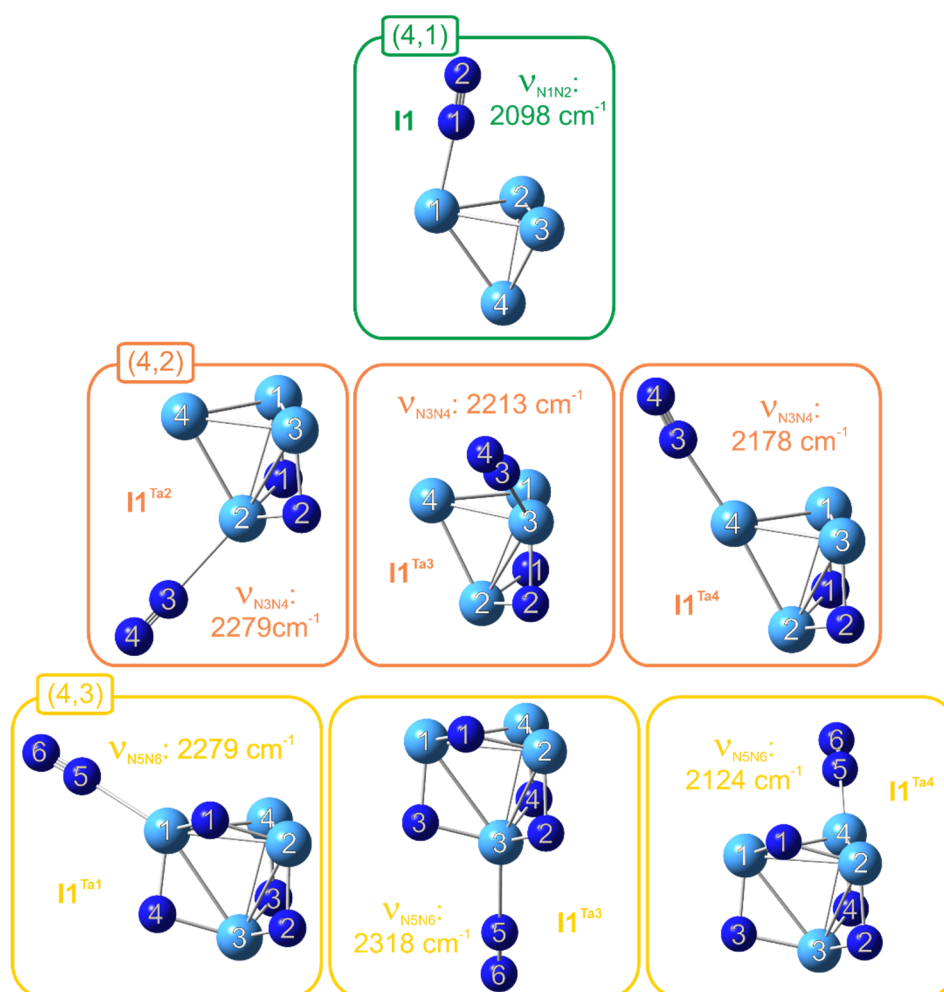


Fig. S7. Model structures with an end on bound N_2 molecule (μ_1 - η^1N_1 coordination) obtained from DFT calculations on the first, second and third N_2 activation pathway. Their scaled vibrational frequencies are within the range of 2100 cm^{-1} to 2300 cm^{-1} (scale factor: 0.9376).

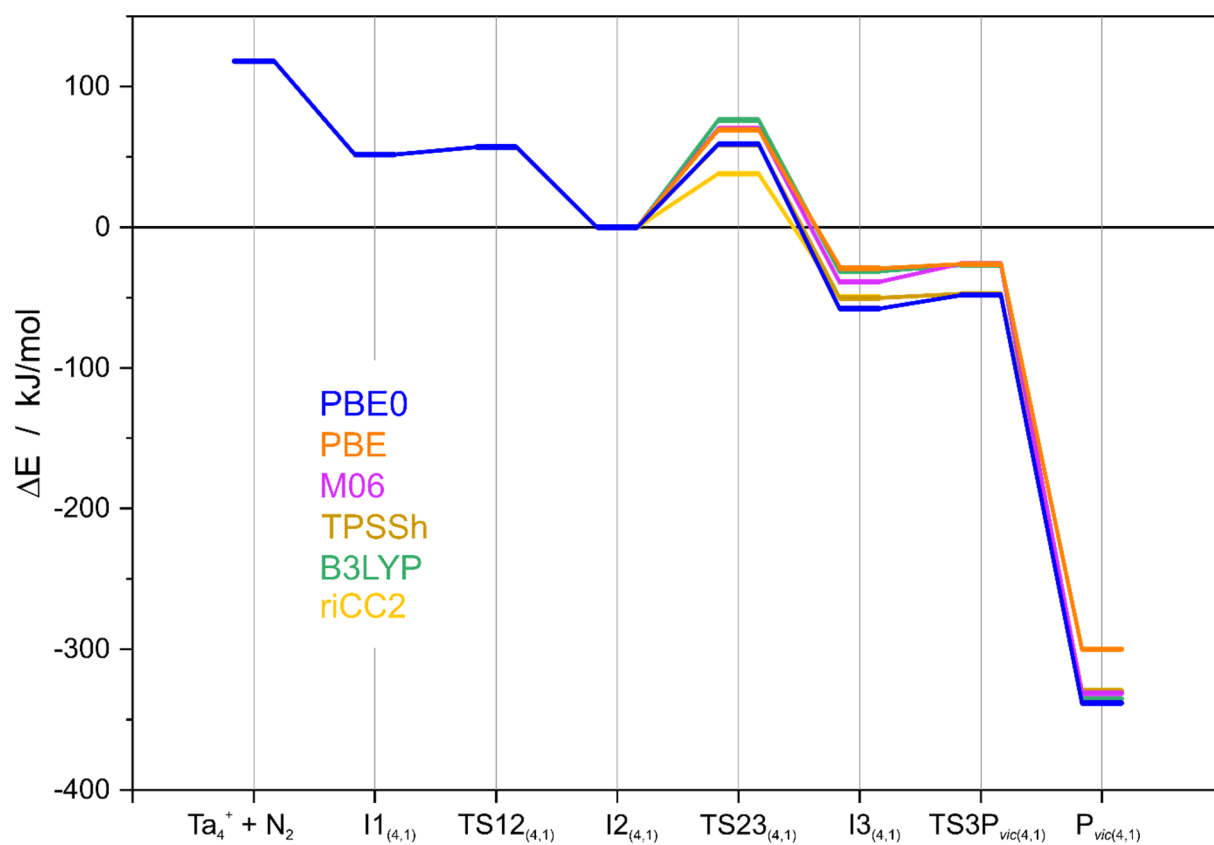


Fig. S8. Reaction path of initial N₂ activation in the case of (n,m)=(4,1) by DFT calculations with a multitude of exchange correlation functionals, and by CC2 calculations. For numerical values refer to Table S14.

Table S1. Relative pseudo-first-order rate constants, absolute rate constants, collision rates and sticking probabilities for the N₂ adsorption on (4,*m*) clusters at a N₂ pressure of $2.6 \cdot 10^{-7}$ mbar. Gray shaded elements highlight sticking probabilities $\gamma > 1$. Orange highlighted values are likely to be questionable as the limits of *evofit* (5) (fit program) have been exceeded.

$2.6 \cdot 10^{-7}$ mbar N₂				
<i>m</i>	$k_{\text{coll}}(4,m) / 10^{-16} \text{ m}^3/\text{s}$	$k_{(4,m)} / \text{s}^{-1}$	$k_{\text{abs}}(4,m) / 10^{-16} \text{ m}^3/\text{s}$	γ
0	6.00	9.58	8.48	1.41
1	6.00	1.88	1.67	0.28
2	5.99	5.10	4.51	0.75
3	5.99	5.65	5.00	0.84
4	5.99	5.01	4.43	0.74
5	5.98	4.60	4.07	0.68
6	5.98	3.72	3.29	0.55
7	5.98	2.31	2.05	0.34
8	5.97	3.02	2.67	0.45
9	5.97	1.23	1.09	0.18
10	5.97	15.43	13.7	2.29
11	5.97	2.37	2.09	0.35
12	5.96	0.09	0.08	0.01

8. Observation and mechanism of cryo N₂ cleavage by a tantalum cluster

Table S2. Calculated distances in Å of atoms within Ta₄⁺, N₂ and [Ta₄(N₂)₁]⁺ in the doublet state along the activation pathway of the first N₂ molecule on a Ta₄⁺ cluster complex.


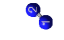
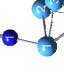









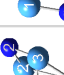

	[Ta ₄] ⁺	N ₂	I ₁ (_{4,1})	TS12(_{4,1})	I2(_{4,1})	TS23(_{4,1})	I3(_{4,1})	TS3P(_{4,1})vic	TS3P(_{4,1})gem	P(_{4,1})vic	TSP _{vic} P _{gem}	P(_{4,1})gem	TSP _{vic} P _{dis}	P(_{4,1})dis
														
Ta1-Ta2	2.64281		2.53029	2.53803	2.63597	2.58405	2.51053	2.9816	2.58642	2.80981	2.81177	2.54861	2.9854	2.65808
Ta2-Ta3	2.52474		2.54831	2.54441	2.57044	2.4606	2.87221	2.80459	2.9635	2.80852	3.05656	2.84528	2.80194	2.77209
Ta3-Ta4	2.55383		2.52596	2.54142	2.60882	2.51033	2.46294	2.55785	2.61668	2.58246	2.57717	2.5485	2.55304	2.65861
Ta1-Ta4	2.52494		2.72035	2.71223	2.55912	2.58949	2.5635	2.57129	2.46981	2.57679	2.55691	2.67861	2.60097	2.66287
Ta2-Ta4	2.52393		2.52819	2.51859	2.57036	2.77776	2.54261	2.44979	2.61663	2.61516	2.55519	2.54854	2.54783	2.65895
Ta1-Ta3	2.5242		2.53039	2.52825	2.55924	2.59023	2.91928	2.51185	2.58647	2.69019	2.66673	2.54863	2.67202	2.65872
Ta1-N1			2.12606	2.08579	2.0197	2.02836	1.91925	1.91264	2.43664	1.83777	1.85736	1.99248	1.8178	1.85619
Ta1-N2														
Ta2-N1			3.1238	2.51358	2.12104	2.16581	2.19976	2.10592	1.94684	1.89471	1.87219	2.00009	1.94786	
Ta2-N2			3.9722		2.17607	2.10638	2.00254	1.92269	1.96373	1.89543	1.95083	1.99998	1.87395	1.85724
Ta3-N1					3.61223		2.2019	2.29594	1.94692			2.00003		
Ta3-N2					4.24793		1.95998	1.9417	1.96381	1.83664	1.84741	1.99997	1.85766	1.85718
Ta4-N1														1.85593
Ta4-N2														
N1-N2		1.08948	1.10833	1.12038	1.18967	1.22901	1.43062	1.66522	1.83186	2.97767		1.99291		4.36624

Table S3. Calculated energies of the cluster adsorbate complex $[\text{Ta}_4(\text{N}_2)_1]^+$ in the doublet and quartet state along the activation pathway of the first N_2 molecule on a Ta_4^+ cluster complex.

	doublet state		quartet state	
	energy E / Ha	ΔE / kJ/mol	energy E / Ha	ΔE / kJ/mol
$\text{Ta}_4^+, \text{N}_2$	-337.05023	0	-337.035182	40
$\text{I1}_{(4,1)}$	-337.07549	-66	-337.054152	-10
$\text{TS12}_{(4,1)}$	-337.07342	-61	-337.050021	1
$\text{I2}_{(4,1)}$	-337.09514	-118	-337.074784	-64
$\text{TS23}_{(4,1)}$	-337.07269	-59	-337.056313	-16
$\text{I3}_{(4,1)}$	-337.11716	-176	-337.10029	-131
$\text{TS3P}_{vic(4,1)}$	-337.1135	-166	-337.094742	-117
$\text{P}_{vic(4,1)}$	-337.22397	-456	-337.192304	-373
$\text{TSP}_{vic} \text{P}_{dis(4,1)}$	-337.20507	-407	-337.175449	-329
$\text{P}_{dis(4,1)}$	-337.22438	-457	-337.205372	-407
$\text{TSP}_{gem} \text{P}_{vic(4,1)}$	-337.20852	-416	-337.17545	-329
$\text{TS3P}_{gem(4,1)}$	-337.09007	-105	-337.05264	-6
$\text{P}_{gem(4,1)}$	-337.22681	-464	-337.179527	-339

Table S4. Calculated NPA charges in electrons (e) of atoms within I3_(4,1), TS3P_{(4,1)vic} and P_{(4,1)vic} in the doublet state.

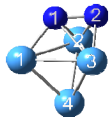


	I3 _(4,1)	TS3P _{(4,1)vic}	P _{(4,1)vic}
			
Ta1	0.61512	0.60802	0.68992
Dif. *I3		-0.0071	0.0748
Dif. *TS3P_{(4,1)vic}			0.0819
Ta2	0.76117	0.85803	1.01663
Dif. *I3		0.09686	0.25546
Dif. *TS3P_{(4,1)vic}			0.1586
Ta3	0.67714	0.68491	0.69468
Dif. *I3		0.00777	0.01754
Dif. *TS3P_{(4,1)vic}			0.00977
Ta4	0.05111	0.04651	0.1791
Dif. *I3		-0.0046	0.12799
Dif. *TS3P_{(4,1)vic}			0.13259
N1	-0.57428	-0.64387	-0.78987
Dif. *I3		-0.06959	-0.21559
Dif. *TS3P_{(4,1)vic}			-0.146
N2	-0.53027	-0.5536	-0.79046

Table S5. Calculated energies of the cluster adsorbate complex $[\text{Ta}_4(\text{N}_2)_2]^+$ in the doublet state along the activation pathway of the second N_2 molecule depending on the adsorption site (Ta2, Ta3 or Ta4) to the $[\text{Ta}_4\text{NN}]^+$ cluster complex.

	N ₂ adsorption on Ta3		N ₂ adsorption on Ta4		N ₂ adsorption on Ta2	
	energy E / Ha	ΔE / kJ/mol	energy E / Ha	ΔE / kJ/mol	energy E / Ha	ΔE / kJ/mol
$[\text{Ta}_4\text{NN}]^+, \text{N}_2$	-446.67025	0	-446.67025	0	-446.67025	0
I1 _(4,2)	-446.68723	-45	-446.68591	-41	-446.69202	-57
TS12 _(4,2)	-446.68534	-40	-446.67966	-25	-446.68012	-26
I2 _(4,2)	-446.69788	-73	-446.70842	-100	-446.68996	-52
TS23 _(4,2)	-446.67392	-10	-446.68283	-33	-446.64057	78
I3 _(4,2)	-446.72388	-141	-446.73011	-157	-446.69561	-67
TS3P _(4,2)	-446.70106	-81	-446.71585	-120		
P _(4,2)	-446.80153	-345	-446.81452	-379		

8. Observation and mechanism of cryo N₂ cleavage by a tantalum cluster

Table S6. Calculated distances in Å of atoms within [Ta₄NN]⁺ (P_{vic(4,1)}), N₂ and [Ta₄(N₂)₂]⁺ in the doublet state along the activation pathway of the second N₂ molecule on a [Ta₄NN]⁺ cluster complex at the adsorption site Ta3.

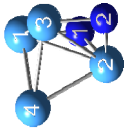





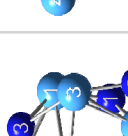
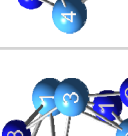

									
	P _{vic(4,1)}	N ₂	I _{1(4,2)}	TS _{12(4,2)}	I _{2(4,2)}	TS _{23(4,2)}	I _{3(4,2)}	TS _{3P(4,2)}	P _(4,2)
Ta1-Ta2	2.80981		2.82055	2.81846	2.81562	2.79044	2.84153	2.83419	2.86942
Ta2-Ta3	2.80852		2.81321	2.8097	2.83041	2.77281	2.7486	2.74203	2.86981
Ta3-Ta4	2.58246		2.58503	2.57503	2.62351	2.72479	2.61416	2.6479	2.86977
Ta1-Ta4	2.57679		2.56888	2.55941	2.61602	2.61317	2.9945	2.9591	2.86938
Ta2-Ta4	2.61516		2.63087	2.62885	2.66096	2.79316	2.7182	2.75419	2.75944
Ta1-Ta3	2.69019		2.71185	2.72558	2.73453	2.66141	2.65038	2.6742	2.75968
Ta1-N1	1.83777		1.83769	1.83437	1.83017	1.81963	1.86045	1.86293	1.87286
Ta1-N3							2.14574	2.31351	
Ta1-N4							1.98228	1.89827	1.87311
Ta2-N1	1.89471		1.89627	1.89915	1.90254	1.92068	1.90306	1.89545	1.87305
Ta2-N2	1.89543		1.88368	1.87654	1.88278	1.837	1.8778	1.87783	1.87285
Ta3-N2	1.83664		1.85651	1.86706	1.85636	1.92233	1.87172	1.87342	1.87306
Ta3-N3			2.30132	2.15797	2.06218	2.00033	2.1264	2.10443	1.87283
Ta4-N3					2.13317	2.1527	2.0368	1.88939	1.87309
Ta4-N4				3.37324	2.24011	1.96456	1.98694	2.02749	1.87284
N1-N2	2.97767		2.98932	2.98721	2.99665	3.06684	3.1244	3.10173	3.08235
N3-N4		1.08948	1.09618	1.11553	1.17958	1.26022	1.44534	1.86585	3.08214

Table S7. Calculated distances in Å of atoms within $[\text{Ta}_4\text{NN}]^+$ ($P_{vic(4,1)}$), N_2 and $[\text{Ta}_4(\text{N}_2)_2]^+$ in the doublet state along the activation pathway of the second N_2 molecule on a $[\text{Ta}_4\text{NN}]^+$ cluster complex at the adsorption site Ta4.

	$P_{vic(4,1)}$	N_2	$\text{I1}_{(4,2)}$	$\text{TS12}_{(4,2)}$	$\text{I2}_{(4,2)}$	$\text{TS23}_{(4,2)}$	$\text{I3}_{(4,2)}$	$\text{TS3P}_{(4,2)}$	$\text{P}_{(4,2)}$
Ta1-Ta2	2.80981		2.83727	2.81923	2.84027	2.79306	2.82791	2.83734	2.89667
Ta2-Ta3	2.80852		2.83709	2.81664	2.81509	2.77074	2.82787	2.81818	2.89051
Ta3-Ta4	2.58246		2.58158	2.58516	2.65604	2.66614	2.61228	2.62146	2.80618
Ta1-Ta4	2.57679		2.58141	2.5747	2.60394	2.57583	2.61193	2.67172	2.73099
Ta2-Ta4	2.61516		2.72586	2.69287	2.68509	2.71478	2.6901	2.7219	2.73246
Ta1-Ta3	2.69019		2.67366	2.68907	2.72829	2.73086	3.13204	3.03091	2.88981
Ta1-N1	1.83777		1.84822	1.84722	1.83673	1.821	1.86045	1.87169	1.87684
Ta1-N3							2.00934	2.26048	
Ta1-N4							2.16871	1.91141	1.85197
Ta2-N1	1.89471		1.88124	1.88215	1.8974	1.91623	1.88128	1.87141	1.87634
Ta2-N2	1.89543		1.88112	1.90161	1.86633	1.86	1.88118	1.86907	1.85192
Ta3-N2	1.83664		1.84818	1.83024	1.87476	1.89818	1.86052	1.87643	1.90732
Ta3-N3				2.78782	2.13583	2.16181	2.16863	2.17606	193905
Ta3-N4					2.13585	2.18539	2.00921	1.9844	1.90715
Ta4-N3			2.28513	2.14424	2.01852	1.94927	1.94453	1.85692	1.82058
N1-N2	2.97767		3.0311	3.02961	3.00888	2.98675	3.04954	3.01691	2.97204
N3-N4		1.08948	1.09805	1.1171	1.19908	1.22114	1.45082	1.88124	3.22509

8. Observation and mechanism of cryo N₂ cleavage by a tantalum cluster

Table S8. Calculated distances in Å of atoms within [Ta₄NN]⁺ (P_{vic(4,1)}), N₂ and [Ta₄(N₂)₂]⁺ in the doublet state along the activation pathway of the second N₂ molecule on a [Ta₄NN]⁺ cluster complex at the adsorption site Ta₂.



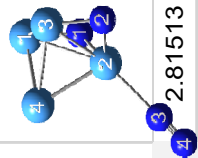

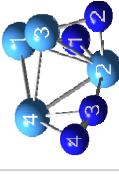


	P _{vic(4,1)}	N ₂	I1 _(4,2)	TS12 _(4,2)	I2 _(4,2)	TS23 _(4,2)	I3 _(4,2)
							
Ta1-Ta2	2.80981		2.81513	2.78882	2.79645	2.79156	2.80208
Ta2-Ta3	2.80852		2.81529	2.78883	2.79699	2.77467	2.6197
Ta3-Ta4	2.58246		2.58552	2.58659	2.63276	2.52906	2.95895
Ta1-Ta4	2.57679		2.58532	2.58658	2.63207	2.64573	2.582
Ta2-Ta4	2.61516		2.62512	2.62782	2.68194	2.65112	3.06341
Ta1-Ta3	2.69019		2.70673	2.70501	2.68166	2.7193	2.71683
Ta1-N1	1.83777		1.83311	1.83438	1.84518	1.8294	1.861
Ta2-N1	1.89471		1.90516	1.91897	1.9048	1.91194	1.88476
Ta2-N2	1.89543		1.90542	1.91897	1.90526	1.89714	1.9482
Ta2-N3			2.36296	2.14761	2.07339	2.19879	2.01995
Ta2-N4							2.39541
Ta3-N2	1.83664		1.83295	1.83437	1.84477	1.83515	1.83541
Ta3-N4							1.97752
Ta4-N3				2.60943	2.13529	2.13624	1.97593
Ta4-N4					2.2617	2.25311	2.01989
N1-N2	2.97767		3.01154	3.15922	3.19045	2.8922	3.14599
N3-N4		1.08948	1.09143	1.12419	1.18514	1.17595	1.43254

Table S9. Calculated distances in Å of atoms within $[\text{Ta}_4\text{NNNN}]^+$ ($\text{P}_{(4,2)}$), N_2 and $[\text{Ta}_4(\text{N}_2)_3]^+$ in the doublet state along the activation pathway of the third N_2 molecule on a $[\text{Ta}_4\text{NNNN}]^+$ cluster complex.

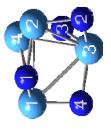
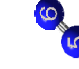
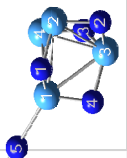
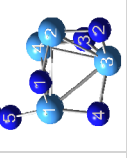
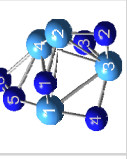
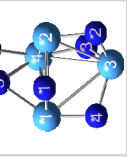
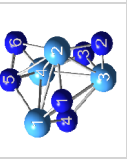
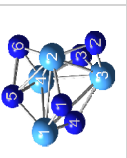
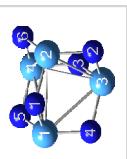
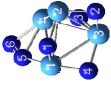
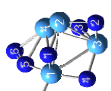
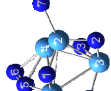

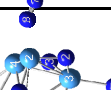
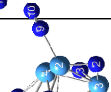
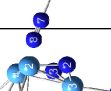
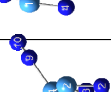

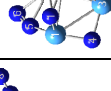

	$\text{P}_{(4,2)}$	N_2	$\text{I1}_{(4,3)}$	$\text{TS12}_{(4,3)}$	$\text{I2}_{(4,3)}$	$\text{TS23}_{(4,3)}$	$\text{I3}_{(4,3)}$	$\text{TS3P}_{(4,3)}$	$\text{P}_{(4,3)}$
									
Ta1-Ta2	2.89667		2.90994	2.87769	2.93005	2.85026	2.72582	2.76575	3.0643
Ta2-Ta3	2.89051		2.90311	2.92722	2.98695	3.01501	2.88929	2.86835	3.06265
Ta3-Ta4	2.80618		2.8047	2.82866	2.83734	2.94419	2.54255	2.57789	3.06413
Ta1-Ta4	2.73099		2.72676	2.71213	2.75695	2.67934	2.85667	2.9236	3.06575
Ta2-Ta4	2.73246		2.75834	2.76559	2.8308	2.75024	2.93891	2.89893	3.06486
Ta1-Ta3	2.88981		2.88935	2.83791	2.85544	3.05579	3.37458	3.38825	3.06333
Ta1-N1	1.87684		1.90147	1.906	1.90697	1.90828	1.83387	1.83147	1.88945
Ta1-N4	1.85197		1.85296	1.88849	1.87502	1.88057	1.97257	1.9503	1.8892
Ta1-N5			2.35714	2.18602	2.0513	2.18602	1.91426	1.89104	1.88959
Ta2-N1	1.87634		1.86135	1.86241	1.85264	1.85229	1.95201	1.96964	1.88959
Ta2-N2	1.85192		1.85731	1.85202	1.84419	1.85237	1.8486	1.85811	1.88944
Ta2-N5							2.34129	2.37533	
Ta2-N6							2.1297	2.04184	1.88967
Ta3-N2	1.90732		1.90617	1.9099	1.91809	1.89812	1.92122	1.91462	1.88953
Ta3-N3	1.93905		1.94295	1.94474	1.91172	1.87877	1.86091	1.85886	1.8894
Ta3-N4	1.90715		1.90975	1.89442	1.90933	1.88815	2.08733	2.04167	1.8898
Ta4-N3	1.82058		1.81801	1.81703	1.85547	1.88415	1.91334	1.91923	1.88949
Ta4-N5					2.1355	2.20318	2.16554	2.13948	1.88935
Ta4-N6					2.12976	2.20298	2.02923	1.94534	1.88927
N1-N2	2.97204		2.98615	2.99346	3.00743	2.7984	2.89833	2.94792	3.09657
N3-N4	3.22509		3.22173	3.23665	3.21198	3.09707	2.79033	2.79851	3.0969
N5-N6		1.08948	1.09095	1.11783	1.20694	1.2035	1.38899	1.86645	3.09568

Table S10. Calculated energies of the cluster adsorbate complex [Ta₄(N₂)₃]⁺ in the doublet state along the activation pathway of the third N₂ molecule to the [Ta₄NNNN]⁺ cluster complex.

	energy E / Ha	ΔE in kJ/mol
[Ta₄NNNN]⁺, N₂	-556.2608	0
I1_(4,3)	-556.28521	-64
TS12_(4,3)	-556.26904	-22
I2_(4,3)	-556.29382	-87
TS23_(4,3)	-556.23984	55
I3_(4,3)	-556.28957	-76
TS3P_(4,3)	-556.25859	6
P_(4,3)	-556.35682	-252

Table S11. Calculated energies and vibrational frequencies of model systems (scaling factor: 0.9376).

	$Ta_4(N_2)_3^+$ I2 (4,3)	$[Ta_4(N_2)_4]^+$			$[Ta_4(N_2)_5]^+$						
		(4,4) ₀₀₀ *Ta1	(4,4) ₀₀₁ *Ta2	(4,4) ₀₀₂ *Ta4	(4,4) ₀₀₃ *Ta3	(4,5) ₀₀₀ *Ta1 *Ta2	(4,5) ₀₀₂ *Ta1 *Ta3	(4,5) ₀₀₁ *Ta1 *Ta4	(4,5) ₀₂₀ *Ta4 *Ta3	(4,5) ₀₁₁ *Ta2 *Ta3	(4,5) ₀₁₀ *Ta2 *Ta4
											
energy E / Ha	-556.29382	-665.76333	-665.76489	-665.76475	-665.76465	-775.2347	-775.23182	-775.23465	-775.23487	-775.23609	-775.23499
energy E / kJ/mol		-1747961.382	-1747965.478	-1747965.11	-1747964.848	-2035378.424	-2035370.863	-2035378.293	-2035378.871	-2035382.074	-2035379.186
$\nu(N-N)_i / cm^{-1}$	1516.31	1473.52	1517.75	1490.68	1475.3	1474.1	1458.64	1423.29	1414.9	1478.16	1475.63
$\nu(N-N)_{i,scal} / cm^{-1}$	1422	1382	1423	1398	1383	1382	1368	1334	1327	1386	1384
$\nu(N-N)_{i,j} / cm^{-1}$		2481.53	2461.79	2403.02	2492.59	2481.4	2480.81	2476.65	2406.97	2415	2476.27
$\nu(N-N)_{i,j,scal} / cm^{-1}$		2326.615362	2308.107672	2253.006511	2336.984918	2326.493477	2325.940309	2322.040006	2256.709924	2264.238634	2321.683728
$\nu(N-N)_{i,j,k} / cm^{-1}$											
$\nu(N-N)_{i,j,k,l} / cm^{-1}$						2423.01	2491.86	2405.77	2488.26	2492.84	2399.66
$\nu(N-N)_{i,j,k,l,m} / cm^{-1}$						2271.748594	2336.30049	2255.584836	2332.925228	2337.219312	2249.856266

8. Observation and mechanism of cryo N₂ cleavage by a tantalum cluster

Table S12. Calculated distances in Å of atoms within model systems in the doublet state.

	Ta ₄ (N ₂) ₂ ⁺ I _{2(C2)}		[Ta ₄ (N ₂) ₂] ⁺				[Ta ₄ (N ₂) ₂] ⁺					
	(4A) _{top} -Ta1	(4A) _{bot} -Ta2	(4A) _{bot} -Ta3	(4A) _{bot} -Ta4	(4A) _{top} -Ta1	(4A) _{top} -Ta2	(4A) _{top} -Ta3	(4A) _{top} -Ta4	(4B) _{top} -Ta1	(4B) _{top} -Ta2	(4B) _{top} -Ta3	(4B) _{top} -Ta4
Ta1-Ta2	2.93005	2.9226	2.91401	2.93769	2.94426	2.92393	2.91832	2.97832	2.92776	2.88943	2.93332	
Ta2-Ta3	2.96695	2.976	3.02814	2.97279	2.92539	2.96623	2.93948	2.93948	3.02048	3.00167	2.96424	
Ta3-Ta4	2.83734	2.84709	2.88121	2.87449	2.83563	2.87097	2.83913	2.87097	2.91576	2.90965	2.88324	
Ta1-Ta4	2.75695	2.77777	2.73511	2.81087	2.82988	2.79881	2.89861	2.78023	2.78023	2.76349	2.8256	
Ta2-Ta4	2.8308	2.83143	2.85005	2.85005	2.80704	2.82047	2.81862	2.82047	2.82894	2.81037	2.85432	
Ta1-Ta3	2.85544	2.86735	2.86287	2.84287	2.92278	2.95135	2.92159	2.92159	2.9092	2.93339	2.85337	
Ta1-N1	1.90697	1.9046	1.91042	1.90687	1.90379	1.91529	1.90649	1.91529	1.91203	1.90209	1.90545	
Ta1-N4	1.87502	1.87602	1.88034	1.87158	1.87555	1.87698	1.87425	1.87425	1.88098	1.88406	1.87392	
Ta1-N5	2.0513	2.05057	2.04029	2.05122	2.0344	2.031	2.03136	2.03477	2.02038	2.03581	2.04593	
Ta2-N1	1.85264	1.86394	1.85238	1.85562	1.87465	1.85735	1.86201	1.85336	1.85336	1.87002	1.8647	
Ta2-N2	1.84419	1.8562	1.8521	1.84425	1.86459	1.86124	1.84785	1.85194	1.85194	1.87132	1.8522	
Ta2-N7		2.37603								2.32757	2.39398	
Ta2-N9					2.33544							
Ta3-N2	1.91609	1.91333	1.91584	1.91986	1.90728	1.90737	1.91846	1.90478	1.91658	1.90478	1.9188	
Ta3-N3	1.91172	1.91408	1.90912	1.91217	1.91959	1.91035	1.91568	1.91285	1.9078	1.91285	1.91335	
Ta3-N4	1.90933	1.91261	1.91061	1.91253	1.91165	1.91806	1.91141	1.90943	1.90751	1.90943	1.91301	
Ta3-N7			2.38548									
Ta3-N9						2.39766			2.38438	2.3876		
Ta4-N3	1.85547	1.85431	1.86258	1.85345	1.85038	1.86262	1.8541	1.85856	1.86273	1.85856	1.85403	
Ta4-N5	2.1355	2.13841	2.11912	2.1306	2.13757	2.1166	2.122	2.12673	2.10771	2.12673	2.13181	
Ta4-N6	2.12976	2.1243	2.10878	2.17063	2.11489	2.10592	2.16231	2.10529	2.143	2.10529	2.16701	
Ta4-N7				2.2843					2.28743			
Ta4-N9							2.28335				2.28658	
N5-N6	1.20694	1.20768	1.21869	1.20584	1.21592	1.22442	1.21875	1.22772	1.22772	1.21933	1.20793	
N7-N8	1.08862	1.8956	1.08629	1.09306	1.08882	1.08881	1.08908	1.09223	1.09308	1.08908	1.08903	
N8-N10					1.09173	1.08817	1.09311	1.08834	1.08834	1.08818	1.09319	

Table S13. Calculated NPA charges in electrons (e) of atoms within model systems in the doublet state.

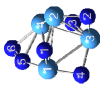
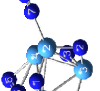
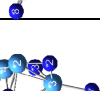
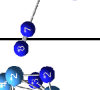
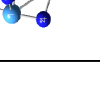

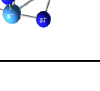
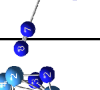
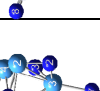
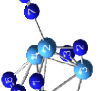
	$[\Gamma_{Ta_1}(N_2)]_d^+$		$[\Gamma_{Ta_1}(N_2)]_d^+$				$[\Gamma_{Ta_1}(N_2)]_d^+$			
	$(4,4)_{\mu 01} \text{Ta1}$	$(4,4)_{\mu 02} \text{Ta2}$	$(4,4)_{\mu 02} \text{Ta4}$	$(4,4)_{\mu 03} \text{Ta3}$	$(4,5)_{\mu 00} \text{Ta1-Ta2}$	$(4,5)_{\mu 02} \text{Ta1-Ta3}$	$(4,5)_{\mu 01} \text{Ta1-Ta4}$	$(4,5)_{\mu 02} \text{Ta4-Ta3}$	$(4,5)_{\mu 11} \text{Ta2-Ta3}$	$(4,5)_{\mu 10} \text{Ta2-Ta4}$
										
	npa	npa	npa	npa	npa	npa	npa	npa	npa	npa
Ta1	1.516	1.527	1.532	1.507	1.458	1.445	1.468	1.544	1.534	1.538
Ta2	1.336	1.209	1.34	1.324	1.182	1.295	1.328	1.33	1.19	1.221
Ta4	1.069	1.093	0.963	1.086	1.133	1.092	0.978	0.999	1.123	0.986
Ta3	1.757	1.757	1.735	1.677	1.738	1.668	1.726	1.676	1.686	1.732
N4	-1.022	-1.028	-1.017	-1.022	-1.027	-1.024	-1.017	-1.021	-1.031	-1.023
N3	-1.003	-1.007	-0.988	-1.001	-1.003	-0.998	-0.985	-0.988	-1.004	-0.991
N2	-1.014	-1.019	-1.013	-1.021	-1.021	-1.022	-1.016	-1.02	-1.026	-1.017
N1	-0.988	-0.996	-0.996	-0.991	-1.001	-0.994	-1.002	-0.999	-0.999	-1.002
N5	-0.426	-0.428	-0.433	-0.451	-0.438	-0.455	-0.455	-0.486	-0.454	-0.437
N6	-0.224	-0.23	-0.207	-0.251	-0.256	-0.267	-0.241	-0.257	-0.256	-0.218
N7		-0.118	-0.123	-0.103	-0.102	-0.098	-0.101	-0.114	-0.125	-0.11
N8		0.235	0.204	0.244	0.233	0.222	0.232	0.196	0.222	0.24
N9					-0.121	-0.1	-0.114	-0.1	-0.103	-0.117
N10					0.225	0.237	0.199	0.241	0.244	0.198

Table S14. Total energies of the activation pathway of the first N₂ molecule in the doublet state from I₂ to P_{vic} by DFT with various functionals. These values are visualized in Fig. S8.

		I _{2(4,1)}	TS _{23(4,1)}	I _{3(4,1)}	TS _{3P_{vic}(4,1)}	P _{vic(4,1)}
B3LYP	energy E / Ha	-337.320685	-337.292027	-337.332639	-337.331014	-337.448346
	ΔE / kJ/mol	0.000000	75.241579	-31.385227	-27.118789	-335.173955
PBE	energy E / Ha	-337.345128	-337.318768	-337.356264	-337.355091	-337.459392
	ΔE / kJ/mol	0.000000	69.208180	-29.237568	-26.157857	-300.000132
M06	energy E / Ha	-337.094349	-337.067648	-337.109171	-337.104272	-337.220527
	ΔE / kJ/mol	0.000000	70.103476	-38.915161	-26.052836	-331.280339
TPSSh	energy E / Ha	-337.266114	-337.243832	-337.285250	-337.284140	-337.391540
	ΔE / kJ/mol	0.000000	58.501391	-50.241568	-47.327263	-329.305963
PBE0	energy E / Ha	-337.095144	-337.072693	-337.117157	-337.113500	-337.223969
	ΔE / kJ/mol	0.000000	58.945100	-57.795132	-48.193678	-338.230038
riCC2	energy E / Ha	-336.227918	-336.213484	-336.246759		
	ΔE / kJ/mol	0.000000	37.896118	-49.467877		

Table S15. Calculated distances in Å of atoms within in the doublet state along the activation pathway of the first N₂ molecule from I_{2(4,1)} to P_{vic(4,1)}.









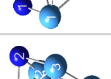
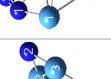
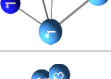








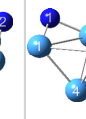



	B3LYP				PBE				M06						
	I _{2(4,1)}	TS23 _(4,1)	I3 _(4,1)	TS3P _{vic(4,1)}	P _{vic(4,1)}	I _{2(4,1)}	TS23 _(4,1)	I3 _(4,1)	TS3P _{vic(4,1)}	P _{vic(4,1)}	I _{2(4,1)}	TS23 _(4,1)	I3 _(4,1)	TS3P _{vic(4,1)}	P _{vic(4,1)}
															
Ta1-Ta2	2.65984	2.63563	2.97672	3.02459	2.84429	2.65862	2.59166	2.97877	3.01261	2.82649	2.65692	2.6092	2.95716	2.99994	2.82557
Ta2-Ta3	2.59167	2.45614	2.90466	2.85321	2.84454	2.5881	2.44783	2.88381	2.83954	2.82677	2.59247	2.45758	2.8774	2.81735	2.82581
Ta3-Ta4	2.62905	2.8013	2.56689	2.57968	2.60001	2.61793	2.55439	2.55891	2.56915	2.59076	2.62944	2.56406	2.56521	2.57954	2.6024
Ta1-Ta4	2.58104	2.5907	2.5904	2.59877	2.59902	2.58246	2.5921	2.57583	2.58239	2.58962	2.58096	2.60473	2.58755	2.593	2.60213
Ta2-Ta4	2.59164	2.5786	2.48043	2.46998	2.64218	2.58799	2.78616	2.47428	2.46988	2.6206	2.59237	2.77211	2.4764	2.47438	2.63388
Ta1-Ta3	2.58115	2.60688	2.5343	2.53295	2.72281	2.58259	2.61781	2.52506	2.52819	2.71311	2.58101	2.61794	2.52864	2.53773	2.72331
Ta1-N1	2.04537	2.04236	1.92841	1.92436	1.85094	2.02556	2.05497	1.94026	1.93317	1.85581	2.04112	2.02827	1.92427	1.90896	1.83591
Ta1-N2															
Ta2-N1	2.15814	2.35143	2.23764	2.15198	1.90701	2.15173	2.23917	2.22235	2.15608	1.9148	2.135	2.18804	2.20343	2.11612	1.8977
Ta2-N2	2.21616	2.42092	1.97115	1.93923	1.9078	2.1951	2.15171	1.96937	1.94022	1.91558	2.19197	2.12912	1.95865	1.91728	1.89802
Ta3-N1			2.23483	2.31594				2.23401	2.30126				2.21046	2.30258	
Ta3-N2			2.01518	1.96782	1.85043			2.02674	1.97954	1.85534			2.00475	1.94323	1.83568
N1-N2	1.18745	1.24672	1.454	1.6375	1.20733	1.25761	1.46239	1.63096	1.63096	1.18614	1.24254	1.43319	1.69166		

Table S16. Calculated distances in Å of atoms within in the doublet state along the activation pathway of the first N₂ molecule from I_{2(4,1)} to P_{vic(4,1)}.

	TPSSh					riCC2		
	I _{2(4,1)}	TS23 _(4,1)	I _{3(4,1)}	TS3P _{vic(4,1)}	P _{vic(4,1)}	I _{2(4,1)}	TS23 _(4,1)	I _{3(4,1)}
								
Ta1-Ta2	2.65011	2.59638	2.94698	2.99392	2.81875	2.60103	2.57941	2.95411
Ta2-Ta3	2.58543	2.47599	2.87627	2.82788	2.81888	2.54261	2.3976	2.79764
Ta3-Ta4	2.61885	2.52904	2.55728	2.56923	2.58887	2.7015	2.64785	2.50717
Ta1-Ta4	2.5768	2.60134	2.57374	2.58095	2.58859	2.5709	2.60455	2.56382
Ta2-Ta4	2.58532	2.77862	2.47722	2.46714	2.63041	2.54215	2.57809	2.41448
Ta1-Ta3	2.57707	2.60288	2.5224	2.5205	2.7055	2.55912	2.64278	2.53324
Ta1-N1	2.02394	2.04654	1.93295	1.9298	1.85178	2.02402	2.22505	2.01614
Ta1-N2								
Ta2-N1	2.13369	2.18569	2.20682	2.14083	1.90694	2.1085	2.27548	2.23521
Ta2-N2	2.18297	2.12726	1.9678	1.94123	1.90725	2.08954	2.20161	1.95075
Ta3-N1			2.21589	2.28349				2.24771
Ta3-N2			2.01536	1.97124	1.85143			2.09205
Ta4-N1								
N1-N2	1.2009	1.23751	1.46539	1.62748		1.23047	1.1583	1.48957

SI References

1. C. Berg, T. Schindler, G. Niedner-Schatteburg and V. E. Bondybey, *J. Chem. Phys.*, 1995, **102**, 4870-4884.
2. V. E. Bondybey and J. H. English, *J. Chem. Phys.*, 1981, **74**, 6978-6979.
3. D. Proch and T. Trickl, *Rev. Sci. Instrum.*, 1989, **60**, 713-716.
4. P. Caravatti and M. Allemann, *Org Mass Spectrom*, 1991, **26**, 514-518.
5. M. Graf, Diploma Technische Universität Kaiserslautern, 2006.
6. T. Su and M. T. Bowers, *International Journal of Mass Spectrometry and Ion Physics*, 1973, **12**, 347-356.
7. I. Balteanu, O. P. Balaj, B. S. Fox-Beyer, P. Rodrigues, M. T. Barros, A. M. C. Moutinho, M. L. Costa, M. K. Beyer and V. E. Bondybey, *Organometallics*, 2004, **23**, 1978-1985.
8. G. Kummerlöwe and M. K. Beyer, *International Journal of Mass Spectrometry*, 2005, **244**, 84-90.
9. M. J. Frisch, G. W. Trucks, H. B. Schlegel, G. E. Scuseria, M. A. Robb, J. R. Cheeseman, G. Scalmani, V. Barone, B. Mennucci, G. A. Petersson, H. Nakatsuji, M. Caricato, X. Li, H. P. Hratchian, A. F. Izmaylov, J. Bloino, G. Zheng, J. L. Sonnenberg, M. Hada, M. Ehara, K. Toyota, R. Fukuda, J. Hasegawa, M. Ishida, T. Nakajima, Y. Honda, O. Kitao, H. Nakai, T. Vreven, J. A. Montgomery Jr., J. E. Peralta, F. Ogliaro, M. J. Bearpark, J. Heyd, E. N. Brothers, K. N. Kudin, V. N. Staroverov, R. Kobayashi, J. Normand, K. Raghavachari, A. P. Rendell, J. C. Burant, S. S. Iyengar, J. Tomasi, M. Cossi, N. Rega, N. J. Millam, M. Klene, J. E. Knox, J. B. Cross, V. Bakken, C. Adamo, J. Jaramillo, R. Gomperts, R. E. Stratmann, O. Yazyev, A. J. Austin, R. Cammi, C. Pomelli, J. W. Ochterski, R. L. Martin, K. Morokuma, V. G. Zakrzewski, G. A. Voth, P. Salvador, J. J. Dannenberg, S. Dapprich, A. D. Daniels, Ö. Farkas, J. B. Foresman, J. V. Ortiz, J. Cioslowski and D. J. Fox, Gaussian 09, Revision D.01, Gaussian, Inc., Wallingford, CT, USA, 2009.
10. M. J. Frisch, G. W. Trucks, H. B. Schlegel, G. E. Scuseria, M. A. Robb, J. R. Cheeseman, G. Scalmani, V. Barone, G. A. Petersson, H. Nakatsuji, X. Li, M. Caricato, A. V. Marenich, J. Bloino, B. G. Janesko, R. Gomperts, B. Mennucci, H. P. Hratchian, J. V. Ortiz, A. F. Izmaylov, J. L. Sonnenberg, Williams, F. Ding, F. Lipparini, F. Egidi, J. Goings, B. Peng, A. Petrone, T. Henderson, D. Ranasinghe, V. G. Zakrzewski, J. Gao, N. Rega, G. Zheng, W. Liang, M. Hada, M. Ehara, K. Toyota, R. Fukuda, J. Hasegawa, M. Ishida, T. Nakajima, Y. Honda, O. Kitao, H. Nakai, T. Vreven, K. Throssell, J. A. Montgomery Jr., J. E. Peralta, F. Ogliaro, M. J. Bearpark, J. J. Heyd, E. N. Brothers, K. N. Kudin, V. N. Staroverov, T. A. Keith, R. Kobayashi, J. Normand, K. Raghavachari, A. P. Rendell, J. C. Burant, S. S. Iyengar, J. Tomasi, M. Cossi, J. M. Millam, M. Klene, C. Adamo, R. Cammi, J. W. Ochterski, R. L. Martin, K. Morokuma, O. Farkas, J. B. Foresman and D. J. Fox, Gaussian 16, Revision C.01, Gaussian, Inc., Wallingford, CT, USA, 2016.
11. J. P. Perdew, K. Burke and M. Ernzerhof, *Phys. Rev. Lett.*, 1996, **77**, 3865-3868.
12. C. Adamo and V. Barone, *J. Chem. Phys.*, 1999, **110**, 6158-6170.
13. F. Weigend and R. Ahlrichs, *PCCP*, 2005, **7**, 3297-3305.
14. D. Andrae, U. Häußermann, M. Dolg, H. Stoll and H. Preuß, *Theoretica Chimica Acta*, 1990, **77**, 123-141.
15. M. P. Klein, A. A. Ehrhard, J. Mohrbach, S. Dillinger and G. Niedner-Schatteburg, *Topics in Catalysis*, 2018, **61**, 106-118.
16. J. Mohrbach, S. Dillinger and G. Niedner-Schatteburg, *The Journal of Physical Chemistry C*, 2017, **121**, 10907-10918.

17. S. Dillinger, M. P. Klein, A. Steiner, D. C. McDonald, M. A. Duncan, M. M. Kappes and G. Niedner-Schatteburg, *The Journal of Physical Chemistry Letters*, 2018, **9**, 914-918.
18. C. Peng and H. Bernhard Schlegel, 1993, **33**, 449-454.
19. L. Fan, D. Harrison, L. Deng, T. K. Woo, D. Swerhone and T. Ziegler, *Can. J. Chem.*, 1995, **73**, 989-998.
20. K. Fukui, *Acc. Chem. Res.*, 1981, **14**, 363-368.
21. F. Weinhold and J. E. Carpenter, in *The Structure of Small Molecules and Ions*, eds. R. Naaman and Z. Vager, Springer US, Boston, MA, 1988, DOI: 10.1007/978-1-4684-7424-4_24, pp. 227-236.
22. E. D. Glendening, C. R. Landis and F. Weinhold, 2013, **34**, 1429-1437.
23. T. A. Albright, J. K. Burdett and M. H. Whangbo, in *Orbital Interactions in Chemistry*, eds. T. A. Albright, J. K. Burdett and M. H. Whangbo, John Wiley & Sons, 2013, DOI: 10.1002/9781118558409.ch18, ch. 18, pp. 503-526.
24. M. D. Fryzuk, S. A. Johnson and S. J. Rettig, *J. Am. Chem. Soc.*, 1998, **120**, 11024-11025.
25. M. Zhou, X. Jin, Y. Gong and J. Li, *Angew. Chem. Int. Ed.*, 2007, **46**, 2911-2914.
26. Y. Gong, Zhao and M. Zhou, *J. Phys. Chem. A*, 2007, **111**, 6204-6207.
27. X. Cheng, Z.-Y. Li, L.-H. Mou, Y. Ren, Q.-Y. Liu, X.-L. Ding and S.-G. He, *Chemistry - A European Journal*, 2019, **25**, 16523-16527.
28. M. D. Fryzuk, S. A. Johnson, B. O. Patrick, A. Albinati, S. A. Mason and T. F. Koetzle, *J. Am. Chem. Soc.*, 2001, **123**, 3960-3973.

9. N₂ Adsorption onto Ta_n⁺ n = 4,5 Clusters: IR-PD Spectroscopy, Cryo-Kinetics, and DFT Modelling

Matthias P. Klein, Daniela V. Fries, Annika Straßner, Maximilian E. Huber,
and Gereon Niedner-Schatteburg¹

*Fachbereich Chemie and Forschungszentrum OPTIMAS,
Technische Universität Kaiserslautern, 67663 Kaiserslautern, Germany*

9.1 Preamble

An experimental team consisting of D. Fries, A. Straßner, M. E. Huber, and myself conducted the experiments. I conducted and evaluated the quantum chemical calculations. Data evaluation was closely accompanied by discussions with G. Niedner-Schatteburg. I wrote the manuscript.

9.2 Abstract

Cryo IR-PD spectroscopy of [Ta_n(N₂)_m]⁺ (n,m), n = 4,5, cluster adsorbate complexes and adsorption kinetics of Ta₅⁺ serve to amend our earlier studies of N₂ cleavage on the Ta₄⁺ cluster. For (4,m) we find co-existing side-on and end-on N₂ adsorbate molecules. In addition, the spectra indicate the coexistence of multiple isomers and possible combination bands of N₂ stretching modes and low-frequency modes. The (5,m) IR-PD spectra provide no evidence for side-on N₂ adsorption or even N₂ dissociation. Bands appear only in the range of end-on N₂ stretching modes. DFT calculations allowed us to tentatively assign cluster structures with trigonal bipyramidal **tbp** cluster cores and we find nearly degenerate singlet and triplet states. The triplet spin state is most stable for the naked Ta₅⁺ cluster and relaxes with addition of N₂ molecules towards singlet state for the (5,10) cluster adsorbate complex. The energies of the higher spin state stabilize in the course of the adsorption and the spin valley curves become shallower. We find a preference of the first N₂ molecule to adsorb to the equatorial Ta atoms.

¹ Corresponding author: Prof. Dr. Gereon Niedner-Schatteburg, Erwin-Schrödinger-Straße 52, 67663 Kaiserslautern, gns@chemie.uni-kl.de

A natural population analysis reveals a localization of the positive charge at the higher next neighbor coordinated equatorial Ta atoms. Spin localizes at the lower coordinated apical Ta atoms of the **tbp** cluster core. Charge distribution and the N₂ stretching frequency correlates with the cluster's spin and the orientation of the N₂ molecule.

9.3 Introduction

Based on studies of N₂ activation for Ta₂⁺ and Ta₆⁺ [1-4], we investigated in a first step the behavior of Ta₄⁺ clusters [5]. We reacted these clusters with N₂ at 26 K and observed stepwise N₂ adsorption kinetics, similar to our earlier studies on Ni, Rh, RhFe and Fe clusters.[6-11] We recorded the IR-PD spectra of each adsorption step and found no indications for end-on bonded N₂ for the first two adsorption steps. These steps reveal particularly low rate constants. DFT calculations helped to understand that N₂ actually dissociates in these first two adsorption steps. We were able to compute dissociation pathways for these reactions with several local minima. The largest barrier in the pathway is between intermediates I2 (N₂ above edge isomer) and I3 (N₂ across surface isomer). To overcome this largest barrier, the N₂ moves according to a newly established AEAS (*Across Edge Above Surface*) mechanism on the tetrahedral Ta₄⁺ cluster core. For the first N₂ adsorbates, this largest barrier is submerged with respect to the Ta₄⁺ + N₂ entrance channel. The N₂ cleavage happens easily. From the first N₂ to the third N₂, this barrier increases, and for the third N₂, it surmounts the entrance channel and the dissociation is hindered. The course of activation cannot proceed beyond I2_(4,3). Indeed, the IR-PD spectrum of [Ta₄(N₂)₃]⁺ comprises of a single band at 1475 cm⁻¹. We could assign the intermediate with an I2 type structure to this band. We concluded that the cluster structure of [Ta₄(N₂)₃]⁺ is trapped at the local minimum I2 in front of the AEAS barrier and IR-PD is a suitable method to prove it. In this paper we complement the IR-PD spectra of [Ta₄(N₂)_m]⁺ *m* = 1,...,5 by spectra up to *m* = 12. In addition, we measured the N₂ adsorption kinetics of [Ta₅(N₂)_m]⁺ and the corresponding IR-PD spectra of *m* = 1,...,10.

9.4 Experimental and theoretical methods

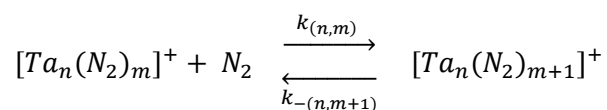
A customized 7 T Fourier Transform-Ion Cyclotron Resonance (FT-ICR)-mass spectrometer (Apex Ultra Bruker Daltonics) serves to produce and isolate the metal clusters, to adsorb N₂ at

various reaction times, to perform mass analysis, and InfraRed Photodissociation (IR-PD) spectroscopy. The detailed construction has been described elsewhere.[12] In short, the second harmonic of a Nd:YAG laser is guided into the home-built laser vaporization cluster ion source chamber as described before.[13, 14] The laser beam is focused on a rotating Ta-target (99.95%, Alfa Aesar, 0.5 mm thick) and produces a plasma, consisting of atoms and ions. A Helium gas pulse (40 μ s, 10-15 bar) is generated and induced into the vaporization chamber by using a homemade piezoelectric valve.[15] This valve operates in synchronization with the laser at 20 Hz. The gas pulse entrains the plasma through a 69 mm long channel (2 mm diameter) where the atoms and ions cool down and aggregate to clusters in the subsequent jet expansion into vacuum ($3.5 \cdot 10^{-7}$ mbar). The ions in the skimmed cluster beam are guided through a 90° ion beam bender and a quadruple mass filter into a cryogenic hexapole ion trap which is cooled to 26 K by a closed cycle He cryostat. We introduce collision gas and reaction gas in the ion trap by a continuous gas inlet. The mass filter serves to select the cluster with the size of interest.

The attachment of nitrogen is achieved by maintaining a constant pressure of about $2.4 - 8.0 \times 10^{-7}$ mbar N_2 , in order to facilitate the recording of IR-PD spectra of cluster adsorbate complexes based on $Ta_{4,5}^+$ clusters. For the $Ta_5^+ N_2$ adsorption kinetics, we chose a partial pressure of 2.6×10^{-7} mbar N_2 . We increase the pressure in the ion trap to roughly 5.0×10^{-6} mbar by adding helium gas to accomplish efficient trapping and cooling of the ions. The ions are stored for a variable time (0 – 20 s). Subsequently, the cluster ions are steered into the ICR-cell, using various electrostatic ion lenses. Our ICR-cell of the so-called infinity-type [16] is cooled down to 10 K by a closed cycle He cryostat to prevent heating of the clusters by black body radiation.

For the investigation of the selected $[Ta_n(N_2)_m]^+$ cluster adsorbate complexes within the ICR cell, we first isolate the $[Ta_n]^+$ metal cluster in the quadrupole mass filter.

Adsorption kinetics. The ICR-cell serves for the detection of the formed cluster adsorbate complexes $[Ta_n(N_2)_m]^+$. By analysis of the mass spectra at various reaction times and pseudo-first-order kinetic fits with the genetic algorithm program 'evofit' [17] we obtain relative rate constants $k_{(n,m)}$ for each N_2 adsorption step $m \rightarrow m+1$, and $k_{-(n,m+1)}$ for each N_2 desorption step $m+1 \rightarrow m$ alike:



The chosen nomenclature is in line with our previous publications. For ease of reference we will utilize in the following the abbreviating nomenclature $[Ta_n(N_2)_m]^+ = (n,m)$ (cf. [8] Text S1 therein).

IR-PD spectroscopy. In order to record IR-PD spectra, we optimize the storage time of the Ta_n⁺ clusters in the hexapole such that we gain maximum intensity of the $[Ta_n(N_2)_m]^+$ cluster adsorbate complex of interest which we isolate afterwards in the ICR cell by removing all other ions by correlated frequency sweeps and shots. A tunable IR laser system coupled to the ICR cell and serves to excite and to dissociate the stored ions. This laser is a KTP/KTA optical parametric oscillator/amplifier (OPO/A, *LaserVision*) system pumped by a pulsed 10 Hz injection seeded Nd:YAG laser (PL8000, *Continuum*) followed by an AgGaSe₂ crystal to generate the difference frequency (DF) between signal and idler waves.[18] This method can generate IR radiation in the range of 1200 – 2400 cm⁻¹. We irradiate each trapped and isolated package of ions by 7 - 10 laser pulses to yield a sufficient amount of fragment ions. A typical pulse energy spectrum is given in Fig. S1. The IR-PD spectra were recorded as ion chromatograms while continuously scanning the IR wavelength. We evaluated the IR-PD signal as $\sum_n F_n / (\sum_n F_n + \sum_x P_x)$, where F_n and P_x indicate fragment and the parent ion signals, respectively. Plotting the fragmentation efficiency as a function of laser frequency yields an IR-PD spectrum. For all cluster adsorbate complexes, the loss of the N₂ was the only observed fragmentation channel.

DFT calculations. Geometry optimizations and vibrational analysis were performed by the Gaussian 09 package [19] at PBE0/ECP(Ta); Def2-TZVP level of theory [20-22] as proven suitable before [5]. We had to tolerate a relaxed SCF convergence criteria of 10⁻⁶ (as compared to 10⁻⁸ in 'standard' DFT calculations) to achieve SCF convergence. Natural Population Analysis was performed using NBO 5.9 as implemented in Gaussian 09.[23] We checked the obtained minimum structures for imaginary vibrational frequencies and found all reported isomers to be true minimum structures. For $[Ta_4(N_2)_m]^+$ we chose an anharmonic linear scaling factor of 0.938 to match the calculated free N₂ stretching frequency (2484 cm⁻¹) to the Raman band of free N₂ at 2330 cm⁻¹. [24]

9.5 Results and Discussion

9.5.1 $[\text{Ta}_4(\text{N}_2)_m]^+$

In order to complement the spectra of the initial five adsorption steps $[\text{Ta}_4(\text{N}_2)_m]^+ = (4,m)$ $m = 1, \dots, 5$ we have published before, we present the IR-PD spectra up to a formal triple N_2 adsorbate layer $m = 12$ (Fig. 1).

(4,1) and (4,2) In combination with extensive DFT modelling, the first steps have provided solid evidence for a full cleavage of the first two N_2 molecules, and the single band at 1475 cm^{-1} of the $m = 3$ spectrum could be assigned to a side-on (above edge, $\mu_2\text{-}\kappa\text{N}:\kappa\text{N},\text{N}$) activated N_2 intermediate.[5]

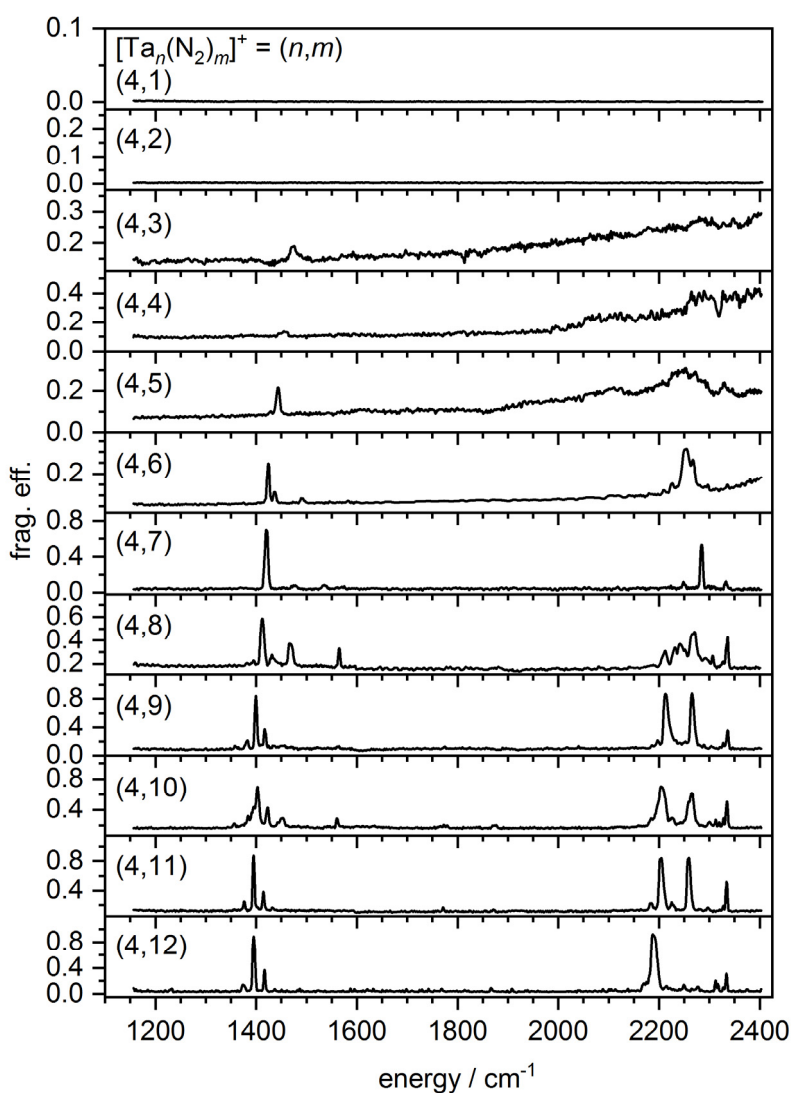


Fig. 1 IR-PD spectra of sequential N_2 adsorption steps onto Ta_4^+ cluster cations $[\text{Ta}_4(\text{N}_2)_m]^+$, $m = 1 - 12$ as recorded after 26 K He buffer gas cooling. The (4,1), ..., (4,5) spectra have been published before ([5] Fig. 2 therein).

(4,3) – (4,5) The fragmentation efficiencies for $m = 3,4,5$ increase with the wavenumber indicating non-resonant absorption. A broad absorption around 2230 cm⁻¹ and a dip in the absorption around 2330 cm⁻¹ may arise from a synergy of an end-on loosely bound roaming N₂ molecule and decrease of the laser power due to CO₂ absorption (cf. power curve Fig. S1). This intense band at 1475 cm⁻¹ ($m = 3$) shifts continuously to the red with increasing amount of adsorbed N₂ up to 1399 cm⁻¹ at $m = 9$.

(4,6) The (4,6) cluster adsorbate complex reveals three bands indicating side-on N₂ adsorption at 1424 and 1436 cm⁻¹ and a weak absorption at 1489 cm⁻¹. At 2254 cm⁻¹ (fwhm = 23 cm⁻¹) a distinct band arises, with a shoulder at 2267 cm⁻¹. These bands clearly indicate the presence of end-on adsorbed N₂ molecules. In general, we assign all bands above 2100 cm⁻¹ to end-on adsorbed N₂ molecules. These bands are usually red shifted with respect to the free N₂ stretching vibration at 2330 cm⁻¹ [24] due to a σ -donor π -acceptor synergism that softens the N-N bond. This concept has been utilized for CO adsorbates in the Blyholder model [25] and for N₂ adsorbates in our earlier studies on Co, Ni, Fe, Ru, Rh, and RhFe alloy clusters [6, 11, 12, 26-30].

(4,7) In the side-on N₂ range of the IR-PD spectrum, one strong bands at 1420 cm⁻¹ (fwhm = 8 cm⁻¹) and two weak bands at 1476 and 1535 cm⁻¹ appear. In the end-on N₂ range, a narrow band at 2284 cm⁻¹ (fwhm = 6 cm⁻¹) appears, accompanied by two weak bands at 2248 and 2333 cm⁻¹. The latter one resembles the stretching frequency of free N₂ and may indicate an N₂ molecule that only weakly interacts with the cluster. It may be loosely bound and attached within a second adsorption shell. Such a band appears in all following (4, m) spectra.

(4,8) We observe four bands in the side-on range: at 1412, 1431, 1466, and 1565 cm⁻¹. An additional very weak feature appears at 1395 cm⁻¹. In the end-on range of the spectrum, we observe a broad absorption pattern with maxima at 2212, 2232, 2242, 2268, 2292, 2307, and 2336 cm⁻¹. The amount of twelve absorption maxima exceeds the number of eight N₂ oscillators and likely arises from coexisting isomers. A formally double occupation of the Ta atoms may lead to reorganization and isomerization.

(4,9) Some of the (4,8) bands remain at (4,9). Three bands in the side-on range shift red by about 12 cm⁻¹: 1383, 1400, and 1417 cm⁻¹. A very weak absorption appears at 1357 cm⁻¹. The

three remaining bands in the end-on range shift only slightly: they appear at 2213, 2265, and 2236 cm^{-1} .

(4,10) The general band pattern of (4,9) continues with addition of further N_2 molecules up to (4,11). We recognize absorption maxima at 1384, 1403, 1423, and 1452 cm^{-1} as well as at 2183, 2205, 2226, 2263, 2300, and 2335 cm^{-1} . The bands of this spectrum are broader than those in the (4,9) spectrum (15 cm^{-1} vs. 10 cm^{-1}). In addition, the weak band at 1357 cm^{-1} survives. As for (4,8), a band at 1561 cm^{-1} is visible. Two additional very weak, but reproducible absorptions appear at 1770 and 1870 cm^{-1} . These features may be combination bands of the N-N stretching mode and bending modes. We used the two most stable calculated (4,5) cluster adsorbate complexes to exemplify the vibrational modes of such complexes (cf. Tables S1 and S2).

(4,11) The bands of (4,11) resemble the (4,9) spectrum almost perfectly. The bands at 1376, 1395, 1414, 2183, 2204, 2225, 2259, 2283, 2298, and 2234 cm^{-1} are only slightly red shifted by up to 7 cm^{-1} and better separated. The good quality of the spectrum allows identifying very weak bands and the assumed combination bands at 1771 and 1871 cm^{-1} appear.

(4,12) The side-on range of the (4,12) spectrum resembles the one of the (4,9) and the (4,11) spectra. In the end-on range, we observe a single strong band at 2188 cm^{-1} with a shoulder at 2174 cm^{-1} . Additional weaker bands at 2215, 2249, 2277, 2313, and 2334 cm^{-1} may resemble those of the (4,11) spectrum albeit less intense. Most of the end-on bands shift red by up to 16 cm^{-1} . The band at 2312 cm^{-1} is specific for the (4,12) spectrum.

Conclusion. The IR-PD spectra of the (4,*m*) cluster comprise a multitude of bands that indicate a coexistence of side-on and end-on N_2 adsorbate molecules. In the case of (4,8), likely two isomers coexist. Weak bands in between the absorption ranges of end-on and of side-on adsorbed N_2 molecules may be combination bands of the stretching vibration of a side-on adsorbed N_2 and one of its bending or wagging modes.

9.5.2 $[\text{Ta}_5(\text{N}_2)_m]^+$

9.5.2.1 Cryo N_2 adsorption kinetics

We recorded the cryo kinetics at 26 K of the N_2 adsorption onto a Ta_5^+ cluster (Fig. 2a). The Ta_5^+ cluster adsorbs N_2 up to a saturation at $m = 16$. We observe a first-order adsorption kinetic behavior up to (5,*m*) $m = 11 = 2n+1$. The intensities of the first three cluster adsorbate

complexes indicate a slow but accelerating attachment of N₂ molecules. We reported slow first adsorption steps for the Rh₅⁺ cluster before [8] and suggest some amount of activation throughout the first three adsorption steps. In earlier studies, we have found intermittent adsorption limits and we have interpreted them in terms of a mono- or double layer of N₂ on the cluster surface. Here, further adsorption steps up to $m = 11$ run swiftly without any indication of an intermittent adsorption limit.

For all further steps, the course of the relative intensities indicates adsorption/desorption equilibria. For these steps, desorption has to be considered in the fits (Fig 2b). However, our intensity curves exhibit steps and discontinuities, and due to this lack of data quality, the fit requires significant desorption for almost every step, with exception of $m = 0$ and 11. As a first step, we evaluated the equilibrium constants which are in most cases close to 1 (except $m = 0$ and 10). The final adsorption/desorption equilibrium $m = 15$ exhibits similar adsorption and desorption rate constants that are both exceedingly high.

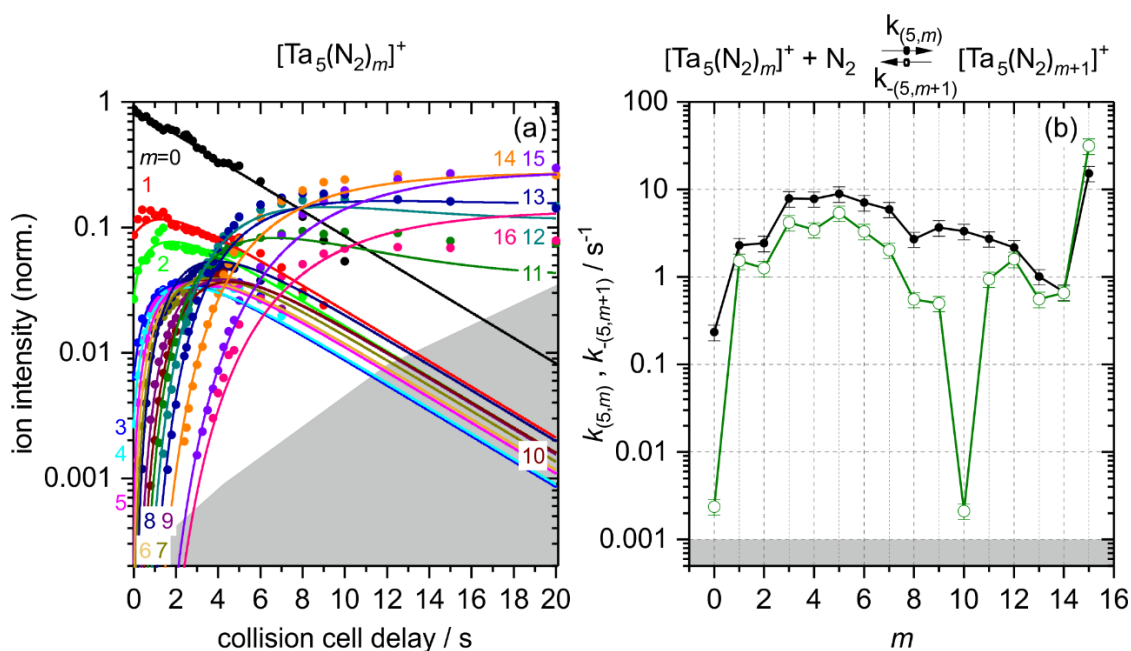


Fig. 2 (a) Isothermal kinetics of the stepwise N₂ adsorption at 26 K by isolated Ta₅⁺ clusters (solid symbols). The fits (solid lines) assume pseudo-first-order kinetics in an adsorption chain of up to 16 consecutive steps. (b) Fitted values of relative rate constants as a function of the stepwise N₂ adsorption (level m). The grey shaded areas indicate the approximate background noise level. Note, that in the most cases the fitted rate constants for the adsorption ($k_{(5,m)}$, black filled circles) are only less than one order of magnitude higher than those of the desorption ($k_{-(5,m+1)}$, green open circles).

Most likely the measurement conditions were not sufficient to yield an acceptable quality and to enable conclusive interpretation. A quantitative and reliable evaluation of the kinetic data would require measurements under more stable conditions such as pressure or temperature. Such work is in progress.

The lack of quality does not affect the IR-PD spectra, where the requirements for storage conditions in the hexapole collision cell are not as crucial as for kinetic measurements. Our following spectroscopic investigations focus on the first ten adsorption steps up to a formal double layer of N₂ adsorbate molecules.

9.5.2.2 Cryo IR-PD spectroscopy

We recorded IR-PD spectra of all cluster adsorbate complexes from (5,1) up to a formal double occupation of Ta sites at (5,10) (Fig. 3).

For all these cluster adsorbate complexes, we observe bands in the range from 2150 – 2300 cm⁻¹. We observed this same range before for Ta₄⁺ clusters and for Rh₆⁺ clusters [5, 29]. For $m = 1, \dots, 6$, we checked for bands below 1900 cm⁻¹ and found no absorption (cf. Fig. S4). The IR-PD spectra consist of a manifold of bands, which persist throughout the increasing N₂ adsorption. The positions of the bands are fixed with increasing number of N₂ molecules. On the other hand, we observe new bands appearing mainly to the red of the already existing ones for increasing number of N₂ molecules. The overall redshift with respect to the free N₂ stretching vibration at 2330 cm⁻¹ relates to a σ -donor and π -acceptor synergism as explained above for Ta₄⁺. We observe no red shifting trend with increasing number of N₂ adsorbate molecules m , in contrast to previous investigations on Rh clusters.

(5,1) For single N₂ adsorption $m = 1$ we found a single band at 2268 cm⁻¹ which is red shifted by 62 cm⁻¹ with respect to the free N₂ stretching vibration at 2330 cm⁻¹.

(5,2) The (5,2) spectrum is more complicated. Instead of the two bands that would arise from two end-on coordinated N₂ molecules, we observe a manifold of at least four weak bands between 2230 and 2300 cm⁻¹ which superimpose strongly. We interpret this in terms of several coexisting isomers with similar energies. We identify absorption maxima at 2236, 2262, and 2273 cm⁻¹. The weakness of the bands might correlate with high adsorption energies. DFT calculations will help to clarify.

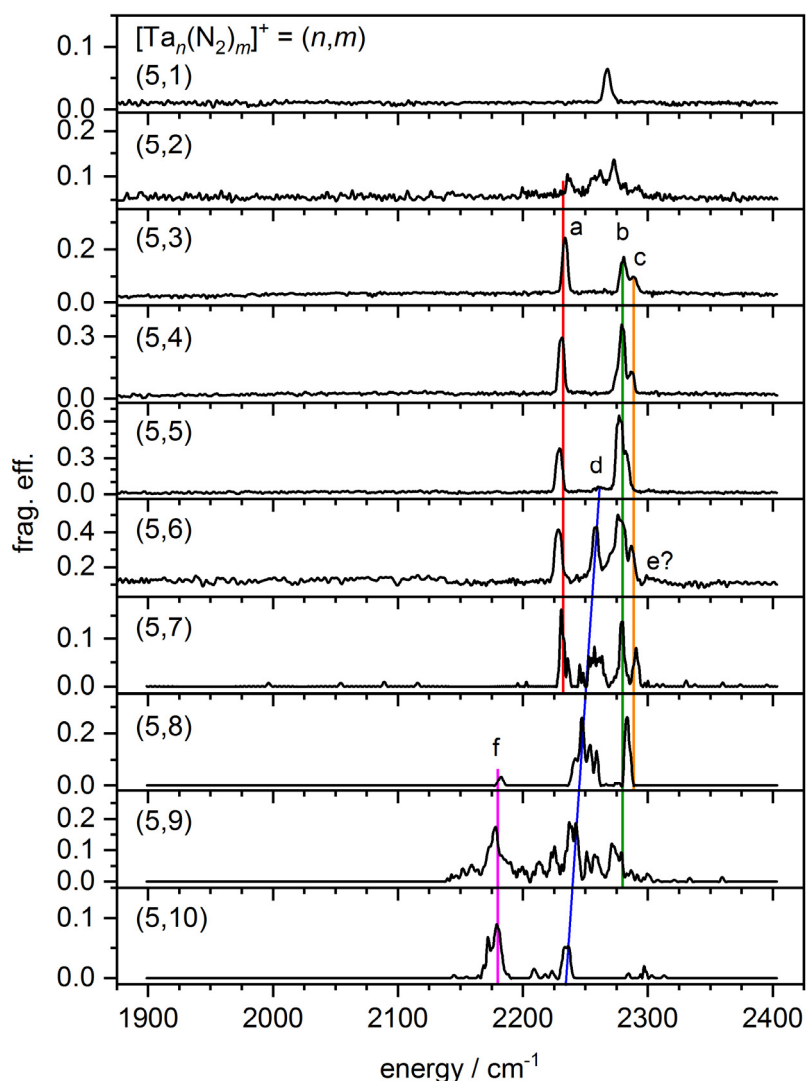


Fig. 3 IR-PD spectra of sequential N₂ adsorption steps onto Ta₅⁺ cluster cations [Ta₅(N₂)_m]⁺, *m* = 1–10 as recorded after 26 K He buffer gas cooling. The colored lines indicate bands that shift throughout the stepwise adsorption process.

(5,3) – (5,5) From *m* = 3,...,5, three bands dominate the spectra: An intense single band (band a, red line) shifts slightly to the red from 2234 to 2229 cm⁻¹. A second band (band b, green line) also shifts to the red from 2281 to 2277 cm⁻¹ (from (5,3) to (5,9)). The second band overlaps with a third band (band c, orange line) at 2289 cm⁻¹ (5,3) that appears as a shoulder in the (5,5) spectrum (band b: 2277 cm⁻¹, band c: 2283 cm⁻¹). Additional weak features appear at 2265 cm⁻¹ for (5,3) and at 2261 cm⁻¹ for (5,5) (band d, blue line). The addition of N₂ molecules does not lead to significant changes in the spectra from (5,3) to (5,5), in particular not of the number of strong bands.

(5,6) The addition of one N₂ molecule onto the formal monolayer at (5,5) makes the band pattern more complicated. We observe bands a, b and c at 2228, 2276, and 2287 cm⁻¹. Band b

comprises shoulders at 2271 and 2280 cm^{-1} . Band d shifts red to 2259 cm^{-1} and intensifies. Additional weak absorptions appear at 2243 and 2300 cm^{-1} .

(5,7) The fragmentation efficiency is reduced for $m = 7$. The spectrum resembles the (5,6) spectrum well, albeit slightly blue shifted. We observe bands at 2231, 2247, 2258, 2280, and 2291 cm^{-1} . The band at 2231 cm^{-1} has a shoulder at 2235 cm^{-1} that is already visible in the (5,6) spectrum. The band around 2258 cm^{-1} is 13 cm^{-1} broad (fwhm) and has a plateau-like shape, without a distinct maximum.

(5,8) The (5,8) spectrum comprises six absorption maxima at 2183, 2242, 2248, 2254, 2259, and 2284 cm^{-1} . The new band at 2183 cm^{-1} (band f, pink line) is outside observed range of bands for less adsorbed N_2 molecules and may indicate an adsorption onto a less next neighbor coordinated Ta atom, likely accompanied by triple geminal N_2 adsorption of three N_2 molecules onto the same Ta atom.

(5,9) For $m = 9$, we observe a broad absorption pattern spread out between 2140 and 2305 cm^{-1} . We identify eleven distinct absorption maxima at 2178 (band f), 2200, 2213, 2225, 2237, 2242 (band d), 2251, 2257, 2271, 2279, and 2299 cm^{-1} . This excess of bands over oscillators may arise from isomerization of the adsorbate shell or a relaxation of the cluster core at high amounts of adsorbed N_2 . In between the distinct peaks, some broad absorptions and shoulders appear that support this assumption.

(5,10) At formal double occupation at $m = 10$, the multitude of bands in the (5,9) spectrum reduces mainly to bands at 2172 and 2180 cm^{-1} (band f) and 2236 cm^{-1} . Additional weaker adsorptions appear at 2208, 2218, 2224, 2284, and 2297 cm^{-1} . The increasing predominance of these red shifted bands (band f) with m supports our hypothesis that the red shifted bands origin from geminal N_2 oscillators adsorbed to low coordinated Ta atoms with a shortage of electrons. However, the spectra do not indicate strong geminal couplings, which would show in the form of double bands.

Summary. Compared to our studies of Rhodium clusters, the IR spectra do not reveal a sequential redshift with increasing number of N_2 adsorbate molecules. One explanation is the difference of number of N_2 molecules. In addition, the low number of electrons inside the cluster may be the cause: There are no lone pairs that donate into the antibonding N_2 orbitals. Instead, additional bands appear at (5,8) around 2175 cm^{-1} , significantly red shifted with respect to the initial range of bands. Consistent band positions throughout the course of

adsorption may indicate less flexible adsorption shells. The (5,*m*) spectra provide no evidence for N₂ activations, in contrast to the (4,*m*) spectra, where an activated intermediate's signature is visible throughout $m = 3, \dots, 10$.

9.5.2.3 DFT calculations of [Ta₅(N₂)_{*m*}]⁺

In order to investigate the effects of stepwise N₂ adsorption on the cluster structure and possible spin relaxations in the course of adsorption, we optimized the Rh₅⁺ cluster core together with the adsorbate shell of (5,*m*) in the cases of $m = 0, 1, 2, 5, 10$. For each *m*, we started with several conceivable adsorption shell isomers, which adsorb N₂ onto reasonable **tbp** and **sp** cluster cores. We obtained fully converged structures for singlet to nonet multiplicities in most cases (Fig. 4). N₂ adsorption energies correspond to the offsets between the resulting curves – each of which resembles the *spin valley* of a single (5,*m*) complex. The recorded spectra of the (5,1) cluster clearly indicate the presence of an intact end-on N₂ adsorbate molecule. We therefore evaluate the most stable cluster isomers comprising such an adsorption motif for all subsequent adsorption steps and find degenerate triplet and singlet isomers most stable.

For the naked Ta₅⁺ cluster, we find a triplet trigonal bipyramidal minimum structure ³**tbp** as most stable isomer, independent of the starting structure. The singlet isomer is only 14 kJ/mol above. Higher multiplicities are more expensive by up to 90 kJ/mol. With a single N₂ adsorbate molecule, singlet and triplet multiplicities become degenerate. This degeneracy persists throughout $m = 2$ and 5. Note that also the higher spin states stabilize and the spin valleys become more shallow. The energy difference between each curve's minimum and the quintet state decreases from 63 kJ/mol ($m = 1$) over 48 kJ/mol ($m = 2$) to 29 kJ/mol ($m = 5$). The $m = 10$ spin valley curve is even less steep. Relative to the most stable singlet ¹**tbp**, the triplet and quintet are less stable by 16 kJ/mol and by 41 kJ/mol.

The found most stable (5,5) cluster adsorbate complex contains a **tbp** cluster core. Its N₂ adsorbate shell concentrates on one side of the molecule: two of the equatorial Ta atoms are singly occupied and one apical Ta atom adsorbs three N₂ molecules. The most stable (5,10) cluster adsorbate complex contains a distorted **tbp** core. Two opposite (apical) Ta atoms adsorb only a single N₂ molecule. Two other Ta atoms adsorb a triplet of N₂ molecules each.

Adsorption energies. We extract adsorption energies from the spin valley curves by evaluating their offsets. By adsorption of N₂ the total energy of the spin valley curves decreases stepwise

by the adsorption energy. We normalize absolute values to the energy of the minimum triplet ${}^3\text{tbp}$ (5,0) cluster. Both vertical (spin conserving) and adiabatic (including relaxation of the spin state) adsorption energies (cf. Fig. S5 and Table S4) refer to this very starting point. Note, that for the most steps, vertical and adiabatic energies are similar due to degenerate singlet and triplet states. Both vertical and adiabatic adsorption energies increase from about -40 kJ/mol for step $m = 0$ to about -50 kJ/mol for step $m = 1$. From $m = 2, \dots, 4$ we obtain reduced interpolated values of -32.4 kJ/mol. For the next five steps $m = 5, \dots, 9$, interpolated adiabatic adsorption energies of -41.5 kJ/mol are slightly higher than the vertical ones (-38.4 kJ/mol). For all ten adsorption steps, the total adiabatic adsorption is only 16 kJ/mol more stable than vertical (triplet) adsorption.

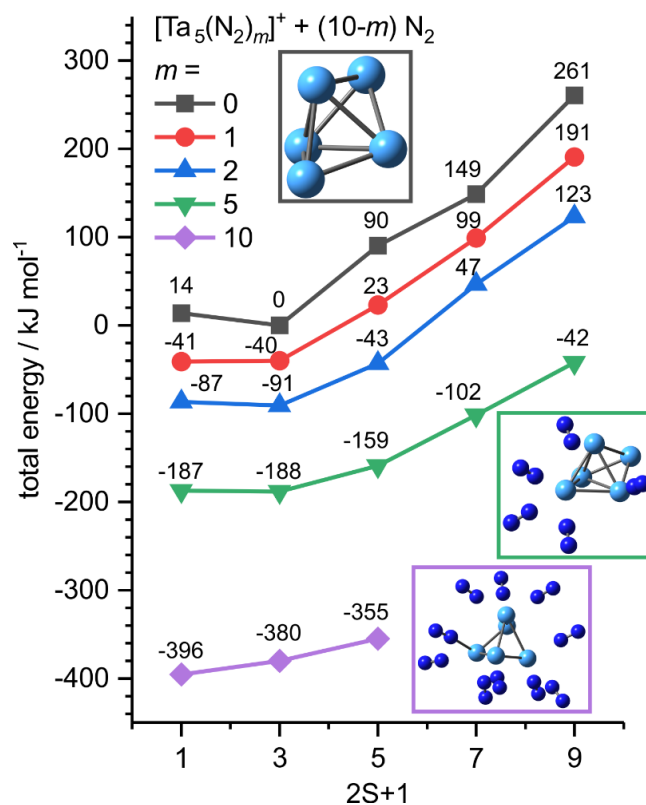


Fig. 4 Total energies of computed $[\text{Ta}_5(\text{N}_2)_m]^+$ intact cluster adsorbate complex structures (5, m) as a function of the spin multiplicity $2S + 1$, normalized to the computed (5,0) spin isomer (trigonal bipyramid, ${}^3\text{tbp}$, triplet). The calculated minimum structures for (5,0), (5,5) and (5,10) are shown as insets. We include ten N_2 molecules in each calculation, increasing the number of adsorbed N_2 and reducing the number of free N_2 .

Electronic properties of the first adsorption step. In a next step, we performed a natural population analysis (NPA) of (5,0) and (5,1) clusters in order to obtain and compare information on their electronic properties with a focus on their charge and spin distribution.

(5,0) The NPA of the most stable (5,0) ³tbp isomer reveals a concentration of the positive charge on the equatorial Ta atoms. The apical Ta atoms comprise more electron density and their respective spin density of ~1 indicates a localization of one unpaired electron to each of them. The apical Ta atoms are coordinated by three next neighbors each, the equatorial Ta atoms are coordinated by four next neighbors each. This most stable isomer is close to D_{3h} symmetry (Fig. 5).

(5,1) The three considered (5,1) isomers (a), (b), and (c) are equally stable (+4 kJ/mol) and differ mainly by the spin or by the angle of the adsorbed N₂ (cf. Fig. 6). The cluster core is relaxed towards a trigonal bipyramid **tbp** in all three cases. Their computed linear absorption spectra are depicted in the Supplement (Fig. S6). The next isomer is 18 kJ/mol less stable than the most stable one.

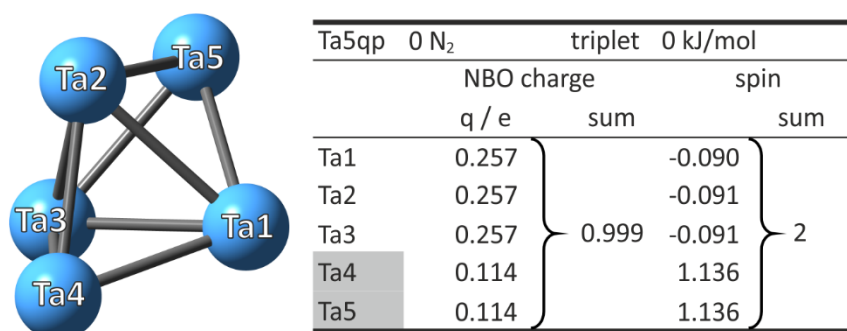
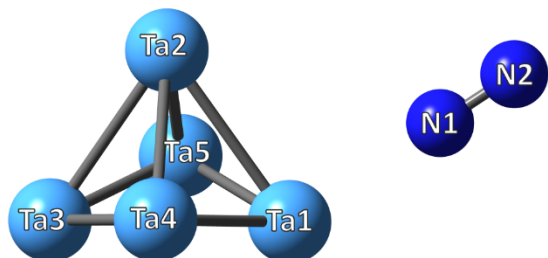


Fig. 5 Most stable isomers of the [Ta₅(N₂)₀]⁺ cluster ³tbp. The charge and spin distribution of each isomer is given. The grey shading indicates the apical Ta atoms.

Also with adsorption of the first N₂ molecule, the charge is concentrated on the equatorial Ta atoms and the electron density at the apical Ta atoms is enhanced. Note that the N₂ molecule adsorbs onto the equatorial Ta atoms that are better electron acceptors. Isomers (a) and (b) are close to C_s symmetry, (c) has C_{2v} symmetry. In the case of the triplet isomers (b) and (c), both apical Ta atoms still comprise of an unpaired electron each and their charge density is reduced with respect to the singlet isomer (a) by 0.04 e per Ta atom. Upon adsorption, the N₂ is polarized ($\Delta q < 0.29$ e) but obtains little charge and spin density. The charge density at the apical Ta atoms is enhanced with respect to the (5,0) cluster. The population of the adsorbing Ta atom strongly depends on the isomer (spin and mainly angle), in particular if compared with the other equatorial Ta atoms: it varies between 0.255 e (b) and 0.174 e (c). In singlet isomer (a) the adsorbing Ta atom is the most positive equatorial atom with a charge density of 0.255 e. The charge density of the adsorbing Ta atom in triplet isomer (b) is in between the

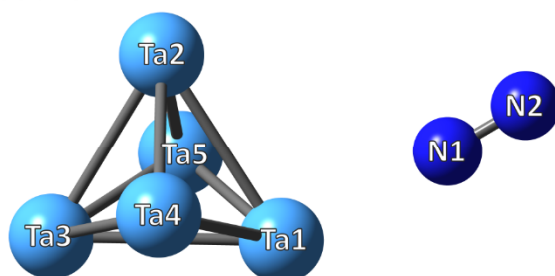
other equatorial atoms $0.219 e < 0.259 e < 0.279 e$. In the highly symmetric triplet isomer (c) the adsorbing isomer comprises the least charge density of the equatorial Ta atoms ($0.174 e < 0.26 e$).

(a) (5,1)_tbp_1a, singlet, 0 kJ/mol



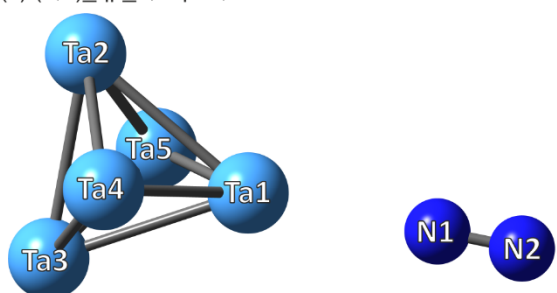
Ta5tpb 1 N ₂		1a		singlet 0 kJ/mol			
		NBO charge		d(N-N)/Å		spin	
	q / e	sum	Δq / e			sum	
Ta1*	0.255	1.018		1.0996	0	0	0
Ta2	0.226						
Ta3	0.209						
Ta4	0.164						
Ta5	0.164						
N1	-0.146	-0.018	0.274	1.0996	0	0	0
N2	0.128						

(b) (5,1)_tbp_1b, triplet, 1 kJ/mol



Ta5tpb 1 N ₂		1b		triplet 1 kJ/mol			
		NBO charge		d(N-N)/Å		spin	
	q / e	sum	Δq / e			sum	
Ta1*	0.259	0.992		1.09654	-0.006	1.995	-0.047
Ta2	0.274						
Ta3	0.219						
Ta4	0.120						
Ta5	0.120						
N1	-0.135	0.006	0.276	1.09654	-0.006	0.005	0.011
N2	0.141						

(c) (5,1)_qp_1, triplet, 4 kJ/mol



Ta5qp 1 N ₂		1		triplet 4 kJ/mol			
		NBO charge		d(N-N)/Å		spin	
	q / e	sum	Δq / e			sum	
Ta1*	0.174	0.926		1.0911	-0.002	2.003	-0.093
Ta2	0.260						
Ta3	0.260						
Ta4	0.116						
Ta5	0.116						
N1	-0.109	0.074	0.292	1.0911	-0.002	-0.004	-0.002
N2	0.183						

Fig. 6 Three most stable isomers of the $[\text{Ta}_5(\text{N}_2)_1]^+$ cluster adsorbate complex. The isomers are equally stable. The corresponding calculated linear absorption spectra are given in Fig. S6. The charge and spin distribution of each isomer is given. The grey shading indicates the apical Ta atoms. The asterisk emphasizes the adsorbing Ta1 atom.

Our investigations on the Ta_5^+ cluster did not yield any evidence for activation precursors or even full dissociation of N_2 . To understand the differences between Ta_4^+ and Ta_5^+ , a calculation of a possible N_2 activation pathway on Ta_5^+ would be an appropriate step. A comparison of these pathways and the height of critical barriers could prove helpful.

We conclude that the adsorption of a single N_2 molecule effects changes of the electron distribution within the Ta_5 cluster core. The specific effect depends strongly on the spin of the

cluster adsorbate complex and the orientation of the adsorbed N₂ molecule. In addition, the N₂ stretching frequency varies with these parameters while a clear correlation cannot be extracted from the data. For a better understanding of the effect of N₂ orientation on the electronic structure and the stretching frequencies, an orbital analysis would be helpful. Such effort is part of ongoing work.

9.6 Conclusion

We recorded cryo IR-PD spectra of [Ta₄(N₂)_m]⁺, (4,*m*), and [Ta₅(N₂)_m]⁺, (5,*m*), cluster adsorbate complexes as well as adsorption kinetics of N₂ onto [Ta₅(N₂)_m]⁺ (5,*m*). For (4,*m*) we find co-existing side-on and end-on N₂ adsorbate molecules. In addition, the spectra indicate the coexistence of multiple isomers and possible combination bands of N₂ stretching modes and low-frequency modes.

Preliminary (5,*m*) adsorption kinetics indicate a stepwise N₂ adsorption process. More precise and reliable measurements are underway and may provide conclusive data. The (5,*m*) IR-PD spectra provide no evidence for side-on N₂ adsorption or even N₂ dissociation. Bands appear only in the range of end-on N₂ stretching modes. DFT calculations allowed us to tentatively assign cluster structures with trigonal bipyramidal **tbp** cluster cores. The evaluation of spin valley curves allows evaluating the spin state dependent stabilities of cluster adsorbate complexes in the course of N₂ adsorption. The triplet spin state is most stable for the naked Ta₅⁺ cluster and relaxes with addition of N₂ molecules towards singlet state for the (5,10) cluster adsorbate complex. In between, for (5,1), (5,2) and (5,5) singlet and triplet state are nearly degenerate. The energies of the higher spin state stabilize in the course of the adsorption and the spin valley curves become shallower. The first N₂ molecule adsorbs preferably to the equatorial Ta atoms. A natural population analysis reveals a localization of the positive charge at the higher next neighbor coordinated equatorial Ta atoms. For triplet isomers, the spin localizes at the lower coordinated apical Ta atoms of the **tbp** cluster core. Charge distribution and the N₂ stretching frequency correlate with the cluster's spin and the orientation of the N₂ molecule. Further theoretical analyses and orbital analysis are work in progress and they will provide insights in the interacting orbitals and their orientation. We showed that the ability of a small Ta cluster to activate dinitrogen vanishes by addition of one single metal atom to the cluster core.

9.7 Acknowledgement

This work was supported by the German research foundation DFG within the transregional collaborative research center SFB/TRR 88 ‘Cooperative effects in homo and heterometallic complexes’ (3MET.de) and by the state research center OPTIMAS. We thank Thomas Kolling for assistance on technical questions of any kind.

9.8 References

1. Geng, C., Li, J., Weiske, T., and Schwarz, H., *Ta₂⁺-mediated ammonia synthesis from N₂ and H₂ at ambient temperature*. Proceedings of the National Academy of Sciences of the United States of America **2018**, *115*, 11680-11687.
2. Geng, C., Li, J., Weiske, T., and Schwarz, H., *Complete cleavage of the N≡N triple bond by Ta₂N⁺ via degenerate ligand exchange at ambient temperature: A perfect catalytic cycle*. Proceedings of the National Academy of Sciences **2019**, 201913664.
3. Mafuné, F., Tawaraya, Y., and Kudoh, S., *Nitrogen Molecule Adsorption on Cationic Tantalum Clusters and Rhodium Clusters and Desorption from Their Nitride Clusters Studied by Thermal Desorption Spectrometry*. J. Phys. Chem. A **2016**, *120*, 4089-4095.
4. Arakawa, M., Ando, K., Fujimoto, S., Mishra, S., Patwari, G.N., and Terasaki, A., *The role of electronegativity on the extent of nitridation of group 5 metals as revealed by reactions of tantalum cluster cations with ammonia molecules*. Phys. Chem. Chem. Phys. **2018**, *20*, 13974-13982.
5. Fries, D.V., Klein, M.P., Steiner, A., Prosenc, M.H., and Niedner-Schatteburg, G., *Observation and Mechanism of Cryo N₂ Cleavage by a Tantalum Cluster*. Phys. Chem. Chem. Phys. **2021**, *23*, 11345-11354.
6. Mohrbach, J., Dillinger, S., and Niedner-Schatteburg, G., *Cryo Kinetics and Spectroscopy of Cationic Nickel Clusters: Rough and Smooth Surfaces*. J. Phys. Chem. C **2017**, *121*, 10907-10918.
7. Mohrbach, J., Dillinger, S., and Niedner-Schatteburg, G., *Probing cluster surface morphology by cryo kinetics of N₂ on cationic nickel clusters*. J. Chem. Phys. **2017**, *147*, 184304.
8. Ehrhard, A.A., Klein, M.P., Mohrbach, J., Dillinger, S., and Niedner-Schatteburg, G., *Cryokinetics and spin quenching in the N₂ adsorption onto rhodium cluster cations*. Mol. Phys. **2021**, e1953172.
9. Ehrhard, A.A., Klein, M.P., Mohrbach, J., Dillinger, S., and Niedner-Schatteburg, G., *Cryo Kinetics of N₂ Adsorption onto Bimetallic Rhodium-Iron Clusters in Isolation*. under review at J. Chem. Phys.
10. Straßner, A., Wiehn, C., Klein, M.P., Fries, D.V., Dillinger, S., Mohrbach, J., Armentrout, P.B., and Niedner-Schatteburg, G., *Kinetics of stepwise nitrogen adsorption by size-selected iron cluster cations: Evidence for some size-dependent nitrophobia*. under review at J. Chem. Phys.
11. Straßner, A., Wiehn, C., Klein, M.P., Fries, D.V., Dillinger, S., Mohrbach, J., Armentrout, P.B., and Niedner-Schatteburg, G., *Cryo spectroscopy of N₂ on cationic iron clusters*. under review at J. Chem. Phys.

12. Dillinger, S., Mohrbach, J., Hewer, J., Gaffga, M., and Niedner-Schatteburg, G., *Infrared spectroscopy of N₂ adsorption on size selected cobalt cluster cations in isolation*. Phys. Chem. Chem. Phys. **2015**, *17*, 10358-10362.
13. Berg, C., Schindler, T., Niedner-Schatteburg, G., and Bondybey, V.E., *Reactions of Simple Hydrocarbons with Nb_n⁺: Chemisorption and Physisorption on Ionized Niobium Clusters*. J. Chem. Phys. **1995**, *102*, 4870-4884.
14. Maruyama, S., Anderson, L.R., and Smalley, R.E., *Direct injection supersonic cluster beam source for FT-ICR studies of clusters*. Rev. Sci. Instrum. **1990**, *61*, 3686-3693.
15. Proch, D. and Trickl, T., *A high-intensity multi-purpose piezoelectric pulsed molecular beam source*. Rev. Sci. Instrum. **1989**, *60*, 713-716.
16. Caravatti, P. and Allemann, M., *The 'infinity cell': A new trapped-ion cell with radiofrequency covered trapping electrodes for fourier transform ion cyclotron resonance mass spectrometry*. Org. Mass Spectrom. **1991**, *26*, 514-518.
17. Graf, M., *Entwicklung eines auf Evolutionsstrategien basierenden Computerprogrammes zum optimierten Anpassen kinetischer Daten aus FT-ICR-Massenspektrometrie-Messungen*. September 2006, TU Kaiserslautern.
18. Gerhards, M., *High energy and narrow bandwidth mid IR nanosecond laser system*. Opt. Commun. **2004**, *241*, 493-497.
19. Frisch, M.J., Trucks, G.W., Schlegel, H.B., Scuseria, G.E., Robb, M.A., Cheeseman, J.R., Scalmani, G., Barone, V., Mennucci, B., Petersson, G.A., Nakatsuji, H., Caricato, M., Li, X., Hratchian, H.P., Izmaylov, A.F., Bloino, J., Zheng, G., Sonnenberg, J.L., Hada, M., Ehara, M., Toyota, K., Fukuda, R., Hasegawa, J., Ishida, M., Nakajima, T., Honda, Y., Kitao, O., Nakai, H., Vreven, T., Montgomery Jr., J.A., Peralta, J.E., Ogliaro, F., Bearpark, M.J., Heyd, J., Brothers, E.N., Kudin, K.N., Staroverov, V.N., Kobayashi, R., Normand, J., Raghavachari, K., Rendell, A.P., Burant, J.C., Iyengar, S.S., Tomasi, J., Cossi, M., Rega, N., Millam, N.J., Klene, M., Knox, J.E., Cross, J.B., Bakken, V., Adamo, C., Jaramillo, J., Gomperts, R., Stratmann, R.E., Yazyev, O., Austin, A.J., Cammi, R., Pomelli, C., Ochterski, J.W., Martin, R.L., Morokuma, K., Zakrzewski, V.G., Voth, G.A., Salvador, P., Dannenberg, J.J., Dapprich, S., Daniels, A.D., Farkas, Ö., Foresman, J.B., Ortiz, J.V., Cioslowski, J., and Fox, D.J., *Gaussian 09, Revision D.01*. 2009, Gaussian, Inc.: Wallingford, CT, USA.
20. Adamo, C. and Barone, V., *Toward reliable density functional methods without adjustable parameters: The PBE0 model*. J. Chem. Phys. **1999**, *110*, 6158-6170.
21. Weigend, F. and Ahlrichs, R., *Balanced basis sets of split valence, triple zeta valence and quadruple zeta valence quality for H to Rn: Design and assessment of accuracy*. Phys. Chem. Chem. Phys. **2005**, *7*, 3297-3305.
22. Andrae, D., Häußermann, U., Dolg, M., Stoll, H., and Preuß, H., *Energy-adjusted ab initio pseudopotentials for the second and third row transition elements*. Theor. Chim. Acta **1990**, *77*, 123-141.
23. Glendening, E.D., Badenhoop, J.K., Reed, A.E., Carpenter, J.E., Bohmann, J.A., Morales, C.M., and Weinhold, F., *NBO 5.9*. 2009, Theoretical Chemistry Institute, University of Wisconsin: Madison, WI.
24. Bendtsen, J., *The rotational and rotation-vibrational Raman spectra of ¹⁴N₂, ¹⁴N¹⁵N and ¹⁵N₂*. J. Raman Spectrosc. **1974**, *2*, 133-145.
25. Blyholder, G., *Molecular Orbital View of Chemisorbed Carbon Monoxide*. J. Phys. Chem. **1964**, *68*, 2772-2777.

-
26. Dillinger, S., Mohrbach, J., and Niedner-Schatteburg, G., *Probing cluster surface morphology by cryo spectroscopy of N₂ on cationic nickel clusters*. J. Chem. Phys. **2017**, *147*, 184305.
 27. Dillinger, S., Klein, M.P., Steiner, A., McDonald, D.C., Duncan, M.A., Kappes, M.M., and Niedner-Schatteburg, G., *Cryo IR Spectroscopy of N₂ and H₂ on Ru₈⁺: The Effect of N₂ on the H-Migration*. J. Phys. Chem. Lett. **2018**, *9*, 914-918.
 28. Klein, M.P., Ehrhard, A.A., Mohrbach, J., Dillinger, S., and Niedner-Schatteburg, G., *Infrared Spectroscopic Investigation of Structures and N₂ Adsorption Induced Relaxations of Isolated Rhodium Clusters*. Top. Catal. **2018**, *61*, 106-118.
 29. Klein, M.P., Straßner, A., Huber, M.E., and Niedner-Schatteburg, G., *IR spectroscopy of sequential N₂ adsorption onto Rh₆⁺ clusters*. unpublished.
 30. Klein, M.P., Ehrhard, A.A., Huber, M.E., Straßner, A., Fries, D.V., Dillinger, S., Mohrbach, J., and Niedner-Schatteburg, G., *Cryo Infrared Spectroscopy of N₂ Adsorption onto Bimetallic Rhodium-Iron Clusters in Isolation*. under review at J. Chem. Phys.

9.9 Supplementary Information

- Fig. S1** Laser pulse energy in dependence of photon energy in the complete measured range.
- Fig. S2** Most stable (4,5) isomers used to investigate the vibrational modes of a cluster adsorbate complex.
- Table S1** Calculated vibrational modes of the ²(4,5)_113 cluster adsorbate complex.
- Table S2** Calculated vibrational modes of the ²(4,5)_106 cluster adsorbate complex.
- Fig. S3** Equilibrium constants derived from the kinetic fit of the [Ta₅]⁺ cluster.
- Fig. S4** IR-PD spectra of sequential N₂ adsorption steps onto Ta₅⁺ cluster cations [Ta₅(N₂)_m]⁺, *m* = 1–10
- Table S4** Energies of the isomers constituting the spin valley
- Table S5** Vertical (triplet) and adiabatic adsorption energies
- Fig. S5** Vertical (triplet) and adiabatic adsorption energies Δ_{ads}E of the adsorption steps *m* = 0 through *m* = 10.
- Fig. S6** Experimental IR-PD spectra and calculated linear absorption spectra of the most stable isomers for [Ta₅(N₂)₁]⁺ cluster adsorbate complex

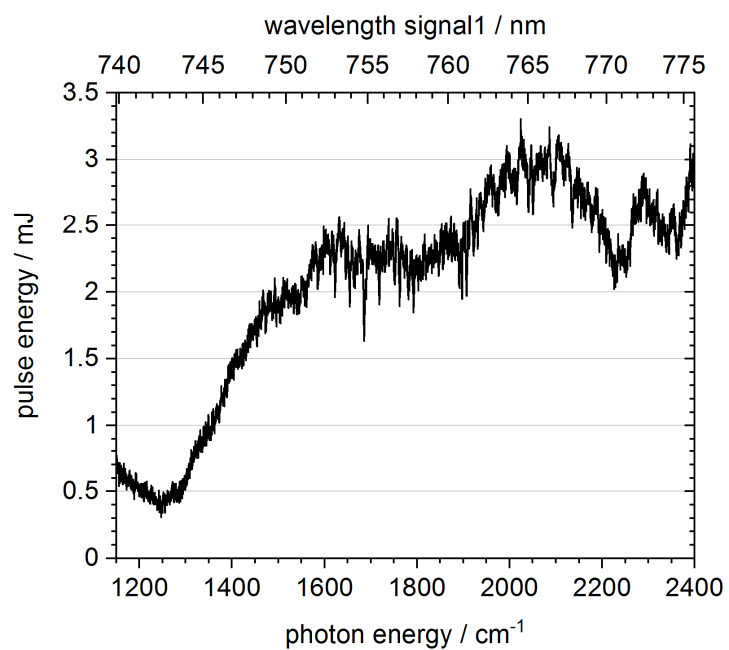


Fig. S1 Laser pulse energy in dependence of photon energy in the complete measured range.

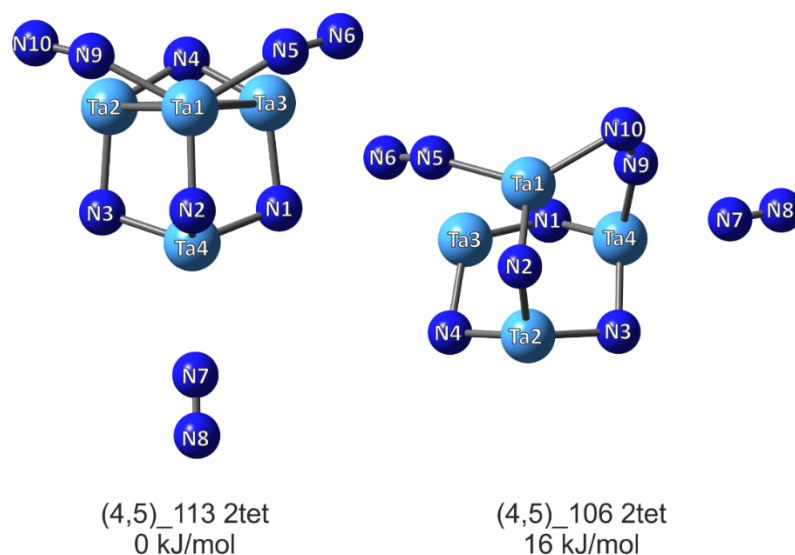


Fig. S2 Most stable (4,5) isomers used to investigate the vibrational modes of a cluster adsorbate complex.

Table S1 Calculated vibrational modes of the ²(4,5)₁₁₃ cluster adsorbate complex. The N₂ stretching frequencies are given unscaled and scaled by 0.9385. The Ta atom numbering is corresponding to Fig. S2. In the case of the stretching vibrations, the position of the oscillators on the cluster is given. N₂ stretching frequencies are scaled by 0.983.

mode	type / site	frequency / cm ⁻¹	scaled frequency / cm ⁻¹	IR intensity / km mol ⁻¹
N₂ wagging modes				
1-4	wagging	27-112		0.22-2.60
Ta₄N₄ cluster skeleton modes				
5-10	cluster core vibrations	133-151		0.29-12.9
N/N₂ bending modes				
10-26	N/N ₂ Bending	180-609		0.0001-104
Ta-N stretching modes				
27-33	Ta-N Stretching	649-897		9.61-212
Single N₂ stretching modes				
34	asym. coupling of N5-N6 and N9-N10	1560	1463	1689
35	sym. coupling of N5-N6 and N9-N10	1687	1582	368
36	N7-N8	2490	2336	7.26

Table S2 Calculated vibrational modes of the ${}^2(4,5)_{106}$ cluster adsorbate complex. The N_2 stretching frequencies are given unscaled and scaled by 0.9385. The Ta atom numbering is corresponding to Fig. S2. In the case of the stretching vibrations, the position of the oscillators on the cluster is given. N_2 stretching frequencies are scaled by 0.983.

mode	type / site	frequency / cm^{-1}	scaled frequency / cm^{-1}	IR intensity / km mol^{-1}
N_2 wagging modes				
1-4	wagging	29-121		0.14-3.91
Ta_4N_4 cluster skeleton modes				
5-9	cluster core vibrations	133-151		3.36-12.36
N/N_2 bending modes				
10-26	N/ N_2 Bending	194-592		0.161-104
Ta-N stretching modes				
27-33	Ta-N Stretching	630-893		11.0-178
Single N_2 stretching modes				
34	N9-N10	1456	1366	447
35	N5-N6	1782	1672	397
36	N7-N8	2479	2325	0.623

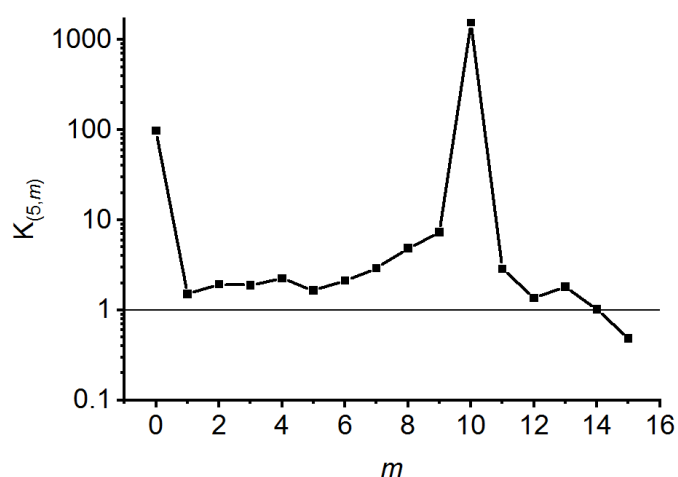


Fig. S3 Equilibrium constants derived from the kinetic fit of the $[\text{Ta}_5]^+$ cluster.

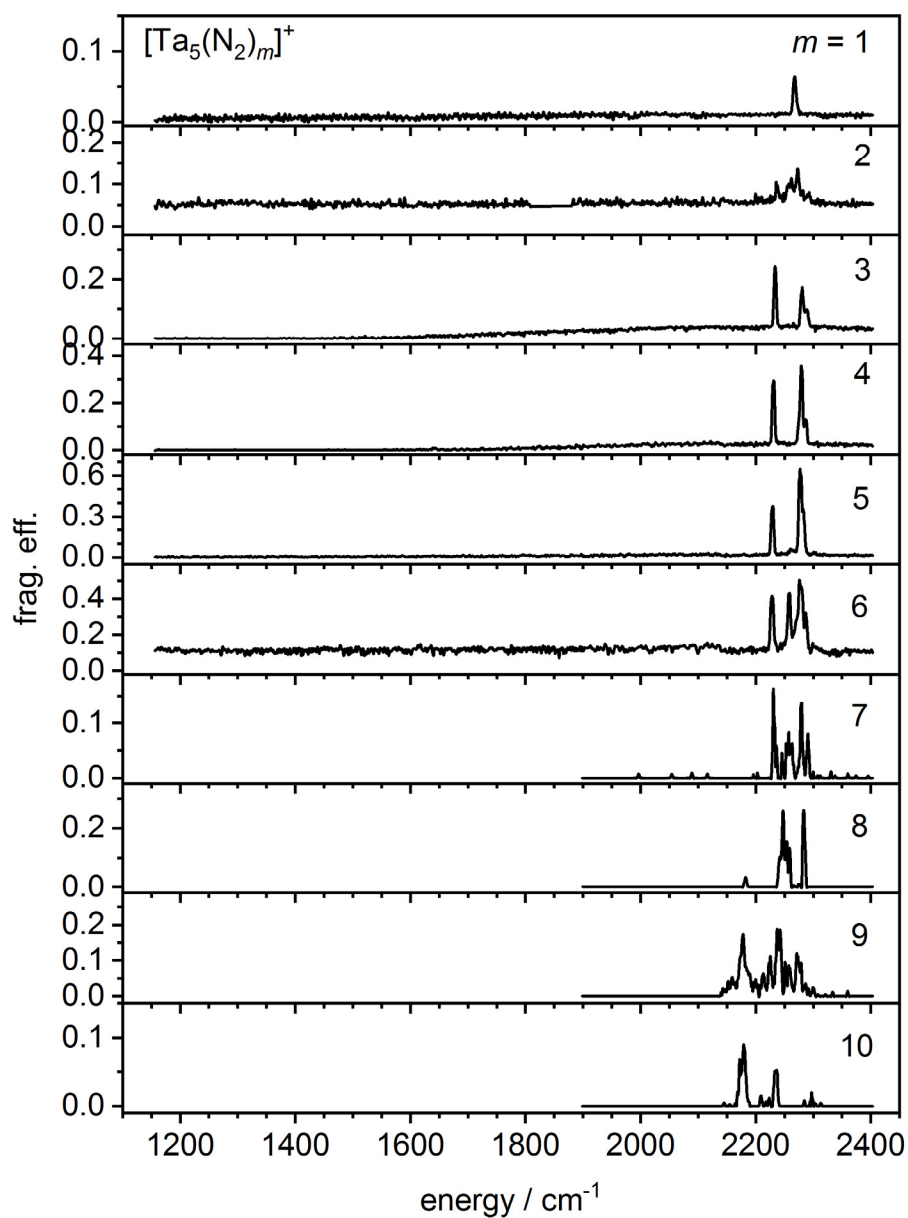


Fig. S4 IR-PD spectra of sequential N₂ adsorption steps onto Ta₅⁺ cluster cations [Ta₅(N₂)_m]⁺, $m = 1-10$ as recorded after 26 K He buffer gas cooling. The measuring range is expanded in order to observe possible side-on N₂ adsorption.

Table S3 Energies of the isomers constituting the spin valley: (a) Absolute energies of the cluster adsorbate complexes, (b) absolute energies of the '(5,*m*) + (10-*m*) N₂' systems, and (c) the relative energies of the '(5,*m*) + (10-*m*) N₂' systems. The grey shaded fields denote the most stable isomer for each *m*.

(a) $E_{\text{abs}}([\text{Ta}_5(\text{N}_2)_m]^+) / \text{a.u.}$

2S+1	<i>m</i>				
	0	1	2	5	10
1	-284.636154	-394.103318	-503.567109	-831.944199	-1379.254958
3	-284.641462	-394.102967	-503.568665	-831.944565	-1379.249108
5	-284.607070	-394.078960	-503.550502	-831.933369	-1379.239387
7	-284.584741	-394.050024	-503.516246	-831.911559	
15	-284.542173	-394.015054	-503.487011	-831.888831	

(b) $E_{\text{abs}}([\text{Ta}_5(\text{N}_2)_m]^+ + (10-m) \text{N}_2) / \text{a.u.}$

2S+1	<i>m</i>				
	0	1	2	5	10
1	-1379.098937	-1379.119823	-1379.137335	-1379.175591	-1379.254958
3	-1379.104245	-1379.119472	-1379.138892	-1379.175956	-1379.249108
5	-1379.069853	-1379.095464	-1379.120729	-1379.164761	-1379.239387
7	-1379.047524	-1379.066529	-1379.086473	-1379.142951	
15	-1379.004956	-1379.031558	-1379.057238	-1379.120223	

(c) $E_{\text{rel}}([\text{Ta}_5(\text{N}_2)_m]^+ + (10-m) \text{N}_2) / \text{kJ/mol}$

2S+1	<i>m</i>				
	0	1	2	5	10
1	13.94	-40.90	-86.88	-187.32	-395.70
3	0.00	-39.98	-90.97	-188.28	-380.34
5	90.29	23.05	-43.28	-158.89	-354.82
7	148.92	99.02	46.66	-101.62	
15	260.68	190.84	123.42	-41.95	

Table S4 Vertical (triplet) and adiabatic adsorption energies as derived from our calculated (5,*m*) *m* = 0, ..., 2, 5, 10 isomers. The values represent the steps 0 and 1 as well as the values for triple adsorption (5,2)→(5,5) and fivefold adsorption (5,5)→(5,10). For the latter two larger steps, we interpolated the multistep values to obtain estimated single-step values and presented them in an additional column (grey shaded).

step <i>m</i>	Adsorption energy / kJ/mol			
	vertical triplet		adiabatic	
0		-40.0		-40.9
1		-50.1		-51.0
2				
3	-97.3	-32.4	-97.3	-32.4
4		-32.4		-32.4
5		-38.4		-41.5
6		-38.4		-41.5
7	-192.1	-38.4	-207.4	-41.5
8		-38.4		-41.5
9		-38.4		-41.5

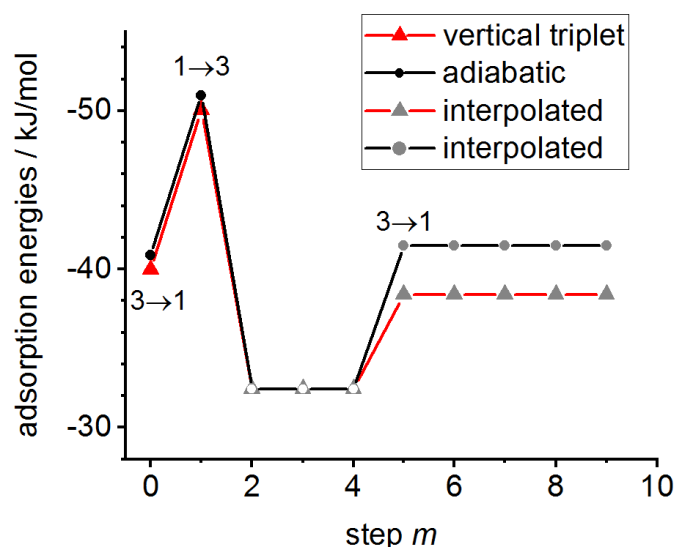


Fig. S5 Vertical (triplet) and adiabatic adsorption energies $\Delta_{\text{ads}}E$ of the adsorption steps *m* = 0 through *m* = 10. The grey points represent interpolated values between (5,2) – (5,5) and (5,5) – (5,10), respectively. The labelling indicates transition between spin states.

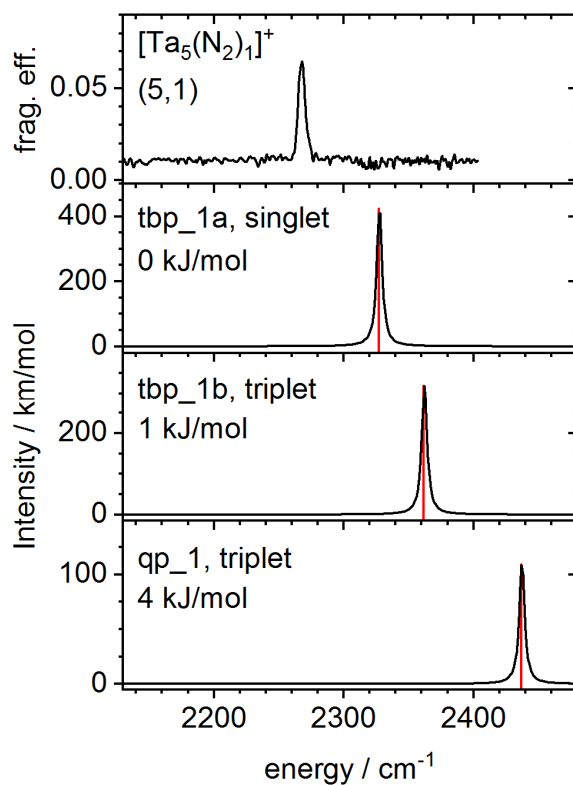


Fig. S6 Experimental IR-PD spectra and calculated linear absorption spectra of the most stable isomers for $[\text{Ta}_5(\text{N}_2)_1]^+$ cluster adsorbate complex. The calculated spectra are not scaled. The structures of the assigned isomers are shown in Fig. 6.

10. Summary and Outlook

The present thesis investigates the interaction of size-selected transition metal clusters with N_2 adsorbate molecules. The influence of the cluster- N_2 interaction on both metal cluster cores as well as on the N_2 adsorbate molecules is elucidated. For our studies, we utilized the FRITZ instrument that enables the generation of metal cluster ions *via* laser vaporization. The size-selected clusters are stored and thermalized in a cryogenic hexapole ion trap. Gas inlets allow the reaction of the stored ions with the reaction gas nitrogen. The resulting cluster adsorbate complexes were analyzed *via* FT-ICR mass spectrometry. Within the ICR cell, the cluster adsorbate complexes could be stored and irradiated with IR radiation generated by a tunable OPO/OPA IR laser system. The experimental setup enabled us to record N_2 adsorption kinetics and IR-PD spectra of cluster adsorbate complexes $[M_n(N_2)_m]^+$. DFT calculations supported these experiments and provided information on the N_2 adsorption process as well as the geometry and electronic structure of the resulting cluster adsorbate complexes. The presented work bases on earlier studies on cobalt, nickel, iron and ruthenium clusters. We focused our investigations on the N_2 adsorption onto cationic rhodium clusters, bimetallic rhodium-iron clusters and tantalum clusters.

Rhodium clusters

In the first part of this thesis (chapters 3 – 5), we studied the stepwise N_2 adsorption onto Rhodium clusters by cryo adsorption kinetics and the resulting cluster adsorbate complexes by means of IR-PD spectroscopy as well as by DFT calculations.

Chapter 3: In a first step, we recorded the IR-PD spectra of $[Rh_i(N_2)_m]^+$ cluster adsorbate complexes (i,m) in the range of $i = 6 - 15$ with a single N_2 adsorbate and in the range of $i = 6 - 11$ with multiple N_2 adsorbates at or close to saturation. DFT calculations of bare clusters Rh_i^+ $i = 6,7,9$ yielded high spin octahedral ($i = 6,7$) and tricapped trigonal prismatic ($i = 9$) structures. The IR-PD bands of single N_2 adsorbates shift continuously red with increasing number of metal atoms, in line with the established charge dilution model. For larger clusters $(i,1)$, $i > 11$, the spectra indicate the coexistence of isomers. Evaluation of the IR-PD spectra in conjunction with DFT modeling allowed the assignment of a $(7,12)$ structure with a capped octahedral Rh_7 core, which resembles the most stable calculated isomer of the naked Rh_7^+ cluster. The high spin state (13tet) of the naked Rh_7^+ cluster quenches upon N_2 adsorption towards triplet multiplicity. This study provides first insights into N_2 adsorbate

localization at rhodium cluster surfaces and into adsorbate induced cluster core relaxation, as evidenced in the cases of (6,11) and (7,13).

Chapter 4: In a second study, we recorded the cryo N₂ adsorption kinetics of Rh_{*i*}⁺ clusters (*i* = 5 – 15) up to saturation. We discussed the presence of intermittent adsorption limits *m_x* as indication for a *rough* cluster surface. In most cases, we observe only maximum adsorption limits *m_{max}* and conclude in a *smooth* cluster surface that consists of equal adsorption sites with similar next neighbor coordination. Relative rate constants derived from pseudo first order kinetic fits serve to quantify the significant trends in adsorption behavior. Equilibria of N₂ adsorption and desorption occur in a large extent for large Rh_{*i*}⁺ clusters (*i* > 10) and we calculated equilibrium constants and Gibbs free energies for these steps. Smaller clusters hold tight to their N₂ adsorbates but for the very last one. The reluctance of the Rh₅⁺ cluster towards N₂ adsorption encouraged us to evaluate the energetics of the adsorption steps by DFT modeling. We postulate an isomerization process from a trigonal bipyramid towards a square pyramid and an accompanying spin quench as indicated by our newly established *spin valley* curves. Deeper understanding of the properties of [Rh₅(N₂)_{*m*}]⁺ cluster adsorbate complexes will require the recording and evaluation of their IR-PD spectra.

Chapter 5: The findings mentioned above include some questions and assumptions that deserved further attention. In particular, some properties of the cluster adsorbate complexes seem to vary with increasing amount of adsorbed N₂. To address these issues, we chose the Rh₆⁺ cluster and recorded IR-PD spectra of each adsorption step (6,*m*) up to saturation at *m_{max}* = 12. We found a continuous red shift of the N-N stretching bands throughout the first seven adsorption steps, which we have tentatively interpreted as a result of an adsorbate dependent charge dilution effect. By virtue of DFT modeling, we assigned structures with an octahedral cluster core to the first five adsorption steps and evaluated the most stable isomers in terms of *spin valley* curves for each adsorption step. A population analysis of the assigned structures confirmed a gradual dissipation of charge and spin density from the metal cluster core over the whole cluster adsorbate complex. An orbital analysis confirmed a σ-bonding π-back bonding synergism that we assumed for the interpretation of the IR spectra.

This study allowed for the following conclusions: (a) We observed no cluster core reorganization in the course of N₂ adsorption. (b) We found dectet spin states for *m* < 5 and a gradual spin quench towards degenerate doublet and quartet isomers above. (c) The adsorption energies between the (6,*m*) cluster adsorbate complexes decrease from the first

to the ultimate step – with some deviations around $m = 4$ and 5, where the spin quench sets in. (d) The IR-PD spectrum of $m_x = 8$ suggests a symmetric cluster adsorbate complex. In addition, we were able to expand the known charge dilution model: Not only an increase of the number of metal atoms but also an increase of the adsorbate shell effects a charge dilution resulting in a softened N_2 stretching vibration.

Rhodium-Iron clusters

The second part of this thesis (chapters 6 and 7) comprises two studies of cryo N_2 adsorption kinetics and IR-PD spectroscopy of mixed $[Rh_iFe_j]^+$ clusters.

Chapter 6: We have recorded the cryo kinetics of N_2 adsorption onto cationic mixed $[Rh_iFe_j]^+$ clusters ($i = 3 - 8$ and $j = 3 - 8$; $i + j = n$) of the three particular cases $[Rh_{n/2}Fe_{n/2}]^+$, $[Rh_{(n-1)/2}Fe_{(n+1)/2}]^+$, and $[Rh_{(n+1)/2}Fe_{(n-1)/2}]^+$. We found differences of the adsorption limits depending on the relative amounts of rhodium and iron within the clusters. From the kinetic fits, we extracted relative rate constants for each N_2 adsorption step and possible desorption steps. For those steps, which are in equilibrium, we determined the Gibbs free energies. We conclude on likely ligand shell reorganization and some weakly bound N_2 ligands for clusters, where multiple N_2 adsorbates are in equilibrium. Transformation of the relative rate constants to absolute rate constants enabled us to determine sticking probabilities, which increase in general with cluster size. Adsorption/desorption equilibria show in a decrease of the sticking probabilities.

Chapter 7: In order to gain information on the geometries and the metal atom distributions within the clusters, we studied size selected N_2 adsorbate complexes of the equiatomic cluster cations $[Rh_{n/2}Fe_{n/2}]^+$ *via* IR-PD spectroscopy and DFT modeling. We found highly symmetric alloy like structures with a maximum amount of Rh-Fe interaction for the $[Rh_3Fe_3]^+$ and $[Rh_4Fe_4]^+$ clusters. The IR-PD spectra comprise a multitude of bands within ranges that coincide with those of N_2 adsorbates on rhodium and iron cluster cations. A band resembling the stretching vibration of free N_2 confirms the presence of weakly bound N_2 adsorbates as indicated by the adsorption kinetics. Our approach allowed us to assign the least red shifted bands to iron sites and to confirm the element sensitivity of the N_2 stretching vibration with respect to adsorption onto rhodium or iron sites. N_2 adsorption onto the $[Rh_3Fe_3]^+$ cluster leads to a monolayer on all metal atoms before the final 7th N_2 molecule is adsorbed onto a rhodium atom in a geminal manner. There is no indication of a spin quench. The IR-PD spectra

of the $[\text{Rh}_4\text{Fe}_4(\text{N}_2)_m]^+$ complexes indicate N_2 adsorption up to $m_x = 4$ exclusively onto the rhodium sites. Additional N_2 attaches to the iron sites, up to $m_{\text{max}} = 8$. Overall, we found adsorption site-specific IR band ranges that allowed us to conclude in preferential adsorption onto rhodium sites and merely secondary adsorption onto iron sites.

Tantalum clusters

The third and last part of this thesis (chapters 8 and 9) comprises of studies of the N_2 adsorption onto and activation by $\text{Ta}_{4,5}^+$ clusters in order to investigate possible N_2 cleavage by means of N_2 cryo adsorption kinetics and cryo IR-PD spectroscopy.

Chapter 8: We recorded adsorption kinetics and IR-PD spectra of the first five N_2 adsorption steps onto the Ta_4^+ cluster. Our rate constants of the initial two adsorption steps and the absence of N-N stretching bands for the corresponding adsorption products (4,1) and (4,2) were first indications for a possible N_2 cleavage. To confirm this assumption, we performed extensive DFT modeling and we found feasible N_2 dissociation pathways on the tetrahedral cluster core with all intermittent barriers submerged for the first and second adsorption steps. Both cleavages proceed via a novel *across edge-above surface (AEAS)* mechanism. The rate determining step is a rearrangement from a μ_2 bonded N_2 ligand across a Ta-Ta edge towards a μ_3 bonded N_2 ligand above a triangular Ta-Ta-Ta surface. Cleavage of the third N_2 ligand is kinetically hindered and we identified the intermediate directly in front of the AEAS barrier by its characteristic vibrational band.

Chapter 9: We recorded the IR-PD spectra of the remaining $[\text{Ta}_4(\text{N}_2)_m]^+$ (4, m) cluster adsorbate complexes up to $m = 12$. The spectra provide no indication of further N_2 cleavage but a variety of bands that we have assigned to coexisting end-on and side-on adsorbed N_2 molecules.

In addition, we recorded IR-PD spectra and preliminary cryo adsorption kinetics of $[\text{Ta}_5(\text{N}_2)_m]^+$ (5, m) cluster adsorbate complexes up to $m = 10$. The IR-PD spectra indicate only end-on adsorbed N_2 molecules. There is no indication of an N_2 cleavage. DFT modeling revealed a trigonal bipyramidal Ta_5^+ minimum structure in triplet spin state that relaxes towards a singlet state at (5,10). An evaluation of *spin valley* curves reveals that, in contrast to rhodium clusters, the high spin states stabilize with increasing N_2 adsorption. The N_2 molecules preferably adsorb onto the higher next neighbor coordinated equatorial tantalum atoms of the trigonal bipyramid. Preliminary population analysis reveals a concentration of the charge density at the equatorial atoms and a concentration of the spin density at the apical atoms. We showed

that the ability of a small tantalum cluster to activate N_2 vanishes by addition of one single metal atom to the cluster core. Further theoretical analyses including orbital analysis are work in progress and they will provide insights in the interacting orbitals and their orientation.

Subsequent research may help to consolidate the understanding of the Rh_5^+ cluster by recording and evaluating IR-PD spectra of its N_2 cluster adsorbate complexes. In the case of the tantalum clusters, the study of H_2 adsorption and N_2/H_2 co-adsorption would be of interest and may reveal possible reactions on the cluster surface. A study of cluster anions would model the effects of changing the clusters' charge on the adsorption of small molecules and may support the understanding of the ligand induced charge dilution that we have found for the Rh_6^+ cluster. In any case, an extension of the investigated size range and of the composition of the clusters would be of great interest as the here presented results showed once more that every atom counts.

11. Zusammenfassung und Ausblick

Die vorliegende Arbeit untersucht die Wechselwirkung zwischen gröÙenselektierten Übergangsmetallclustern und N₂-Adsorbatmolekülen. Dabei berücksichtigt sowohl den Einfluss der Cluster-N₂-Wechselwirkung auf den Metallcluster-Kern als auch auf die N₂-Adsorbatmoleküle. Für unsere Untersuchungen haben wir den FRITZ-Aufbau verwendet, der die Erzeugung von Metallclusterionen mittels Laserverdampfung ermöglicht. Die gröÙenselektierten Cluster werden in einer kryogenen Hexapolionenfalle gespeichert und thermalisiert. Die gespeicherten Ionen können mit dem eingeleiteten Reaktionsgas Stickstoff reagieren. Die dabei entstandenen Cluster-Adsorbat-Komplexe werden mittels FT-ICR-Massenspektrometrie analysiert. In der ICR-Zelle können die Cluster-Adsorbat-Komplexe gespeichert und mit Infrarotstrahlung bestrahlt werden, welche mit einem durchstimmbaren OPO/OPA Infrarot-Lasersystem erzeugt wird. Dieser experimentelle Aufbau ermöglicht das Messen von N₂-Adsorptionskinetiken und von IR-PD-Spektren der Cluster-Adsorbat-Komplexe. Begleitende Dichtefunktionalrechnungen liefern Erkenntnisse über die Adsorptionsprozesse sowie über die geometrische und elektronische Struktur der dabei entstehenden Cluster-Adsorbat-Komplexe. Die hier präsentierte Arbeit baut auf Vorarbeiten an Kobalt-, Nickel-, Eisen- und Rutheniumclustern auf. Wir haben unsere Untersuchungen auf kationische Rhodium-, Rhodium-Eisen- und Tantalcluster fokussiert.

Rhodiumcluster

Im ersten Teil dieser Arbeit (Kapitel 3–5) haben wir die schrittweise N₂-Adsorption auf Rhodiumcluster mittels Kryo-Adsorptionskinetik und die dabei entstandenen Cluster-Adsorbat-Komplexe mittels IR-PD-Spektroskopie sowie mithilfe von DFT-Rechnungen untersucht.

Kapitel 3: In einem ersten Schritt haben wir die IR-PD-Spektren von [Rh_{*i*}(N₂)_{*m*}]⁺-Cluster-Adsorbat-Komplexen (*i, m*) im Größenbereich *i* = 6–15 mit einem einzelnen N₂-Adsorbatmolekül und im Bereich *i* = 6–11 bei oder nahe der Adsorbatsättigung gemessen. DFT-Rechnungen an nackten Rh_{*i*}⁺-Clustern *i* = 6,7,9 offenbarten *high-spin* Cluster mit oktaedrischen Grundstrukturen (*i* = 6,7) und ein dreifach überkapptes trigonales Prisma (*i* = 9). Die Rotverschiebung der IR-PD Banden einzelner N₂ Adsorbate steigt in Übereinstimmung mit dem bewährten *charge-dilution*-Modell mit zunehmender Anzahl der Metallatome an. Die Spektren der größeren Cluster (*i, 1*), *i* > 11 weisen auf die Koexistenz verschiedener Isomere hin. Durch den Vergleich der IR-PD-Spektren mit DFT-Rechnungen konnten wir dem (7,12)

Cluster-Adsorbat-Komplex eine Struktur mit einem überkappt-oktaedrischen Rh_7 -Kern zuordnen, welcher der Struktur des stabilsten berechneten Isomers des nackten Rh_7^+ -Clusters entspricht. Mit zunehmender N_2 -Adsorbatmenge sinkt die Spin-Multiplizität von einem 13tet bei dem nackten Rh_7^+ -Cluster zu einem Triplet bei maximaler Adsorbatmenge (*spin-quench*). Diese Untersuchung bietet erste Einblicke in die Position der N_2 -Moleküle auf der Rhodium-Cluster-Oberfläche. Die Daten für die (6,11) und (7,13) Cluster-Adsorbat-Komplexe weisen auf eine Adsorbat-induzierte Relaxation des Clusterkerns hin.

Kapitel 4: In einer zweiten Untersuchung haben wir die Kryo-Adsorptionskinetiken von N_2 auf Rh_i^+ -Cluster ($i = 5 - 15$) bis zur Adsorbatsättigung (*maximum adsorption limits* m_{max}) gemessen und ausgewertet. Die Existenz zusätzlicher *intermittent adsorption limits* m_x deutet auf raue Clusteroberflächen hin. In den meisten Fällen haben wir lediglich *maximum adsorption limits* beobachtet und schließen daher auf eine glatte Clusteroberfläche, die aus äquivalenten Adsorptionsstellen mit ähnlicher Koordinationsumgebung durch die nächsten Nachbarn besteht. An die kinetischen Messungen haben wir ein kinetisches Modell pseudo-erster Ordnung angepasst und die daraus erhaltenen relativen Geschwindigkeitskonstanten haben wir verwendet, um signifikante Trends im Adsorptionsverhalten zu quantifizieren. Die Kinetiken großer Rh_i^+ -Cluster ($i > 10$) zeigen ausgeprägte N_2 -Adsorptions-Desorptions-Gleichgewichte, für die wir Gleichgewichtskonstanten und Freie Enthalpien berechnet haben. Bei kleinen Clustern haben wir lediglich für das letzte N_2 Adsorbatmolekül eine Desorption beobachtet. Die N_2 -Adsorption auf dem Rh_5^+ -Cluster läuft besonders langsam ab, weshalb wir die Energetik der Adsorptionsschritte mithilfe von DFT-Rechnungen genauer untersucht haben. Wir postulieren in diesem Fall, dass die zunehmende Menge an adsorbiertem N_2 eine Isomerisierung von einer trigonalen Bipyramide zu einer quadratischen Pyramide bewirkt und zusätzlich von einem *spin-quench* begleitet wird. Im Zuge dieser Untersuchungen haben wir die Darstellung der DFT-Ergebnisse in Form von *spin-valley*-Kurven eingeführt. Um die Eigenschaften der $Rh_5(N_2)_m]^+$ Cluster-Adsorbat-Komplexe besser zu verstehen, sollten zukünftig deren IR-PD-Spektren gemessen und ausgewertet werden.

Kapitel 5: Im Zuge der vorherigen Untersuchungen haben sich einige Fragen aufgetreten, die insbesondere solche Eigenschaften der Cluster-Adsorbat-Komplexe betreffen, die mit der adsorbierten N_2 -Menge variieren. Zur Beantwortung dieser Fragen haben wir die IR-PD-Spektren der (6, m) Cluster-Adsorbat-Komplexe bis zu m_{max} gemessen. Wir haben eine kontinuierliche Rotverschiebung der N-N-Streckschwingung während der ersten sieben

Adsorptionsschritte beobachtet. Diese Rotverschiebung konnten wir mit einer Umverteilung der positiven Ladung auf die Adsorbatmoleküle erklären, und so das bereits existierende *charge-dilution*-Modell um eine Abhängigkeit von der Adsorbatmenge erweitern. Mithilfe von DFT-Rechnungen konnten wir den ersten fünf Adsorptionsschritten Strukturen mit oktaedrischem Clusterkern zuordnen. Für alle Adsorptionsschritte haben wir die stabilsten Isomere in Form von *spin-valley*-Kurven ausgewertet. Eine Populationsanalyse der zugeordneten Strukturen hat eine schrittweise Verteilung der Ladungsdichte vom Clusterkern über den gesamten Cluster-Adsorbat-Komplex einschließlich der Adsorbathülle bestätigt. Eine Orbitalanalyse hat das Konzept einer Synergie aus σ -Hinbindung und π -Rückbindung bestätigt, das wir zur Interpretation der IR-PD-Spektren verwenden.

Unsere Untersuchungen erlauben folgende Schlussfolgerungen: (a) Wir haben keine Isomerisierung des Clusterkerns mit fortschreitender N_2 -Adsorption beobachtet. (b) Wir haben Dectet-Multiplizitäten für $m < 5$ erhalten und darüber einen *spin-quench* zu entarteten Quartett- und Dublett-Isomeren beobachtet. (c) Die Adsorptionsenergien nehmen vom ersten zum letzten Adsorptionsschritt ab, mit Schwankungen beim Einsetzen des *spin-quenches*. (d) Das IR-PD-Spektrum von $m_x = 8$ deutet auf einen symmetrischen Cluster-Adsorbat-Komplex hin. Außerdem konnten wir das bekannte *charge-dilution*-Modell erweitern: Zusätzlich zu einer Zunahme der Anzahl der Metallatome kann auch die Zunahme der N_2 -Adsorbatmoleküle eine Verringerung der positiven Ladungsdichte und damit eine Schwächung der N-N-Bindung bewirken.

Rhodium-Eisen-Cluster

Der zweite Teil dieser Arbeit (Kapitel 6 und 7) besteht aus zwei Untersuchungen zur Kryoadsorptionskinetik und IR-PD-Spektroskopie von gemischten $[Rh_iFe_j]^+$ -Clustern.

Kapitel 6: Wir haben die Kryoadsorptionskinetiken von N_2 auf kationische gemischte $[Rh_iFe_j]^+$ -Cluster ($i = 3 - 8$ and $j = 3 - 8$; $i + j = n$) der drei Zusammensetzungen $[Rh_{n/2}Fe_{n/2}]^+$, $[Rh_{(n-1)/2}Fe_{(n+1)/2}]^+$, und $[Rh_{(n+1)/2}Fe_{(n-1)/2}]^+$ gemessen. Die *maximum adsorption limits* unterscheiden sich entsprechend der relativen Rhodium- und Eisen-Anteile. Wir haben relative Geschwindigkeitskonstanten für die Adsorptionsschritte und mögliche Desorptionsschritte bestimmt. Für Adsorptions-/Desorptionsgleichgewichte haben wir Freie Enthalpien bestimmt. In den Fällen, in denen sich das Gleichgewicht auf mehrere Cluster-Adsorbat-Komplexe erstreckt, schließen wir daher auf eine Reorganisation der Adsorbathülle

und schwach gebundene N₂-Moleküle. Durch Umrechnung der relativen in absolute Geschwindigkeitskonstanten konnten wir *sticking probabilities* (Haftwahrscheinlichkeiten) bestimmen, die im Allgemeinen mit der Clustergröße zunehmen. Ausnahmen beobachten wir in den Fällen von Adsorptions-/Desorptions-Gleichgewichten.

Kapitel 7: Um Informationen über die Strukturen der Cluster und über die Verteilungen der Metallatome darin zu erhalten, haben wir gröÙenselektierte N₂-Adsorbatkomplexe der äquiatomaren Clusterkationen [Rh_{n/2}Fe_{n/2}]⁺ mittels IR-PD-Spektroskopie und DFT-Rechnungen untersucht. Wir haben für die [Rh₃Fe₃]⁺- und [Rh₄Fe₄]⁺-Cluster hochsymmetrische Strukturen mit einer maximalen Anzahl von Rh-Fe-Kontakten gefunden. Die IR-PD-Spektren enthalten eine Vielzahl an Banden in Bereichen, die mit denen von N₂-Adsorbaten auf reinen Rhodium- und Eisen-Clustern übereinstimmen. Eine Bande an der Position der Streckschwingung von freiem N₂ bestätigt das Vorhandensein von schwach gebundenen Adsorbaten, worauf bereits die kinetischen Untersuchungen hingewiesen haben. Unsere Herangehensweise hat es uns ermöglicht, die am wenigsten rotverschobenen Banden N₂-Molekülen zuzuordnen, die auf Eisenatomen adsorbiert sind. Somit wurde die Elementsensitivität der N₂-Streckschwingung bezüglich der Adsorption auf Rhodiumatomen oder Eisenatomen bestätigt. N₂-Adsorption auf den [Rh₃Fe₃]⁺-Cluster führt zu einer einfachen Adsorption auf allen Metallatomen bevor das siebte N₂-Molekül auf einem bereits belegten Rhodiumatom adsorbiert wird. Es gibt dabei keine Hinweise auf einen *spin quench*. Die IR-PD-Spektren der [Rh₄Fe₄(N₂)_m]⁺-Cluster-Adsorbat-Komplexe deuten darauf hin, dass die N₂-Adsorption bis zu $m_x = 4$ ausschließlich auf die Rhodiumatome erfolgt. Weitere Adsorption bis zu $m_{max} = 8$ erfolgt auf die Eisenatome. Spezifische Bereiche in den IR-PD-Spektren für eine N₂-Adsorption auf Rhodium- oder Eisenatomen ermöglichen die Feststellung, dass die N₂-Adsorption bevorzugt auf Rhodiumatome und nur sekundär auf Eisenatome erfolgt.

Tantalcluster

Der dritte und letzte Teil dieser Arbeit (Kapitel 8 und 9) enthält Untersuchungen der N₂-Adsorption auf und Aktivierung durch Ta_{4,5}⁺-Cluster, die dem Zweck dienen mögliche N₂-Dissoziation auf den Clustern mithilfe von Kryo-Adsorptionskinetiken und Kryo-IR-PD-Spektroskopie zu erforschen.

Kapitel 8: Wir haben die Adsorptionskinetiken und die IR-PD-Spektren der ersten fünf N₂-Adsorbate von Ta₄⁺-Clustern (4,*m*), *m* = 1-5, gemessen. Die für die ersten zwei Adsorptions-

schritte erhaltenen Geschwindigkeitskonstanten und das Fehlen einer N-N-Streckschwingung der entsprechenden Adsorptionsprodukte (4,1) und (4,2) sind erste Hinweise auf eine mögliche N₂-Dissoziation. Um diese Annahme zu bestätigen, haben wir umfangreiche DFT-Rechnungen durchgeführt. Dabei haben wir für den ersten und zweiten Adsorptionsschritt mögliche Dissoziationspfade von N₂ auf dem tetraedrischen Clusterkern gefunden, deren Energiebarrieren alle unterhalb des Eingangskanals liegen. Beide Dissoziationsprozesse folgen einem neuen *across edge-above surface (AEAS)* Mechanismus. Der geschwindigkeitsbestimmende Schritt ist dabei eine Umorientierung des N₂-Adsorbatmoleküls von einem μ_2 über einer Ta-Ta-Kante gebundenen zu einem μ_3 über einer Ta-Ta-Ta-Fläche gebundenem Zustand. Die Dissoziation eines dritten N₂-Moleküls ist kinetisch gehindert und wir konnten das direkt vor der Barriere liegende Intermediat durch seine charakteristische N-N-Streckschwingungsbande identifizieren.

Kapitel 9: Wir haben die IR-PD-Spektren der verbleibenden [Ta₄(N₂)_m]⁺-Cluster-Adsorbat-Komplexe (4,*m*) bis *m* = 12 gemessen. Die Spektren bieten zwar keine Hinweise auf weitere N₂-Dissoziation, aber dennoch eine Vielzahl an Banden, die wir koexistierenden *side-on* und *end-on* Adsorbatmolekülen zuordnen konnten.

Zusätzlich haben wir die IR-PD-Spektren und vorläufige Kryo-Adsorptionskinetiken von [Ta₅(N₂)_m]⁺-Cluster-Adsorbat-Komplexen (5,*m*) bis zu *m* = 10 gemessen. Die IR-PD-Spektren weisen ausschließlich auf *end-on* gebundene N₂-Moleküle hin und es gibt keine Hinweise auf eine N₂-Dissoziation. DFT-Rechnungen ergaben eine trigonal-bipyramidale Ta₅⁺ Grundstruktur in einem Triplettzustand, der im Laufe zunehmender N₂-Adsorption in einen Singulettzustand bei (5,10) relaxiert. Eine Auswertung der *spin-valley*-Kurven zeigte, dass im Gegensatz zu Rhodiumclustern die relativen Energien der höheren Spinzustände mit zunehmender N₂-Adsorption absinken. Die N₂-Moleküle adsorbieren bevorzugt an die äquatorialen Tantalatome in der trigonalen Bipyramide, deren Anzahl nächster Nachbarn höher ist als die der apikalen Tantalatome. Eine erste Populationsanalyse zeigte eine Konzentration der Ladungsdichte auf den äquatorialen Atomen und eine Konzentration der Spindichte auf den apikalen Atomen. Wir haben gezeigt, dass die Fähigkeit kleiner Tantalcluster ein N₂-Molekül zu spalten durch Hinzufügen eines einzigen Metallatoms verschwindet. Weitere theoretische Untersuchungen einschließlich Orbitalanalysen sind in Arbeit und sollen Einblicke in die wechselwirkenden Orbitale und ihre relative Orientierung zueinander bieten.

Zukünftige Untersuchungen können mithilfe von IR-PD-Spektroskopie dabei helfen, das Verhalten des Rh_5^+ -Clusters besser zu verstehen. Im Fall der Tantalcluster könnten Untersuchungen von H_2 -Adsorbaten und von N_2/H_2 -Koadsorbaten Hinweise auf mögliche Reaktionen auf der Clusteroberfläche bieten. Mit einer Untersuchung von Clusteranionen könnte man Erkenntnisse über die Auswirkungen der Änderung der Clusterladung auf die Adsorption kleiner Moleküle gewinnen und das Verständnis der Ladungsdichteverteilung auf Adsorbatmoleküle, die wir bei dem Rh_6^+ -Cluster beobachtet haben, vertiefen. Auf jeden Fall ist eine Erweiterung des untersuchten Größenbereiches und der Zusammensetzung der Cluster von großem Interesse, da die hier präsentierten Ergebnisse einmal mehr gezeigt haben, dass jedes Atom zählt.

Appendices

12. Appendix 1: Manuals for kinetic fit procedures

For the acquisition of rate constants from kinetic measurements and their interpretation, adequate fitting procedures are necessary. In the AK Niedner-Schatteburg, several fit programs and tools were developed in the last decades. Over the years, the handling of these helpful tools changed and this section serves to document the current usage procedures providing detailed using descriptions, along with illustrations.

The *evofit* program has been developed by Michael Graf [1]. The *manufit* (Formerly simply “fit”) and *2isofit* programs were used since the works of Thomas Schindler [2].

The *Mathematica* notebooks were developed in the course of elaborating this thesis and helped to evaluate the kinetic data as presented in earlier chapters.

12.1 Evofit

12.1.1 Introduction

Evofit creates a pseudo-first-order kinetic fit of time dependent ion intensity data using an evolutionary algorithm. The fitting procedure may take some time, so I recommend performing the calculations as a batch job on a server as described below.

Input: experimental time dependent intensity data, start matrix consisting of 1 and 0 values

Output: rate constant matrix, calculated normalized time dependent intensity data, experimental normalized time dependent intensity data

12.1.2 Preparatory work

a) Where to get the intensity data from? *DataAnalysis*!!

Open the measurement [measurement].d in *DataAnalysis* and apply a data evaluation method from a previous evaluation to create an intensity file. In this method, you have to define a file name for the intensity file. Make a good choice to make sure that you recognize this file as an intensity file in future, e.g. by beginning the name with [Int...].txt. In one of the next lines, you have to define a **modified** delay file (vd-list) you used. This file has a *.txt file extension.

In the following lines you have to define your “parent” and “fragment” masses. The parent mass is usually the bare precursor cluster and the fragment masses the product cluster adsorbate complexes in the order of reaction/adsorption progress. You also have to define the m/z window that is used to read out the intensities of each species from the [measurement].d.

b) What is the vd-list and why do you have to modify it?

During the measurement, the original vd-list is read by *Compass* measuring program and defines the collision cell delays applied one after another. It consists of a simple list of all collision cell delays, usually starting with 0, increasing up to your maximum collision cell delay and is terminated by the starting value, usually 0. That means, after collecting a full kinetic data set, an additional mass spectrum at 0 s collision cell delay is recorded. This file has NO file extension. An example for a typical VD-list name would be “vd_Ta_48_20s”. “vd” indicates a delay file, “Ta” the investigated species, “48” the number of delays in the file excluding the terminating 0 and “20s” the maximum delay defined in the file.

You will chose the duration of your chromatogram according to the total duration of collecting all data points defined in the vd-list and add an additional time buffer. In the additional time, *Compass* starts to read out the delays at the beginning of the vd-list, again.

The evaluation method in *DataAnalysis* correlates the mass spectra in your measurement with a delay in the vd-list. Because you added a time buffer and re-read the vdlst from the beginning, you have to attach the delays of the additional measurements at the end of the file. Save this file as a *.txt file and use it in your *Data Analysis* method.

12.1.3 The actual *evofit* procedure

a) Requirements:

- An account at a batch server system e.g. lca/b
- Time dependent ion intensity data. You may generate them by applying a method *via DataAnalysis* to your kinetic measurement. The measurement data consists of a chromatogram of mass spectra. Each mass spectrum is the sum of usually up to 40 mass spectra at a certain storage time. Each mass spectrum in the chromatogram is recorded at a different storage time of the mass selected cluster ions in the hexapole ion trap.
- An *evofit* version located in your bin folder of the server, e.g. lca:"user"\bin\evofit.exe
- The executable startevo.sh script located in your bin folder of the server (Fig. 1), e.g. lca:"user"\bin\evofit.exe

This script generates an input.sh file in your current evaluation folder containing all required information and submits input.sh as a batch jobfile. Startevo.sh reads in the name of the [output].out file as job name and defines e.g. the number of CPUs and the maximum calculation time.

Alternatively, you may run your job as a local job on the server. You will have no control via SLURM workload manager. In this case, use localevo.sh

- An executable input.sh file in your current evaluation folder. This file may be generated using startevo.sh.
- An input file [inputfile].txt in your current evaluation folder. This file contains the required information for evofit.exe. The content of the input file is described below

and a sample input file is attached (Fig. 2 and 3). For a more detailed description of its contents, refer to M. Graf [1].

b) The input file

The [input file].txt contains the required information for evofit.exe in the following order:

- "number of turns:" The number of calculation steps to be done; e.g. 3. In general, there should be several turns to verify reproducibility.
- "size of child generation:" The number of created childs per generation/size of population; e.g. 40. Increase this number if the reproducibility is not sufficient.
- "size of parent generation:" The number of parents taken into account per generation out of the population size; e.g. 20. This value must be proportionally adapted to the size of child generation if the size of child generation is changed to preserve the selection pressure. An increase of the child/parent ration increases the selection pressure.
- "number of generations before termination:" A bigger value increases accuracy and lowers the scattering. A bigger value also increases the calculation time.
- "time interval (s):" defines the time grid of the calculation and of the output. Only use the values 0.001, 0.0001 or 0.00001; not larger, not smaller! Higher values may cause floating-point errors, smaller values increase the calculation time immensely.
- "end of data creation (s):" The maximum reaction time for the fit, usually consistent with the experimental data.
- "signal threshold:" signal threshold for the fit (usually 0.01, not to change). Relative intensities below this value are not taken into account.
- "mutation probability:" usually 1, not to change in every-day-use
- "standard deviation of mutation (start value):" start value for the standard deviation of the mutation process; e.g. 0.1. This value may be decreased if the data has been already fitted *via manufit*. For a higher value of the k matrix elements (larger initial scattering), a higher initial standard deviation should be chosen.
- "decrementation factor:" The factor by which the standard deviation is reduced (or increased) adaptively; e.g. 0.75. A higher value decelerates the adaption process and can improve the fit for larger matrices.
- "rate constant matrix:" The rate constant matrix is tab separated and contains the rate constants. The diagonal elements are 0. The elements (n+1,n) (below the diagonal) are the k starting values for the reaction, the elements (n,n+1) (above the diagonal) are the k starting values for the back reaction. If there are no estimated or fitted values for k yet, use 1 for all cases. The back reaction may be omitted in the first step: all (n,n+1) = 0. If necessary, you may stepwise „activate“ back reaction steps by exchange of 0 against 1 in following fits. If start values for k already exist, use these values instead of 1. You may obtain suitable starting values from previous *evofit* runs or a manual *manufit* procedures.

Terminate the matrix by the terminator "<" in the following line! Make sure the terminator is not in the last line of the rate constant matrix, but in the following line!

Otherwise the fit process will not work. An error message like the following may occur in this case: "slurmstepd: error: Job ##### exceeded memory limit (104499848 > 102400000), being killed slurmstepd: error: Exceeded job memory limit"

- "start intensity:" The start intensities at t=0 (without the delay!). The intensities do not need to be normalized. Use the data produced by a script *via DataAnalysis*. These values also must be terminated by "<". In this case, the terminator may be in the same line as the start values.
- "time and signal intensities:" (3-)Space separated list. Contains the experimental reaction times/delays in the first column. The other columns contain the experimental intensities of each species taken into account. The intensities do not need to be normalized. Use the data produced by a script *via DataAnalysis*. The first line, except for the first element (time) consists of the start intensities used in the previous point. These list also must be terminated by "<". Place the terminator in the next line below the list.
- "strategy:" (m,l) or (m+l): Choice of the strategy: "+" indicates immortal individuals. The individuals survive throughout a whole turn. For ",", the lifetime of each individual is only 1 generation. The unwanted strategy is commented out with "#".
- "use recombination:" yes or no: Indicates if a recombination is allowed. Usually, this option is activated.
- "check nonreactive educts:" yes or no: Checks for non reactive educts. Choice depends on the experimental data.

c) Procedure:

- 1) Get the intensity data from a kinetic measurement.
- 2) Log in to the computation server; e.g. lca/b
- 3) Make sure that the startevo.sh file refers to the right version of evofit (newer compiled: "evofit.exe"; older compilation "evofit")
- 4) Open the path in WinSCP
- 5) Go to your evaluation folder
- 6) Make an evofit_[input file].txt file in your evaluation folder (A sample input file is depicted in Fig. 2 and 3.
 - o You may also prepare it on your computer and copy it to your evaluation folder on lca/b. In this case take care of the end-of-line (EOL) characters
 - o Choose a meaningful name for this file
 - o Copy your starting intensities to the right place in this file
 - o Copy your intensity data including the time column to the right place in this file
 - o Choose a suitable starting matrix for the fit.
 - o Check the values of the other parameters
- 7) Submit job with the command: startevo.sh [outputfile].txt evofit_[inputfile].txt
 - a. Startevo.sh will generate an input.sh in your evaluation folder and execute it
 - b. Alternatively, you may write the input and output file names directly into input.sh and execute it.

- 8) *Evofit* generates the following files:
 - a. [Outputfile].log: logs the fit process, the quality statistics and the new best rate constant matrices.
 - b. [Outputfile].txt: summarizes the input file. In addition, it contains the rate constant matrices of all turns, the according standard deviation matrices and the total qualities for each ion in each turn. The last two matrices, are the best matrix of all turns and standard deviation matrix of all turns, together with the respective values of the quality function for each species. You may use this best matrix for further work (Fig. 4).
 - c. [Outputfile]_calculated.dat: Contains the calculated normalized intensity data for the best rate constant matrix.
 - d. [Outputfile]_measured.dat: Contains the experimental normalized intensity data. You may use part of this data as input for a manual fit, e.g. with *manufit* [2].
 - e. [Outputfile]_startmatrix.dat: Contains the calculated normalized intensity data for the starting rate constant matrix.
 - f. The batch system SLURM generates also [Outputfile].e##### and [Outputfile].o##### files. These contain error messages, warnings or shell output.
- 9) Plot the content of [Outputfile]_calculated.dat as line diagrams and the content of [Outputfile]_measured.dat as point diagrams and compare the data sets.
- 10) Check if the result is satisfying. The total value of the quality function should be above 99 % and both experimental and calculated intensities should be in good agreement.
 - a. If the result is not satisfying:
 - Change parameters in the Input file, e.g. the population parameters (take care of proportionality)
 - You may use the fitted rate constant matrix.
 - If you have indications of back reactions or an equilibrium, add back reactions in your start matrix.
 - Save the input file with a new meaningful name and repeat steps 7-9.
 - If you still cannot get satisfying results, use your normalized starting intensities and your best rate constant matrix and try to improve the rate constants stepwise using *manufit* as described below.
 - b. If the result is satisfying: Congratulations!

If the result of the evolutionary algorithm procedure is not satisfying, use the manual *manufit* procedure as described in the following section 12.2.

12.1.4 Illustrations for the evofit procedure

```
#!/bin/csh
cat > input.sh <<EOF
#!/bin/csh
#SBATCH --job-name=$1
#SBATCH --partition=normal
#SBATCH --ntasks=1
#SBATCH --cpus-per-task=1
#SBATCH --time=240:00:00
cd $PWD
#Choose new (upper) or old (lower row) compiled evofit version
$HOME/bin/evofit.exe -o $1 $2
#~/bin/evofit -o $1 $2
EOF
chmod +x input.sh
```

Fig. 23 Startevo.sh. This script, located on the Linux server, generates and submits an input file suitable for SLURM job management.

```
"number of turns:"
3
# Gibt die Anzahl der Rechendurchläufe an. Es sollten grundsätzlich mehrere Rechnungen
# durchgeführt werden, um die Reproduzierbarkeit zu erhöhen.
"size of child generation:"
40
# bei vielen Geschwindigkeitskonstanten sollte die Populationsgröße vergrößert werden.
# bei schlecht reproduzierbaren Ergebnissen hilft oft ein Erhöhen des Wertes.
"size of parent generation:"
20
# wird der obige Wert geändert, muss dieser proportional geändert werden, wenn
# der Selektionsdruck gleich bleiben soll. Der kann durchaus noch erhöht werden.
"number of generations before termination:"
50
# Dieser Parameter hat großen Einfluss auf die Genauigkeit und auf die Reproduzierbarkeit
# der Ergebnisse. Je größer, desto genauer und weniger gestreut sind diese. Allerdings zum
# Preis einer erhöhten Rechenzeit.
"time interval (s):"
0.001
# Grundsätzlich sollten hier nur die Werte 0,00001, 0,0001 und 0,001 benutzt werden. Noch
# größere Werte führen zu (aufgrund des Berechnungsalgorithmus' im Programm) zu Fließkomma-
# Fehlern, zu kleine erhöhen die Rechenzeit immens.
"end of data creation (s):"
4.6
# gibt an, bis zu welcher Zeit aus einer gegebenen Geschwindigkeitskonstantenmatrix
# Intensitätswerte berechnet werden sollen.
"signal threshold:"
0.01
# Ist die Schwelle, unterhalb derer man auch beim visuellen Fitten Intensitätswerte
# nicht zum Fitten heranzieht. Muss i.d.R. nicht geändert werden.
"mutation probability:"
1
# Sollte im "Alltagsbetrieb" nicht geändert werden.
"standard deviation of mutation (start value):"
0.1
# Gibt die Startstandardabweichung für den Mutationsprozess an. Kann verkleinert werden, wenn
# das Datenmaterial bereits visuell gefittet wurde, aber auch vergrößert, wenn die Elemente der
# Matrix" (s.u.) größer gewählt werden (größere Startstreuung)
"decrementation factor:"
0.75
# gibt den Faktor an, mit dem die Standardabweichung adaptiv erniedrigt (b.z.w. in Umkehrung
# auch wieder erhöht) wird. eine Erhöhung des Wertes verlangsamt den Adaptionsprozess, was bei
# großen Matrizen sinnvoll sein kann.
```

Fig. 24 Sample input file:

"evofit_20160429_26.OK_RhN2_pos_kin_n 5_10T_10.txt", first part.

12. Appendix 1: Manuals for kinetic fit procedures

```
best calculated matrix in 3 turns:
  0 6.1676192      0      0      0      0      0      0      0      0      0
1.0162565      0 3.0677979      0      0      0      0      0      0      0      0
  0 3.4172604      0 0.3614492      0      0      0      0      0      0      0
  0      0 4.4056368      0 0.0004113      0      0      0      0      0      0
  0      0      0 5.0022387      0 1.07E-05      0      0      0      0      0
  0      0      0      0 5.1236546      0 9.15E-05      0      0      0      0
  0      0      0      0      0 4.9969205      0 5.75E-07      0      0      0
  0      0      0      0      0      0 6.2397784      0 1.5431323      0      0
  0      0      0      0      0      0      0 2.409902      0 7.64E-07      0
  0      0      0      0      0      0      0      0 2.6879302      0 8.81E-08
  0      0      0      0      0      0      0      0      0 3.0159887      0

total value of quality function (high accuracy):0.982378542423248291
interpolation qualities for each ion graph separately (high accuracy):
ion No. 1:0.968643486499786377
ion No. 2:0.990638077259063721
ion No. 3:0.997715830802917480
ion No. 4:0.995529353618621826
ion No. 5:0.996549665927886963
ion No. 6:0.995319724082946777
ion No. 7:0.997494697570800781
ion No. 8:0.987049698829650879
ion No. 9:0.989723682403564453
ion No. 10:0.993508279323577881
ion No. 11:0.944090723991394043

standard deviations of all rate constants calculated:
  0 0.4407613      0      0      0      0      0      0      0      0      0
0.0591355      0 0.9204181      0      0      0      0      0      0      0      0
  0 0.4067487      0 0.276924      0      0      0      0      0      0      0
  0      0 0.220605      0 0.4176631      0      0      0      0      0      0
  0      0      0 0.3862051      0 0.8221014      0      0      0      0      0
  0      0      0      0 0.3408461      0 0.9334768      0      0      0      0
  0      0      0      0      0 0.547493      0 0.3215786      0      0      0
  0      0      0      0      0      0 0.3767808      0 1.0195917      0      0
  0      0      0      0      0      0      0 1.1469856      0 0.2676393      0
  0      0      0      0      0      0      0      0 1.0797932      0 0.1133531
  0      0      0      0      0      0      0      0      0 1.3469059      0
```

Fig. 26 Best rate constant matrix, quality functions and standard deviation matrix as written by evofit in the [output].txt file. Sample file: Rh5_pos_10T_2_20200430_1a.txt.

12.2 Manufit

12.2.1 Introduction

Manufit can perform pseudo-first-order fits on normalized kinetic data. The program calculates time dependent ion intensities using normalized starting values and a (guessed) rate constant matrix. This rate constant matrix may be a result of an *evofit* procedure. The *manufit* calculation is finished in a few seconds and may be easily performed on your desktop PC.

Input: (guessed) rate constant matrix, experimental normalized start intensities

Output: calculated normalized time dependent intensity data

Manufit is used, if the genetic *evofit* algorithm fails. I recommend using a rate constant matrix created by *evofit* as an input for *manufit*.

If your intensity data is not normalized yet, feel free to use the *Mathematica* script "NormalizeKinetics.nb" to do so.

12.2.2 The actual *manufit* procedure

a) Requirements:

- A *manufit* version in a file located on your computer, e.g. C:\Path\manufit3.0.exe
- A Fit input file *.fit in your current evaluation folder (described in more detail below)
 - o This file contains among others a rate constant matrix, preferably preoptimized and an output of a first *evofit* trial
- A file containing normalized experimental intensity data, e.g. created by *evofit* "Rh15_18T_2_20160428_measured.dat". You may also generate normalized intensity data using the NormalizeKinetics.nb Mathematica file as described in Section 12.3 below.
- The startmanu.bat script in your current evaluation folder, containing
C:\Path\manufit3.0.exe > "Output file" < "[Input file].fit", e.g.
C:\Users\Matthias\Documents\fit3.0.exe > Rh15_18T_2_3_fit.dat < Rh15_18T_2_fit
 - o This script executes *manufit*, reads in the input file and writes the output in the chosen file
 - o A similar procedure is possible with a Shell script on a Linux server
- A valid *Mathematica* installation on your PC and the latest version of fitplot"x".nb in your current data folder

b) Procedure:

- 1) Open with GUI the data folder containing the input file, the *measured.dat file and startmanu.bat
- 2) Modify startmanu.bat:
 - Make sure it refers to manufit3.0.exe in the right directory
 - Check/change the name of the output file
 - Check/change the name of the input file
 - Save and close startmanu.bat
- 3) Modify fitplot.nb
 - Check/change the name of the normalized experimental data (*measured.dat) file in “Load Data” section (marked red in Fig. 5)
 - Check/change the name of the *manufit* output file in “Load Data” section
 - Check/change the time delays in the “Create Plots” section (marked red in Fig. 7; should be consistent with your experimental data)
 - Save Mathematica file and do not close it, you will need it later on
- 4) Open the input file in a text editor, e.g. notepad++ or pspad
 - Check/change number of data points
 - Check/change minimum intensity for output
 - Fill in the number of ions including all parents and daughters
 - Check/change the start time
 - Check/change the delay time (should be consistent with the experimental data)
 - Add your normalized starting intensities
 - Add the rate constant matrix (e.g. output from *evofit*)
 - Check/change the incrementation step for fit
 - Save input file and do not close it, you will need it later on
- 5) Double-click on startmanu.bat: execution of manufit3.0.exe and creation of the output file.
alternatively, you may navigate in your *Windows* command line to the data folder and type in content of startmanu.bat. Hitting [Enter] executes *manufit*
- 6) Click somewhere in the input cell of fitplot3.nb and hit [SHIFT]+[ENTER]. Experimental data (dots) and the data calculated using your input file (lines) are plotted in the output cell (Fig. 8)
- 7) Check if the result is satisfying
 - a. If it is not satisfying:
 - i. change a rate constant in the input file
 - ii. save the input file and let it open
 - iii. repeat steps 5-7 until 7b
 - b. If it is satisfying: Congratulations!

12.2.3 The code

This script consists of three sections:

- 1) Header Section and “Load Data” section (Fig. 5)
Experimental and calculated data are read in and written to the variables “expdata” and “calcddata”.
- 2) The “Plot Data” section
 - a. “preparation for plot” (Fig. 6): The read-in data is processed to prepare a plot. This section stores the time dependent intensity data in a variable (“tde” for experimental data and “tdc” for the calculated data. The variable “tdi” enables the treatment of kinetic fits with the program “2isofit”. This is required, if the initial species comprises a second non-reactive isomer.
 - b. The “create plots” section (Fig. 7): This section performs the actual plots of experimental and calculated intensity data in one graph. The experimental data points are presented as dots, the calculated data appears as lines.

The code of “fitplot.nb” is as follows:

```

(* fitplot.
nb: Mathematica Script for Visualization of Fit-Output data compared to experimental
    _passe an
    kinetic data during iterative Fit procedure with FIT-
    _passe an
    Program ((c)Thomas Schindler 1994) scripted by Matthias Klein 2018*)
(* Warning: It might be no elegant programming style,
but it works fine in connection with "fit" and a shell script (e.g. startfit.sh)
that executes fit and writes the output data to a file called by the command
in program line 2. Please take care to use the right directories. *)
(*##### Load Data #####*)

(* reads calculation input/normalized data from evofit
into stream. The data must consist of a column for the applied
delays and an additional column for each evaluated species. *)
estrm = OpenRead["Documents/Manutest/Rh15_18T_2_20160428_measured.dat"];
    _öffne,um zu lesen
(* modify directory and file name *)
(* reads calculation output into stream *)
cstrm = OpenRead["Documents/Manutest/Rh15_18T_2_3_fit.dat"];
    _öffne,um zu lesen

(* writes streamed data to variable and closes streams *)
expdata = ReadList[estrm, Number, RecordLists -> True];
    _lese Liste      _Zahl      _separate Liste pr... _wahr
calcdata = ReadList[cstrm, Number, RecordLists -> True];
    _lese Liste      _Zahl      _separate Liste pr... _wahr
Close[estrm];
    _schließe
Close[cstrm];
    _schließe

```

Fig. 27 The header and “Load Data” Section: Read-In of the measured and calculated Data used in the Fit procedure. The file names are marked red and may be adapted to the actual file names.

```

(*##### Plot Data #####*)
    [stelle Funktion graphisch dar]
(*##### preparation for plot #####*)

edelays = expdata[[All, 1]];
    [alle]

(* reads delay vector from imported experimental data (1st column) *)
eintensities = expdata[[1 ;; Length[expdata[[All, 1]]], 2 ;; Length[expdata[[1]]]];
    [Länge] [alle] [Länge]

(* reads intensities from imported experimental data (all but 1st column) *)
cdelays = calcddata[[All, 1]];
    [alle]

(* reads delay vector from imported calculated data (1st column) *)

cintensities =
    calcddata[[1 ;; Length[calcddata[[All, 1]]], 2 ;; Length[calcddata[[1]]]];
    [Länge] [alle] [Länge]

(* reads intensities from imported calculated data (all but 1st column) *)
cisoHELP = cintensities;
cisoHELP[[All, 2]] = cintensities[[All, Length[cintensities[[1]]]];
    [alle] [alle] [Länge]

cisoINT =
    cisoHELP[[1 ;; Length[calcddata[[All, 1]]], 2 ;; Length[calcddata[[1]]] - 1]];
    [Länge] [alle] [Länge]

(*cisoINT=PadLeft[cdaughters,18,ConstantArray[0,Length[calcddata[[All,1]]]]*)
    [fülle auf von links]

tde = TemporalData[eintensities, {edelays}]; (* Defines experimental
    [Zeitdaten]
    intensities as time dependent data with delay vector as time row *)
tdc = TemporalData[cintensities, {cdelays}]; (* Defines calculated
    [Zeitdaten]
    intensities as time dependent data with delay vector as time row *)
tdi = TemporalData[cisoINT, {cdelays}];
    [Zeitdaten]

legend = Range[0, Length[expdata[[1]]] - 1];
    [Liste aufe...] [Länge]

(* makes legend out of number of colums. Legend
    consists of number of reactions species has undergone *)

```

Fig. 28 The “preparation for plot” section. No input and changes need to be made here. The violet parts indicate the possibility to process data from a 2isofit program, which takes into account two isomers of the initial species reacting with different rates. The variable “tdi” comprises the time dependent intensity data

```
(*##### Create Plots #####*)

g1 = ListLogPlot [tde, PlotRange → {{-0.1, 5.5(**)}, {0.001, 1.1}}, PlotLegends →
  [listenbezogene logari... [Koordinatenbereich der Graphik [Legenden der Graphik
  SwatchLegend[{legend}], LegendMarkerSize → 15(**), LegendMarkers → "Bubble"],
  [Farbfeld-Legende [Größe der Legendenmarkierung [Legendenmarkierungen
  PlotStyle → PointSize[0.0075], ImageSize → 1200];
  [Darstellungsstil [Punktgröße [Bildgröße

(* You may modify the delay range plotted (**) and the other underlined
parameters like size of dots and thickness of lines! *)

g2 = ListLogPlot[tdc, PlotRange → {{-0.1, 5.5(**)}, {0.001, 1.1}},
  [listenbezogene logari... [Koordinatenbereich der Graphik
  Joined → True, PlotStyle → Thickness[0.0015], ImageSize → 1200];
  [verknüpft? [wahr [Darstellungsstil [Dicke [Bildgröße

Show[g1, g2] (* only visible output of this script is a Plot combining
zeige an [stelle Funktion graphisch dar
experimental data (dots) and calculated data (lines) *)

(*OutputOutputOutputOutputOutputOutputOutputOutputOutputOutputOutput*)
```

Fig. 29 The “Create Plots” section. You may vary the red parameters: The plotted delay range has to be the same for the experimental and calculated data plot. Exchange the plotted calculated variable “tdc” by “tdi” if you are working with the “2isofit” program.

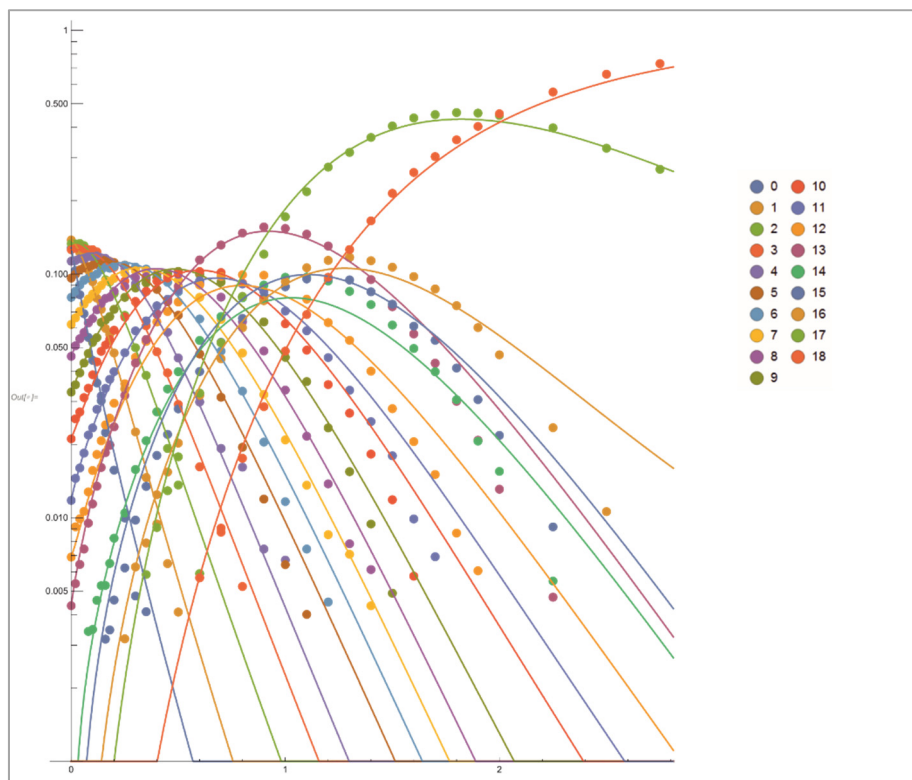


Fig. 30 Typical output diagram of fitplot3.nb

12.3 Normalize kinetic data

EvoFit automatically normalizes the measured kinetic data and prints it into a special file. However, *manuFit* does not include this functionality. If you want to perform a manual kinetic fit on a measurement that has not been undergone the genetic *evoFit* algorithm, you have to perform the normalization in a previous step. The Mathematica file “NormalizeKinetics.nb” may be helpful here.

This script consists of four sections:

- 1) Read in the intensity file
- 2) Normalization of the intensity file
- 3) Output of the normalized data

There are two options of the output: a) Output of bare intensity data and b) Output of intensity data with delays in first column. One of them is commented out.

- 4) Plot of the normalized Data

After modifying the file names, the script can be executed by pressing [Shift]+[Enter] and the normalized intensity data are plotted:

The code is as follows:

```

1) (* Matthias Klein 2019*)
(* Programm normiert Intensitätsfiles, die zuvor mit DataAnalysis erstellt wurden*)
(***) Import der experimentellen Daten: (***)
    [importiere
(***) Namen der Intensitätsdatei angeben (In "Anführungszeichen"): (***)
    [eingegebenes Objekt
strm = OpenRead[ (**) "20190116_26.0K_Fe17N2_9T.txt" (**) ]; Fill in intensity file name
    [öffne,um zu lesen
Skip[strm, Record, 1, NullRecords → True];
[überspringe [Aufzeichnung [leere Einträge [wahr
expdata = ReadList[strm, Number, RecordLists → True];
    [lese Liste [Zahl [separate Liste pr [wahr
Close[strm];
[schließe

delays = expdata[[All, 1]]; (*Speichert die erste Spalte der Daten als Delays. *)
    [alle

2) (*-----*)
(***) normiert die experimentellen Daten (***)
intensities = expdata[[1 ;; Length[expdata[[All, 1]]], 2 ;; Length[expdata[[1]]]];
    [Länge [alle [Länge
transint = Transpose[intensities];
    [transponiere
sumrowsint = Total[Transpose[intensities]];
    [Gesam... [transponiere
normA = intensities / sumrowsint // N;
    [numerischer Wert
normdata = MapThread[Insert, {normA, delays, Table[1, {Length[delays]}]}];
    [wende auf ... [füge ein [Tabelle [Länge

3) (*-----*)
(***) Export der normierten Daten: (***)
    [exportiere
(***) Namen der Output-Dateien angeben (In "Anführungszeichen"): (***)
    [eingegebenes Objekt
(*Export[ (**) "norm20190116_26.0K_Fe17N2_9T.dat" (**), normA]; Fill in output file name for
    [exportiere bare intensity data
(*Exportiert ohne Delays*)*)
Export[ (**) "delaynorm20190116_26.0K_Fe17N2_9T.dat" (**), normdata];
    [exportiere Fill in output file name for
    [erste Spalte sind die Delays*) intensity data with delays
    [in first column

4) (*-----*)
(***) Plot der normierten Daten: (***)
    [stelle Funktion graphisch dar
td = TemporalData[normA, {delays}];
    [Zeitdaten
legend = Range[0, Length[normA[[1]]] - 1];
    [Liste aufe... [Länge
g1 = ListLogPlot[td, PlotRange → {0.001, 1}, PlotLegends → {legend}];
    [listenbezogene logar... [Koordinatenbereich der Graphik [Legenden der Graphik
Show[g1]
    [zeige an

```

Fig. 31 The NormalizeKinetics.nb file. The four steps are emphasized and the lines where to modify the file names are marked.

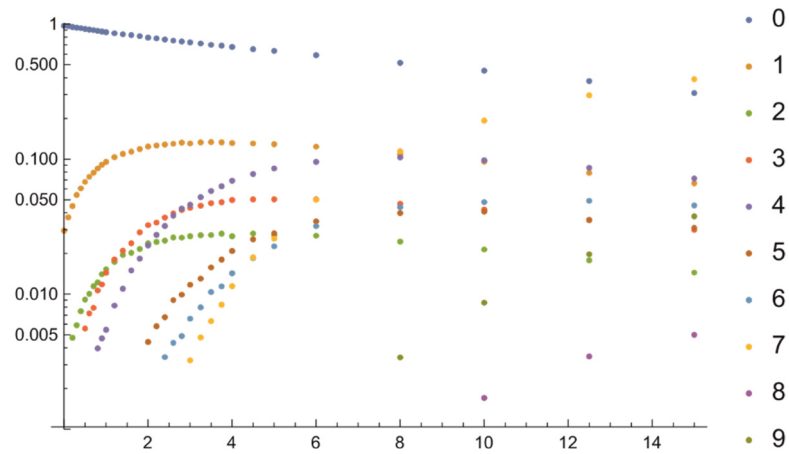


Fig. 23: Plot of normalized intensity data as generated by “NormalizeKinetics.nb”.

12.4 Literature

1. Graf, M., *Entwicklung eines auf Evolutionsstrategien basierenden Computerprogrammes zum optimierten Anpassen kinetischer Daten aus FT-ICR-Massenspektrometrie-Messungen*. September 2006, TU Kaiserslautern.
2. Schindler, T., *Reaktivität und Stabilität molekularer Cluster*. 1995, TU München.

13. Appendix 2: Further Joint Publications

13.1 Cryo IR Spectroscopy of N₂ and H₂ on Ru₈⁺: The Effect of N₂ on the H-Migration

Sebastian Dillinger^a, Matthias P. Klein^a, Annika Steiner^a, David C. McDonald II^b,
Michael A. Duncan^b, Manfred M. Kappes^{c,d}, and Gereon Niedner-Schatteburg^a

*a) Fachbereich Chemie and Forschungszentrum OPTIMAS, Technische Universität
Kaiserslautern, 67663 Kaiserslautern, Germany*

b) Department of Chemistry, University of Georgia, Athens, Georgia 30602, USA

*c) Institute of Physical Chemistry, Karlsruhe Institute of Technology (KIT), Fritz-Haber-Weg 2,
76131 Karlsruhe, Germany*

*d) Institute of Nanotechnology, Karlsruhe Institute of Technology (KIT), Hermann-von-
Helmholtz-Platz 1, 76344 Eggenstein-Leopoldshafen, Germany*

13.1.1 Preamble

The following chapter is a reprint of a publication in the journal “Journal of Physical Chemistry Letters”.

An experimental team consisting of S. Dillinger, A. Steiner, D. C. Mc Donald II, and myself conducted the experiments. S. Dillinger conducted the data evaluation and the quantum chemical calculations. The initial manuscript was written by S. Dillinger and revised with the help of G. Niedner-Schatteburg, M. M. Kappes, and M. A. Duncan.

Full Reference:

Cryo IR Spectroscopy of N₂ and H₂ on Ru₈⁺: The Effect of N₂ on the H-Migration

S. Dillinger, **M. P. Klein**, A. Steiner, D. C. McDonald II, M. A. Duncan, M. M. Kappes, and G. Niedner-Schatteburg, *J. Phys. Chem. Lett.* **2018**, 9, 4, 914–918.

<https://doi.org/10.1021/acs.jpcllett.8b00093>

13.1.2 Reprint

Reprinted with permission from S. Dillinger et al., *J. Phys. Chem. Lett.* **2018**, *9*, 4, 914–918.

Copyright 2018 American Chemical Society.

Cryo IR Spectroscopy of N₂ and H₂ on Ru₈ : The Effect of N₂ on the H-Migration

Author: Sebastian Dillinger, Matthias P. Klein, Annika Steiner, et al

Publication: Journal of Physical Chemistry Letters

Publisher: American Chemical Society

Date: Feb 1, 2018

Copyright © 2018, American Chemical Society



PERMISSION/LICENSE IS GRANTED FOR YOUR ORDER AT NO CHARGE

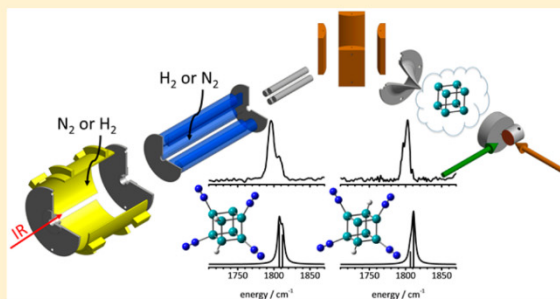
This type of permission/license, instead of the standard Terms & Conditions, is sent to you because no fee is being charged for your order. Please note the following:

- Permission is granted for your request in both print and electronic formats, and translations.
- If figures and/or tables were requested, they may be adapted or used in part.
- Please print this page for your records and send a copy of it to your publisher/graduate school.
- Appropriate credit for the requested material should be given as follows: "Reprinted (adapted) with permission from (COMPLETE REFERENCE CITATION). Copyright (YEAR) American Chemical Society." Insert appropriate information in place of the capitalized words.
- One-time permission is granted only for the use specified in your request. No additional uses are granted (such as derivative works or other editions). For any other uses, please submit a new request.

Cryo IR Spectroscopy of N₂ and H₂ on Ru₈⁺: The Effect of N₂ on the H-MigrationSebastian Dillinger,[†] Matthias P. Klein,[†] Annika Steiner,[†] David C. McDonald, II,[‡] Michael A. Duncan,[‡] Manfred M. Kappes,^{§,||} and Gereon Niedner-Schatteburg^{*,†,||}[†]Fachbereich Chemie and Forschungszentrum OPTIMAS, Technische Universität Kaiserslautern, 67663 Kaiserslautern, Germany[‡]Department of Chemistry, University of Georgia, Athens, Georgia 30602, United States[§]Institute of Physical Chemistry, Karlsruhe Institute of Technology (KIT), Fritz-Haber-Weg 2, 76131 Karlsruhe, Germany^{||}Institute of Nanotechnology, Karlsruhe Institute of Technology (KIT), Hermann-von-Helmholtz-Platz 1, 76344 Eggenstein-Leopoldshafen, Germany

Supporting Information

ABSTRACT: We present the cryo IR-PD spectra of the coadsorbed [Ru₈(H₂)₁(N₂)₄]⁺ and [Ru₈(N₂)₄(H₂)₁]⁺ species differing in the adsorption sequence of H₂ and N₂, which we record via application of tandem cryo ion trapping. We observe strong evidence for dissociative H₂ adsorption, and the spectra reveal differences in the Ru–H stretching region, which we assign to distal and proximal hydrogen atom locations on the Ru₈⁺ cluster, their migration likely hindered by preloaded nitrogen molecules and unaffected by subsequent N₂ adsorption.



Ru-based catalysts make it possible to run the Haber-Bosch process under milder conditions than with widespread Fe-based catalysts.¹ This is underlined by the industrial Kellogg Advanced Ammonia Process, which uses supported Ru nanoparticles as the catalyst and works at lower pressures and temperatures.² Ammonia synthesis on Ru catalysts is highly structure sensitive.³ Highly reactive “BS sites” (5 Ru atoms interact with N₂) are thought to mediate the rate-limiting step in ammonia synthesis—the N₂ activation.^{4,5} Studies on isolated clusters can provide valuable information to elucidate such structure-sensitive reactions. Yet, mass spectrometric investigations of reactions of Ru clusters with small molecules like H₂ are very challenging due in part to the broad isotopic distribution of Ru.

Various spectroscopic studies of the N₂/Ru(001) surface–adsorbate system indicate that at low temperatures N₂ adsorbs in a head-on position.^{6,7} High-resolution electron energy loss spectroscopy (HREELS) has identified the same type of adsorption on Ru(1010), as opposed to Fe(111) where N₂ binds side-on.^{8,9} Dissociative adsorption of N₂ on Ru(0001) only sets in at higher surface temperatures.¹⁰ In contrast H₂ dissociatively chemisorbs on Ru(001) at temperatures as low as 50 K.¹¹ The corresponding change in work function has been associated with two different adsorption states, as also observed in thermal desorption studies.¹² HREELS measurements of hydride monolayers have allowed determination of the Ru–H stretch and bend vibrations (around 820 and 1137 cm^{−1}).¹³ More recently, fast quantum tunneling effects of H on Ru

(0001) have been observed at low temperatures.¹⁴ These may also play a role in the formation of NH on a Ru(001) surface when nitrogen is coadsorbed.¹⁵

The magnetic properties of isolated neutral Ru clusters in the size range between 10 and 100 atoms have been investigated by cluster beam deflection experiments, which showed no evidence for significant ferromagnetism.¹⁶ Several computational studies predict that small Ru clusters favor cubic structures.^{17–19} This prediction was substantiated by far-IR spectroscopy of small cationic Ru clusters, which provided evidence for cubic structures.²⁰ Trapped-ion electron diffraction (TIED) found a cubic motif for the Ru₈[−] cluster.²¹ There are several reaction studies with Ru clusters, although these are complicated by the mentioned difficulties with the isotopic distribution. Mass spectrometry in conjunction with density functional calculations has revealed water activation by cationic ruthenium oxide clusters.²² TIED experiments have shown that Ru₁₉[−] undergoes a structural transition upon H₂ adsorption.²³ H₂ on neutral Ru clusters has also been the subject of extensive theoretical investigations.^{24–26} IR spectroscopy has yielded fundamental insights into the binding of CO to cationic and anionic Ru²⁷ clusters as well as into the adsorption of N₂ on neutral Ru clusters.²⁸ Primarily, head-on μ₁ adsorption of CO and N₂ have been inferred.

Received: January 10, 2018

Accepted: February 6, 2018

Published: February 6, 2018

To our knowledge, there have been no experiments aimed at elucidating the coadsorption of H₂ and N₂ on isolated Ru clusters (in order to explore precursor states leading to catalytic activation). Our tandem cryo trap instrument provides the unique opportunity to conduct these experiments, as shown by our previous work on N₂ on Co²⁹ and Ni clusters.³⁰

This study reports IR spectra the coadsorbed [Ru₈(H₂)₁(N₂)₄]⁺ and [Ru₈(N₂)₄(H₂)₁]⁺ species (differing in adsorption sequence) under isolated conditions. It elucidates the interplay of H₂-N₂ coadsorption in unprecedented detail. In particular, it provides clear evidence for dissociative chemisorption of H₂ and demonstrates that subsequent mobility of hydrogen atoms can be constrained by N₂ adsorption.

Using our tandem cryo trapping technique, we were able to produce H₂-N₂ coadsorbates by sequential addition in **either order**. We find that the IR-PD spectra of the “mixed” adsorbates can depend on this order. To demonstrate this, we have selected the two species [Ru₈(H₂)₁(N₂)₄]⁺ and [Ru₈(N₂)₄(H₂)₁]⁺, where the notation signifies the order of attachment: the [Ru₈(H₂)₁(N₂)₄]⁺ species is assembled by first adsorbing a single H₂ in the cryo hexapole trap followed by four N₂ adsorbates in the cryo FT-ICR trap. Conversely, the [Ru₈(N₂)₄(H₂)₁]⁺ species is formed by adding four N₂ adsorbates in the cryo hexapole trap and one H₂ adsorbate in the subsequent cryo FT-ICR trap.

At first sight, the IR-PD spectra of both species reveal similar Ru–H and N₂ stretching features (Figure 1), much like those seen with separate adsorbates (corresponding to the stretching modes of Ru–H and of head-on coordinated N₂, cf. Figure S2);

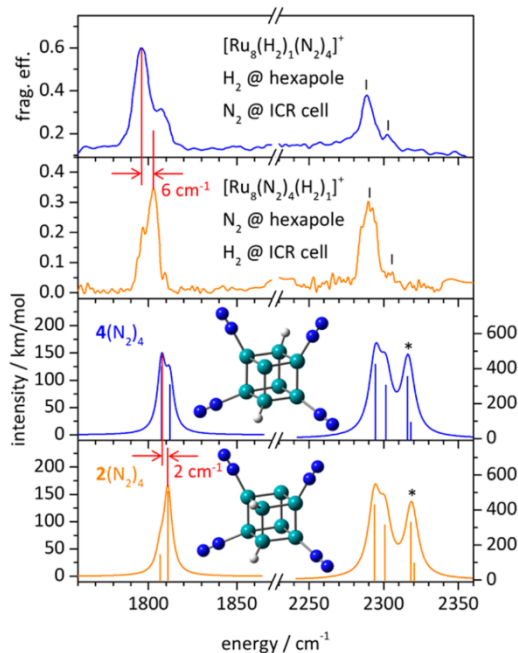


Figure 1. IR-PD spectra of [Ru₈(H₂)₁(N₂)₄]⁺ (blue) and [Ru₈(N₂)₄(H₂)₁]⁺ (orange) compared to the predictions of theory. The red lines serve to highlight the shifts induced by varying the sequence of N₂/H₂ addition. For a discussion of the predicted bands (including * features) refer to the text and the Supporting Information.

the Supporting Information provides extended spectra (Figures S5 and S6), void of additional features, which document the excellent reproducibility of individual features over multiple measurements (Figure S19).

Upon closer inspection, the Ru–H bands differ in the [Ru₈(H₂)₁(N₂)₄]⁺ and [Ru₈(N₂)₄(H₂)₁]⁺ spectra: the former reveals a resolved side peak 10 cm⁻¹ to the blue of the main peak at 1796 cm⁻¹, which is not present in the latter. The latter has an asymmetric peak shape with some red shading, which is absent in the former. The dominant Ru–H stretch blue shifts by 6 cm⁻¹ from the former to the latter.

In the N₂ stretch region both the [Ru₈(H₂)₁(N₂)₄]⁺ and the [Ru₈(N₂)₄(H₂)₁]⁺ species reveal a strong main peak at about 2290 cm⁻¹ with a weak feature about 13 cm⁻¹ to the blue; this is well resolved in the former and somewhat blurry in the latter.

We refer the reader to the Supporting Information (Figure S7) for a figure contrasting the spectra of the coadsorbed species with those of [Ru₈(H₂)_k]⁺ and [Ru₈(N₂)_m]⁺, respectively. In the case of [Ru₈(H₂)₁(N₂)₄]⁺, the H₂ is already dissociated on the cluster. These hydrogen atoms had the possibility to migrate to the energetically most favored spot.

We extended our DFT calculations to model H₂-N₂ coadsorption. In particular, we checked relative energies and predicted IR-allowed vibrational transitions for numerous plausible structural variants of [cubic Ru₈, 4N₂, 2H]⁺ (for structures and corresponding spectra, see Figures S8–S15; for structural labels, see Figure 2). Note that the spin quenches

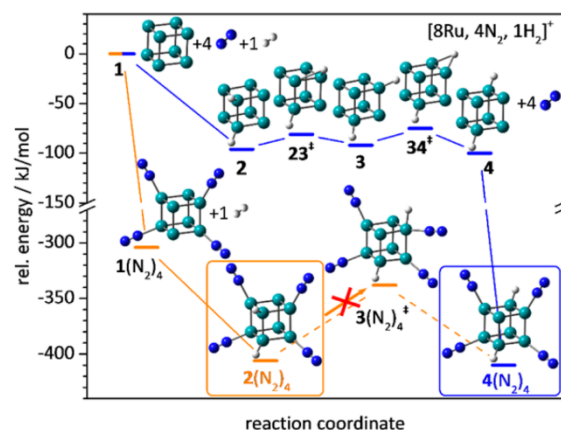


Figure 2. Predicted reaction paths for the formation of [Ru₈(H₂)₁(N₂)₄]⁺/4(N₂)₄ and [Ru₈(N₂)₄(H₂)₁]⁺/2(N₂)₄.

from a quartet in the case of cubic Ru₈^{+/1} and [Ru₈(N₂)₄]^{+/1}(N₂)₄ to a doublet upon further addition of 2H. On the basis of energetics and spectral features, we conclude that the two most likely structures of [cubic Ru₈, 4N₂, 2H]⁺ have doublet spin states (see insets to Figure 1). We present their predicted IR absorption spectra in the lower traces of Figure 1.

The assigned calculated spectra show features that are quite similar to the experimental IR-PD spectra, except for the predicted * bands that occur significantly weaker in the experiment. This deviation is likely due to a lack of efficient internal vibrational redistribution (IVR) in these cases (for further details, refer to text 2 in the Supporting Information), which limits the dissociation yield.

In the Ru–H band region, we find a close resemblance of the IR absorption spectra predicted by DFT for isomers 4(N₂)₄

and 2(N₂)₄ with the IR-PD spectra recorded for the two distinct species [Ru₈(H₂)₁(N₂)₄]⁺ and [Ru₈(N₂)₄(H₂)₁]⁺: DFT modeling reveals a shoulder to the blue of the RuH stretching band in 4(N₂)₂ and asymmetric red shading in the case of 2(N₂)₄. The predicted blue shift of the RuH band of 4(N₂)₄ with respect to that of 2(N₂)₄ (about 2 cm⁻¹) closely corresponds to the IR-PD bands of [Ru₈(H₂)₁(N₂)₄]⁺ and [Ru₈(N₂)₄(H₂)₁]⁺, which differ by a blue shift of about 6 cm⁻¹.

On the basis of all of the above findings, we are confident to assign the 4(N₂)₄ structure to the [Ru₈(H₂)₁(N₂)₄]⁺ species and the 2(N₂)₄ structure to the [Ru₈(N₂)₄(H₂)₁]⁺ species. Both have the same arrangement of N₂ on the cubic Ru₈⁺ cluster as in 1(N₂)₄ (that can be assigned by comparison of DFT-calculated spectra with the experimental spectrum of [Ru₈(N₂)₄]⁺, cf. Figure S8 and text 2 in the Supporting Information). They merely differ in their RuH positions: in the case of [Ru₈(H₂)₁(N₂)₄]⁺/4(N₂)₄, the hydrogens are located on two opposing Ru atoms (distal “trans” HH arrangement), and in the case of [Ru₈(N₂)₄(H₂)₁]⁺/2(N₂)₄, they are on two neighboring Ru atoms (proximal “cis” HH arrangement).

Our vibrational band assignments lead to the tentative conclusion that hydrogen atom migration is hindered on N₂ preloaded Ru₈⁺ clusters, whereas on naked Ru₈⁺, hydrogen atoms swiftly migrate through cooperation of adjacent Ru atoms to the most favorable Ru binding sites (see Figure S15). These lie on two (space) diagonally opposing Ru atoms (distal “trans” HH arrangement). Once formed, this arrangement apparently persists upon subsequent N₂ adsorption. When H₂ adsorbs to a N₂ preloaded Ru₈⁺ cluster (1(N₂)₄), it dissociates as well, but the adsorbed nitrogen molecules likely hinder H migration. The hydrogen atoms are forced to stay on two neighboring Ru atoms (proximal “cis” HH arrangement).

In order to further support the above interpretation, we calculated a range of possible reaction paths for H-migration on a cubic Ru₈⁺ cluster, thereby confirming the effect of coadsorbed N₂ (Figure 2). We predict facile hydrogen atom hopping among adjacent (unloaded) Ru atoms, whereas H migration across a face of the Ru₈⁺ cube is energetically precluded (Figure S16). In the case of H₂ adsorption on a naked Ru₈⁺ (blue reaction path in Figure 2), the migration from two neighboring Ru–H (2) occurs via an intermediate with the hydrogen atoms on two (face) diagonal Ru atoms (3) and via two low-lying Ru–H–Ru “on bridge” transition states (23[‡] and 34[‡]) with barriers of about 15 and 17 kJ/mol, ultimately to two opposing Ru–H (4) (distal “trans” HH arrangement), which convert without a barrier by stepwise N₂ adsorption into 4(N₂)₄. The excess energy from the H₂ adsorption is most likely dissipated by the collision gas. Yet it may serve to overcome the low barriers as the H migration may be faster than the cooling process.

The H₂ adsorption on a preloaded [Ru₈(N₂)₄]⁺/1(N₂)₄ species (orange reaction path in Figure 2) results in the 2(N₂)₄ species with the hydrogen atoms on two neighboring Ru atoms (proximal “cis” HH arrangement). It is essentially impossible to reach the 4(N₂)₄ species by further hydrogen hopping, which would involve a high-energy transition state (with a barrier of about 68 kJ/mol) where the hydrogen atom would be located on a N₂ loaded Ru site (3(N₂)₄[‡]). Thus, the 2(N₂)₄ species is the final product upon N₂ preloading.

We have presented the cryo IR-PD spectra of the [Ru₈(H₂)₁(N₂)₄]⁺ and [Ru₈(N₂)₄(H₂)₁]⁺ species, where the listed order signifies the order of adsorption. Our IR-PD spectra show tantalizing differences, in particular, in the Ru–H bands.

We interpret this in terms of distal or proximal hydrogen locations on the Ru₈⁺ cluster as well as by differences in hydrogen migration kinetics. Such migration is likely hindered by preloading with nitrogen molecules but unaffected by subsequent N₂ adsorption. We elucidate this interplay of low-temperature H₂–N₂ coadsorption in unprecedented detail and, in particular, at low-coordinated Ru sites as present in rough/open bulk surfaces. Such information is particularly valuable for gauging of future nano- and multiscale modeling of N₂ activation and its catalytic conversion. It is imperative to extend our studies toward further adsorbate species such as HD and NH₃ and toward conceivable photoactivation and product identification.

EXPERIMENTAL AND COMPUTATIONAL METHODS

We performed all experiments in a customized Fourier transform-ion cyclotron resonance (FT-ICR) mass spectrometer (Apex Ultra Bruker Daltonics), in particular, cluster production, isolation, N₂/H₂ adsorption, infrared photodissociation (IR-PD) spectroscopy, and mass analysis. The metal cluster ions were generated from a monoisotopic ¹⁰²Ru (99.38%, Oak Ridge National Laboratories; Figure S1) foil using a home-built laser vaporization source.^{31,32} After mass selection, the Ru clusters were stored in a cryogenic hexapole ion trap (17 K for H₂ and 26 K for N₂). Reaction gas (H₂ or N₂) was continuously introduced up to a pressure of 5.0 × 10⁻⁷ mbar to yield sufficient reaction products. Helium was used to increase the pressure up to 5.0 × 10⁻⁶ mbar to accomplish efficient trapping and cooling (cf. extended experimental description in the Supporting Information). After a variable storage time (0–10 s), the ions were guided into the FT-ICR cell that was held at a temperature below 10 K for the spectroscopy of the [Ru₈(H₂)_k]⁺ and [Ru₈(N₂)_m]⁺ species. The cell was used for isolation and detection of the ions. For the coadsorption experiments, the ICR cell served as the second reaction cell that was heated to 19 K for reactions with H₂ or to 49 K for N₂ to avoid condensation. The pressure was increased from 2.0 × 10⁻⁹ up to 1.0 × 10⁻⁸ mbar, and the ions were stored up to 2 s. For acquisition of the IR-PD spectra, the FT-ICR cell was coupled to a tunable IR laser that generates radiation in the range of 1000–2400 cm⁻¹. Each trapped and isolated packet of ions was irradiated by 7–10 laser pulses (0.1–1.5 mJ/pulse). The IR spectra were recorded by acquiring fragmentation mass spectra while continuously scanning the IR wavelength. The IR-PD signal was evaluated as $\sum_i F_i / (\sum_i F_i + \sum_i P_i)$, where F_i and P_i indicate the fragment and the parent ion signals, respectively. An experimental IR-PD spectrum is then obtained from a plot of the fragmentation efficiency as a function of laser frequency. In the case of the coadsorbed species, the loss of N₂ was the only observed fragmentation channel. Linear (harmonic) IR absorption spectra were calculated at the PBE³³ level of theory using the cc-pVTZ basis sets³⁴ (H, N) and the Stuttgart RSC 1997³⁵ effective core potential (Ru), respectively, as implemented in the Gaussian 09 program package,³⁶ with appropriately gauged scaling factors correcting for the vibrational anharmonicities and for the deficiency in the DFT harmonic force field.

ASSOCIATED CONTENT

Supporting Information

The Supporting Information is available free of charge on the ACS Publications website at DOI: 10.1021/acs.jpcllett.8b00093.

Detailed experimental and computational methods; mass spectra recorded in the Ru_8^+ cluster mass range with a natural isotope ratio and a monoisotopic ^{102}Ru foil; IR-PD spectra of $[\text{Ru}_8(\text{H}_2)_k]^+$ $k = 1-8$, $[\text{Ru}_8(\text{D}_2)_6]^+$, and $[\text{Ru}_8(\text{N}_2)_m]^+$ $m = 1-8$; IR-PD spectra of the $[\text{Ru}_8(\text{H}_2)_1(\text{N}_2)_4]^+$ and $[\text{Ru}_8(\text{N}_2)_4(\text{H}_2)_1]^+$ species with an extended spectral range; DFT calculations of $[\text{Ru}_8(\text{H}_2)_1]^+$, $[\text{Ru}_8(\text{N}_2)_4]^+$, $[\text{Ru}_8(\text{H}_2)_1(\text{N}_2)_4]^+$, and $[\text{Ru}_8(\text{N}_2)_4(\text{H}_2)_1]^+$; and alternative reaction paths for the formation of **4** from **2** and for the formation of $4(\text{N}_2)_4$ from $2(\text{N}_2)_4$ (PDF)

AUTHOR INFORMATION

Corresponding Author

*E-mail: gns@chemie.uni-kl.de.

ORCID

Michael A. Duncan: 0000-0003-4836-106X

Geron Niedner-Schatteburg: 0000-0001-7240-6673

Notes

The authors declare no competing financial interest.

ACKNOWLEDGMENTS

This work was supported by the German research foundation DFG within the transregional collaborative research center SFB/TRR 88 “Cooperative effects in homo and heterometallic complexes” (3MET.de) and by the state research center OPTIMAS. We gratefully acknowledge the generous support for D.C.M. from the Air Force Office of Scientific Research through Grant No. FA9550-15-1-0088. The isotopes used in this research were supplied by the United States Department of Energy Office of Science by the Isotope Program in the Office of Nuclear Physics. We thank the reviewers for valuable comments.

DEDICATION

This work is dedicated to Professor Helmut Schwarz in recognition of his seminal contributions to the field of single site catalysis.

REFERENCES

- Schlögl, R. In *Handbook of Heterogeneous Catalysis*; Wiley-VCH Verlag GmbH & Co. KGaA: Weinheim, Germany, 2008.
- Bielawa, H.; Hinrichsen, O.; Birkner, A.; Muhler, M. The Ammonia-Synthesis Catalyst of the Next Generation: Barium-Promoted Oxide-Supported Ruthenium. *Angew. Chem., Int. Ed.* **2001**, *40*, 1061–1063.
- Jacobsen, C. J. H.; Dahl, S.; Hansen, P. L.; Törnqvist, E.; Jensen, L.; Topsøe, H.; Prip, D. V.; Møenshaug, P. B.; Chorkendorff, I. Structure Sensitivity of Supported Ruthenium Catalysts for Ammonia Synthesis. *J. Mol. Catal. A: Chem.* **2000**, *163*, 19–26.
- van Hardeveld, R.; van Montfoort, A. The Influence of Crystallite Size on the Adsorption of Molecular Nitrogen on Nickel, Palladium and Platinum. *Surf. Sci.* **1966**, *4*, 396–430.
- Shetty, S.; Jansen, A. P. J.; van Santen, R. A. Active Sites for N_2 Dissociation on Ruthenium. *J. Phys. Chem. C* **2008**, *112*, 17768–17771.
- de Paola, R. A.; Hoffmann, F. M.; Heskett, D.; Plummer, E. W. Adsorption of Molecular Nitrogen on Clean and Modified Ru(001) Surfaces: The Role of σ Bonding. *Phys. Rev. B: Condens. Matter Mater. Phys.* **1987**, *35*, 4236–4249.
- Shi, H.; Jacobi, K. Evidence for Physisorbed N_2 in the Monolayer on Ru(001) at 40 K. *Surf. Sci.* **1992**, *278*, 281–285.
- Gruyters, M.; Jacobi, K. High-Resolution Electron Energy Loss Spectroscopy Study of Chemisorbed and Physisorbed N_2 on Ru(1010). *Surf. Sci.* **1995**, *336*, 314–320.
- Grunze, M.; Golze, M.; Hirschwald, W.; Freund, H.-J.; Pulm, H.; Seip, U.; Tsai, M. C.; Ertl, G.; Küppers, J. π -Bonded N_2 on Fe(111): The Precursor for Dissociation. *Phys. Rev. Lett.* **1984**, *53*, 850–853.
- Shi, H.; Jacobi, K.; Ertl, G. Dissociative Chemisorption of Nitrogen on Ru(0001). *J. Chem. Phys.* **1993**, *99*, 9248–9254.
- Tatarkhanov, M.; Rose, F.; Fomin, E.; Ogletree, D. F.; Salmeron, M. Hydrogen Adsorption on Ru (001) Studied by Scanning Tunneling Microscopy. *Surf. Sci.* **2008**, *602*, 487–492.
- Feulner, P.; Menzel, D. The Adsorption of Hydrogen on Ruthenium (001) – Adsorption States, Dipole-Moments and Kinetics of Adsorption and Desorption. *Surf. Sci.* **1985**, *154*, 465–488.
- Kostov, K. L.; Widdra, W.; Menzel, D. Hydrogen on Ru(001) Revisited: Vibrational Structure, Adsorption States, and Lateral Coupling. *Surf. Sci.* **2004**, *560*, 130–144.
- McIntosh, E. M.; Wikfeldt, K. T.; Ellis, J.; Michaelides, A.; Allison, W. Quantum Effects in the Diffusion of Hydrogen on Ru(0001). *J. Phys. Chem. Lett.* **2013**, *4*, 1565–1569.
- Waluyo, I.; Ren, Y.; Trenary, M. Observation of Tunneling in the Hydrogenation of Atomic Nitrogen on the Ru(001) Surface to Form NH. *J. Phys. Chem. Lett.* **2013**, *4*, 3779–3786.
- Cox, A. J.; Louderback, J. G.; Apsel, S. E.; Bloomfield, L. A. Magnetism in 4d-Transition Metal Clusters. *Phys. Rev. B: Condens. Matter Mater. Phys.* **1994**, *49*, 12295–12298.
- Li, S. F.; Li, H. S.; Liu, J.; Xue, X. L.; Tian, Y. T.; He, H.; Jia, Y. Structural and Electronic Properties of Ru_n Clusters ($n = 2-14$) Studied by First-Principles Calculations. *Phys. Rev. B: Condens. Matter Mater. Phys.* **2007**, *76*, 045410/1–045410/9.
- Aguilera-Granja, F.; Balbás, L. C.; Vega, A. Study of the Structural and Electronic Properties of Rh_N and Ru_N Clusters ($N < 20$) within the Density Functional Theory. *J. Phys. Chem. A* **2009**, *113*, 13483–13491.
- Zhang, W. Q.; Zhao, H. T.; Wang, L. C. The Simple Cubic Structure of Ruthenium Clusters. *J. Phys. Chem. B* **2004**, *108*, 2140–2147.
- Kerpál, C.; Harding, D. J.; Rayner, D. M.; Lyon, J. T.; Fielicke, A. Far-IR Spectra and Structures of Small Cationic Ruthenium Clusters: Evidence for Cubic Motifs. *J. Phys. Chem. C* **2015**, *119*, 10869–10875.
- Waldt, E.; Hehn, A.-S.; Ahlrichs, R.; Kappes, M. M.; Schooss, D. Structural Evolution of Small Ruthenium Cluster Anions. *J. Chem. Phys.* **2015**, *142*, 024319/1–024319/8.
- Lang, S. M.; Bernhardt, T. M.; Krstic, M.; Bonacic-Koutecky, V. Water Activation by Small Free Ruthenium Oxide Clusters. *Phys. Chem. Chem. Phys.* **2014**, *16*, 26578–26583.
- Bumüller, D.; Hehn, A.-S.; Waldt, E.; Ahlrichs, R.; Kappes, M. M.; Schooss, D. Ruthenium Cluster Structure Change Induced by Hydrogen Adsorption: Ru_{19}^- . *J. Phys. Chem. C* **2017**, *121*, 10645–10652.
- Ge, G.-X.; Yan, H.-X.; Jing, Q.; Luo, Y.-H. Theoretical Study of Hydrogen Adsorption on Ruthenium Clusters. *J. Cluster Sci.* **2011**, *22*, 473.
- Takahashi, K.; Isobe, S.; Ohnuki, S. The Stabilization of Fe, Ru, and Os Clusters upon Hydrogenation. *RSC Adv.* **2013**, *3*, 21841–21847.
- Cusinato, L.; Martínez-Prieto, L. M.; Chaudret, B.; Del Rosal, I.; Poteau, R. Theoretical Characterization of the Surface Composition of Ruthenium Nanoparticles in Equilibrium with Syngas. *Nanoscale* **2016**, *8*, 10974–10992.
- Lyon, J. T.; Gruene, P.; Fielicke, A.; Meijer, G.; Rayner, D. M. Probing C-O Bond Activation on Gas-Phase Transition Metal Clusters: Infrared Multiple Photon Dissociation Spectroscopy of Fe, Ru, Re, and W Cluster CO Complexes. *J. Chem. Phys.* **2009**, *131*, 184706.
- Kerpál, C.; Harding, D. J.; Lyon, J. T.; Meijer, G.; Fielicke, A. N_2 Activation by Neutral Ruthenium Clusters. *J. Phys. Chem. C* **2013**, *117*, 12153–12158.

(29) Dillinger, S.; Mohrbach, J.; Hewer, J.; Gaffga, M.; Niedner-Schatteburg, G. Infrared Spectroscopy of N₂ Adsorption on Size Selected Cobalt Cluster Cations in Isolation. *Phys. Chem. Chem. Phys.* **2015**, *17*, 10358–10362.

(30) Mohrbach, J.; Dillinger, S.; Niedner-Schatteburg, G. Cryo Kinetics and Spectroscopy of Cationic Nickel Clusters: Rough and Smooth Surfaces. *J. Phys. Chem. C* **2017**, *121*, 10907–10918.

(31) Maruyama, S.; Anderson, L. R.; Smalley, R. E. Direct Injection Supersonic Cluster Beam Source for FT-ICR Studies of Clusters. *Rev. Sci. Instrum.* **1990**, *61*, 3686–3693.

(32) Berg, C.; Schindler, T.; Niedner-Schatteburg, G.; Bondybey, V. E. Reactions of Simple Hydrocarbons with Nb_n⁺: Chemisorption and Physisorption on Ionized Niobium Clusters. *J. Chem. Phys.* **1995**, *102*, 4870–4884.

(33) Adamo, C.; Barone, V. Toward Reliable Density Functional Methods without Adjustable Parameters: The PBE0Model. *J. Chem. Phys.* **1999**, *110*, 6158–6170.

(34) Dunning, T. H. Gaussian-Basis Sets for Use in Correlated Molecular Calculations 1. The Atoms Boron through Neon and Hydrogen. *J. Chem. Phys.* **1989**, *90*, 1007–1023.

(35) Andrae, D.; Haeussermann, U.; Dolg, M.; Stoll, H.; Preuss, H. Energy-Adjusted *ab initio* Pseudopotentials for the Second and Third Row Transition Elements. *Theor. Chem. Acc.* **1990**, *77*, 123–141.

(36) Frisch, M. J.; Trucks, G. W.; Schlegel, H. B.; Scuseria, G. E.; Robb, M. A.; Cheeseman, J. R.; Scalmani, G.; Barone, V.; Petersson, G. A.; Nakatsuji, H.; Li, M. C. X.; Marenich, A.; Bloino, J.; Janesko, B. G.; Gomperts, R.; Mennucci, B.; Hratchian, H. P.; Ortiz, J. V.; Izmaylov, A. F.; Sonnenberg, J. L.; Williams-Young, D.; Ding, F.; Lipparini, F.; Egidi, F.; Goings, J.; Peng, B.; Petrone, A.; Henderson, T.; Ranasinghe, D.; Zakrzewski, V. G.; Gao, J.; Rega, N.; Zheng, G.; Liang, W.; Hada, M.; Ehara, M.; Toyota, K.; Fukuda, R.; Hasegawa, J.; Ishida, M.; Nakajima, T.; Honda, Y.; Kitao, O.; Nakai, H.; Vreven, T.; Throssell, K.; Montgomery, J. A., Jr.; Peralta, J. E.; Ogliaro, F.; Bearpark, M.; Heyd, J. J.; Brothers, E.; Kudin, K. N.; Staroverov, V. N.; Keith, R. K. T.; Normand, J.; Raghavachari, K.; Rendell, A.; Burant, J. C.; Iyengar, S. S.; Tomasi, J.; Cossi, M.; Millam, J. M.; Klene, M.; Adamo, C.; Cammi, R.; Ochterski, J. W.; Martin, R. L.; Morokuma, K.; Farkas, O.; Foresman, J. B.; Fox, D. J. *Gaussian 09*, revision D.01; Gaussian, Inc., Wallingford, CT, 2013.

13.2 A Phosphino-Carboxylic Acid-Based Ru Dimeric Complex

Christian K. Rank^a, Tatjana Wall^{ab}, Fabian Dietrich^{ab}, Marko Vidovic^{ab}, Matthias P. Klein^{ab}, Yu Sun^a, Gereon Niedner-Schatteburg^{ab}, Markus Gerhards^{ab}, and Frederic W. Patureau^a

*a) Fachbereich Chemie, Technische Universität Kaiserslautern,
67663 Kaiserslautern, Germany*

*b) Forschungszentrum OPTIMAS, Technische Universität Kaiserslautern,
67663 Kaiserslautern, Germany*

13.2.1 Preamble

The following chapter is a reprint of a publication in the journal “European Journal of Inorganic Chemistry”.

I performed the MS analysis and revised the manuscript.

Full Reference:

A Phosphino-Carboxylic Acid-Based Ru Dimeric Complex

C. K. Rank, T. Wall, F. Dietrich, M. Vidovic, **M. P. Klein**, Yu Sun, G. Niedner-Schatteburg, M. Gerhards, and F. W. Patureau, *Eur. J. Inorg. Chem.* **2018**, 1394–1398.

<https://doi.org/10.1002/ejic.201701382>

13.2.2 Reprint

License Number	5101331169971
License date	Jul 03, 2021
 Licensed Content	 Order Details
Licensed Content Publisher	John Wiley and Sons
Licensed Content Publication	European Journal of Inorganic Chemistry
Licensed Content Title	A Phosphino-Carboxylic Acid-Based Ru Dimeric Complex
Licensed Content Author	Frederic W. Patureau, Markus Gerhards, Gereon Niedner-Schatteburg, et al
Licensed Content Date	Mar 25, 2018
Licensed Content Volume	2018
Licensed Content Issue	12
Licensed Content Pages	5
 About Your Work	 Additional Data
Title	Dinitrogen Adsorption and Activation on Pure and Alloy Metal Cluster Cations Studied by Cryo Adsorption Kinetics and Infrared Spectroscopy
Institution name	TU Kaiserslautern
Expected presentation date	Jul 2021
 Requestor Location	 Tax Details
Requestor Location	Mr. Matthias Klein Erwin-Schroedinger-Str. 52 Kaiserslautern, 67663 Germany Attn: TU Kaiserslautern
\$ Price	Publisher Tax ID EU826007151
Total	0.00 EUR

Supramolecular Ru Dimers

A Phosphino-Carboxylic Acid-Based Ru Dimeric Complex

Christian K. Rank,^[a] Tatjana Wall,^[a,b] Fabian Dietrich,^[a,b] Marko Vidovic,^[a,b]
Matthias P. Klein,^[a,b] Yu Sun,^[a] Gereon Niedner-Schatteburg,^{*[a,b]} Markus Gerhards,^{*[a,b]} and
Frederic W. Patureau^{*[a]}

Abstract: A new supramolecular Ru dimer is described, notably by X-ray crystallography, ESI-MS and solution IR spectroscopy.

The properties and C–H bond activation catalytic activity of this new H-bonded binuclear complex are discussed.

Introduction

The field of C–H bond activation has grown exponentially over the past decade.^[1] This reactivity concept is developing rapidly because it allows the direct-step and atom-economical construction of molecular complexity compared to classical cross-coupling techniques. The most popular catalysts are often based on Pd, Rh, or Ru organometallic complexes, which is due in part to their redox versatility.^[1] Of the three, Ru is particularly interesting for future developments because it is the least expensive metal. The vast majority of Ru-catalyzed C–H bond-activation systems however rely solely on [(*p*-cymene)RuCl₂]₂, which is the most commercially available Ru^{II} source.^[2] Some recent work by Larossa,^[3] and also by us,^[4] suggest that [(*p*-cymene)RuCl₂]₂ may not always be the most optimal precatalyst. Some other works have also suggested that the addition of a phosphine ligand may in some cases significantly increase the catalytic efficiency of [(*p*-cymene)RuCl₂]₂ in some C–H arylation coupling reactions.^[2h] Therefore, there is much potential

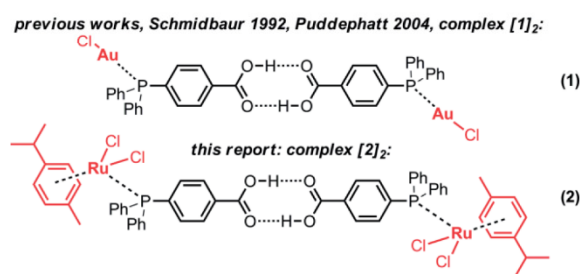
for C–H bond-activation catalytic activity through optimization of ligand effects. We thus report here a new phosphino-carboxylic acid-based Ru dimeric complex. Previously, only a Au^I H-bonded binuclear analogous structure had been described by Schmidbaur and independently by Puddephatt (Complex **[1]**₂, Scheme 1).^[5]

Results and Discussion

Reacting [(*p*-cymene)RuCl₂]₂ and commercially available 4-(diphenylphosphanyl) benzoic acid in CDCl₃ instantaneously affords complex **[2]** at room temperature. ³¹P NMR shows a single characteristic peak at +25.2 ppm. The X-ray structure and the H-bonding dimeric disposition are shown in Figure 1.

Although we had expected a direct interaction between the carboxylic moieties and the Ru centers, the distance between Ru and the closest oxygen atom forbids any such interpretation. For comparison, in the binuclear gold complex **[1]**₂, the intermolecular O–O distance is 2.637 and 2.611 Å (two dimers in the unit cell),^[5] compared to 2.619 Å in the X-ray structure of the free ligand 4-(diphenylphosphanyl) benzoic acid.^[5c] Thus, Au^I coordination does not seem to greatly affect the H-bonding between the two carboxylic acid moieties. In binuclear Ru complex **[2]**₂, the O–O intermolecular distance is 2.666 Å, suggesting a slightly weaker H-bonding between the carboxylic moieties. The robustness of binuclear complex **[2]**₂ was then probed with ESI MS (Figure 2).

Clearly, complex **[2]** remains dimeric under ESI ionization conditions. In contrast, complex **[3]** resulting from the coordination of 4-(diphenylphosphanyl) benzoic methyl ester with [(*p*-cymene)RuCl₂]₂, displays a characteristic mononuclear ESI MS pattern (Figure 3). The solid state ATR spectrum of the binuclear complex **[2]**₂ shows two bands at around 3055 cm⁻¹ and 2963 cm⁻¹, on top of a broader signal (Figure 4). DFT calculations show that the band of the monomer is expected at 3591 cm⁻¹, whereas the double H-bonded structure such as found in the X-ray of complex **[2]**₂ should yield a very red-shifted and intense band at 2938 cm⁻¹. The comparison of measured and calculated spectra is thus consistent with the existence of the H-bonded structure in the solid state. In con-



Scheme 1. Comparison of the solid-state structures of carboxylic acid bridged phosphine Au and Ru dimers.

[a] FB Chemie & Research Center Optimas, TU Kaiserslautern, Erwin-Schrödinger Str. 52, 67663 Kaiserslautern, Germany
E-mail: gns@chemie.uni-kl.de
gerhards@chemie.uni-kl.de
patureau@chemie.uni-kl.de

[b] Forschungszentrum Optimas, TU Kaiserslautern
Kaiserslautern, Germany

Supporting information and ORCID(s) from the author(s) for this article are available on the WWW under <https://doi.org/10.1002/ejic.201701382>.

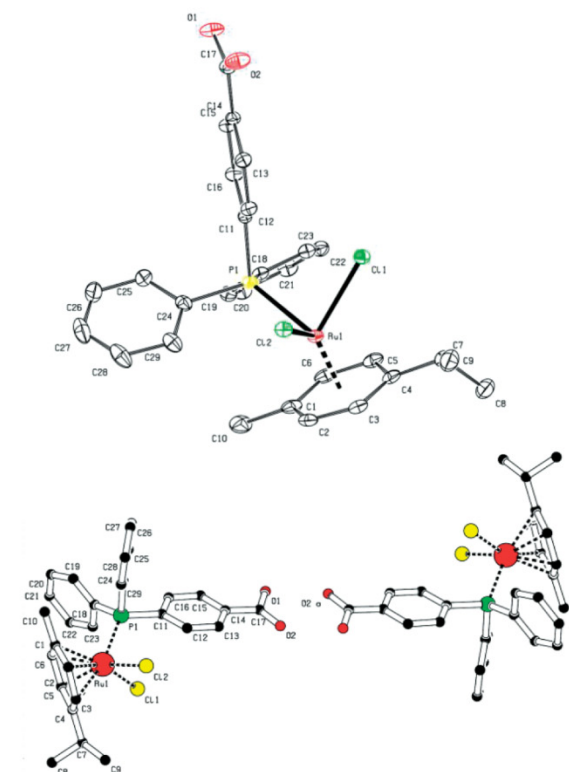


Figure 1. X-ray structure of binuclear complex **[2]₂**, ORTEP view 30 %, hydrogen atoms and two solvent molecules (dichloromethane) are omitted for clarity.

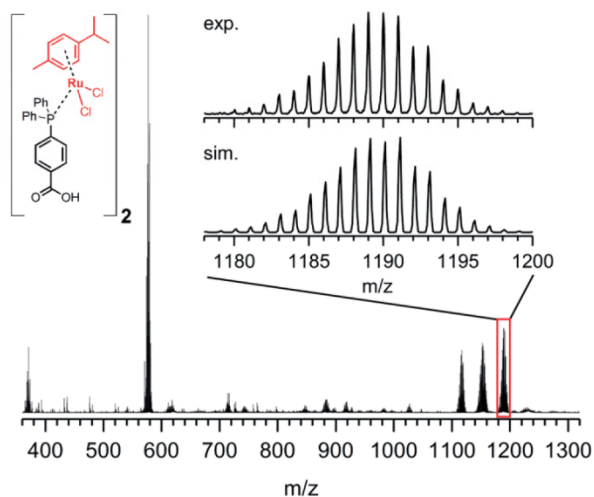


Figure 2. (Top) ESI-MS of binuclear complex **[2]₂** (top), and largest fragment (zoom), which simulations suggest should correspond to $[(C_{29}H_{29}ClO_2PRu)_2Cl]^+$ (beneath).

trast, an acetonitrile solution of **[2]** yielded two O–H IR stretches at respectively 3630 and 3540 cm^{-1} , whereas a dichloromethane solution of **[2]** yielded a broad O–H IR stretch at 3494 cm^{-1} . A similar IR profile was obtained in CD_2Cl_2 . These

results show the relative fragility of the H-bonded dimer, even in moderately polar dichloromethane solution (see Supporting Information).

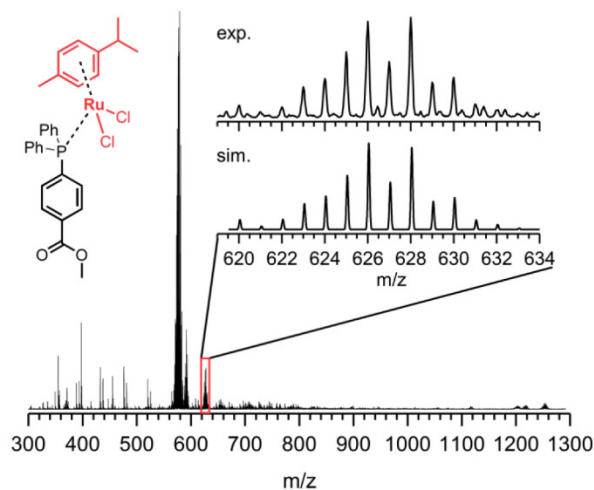


Figure 3. ESI-MS of monomeric complex **[3]**, largest fragment (zoom) belonging to $[RuCl_2(C_{10}H_{14})P(C_6H_5)_2(C_6H_4)COOCH_3]^+$ according to simulation (beneath).

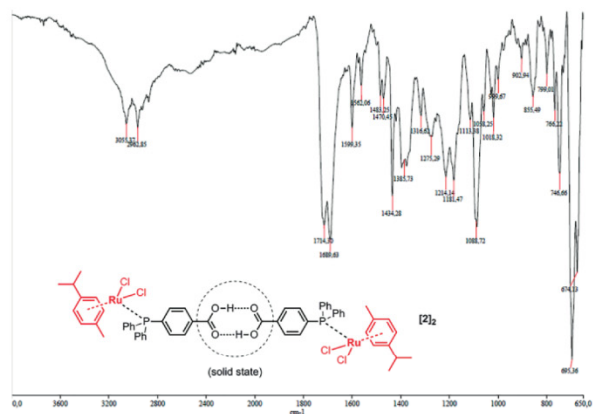


Figure 4. Neat ATR-IR spectrum of binuclear complex **[2]₂**.

Intrigued, we then looked at rationalizing the FTIR spectrum of the acetonitrile solution of complex **[2]**, displaying the two O–H stretching bands at 3630 and 3540 cm^{-1} , respectively (see Supporting Information). This indicates that such originally dimeric structures may be arranged very differently in solution, particularly in polar solvents. H-bonding between the carboxylic acid moieties and the chlorides was notably considered, however the correct attribution for the observed bands could not be convincingly calculated so far, despite our best efforts. UV/Vis and fluorescence spectra were also acquired, notably in KBr, in cyclohexane and acetonitrile, respectively (Figure 5). It should be noted that the spectra in acetonitrile are strongly dependent on the concentration, indicating that some dynamic association/dissociation processes may take place in that solvent (see Supporting Information for details).

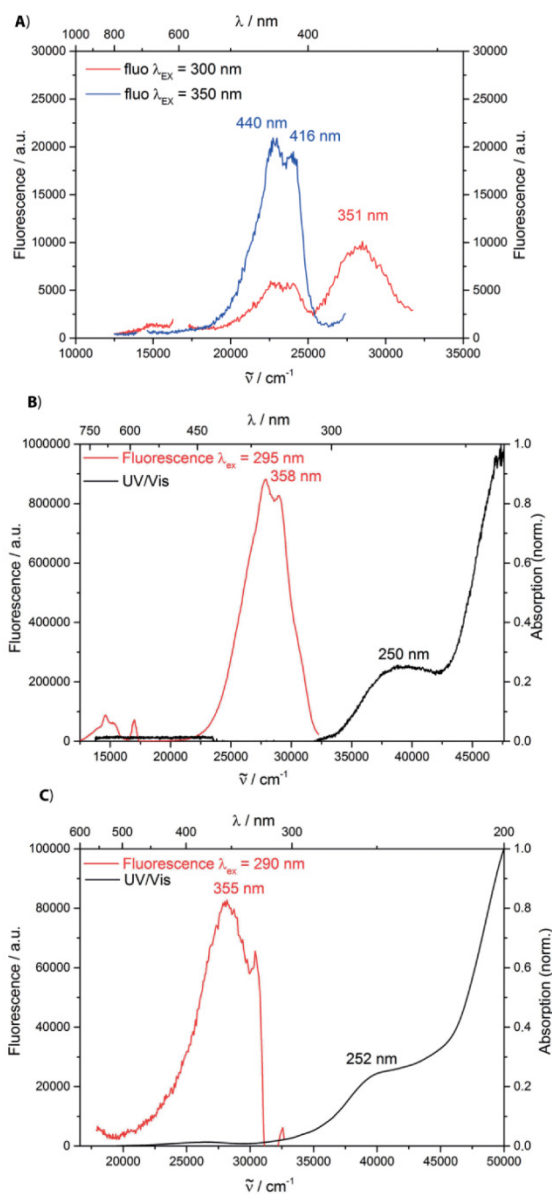
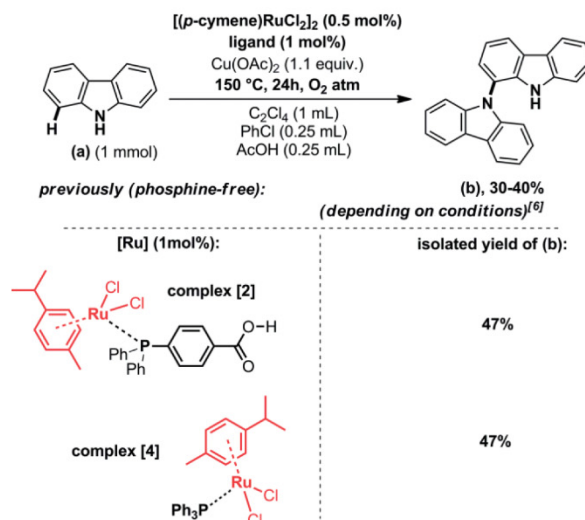


Figure 5. **A)** Fluorescence spectra of complex **[2]** in KBr matrix, with different excitation wavelengths. **B)** UV/Vis spectra (black) and fluorescence (red) spectra of complex **[2]** in cyclohexane. **C)** in acetonitrile.

We finally evaluated the catalytic activity of binuclear complex **[2]₂**, in a Ru catalyzed intermolecular dehydrogenative C–N bond forming dimerization reaction, which we had previously developed (Scheme 2).^[6] Complex **[2]** showed significantly superior activity (47 % isolated yield of the bicarbazole) compared to naked $[(p\text{-cymene})\text{RuCl}_2]_2$ (in all reaction conditions that were tested, 40 % yield or less were generally obtained within the first 24 h reaction time).^[6] However, control monomeric complex **[4]** based on simple triphenylphosphine showed the same increased catalytic efficiency. This suggests that the carboxylic acid functional group does not significantly contribute in

a cooperative fashion to the acceleration of the catalytic activity. Thus, the increased catalytic activity is solely due to a phosphine-accelerating effect, a phenomenon already observed in other Ru catalyzed C–H activation reactions.^[2h]

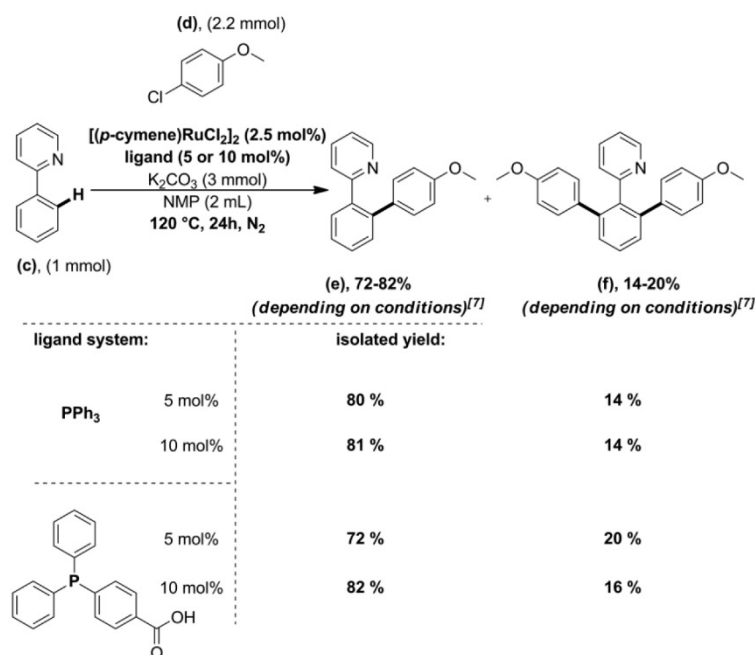


Scheme 2. Catalytic activity in an intermolecular cross dehydrogenative C–N bond forming reaction with carbazoles.

In order to confirm this trend in a second test reaction, complexes **[2]** and **[4]** were evaluated as catalysts in the notorious Ru-catalyzed arylation of phenyl pyridines (Scheme 3).^[7] Likewise, no significant differences were observed in terms of catalytic behavior, both ligand systems affording high yields of the C–H arylated products. Moreover, similar ratios of mono-/diarylation were observed.

Conclusions

In conclusion, we reported here a new phosphino-carboxylic acid based Ru dimeric complex. So far, only the Au^I analogue had been known (complex **[1]₂**). The dimeric H-bonded character of complex **[2]₂** could be unambiguously confirmed in the solid state with X-ray crystallography (see also ESI MS). The double H-bonding system seems to change significantly in solution, as evidenced by solution IR studies (in acetonitrile or alternatively in dichloromethane). Absorption/emission spectra of the complex in both apolar (cyclohexane) and polar media (acetonitrile) do not show significant differences, suggesting a mostly monomeric disposition in dilute conditions. The catalytic activity in a cross-dehydrogenative C–N bond forming reaction is superior to previously reported $[(p\text{-cymene})\text{RuCl}_2]_2$. However, this does not arise from a cooperative effect of the carboxylic moieties, or any sort of proximal cooperativity between the two Ru centers that would be enforced by the μ -bridging ligand, since the control triphenylphosphine ligand performed just as well. The Ru-catalyzed C–H arylation of phenylpyridine also showed similar activity for the two ligand systems. However, these results show that $[(p\text{-cymene})\text{RuCl}_2]_2$ is not an optimal pre-catalyst for such cross dehydrogenative coupling reactions,



Scheme 3. Catalytic activity in the Ru catalysed C–H arylation of phenyl pyridines.

and that better performance can still be achieved by ligand optimization. Such ligand optimization efforts for improved catalytic activity are currently under way in our laboratory.

Experimental Section

Catalysis experiments were carried out in 170 mL dried reaction vessels with sealed Teflon screw caps under air, unless otherwise specified. NMR spectra were obtained on Bruker AMX 400 or on Bruker Avance 600 systems using CDCl₃ as solvents, with proton and carbon resonances at 400/600 MHz and 101/151 MHz, respectively. Coupling constants (*J*) are quoted in Hz. Flash chromatography was performed on silica gel (40–63 mesh) by standard technique. HRMS data were determined on a WATERS GCT-Premier™ mass spectrometer. Electrospray ionization mass spectrometry (ESI-MS) was performed with an ion trap instrument (Bruker amazon ETD). The investigated cations were produced in the positive electrospray ionization mode. The scan speed was 4650 *m/z* s⁻¹ in maximum-resolution scan mode (0.18 *fwhm/m/z*). The scan range was at least 70 to 3000 *m/z*. Sample solutions of complexes [2] and [3] in acetonitrile at concentrations of approximately 10⁻⁵ M were continuously infused into the ESI chamber at a flow rate of 2 μL min⁻¹ by using a syringe pump. N₂ gas was used as the drying gas at a flow rate of 3.0 to 4.0 L min⁻¹ heated to 220 °C. The solutions were sprayed at a nebulizer gas pressure of 0.2 to 0.28 bar with the electrospray needle held at 4.5 kV. Helium was used as a buffer gas with a partial pressure of ca. 3 × 10⁻³ mbar inside the ion trap. Bruker trapControl 7.2 software controlled the instrument and data analysis was performed with Data Analysis 4.2 software. Theoretical methods: initial structures of the monomer are generated by application of the simulated annealing algorithm of the XTB package.^[8] The obtained minimum structures are optimized with B3LYP-D3(BJ)/def2-TZVP using the Bery algorithm of Gaussian 09^[9] and the energies and gradients calculated by Turbomole

7.1.^[10] This procedure yield two structures, which are used to generate dimers with different symmetries. The dimerization via the carbonyl moieties is considered as well as chelation of one ruthenium by the second molecule. For all structures vibrational spectra are calculated, scaled with the factor 0.9608^[11] and convolved with a Gaussian (FWHM = 15 cm⁻¹). Characterization of C1–N bicarbazole product: see ref.^[7] UV/Vis/Luminescence spectroscopy: For all measurements, only spectroscopy grade solvents from Fluka were used. All measured solutions had a concentration in the range of 2 × 10⁻⁵ mol L⁻¹, 2 × 10⁻⁴ mol L⁻¹ and 2 × 10⁻³ mol L⁻¹ and were prepared with the common Schlenk technique under Argon atmosphere. The absorption spectra were recorded with a Perkin–Elmer Lambda 900 double beam UV/Vis/NIR spectrophotometer. Cylindrical quartz cuvettes with a path length of 1 cm were used. For detection of the emission a Horiba Jobin Yvon Fluorolog 3–22 τ and 1 cm × 1 cm quartz cuvettes were applied.

Complex [1]₂: see ref.^[5]

Complex [2]₂: [(*p*-cymene){(C₆H₅)₂P(C₆H₄)CO₂H}RuCl₂]₂: (*p*-cymene)RuCl₂ (commercial from TCI-Chemicals, 0.66 mmol, 202 mg) was united with 4-(diphenylphosphanyl)benzoic acid (commercial from Sigma Aldrich, 0.66 mmol, 203 mg) and submitted with CH₂Cl₂ (10 mL) under air. The solution was crushed with hexane (excess) and filtered through a P4-frit. Afterwards the orange solid was dried in vacuo, (0.60 mmol, 377 mg, 91 %). ¹H NMR (400 MHz, CDCl₃): δ = 8.01–7.91 (m, 4 H), 7.84–7.79 (m, 4 H), 7.46–7.37 (m, 6 H), 5.23 (d, ³J = 6.1 Hz, 2 H), 4.99 (d, ³J = 5.5 Hz, 2 H), 2.86 (hept, ³J = 6.9 Hz), 1.86 (s, 3 H), 1.11 (d, ³J = 6.9 Hz, 6 H) ppm. ³¹P{¹H} NMR (162 MHz, CDCl₃): δ = 25.26 (s, P) ppm. C₂₉H₂₉Cl₂O₂Ru (581.52): calcd. C 56.87, H 4.77; found C 55.62, H 4.98, MS-ESI (CH₃CN): see Figure 2. IR (neat): $\tilde{\nu}$ = 3055, 2963, 1714, 1690, 1599, 1562, 1483, 1470, 1434, 1386, 1275, 1214, 1181, 1088, 1018, 855, 766, 747, 695, 674 cm⁻¹. Crystallization from CH₂Cl₂.

Complex [3]₂: [(*p*-cymene){(C₆H₅)₂P(C₆H₄)CO₂CH₃}RuCl₂]₂: (*p*-cymene)RuCl₂ (commercially available from TCI-Chemicals, 0.33 mmol,

200 mg) was united with methyl 4-(diphenylphosphanyl)benzoic methyl ester (0.25 mmol, 80.1 mg) and submitted with CH_2Cl_2 (3 mL) under air. The solution was crushed with hexane (excess) and filtered through a P4-frit. Afterwards the orange solid was dried in vacuo, yielding a red, orange solid (0.25 mmol, 159 mg, > 99 %). ^1H NMR (400 MHz, CDCl_3): δ = 7.96–7.88 (m, 4 H), 7.83–7.79 (m, 4 H), 7.45–7.37 (m, 6 H), 5.21 (d, 3J = 6.1 Hz, 2 H), 4.98 (d, 3J = 5.5 Hz, 2 H), 3.88 (s, 3 H), 2.85 (sept, 3J = 6.95 Hz, 1 H), 1.86 (s, 3 H), 1.10 (d, 3J = 6.9 Hz, 6 H) ppm. $^{31}\text{P}\{^1\text{H}\}$ NMR (162 MHz, CDCl_3): δ = 24.84 ppm. $\text{C}_{30}\text{H}_{31}\text{Cl}_2\text{O}_2\text{PRu}$ (626.52): calcd. C 57.51, H 4.99; found C 56.97, H 5.43. MS-ESI (CH_3CN): see Figure 3. IR (neat): $\tilde{\nu}$ = 3052, 2958, 1718, 1598, 1483, 1471, 1434, 1392, 1476, 1190, 1114, 1087, 1019, 854, 763, 748, 721, 693 cm^{-1} .

Acknowledgments

The Deutsche Forschungsgemeinschaft (DFG)-funded transregional collaborative research center SFB/TRR 88 “Cooperative effects in homo and heterometallic complexes” (<http://3MET.de>), DFG funded project PA 2395/2-1, and COST Action CA15106 (CHAOS), and state research center OPTIMAS are acknowledged for financial support.

Keywords: Binuclear complexes · Cooperative catalysis · Hydrogen bonding · Cross-dehydrogenative coupling · Carbazole

- [1] P. H. Dixneuf, H. Doucet (Eds.), C–H Bond Activation and Catalytic Functionalization, *Top. Organomet. Chem.* **2016**, 55.
- [2] Selected reviews on Ru-catalysed C–H bond functionalization: a) S. Ruiz, P. Villuendas, E. P. Urriolabeitia, *Tetrahedron Lett.* **2016**, 57, 3413; b) R. Manikandan, M. Jeganmohan, *Org. Biomol. Chem.* **2015**, 13, 10420; c) S. De Sarkar, W. Liu, S. I. Kozhushkov, L. Ackermann, *Adv. Synth. Catal.* **2014**, 356, 1461; d) V. S. Thirunavukkarasu, S. I. Kozhushkov, L. Ackermann, *Chem. Commun.* **2014**, 50, 29; e) F. J. Hernandez, M. Simonetti, I. Larrosa, *Angew. Chem. Int. Ed.* **2013**, 52, 11458; *Angew. Chem.* **2013**, 125, 11670; f) L. Ackermann, *Acc. Chem. Res.* **2014**, 47, 281; g) P. B. Arockiam, C. Bruneau, P. H. Dixneuf, *Chem. Rev.* **2012**, 112, 5879; h) G.-F. Zha, H.-L. Qin, E. A. B. Kantchev, *RSC Adv.* **2016**, 6, 30875.
- [3] M. Simonetti, G. J. P. Perry, X. C. Cambeiro, F. Julia-Hernandez, J. N. Arokianathar, I. Larrosa, *J. Am. Chem. Soc.* **2016**, 138, 3596.
- [4] C. Heitz, A. W. Jones, B. S. Oezkaya, C. L. Bub, M.-L. Louillat-Habermeyer, V. Wagner, F. W. Patureau, *Chem. Eur. J.* **2016**, 22, 17980.
- [5] a) H. Schmidbaur, B. Brachthäuser, S. Gamper, A. Schier, O. Steigelmann, *Z. Naturforsch. B* **1992**, 47, 1725; b) F. Mohr, M. C. Jennings, R. J. Puddephatt, *Angew. Chem. Int. Ed.* **2004**, 43, 969; *Angew. Chem.* **2004**, 116, 987. For the X-ray structure of 4-(diphenylphosphanyl)benzoic acid, see: c) P.-H. Zhao, F.-Y. Sun, J.-J. Liu, *Acta Crystallogr., Sect. E: Struct. Rep. Online* **2011**, 67, o2454. CCDC 221124 (for [2]) contains the supplementary crystallographic data for this paper. These data can be obtained free of charge from The Cambridge Crystallographic Data Centre.
- [6] M.-L. Louillat, F. W. Patureau, *Org. Lett.* **2013**, 15, 164.
- [7] For a selection, see: a) S. Oi, Y. Ogino, S. Fukita, Y. Inoue, *Org. Lett.* **2002**, 4, 1783; b) L. Ackermann, *Org. Lett.* **2005**, 7, 3123; c) F. Pozgan, P. H. Dixneuf, *Adv. Synth. Catal.* **2009**, 351, 1737; d) L. Ackermann, R. Vicente, H. K. Potukuchi, V. Pirovano, *Org. Lett.* **2010**, 12, 5032; e) N. Luo, Z. Yu, *Chem. Eur. J.* **2010**, 16, 787; f) A. Prades, M. Poyatos, E. Peris, *Adv. Synth. Catal.* **2010**, 352, 1155; g) B. Yu, X. Yan, S. Wang, N. Tang, C. Xi, *Organometallics* **2010**, 29, 3222; h) P. B. Arockiam, C. Fischmeister, C. Bruneau, P. H. Dixneuf, *Green Chem.* **2013**, 15, 67; i) Y.-L. Zou, Z.-Y. Wang, Y.-M. Feng, Y.-G. Li, E. A. B. Kantchev, *Eur. J. Org. Chem.* **2017**, 2017, 6274.
- [8] S. Grimme, C. Bannwarth, P. Shushkov, *J. Chem. Theory Comput.* **2017**, 13, 1989.
- [9] M. J. Frisch, G. W. Trucks, H. B. Schlegel, G. E. Scuseria, M. A. Robb, J. R. Cheeseman, G. Scalmani, V. Barone, B. Mennucci, G. A. Petersson, H. Nakatsuji, M. Caricato, X. Li, H. P. Hratchian, A. F. Izmaylov, J. Bloino, G. Zheng, J. L. Sonnenberg, M. Hada, M. Ehara, K. Toyota, R. Fukuda, J. Hasegawa, M. Ishida, T. Nakajima, Y. Honda, O. Kitao, H. Nakai, T. Vreven, J. A. Montgomery Jr., J. E. Peralta, F. Ogliaro, M. Bearpark, J. J. Heyd, E. Brothers, K. N. Kudin, V. N. Staroverov, R. Kobayashi, J. Normand, K. Raghavachari, A. Rendell, J. C. Burant, S. S. Iyengar, J. Tomasi, M. Cossi, N. Rega, J. M. Millam, M. Klene, J. E. Knox, J. B. Cross, V. Bakken, C. Adamo, J. Jaramillo, R. Gomperts, R. E. Stratmann, O. Yazyev, A. J. Austin, R. Cammi, C. Pomelli, J. W. Ochterski, R. L. Martin, K. Morokuma, V. G. Zakrzewski, G. A. Voth, P. Salvador, J. J. Dannenberg, S. Dapprich, A. D. Daniels, Ö. Farkas, J. B. Foresman, J. V. Ortiz, J. Cioslowski, D. J. Fox, *Gaussian 09, Revision D.01*, Gaussian, Inc., Wallingford CT, **2009**.
- [10] F. Furche, R. Ahlrichs, C. Hättig, W. Klopper, M. Sierka, F. Weigend, *WIREs Comput. Mol. Sci.* **2014**, 4, 91.
- [11] A. Stamm, D. Maué, A. Schaly, S. Schlicher, J. Bartl, S. Kubik, M. Gerhards, *Phys. Chem. Chem. Phys.* **2017**, 19, 10718.

Received: November 26, 2017

13.3 Generation of a zinc and rhodium containing metallomacrocycle by rearrangement of a six-coordinate precursor complex

Cedric Groß^a, Yu Sun^a, Tobias Jost^a, Tobias Grimm^a, Matthias P. Klein^{ab}, Gereon Niedner-Schatteburg^{ab}, Sabine Becker^a, and Werner R. Thiel^a

a) Fachbereich Chemie, Technische Universität Kaiserslautern, 67663 Kaiserslautern, Germany

b) Forschungszentrum OPTIMAS, Technische Universität Kaiserslautern, 67663 Kaiserslautern, Germany

13.3.1 Preamble

The following chapter is a reprint of a publication in the journal “Chemical Communications”.

I performed the MS analysis and revised the manuscript.

Full Reference:

Generation of a zinc and rhodium containing metallomacrocycle by rearrangement of a six-coordinate precursor complex

C. Groß, Y. Sun, T. Jost, T. Grimm, **M. P. Klein**, G. Niedner-Schatteburg, S. Becker, and W. R. Thiel, *Chem. Commun.* **2020**, *56*, 368-371.

<https://doi.org/10.1039/C9CC07723E>

13.3.2 Reprint

Reproduced from C. Groß et al., *Chem. Commun.* **2020**, 56, 368-371 with permission from The Royal Society of Chemistry.

Generation of a zinc and rhodium containing metallomacrocycle by rearrangement of a six-coordinate precursor complex

C. Groß, Y. Sun, T. Jost, T. Grimm, M. P. Klein, G. Niedner-Schatteburg, S. Becker and W. R. Thiel, *Chem. Commun.*, 2020, **56**, 368 DOI: 10.1039/C9CC07723E

To request permission to reproduce material from this article, please go to the [Copyright Clearance Center request page](#).

If you are **an author contributing to an RSC publication, you do not need to request permission** provided correct acknowledgement is given.

If you are **the author of this article, you do not need to request permission to reproduce figures and diagrams** provided correct acknowledgement is given. If you want to reproduce the whole article in a third-party publication (excluding your thesis/dissertation for which permission is not required) please go to the [Copyright Clearance Center request page](#).

Read more about [how to correctly acknowledge RSC content](#).

Cite this: *Chem. Commun.*, 2020, 56, 368Received 1st October 2019,
Accepted 25th November 2019

DOI: 10.1039/c9cc07723e

rsc.li/chemcomm

Generation of a zinc and rhodium containing metallomacrocyclic by rearrangement of a six-coordinate precursor complex†

C. Groß,^a Y. Sun,^a T. Jost,^a T. Grimm,^a M. P. Klein,^{ab} G. Niedner-Schatteburg,^{ab} S. Becker^{ab} and W. R. Thiel^{ab*}

Two pentadentate N₃P₂ ligands coordinate zinc(II) by their N₃ pocket. Four free phosphine donors allow the coordination of four AuCl moieties leading to a pentanuclear ZnAu₄ complex. In contrast, the attempt to use the phosphines for chelating coordination of two Rh(CO)Cl units results in a well-organized rearrangement that ends up with the formation of a metallomacrocyclic in high yields.

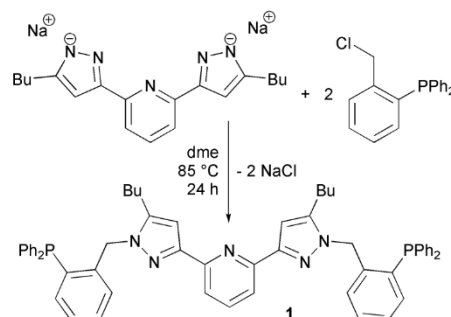
Metallomacrocyclics are formed by coordinative bonds between ligands and metal ions, which makes them perfect building blocks in supramolecular chemistry. Bond cleavage and formation allow the system to correct misfits and thus to reach its optimal structure. Due to this, metallomacrocyclics have found applications in different areas of chemistry and physics.¹ They have been used as components of molecular machines,² as sensors,³ as molecular containers,⁴ as parts in redox-active architectures⁵ and in photophysics.⁶ Although these compounds are mainly formed by hard donors such as heteroarenes,⁷ the relevance of hard/soft interactions had already been discussed in the 1990ies by Reinhoudt and co-workers.⁸ Phosphine coordination has rarely been used for the construction of metallomacrocyclics.⁹ We here report the synthesis of a metallomacrocyclic containing two phosphine-coordinated rhodium(I) sites in the ring, which is formed by rearrangement of a six-coordinated zinc(II) complex that acts as a template.

The N₃P₂ ligand **1** was synthesized by deprotonation of 2,6-di(5-butylpyrazol-3-yl)pyridine¹⁰ with NaH in thf solution followed by removal of the solvent and treatment of the resulting dianion with (2-chloromethylphenyl)diphenylphosphine¹¹ in dimethoxyethane (dme) under heating to reflux for 24 h (Scheme 1). The two *n*-butyl side chains provide much better

solubility to the transition metal complexes derived from this ligand. Ligand **1** carries orthogonal donor functions which means that the nitrogen pocket will preferentially react with hard while the phosphine moieties will undergo coordination to soft Lewis-acids. It therefore allows to direct metal sites into a specific coordination environment.

The ³¹P NMR resonance (−15.6 ppm) measured for compound **1** is in the typical range for triarylphosphines. In the ¹H NMR spectrum there is the typical singlet at 5.50 ppm for the methylene groups linking the 2,6-di(5-butylpyrazol-3-yl)pyridine and the triphenylphosphine units as well as a singlet at 6.88 ppm for the hydrogen atoms at the pyrazole rings. The resonance of the pyridine *meta*-protons (7.87 ppm) is shifted to lower field indicating that, due to weak N⋯H-C interactions, the molecule preferentially occupies the stretched, *all-transoid* conformation as shown in Scheme 1. An X-ray structure analysis confirms this indication (Fig. 1). The three central five- and six-membered rings are found in almost co-planar orientation.

Treatment of **1** with half an equivalent of Zn(OTf)₂ (TfO[−]: trifluoromethylsulfonate) and one equivalent of NaBF₄ according to a procedure published in the literature for the synthesis of [(4-PhTpy)₂Zn](BF₄)₂ (4-PhTpy: 4-phenyl-2,2':6',2''-terpyridine)¹² provides the dicationic, homoleptic, six-coordinated zinc(II)

Scheme 1 Synthesis of the N₃P₂-ligand **1**.

^a Fachbereich Chemie, TU Kaiserslautern, Erwin-Schrödinger-Str. 54, 67663 Kaiserslautern, Germany. E-mail: thiel@chemie.uni-kl.de

^b Forschungszentrum OPTIMAS, Technische Universität Kaiserslautern, 67663 Kaiserslautern, Germany

† Electronic supplementary information (ESI) available: Synthesis procedures, NMR, IR and mass spectra, semi-empirical calculations, X-ray data. CCDC 1954209 and 1954210. For ESI and crystallographic data in CIF or other electronic format see DOI: 10.1039/c9cc07723e

Communication

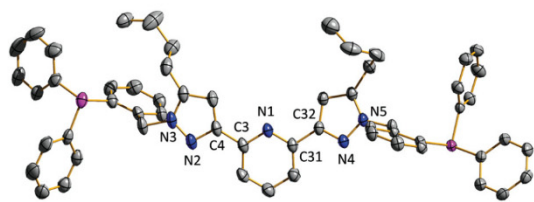
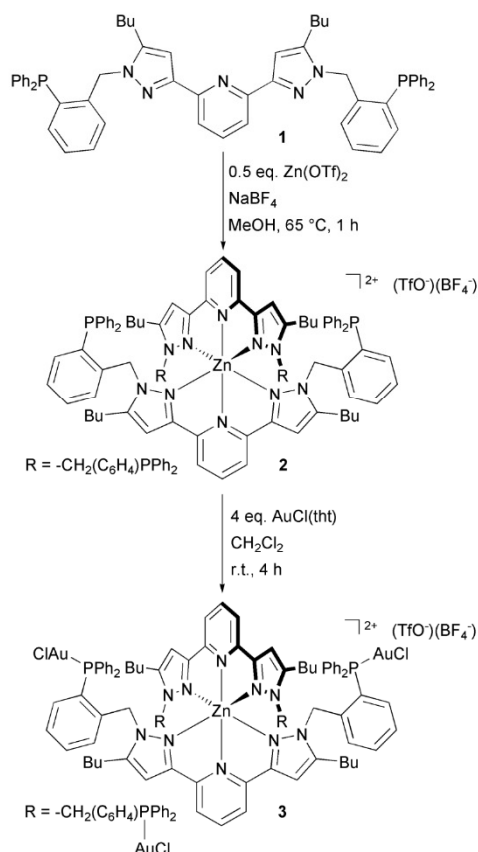


Fig. 1 Molecular structure of compound **1** in the solid state. Selected dihedral angles [°]: N1–C3–C4–N2 –175.5(2), N1–C31–C32–N4 –162.1(1). Hydrogen atoms and the disordering of one of the butyl side chains are omitted for clarity.

complex **2** (Scheme 2). One equivalent of NaBF₄ was applied to achieve a complete exchange of the trifluoromethylsulfonate anions. However, reproducibly only half of them were exchanged. Probably, the compound with the mixed anions has the poorest solubility. ESI mass spectrometry, ¹⁹F NMR spectroscopy and elemental analysis were applied to prove the presence of the mixed anions. The complexation of the zinc(II) cation results in a shift of the resonance of the pyridine *meta*-protons by 0.26 ppm to higher and of the pyridine *para*-protons by 0.38 ppm to lower field. This clearly proves the coordination of the central N₃-donor

unit to the metal site.¹³ Parallel, the resonance of the pyrazole protons is shifted by 0.22 ppm to higher field. The signal of the bridging methylene groups is shifted strongly to higher field ($\Delta\delta$: 1.45 ppm). This can be explained by the fact that, in order to avoid steric interference, the bridging methylene protons of one N₃-donor have to point towards the other N₃-donor and thus receive a strong shielding by the aromatic rings. The resonances of the phosphine units stay almost unaffected (³¹P NMR: –16.7 ppm) compared to compound **1**. This proves, that there is no interaction between these donors and the zinc(II) centers. Even in a heteroleptic, five-coordinated complex that was obtained by treating ZnCl₂ with ligand **1**,¹⁴ the phosphine donors stay spectators, which is in complete agreement with Pearson's concept of hard and soft Lewis-acids and bases.¹⁵ ESI mass spectrometry (positive mode) provides a signal at $m/z = 904.34$ (calcd. for [C₁₁₄H₁₁₀N₁₀P₄Zn]²⁺: 904.36). In addition signals for the cations [C₁₁₄H₁₁₀N₁₀O_nP₄Zn]²⁺ are observed, formed by oxidation at the phosphorous atoms during the ESI-MS process.

Treating compound **2** with four equiv. of [AuCl(tht)] (tht: tetrahydrothiophene) results in the generation of the pentanuclear ZnAu₄ complex **3** with linear coordination of AuCl fragments to all four phosphine sites of the ligand (Scheme 2). Elemental analysis and ESI mass spectrometry clearly prove the existence of compound **3**. A peak in the ESI-MS spectrum at $m/z = 1369.13$ can be assigned to the cation [C₁₁₄H₁₁₀Au₄Cl₄N₁₀P₄Zn]²⁺ (calcd.: 1369.23). There are no hints for oxidation occurring at the phosphorous sites, which are protected by coordination to gold. A second peak in the ESI-MS spectrum at $m/z = 1300.27$ is assigned to [C₅₇H₅₅Au₂ClN₅P₂]⁺ (calcd.: 1300.29) which is ligand **1** coordinating to two gold(I) centers. For charge balance, one chloride anion is present. This peak is the only one that is formed when the dication is treated in the MS trap under CID conditions. In contrast to the mass spectrometry data, the NMR spectra of compound **3** are rather complicated. In CDCl₃ solution there are two main resonances at 20.90 and 20.28 ppm and four resonances of lower intensities in the ³¹P NMR spectrum. The resonances are found shifted to lower field compared to other complexes of the type (PAr₃)AuCl (Ar: aryl substituent, δ (³¹P NMR) *ca.* 33 ppm).¹⁶ We assign this to a strong shielding of the phosphorous atoms due to the confined space around the phosphine side chains (see ESI[†]). A similar pattern caused by two major and some minor conformers is observed in the ¹H NMR spectrum, where two intense pairs of resonances for protons of methylene groups bound to pyrazole nitrogen atoms are accomplished by a series of resonances of lower intensities. *H,H*-Coupling constants of about 17 Hz prove the presence of diastereotopic methylene protons. We therefore assign two main components having local S₄ and D_{2d} symmetry and one component of C₁ symmetry (see ESI[†]). Their interconversion is slow with respect to the NMR timescale due to hindered rotation around the N–CH₂–C₆H₄ single bonds, while the rotation around the Ph₂P–(C₆H₄) bond is rapid enough that the orientation of the AuCl moiety does not lead to further resonances in the NMR spectra. Nevertheless, all species are in equilibrium in solution since their ratios are strongly solvent dependent.



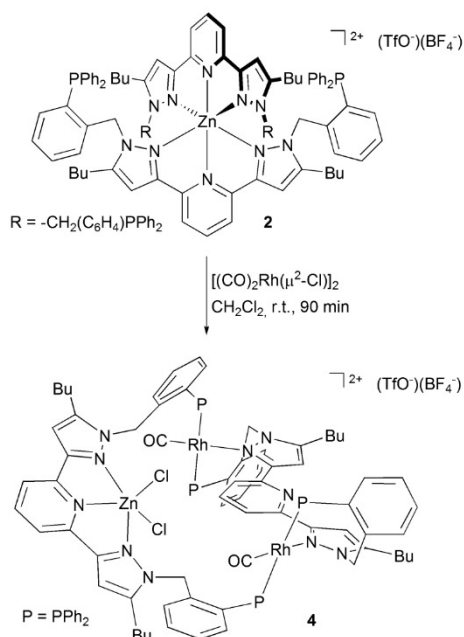
Scheme 2 Synthesis of the Zn₁ and ZnAu₄ complexes **2** and **3**.

13.3. Generation of a zinc and rhodium containing metallomacrocyclic by rearrangement of a six-coordinate precursor complex

View Article Online

ChemComm

Communication



Scheme 3 Synthesis of the macrocyclic ZnRh_2 complex **4**.

Treating complex **2** with two equivalents of $[(\text{CO})_2\text{Rh}(\mu^2\text{-Cl})_2]$ did not lead to a compound having the shape of an “8” by bridging two pairs of phosphine sites with rhodium(i). Instead, three of the Zn–N bonds in the core are cleaved and the structure rearranges to the macrocyclic complex **4** (Scheme 3).

By recrystallization from dichloromethane, crystals suitable for an X-ray structure analysis could be obtained (Fig. 2).

In compound **4**, the two rhodium(i) sites are coordinated by two phosphine donors and a carbonyl ligand as expected. However, in the *trans*-position to the carbonyl ligand there is a pyrazole bound instead of a chlorido ligand, leading to two cationic $(\text{CO})\text{RhP}_2\text{N}$ units with an overall square-planar geometry. A related structure has been reported in the literature.¹⁷ To liberate the two pyrazole donors, the zinc(II) site has lost one of its tridentate ligands, which now occupies a relaxed, *all-transoid* conformation similar to compound **1**. To complete its coordination environment, the zinc(II) cation binds two chlorido ligands. There are close contacts of 2.81 and 2.88 Å between the hydrogen atom (H58) in the *trans*-position to N6 and the two chlorido ligands at Zn1 leading to a strong deshielding of this proton (9.39 ppm) and the neighboring *meta*-protons (9.13 ppm) as documented by the ^1H NMR spectrum of **4**. In the ^{31}P NMR spectrum of **4** there are two doublets of doublets at 21.03 and 14.96 ppm ($^1J_{\text{RhP}} = 294.2$, $^2J_{\text{PP}} = 122.5$ Hz) representing two chemically different phosphorous sites. In addition, there are two pairs of resonances for the N–CH₂ protons in the ^1H NMR spectrum, proving the structural rigidity of the large ring system. Two IR absorptions at 2000 and 1978 cm^{-1} can be assigned to an antisymmetric and a symmetric combination of the CO stretching vibrations. The number of ring-atoms depends on the mode of counting.

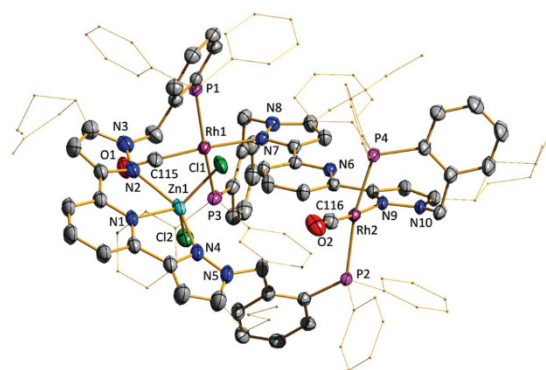


Fig. 2 Molecular structure of the dication of the ZnRh_2 complex **4** in the solid state. For clarity, the anions, disordered solvent molecules and hydrogen atoms are omitted. In addition, the phenyl and the butyl groups are drawn with thin lines to allow a better view on the core structure of complex **4**. Characteristic bond lengths [Å] and angles [°]: Rh1–P1 2.377(1), Rh1–P3 2.314(1), Rh1–N7 2.121(4), Rh1–C115 1.824(5), Rh2–P2 2.378(1), Rh2–P4 2.313(1), Rh2–N9 2.125(5), Rh2–C116 1.826(6), Zn1–Cl1 2.236(1), Zn1–Cl2 2.240(2), Zn1–N1 2.115(4), Zn1–N2 2.264(4), Zn1–N4 2.274(4), O1–C115 1.139(7), O2–C116 1.134(8), H58···Cl1 2.8100, H58···Cl2 2.8800, P1–Rh1–P3 169.60(5), P1–Rh1–N7 93.3(1), P1–Rh1–C115 91.5(2), P3–Rh1–N7 82.1(1), P3–Rh1–C115 93.2(2), N7–Rh1–C115 175.2(2), P2–Rh2–P4 169.34(5), P2–Rh2–N9 93.6(1), P2–Rh2–C116 92.0(2), P4–Rh2–N9 82.5(1), P4–Rh2–C116 91.9(2), N9–Rh2–C116 174.4(2), Cl1–Zn1–Cl2 121.97(6), Cl1–Zn1–N1 119.0(1), Cl1–Zn1–N2 100.3(1), Cl1–Zn1–N4 94.0(1), Cl2–Zn1–N1 119.0(1), Cl2–Zn1–N2 95.8(1), Cl2–Zn1–N4 100.7(1), N1–Zn1–N2 74.2(2), N1–Zn1–N4 73.7(2), N2–Zn1–N4 147.9(2), Rh1–C115–O1 179.6(5), Rh2–C116–O2 178.6(4).

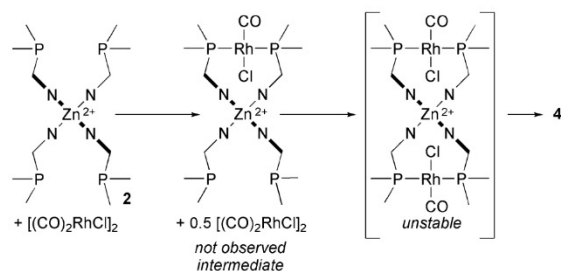
In case the zinc(II) site is excluded from counting, the macrocycle contains 26 ring-atoms.

The ESI mass spectrum of compound **4** provides a strong signal for the dication $[(\text{C}_{57}\text{H}_{55}\text{N}_5\text{P}_2)_2\text{ZnCl}_2(\text{Rh}(\text{CO}))_2]^{2+}$ (m/z : found 1070.19, calcd. 1070.22) in the positive mode. The spectra and the proposed fragmentation channels are summarized in the ESI.† Additionally a series of other signals are present, that can be explained by fragmentation along some critical bonds: $m/z = 1138.09$ (calcd. 1138.16) can be assigned to $[(\text{C}_{57}\text{H}_{55}\text{N}_5\text{P}_2)\text{ZnCl}_2(\text{Rh}(\text{CO}))]^+$. To achieve this product, the fragment $[(\text{C}_{57}\text{H}_{55}\text{N}_5\text{P}_2)\text{Rh}(\text{CO})]^+$ has to be split off from the mother ion. The signal for this species (m/z : 1002.28) is found in the spectrum as well as the signal for $[(\text{C}_{57}\text{H}_{55}\text{N}_5\text{P}_2)\text{Rh}]^+$ (m/z : found 974.28, calcd. 974.30). On the other hand, there are strong signals for $[(\text{C}_{57}\text{H}_{55}\text{N}_5\text{P}_2)\text{Rh}_2(\text{CO})_2\text{Cl}]^+$ (m/z : found 1168.13, calcd. 1168.16) and $[(\text{C}_{57}\text{H}_{55}\text{N}_5\text{OP}_2)\text{ZnCl}]^+$ (m/z : found 988.31, calcd. 988.29, oxidation of one phosphine site).

The molecular structure of **4** is the result of a complete but nevertheless well-organized rearrangement of the zinc(II) complex **2**. If **1** is treated with $[(\text{CO})_2\text{Rh}(\mu^2\text{-Cl})_2]$ in the absence of zinc(II), only insoluble, probably polymeric material is obtained. Therefore, the formation of **4** requires the preorganisation of the phosphine sites in **2** (Scheme 4).

We assume, that the introduction of the first rhodium(i) site, starting from the D_{2d} symmetric isomer of **2**, is still possible without breaking the ZnN_6 core, while the attack of the second rhodium site sufficiently destabilizes the intermediate which then rearranges to **4**. At the moment, we investigate the exchange of the central ZnCl_2 unit against other metal halides.

Communication



Scheme 4 Stepwise and organized formation of ZnRh_2 complex **4** under a templating direction of the zinc(II) core of **2**.

This work was supported by the German research foundation DFG within the transregional collaborative research centre SFB/TRR 88 "Cooperative effects in homo and heterometallic complexes" (3MET).

Conflicts of interest

There are no conflicts to declare.

Notes and references

- D. Rota Martir and E. Zysman-Colman, *Chem. Commun.*, 2019, **55**, 139–158.
- J. P. Sauvage, *Angew. Chem., Int. Ed.*, 2017, **56**, 11080–11093; B. Champin, Pierre Mobian and J.-P. Sauvage, *Chem. Soc. Rev.*, 2007, **36**, 358–366.
- K. Severin, *Coord. Chem. Rev.*, 2003, **245**, 3–10; L.-Y. Guo, H.-F. Su, M. Kurmoo, X.-P. Wang, Q.-Q. Zhao, S.-C. Lin, C.-H. Tung, D. Sun and L.-S. Zheng, *ACS Appl. Mater. Interfaces*, 2017, **9**, 19980–19987; J. Dong, C. Tan, K. Zhang, Y. Liu, P. J. Low, J. Jiang and Y. Cui, *J. Am. Chem. Soc.*, 2017, **139**, 1554–1564.
- Y.-Y. Zhang, W.-X. Gao, L. Lin and G.-X. Jin, *Coord. Chem. Rev.*, 2017, **344**, 323–344; C. J. Jones, *Chem. Soc. Rev.*, 1998, **27**, 289–299.
- V. Croué, S. Goeb and M. Sallé, *Chem. Commun.*, 2015, **51**, 7275–7289; D. A. Leigh, J.-F. Lemonnier and S. L. Woltering, *Angew. Chem., Int. Ed.*, 2018, **57**, 12212–12214; D. H. Kim, N. Singh, J. Oh, E.-H. Kim, J. Jung, H. Kim and K.-W. Chi, *Angew. Chem., Int. Ed.*, 2018, **57**, 5669–5673; A. Mishra, S. C. Kang and K.-W. Chi, *Eur. J. Inorg. Chem.*, 2013, 5222–5232.
- P. Thanasekaran, R.-T. Liao, Y.-H. Liu, T. Rajendran, S. Rajagopal and K.-L. Lu, *Coord. Chem. Rev.*, 2005, **249**, 1085–1110.
- C. E. Housecroft, *Dalton Trans.*, 2014, **43**, 6594–6604.
- F. C. J. M. van Veggel, W. Verboom and D. N. Reinhoudt, *Chem. Rev.*, 1994, **94**, 279–299.
- M. Zábranský, I. Cisařová and P. Štěpnička, *Eur. J. Inorg. Chem.*, 2017, 2557–2572; M. V. Ovchinnikov, A. M. Brown, X. Liu, C. A. Mirkin, L. N. Zakharov and A. L. Rheingold, *Inorg. Chem.*, 2004, **43**, 8233–8235; T. Brasey, R. Scopelliti and K. Severin, *Inorg. Chem.*, 2005, **44**, 160–162; J. M. Martín-Alvarez, F. Hampel, A. M. Arif and J. A. Gladysz, *Organometallics*, 1999, **18**, 955–957; A. L. Balch, M. M. Olmstead, D. E. Oram, R. E. Reedy Jr. and S. H. Reimer, *J. Am. Chem. Soc.*, 1989, **111**, 4021–4028.
- L. Taghizadeh Ghoochany, S. Farsadpour, Y. Sun and W. R. Thiel, *Eur. J. Inorg. Chem.*, 2011, 3431–3437; P. Weingart and W. R. Thiel, *ChemCatChem*, 2018, **10**, 4844–4848.
- A.-E. Wang, J.-H. Xie, L.-X. Wang and Q.-L. Zhou, *Tetrahedron*, 2005, **61**, 259–266; A.-E. Wang, J. Zhong, J.-H. Xie, K. Li and Q.-L. Zhou, *Adv. Synth. Catal.*, 2004, **346**, 595–598; J. Zhong, J.-H. Xie, A.-E. Wang, W. Zhang and Q.-L. Zhou, *Synlett*, 2006, 1193–1196; J. Trampert, M. Nagel, T. Grimm, Y. Sun and W. R. Thiel, *Z. Allg. Anorg. Chem.*, 2018, **644**, 963–972.
- E. C. Constable, J. Lewis, M. C. Liptrot and P. R. Raithby, *Inorg. Chim. Acta*, 1990, **178**, 47–54.
- T. D. Roberts and M. A. Halcrow, *Polyhedron*, 2016, **103**, 79–86.
- C. Groß, PhD thesis, Technische Universität Kaiserslautern, 2019.
- R. G. Pearson, *J. Am. Chem. Soc.*, 1963, **85**, 3533; R. G. Pearson, *Coord. Chem. Rev.*, 1990, **100**, 403; R. G. Pearson, *J. Chem. Educ.*, 1987, **64**, 561; R. G. Pearson, *J. Chem. Educ.*, 1968, **45**, 643; R. G. Pearson, *J. Chem. Educ.*, 1968, **45**, 581.
- G. H. Woehrle, L. O. Brown and J. E. Hutchison, *J. Am. Chem. Soc.*, 2005, **127**, 2172–2183; Y. Li, P. Tang, Y. Chen and B. Yu, *J. Org. Chem.*, 2008, **73**, 4323–4325.
- F. Neve, M. Ghedini and A. Crispini, *Organometallics*, 1992, **11**, 3324–3327.

13.4 Complexes of Platinum Group Elements Containing the Intrinsically Chiral Cyclopentadienide Ligand (Cp^C)⁻¹

Florian Nährig^a, Gerd Gemmecker^b, Jae-Yeon Chung^a, Patrick Hütchen^a, Sergej Lauk^a,
Matthias P. Klein^a, Yu Sun^a, Gereon Niedner-Schatteburg^{ac}, Helmut Sitzmann^a,
and Werner R. Thiel^a

a) *Fachbereich Chemie, Technische Universität Kaiserslautern,
67663 Kaiserslautern, Germany*

b) *Technische Universität München, BNMRZ, Fakultät für Chemie,
85748 Garching, Germany*

c) *Forschungszentrum OPTIMAS, Technische Universität Kaiserslautern,
67663 Kaiserslautern, Germany*

13.4.1 Preamble

The following chapter is a reprint of a publication in the journal “Organometallics”.

I performed the MS analysis and revised the manuscript.

Full Reference:

*Complexes of Platinum Group Elements Containing the Intrinsically Chiral Cyclopentadienide
Ligand (Cp^C)⁻¹*

F. Nährig, G. Gemmecker, J.-Y. Chung, P. Hütchen, S. Lauk, **M. P. Klein**, Y. Sun, G. Niedner-
Schatteburg, H. Sitzmann, and W. R. Thiel, *Organometallics* **2020**, 39, 10, 1934–1944.

<https://doi.org/10.1021/acs.organomet.0c00138>

13.4.2 Reprint

Reprinted with permission from F. Nährig et al., *Organometallics* **2020**, *39*, 10, 1934–1944.
Copyright 2020 American Chemical Society.



Complexes of Platinum Group Elements Containing the Intrinsically Chiral Cyclopentadienide Ligand (CpC)–1

Author: Florian Nährig, Gerd Gemmecker, Jae-Yeon Chung, et al

Publication: *Organometallics*

Publisher: American Chemical Society

Date: May 1, 2020

Copyright © 2020, American Chemical Society

PERMISSION/LICENSE IS GRANTED FOR YOUR ORDER AT NO CHARGE

This type of permission/license, instead of the standard Terms & Conditions, is sent to you because no fee is being charged for your order. Please note the following:

- Permission is granted for your request in both print and electronic formats, and translations.
- If figures and/or tables were requested, they may be adapted or used in part.
- Please print this page for your records and send a copy of it to your publisher/graduate school.
- Appropriate credit for the requested material should be given as follows: "Reprinted (adapted) with permission from (COMPLETE REFERENCE CITATION). Copyright (YEAR) American Chemical Society." Insert appropriate information in place of the capitalized words.
- One-time permission is granted only for the use specified in your request. No additional uses are granted (such as derivative works or other editions). For any other uses, please submit a new request.

ORGANOMETALLICS

pubs.acs.org/Organometallics

Article

Complexes of Platinum Group Elements Containing the Intrinsically Chiral Cyclopentadienide Ligand (Cp^C)⁻¹

Florian Nährig, Gerd Gemmecker, Jae-Yeon Chung, Patrick Hütchen, Sergej Lauk, Matthias P. Klein, Yu Sun, Gereon Niedner-Schatteburg, Helmut Sitzmann, and Werner R. Thiel*

Cite This: *Organometallics* 2020, 39, 1934–1944

Read Online

ACCESS |



Metrics & More

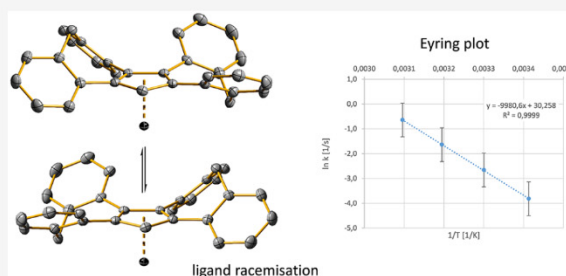


Article Recommendations



Supporting Information

ABSTRACT: Cyclopentadienide derivatives possessing intrinsic helical chirality have only rarely been published in the past. The ligand Cp^CH, which is well-accessible from inexpensive dibenzosuberenone, is paradigm for such a ligand. Here, the synthesis as well as the spectroscopic and structural characterization of a series of platinum group metal complexes containing this ligand are presented. While alkaline metal salts of Cp^CH failed in transferring the (Cp^C)⁻¹ unit to this type of metal sites, (Cp^C)Tl turned out to be an excellent precursor for the synthesis of ruthenium ($[(\eta^5\text{-Cp}^{\text{C}})\text{Ru}(\eta^6\text{-arene})]\text{PF}_6$, $[(\eta^5\text{-Cp}^{\text{C}})\text{Ru}(\text{NCCH}_3)_3]\text{PF}_6$), rhodium ($(\eta^5\text{-Cp}^{\text{C}})\text{Rh}(\eta^4\text{-COD})$), and iridium ($(\eta^5\text{-Cp}^{\text{C}})\text{Ir}(\eta^4\text{-COD})$, $[(\eta^5\text{-Cp}^{\text{C}})\text{Ir}(\eta^5\text{-Cp}^{\text{C}})]\text{PF}_6$) complexes with Cp^C ligands. EXSY NMR studies were carried out to obtain a deeper insight into the ligand

dynamics of Cp^C complexes.

INTRODUCTION

Chiral cyclopentadienide (Cp) metal complexes have gained broad interest mainly due to applications in stereoselective reactions.¹ During the past decades, five principle strategies were developed to synthesize such compounds: (a) the use of chiral (auxiliary) ligands such as phosphines in addition to a Cp ligand,² (b) the generation of chiral metal centers,³ (c) the substitution of a Cp hydrogen atom against a chiral side chain,⁴ (d) the generation of a metal complex possessing planar chirality mostly realized with ferrocenes by the introduction of two different substituents in the 1- and 2-position of the Cp ligand,⁵ and (e) the use of Cp derivatives possessing helical chirality or introducing it when bound to a metal site.⁶ Strategies (a) and (b) are based on ligand exchange reactions proceeding with Cp transition metal complexes and are often combined with each other.⁷ Strategies (c) and (d) can be realized because of the typical chemistry of Cp ligands. Deprotonation followed by substitution allows to introduce side-chains either on a free CpH system or at a (transition) metal complex. Cp complexes resulting from strategy (e) can thus be divided into two classes of different structures: (1) systems with *ansa*-bridged di-Cp-type ligands in *rac*-configuration which have found broad application, e.g., as catalysts for stereoselective propene polymerization⁸ and (2) complexes where one Cp ligand provides a helical environment by its own molecular structure.

Some years ago we published a series of transition metal complexes of 7*H*-dibenzo[*c,g*]fluorenone (Dbf⁻¹), a 2-fold benzannulated fluorenone ligand which not only contains a Cp

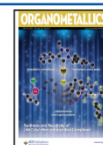
center but also a 1,1'-binaphthyl structure that leads to an intrinsic helical chirality.⁹ However, the racemization barrier of Dbf⁻¹ and its metal complexes is low. Therefore, we recently introduced a new cyclopentadiene named Cp^CH (1, IUPAC name: 5*H*-dibenzo[*e,h*]dibenzo[3,4:6,7]cyclohept-[1,2-*a*]-azulene) which turned out to have a much higher racemization barrier due to the (formal) introduction of an additional sp³ hybridized carbon atom into a six-membered aromatic ring.¹⁰ This results in two seven-membered rings in the molecule and introduces a bent conformation as known from the structurally related compound dibenzosuberenone. The suffix "C" should symbolize this bent geometry. Starting from rather inexpensive 5-dibenzosuberenone, the ligand Cp^CH (1) can be obtained in multigram amounts and in excellent yields following one of the classical strategies of Cp*H (Cp*H: 1,2,3,4,5-pentamethylcyclopentadiene) synthesis. In this manuscript, we focus on the synthesis and characterization of a series of novel platinum group metal complexes containing the (Cp^C)⁻¹ ligand.

RESULTS AND DISCUSSION

Deprotonation of Cp^CH with a strong base such as *n*-butyllithium or potassium bis(trimethylsilyl)amide gives

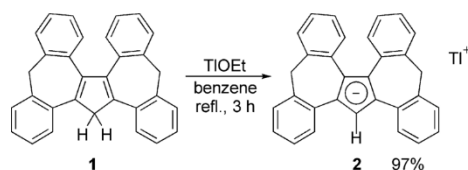
Received: February 26, 2020

Published: May 13, 2020



quantitatively the corresponding alkaline metal salts of $(\text{Cp}^{\text{C}})^{1-}$ which we recently used for the synthesis of iron and titanium(IV) complexes.^{10,11} However, attempts to transfer $(\text{Cp}^{\text{C}})^{1-}$ to late and thus more electron-rich transition metal precursors by applying its lithium, sodium, or potassium salts failed probably due to the strongly reducing nature of these salts. Since the benefits of TlCp and TlCp^* as Cp- or Cp*-transferring agents is well-documented in the literature,¹² $(\text{Cp}^{\text{C}})\text{Tl}$ (**2**) seemed to be the reagent of choice to enter late transition metal Cp^{C} chemistry. The thallium(I) compound **2** was obtained in almost quantitative yield by treating **1** with TlOEt in benzene solution (Scheme 1).

Scheme 1. Synthesis of $(\text{Cp}^{\text{C}})\text{Tl}$ (**2**)



According to its light-sensitivity, all processes involving **2** were protected from light. In its aromatic region, the ^1H NMR spectrum of $(\text{Cp}^{\text{C}})\text{Tl}$ (**2**) resembles the ^1H NMR spectrum of $\text{Cp}^{\text{C}}\text{H}$ (**1**). The only exception is the resonance of the Cp-bound hydrogen atom that appears at 6.56 ppm and is thus shifted largely to lower field as compared to the resonance of the Cp methylene unit in **1** (4.36 ppm). Due to the bending of the two wings of Cp^{C} derivatives, the methylene protons of seven-membered rings are magnetically inequivalent, giving two doublets with typical germinal coupling constants of 12.4 Hz. This proves that the thallium(I) cation is—with respect to the NMR time scale—not permanently bound to one side of the $(\text{Cp}^{\text{C}})^{1-}$ anion but is able to move to the other side. Recrystallization of **2** from tetrahydrofuran resulted in crystals suitable for X-ray structure analysis. Figure 1 shows the molecular structure of **2** and summarizes typical bond parameters.

Compound **2** crystallizes as a centrosymmetric dimer with the two thallium(I) cations connecting two $(\text{Cp}^{\text{C}})^{1-}$ units by interactions with the cyclopentadienide moiety and two benzene rings. In 1997 C. Janiak reviewed the chemistry of organothallium compounds and discussed their structures in detail.¹³ Tl–Cp distances depend strongly on the coordination mode of the thallium(I) site, which is typical for compounds of a largely ionic nature. With a Tl–Cp (centroid) distance of 2.654 Å compound **2** is ranked at the bottom end of the distance range, among a group of Cp derivatives with bulky substituents preventing $\text{Cp}\cdots\text{Tl}\cdots\text{Cp}$ interactions.¹⁴ The Tl–C_{Cp} distances in the solid state structure of **2** differ by approximately 0.1 Å, due to steric interference between the thallium(I) site, the two wings of the $(\text{Cp}^{\text{C}})^{1-}$ ligand and the coordinated tetrahydrofuran ligand. Two of the arene rings provide coordinative saturation to the thallium(I) site. Such M–arene interactions are typical for low valent late main group element cations.¹⁵ The corresponding Tl–Ar distances are found to be largely longer than reported for typical thallium(I) arene species probably due to steric reasons.

Although Tl–H and Tl–C coupling had been reported for the ^1H and ^{13}C NMR spectra of $\text{C}_5\text{Me}_5\text{Tl}$ recorded in benzene,^{14b} such couplings could not be observed in the ^1H and ^{13}C NMR spectra of compound **2**. These spectra had to be

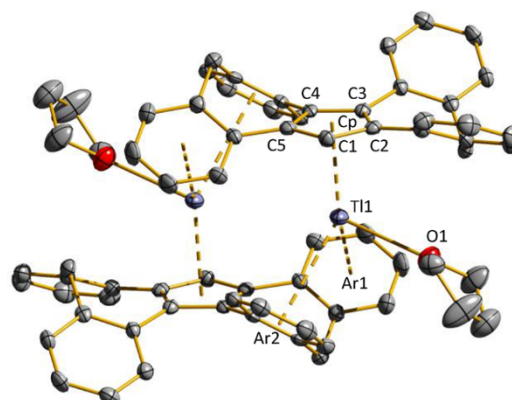
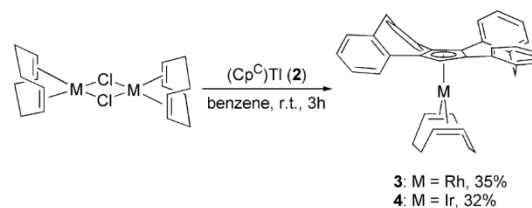


Figure 1. Molecular structure of the compound $(\text{Cp}^{\text{C}})\text{Tl}$ (**2**) in the solid state. Characteristic bond lengths [Å] and angles [°]: Tl1–Tl1' 4.225(5), Tl1–C1 2.865(4), Tl1–C2 2.942(4), Tl1–C3 2.967(4), Tl1–C4 2.930(4), Tl1–C5 2.878(4), Tl1–Cp 2.654(3), Tl1–O1 2.833(3), Tl1–Ar1 3.421(4), Tl1–Ar2 3.532(4), Cp–Tl1–Ar1 132.09(1), Cp–Tl1–Ar2 133.00(1), Ar1–Tl1–Ar2 87.25(1). Cp is the center of the five-membered ring and Ar1 and Ar2 are the centers of the six-membered rings. Hydrogen atoms are omitted for clarity.

measured in DMSO solution according to the limited solubility of the thallium(I) salt in nonpolar solvents. The number of resonances, both in the ^1H and ^{13}C NMR spectrum, and the presence of just two magnetically inequivalent methylene protons clearly prove that there is only weak interaction between the cation and the anion in a strongly coordinating solvent such as DMSO.

$(\text{Cp}^{\text{C}})\text{Tl}$ (**2**) turned out to be the perfect reagent for transferring the $(\text{Cp}^{\text{C}})^{1-}$ ligand to late transition metal sites. Complexes of the type $(\eta^5\text{-Cp}^{\text{C}})\text{M}(\eta^4\text{-COD})$ (**3**: M = Rh; **4**: M = Ir) are for example accessible from the corresponding dimeric precursors $[\text{M}(\eta^4\text{-COD})(\mu^2\text{-Cl})_2]$ (Scheme 2).¹⁶

Scheme 2. Synthesis of the Cyclooctadiene Rhodium(I) and Iridium(I) Complexes **3** and **4**



Structurally closely related rhodium(I) complexes such as $(\eta^5\text{-Cp})\text{Rh}(\eta^4\text{-COD})$ or $(\eta^5\text{-Cp}^*)\text{Rh}(\eta^4\text{-COD})$ have found applications as catalysts for the cyclotrimerization of alkynes and alkynes/nitriles leading to benzene and pyridine derivatives.¹⁷ The according iridium compounds are starting materials for a series of iridium(III) complexes.¹⁸

Slow diffusion of *n*-pentane into solutions of complexes **3** and **4** in dichloromethane gave single crystals suitable for X-ray structure analysis. According to the similar ion radii of rhodium(I) and iridium(I) both complexes crystallize in the monoclinic space group $P2_1/n$ with almost identical cell parameters, bond distances and angles. Figure 2 therefore only shows the molecular structure of the rhodium(I) complex **3**

but provides the bond parameters of both compounds in the figure caption.

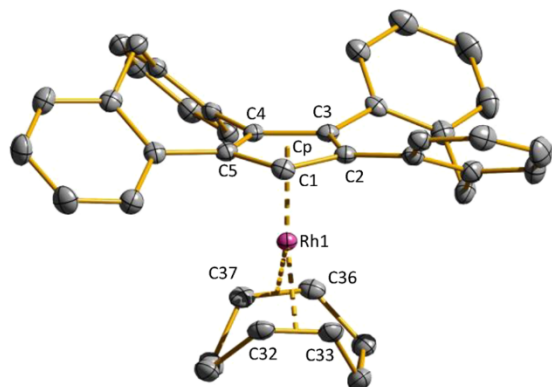


Figure 2. Molecular structure of compound $(\eta^5\text{-Cp}^{\text{C}})\text{Rh}(\eta^4\text{-COD})$ (**3**) in the solid state. Characteristic bond lengths [Å]: **3**: Rh1–C1 2.210(2), Rh1–C2 2.298(2), Rh1–C3 2.282(2), Rh1–C4 2.313(2), Rh1–C5 2.295(2), Rh1–Cp 1.924(2), Rh1–C32 2.127(2), Rh1–C33 2.116(2), Rh1–C36 2.129(2), Rh1–C37 2.133(2). **4**: Ir1–C1 2.208(3), Ir1–C2 2.275(3), Ir1–C3 2.269(3), Ir1–C4 2.308(3), Ir1–C5 2.297(3), Ir1–Cp 1.913(2), Ir1–C32 2.125(3), Ir1–C33 2.117(3), Ir1–C36 2.124(3), Ir1–C37 2.135(3). Cp is the center of the five-membered ring. Hydrogen atoms are omitted for clarity.

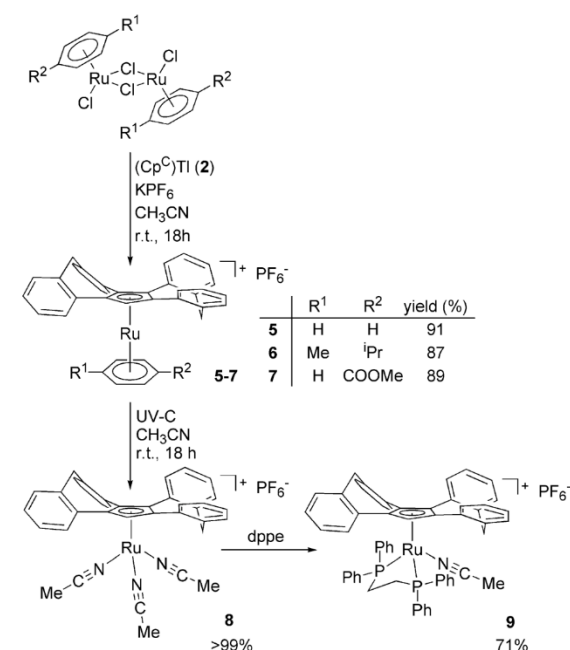
The M1–C1 distance is by about 0.1 Å shorter than the other distances between the metal site and the other Cp carbon atoms. Slight differences in these distances as well as in the distances M1–C of the metal–COD bonds are due to steric interactions in the molecule. The measured bond lengths of **3** and **4** are close to values reported for related compounds in the literature. Bonegardt et al. and Zherikova et al. reported Ir–C_{Cp} bond lengths of 2.192–2.275 Å and Ir–C_{COD} bond lengths of 2.101–2.133 Å for $(\eta^5\text{-C}_5\text{Me}_5)\text{Ir}(\eta^4\text{-COD})$ and $(\eta^5\text{-C}_5\text{H}_4\text{Me})\text{Ir}(\eta^4\text{-COD})$, which are close to the data measured for **4**.¹⁹ From rhodium(I), $(\eta^5\text{-C}_5\text{H}_5)\text{Rh}(\eta^4\text{-COD})$ and $(\eta^5\text{-C}_9\text{H}_7)\text{Rh}(\eta^4\text{-COD})$ ($\eta^5\text{-C}_9\text{H}_7\text{:}\eta^5\text{-indenide}$) have structurally been characterized, showing bond parameters similar to those of **3**.²⁰

Due to the fixed position of the metal site on one side of the (Cp^C)⁻¹ ligand and the fixed conformation of the ligand, the overall symmetry of compounds **3** and **4** and all of the following transition metal complexes is C₁ leading to four different benzene rings, five different Cp carbon ring atoms and two different methylene units with magnetically inequivalent hydrogen atoms and thus to rather complicated ¹H and ¹³C NMR spectra for this part of the molecules. Consequently there are four doublets for the methylene protons in the ¹H NMR spectrum, a pattern that is typical for all Cp^C complexes discussed in the following. The positions of these resonances differ due to shielding effects of the metal sites and of the ligands *trans* to the (Cp^C)⁻¹ moiety. In case of compounds **3** and **4**, one of these resonances is largely shifted to lower field. We assign this resonance to the hydrogen atom pointing downward and to the metal site. The resonances of the Cp bound hydrogen atoms appear at 5.58 (for **3**) and 5.62 ppm (for **4**). Coupling to the ¹⁰³Rh nucleus results in doublets for all rhodium-bound carbon atoms in the ¹³C NMR spectrum of compound **3**. The Cp carbon atoms are found between 108 and 103 ppm with ¹J_{RhC} coupling constants of about 2–4 Hz,

while the olefinic COD carbon atoms as expected appear shifted to higher field (75–69 ppm) with ¹J_{RhC} coupling around 14 Hz.^{20a} Free rotation of the COD ligand (in terms of the NMR time scale) leads to a local C₂ symmetry for this part of the molecule and therefore to two sets of signals for the methylene (CH₂) and the methine (CH) units.

Treating (Cp^C)Ti (**2**) with precursors of the type $[(\eta^6\text{-arene})\text{Ru}(\mu^2\text{-Cl})\text{Cl}]_2$ (arene = C₆H₆, 1,4-(Me)C₆H₄(^{*i*}Pr), C₆H₅COOMe)²¹ resulted in the formation of the cationic complexes $[(\eta^5\text{-Cp}^{\text{C}})\text{Ru}(\eta^6\text{-arene})]^+$ (**5–7**), which were isolated as their hexafluorophosphate salts (Scheme 3).

Scheme 3. Synthesis of the Arene Ruthenium(II) Complexes 5–7, the Acetonitrile Derivative 8, and the dppe Complex 9



While $[(\eta^6\text{-arene})\text{Ru}(\mu^2\text{-Cl})\text{Cl}]_2$ (arene = C₆H₆ and 1,4-(Me)C₆H₄(^{*i*}Pr)) are commercially available, the derivative bearing a benzoic acid methyl ester was synthesized from 1,4-dihydrobenzoic acid methyl ester and RuCl₃ according to a procedure published in the literature.^{21b} Cationic $[(\eta^5\text{-Cp}^{\text{C}})\text{Ru}(\eta^6\text{-arene})]^+$ complexes have widely been studied in the past as precursors for catalyst synthesis which mainly proceeds via exchange of the arene ligand against acetonitrile or other ligands.²² This type of reactivity was also investigated for compounds **5–7**. UV irradiation in acetonitrile solution gives quantitatively the trisacetonitrile derivative **8**. However, compounds of the type $[(\eta^5\text{-Cp}^{\text{C}})\text{Ru}(\eta^6\text{-arene})]^+$ themselves exhibit activity as catalysts²³ and show interesting photochemical behavior, e.g., the exchange of the arene ligand under irradiation.²⁴

Slow diffusion of diethyl ether into a concentrated solution of **7** in acetonitrile produced colorless crystals which were suitable for X-ray structure analysis. The compound crystallizes in the triclinic space group P1̄ with two crystallographically independent molecules in the unit cell. Figure 3 shows the molecular structure of the cation of **7** and summarizes typical bond parameters.

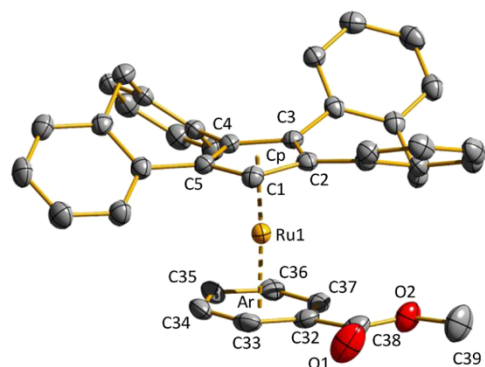


Figure 3. Molecular structure of the cation of compound $[(\eta^5\text{-CpC})\text{Ru}(\eta^6\text{-C}_6\text{H}_5\text{COOMe})\text{PF}_6]$ (**7**) in the solid state. Characteristic bond lengths [Å] and angles [°]: Ru1–C1 2.160(3), Ru1–C2 2.219(3), Ru1–C3 2.259(3), Ru1–C4 2.194(3), Ru1–C5 2.201(3), Ru1–Cp 1.836(3), Ru1–C32 2.216(3), Ru1–C33 2.204(3), Ru1–C34 2.198(3), Ru1–C35 2.222(3), Ru1–C36 2.258(3), Ru1–C37 2.258(3), Ru1–Ar 1.721(3), C32–C38 1.498(4), O1–C38 1.197(4), O2–C38 1.327(4), Cp–Ru1–Ar 175.58(2). Cp is the center of the five-membered ring of $(\text{Cp}^{\text{C}})^{-1}$ and Ar is the center of the six-membered ring of the $\text{C}_6\text{H}_5\text{COOMe}$ ligand. The second, crystallographically independent molecule in the unit cell is omitted for clarity. It shows closely related bond parameters. Furthermore the hydrogen atoms and the PF_6^- anions are omitted.

Probably the most striking feature of this structure is the slight bending of the Cp–Ru1–Ar angle (175.58°), which originates from steric interactions between the downward bound methylene unit of $(\text{Cp}^{\text{C}})^{-1}$ and the benzoic acid methyl ester ligand. The methoxycarbonyl group of this ligand is almost coplanar to the benzene ring and is located in a void below carbon atoms C1 and C2 of the $(\text{Cp}^{\text{C}})^{-1}$ ligand. In the second, crystallographically independent unit that is found in the solid state structure of **7**, the methoxycarbonyl group is located in the void below the left wing of the $(\text{Cp}^{\text{C}})^{-1}$ ligand (see Figure 3) which is pointing upward. At this point it becomes clear, that the $(\text{Cp}^{\text{C}})^{-1}$ ligand obviously discriminates the space at the opposite site of the metal by directing bulky groups of other ligands to well-defined positions. With the exception of the bending mentioned above, all bond parameters found for **7** are close to data from the literature for cationic complexes of the type $[(\eta^5\text{-Cp})\text{Ru}(\eta^6\text{-arene})]^+_{24b,25}$.

The NMR spectroscopic characterization of compounds **5**–**8** is graphically summarized in Figure S57 and S58 in the Supporting Information to this manuscript. Slight differences in the ^1H NMR chemical shifts of the $(\text{Cp}^{\text{C}})^{-1}$ units of complexes **5**–**7**, all containing an arene ligand, are due to shielding effects of these arene groups. Furthermore, the resonances of the arenes themselves display the chiral nature of the $(\text{Cp}^{\text{C}})^{-1}$ ligand: All aromatic protons of the cymene and the benzoic acid methyl ester ligand in complexes **6** and **7** are magnetically inequivalent. The same is true for the carbon

atoms of these ligands. In addition, there are two doublets for the diastereotopic methyl units of the isopropyl group in the ^1H NMR spectrum of **6** as well as two of the signals for these groups in the ^{13}C NMR spectrum. There is a pronounced shift to lower field for the Cp^{C} ring proton in the ^1H NMR spectrum of the trisacetonitrile complex **8**, which can be explained by a reduced shielding effect of the acetonitrile ligands compared to the arene ligands in complexes **5**–**7**. Furthermore, the ^1H NMR resonance of one of the magnetically inequivalent methylene groups is also shifted strongly to lower field, probably also due to some deshielding in this ligand environment compared to complexes **5**–**7**.

In order to elucidate the conformational stability of such complexes as well as the barrier for the inversion of the two stereoisomers, temperature dependent ^1H NMR spectra up to a temperature of 80°C were recorded for compounds **6** and **7**. Neither the half widths of these resonances nor of their position changes, which speaks for a rather high barrier of inversion of the $(\text{Cp}^{\text{C}})^{-1}$ ligand. This is in agreement with the results of DFT calculations on the isomerization process we had published some time ago.¹⁰ The inversion proceeds via a transition state wherein one of the wing becomes flattened and an intermediate with C_2 symmetry is formed. For the inversion barrier, a $\Delta\Delta G^\ddagger$ value of 83.7 kJ/mol was calculated (at 0 K), the barrier for the lithium complex $\text{Li}(\text{Cp}^{\text{C}})$ is in the same range (83.4 kJ/mol). This barrier is too high to be observed by conventional dynamic NMR spectroscopy. To get a deeper insight in the ligand dynamics of a transition metal Cp^{C} complex, EXSY spectra were recorded.

In the 2D EXSY spectra of compounds **5** and **9** (for the synthesis and characterization of **9**: see below), exchange cross-peaks could be observed between the ^1H signals of the methylene bridges. Specifically, at long exchange times (0.5–1 s) signals A and D showed mutual exchange, as well as signals B and C (cf. Figures S17, S49, S61, and S62). While the B–C signals are located too close to the diagonal for quantification, the A–D signals could be readily integrated for both compounds, together with the A and D diagonal peaks. For the chosen measurement conditions (for **5**, $T = 293\text{--}323\text{ K}$, exchange time 1 s; for **9**, $T = 278\text{--}318\text{ K}$, exchange times 0.5–1 s), the exchange cross-peaks were still weak compared to the diagonal peaks (0.7–37%), so that exchange rates could be readily extracted, based on two-site exchange with equal populations.²⁶ With those rates, the thermodynamic activation parameters for the inversion process could be extracted from an Eyring plot (Table 1, cf. Figure S63 and S64). Within the error margins, both compounds **5** and **9** are showing practically identical barriers.

Reacting compound **8** with 1 equiv of dppe (1,2-bis(diphenyl)diphosphinoethane) gives the phosphine complex **9** in excellent yields by displacement of two acetonitrile ligands (Scheme 3). The third acetonitrile ligand stays coordinated, leading to an overall 18VE compound. Slow diffusion of diethyl ether into a concentrated solution of **9** in dichloromethane produced yellow crystals suitable for X-ray structure

Table 1. Thermodynamic Data of the Barriers for the Isomerization Process Derived from EXSY Measurements

compound	$\Delta\Delta G^\ddagger$ [kJ/mol]	error [kJ/mol]	$\Delta\Delta H^\ddagger$ [kJ/mol]	error [kJ/mol]	$\Delta\Delta S^\ddagger$ [kJ/K·mol]	error [kJ/K·mol]	$T \cdot \Delta\Delta S^\ddagger$ at 298 K [kJ/mol]	error [kJ/mol]
5	83.0	± 0.7	80.4	± 0.7	0.002	± 0.002	−0.58	± 0.66
9	83.8	± 4.3	81.3	± 4.3	0.013	± 0.013	3.75	± 3.78

analysis. The compound crystallizes in the monoclinic space group $P2_1/n$ with a disordered PF_6^- counteranion. Figure 4 shows the molecular structure of the cation of **9** and summarizes typical bond parameters.

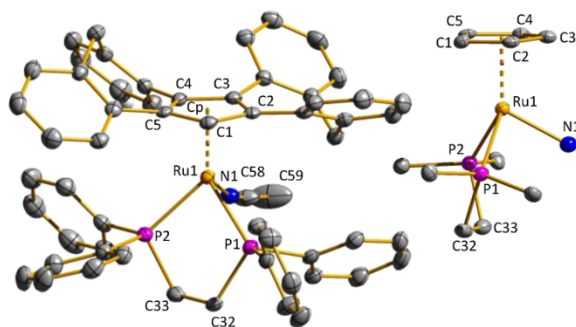


Figure 4. Molecular structure of the cation of compound $[(\eta^5\text{-Cp}^*)\text{Ru}(\text{dppf})(\text{CH}_3\text{CN})]\text{PF}_6$ (**9**) in the solid state. Characteristic bond lengths [Å], angles [°] and dihedral angles [°]: Ru1–P1 2.3397(8), Ru1–P2 2.2995(7), Ru1–N1 2.027(3), Ru1–C1 2.222(3), Ru1–C2 2.261(3), Ru1–C3 2.286(3), Ru1–C4 2.265(3), Ru1–C5 2.297(3), Ru1–Cp 1.906(3), N1–C58 1.131(4), P1–Ru1–P2 81.96(3), P1–Ru1–N1 88.06(8), P2–Ru1–N1 85.36(7), P1–Ru1–Cp 133.18(2), P2–Ru1–Cp 133.09(2), N1–Ru1–Cp 119.42(7), P1–C32–C33–P2–43.2(2). The disordered anion PF_6^- and the hydrogen atoms are omitted for clarity. Cp is the center of the five-membered ring of $(\text{Cp}^{\text{C}})^{-1}$. The inset shows a side view of the central unit of the complex, exhibiting the large Cp–Ru1–P angles in more detail.

As already observed for the compounds discussed above, orientation of bulky groups in voids below the $(\text{Cp}^{\text{C}})^{-1}$ ligand allows minimization of steric repulsion. The PPh_2 unit containing phosphorus atom P2 is located below the left wing of the $(\text{Cp}^{\text{C}})^{-1}$ ligand, which is pointing upward (see Figure 4). This brings the second PPh_2 unit containing P1 in a position where at least one of its phenyl substituents can be located in the void below C1 and C2, the acetonitrile ligand is located in the void below C3. The sterically more relaxed situation of the PPh_2 unit containing phosphorus atom P2 results in a Ru1–P2 distance that is 0.04 Å shorter than Ru1–P1. All bond parameters are in general close to those measured for the structurally related $[\text{Cp}^*\text{Ru}(\text{dppf})(\text{NCCH}_3)]^+$ cation.²⁷ In agreement with the data of analogous Cp^* complexes from the literature, the bulky $(\text{Cp}^{\text{C}})^{-1}$ ligands leads to rather large Cp–Ru1–P angles of about 133°. For ruthenium(II) complexes of this type bearing less bulky Cp^{1-} derivatives, smaller angles have been reported.²⁸ Consequently the Cp–Ru1–N1 angle becomes larger in these cases than same angle measured for compounds with bulky Cp derivatives.

Due to the presence of overall eight six-membered aromatic rings, the ¹³C and ¹H NMR spectra of compound **9** become rather complicated. However, the number of proton and carbon resonances in these spectra is correct (see the Supporting Information to this manuscript) and a few of the signals can be taken to further support the structural assignment. As usual in Cp^{C} metal complexes, there are four resonances for the magnetically inequivalent methylene protons of the $(\text{Cp}^{\text{C}})^{-1}$ ligand, two of them having exactly the same chemical shift. The resonances of the four magnetically inequivalent methylene protons of the dppf backbone appear as complex multiplets according to three HH

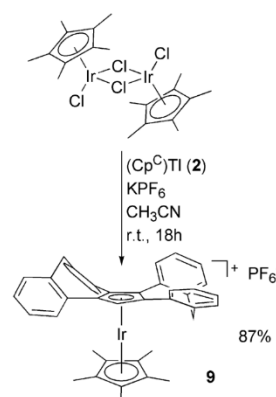
and two PH couplings for each of this nuclei. In the ¹³C NMR spectrum, there is PC coupling not only to the carbon atoms of the dppf unit but also to some of the carbon atoms (²J_{PH} = 0.0–9.5 Hz) of the central five-membered ring of the $(\text{Cp}^{\text{C}})^{-1}$ ligand. The magnetically inequivalent methylene protons of the dppf backbone show ¹J_{PH} coupling constants of about 32 Hz and ²J_{PH} coupling constants of about 13 Hz. As expected, there are two resonances in the ³¹P NMR spectrum for the magnetically different dppf phosphorus atoms (63.6, 61.8 ppm, ²J_{PP} ca. 19 Hz).

To obtain information whether the bulky dppf ligand influences the dynamics of the $(\text{Cp}^{\text{C}})^{-1}$ ligand, an EXSY study was carried out with compound **9**. The resulting data show (Table 1) that there is no shift of the activation parameters compared to compound **5**. Together with the DFT data of our former study it becomes evident, that an inversion barrier of approximately 80–90 kJ/mol can generally be expected for Cp^{C} transition metal complexes. At this point one can conclude that the calculated barriers are too low to allow the isolation of an enantiomerically pure $(\text{Cp}^{\text{C}})^{-1}$ compound. However, there are ways to solve this issue: One possibility is the introduction of bulky substituents to the Cp^{C} -backbone. This can either be done at the inward-pointing positions of the benzene rings, which would require an accordingly substituted dibenzosuberone as the precursor. Alternatively the CH-position at the central five-membered ring can be substituted. We have already synthesized the according methyl derivative and have found by DFT calculations that the barrier of equilibration rises by about 12 kJ/mol (see the Supporting Information). The second possibility is to introduce an enantiomerically pure substituent to this position which results in diastereomers which should be energetically different. This is the way we will proceed in the future.

Similar to the use of $[(\eta^6\text{-arene})\text{Ru}(\mu^2\text{-Cl})\text{Cl}]_2$ -type compounds in areneruthenium(II) chemistry, $[(\eta^5\text{-Cp}^*)\text{Ir}(\mu^2\text{-Cl})\text{Cl}]_2$ ²⁹ is a frequently used precursor for the synthesis of Cp^* iridium(III) complexes.³⁰ Treatment of $[(\eta^5\text{-Cp}^*)\text{Ir}(\mu^2\text{-Cl})\text{Cl}]_2$ with $(\text{Cp}^{\text{C}})\text{Ti}$ (**2**) and KPF_6 in acetonitrile results in the formation of $[(\eta^5\text{-Cp}^*)\text{Ir}(\eta^5\text{-Cp}^{\text{C}})]\text{PF}_6$ (**10**) in 87% yield (Scheme 4).

Slow diffusion of diethyl ether into a concentrated solution of **10** in dichloromethane produced colorless crystals which were suitable for X-ray structure analysis. The compound crystallizes in the orthorhombic space group $Pbca$ with eight

Scheme 4. Synthesis of the Cp^* Iridium(III) Complex **9**



molecules in the unit cell. Figure 5 shows the molecular structure of **10** and summarizes typical bond parameters.

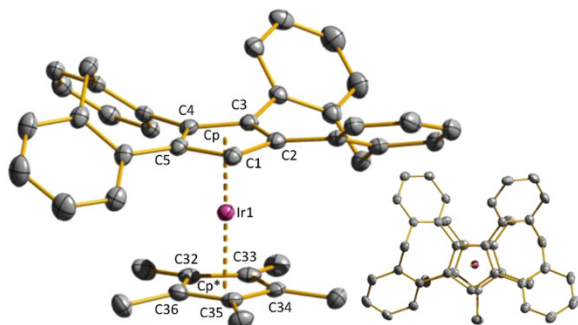


Figure 5. Molecular structure of the cation of compound $[(\eta^5\text{-Cp}^{\text{C}})\text{Ir}(\eta^5\text{-C}_5\text{Me}_5)]\text{PF}_6$ (**10**) in the solid state. Characteristic bond lengths [Å] and angles [$^\circ$]: Ir1–C1 2.181(2), Ir1–C2 2.229(2), Ir1–C3 2.247(2), Ir1–C4 2.219(2), Ir1–C5 2.215(2), Ir1–Cp 1.847(2), Ir1–C32 2.205(2), Ir1–C33 2.209(2), Ir1–C34 2.202(2), Ir1–C35 2.192(2), Ir1–C36 2.208(2), Ir1–Cp* 1.833(2), Cp–Ir1–Cp* 177.09(2). Cp is the center of the five-membered ring of $(\text{Cp}^{\text{C}})^{-1}$ and Cp* is the center of the $(\text{C}_5\text{Me}_5)^{-1}$ ligand. Hydrogen atoms and the PF_6^- anion are omitted for clarity. The inset presents a view along the axis Cp–Ir1–Cp* showing the eclipsed conformation of the two η^5 -coordinated ligands.

In this case, two ligands with five-membered rings are combined in one molecule. If the two ligands were Cp^{*-} they would arrange in a staggered conformation to avoid steric stress as it is realized, e.g., in the solid state structure of the $[(\eta^5\text{-Cp}^*)_2\text{Ir}]^+$ cation or in $[(\eta^5\text{-Cp}^*)_2\text{Fe}]$.³¹ However, in compound **10** the $(\text{Cp}^{\text{C}})^{-1}$ ligand possesses one CH_2 group pointing downward (into the direction of the Cp^{*-} ligand) and thus a motif which strongly interferes with the Cp^{*-} methyl groups. To minimize this unfavorable interaction, the two η^5 -coordinating ligands are arranging in an eclipsed conformation. Consequently the Cp–Ir1–Cp* can come close to 180° . As expected, there is no large difference between the Ir–C distances in compound **10**. They are found in the same range that has been reported for the $[(\eta^5\text{-Cp}^*)_2\text{Ir}]^+$ cation.^{31a}

Compared to compound **5**, the ^1H NMR resonance of the hydrogen atom attached to the five-membered ring of the $(\text{Cp}^{\text{C}})^{-1}$ ligand $\text{Cp}^{\text{C}}\text{H}$ is shifted by about 0.5 ppm to lower field assigning a deshielding due to the higher oxidation state of the iridium center.

CONCLUSION

$(\text{Cp}^{\text{C}})\text{Ti}$ (**2**) has turned out to be the ideal $(\text{Cp}^{\text{C}})^{-1}$ transferring reagent for the synthesis of a series of novel (Cp^{C}) complexes of late, electron-rich transition metals. Rhodium(I) and iridium(I) cyclooctadiene complexes, ruthenium(II) arene complexes, and an iridium(III) Cp^* complex were accessible following this route in high yields. The exchange of the arene ligand of $[(\eta^6\text{-arene})\text{Ru}(\eta^6\text{-arene})]\text{PF}_6$ against three acetonitrile ligands opens up the access to new chiral ruthenium(II) phosphine complexes. However, EXSY spectroscopy proved that the barriers of inversion of (Cp^{C}) transition metal complexes are too low to allow the isolation of enantiomerically pure compounds. We are presently working to solve this problem by following three different strategies: (a) The introduction of enantiomerically

pure auxiliary ligands such as BINAP. This will result in two diastereomeric complexes, one of them being lower in energy than the other one and thus being the major product. The use of such compounds in stereoselective catalysis may benefit from the bulky (Cp^{C}) moiety in addition to the chiral phosphine site. (b) Reacting $(\text{Cp}^{\text{C}})^{-1}$, e.g., with enantiomerically pure epoxides will generate two diastereomeric (Cp^{C}) -type ligands and thus allow synthesis of diastereomeric (Cp^{C}) complexes, which should be separable. (c) The introduction of substituents into the right positions at the (Cp^{C}) structure may raise the equilibration barrier to a value that allows the separation of the two enantiomers.

EXPERIMENTAL SECTION

General Remarks. All reactions were carried out under an inert atmosphere of dry nitrogen using standard Schlenk techniques. Chemicals were commercially achieved and used without further purifications. Solvents used in reactions were dried by standard methods and degassed prior to use. The ^1H and ^{13}C NMR spectra were recorded on a Bruker AVANCE 400 (^1H , 400 MHz; ^{13}C , 101 MHz; ^{31}P , 162 MHz; ^{19}F , 377 MHz) and a Bruker AVANCE 600 spectrometer (^1H , 600 MHz; ^{13}C , 151 MHz; ^{31}P , 243 MHz; ^{19}F , 565 MHz). The chemical shifts are referenced to internal solvent resonances. Infrared (IR) spectra were recorded on an FT-ATR IR 100 spectrometer with a diamond coated ZnSe ATR cell. ESI-mass spectrometric measurements were performed on a BRUKER Esquire 6000plus device by using solutions of all cationic compounds in acetonitrile. Elemental analyses were carried out with a Hanau Analyzer Vario MICRO cube. Copies of the NMR, IR, and ESI-spectra are deposited in the Supporting Information to this manuscript. The X-ray structure analyses were recorded on an Oxford Diffraction Gemini S Ultra device. Irradiation of complexes **5**, **6**, and **7** was carried out with a 254 nm Narva UVC lamp (LT-T8 18W/UVC HRA). The ligand $\text{Cp}^{\text{C}}\text{H}$ (**1**) was synthesized according to a published procedure.¹⁰

$(\text{Cp}^{\text{C}})\text{Ti}$ (2**).** A solution of 1.76 g (1.89 mmol) of $\text{Cp}^{\text{C}}\text{H}$ (**1**) in 12 mL of dry benzene was slowly added to a solution of 519 mg (2.08 mmol) thalliummethoxide in 6 mL of dry benzene at room temperature. The reaction mixture was stirred for 3 h under protection from light at 80°C . During this time a pale yellowish solid precipitated. After cooling to room temperature, the reaction mixture was filtered and the obtained yellow solid washed three times with 10 mL of dry benzene and dried under a vacuum. Yellow crystals of **2** suitable for X-ray structure analysis were obtained by recrystallization of the crude product from tetrahydrofuran. Yield 1.10 g (1.83 mmol, 97%). Elemental analysis calcd. for $\text{C}_{31}\text{H}_{21}\text{Ti}$ (597.88): C 62.28, H 3.54, found C 61.91, H 3.71%. ^1H NMR (400 MHz, $\text{DMSO}-d_6$) δ 7.53 (dd, $^3J_{\text{HH}} = 7.6$, $^4J_{\text{HH}} = 0.9$ Hz, 2H, H_{Ar}), 7.31 (m, 4H, H_{Ar}), 7.12 (td, $^3J_{\text{HH}} = 7.5$, $^4J_{\text{HH}} = 1.2$ Hz, 2H, H_{Ar}), 7.04 (m, 4H, H_{Ar}), 6.90 (td, $^3J_{\text{HH}} = 7.3$, $^4J_{\text{HH}} = 1.3$ Hz, 2H, H_{Ar}), 6.77 (td, $^3J_{\text{HH}} = 7.6$, $^4J_{\text{HH}} = 1.2$ Hz, H_{Ar}), 6.56 (s, 1H, H_{Cp}), 3.86 (d, $^2J_{\text{HH}} = 12.3$ Hz, 2H, CH_2), 3.78 (d, $^2J_{\text{HH}} = 12.4$ Hz, 2H, CH_2). ^{13}C NMR (101 MHz, $\text{DMSO}-d_6$) δ 137.5, 137.3, 137.1, 136.6, 130.3, 127.2, 127.2, 127.1, 125.8, 125.5, 124.7, 123.8, 123.2, 120.4, 106.0 (C_{CpH}), 42.1 (CH_2).

$(\eta^5\text{-Cp}^{\text{C}})\text{Rh}(\eta^4\text{-COD})$ (3**).** A solution of 61.6 mg (0.13 mmol) of $[\text{Rh}(\eta^4\text{-COD})(\mu^2\text{-Cl})_2]$ in 5 mL of dry benzene was slowly added to a suspension of 155 mg (0.26 mmol) of **2** in 10 mL of dry benzene at room temperature. The reaction mixture was stirred for 3 h under protection from light at room temperature. Then the precipitated thallium(I)chloride was removed by filtration and the remaining solvent was concentrated and overlaid with *n*-pentane. After several days, yellow crystals of **3** suitable for X-ray structure analysis were obtained. Yield 53.0 mg (0.09 mmol, 35%). Elemental analysis calcd. for $\text{C}_{39}\text{H}_{33}\text{Rh}$ (604.58): C 77.48, H 5.50, found C 77.51, H 5.66%. ^1H NMR (600 MHz, benzene- d_6) δ 8.01 (d, $^3J_{\text{HH}} = 7.6$ Hz, 1H, H_{Ar}), 7.41 (d, $^3J_{\text{HH}} = 7.2$ Hz, 1H, H_{Ar}), 7.38 (d, $^3J_{\text{HH}} = 7.5$ Hz, 2H, H_{Ar}), 7.33–7.26 (m, 1H, H_{Ar}), 7.22–7.17 (m, 2H, H_{Ar}), 7.12 (d, $^3J_{\text{HH}} = 7.8$ Hz, 1H, H_{Ar}), 7.08–7.03 (m, 2H, H_{Ar}), 7.03–6.99 (m, 1H, H_{Ar}), 6.83

(t, $^3J_{\text{HH}} = 7.2$ Hz, 1H, H_{Ar}), 6.75 (t, $^3J_{\text{HH}} = 7.2$ Hz, 1H, H_{Ar}), 6.65 (d, $^3J_{\text{HH}} = 7.6$ Hz, 1H, H_{Ar}), 5.75 (d, $^2J_{\text{HH}} = 12.3$ Hz, 1H, CH₂), 5.58 (s, H1, 1H, H_{Cp}), 4.18 (d, $^2J_{\text{HH}} = 12.3$ Hz, 1H, CH₂), 4.10 (m, $^2J_{\text{HH}} = 13.3$ Hz, 1H, CH₂), 4.00 (m, 2H, -HC=CH-), 3.55 (d, $^2J_{\text{HH}} = 13.3$ Hz, 1H, CH₂), 3.04 (m, 2H, -HC=CH-), 2.13–2.04 (m, 2H, -H₂C-CH₂-), 1.93 (ddt, $^2J_{\text{HH}} = 13.9$, $^3J_{\text{HH}} = 10.6$, 7.0 Hz, 2H, -H₂C-CH₂-), 1.72–1.64 (m, 2H, -H₂C-CH₂-), 1.64–1.56 (m, 2H, -H₂C-CH₂-) ppm. $^{13}\text{C}\{^1\text{H}\}$ NMR (151 MHz, benzene-*d*₆) δ 140.8, 140.5, 140.4, 140.2, 135.0, 132.7, 131.5, 130.9, 130.7, 130.4, 128.8, 128.8, 128.6, 128.5, 128.4, 128.4, 128.0, 127.6, 127.4, 127.3, 126.8, 126.5, 126.0, 125.5, 107.8 (d, $J_{\text{RhC}} = 3.3$ Hz, C_{Cp}), 105.9 (d, $J_{\text{RhC}} = 1.8$ Hz, C_{Cp}), 105.6 (d, $J_{\text{RhC}} = 2.3$ Hz, C_{Cp}), 103.2 (d, $J_{\text{RhC}} = 2.1$ Hz, C_{Cp}), 84.2 (d, $J_{\text{RhC}} = 3.7$ Hz, C_{CpH}), 75.4 (d, $J_{\text{RhC}} = 13.7$ Hz, -HC=CH=), 68.9 (d, $J_{\text{RhC}} = 14.2$ Hz, -HC=CH-), 43.2 (CH₂), 42.0 (CH₂), 32.8 (-H₂C-CH₂-), 31.2 (-H₂C-CH₂-) ppm. IR (ATR) $\tilde{\nu}$ 3059w, 3027w, 2987m, 2936m, 2871m, 2827m, 1599m, 1571w, 1493m, 1478m, 1425m, 1238m, 1200m, 1148m, 1120m, 1073m, 1038m, 992m, 923m, 874m, 864m, 750s, 732vs, 712s, 680vs, 656s cm⁻¹.

(η^5 -Cp^C)Ir(η^4 -COD) (4). Following the same procedure as described for complex 3, 72.9 mg (0.11 mmol) of [Ir(η^4 -COD)(μ^2 -Cl)]₂ were reacted with 130 mg (0.22 mmol) of 2. Layering a concentrated solution of the crude product in benzene with *n*-pentane produced red crystals of 4 which were suitable for X-ray structure analysis. Yield: 48.0 mg (0.07 mmol, 32%). Elemental analysis calcd. for C₃₉H₃₃Ir (693.91): C 67.51, H 4.79, found C 67.63, H 4.96%. ^1H NMR (400 MHz, benzene-*d*₆) δ 7.91 (d, $^3J_{\text{HH}} = 7.4$ Hz, 1H, H_{Ar}), 7.38 (dd, $^3J_{\text{HH}} = 7.7$, $^4J_{\text{HH}} = 1.1$ Hz, 1H, H_{Ar}), 7.32 (d, $^3J_{\text{HH}} = 6.7$ Hz, 2H, H_{Ar}), 7.26–7.21 (m, 1H, H_{Ar}), 7.14–7.09 (m, 4H, H_{Ar}), 7.06–6.95 (m, 3H, H_{Ar}), 6.83 (d, $^4J_{\text{HH}} = 1.1$ Hz, 1H, H_{Ar}), 6.72 (d, $^4J_{\text{HH}} = 1.1$ Hz, 1H, H_{Ar}), 6.63 (dd, $^3J_{\text{HH}} = 7.8$, $^4J_{\text{HH}} = 1.0$ Hz, 1H, H_{Ar}), 5.62 (s, 1H, H1, H_{Cp}), 5.48 (d, $^2J_{\text{HH}} = 12.3$ Hz, 1H, CH₂), 4.14 (d, $^2J_{\text{HH}} = 13.2$ Hz, 1H, CH₂), 4.12 (d, $^2J_{\text{HH}} = 12.3$ Hz, 1H, CH₂), 3.92 (td, $^3J_{\text{HH}} = 7.9$, $^4J_{\text{HH}} = 3.2$ Hz, 2H, -HC=CH-), 3.50 (d, $^2J_{\text{HH}} = 13.3$ Hz, 1H, CH₂), 3.01 (td, $^3J_{\text{HH}} = 7.6$, $^4J_{\text{HH}} = 2.4$ Hz, 2H, -HC=CH-), 2.16–2.01 (m, 2H, -H₂C-CH₂-), 1.87 (ddt, $^3J_{\text{HH}} = 13.9$, $^3J_{\text{HH}} = 11.1$, $^3J_{\text{HH}} = 6.9$ Hz, 2H, -H₂C-CH₂-), 1.76–1.65 (m, 2H, -H₂C-CH₂-), 1.57 (dtd, $^3J_{\text{HH}} = 10.6$, $^3J_{\text{HH}} = 7.4$, $^4J_{\text{HH}} = 3.2$ Hz, 2H, -H₂C-CH₂-) ppm. $^{13}\text{C}\{^1\text{H}\}$ NMR (101 MHz, benzene-*d*₆) δ 141.8, 141.5, 141.4, 140.8, 134.9, 132.0, 130.7, 130.6, 130.5, 129.4, 129.3, 128.8, 128.7, 128.6, 128.6, 128.5, 128.2, 128.2, 127.9, 127.5, 127.0, 126.6, 126.2, 125.7, 102.75 (C_{Cp}), 102.0 (C_{Cp}), 99.7 (C_{Cp}), 98.1 (C_{Cp}), 80.7 (C_{CpH}), 58.6 (-HC=CH-), 52.6 (-HC=CH-), 43.1 (CH₂), 41.7 (CH₂), 34.2 (-H₂C-CH₂-), 32.7 (-H₂C-CH₂-) ppm. IR (ATR) $\tilde{\nu}$ 3060w, 3030w, 2969m, 2954m, 2918m, 2873m, 2824m, 1604w, 1572w, 1498m, 1427m, 1315m, 1232m, 1200m, 1153m, 1119m, 1076m, 1040m, 1007m, 952m, 949m, 912m, 859m, 835m, 805m, 768s, 755vs, 733s, 675m cm⁻¹.

(η^5 -Cp^C)Ru(η^6 -C₆H₆)PF₆ (5). A solution 400 mg of (0.80 mmol) of [(η^6 -C₆H₆)Ru(μ^2 -Cl)Cl]₂ in 10 mL of dry acetonitrile and 294 mg (1.60 mmol) of KPF₆ was slowly added to a suspension of 1.02 g (1.71 mmol) of 2 in 5 mL of dry acetonitrile at room temperature. The reaction mixture was stirred for 18 h at room temperature while protected from light. The precipitated thallium(I)chloride was removed by filtration and the solvent was evaporated under reduced pressure. The remaining residue was washed three times with 10 mL of diethyl ether and dried under a vacuum. Complex 5 was obtained as a gray solid. Colorless crystals of 5 suitable for X-ray structure analysis were obtained by slow evaporation of a saturated solution of 5 in chloroform. Yield 1.05 g (1.46 mmol, 91%). Elemental analysis calcd. for C₃₇H₂₇F₆PRu (717.66): C 61.92, H 3.79, found C 61.96, H 3.93. ^1H NMR (400 MHz, CD₃CN) δ 7.86–7.81 (m, 1H, H_{Ar}), 7.69 (d, $^3J_{\text{HH}} = 7.4$ Hz, 1H, H_{Ar}), 7.54 (dd, $^3J_{\text{HH}} = 7.5$, $^4J_{\text{HH}} = 2.4$ Hz, 2H, H_{Ar}), 7.49–7.42 (m, 6H, H_{Ar}), 7.40–7.34 (m, 2H, H_{Ar}), 7.31 (t, $^3J_{\text{HH}} = 7.2$ Hz, 1H, H_{Ar}), 7.14 (td, $^3J_{\text{HH}} = 7.6$, 0.7 Hz, 1H, H_{Ar}), 6.94–6.88 (m, 2H, H_{Ar}), 6.70 (s, 1H, H_{Cp}), 5.97 (s, 6H, C₆H₆), 4.46 (d, $^2J_{\text{HH}} = 13.5$ Hz, 1H, CH₂), 4.29 (d, $^2J_{\text{HH}} = 13.5$ Hz, 1H, CH₂), 4.18 (d, $^2J_{\text{HH}} = 13.8$ Hz, 1H, CH₂), 3.85 (d, $^3J_{\text{HH}} = 13.8$ Hz, 1H, CH₂). $^{13}\text{C}\{^1\text{H}\}$ NMR (101 MHz, CD₃CN) δ 142.7, 142.6, 142.1, 141.5, 134.3, 132.4, 131.2, 131.1, 130.9, 130.9, 130.8, 130.7, 130.7, 130.1, 130.1, 130.0, 129.6, 129.6, 129.5, 128.5, 128.3, 128.0, 127.3, 126.6, 102.4 (C_{Cp}),

100.4 (C_{Cp}), 98.8 (C_{Cp}), 97.4 (C_{Cp}), 90.8 (C₆H₆), 79.2 (C_{CpH}), 42.8 (CH₂), 40.6 (CH₂). ^{31}P NMR (162 MHz, CD₃CN) δ -144.6 (hept, $^1J_{\text{PF}} = 706.5$ Hz). ^{19}F NMR (377 MHz, CD₃CN) δ -72.88 (d, $^1J_{\text{FP}} = 706.2$ Hz). MS (ESI) calcd. for [C₃₇H₂₇Ru]⁺: 573.12, found 573.10 *m/z*. IR (ATR) $\tilde{\nu}$ 3100w, 3078w, 2945w, 2854w, 1599w, 1579w, 1503w, 1441m, 1400m, 1160w, 1123w, 1078w, 878m, 832vs, 767s, 739s, 715m, 688m cm⁻¹.

(η^5 -Cp^C)Ru(η^6 -C₁₀H₁₄)PF₆ (6). Following the same procedure as described for complex 5, 325 mg (0.53 mmol) of [(η^6 -C₁₀H₁₄)Ru(μ^2 -Cl)Cl]₂ were reacted with 195 mg (1.06 mmol) of KPF₆ and 700 mg (1.17 mmol) of 2. Complex 6 was obtained as a gray solid. Yield 710 mg (0.92 mmol, 87%). Elemental analysis calcd. for C₄₁H₃₅F₆PRu (773.76): C 63.64, H 4.56, found C 63.43, H 4.76%. ^1H NMR (400 MHz, CD₃CN) δ 7.99–7.93 (m, 1H, H_{Ar}), 7.72–7.66 (m, 1H, H_{Ar}), 7.56 (t, $^3J_{\text{HH}} = 8.6$ Hz, 2H, H_{Ar}), 7.50–7.42 (m, 5H, H_{Ar}), 7.39–7.30 (m, 3H, H_{Ar}), 7.18–7.11 (m, 1H, H_{Ar}), 6.99 (dd, $^3J_{\text{HH}} = 7.8$, $^4J_{\text{HH}} = 1.1$ Hz, 1H, H_{Ar}), 6.96–6.89 (m, 1H, H_{Ar}), 6.76 (s, 1H, H_{Cp}), 6.26 (d, $^3J_{\text{HH}} = 6.1$ Hz, 1H, H_{Cym}), 6.18 (d, $^3J_{\text{HH}} = 6.1$ Hz, 1H, H_{Cym}), 5.87 (d, $^3J_{\text{HH}} = 6.0$ Hz, 1H, H_{Cym}), 5.79 (d, $^3J_{\text{HH}} = 6.2$ Hz, 1H, H_{Cym}), 4.40 (d, $^2J_{\text{HH}} = 13.3$ Hz, 1H, CH₂), 4.28 (d, $^2J_{\text{HH}} = 13.3$ Hz, 1H, CH₂), 4.17 (d, $^2J_{\text{HH}} = 13.8$ Hz, 1H, CH₂), 3.87 (d, $^2J_{\text{HH}} = 13.8$ Hz, 1H, CH₂), 2.06–1.97 (m, 1H, CH(CH₃)₂), 1.21 (s, 3H, CH₃-Cym), 0.62 (d, $^3J_{\text{HH}} = 6.9$ Hz, 3H, CH(CH₃)₂), 0.41 (d, $^3J_{\text{HH}} = 6.9$ Hz, 3H, CH(CH₃)₂). $^{13}\text{C}\{^1\text{H}\}$ NMR (101 MHz, CD₃CN) δ 142.5, 142.2, 141.7, 141.3, 134.2, 132.6, 131.1, 131.1, 131.1, 130.9, 130.9, 130.5, 130.4, 130.2, 130.2, 129.8, 129.7, 129.6, 129.0, 129.0, 128.3, 128.2, 127.1, 126.7, 112.3 (C_{Cym}), 102.3 (C_{Cp}), 101.4, 99.7, 98.1, 96.2 (3 × C_{Cp} C_{Cym}), 94.4 (C_{Cym}), 91.0 (C_{Cym}), 90.8 (C_{Cym}), 87.4 (C_{Cym}), 78.2 (C_{CpH}), 42.6 (CH₂), 40.7 (CH₂), 31.1 (CH(CH₃)₂), 21.8, 21.8 (2 × CH(CH₃)₂), 16.4 (CH₃-Cym). ^{31}P NMR (162 MHz, CD₃CN) δ -144.6 (hept, $^1J_{\text{PF}} = 706.2$ Hz). ^{19}F NMR (377 MHz, CD₃CN) δ -72.92 (d, $^1J_{\text{FP}} = 706.0$ Hz). MS (ESI) calcd. for [C₄₁H₃₅Ru]⁺: 629.18, found 629.14 *m/z*. IR (ATR) $\tilde{\nu}$ 3065w, 3023w, 2972w, 2863w, 1597w, 1481w, 1439m, 1396m, 1329w, 1165w, 1123w, 1057w, 1039w, 878m, 828vs, 764s, 739m, 715m cm⁻¹.

(η^5 -Cp^C)Ru(η^6 -C₈H₈O₂)PF₆ (7). Following the same procedure as described for complex 5, 300 mg (0.49 mmol) of [(η^6 -C₈H₈O₂)Ru(μ^2 -Cl)Cl]₂ were reacted with 179 mg (0.974 mmol) of KPF₆ and 658 mg (1.10 mmol) of 2. Complex 7 was obtained as a gray solid. Slow diffusion of diethyl ether into a concentrated solution of 7 in acetonitrile produced colorless crystals which were suitable for X-ray structure analysis. Yield 670 mg (0.864 mmol, 89%). Elemental analysis calcd. for C₃₉H₂₉F₆O₂PRu (775.69): C 60.39, H 3.77, found C 59.95, H 4.02%. ^1H NMR (400 MHz, CD₃CN) δ 7.85–7.80 (m, 1H, H_{Ar}), 7.66 (d, $^3J_{\text{HH}} = 7.7$ Hz, 1H, H_{Ar}), 7.55 (d, $^3J_{\text{HH}} = 7.5$ Hz, 1H, H_{Ar}), 7.52–7.43 (m, 1H, H_{Ar}), 7.37 (dd, $^3J_{\text{HH}} = 13.0$, $^3J_{\text{HH}} = 6.3$ Hz, 1H, H_{Ar}), 7.31 (t, $^3J_{\text{HH}} = 7.5$ Hz, 1H, H_{Ar}), 7.14 (t, $^3J_{\text{HH}} = 7.5$ Hz, 1H, H_{Ar}), 6.92 (d, $^3J_{\text{HH}} = 4.0$ Hz, 1H, H_{Ar}), 6.72 (s, 1H, H_{Cp}), 6.63 (d, $^3J_{\text{HH}} = 6.2$ Hz, 1H, C₆H₅), 6.54 (d, $^3J_{\text{HH}} = 6.1$ Hz, 1H, C₆H₅), 6.37 (t, $^3J_{\text{HH}} = 6.1$ Hz, 1H, C₆H₅), 6.16 (t, $^3J_{\text{HH}} = 6.1$ Hz, 1H, C₆H₅), 5.89 (t, $^3J_{\text{HH}} = 5.9$ Hz, 1H, C₆H₅), 4.36–4.24 (m, 2H, 2 × CH₂), 4.15 (d, $^2J_{\text{HH}} = 13.9$ Hz, 1H, CH₂), 3.84 (d, $^2J_{\text{HH}} = 13.9$ Hz, 1H, CH₂), 3.09 (s, 1H, CH₃). $^{13}\text{C}\{^1\text{H}\}$ NMR (101 MHz, CD₃CN) δ 164.2 (C = O), 142.5, 142.5, 142.1, 141.5, 134.0, 132.6, 131.5, 131.4, 131.1, 131.1, 130.7, 130.2, 130.1, 130.1, 129.9, 129.9, 129.7, 129.6, 128.5, 128.5, 128.1, 127.9, 127.3, 126.7, 104.0 (C_{Cp}), 102.0 (C_{Cp}), 99.8 (C_{Cp}), 98.1 (C_{Cp}), 92.4, 91.9, 91.8, 90.8, 90.4, 89.8 (6 × C₆H₅), 79.9 (C_{CpH}), 53.9 (CH₃), 42.7 (CH₂), 40.6 (CH₂). ^{31}P NMR (162 MHz, CD₃CN) δ -144.6 (hept, $^1J_{\text{PF}} = 706.4$ Hz). ^{19}F NMR (377 MHz, CD₃CN) δ -72.78 (d, $^1J_{\text{FP}} = 706.3$ Hz). MS (ESI) calcd. for [C₃₉H₂₉O₂Ru]⁺: 631.12, found 631.08 *m/z*. IR (ATR) $\tilde{\nu}$ 3102w, 3064w, 2955w, 2852w, 1736s, 1600w, 1529w, 1501w, 1440m, 1404m, 1302m, 1287m, 1201w, 1121m, 1049w, 954w, 878m, 834vs, 766s, 736m, 715s, 681w, 668w, 654w cm⁻¹.

(η^5 -Cp^C)Ru(NCCH₃)₃PF₆ (8). This reaction follows known literature procedures and can be realized starting from complexes 5, 6, or 7. A 0.02 M solution of 300 mg (0.418 mmol) of complex 5 in 21 mL of dry acetonitrile was degassed with nitrogen for several minutes in a quartz glass Schlenk tube. Subsequently, the red reaction

mixture was irradiated for 18 h with a 254 nm Narva UVC lamp (LT-T8 18W/UVC HRA). The solvent was removed under reduced pressure yielding complex **8** as a bright brown powder in quantitative yield. Elemental analysis calcd. for $C_{37}H_{30}F_6N_3PRu$ (597.88): C 58.27, H 3.96, N 5.51, found C 57.93, H 3.74, N 5.17%. 1H NMR (600 MHz, CD_3CN) δ 7.77–7.74 (m, 1H, H_{Ar}), 7.65 (dd, $^3J_{HH} = 7.7$, $^4J_{HH} = 1.1$ Hz, 1H, H_{Ar}), 7.49 (d, $^3J_{HH} = 7.5$ Hz, 2H, H_{Ar}), 7.44–7.40 (m, 5H), 7.38 (d, $^3J_{HH} = 7.5$ Hz, 1H, H_{Ar}), 7.30 (ddd, $^3J_{HH} = 7.6$, $^3J_{HH} = 6.6$, $^4J_{HH} = 2.1$ Hz, 1H, H_{Ar}), 7.26 (ddd, $^3J_{HH} = 7.2$, $^3J_{HH} = 6.6$, $^4J_{HH} = 1.0$ Hz, 2H, H_{Ar}), 7.08 (td, $^3J_{HH} = 7.5$, $^4J_{HH} = 1.1$ Hz, 1H, H_{Ar}), 6.90–6.86 (m, 2H, H_{Ar}), 5.16 (s, 1H, H_{Cp}), 4.79 (d, $^2J_{HH} = 13.3$ Hz, 1H, CH_2), 4.23 (d, $^2J_{HH} = 13.6$ Hz, 1H, CH_2), 4.09 (d, $^2J_{HH} = 13.4$ Hz, 1H, CH_2), 3.79 (d, $^2J_{HH} = 13.6$ Hz, 1H, CH_2), 1.96 (s, 9H, CH_3CN). ^{13}C NMR (151 MHz, CD_3CN) δ 142.6, 142.0, 142.0, 141.9, 134.2, 133.3, 132.3, 132.1, 132.1, 131.3, 130.7, 130.2, 129.9, 129.7, 129.6, 129.4, 129.3, 129.1, 129.1, 128.8, 127.6, 127.4, 126.7, 126.2, 118.5 (NCCH₃), 99.2 (C_{Cp}), 88.1 (C_{Cp}), 87.6 (C_{Cp}), 75.7 (C_{CpH}), 60.8 (NCCH₃), 7.08 (CH₂), 41.3 (CH₂), 1.77 (NCCH₃). ^{31}P NMR (243 MHz, CD_3CN) δ -144.6 (hept, $^1J_{PF} = 706.6$ Hz). ^{19}F NMR (565 MHz, CD_3CN) δ -72.87 (d, $^1J_{FP} = 706.5$ Hz). MS (ESI) calcd. for $[C_{31}H_{21}Ru(CH_3CN)_3]^+$: 618.15, found 618.73 *m/z*; calcd. for $[C_{31}H_{21}Ru(CH_3CN)_2]^+$: 577.12, found 577.10 *m/z*; calcd. for $[C_{31}H_{21}Ru(CH_3CN)]^+$: 536.09, found 536.11 *m/z*. IR (ATR) $\tilde{\nu}$ 3064w, 3028w, 2935w, 2841w, 1980w, 1957w, 1599w, 1499m, 1436m, 1370m, 1163w, 1122w, 1077w, 1039w, 832vs, 826vs, 763s, 739s, 703m, 676m cm^{-1} .

$[(\eta^5-Cp^*)Ru(dppe)(C_2H_5N)]PF_6$ (9**)**. A solution of 1,2-bis-(diphenylphosphino)ethane (dppe, 98 mg, 0.25 mmol) in 5 mL of dry acetonitrile was slowly added to a solution of **8** (188 mg, 0.25 mmol) in 5 mL of dry acetonitrile at room temperature. The reaction mixture was stirred for 2 h at room temperature while changing its color from brown to bright yellow. After removing the solvent under reduced pressure and the remaining brown solid was dissolved in 3 mL of dry tetrahydrofuran. Partial removing of the solvent under reduced pressure led to the precipitation of a yellow solid. Slow evaporation of diethyl ether into a concentrated solution of the solid in dichloromethane resulted in the formation of yellow crystals of **9** which were suitable for X-ray structure analysis. Yield: 189 mg (0.175 mmol, 71%). Elemental analysis calcd. for $C_{59}H_{48}F_6N_3Ru$ (1079.02): C 65.68, H 4.48, N 1.30, found C 65.20, H 4.52, N 1.22. 1H NMR (400 MHz, CD_3CN) δ 7.51–7.43 (m, 3H), 7.42–7.28 (m, 12H), 7.24 (d, $^3J_{HH} = 7.6$ Hz, 1H), 7.21–7.00 (m, 11H), 6.99–6.93 (m, 2H), 6.89 (t, $^3J_{HH} = 7.5$ Hz, 1H), 6.62 (dd, $^3J_{HH} = 10.7$, 4.7 Hz, 3H), 6.51–6.41 (m, 3H), 4.49 (d, $^3J_{PH} = 2.2$ Hz, 1H, H_{Cp}), 4.11 (d, $^2J_{HH} = 13.7$ Hz, 1H, CH_2), 4.01 (d, $^2J_{HH} = 13.0$ Hz, 1H, CH_2), 3.66 (d, $^2J_{HH} = 12.9$ Hz, 2H, CH_2), 3.22–2.88 (m, 2H, PCH_2), 2.61–2.29 (m, 2H, PCH_2), 1.96 (s, 3H, CH_3CN). ^{13}C NMR (101 MHz, CD_3CN) δ 142.8, 141.5 (d, $J_{PC} = 1.8$ Hz), 141.3 (d, $J_{PC} = 1.6$ Hz), 141.0, 137.4 (d, $J_{PC} = 45.0$ Hz), 134.6 (d, $J_{PC} = 2.0$ Hz), 134.5 (d, $J_{PC} = 2.0$ Hz), 134.1 (d, $J_{PC} = 2.1$ Hz), 133.5 (d, $J_{PC} = 38.9$ Hz), 133.4, 133.0, 132.5 (d, $J_{PC} = 9.4$ Hz), 132.1 (d, $J_{PC} = 9.9$ Hz), 131.9 (d, $J_{PC} = 9.1$ Hz), 131.5 (d, $J_{PC} = 13.8$ Hz), 131.4, 131.4, 131.3, 131.0, 130.9, 130.6, 130.5 (d, $J_{PC} = 2.1$ Hz), 130.3, 130.1 (d, $J_{PC} = 2.4$ Hz), 129.9, 129.8, 129.8, 129.6, 129.5, 129.5, 129.5, 129.4, 129.4, 129.1 (d, $J_{PC} = 9.8$ Hz), 129.0, 127.7, 127.5, 126.9, 126.3, 118.7 (CH₃CN), 111.4 (d, $J_{PC} = 2.6$ Hz, C_{Cp}), 104.0 (C_{Cp}), 93.8 (d, $J_{PC} = 8.3$ Hz, C_{Cp}), 89.9 (d, $J_{PC} = 9.5$ Hz, C_{Cp}), 79.2 (C_{CpH}), 42.1 (CH₂), 41.5 (CH₂), 28.1 (dd, $J_{PC} = 31.2$, 12.0 Hz, PCH_2), 27.1 (dd, $J_{PC} = 33.2$, 14.2 Hz, PCH_2), 2.0 (CH₃CN). ^{31}P NMR (243 MHz, CD_3CN) δ 63.6 (d, $^2J_{PP} = 18.9$ Hz), 61.8 (d, $^2J_{PP} = 19.2$ Hz), -144.6 (hept, $^1J_{PF} = 706.2$ Hz). ^{19}F NMR (565 MHz, CD_3CN) δ -72.93 (d, $^1J_{FP} = 706.4$ Hz). MS (ESI) calcd. for $[C_{31}H_{21}Ru(dppe)(CH_3CN)]^+$: 934.24, found 934.21 *m/z*; calcd. for $[C_{31}H_{21}Ru(dppe)]^+$: 893.21, found 893.21 *m/z*. IR (ATR) $\tilde{\nu}$ 3061w, 2929w, 2854w, 2050vw, 2035vw, 1602w, 1572w, 1485w, 1433s, 1310w, 1195w, 1161w, 1094m, 1026w, 831vs, 764s, 736s, 696s, 673s cm^{-1} .

$[(\eta^5-Cp^*)Ir(\eta^5-Cp^*)PF_6$ (10**)**. Following the same procedure as described for complex **5**, 367 mg (0.46 mmol) of $[(\eta^5-Cp^*)Ir(\mu^2-Cl)_2]$ were reacted with 170 mg (0.92 mmol) of KPF₆ and 598 mg (1.00 mmol) of **2**. Complex **10** was obtained as a gray solid. Slow

diffusion of diethyl ether into a concentrated solution of **10** in dichloromethane produced colorless crystals which were suitable for X-ray structure analysis. Yield 710 mg (0.918 mmol, 87%). Elemental analysis calcd. for $C_{41}H_{36}F_6IrP$ (865.92): C 56.87, H 4.19, found C 56.60, H 4.34%. 1H NMR (400 MHz, CD_3CN) δ 7.76–7.71 (m, 1H, H_{Ar}), 7.62–7.32 (m, 11H, H_{Ar}), 7.15 (t, $^3J_{HH} = 7.3$ Hz, 1H, H_{Ar}), 7.01–6.93 (m, 2H, H_{Ar}), 6.75 (d, $^3J_{HH} = 7.2$ Hz, 1H, H_{Ar}), 6.58 (s, 1H, H_{Cp}), 4.36 (d, $^2J_{HH} = 16.0$ Hz, 1H, CH_2), 4.32 (d, $^2J_{HH} = 13.5$ Hz, 1H, CH_2), 3.91 (d, $^2J_{HH} = 14.0$ Hz, 1H, CH_2), 3.73 (d, $^2J_{HH} = 12.9$ Hz, 1H, CH_2), 1.54 (s, 15H, CH_3) ppm. ^{13}C NMR (101 MHz, CD_3CN) δ 143.1, 142.7, 141.2, 140.9, 133.8, 132.3, 131.4, 131.3, 131.0, 130.8, 130.4, 130.4, 130.3, 130.0, 129.9, 129.9, 128.7, 128.5, 128.2, 127.8, 127.5, 127.2, 126.8, 126.7, 101.7 (C_{Cp}), 98.5 (C_{Cp}), 96.6 (C_{Cp}), 96.3 (C_{Cp}), 96.2 (C(CH₃)₃), 79.9 (C_{CpH}), 41.5 (CH₂), 40.8 (CH₂), 9.00 (C(CH₃)₃). ^{31}P NMR (162 MHz, CD_3CN) δ -144.6 (hept, $^1J_{PF} = 706.5$ Hz). ^{19}F NMR (377 MHz, CD_3CN) δ -72.87 (d, $^1J_{FP} = 706.9$ Hz). MS (ESI) calcd. for $[C_{41}H_{36}Ir]^+$: 721.24, found 721.18 *m/z*. IR (ATR) $\tilde{\nu}$ 3120w, 3061w, 2956w, 2927w, 2848w, 1606w, 1501m, 1476m, 1438m, 1399m, 1382m, 1261m, 1163w, 1126w, 1076m, 1028m, 917w, 879m, 831vs, 764s, 737s, 715s, 675m cm^{-1} .

EXSY Spectroscopy. 2D EXSY spectra were recorded at 600 MHz 1H frequency on a Bruker Avance III NMR spectrometer equipped with an inverse-detection room temperature probe. Sample temperatures were set with a variable temperature unit calibrated on 99.8% methanol-d₄. Sample concentrations were ca. 3.0 mg in 520 μ L of $CDCl_3$ for compound **5**, and 2.7 mg in 500 μ L of $CDCl_3$ for compound **9**. Spectra were acquired with 4096–400 real data points in F2 and F1, corresponding to acquisition times of ca. 340 ms (t_2) and 33 ms (t_1) for **5**, and 310 ms (t_2) and 30 ms (t_1) for **9**, with 8 or scans per t_1 increment. Processing was done with shifted square sinebell apodization and linear prediction to 512 t_1 increments and zero-filling to 1024 t_1 points. For compound **5**, EXSY spectra were acquired at 273, 283, 293, 303, 313, and 323 K; exchange time 1 s. Measurements at the two lowest temperatures 273 and 283 K were excluded from evaluation because no exchange was visible. For compound **9**, EXSY spectra were acquired at 278, 288, 298, 308, and 318 K; exchange time 1 and 0.5 s at 318 K. Data at 288 K were later excluded due to artifacts probably stemming from temperature instabilities during the measurement. Integration of diagonal and cross-peaks was performed within the Bruker Topspin software package (version 3.5pl7) after manual definition of the peak areas.

X-ray Structure Analyses. Crystal data and refinement parameters are collected in Table S1 in the Supporting Information. All structures were solved using direct the method implemented in SIR92,³² completed by subsequent difference Fourier syntheses, and refined by full-matrix least-squares procedures.³³ Analytical numeric absorption corrections were applied on all compounds.³⁴ All non-hydrogen atoms were refined with anisotropic displacement parameters. All hydrogen atoms were placed in calculated positions and refined by using a riding model. CCDC 1946697–1946702 contain the supplementary crystallographic data for compounds **2**, **3**, **4**, **7**, **9**, and **10** in this paper. These data can be obtained free of charge from The Cambridge Crystallographic Data Centre via www.ccdc.cam.ac.uk/data_request/cif.

■ ASSOCIATED CONTENT

Supporting Information

The Supporting Information is available free of charge at <https://pubs.acs.org/doi/10.1021/acs.organomet.0c00138>.

All recorded NMR spectra (PDF)

Accession Codes

CCDC 1946697–1946702 contain the supplementary crystallographic data for this paper. These data can be obtained free of charge via www.ccdc.cam.ac.uk/data_request/cif, or by emailing data_request@ccdc.cam.ac.uk, or by contacting The

Cambridge Crystallographic Data Centre, 12 Union Road, Cambridge CB2 1EZ, UK; fax: +44 1223 336033.

AUTHOR INFORMATION

Corresponding Author

Werner R. Thiel – Technische Universität Kaiserslautern, Fachbereich Chemie, 67663 Kaiserslautern, Germany; orcid.org/0000-0001-5283-2368; Email: thiel@chemie.uni-kl.de

Authors

Florian Nährig – Technische Universität Kaiserslautern, Fachbereich Chemie, 67663 Kaiserslautern, Germany
 Gerd Gemmecker – Technische Universität München, BNMRZ, Fakultät für Chemie, 85748 Garching, Germany
 Jae-Yeon Chung – Technische Universität Kaiserslautern, Fachbereich Chemie, 67663 Kaiserslautern, Germany
 Patrick Hütchen – Technische Universität Kaiserslautern, Fachbereich Chemie, 67663 Kaiserslautern, Germany
 Sergej Lauk – Technische Universität Kaiserslautern, Fachbereich Chemie, 67663 Kaiserslautern, Germany
 Matthias P. Klein – Technische Universität Kaiserslautern, Fachbereich Chemie, 67663 Kaiserslautern, Germany
 Yu Sun – Technische Universität Kaiserslautern, Fachbereich Chemie, 67663 Kaiserslautern, Germany
 Gereon Niedner-Schatteburg – Technische Universität Kaiserslautern, Fachbereich Chemie, 67663 Kaiserslautern, Germany; Research Center OPTIMAS, 67663 Kaiserslautern, Germany; orcid.org/0000-0001-7240-6673
 Helmut Sitzmann – Technische Universität Kaiserslautern, Fachbereich Chemie, 67663 Kaiserslautern, Germany

Complete contact information is available at: <https://pubs.acs.org/10.1021/acs.organomet.0c00138>

Notes

The authors declare no competing financial interest.

ACKNOWLEDGMENTS

The authors wish to thank the Carl Zeiss-Stiftung for donating a research grant to F.N. and the DFG-funded transregional collaborative research center SFB/TRR 88 “Cooperative effects in homo- and heterometallic complexes (3MET)” for the financial support.

REFERENCES

- (1) (a) Wagner, G.; Herrmann, R. Central Chiral Ferrocene Derivatives. In *Ferrocenes: Homogeneous Catalysis, Organic Synthesis, Material Science*; Togni, A., Hayashi, T., Eds.; Wiley-VCH: Weinheim, 1995. (b) *Chiral Ferrocenes in Asymmetric Catalysis*; Dai, L.-X., Hou, X.-L., Eds.; Wiley-VCH: Weinheim, 2010. (c) Blaser, H.-U.; Chen, W.; Camponovo, F.; Togni, A. Chiral 1,2-disubstituted ferrocene diphosphines for asymmetric catalysis. In *Ferrocenes: Ligands, Materials and Biomolecules*; Štěpnička, P., Ed.; John Wiley and Sons: Chichester, 2008; pp 205–235. (d) Gómez Arrayás, R.; Adrio, J.; Carretero, J. C. Recent Applications of Chiral Ferrocene Ligands in Asymmetric Catalysis. *Angew. Chem., Int. Ed.* **2006**, *45*, 7674–7715.
- (2) (a) Alezra, V.; Bernardinelli, G.; Corminboeuf, C.; Frey, U.; Kündig, E. P.; Merbach, A. E.; Saudan, C. M.; Viton, F.; Weber, J. [CpRu(R)-Binop-F](H₂O)] [SbF₆], a New Fluxional Chiral Lewis Acid Catalyst: Synthesis, Dynamic NMR, Asymmetric Catalysis, and Theoretical Studies. *J. Am. Chem. Soc.* **2004**, *126*, 4843–4853. (b) Kündig, E. P.; Saudan, C. M.; Alezra, V.; Viton, F.; Bernardinelli, G. [(Indenyl)Ru(biphop-F)]⁺: A Lewis Acid Catalyst That Controls

both the Diene and the Dienophile Facial Selectivity in Diels–Alder Reactions. *Angew. Chem., Int. Ed.* **2001**, *40*, 4481–4485.

(3) (a) Brunner, H. Optically Active Organometallic Compounds of Transition Elements with Chiral Metal Atoms. *Angew. Chem., Int. Ed.* **1999**, *38*, 1194–1208. (b) Romerosa, A.; Campos-Malpartida, T.; Lidrissi, C.; Saoud, M.; Serrano-Ruiz, M.; Peruzzini, M.; Garrido-Cardenas, J. A.; Garcia-Maroto, F. Synthesis, Characterization, and DNA Binding of New Water-Soluble Cyclopentadienyl Ruthenium-(II) Complexes Incorporating Phosphines. *Inorg. Chem.* **2006**, *45*, 1289–1298. (c) Jiménez-Tenorio, M.; Palacios, M. D.; Puerta, M. C.; Valerga, P. Preparation and Reactivity of Organometallic Complexes Bearing the Fragment “Cp*₂Ru(CO)(PR₃)” (PR₃ = PMe₂Pr, PEt₃): Dinuclear Complexes [(Cp*₂Ru(CO)(PR₃)₂ (-Cl))⁺ Containing Two Chiral Centers, ²-Alkene, and Other Mononuclear Complexes. *Organometallics* **2004**, *23*, 504–510.

(4) (a) Doppiu, A.; Salzer, A. A New Route to Cationic Half-Sandwich Ruthenium(II) Complexes with Chiral Cyclopentadienyl-phosphane Ligands. *Eur. J. Inorg. Chem.* **2004**, *2004*, 2244–2252. (b) Ciruelos, S.; Doppiu, A.; Englert, U.; Salzer, A. New Optically Active ‘Constrained-geometry’ Cyclopentadienyl-phosphine Ligands and their Metal Complexes. *J. Organomet. Chem.* **2002**, *663*, 183–191. (c) Moriarty, K. J.; Rausch, M. D. Synthesis and Properties of Optically Active Organomolybdenum Compounds. *J. Organomet. Chem.* **1989**, *370*, 75–80.

(5) (a) Marquarding, D.; Klusacek, H.; Gokel, G.; Hoffmann, P.; Ugi, I. Correlation of Central and Planar Chirality in Ferrocene Derivatives. *J. Am. Chem. Soc.* **1970**, *92*, 5389–5393. (b) Wechsler, D.; Rankin, M. A.; McDonald, R.; Ferguson, M. J.; Schatte, G.; Stradiotto, M. New Racemic Planar-Chiral Metallocene Ligands Derived from Donor-Substituted Indenes: A Synthetic, Structural, and Catalytic Investigation. *Organometallics* **2007**, *26*, 6418–6427. (c) Faller, J. W.; D’Alliessi, D. G. Planar Chirality in Tethered ⁶:¹-(Phosphinophenylenearene-P)ruthenium(II) Complexes and Their Potential Use as Asymmetric Catalysts. *Organometallics* **2003**, *22*, 2749–2757.

(6) Wild, F. R. W. P.; Zsolnai, L.; Huttner, F.; Brintzinger, H. H. *ansa*-Metallocene derivatives. IV. Synthesis and Molecular Structures of Chiral *ansa*-Titanocene Derivatives with Bridged Tetrahydroindenyl Ligands. *J. Organomet. Chem.* **1982**, *232*, 233–247.

(7) (a) Pardo, P.; Carmona, D.; Lamata, P.; Rodríguez, R.; Lahoz, F. J.; García-Orduña, P.; Oro, L. A. Reactivity of the Chiral Metallic Brønsted Acid [(η⁶-p-MeC₆H₄Pr)Ru(κ³P, O, O’-POH)] [SbF₆]₂ (POH = (S_{C1},R_{C2})-Ph₂PC(Ph)HC(OH)HCH₂OMe) toward Aldimines. *Organometallics* **2014**, *33*, 6927–6936. (b) Carmona, D.; Lamata, M. P.; Pardo, P.; Rodríguez, R.; Lahoz, F. J.; García-Orduña, P.; Alkorta, I.; Elguero, J.; Oro, L. A. Arene-Ruthenium Chemistry and Brønsted Acid Catalysis of a Chiral Phosphane-Hydroxyl Ligand. *Organometallics* **2014**, *33*, 616–619. (c) Brunner, H.; Henning, F.; Weber, M.; Zabel, M.; Carmona, D.; Lahoz, F. J. Chiral-at-Metal (e⁶-p-Cymene)Ruthenium(II) Complexes of Binaphthyl Ligands - Synthesis, Characterization, and Enantioselective Catalysis. *Synthesis* **2003**, *2003*, 1091–1099. (d) Carmona, D.; Lahoz, F. J.; Elipse, S.; Oro, L. A.; Lamata, M. P.; Viguri, F.; Sánchez, F.; Martínez, S.; Catiuela, C.; López-Ram de VÍu, M. P. Synthesis, Characterization, Properties, and Asymmetric Catalytic Diels–Alder Reactions of Chiral-at-Metal Phosphinooxazoline-Rhodium(III) and -Iridium(III) Complexes. *Organometallics* **2002**, *21*, 5100–5114.

(8) (a) Halterman, R. L. Synthesis and Applications of Chiral Cyclopentadienylmetal Complexes. *Chem. Rev.* **1992**, *92*, 965–994. (b) Halterman, R. L. Synthesis of chiral titanocene and zirconocene dichlorides. In *Metallocenes*; Togni, A., Halterman, R. L., Eds.; Wiley-VCH: New York, 1998. (c) Resconi, L.; Cavallo, L.; Fait, A.; Piemontesi, F. Selectivity in Propene Polymerization with Metallocene Catalysts. *Chem. Rev.* **2000**, *100*, 1253–1346. (d) Alt, H. G.; Köppl, A. Effect of the Nature of Metallocene Complexes of Group IV Metals on Their Performance in Catalytic Ethylene and Propylene Polymerization. *Chem. Rev.* **2000**, *100*, 1205–1222.

(9) (a) Pammer, F.; Sun, Y.; May, C.; Wolmershäuser, G.; Kelm, H.; Krüger, H.-J.; Thiel, W. R. Dibenzo[*c*,*g*]fluorene, the Combination of

- Cyclopentadiene and 1,1'-Binaphthyl in one Ligand. *Angew. Chem., Int. Ed.* **2007**, *46*, 1270–1273. (b) Pammer, F.; Sun, Y.; Thiel, W. R. Group VI Allyl Complexes of Dibenzo[c, g]fluorene. *Organometallics* **2008**, *27*, 1015–1018. (c) Pammer, F.; Sun, Y.; Pagels, M.; Weismann, D.; Sitzmann, H.; Thiel, W. R. Dibenzo[c, g]-fluoreneiron: a Metallorganic Relative to Pentahelicene. *Angew. Chem., Int. Ed.* **2008**, *47*, 3271–3274. (d) Pammer, F.; Sun, Y.; Weismann, D.; Sitzmann, H.; Thiel, W. R. Exploring the Concept of Aromaticity on Complexes of a Fourfold Benzannulated Cp-Ligand. *Chem. - Eur. J.* **2010**, *16*, 1265–1270. (e) Pammer, F.; Sun, Y.; Sieger, M.; Fiedler, J.; Sarkar, B.; Thiel, W. R. A Cobaltocenium Complex of Dibenzo[c, g]fluorene and its Structural and Electrochemical Properties. *Organometallics* **2010**, *29*, 6165–6168. (f) Pammer, F.; Sun, Y.; Thiel, W. R. Dbf-Ruthenocenes: Towards Chiral Half-sandwich Lewis Acidic Dbf Complexes. *Inorg. Chim. Acta* **2011**, *374*, 205–210. (g) Pammer, F.; Thiel, W. R. Benzannulated Homologues of Cyclopentadiene as Ligands in Organometallic Chemistry. *Coord. Chem. Rev.* **2014**, *270–271*, 14–30.
- (10) Chung, J.-Y.; Schulz, C.; Bauer, H.; Sun, Y.; Sitzmann, H.; Auerbach, H.; Pierik, A. J.; Schünemann, V.; Neuba, A.; Thiel, W. R. The Novel Cyclopentadiene Ligand CpC⁻ Possessing Intrinsic Helical Chirality and its Ferrocene Analogues. *Organometallics* **2015**, *34*, 5374–5382.
- (11) Chung, J.-Y.; Sun, Y.; Thiel, W. R. Titanium(IV) complexes bearing the Cp⁻ ligand. *J. Organomet. Chem.* **2017**, *829*, 31–36.
- (12) (a) Shoshani, M. M.; Liu, J.; Johnson, S. A. Mechanistic Insight into H/D Exchange by a Pentanuclear Ni-H Cluster and Synthesis and Characterization of Structural Analogues of Potential Intermediates. *Organometallics* **2018**, *37*, 116–126. (b) Masi, S.; Top, S.; Jaouen, G. Reaction of [Re(CO)₆]⁺ Cation with Cyclopentadienylthallium Derivatives. Formation of Cyclopentadienylrhodiumtricarboxyl Derivatives via [Re(CO)₃L₃]⁺ (L = solvent). *Inorg. Chim. Acta* **2003**, *350*, 665–668. (c) Dysard, J. M.; Tilley, T. D. Tantalum-Mediated Substitution at Germanium: A Germolyl-to-Germole Transformation Leading to f⁴-C₄Me₄GeMeCl Complexes. *Organometallics* **2000**, *19*, 4720–4725. (d) Janiak, C. Cyclopentadienylthallium(I) as a Ligand Transfer Reagent. *J. Prakt. Chem./Chem.-Ztg.* **1998**, *340*, 181–183. (e) Herrmann, W. A.; Thiel, W. R.; Herdtweck, E. Chrom(III)- und Chrom(IV)-Komplexe der-Aromaten-Reihe: Präparative und Strukturchemische Aspekte. *J. Organomet. Chem.* **1988**, *353*, 323–336. (f) Kraus, H. J.; Werner, H.; Krüger, C. Synthese und Struktur von C₅Me₃Pd(PR₃)X: Palladiumkomplexe mit einem Unsymmetrisch Gebundenen Pentamethylcyclopentadienylring. *Z. Naturforsch., B: J. Chem. Sci.* **1983**, *38B*, 733–737.
- (13) Janiak, C. (Organo)thallium(I) and (II) Chemistry: Syntheses, Structures, Properties and Applications of Subvalent Thallium Complexes with Alkyl, Cyclopentadienyl, Arene or Hydrotris-(pyrazolyl)borate Ligands. *Coord. Chem. Rev.* **1997**, *163*, 107–216.
- (14) (a) Frasson, E.; Menegus, F.; Panattoni, C. Chain Structure of the Cyclopentadienyls of Monovalent Indium and Thallium. *Nature* **1963**, *199*, 1087–1089. (b) Werner, H.; Otto, H.; Kraus, H. J. Die Kristallstruktur von TIC₃Me₃. *J. Organomet. Chem.* **1986**, *315*, C57–C60. (c) Schumann, H.; Kucht, H.; Dietrich, A.; Esser, L. [(Dimethylphenylsilyl)tetramethylcyclopentadienyl]thallium(I) und [(Benzoldimethylsilyl)tetramethylcyclopentadienyl]thallium(I) - Polymere Metallorganyle mit Kettenstruktur. *Chem. Ber.* **1990**, *123*, 1811–1816.
- (15) (a) Schmidbaur, H. Arene Complexes of Univalent Gallium, Indium, and Thallium. *Angew. Chem., Int. Ed. Engl.* **1985**, *24*, 893–904. (b) Schmidbaur, H.; Bublak, W.; Riede, J.; Müller, G. [(1,3,5-(CH₃)₃H₃C₆]₂[GaBr₄]₄ - Synthesis and Structure of a Mixed Mono- and Bis(arene)thallium Complex. *Angew. Chem., Int. Ed. Engl.* **1985**, *24*, 414–415.
- (16) (a) Baghurst, D. R.; Mingos, D. M. P.; Watson, M. J. Application of Microwave Dielectric Loss Heating Effects for the Rapid and Convenient Synthesis of Organometallic Compounds. *J. Organomet. Chem.* **1989**, *368*, C43–C45. (b) Axelson, D. A. In *Inorg. Synth.*; Shriver, D. F., Ed.; Wiley Interscience: Chichester, 1979; Vol. 19. (c) Herde, J. L.; Lambert, J. C.; Senoff, C. V. In *Inorg. Synth.*; Parshall, G. W., Ed.; Wiley Interscience: Chichester, 1974; Vol. 19.
- (17) (a) Abdulla, K.; Booth, B. L.; Stacey, C. Cyclotrimerization of Acetylenes Catalyzed by (1⁵-Cyclopentadienyl)rhodium Complexes. *J. Organomet. Chem.* **1985**, *293*, 103–114. (b) Dazinger, G.; Torres-Rodrigues, M.; Kirchner, K.; Calhorda, M. J. P. J.; Costa, P. J. Formation of Pyridine from Acetylenes and Nitriles Catalyzed by RuCpCl, CoCp, and RhCp Derivatives - A Computational Mechanistic Study. *J. Organomet. Chem.* **2006**, *691*, 4434–4445. (c) Orian, L.; van Stralen, J. N. P.; Bickelhaupt, F. M. Cyclotrimerization Reactions Catalyzed by Rhodium(I) Half-Sandwich Complexes: A Mechanistic Density Functional Study. *Organometallics* **2007**, *26*, 3816–3830.
- (18) Datsenko, V. P.; Nelyubina, Y. V.; Smol'yakov, A. F.; Loginov, D. A. Cyclooctadiene Iridium Complexes [Cp^{*}Ir(COD)X]⁺ (X = Cl, Br, I): Synthesis and Application for Oxidative Coupling of Benzoic Acid with Alkynes. *J. Organomet. Chem.* **2018**, *874*, 7–12.
- (19) (a) Bonegardt, D. V.; Il'in, I. Y.; Sukhikh, T. S.; Morozova, N. B. Crystal Structure and Properties of (1,5-Cyclooctadiene)(η⁵-pentamethylcyclopentadienyl) Iridium(I) [Ir(cod)Cp^{*}]. *J. Struct. Chem.* **2017**, *58*, 983–988. (b) Zherikova, K. V.; Morozova, N. B.; Baidina, I. A. Crystal Structure of (5-Methylcyclopentadienyl)-(1,5-cyclooctadiene) Iridium(I). *J. Struct. Chem.* **2009**, *50*, 570–573.
- (20) (a) Graf, M.; Böttcher, H.-C.; Mayer, P.; Scheer, M. Synthesis and Molecular Structures of [Rh(η⁵-C₅H₅)(coe)₂] (coe = cis-cyclooctene) and [Rh(η⁵-C₅H₅)(cod)] (cod = cis-η⁵-1,5-cyclooctadiene). *Z. Anorg. Allg. Chem.* **2017**, *643*, 1323–1325. (b) Kakkar, A. K.; Jones, S. F.; Taylor, N. J.; Collins, S.; Marder, T. B. The Hapticity of 1-Indenyl Complexes: Molecular Structures of [(⁵-C₉R₇)Rh(⁴-cod)] (R = H, Me) (cod = Cyclo-octa-5-diene). *J. Chem. Soc., Chem. Commun.* **1989**, 1454–1456.
- (21) (a) Bennett, M. A.; Smith, A. K. Arene Ruthenium(II) Complexes Formed by Dehydrogenation by Cyclohexadienes with Ruthenium(III) Trichloride. *J. Chem. Soc., Dalton Trans.* **1974**, 233–241. (b) Pinto, P.; Marconi, G.; Heinemann, F. W.; Zenneck, U. Chiral Arene Ruthenium Complexes. 6. Diastereoselective Formation of Chiral-At-Metal P-Tethered Arene Ruthenium(II) Complexes. *Organometallics* **2004**, *23*, 374–380.
- (22) (a) Wang, S.-G.; Park, S. H.; Cramer, N. A Readily Accessible Class of Chiral Cp Ligands and their Application in RuII-Catalyzed Enantioselective Syntheses of Dihydrobenzoindoles. *Angew. Chem., Int. Ed.* **2018**, *57*, 5459–5462. (b) Smarun, A. V.; Shahreel, W.; Pramono, S.; Koo, S. Y.; Tan, L. Y.; Ganguly, R.; Vidović, D. Influence of Increasing Steric Demand on Isomerization of Terminal Alkenes Catalyzed by Bifunctional Ruthenium Complexes. *J. Organomet. Chem.* **2017**, *834*, 1–9. (c) Kossler, D.; Cramer, N. Neutral Chiral Cyclopentadienyl Ru(II)Cl Catalysts Enable Enantioselective [2 + 2]-Cycloadditions. *Chem. Sci.* **2017**, *8*, 1862–1866. (d) Trost, B. M.; Rao, M.; Dieskau, A. P. A Chiral Sulfoxide-Ligated Ruthenium Complex for Asymmetric Catalysis: Enantio- and Regioselective Allylic Substitution. *J. Am. Chem. Soc.* **2013**, *135*, 18697–18704. (e) Imazaki, Y.; Shirakawa, E.; Ueno, R.; Hayashi, T. Ruthenium-Catalyzed Transformation of Aryl and Alkenyl Triflates to Halides. *J. Am. Chem. Soc.* **2012**, *134*, 14760–14763. (f) Gutierrez, A. C.; Jamison, T. F. Continuous Photochemical Generation of Catalytically Active [CpRu]⁺ Complexes from CpRu(η⁶-C₆H₆)PF₆. *Org. Lett.* **2011**, *13*, 6414–6417. (g) Zhang, H.-J.; Demerseman, B.; Toupet, L.; Xi, Z.; Bruneau, C. Ruthenium-Catalyzed Nucleophilic Allylic Substitution Reactions from β-Silylated Allylic Carbonates. *Organometallics* **2009**, *28*, 5173–5182.
- (23) (a) Takemoto, S.; Shibata, E.; Nakajima, M.; Yumoto, Y.; Shimamoto, M.; Matsuzaka, H. Ruthenium-Sulfonamide-Catalyzed Direct Dehydrative Condensation of Benzylic C-H Bonds with Aromatic Aldehydes. *J. Am. Chem. Soc.* **2016**, *138*, 14836–14839. (b) Kononov, A. I.; Gorbacheva, E. O.; Miloserdov, F. M.; Grushin, V. V. Ruthenium-Catalyzed Nucleophilic Fluorination of Halobenzenes. *Chem. Commun.* **2015**, *51*, 13527–13530.
- (24) (a) George, S. P.; Moore, C. E.; Carpenter, A. E.; Rheingold, A. L.; Blackwell, J. M.; Figueroa, J. S. Development of [CpRu(B⁶

- benzylcarbamate)]X Salts as Two-stage Photobase Generators. *Inorg. Chim. Acta* **2014**, *422*, 146–151. (b) Perekalin, D. S.; Karslyan, E. E.; Petrovskii, P. V.; Borissova, A. O.; Lyssenko, K. A.; Kudinov, A. R. Arene Exchange in the Ruthenium-Naphthalene Complex [CpRu(C₁₀H₈)]⁺. *Eur. J. Inorg. Chem.* **2012**, *2012*, 1485–1492. (c) Uchida, K.; Inagaki, A.; Akita, M. Preparation and Photochemical Behavior of Organoruthenium Derivatives of Photochromic Dithienylethene (DTE): DTE - (RRuL_m)_n (RRuL_m) = ((⁶-C₆H₅)Ru(⁵-C₅Me₅), (⁶-C₆H₅)RuCl₂(PPh₃), (⁵-C₅Me₄)Ru(CO)₂; n = 1,2). *Organometallics* **2007**, *26*, 5030–5041.
- (25) (a) Navarro Clemente, M. E.; Juárez Saavedra, P.; Cervantes Vásquez, M.; Paz-Sandoval, M. A.; Arif, A. M.; Ernst, R. D. Syntheses, Structures, and Reactivity Studies of Half-Open Ruthenocenes and Their Oxidienyl Analogues. *Organometallics* **2002**, *21*, 592–605. (b) Grepioni, F.; Cojazzi, G.; Braga, D.; Marseglia, E.; Scaccianoce, L.; Johnson, B. F. G. Crystal Architecture of the Cocrystalline Salt [Ru(⁵-C₅H₅)(⁶-trans-PhCH = CHPh)][PF₆][•]0.5trans-PhCH = CHPh and the Reversible Order-disorder Phase Transition in [Ru(d⁵-C₅H₅)(⁶-C₆H₆)]PF₆. *J. Chem. Soc., Dalton Trans.* **1999**, 553–558. (c) Morisaki, Y.; Kondo, T.; Mitsudo, T. Ruthenium-Catalyzed Allylic Substitution of Cyclic Allyl Carbonates with Nucleophiles. Stereoselectivity and Scope of the Reaction. *Organometallics* **1999**, *18*, 4742–4746. (d) Loughrey, B. T.; Cuning, B. V.; Healy, P. C.; Brown, C. L.; Parsons, P. G.; Williams, M. L. Selective, Cytotoxic Organoruthenium(II) Full-Sandwich Complexes: A Structural, Computational and In Vitro Biological Study. *Chem. - Asian J.* **2012**, *7*, 112–121. (e) He, X. D.; Chaudret, B.; Dahan, F.; Huang, Y.-S. Synthesis and Reactivity of Neutral and Ionic π -Adducts of Functional Arenes. X-ray Crystal Structures of {[(C₅Me₅)Ru]₂(^{6,6}-PhC≡CPh)(CF₃SO₃)₂}, (C₅Me₅)Ru(⁶-PhCO), and [(C₅Me₅)(MeCN)Ru(^{2,2',4}-C₄H₂Ph₂)Ru(C₅Me₅)](CF₃SO₃). *Organometallics* **1991**, *10*, 970–979.
- (26) Perrin, C. L.; Dwyer, T. J. Application of Two-Dimensional NMR to Kinetics of Chemical Exchange. *Chem. Rev.* **1990**, *90*, 935–967.
- (27) (a) Perekalin, D. S.; Shvydkiy, N. V.; Nelyubina, Y. V.; Kudinov, A. R. Synthesis of the half-sandwich ruthenium complexes [Cp*^{Ru}L₃]⁺ via naphthalene replacement in [Cp*^{Ru}(C₁₀H₈)]⁺. *Mendeleev Commun.* **2015**, *25*, 29–31. (b) Cordiner, R. L.; Albesa-Jové, D.; Roberts, R. L.; Farmer, J. D.; Puschmann, H.; Corcoran, D.; Goeta, A. E.; Howard, J. A. K.; Low, P. J. Syntheses and molecular structures of group 8 benzonitrile complexes. *J. Organomet. Chem.* **2005**, *690*, 4908–4919. (c) Beach, M. T.; Walker, J. M.; Wang, R.; Spivak, G. J. Ruthenium Piano-stool Complexes Containing Mono- or Bidentate Pyrrolidinylalkylphosphines and their Reactions with Small Molecules. *J. Organomet. Chem.* **2011**, *696*, 3198–3205.
- (28) (a) Morandini, F.; Consiglio, G.; Ciani, G.; Sironi, A. Stereospecific Substitution of the Choro-ligand by Acetonitrile in the Diastereomeric (η^5 -C₅H₅)RuCl[(R)-Ph₂PCH(CH₃)CH₂PPh₂]-complexes. *Inorg. Chim. Acta* **1984**, *82*, L27–L28. (b) Keisham, S. S.; Mozharivskiy, Y. A.; Carroll, P. J.; Kollipara, M. R. Syntheses and Characterization of Indenylruthenium(II) Complexes Containing N, N' Donor Schiff Base Ligands. Molecular Structures of [(⁵-C₉H₇)Ru(PPh₃)₂(CH₃CN)]BF₄ and [(⁵-C₉H₇)Ru(PPh₃)(C₅H₄-N-2-CH = N-C₆H₄-p-CH₃)]BF₄. *J. Organomet. Chem.* **2004**, *689*, 1249–1256. (c) Belli, R. G.; Burton, K. M. E.; Rufh, S. A.; McDonald, R.; Rosenberg, L. Inner- and Outer-Sphere Roles of Ruthenium Phosphido Complexes in the Hydrophosphination of Alkenes. *Organometallics* **2015**, *34*, 5637–5646.
- (29) Ball, R. G.; Graham, W. A. G.; Heinekey, D. M.; Hoyano, J. K.; McMaster, A. D.; Mattson, B. M.; Michel, S. T. Synthesis and Structure of [(-C₅Me₅)Ir(CO)]₂. *Inorg. Chem.* **1990**, *29*, 2023–2025.
- (30) (a) Dialer, H.; Polborn, K.; Ponikvar, W.; Sünkel, K.-H.; Beck, W. nnnnnnn-Amino Acids with Metallocenyl Side Chains. *Chem. - Eur. J.* **2002**, *8*, 691–699. (b) Schön, F.; Leist, M.; Neuba, A.; Lang, J.; Braun, C.; Sun, Y.; Niedner-Schatteburg, G.; Bräse, S.; Thiel, W. R. A Direct Access to Heterobimetallic Complexes by Roll-over Cyclo-metallation. *Chem. Commun.* **2017**, *53*, 12016–12019. (c) Kerner, C.; Neu, J. P.; Gaffga, M.; Lang, J.; Oelkers, B.; Sun, Y.; Niedner-Schatteburg, G.; Thiel, W. R. Gas-phase reactivity of Cp* Group IX metal complexes bearing aromatic N, N'-chelating ligands. *New J. Chem.* **2017**, *41*, 6995–7006. (d) Schnitzler, V.; Frank, W.; Ganter, C. Straightforward synthesis of phosphametalocenium cations of Rh and Ir. *J. Organomet. Chem.* **2008**, *693*, 2610–2614. (e) Blasberg, F.; Bolte, M.; Lerner, H.-W.; Wagner, M. Mononuclear (O,O' or N,N') and Heterodinuclear (O,O' and N,N') Transition-Metal Complexes of ortho-Quinoid Bis(pyrazol-1-yl)methane Ligands. *Organometallics* **2012**, *31*, 3213–3221.
- (31) (a) Struchkov, Y. T.; Antipin, M. Y.; Lyssenko, K. A.; Gusev, O. V.; Peganova, T. A.; Ustynyuk, N. A. X-ray Structures of Decamethylplatinocene Dication in the Crystal of [Pt(⁵-C₅Me₅)₂]²⁺(PF₆⁻)₂ and Decamethyliridocenium Cation in the Crystal of [Ir(⁵-C₅Me₅)₂]⁺(BPh₄⁻)•CH₂Cl₂. *J. Organomet. Chem.* **1997**, *536*, 281–284. (b) Struchkov, Y. T.; Andrianov, V. G.; Sal'nikova, T. N.; Lyatfifov, I. R.; Materikova, R. B. Crystal and Molecular Structure of two Polymethylferrocenes: Sym-Octamethylferrocene and Decamethylferrocene. *J. Organomet. Chem.* **1978**, *145*, 213–23.
- (32) Altomare, A.; Cascarano, G.; Giacovazzo, C.; Guagliardi, A.; Burla, M. C.; Polidori, G.; Camalli, M. SIR92 - a program for automatic solution of crystal structures by direct methods. *J. Appl. Crystallogr.* **1994**, *27*, 435–435.
- (33) Sheldrick, G. M. A short history of SHELX. *Acta Crystallogr., Sect. A: Found. Crystallogr.* **2008**, *A64*, 112–122.
- (34) *CrysAlisPro*, ver. 1.171.38.41, 1.171.38.43, and 1.171.38.46; Rigaku Oxford Diffraction, 2015.

Curriculum Vitae

Matthias Klein

Doctoral studies

Since 12/2016 Technische Universität Kaiserslautern, Department of Chemistry,
Niedner-Schatteburg group
Doctoral studies in Physical Chemistry

Education

10/2011 – 11/2016 Technische Universität Kaiserslautern
Field of study: Chemistry, Focus Physical Chemistry
Degree: Diploma
Thesis title: „Cryo-Infrarotspektroskopie an Stickstoffadsorbaten auf
kationischen Rhodium- und Rhodium-Eisen-Clustern“

Awards

PCCP Poster Prize, Bunsentagung 2017, Kaiserslautern
Steinhofer Prize 2017, Prof. Dr. Drs. h.c. A. Steinhofer foundation for
outstanding achievements during the diploma thesis work

List of Publications

1. *Infrared spectroscopic investigation of structures and N₂ adsorption induced relaxations of isolated Rhodium clusters*
M. P. Klein, A. A. Ehrhard, J. Mohrbach, S. Dillinger, and G. Niedner-Schatteburg
Top. Catal. **2018**, *61*, 106-118.
<http://doi.org/10.1007/s11244-017-0865-2>
2. *A phosphino-carboxylic acid based Ru dimeric complex*
C. K. Rank, T. Wall, F. Dietrich, M. Vidovic, M. P. Klein, Y. Sun, G. Niedner-Schatteburg, M. Gerhards, and F. W. Patureau
Eur. J. Inorg. Chem. **2018**(12), 1394-1398.
<https://doi.org/10.1002/ejic.201701382>
3. *Cryo IR Spectroscopy of N₂ and H₂ on Ru₈⁺: The Effect of N₂ on the H-Migration*
S. Dillinger, M. P. Klein, A. Steiner, D. C. McDonald II, M. A. Duncan, M. M. Kappes, and G. Niedner-Schatteburg
J. Phys. Chem. Lett. **2018**, *9*, 914-918.
<https://doi.org/10.1021/acs.jpcclett.8b00093>
4. *Generation of a zinc and rhodium containing metallomacrocycle by rearrangement of a six-coordinate precursor complex*
C. Groß, Y. Sun, T. Jost, T. Grimm, M. P. Klein, G. Niedner-Schatteburg, S. Becker, and W. R Thiel
Chem. Commun. **2020**, *56*, 368-371.
<https://doi.org/10.1039/C9CC07723E>
5. *Complexes of Platinum Group Elements Containing the Intrinsically Chiral Cyclopentadienide Ligand (Cp^C)⁻¹*
F. Nährig, G. Gemmecker, J.-Y. Chung, P. Hütchen, S. Lauk, M. P. Klein, Y. Sun, G. Niedner-Schatteburg, H. Sitzmann, and W. R. Thiel
Organometallics **2020**, *39*, 10, 1934-1944.
<https://doi.org/10.1021/acs.organomet.0c00138>
6. *Observation and mechanism of cryo N₂ cleavage by a tantalum cluster*
D. V. Fries, M. P. Klein, A. Steiner, M. H. Prosenc, and G. Niedner-Schatteburg
Phys. Chem. Chem. Phys. **2021**, *23*, 11345-11354.
<https://doi.org/10.1039/D0CP06208A>
7. *Cryokinetics and Spin Quenching in the N₂ Adsorption onto Rhodium Cluster Cations*
A. A. Ehrhard*, M. P. Klein*, J. Mohrbach, S. Dillinger, and G. Niedner-Schatteburg
(* equally contributing)
Molecular Physics **2021**, accepted.
<https://doi.org/10.1080/00268976.2021.1953172>

8. *Cryo Kinetics of N₂ Adsorption onto Bimetallic Rhodium-Iron Clusters in Isolation*
A. A. Ehrhard, **M. P. Klein**, J. Mohrbach, S. Dillinger, and G. Niedner-Schatteburg
under review at J. Chem. Phys.

9. *Cryo Infrared Spectroscopy of N₂ Adsorption onto Bimetallic Rhodium-Iron Clusters in Isolation*
M. P. Klein, A. A. Ehrhard, M. E. Huber, S. Dillinger, J. Mohrbach, and G. Niedner-Schatteburg
under review at J. Chem. Phys.

Conference Contributions

Oral Presentations

Matthias P. Klein, Amelie Ehrhard, Sebastian Dillinger, Joachim M. Hewer, Johannes Lang, Jennifer Mohrbach, and Gereon Niedner-Schatteburg, "Cryo spectroscopy on N₂ adducts of cold transition metal complexes and cluster cations", 3MET PhD Workshop, Heidelberg, 27.09.2017.

Matthias P. Klein, Daniela V. Fries, Annika Steiner, and Gereon Niedner-Schatteburg, "Adsorption of Diatomics on Rhodium and Tantalum clusters: Cryo spectroscopy and kinetics", 6. Promovierendenseminar des Fachbereichs Chemie, Kaiserslautern, 02.04.2019.

Matthias P. Klein, Daniela V. Fries, Annika Steiner, Helmut Schwarz, and Gereon Niedner-Schatteburg, "Cryo kinetics and IR spectroscopy of N₂ adsorbed to size selected Tantalum clusters using an FT-ICR-MS instrument", FTMS-Meeting, Berlin, 19.09.-20.09.2019.

Matthias P. Klein, Michael Lembach, Annika Steiner, Daniela V. Fries, and Gereon Niedner-Schatteburg, "Magnetism and functional cooperativity of isolated oligo-nuclear transition metal complexes (and clusters) within cryo ion traps", 3MET PhD Workshop, Heidelberg, 08.10.2019.

Talks in 2020 accepted by organizer but cancelled due to Corona pandemic:

Matthias P. Klein, Daniela V. Fries, Annika Steiner, Helmut Schwarz, and Gereon Niedner-Schatteburg, "N₂ activation on size selected Tantalum clusters investigated by cryo kinetics and IR spectroscopy", DPG Frühjahrstagung, Hannover, 08.03.-13.03.2020.

Matthias P. Klein, Daniela V. Fries, Annika Steiner, Helmut Schwarz, and Gereon Niedner-Schatteburg, "N₂ activation on size selected Tantalum clusters investigated by cryo kinetics and IR spectroscopy", Bunsentagung, Gießen, 31.08.-02.09.2020.

Poster Presentations

Matthias Klein, Amelie Ehrhard, Sebastian Dillinger, Jennifer Mohrbach, and Gereon Niedner-Schatteburg, "Infrared spectroscopic investigations of N₂ adsorbed to cold Rhodium Iron alloy cluster cations", Frühjahrstagung der Deutschen Physikalischen Gesellschaft, Mainz, 06.-10.03.2017.

Matthias P. Klein, Amelie Ehrhard, Sebastian Dillinger, Jennifer Mohrbach, and Gereon Niedner-Schatteburg, "Infrared spectroscopic investigations of N₂ adsorbed to cold Rhodium Iron alloy cluster cations", 116. Bunsentagung, Kaiserslautern, 25.-27.05.2017, **awarded with PCCP Poster Prize**.

Matthias P. Klein, Amelie Ehrhard, Sebastian Dillinger, Jennifer Mohrbach, and Gereon Niedner-Schatteburg, "FT-ICR based characterization of cold Rhodium Iron alloy cations and their N₂ adducts", FT-MS Tagung, Kaiserslautern, 21.09.-22.09.2017.

Matthias P. Klein, Amelie Ehrhard, Sebastian Dillinger, Joachim. M. Hewer, Johannes Lang, Jennifer Mohrbach, and Gereon Niedner-Schatteburg, "Cryo spectroscopy on N₂ adducts of cold transition metal complexes and cluster cations", 3MET PhD Workshop, Heidelberg, 27.09.2017.

Matthias P. Klein, Amelie Ehrhard, Sebastian Dillinger, Jennifer Mohrbach, Annika Steiner, and Gereon Niedner-Schatteburg, "Cryo kinetics and IR spectroscopy of N₂ adsorbed to size selected Rhodium and Rhodium Iron alloy cluster cations" GRS: Molecular and Ionic Clusters, Barga, Italy, 24.-25.02.2018.

Matthias P. Klein, Amelie Ehrhard, Sebastian Dillinger, Jennifer Mohrbach, Annika Steiner, and Gereon Niedner-Schatteburg, "Cryo kinetics and IR spectroscopy of N₂ adsorbed to size selected Rhodium and Rhodium Iron alloy cluster cations" GRC: Molecular and Ionic Clusters, Barga, Italy, 25.02.-02.03.2018.

Matthias P. Klein, Amelie Ehrhard, Sebastian Dillinger, Jennifer Mohrbach, Annika Steiner, and Gereon Niedner-Schatteburg, "Cryo kinetics and IR spectroscopy of N₂ adsorbed to size selected Rhodium and Rhodium Iron alloy cluster cations", EFTMS Workshop, Freising, 23.04.-27.04.2018.

Matthias P. Klein, Amelie Ehrhard, Sebastian Dillinger, Jennifer Mohrbach, Annika Steiner, and Gereon Niedner-Schatteburg, "Cryo kinetics and IR spectroscopy of N₂ adsorbed to size selected Rhodium and Rhodium Iron alloy cluster cations", 117. Bunsentagung, Hannover, 10.05.-12.05.2018.

Matthias P. Klein, Amelie Ehrhard, Sebastian Dillinger, Jennifer Mohrbach, Annika Steiner, and Gereon Niedner-Schatteburg, "Cryo kinetics and IR spectroscopy of N₂ adsorbed to size selected Rhodium and Rhodium Iron alloy cluster cations", International Bunsen Discussion Meeting "Gas Phase Model Systems in Catalysis", Ulm, 17.06.-20.06.2018.

Matthias P. Klein, Amelie Ehrhard, Daniela V. Fries, Annika Steiner, Sebastian Dillinger, Jennifer Mohrbach, and Gereon Niedner-Schatteburg, "Cryo kinetics and IR spectroscopy of N₂ and H₂ adsorbed to size selected Rhodium and Tantalum clusters", DPG Frühjahrstagung, Rostock, 10.03.-15.03.2019.

Matthias P. Klein, Daniela V. Fries, Annika Steiner, Amelie Ehrhard, Sebastian Dillinger, Jennifer Mohrbach, and Gereon Niedner-Schatteburg, "Cryo kinetics and IR spectroscopy of N₂ and H₂ adsorbed to size selected Rhodium and Tantalum clusters", 118. Bunsentagung, Jena, 30.05.-01.06.2019.

Matthias P. Klein, Daniela V. Fries, Annika Steiner, and Gereon Niedner-Schatteburg, "Cryo kinetics and IR spectroscopy of N₂ and H₂ adsorbed to size selected Tantalum clusters", GRS: Clusters and Nanostructures, Les Diablerets, Switzerland, 15.06.-16.06.2019.

Matthias P. Klein, Daniela V. Fries, Annika Steiner, and Gereon Niedner-Schatteburg, "Cryo kinetics and IR spectroscopy of N₂ and H₂ adsorbed to size selected Tantalum clusters", GRC: Clusters and Nanostructures, Les Diablerets, Switzerland, 16.06.-21.06.2019.

Matthias P. Klein, Daniela V. Fries, Annika Steiner, Helmut Schwarz, and Gereon Niedner-Schatteburg, "Cryo kinetics and IR spectroscopy of N₂ adsorbed to size selected Tantalum clusters", 705. Heraeus Seminar: Frontiers in Size-Selected Cluster Research: Bridging the Gap, "Clustertreffen", 29.09.-04.10.2019.

I have presented these posters and contributed to 13 additional posters.

Danksagung

Ich danke Prof. Dr. Gereon Niedner-Schatteburg für die Möglichkeit, in seinem Arbeitskreis diese Promotionsarbeit anfertigen zu können. Ich bedanke mich insbesondere für die gute Zusammenarbeit und Betreuung, die eingeräumten Freiräume und die stete Diskussionsbereitschaft. Weiterhin bedanke ich mich für seine Ansprechbarkeit bei Problemen aller Art.

Ich danke PD Dr. Christoph Riehn für die Übernahme des Zweitgutachtens und Prof. Dr. Werner Thiel für die Übernahme des Vorsitzes der Promotionskommission.

Ich danke Prof. Dr. Markus Gerhards† für seine Bereitschaft, das Zweitgutachten zu übernehmen, unterhaltsame Gespräche und die Gewissheit nie alleine auf dem Flur zu sein.

Ich danke allen meinen Kollegen und Leidensgenossen für die Unterstützung in und außerhalb der Uni:

Ich danke der vorherigen Generation des AK GNS Matthias Tombers, Joachim Hewer, Johannes Lang, Dimitri Imanbaew, und Sebastian Kruppa, die mir den Einstieg in den Arbeitskreis erleichtert haben. Besonderer Dank gilt dabei Sebastian Dillinger, Jennifer Mohrbach für die Einarbeitung an Fritz und die Möglichkeit von Anfang an eigene fruchtbare Projekte zu bearbeiten.

Ich danke meinen Kollegen Annika Straßner, Björn Kwasigroch und Mike Lembach für die gute Zusammenarbeit und gegenseitige Unterstützung und Aufmunterung. Besonders danke ich Annika, die mich in den letzten Jahren als Kollegen an Fritz und als Büronachbarn ertragen hat.

Ich danke der nachfolgenden Generation, insbesondere Daniela Fries, Maximilian Huber, Maximilian Luczak und Christopher Wiehn für die Weiterführung der Projekte und ihre neuen Ideen und wünsche ihnen dabei ein glückliches Händchen und Durchhaltevermögen.

Ich danke Amelie Ehrhard für die gute und ergebnisreiche Zusammenarbeit während unser Diplomarbeiten und dafür, dass sie auch nach ihrer Kaiserslauterer Zeit den Fortschritt unserer gemeinsam begonnenen Rhodium- und Rhodium-Eisen-Projekte weiter aktiv begleitet hat.

Ich danke Thomas Kolling und Yevgeniy Nosenko für ihre geduldige und stete Hilfsbereitschaft bei Problemen aller Art.

Ich danke allen, die ich in ihrem Studium insbesondere bei Abschlussarbeiten, Forschungspraktika und Hiwi-Tätigkeiten (mit-)betreuen durfte: Heinrich Schneider, Jörg

Schild, Annika Straßner, Yannick Mees, Daniela Fries, Maximilian Huber, Christopher Wiehn, Anja Helbig, Sophie Thommes, Isabel Manes und Benedict Kirchner.

Ich danke unseren Sekretärinnen Hilde Seelos, Sybille Heieck, Petra Wetzels, Birgit Harrison-Weber und Bärbel Stemler für die Hilfe bei allen Verwaltungsangelegenheiten und auflockernde Gespräche abseits des täglichen Trubels.

Ich danke allen ehemaligen und aktuellen Mitarbeitern unseres Flurs im 5. Stock für die angenehme Atmosphäre und gegenseitige Hilfsbereitschaft.

Meiner „ESI-Kundschaft“ danke ich für die vielen interessanten Proben und auch die daraus entstandenen Veröffentlichungen.

Ich danke meinen Kommilitonen, insbesondere Andrea, Björn, Johannes, Marius, Dominique und Marko, für die schöne gemeinsame Zeit und die Ablenkung vom Uni-Alltag.

Zu guter Letzt danke ich meiner Familie, ohne deren beständige Unterstützung mein Weg so nicht möglich gewesen wäre.

Eidesstattliche Erklärung

Hiermit bestätige ich, Matthias Klein, dass die vorliegende Arbeit mit dem Titel „*Dinitrogen Adsorption and Activation on Pure and Alloy Metal Cluster Cations Studied by Cryo Adsorption Kinetics and Infrared Spectroscopy*“ gemäß der Promotionsordnung des Fachbereichs Chemie der Technischen Universität Kaiserslautern selbstständig und unter Verwendung der angegebenen Quellen und Hilfsmitteln angefertigt wurde.

Kaiserslautern, den

Matthias Klein